frontiers | Research Topics

Gas-water-rock interaction and multi physical field coupling mechanism

Edited by
Leilei Si, Yong Liu, Guangyao Si, Jian Zhang and Hongtu Zhang

Published in
Frontiers in Earth Science

ISSN 1664-8714
ISBN 978-2-8325-2329-2
DOI 10.3389/978-2-8325-2329-2

About Frontiers

Frontiers is more than just an open access publisher of scholarly articles: it is a pioneering approach to the world of academia, radically improving the way scholarly research is managed. The grand vision of Frontiers is a world where all people have an equal opportunity to seek, share and generate knowledge. Frontiers provides immediate and permanent online open access to all its publications, but this alone is not enough to realize our grand goals.

Frontiers journal series

The Frontiers journal series is a multi-tier and interdisciplinary set of open-access, online journals, promising a paradigm shift from the current review, selection and dissemination processes in academic publishing. All Frontiers journals are driven by researchers for researchers; therefore, they constitute a service to the scholarly community. At the same time, the *Frontiers journal series* operates on a revolutionary invention, the tiered publishing system, initially addressing specific communities of scholars, and gradually climbing up to broader public understanding, thus serving the interests of the lay society, too.

Dedication to quality

Each Frontiers article is a landmark of the highest quality, thanks to genuinely collaborative interactions between authors and review editors, who include some of the world's best academicians. Research must be certified by peers before entering a stream of knowledge that may eventually reach the public - and shape society; therefore, Frontiers only applies the most rigorous and unbiased reviews. Frontiers revolutionizes research publishing by freely delivering the most outstanding research, evaluated with no bias from both the academic and social point of view. By applying the most advanced information technologies, Frontiers is catapulting scholarly publishing into a new generation.

What are Frontiers Research Topics?

Frontiers Research Topics are very popular trademarks of the *Frontiers journals series*: they are collections of at least ten articles, all centered on a particular subject. With their unique mix of varied contributions from Original Research to Review Articles, Frontiers Research Topics unify the most influential researchers, the latest key findings and historical advances in a hot research area.

Find out more on how to host your own Frontiers Research Topic or contribute to one as an author by contacting the Frontiers editorial office: frontiersin.org/about/contact

Gas-water-rock interaction and multi physical field coupling mechanism

Topic editors
Leilei Si — Henan Polytechnic University, China
Yong Liu — Henan Polytechnic University, China
Guangyao Si — University of New South Wales, Australia
Jian Zhang — Henan Polytechnic University, China
Hongtu Zhang — Henan Polytechnic University, China

Citation
Si, L., Liu, Y., Si, G., Zhang, J., Zhang, H., eds. (2023). *Gas-water-rock interaction and multi physical field coupling mechanism*. Lausanne: Frontiers Media SA.
doi: 10.3389/978-2-8325-2329-2

Table of contents

05 Instability and failure characteristics of surrounding rock of water drenching roadway in thick coal seam
Ce Jia, Sheng Li, Chaojun Fan, Mingkun Luo, Zhenhua Yang, Lei Yang and Ziang Pu

17 Numerical simulation on spatial steering rule of directional perforation hydraulic fractures in low-permeability reservoir
Weiyong Lu, Erhu Bai, Le Wei, Changchun He, Yaohui Sun and Lei Shi

31 On the acoustic attenuation characteristics of sonar detection in the salt-cavern gas storage environment
Haiyan Yang, Yu Wang, Yao Dai, Junfu Zhang and Gang Chen

40 Influence radius of pressure relief of energy-accumulating blasting and water injection in the heading face of the liangbei coal mine
Zhenfeng Wang, Yu Wang and Feng Wang

54 Study on the test of coal mass fracture grouting sealing with coal-based materials and its application
Yingjun Gao, Banghua Yao, Hongtu Zhang, Boyang Zhang, Jinhu Song, Qian Wang, Jinming Niu and Jinhua Li

66 Effects of surface roughness on wettability and surface energy of coal
Jian Zhang, Bo Xu, Pengyan Zhang, Maolin Cai and Bo Li

76 Methane emission characteristics and model of CBM wells
Qingxiang Dong, Shengwei Wang, Jinkui Ma, Shuaifeng Lyu and Weiyong Lu

87 Study on the dynamic response and the hazard of rock burst under the influence of fault slip
Peng Kong, Rong Liu, Luyi Xing, Zhihong Li, Chuanwei Xu and Zhongteng Zhang

103 Accumulation and evolution of ice jams influenced by different ice discharge: An experimental analysis
Pangpang Chen, Tiejie Cheng, Jun Wang and Guangxue Cao

113 Studies of natural gas production prediction and risk assessment for tight gas in Sichuan Basin
Haitao Li, Guo Yu, Yizhu Fang, Yu Chen and Dongming Zhang

128 Experimental study on mechanical properties of single fracture-hole red sandstone
Ning Jiang, Ke Lv, Zhiyou Gao, Chuanbao Jia, Lei Ye, Shuyu Meng and Quanbao Su

143 A comprehensive insight into the effects of acidification on varied-sized pores in different rank coals
Peiwen Jiang, Chengtao Yang, Feng Chen, Bing Li, Jiangang Ren, Jianbao Liu and Zhimin Song

159 **Study on stability of underlying room and pillar old goaf in close coal seam and mining of the upper coal seam**
Hongtao Liu, Cheng Hao, Zhiwen Wang, Chong Li, Linfeng Guo, Jialu Liang and Haozhu Wang

173 **Prediction method of shield tunneling parameters in pebble stratum formed by weathered granite and quartzite**
Meiyan Wang, Dajun Zhao, Yan Lv, Wei Wang and Xing Wang

186 **The invasion law of drilling fluid along bedding fractures of shale**
Hong Li, Qing Wang, Kun Zhang, Qing Hui Zhang, Tao Song, Chuang Zhang, Lu Bin Zhuo, Chen Hao, Fu Ping Feng, He Yuan Wang and Yin Quan Zhang

201 **Experiment research and mechanism analysis on rheological properties of tailings slurry**
Zhiliu Wang, Linlin Chen and Mengxin Hu

frontiers | Frontiers in Earth Science

TYPE Original Research
PUBLISHED 13 September 2022
DOI 10.3389/feart.2022.1013715

Instability and failure characteristics of surrounding rock of water drenching roadway in thick coal seam

Ce Jia[1], Sheng Li[1]*, Chaojun Fan[1], Mingkun Luo[2], Zhenhua Yang[1], Lei Yang[1] and Ziang Pu[1]

[1]College of Mining, Liaoning Technical University, Fuxin, China, [2]Institute of Science and Technology, Shanxi Lu'an Chemical (Group) Co., Ltd., Changzhi, China

EDITED BY
Hongtu Zhang,
Henan Polytechnic University, China

REVIEWED BY
Lianpeng Dai,
Liaoning University, China
Bo Zhao,
Taiyuan University of Technology, China
Gan Feng,
Sichuan University, China

*CORRESPONDENCE
Sheng Li,
13941811946@139.com

SPECIALTY SECTION
This article was submitted to Economic Geology,
a section of the journal
Frontiers in Earth Science

RECEIVED 07 August 2022
ACCEPTED 25 August 2022
PUBLISHED 13 September 2022

CITATION
Jia C, Li S, Fan C, Luo M, Yang Z, Yang L and Pu Z (2022), Instability and failure characteristics of surrounding rock of water drenching roadway in thick coal seam.
Front. Earth Sci. 10:1013715.
doi: 10.3389/feart.2022.1013715

Aiming at the water drenching problem in the roof of transport roadway 2,606 of the Zhangcun coal mine, the instability and failure law of the drenching roadway was studied by borehole peephole, soaking water softening test and numerical simulation in this study. It is found that the relation between compressive strength, elastic modulus, tensile strength and moisture content is a negative exponential function. Subsequently, the Fish language was used to embed the functional relationship between mechanical parameters of surrounding rock in the roadway and moisture content into Flac^{3D} software to simulate the failure law of surrounding rock under different moisture contents. The influence of moisture content on the surrounding rock is ordered as roof > two sides > floor. Through the comparison between borehole peeping and plastic zone, the roof water content is obtained by inversion. The results provide a reference basis for the selection of the surrounding rock support method for drenching roadway in thick coal seam.

KEYWORDS

water drenching roadway, water-rock coupling, surrounding rock deformation, particle flow, borehole peephole

Introduction

China has a wide distribution of coal resources, and is the largest coal producer in the world (Xie et al., 2018; Fan et al., 2020). Nearly 76.3% of coal resources are buried above 600 m, and 59.5% are buried above 1,000 m (Su et al., 2021; Wang et al., 2022). Due to the increase in mining intensity, the depth of coal mining in China is increasing with a growth rate of 8–12 m per year (Fan et al., 2022a). With the increase of mining depth, geological anomalies, roof permeability, and other problems have been encountered during the mining process (Yang et al., 2017a; Chen et al., 2021; Dou et al., 2021). To effectively control the roadway surrounding rock, deformation characteristics and the mechanism of the roadway surrounding rock under the influence of water drenching and the control of roadway stability under the condition of water drenching roof have been widely concerned at present

(Gao et al., 2021; Zhao et al., 2022). The roadway surrounding rock under drenching conditions shows prominent soft rock characteristics. Therefore, the large deformation of roadway surrounding rock is difficult to control, which seriously hinders coal mines' high-yield and high-efficiency production (Zhu et al., 2022a; Fan et al., 2022b).

Recently, Li and He (He, 2014; Li et al., 2016; Fan et al., 2021) proposed that the deformation of the surrounding rock is caused by various factors such as soft features, poor support, high ground stress, groundwater, and geological formations. The research on the surrounding rock control technology of water drenching and soft rock roadways is mainly carried out through numerical simulation, industrial tests, and laboratory tests (Zhang et al., 2016; Tao et al., 2020; Zhai et al., 2022). Yang (Yang et al., 2017b) revealed the damage mechanism of soft rock roadways under high stress, long-term water immersion conditions by numerical simulation and field industrial tests. Through scanning electron microscopy, Yu (Yu et al., 2021) obtained that the weakly cemented siltstone is composed of coarse-grained minerals with highly developed pores, revealing the instability of the soft rock roadway. Ma (Ma et al., 2021) conducted indoor experimental tests on red shale to obtain mineral composition and microstructure, anisotropy, hydraulic properties, and other mechanical parameters to reveal its deformation and damage characteristics. Besides, the damage law of the red shale soft rock roadway was obtained by the FLac^{3D} software. Wen (Wen et al., 2021) investigated the support method for large section soft rock roadway and obtained the displacement, plastic zone, and stress field distribution law of the surrounding rock by numerical simulation. By using the numerical simulation inversion, Chen (Chen et al., 2020) reported that as the moisture content increases, the failure zone further extends to the deep surrounding rock, leading to increased stress relaxation around the roadway, especially in the roof. Wei (Zhu et al., 2022b) proposed a new concept of internal and external self-bearing structures for the surrounding rock and determined the shape of the internal and external bearing structures based on the results of field monitoring. Through indoor tests, numerical calculations, and field tests, Li (Li et al., 2015) analyzed the composition and microstructure of mudstone and obtained the hydration law of mudstone and its characteristics of strength weakening as well as the deformation and damage characteristics of surrounding rock under the action of the hydration. Zheng (Zheng et al., 2021) studied the effects of different factors on the stability of soft rock roadways based on numerical simulation techniques. It was found that high ground stress, rock fragmentation, and poor lithology are the factors that lead to the instability of the roadway; besides, physical and mechanical properties of the surrounding rock and the bearing capacity of the surrounding rock layer can be promoted to maintain the stability of the roadway with broken soft rock. Chen (Chen et al., 2018) analyzed the mineral composition of the surrounding rock by X-ray diffraction. The results showed that the surrounding rock contains clay minerals that tend to expand upon water contact, leading to instability and damage of the surrounding rock of the roadway. Bai (Bai and Tu, 2016) analyzed the failure of large span long-wall roadways under water-rich roofs by field observation and numerical simulation, and found that large span excavation induces rock fracture to form seepage pathways. The water drenching not only weakens the rock mass but also reduces the bond between the surrounding rock and the anchor rods, resulting in the failure of the anchor rods and anchor cables.

In this study, the instability and damage law of the water drenching roadway was studied by drilling peephole, soaking water softening experiment, and numerical simulation to provide guidance for surrounding rock control of 2,606 transport roadway in Zhangcun coal Mine.

Research background

Zhangcun coal mine is located in Changzhi City, Shanxi Province. No.3 coal seam in the lower part of Shanxi Formation of Permian was exploited in working face 2,606. This coal seam has a stable occurrence, a small variation in coal thickness, and a simple coal seam structure. The buried depth of the coal seam is about 537 m, the thickness of the coal seam is 5.33–6.19 m, and the average thickness is 5.86 m. The original gas content during the tunneling of the transport roadway 2,606 was 8.5–10.0 m^3/t and the temperature was 15–17°C. Transport roadway 2,606 was located in the north of belt road 26, 300 m east from transport roadway 2,605. For transport roadway 2,606, the bottom of the coal seam was designed to be excavated, leaving 1.5–2 m thick top coal. The layout of the roadway and the design section of transport roadway 2,606 was 5.8m×4 m (length × width), as shown in Figure 1A. The direct top of No.3 coal seam roof was mudstone with a thickness of 2.49 m, and the old top above the direct top was medium and fine-grained sandstone, with a thickness of about 7.83 m. The direct bottom was mudstone, with a thickness of 2.83 m, and the old bottom was gray-white fine-grained sandstone, with a thickness of 5.04 m, as shown in Figure 1B.

According to the hydrogeological conditions of the mine, the No. VII water-bearing layer was 2.49 m below the No. 3 coal seam. The thickness of this water-bearing layer was 7.83 m, and its lithology was gray-white medium and fine-grained sandstone. During the excavation process, the roof water drenching occurred in transport roadway 2,606, and the water seeping down at the anchor pallet was collected through the drencher into the drainage tank. The roof water drenching led to the softening of the coal rock body, severe deformation of the roadway roof, and the corrosion of anchor rods and anchor cable pallets, as shown in Figure 2.

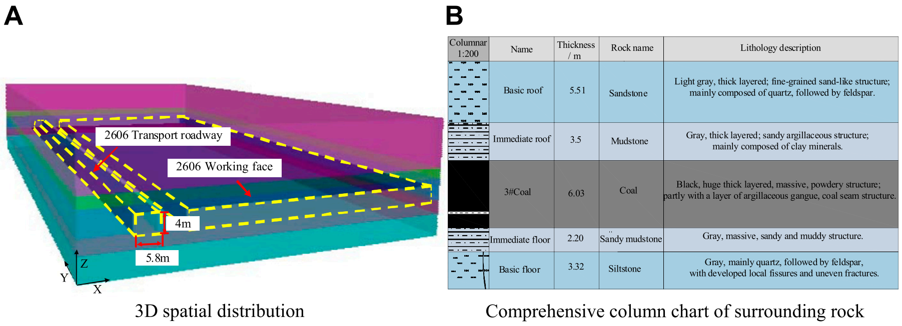

3D spatial distribution

Columnar 1:200	Name	Thickness / m	Rock name	Lithology description
	Basic roof	5.51	Sandstone	Light gray, thick layered; fine-grained sand-like structure; mainly composed of quartz, followed by feldspar.
	Immediate roof	3.5	Mudstone	Gray, thick layered; sandy argillaceous structure; mainly composed of clay minerals.
	3#Coal	6.03	Coal	Black, huge thick layered, massive, powdery structure; partly with a layer of argillaceous gangue, coal seam structure.
	Immediate floor	2.20	Sandy mudstone	Gray, massive, sandy and muddy structure.
	Basic floor	3.32	Siltstone	Gray, mainly quartz, followed by feldspar, with developed local fissures and uneven fractures.

Comprehensive column chart of surrounding rock

FIGURE 1
Geological overview of transport roadway 2,606. **(A)** 3D spatial distribution. **(B)** Comprehensive column chart of surrounding rock.

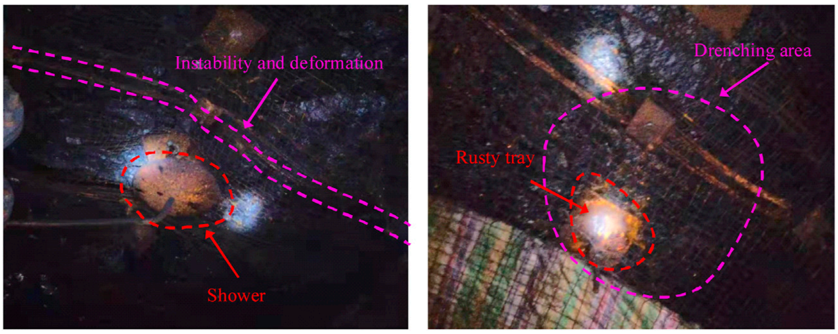

FIGURE 2
Roof drenching and damage pictures on-site.

Macroscopic evolution law of mudstone under the action of water-mechanical coupling

When mudstone encounters water, it will expand, argillite, disintegrate, and break, resulting in the softening of mudstone (Liu et al., 2020). The softening effect of water on rock is by affecting the microstructure of rock, resulting in the reduction of macroscopic mechanical properties. Therefore, the PFC^{2D} software was used to explore the mechanical properties and fracture evolution laws of mudstone under different water contents. PFC^{2D} software was used to build a cuboid sample with a model size of 100mm × 50 mm (length × width). The cuboid sample was composed of round particles. Due to the non-uniform characteristics of rock materials, the rock particle radius is randomly generated between 0.3 and 0.75 mm (Yang et al., 2019), and finally, the particles are continuously vibrated within the specified range to reach a balanced state. Uniaxial Compression and Tensile Testing of Rocks by Loading Walls, as shown in Figure 3.

Mudstone belongs to argillaceous cemented rock. To better reflect the mechanical properties of rock materials, the parallel cementation model (PBM) is used to simulate the rock laboratory test. According to the PFC micromechanical parameters analysis method introduced by U. Castro-Filgueira (Castro-Filgueira et al., 2017), a large number of trial calculations were carried out to determine the initial parameters of the model micromechanical parameters, as shown in Table 1. According to the literature (Zhao et al., 2021), it can be known that the water content influences the normal, tangential bond strength and bond strength ratio parameters of the rock. Combined with the data in the literature (He, 2021; Jing et al., 2021; Liu et al., 2021), the functions of rock normal, tangential bond strength, bond strength ratio, and water content are obtained.

$$\begin{cases} \sigma_c = 32\exp\left(-w/0.41\right) + 1.4 \\ \tau_c = 59\exp\left(-w/0.34\right) + 1.46 \\ k_c = -13.5\exp\left(-w/0.37\right) + 3.7 \end{cases} \tag{1}$$

Where: σ_c is the normal bond strength, MPa; τ_c is the tangential bond strength, MPa; k_c is the bond strength ratio; w is the moisture content, %.

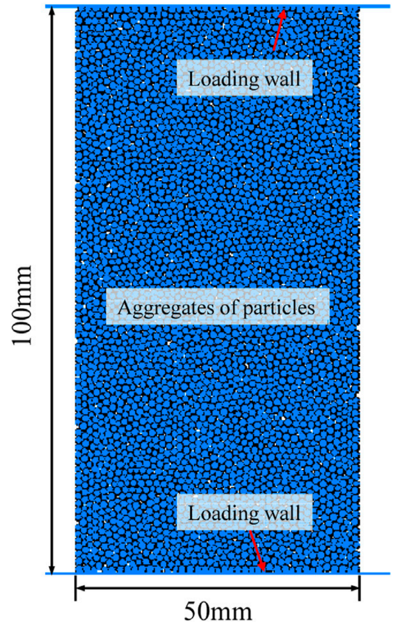

FIGURE 3
Generation of balls and walls.

Evolution law of mechanical properties of mudstone with different water content

Figure 4 shows the evolution law of mudstone mechanical properties under different water contents. In Figure 4A, the evolution law of compressive strength of mudstone under different water content. With the increase in water content, the compressive strength decreased from 20.2 to 3.3 MPa, and the compressive strength decreased by 84%. In Figure 4B, the law of tensile strength enhancement of mudstone under different water content. With the increase in water content, the tensile strength decreased from 5.7 to 1.02 MPa, and the compressive strength decreased by 82.1%. According to the data fitting in Figure 4, the elastic modulus, shear modulus, and tensile strength of rock under different water contents are obtained. The functional relationship is as follows:

$$\begin{cases} y_1 = 3.7251e^{-1.0w} + 0.82509 \\ y_2 = 15.7090e^{-1.045w} + 9.0847 \\ y_3 = -3.69386e^{-0.23106w} + 10.3261 \end{cases} \tag{2}$$

where y_1, y_2, and y_3 are shear modulus, bulk modulus, and tensile strength, Mpa; w is the moisture content, %.

TABLE 1 Model meso-initial parameters.

Meso parameters	Symbol	Numerical value
Minimum particle radius/m	$R_{\min}$	0.5e-3
Maximum to minimum particle radius ratio	$R_{\max}/R_{\min}$	1.5
Particle density/kg/m^3	ρ	2,500
Porosity/%	n	0.1
Damping coefficient	ζ	0.7
Particle normal to tangential contact stiffness ratio	K_n/k_s	2.5
Particle Elastic Modulus/GPa	$\bar{E}_c$	3
Parallel Bond Radius Coefficient	$\bar{\lambda}$	1.0
Friction coefficient	μ	0.9

TABLE 2 Physical and mechanical parameters of coal and rock.

Name	Density g/cm^3	Bulk modulus /GPa	Shear modulus /GPa	Cohesion /MPa	Internal friction angle/°	Tensile strength /MPa
Basic roof	2,873	1.84	0.80	2.3	28	2.0
Immediate roof	2,487	y_1	y_2	1.9	30	y_3
3#coal	1,400	1.66	0.85	2.1	32	1.28
Immediate floor	2,483	1.84	0.80	2.3	28	2.0
Basic floor	2,460	1.79	0.97	1.9	30	1.6

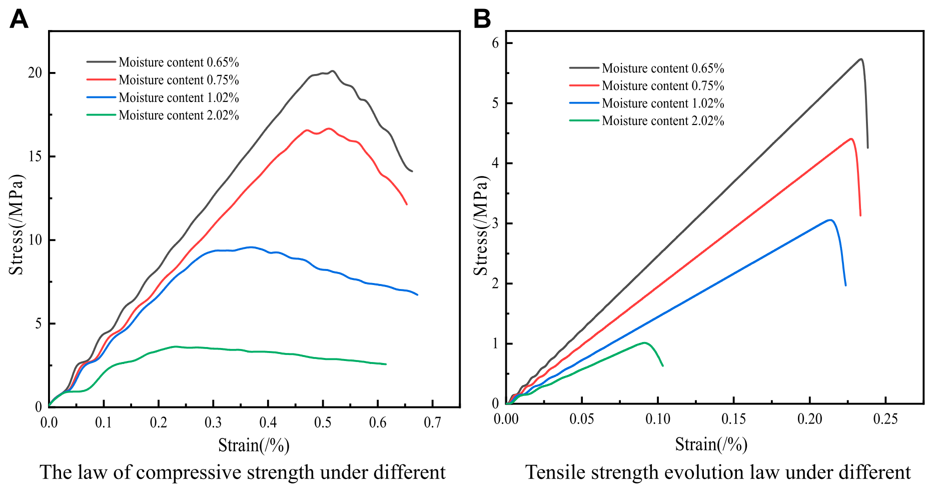

FIGURE 4
Evolution law of mudstone mechanical properties under different water content. **(A)** The law of compressive strength under different moisture content. **(B)** Tensile strength evolution law under different moisture content.

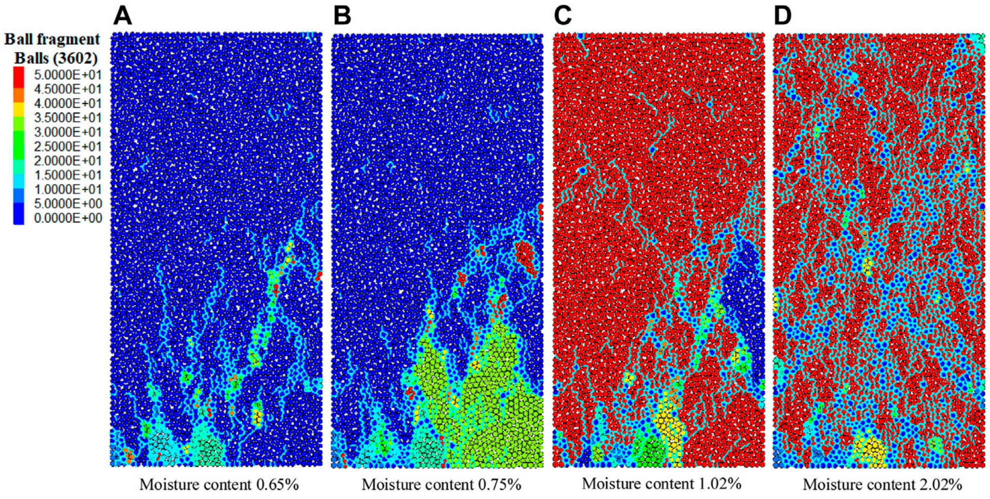

FIGURE 5
Evolution law of rock compression cracks. **(A)** Moisture content 0.65% **(B)** Moisture content 0.75% **(C)** Moisture content 1.02% **(D)** Moisture content 2.02%

Evolution law of mudstone fissures under different water contents

Figure 5 shows the crack evolution law of rock under compression under different water contents. In Figure 5A, when the water content of mudstone is 0.65%, the bottom of the sample cracks, and the cracks are mainly concentrated in the lower part of the sample. In Figure 5B, when the moisture content increases to 0.75%, the cracks extend from bottom to top, the number of cracks increases, and the lower-left sample breaks. In Figure 5C, when the moisture content increased to 1.02%, the entire sample was damaged, and the crack penetrated the middle and upper part of the sample. In Figure 5D, when the moisture content is 2.02%, the entire sample is broken, and the crack penetrates the entire sample. In summary, with the increase of water content, the number of crack penetrations increases, providing channels for the movement of water molecules, resulting in crack expansion and rock softening.

Figure 6 shows the crack evolution law of rock under tension under different water contents. In Figure 6A, when the moisture

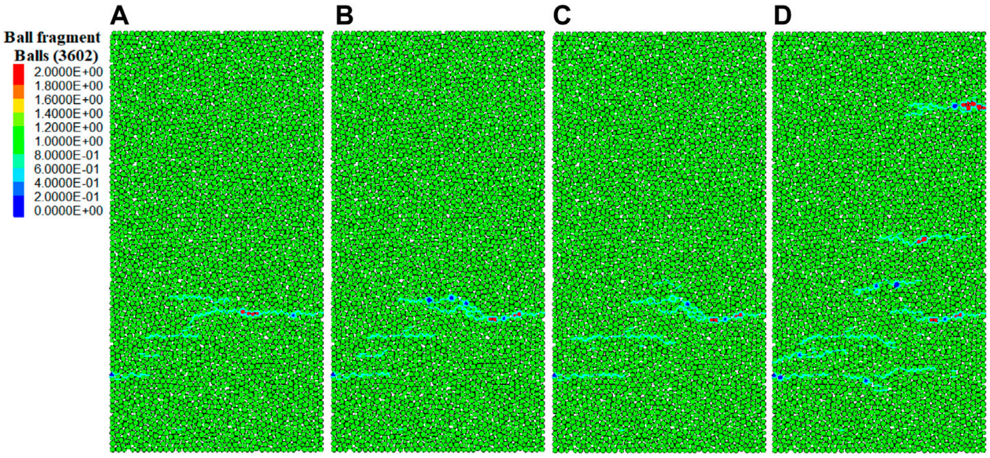

Moisture content 0.65% Moisture content 0.75% Moisture content 1.02% Moisture content 2.02%

FIGURE 6
Evolution law of tensile cracks in rock. Please add a legend **(A)** Moisture content 0.65% **(B)** Moisture content 0.75% **(C)** Moisture content 1.02% **(D)** Moisture content 2.02%

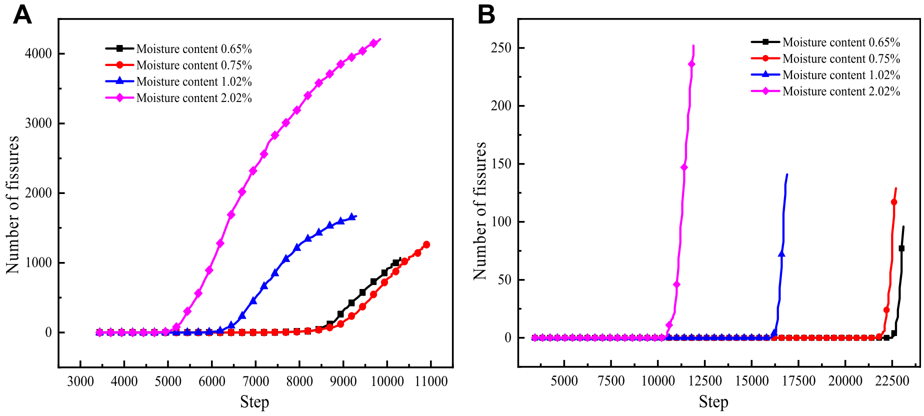

Compression test crack monitoring evolution law Tensile test crack monitoring evolution law

FIGURE 7
Evolution law of crack monitoring. **(A)** Compression test crack monitoring evolution law. **(B)** Tensile test crack monitoring evolution law.

content is 0.65%, the tensile failure of the sample occurs in the lower part. In Figure 6B, when the moisture content is 0.75%, tensile failure occurs in the lower part of the sample, and the crack expansion length increases. In Figure 6C, when the moisture content is 1.02%, tensile failure occurs in the lower part of the sample, mainly showing three macroscopic cracks. In Figure 6D, when the moisture content is 2.02%, the overall tensile failure of the sample occurs. In summary, with the increase of water content, the internal cementation of the rock decreases, the bonding force between the rock molecules decreases, and the tensile strength of the surrounding rock deteriorate.

Figure 7 shows the evolution law of crack monitoring of mudstone under uniaxial compression and tensile tests. In Figure 7A, when the mudstone with a moisture content of 2.02% is subjected to a uniaxial compression test under the same conditions, cracks are generated first and the number of cracks is the largest. Figure 7B shows the evolution law of crack monitoring in the mudstone tensile test under different water contents. The time of crack appearance from early to late is moisture content 2.02%> moisture content 1.02%> moisture content 0.75%> moisture content 0.65%. The maximum number of cracks in the sample with a moisture content of

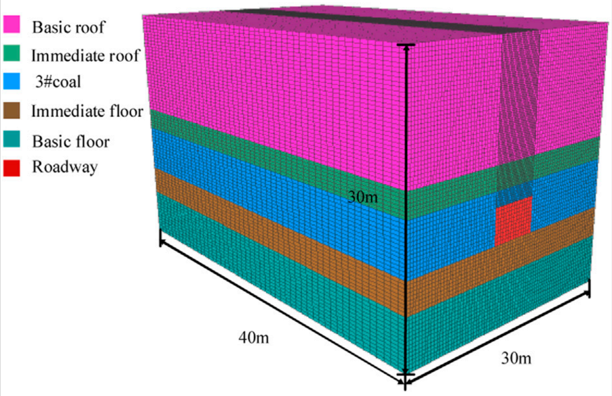

FIGURE 8
3D model meshing.

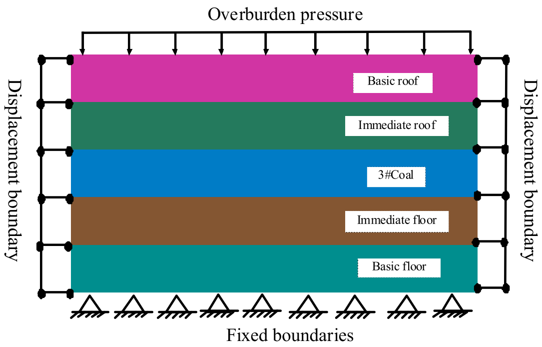

FIGURE 9
Static calculation model.

2.02% is 252, and the minimum number of cracks in the sample with a moisture content of 0.65% is 96. To sum up, as the water content increases, the earlier the mudstone is damaged, the more cracks and the greater the softening degree.

Failure and evolution law of roadway surrounding rock under different moisture content

According to the geological situation of the Zhangcun coal mine, transport roadway 2,606 was selected as the research object. The FLAC^{3D} software was used to establish the computational model, and the effect of moisture content on the unstable deformation of the roadway was analyzed by using the coupling of large deformation and hydrostatic modules. It should be noted that pores and joint fissures of various morphologies in the natural coal rock structure were not considered (Wang et al., 2021). The model was assumed to be isotropic and the Moore Coulomb criterion was used in the simulation (Jia et al., 2021). The physical and mechanical parameters of the surrounding rock were fitted into the moisture content relationship curve as exponential functions of y_1~y_3. The model was assigned by compiling the function in the FISH language. Table 2 shows the specific parameters of the model. The size of the model is 30 m × 40 m × 30 m (length × width × height), as shown in Figure 8. The roadway is excavated along the No.3 coal floor, with a rectangular section and a size of 5.8m × 4 m (width × height). Figure 9 shows the overall model. In the static calculation, the left and right boundaries of the model are constrained by horizontal hinges, the bottom boundary is fixed and constrained, and the upper boundary is free and bears the uniform load acting on the boundary by the overburden.

Evolution law of displacement field of roadway surrounding rock

Figure 10 illustrates the effect of different moisture contents on the displacement change of roof, floor and two sides of the roadway. Monitoring points were arranged at the roof and floor of the roadway and in the middle of the two sides to monitor the displacement of the surrounding rock. Figure 10A shows the failure deformation of surrounding rock and roof subsidence caused by initial rock stress field failure at the initial stage of roadway excavation. With the continuous increase of the moisture content, the vertical displacement and subsidence of the roof also increase. Before the time step of 18,000 step, the roof subsidence changes drastically, and the subsidence amount tends to be stable from 18,000 step to 22,000 step, reaching a new equilibrium state. The increase in moisture content leads to the softening of the top coal, and the top coal is more likely to be broken and deformed. Figure 10B shows that the bottom heave phenomenon occurs in the floor, and the moisture content has little effect on the bottom heave of the roadway floor. Figure 10C shows the relationship between the left side of the roadway and the moisture content. As the moisture content increases, the horizontal displacement of the left side increases. When the moisture content increases from 0.67 to 2.02%, the maximum displacement of the left side deformation increases from 19.47 to 53.75 mm, increasing by 67.49%. Figure 10D shows the relationship between the right side of the roadway and the moisture content. With the excavation of the roadway, the horizontal displacement of the right side occurs, which increases rapidly at first and then gradually changes steadily. With the increase of moisture content, the maximum horizontal displacement of the right side also increases, and the maximum value reaches 53.45 mm. The above analysis shows that water drenching has a serious impact on the displacement of the roof and has the least impact on the floor. According to the analysis of on-site drilling exploration data, it can be found that No. VII on the

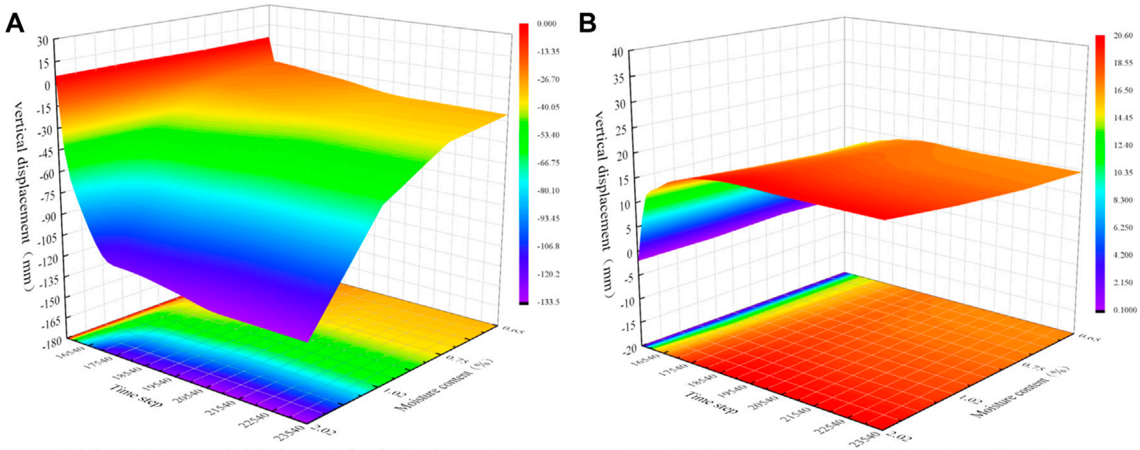

Relationship between vertical displacement of roof and moisture content

The relationship between the displacement of the bottom floor and the moisture content

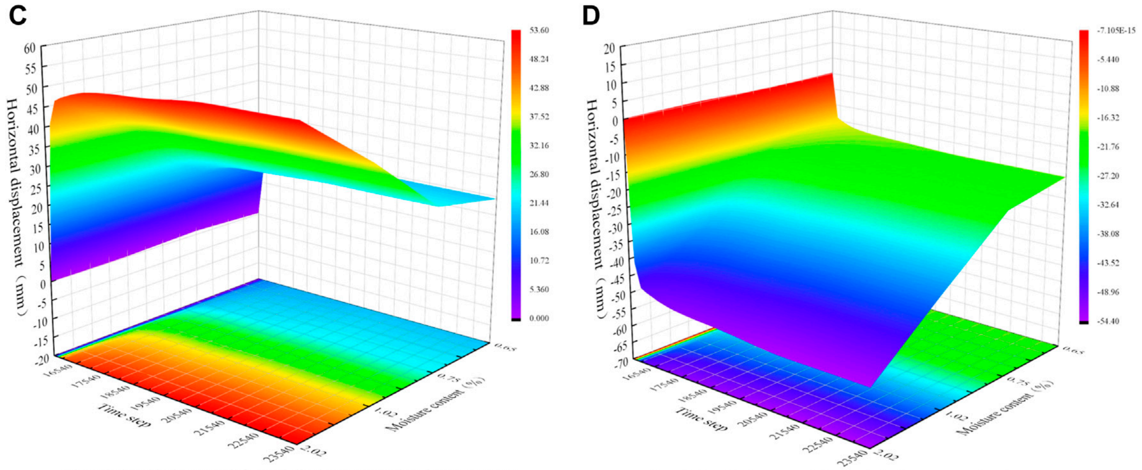

The relationship between left-hand displacement and moisture content

The relationship between right-hand displacement and moisture content

FIGURE 10
Relationship between deformation of surrounding rock and water content of roadway. **(A)** The relationship between vertical displacement of roof and moisture content **(B)** The relationship between vertical displacement of floor and moisture content **(C)** The relationship between horizontal displacement of left side and moisture content **(D)** The relationship between horizontal displacement of right side and moisture content

roof of the No. 3 coal seam is an aquifer that has a great influence on the roof, which is in line with the actual situation on site.

In Figure 11, exponential fitting is performed between the displacement of the roof, floor and two sides and the water content, and four exponential equations are obtained as y_1-y_4. The exponential relationship between roof displacement and water content is represented by equation y_1, and $R^2=0.99$ has a significant fitting effect. The exponential relationship between the displacement of the right side and the water content is represented by the equation y_2, and the fitting effect of $R^2=0.98$ is significant. The exponential relationship between the displacement of the left side and the water content is represented by the equation y_3, and the fitting effect of $R^2=0.98$ is significant. The exponential relationship between the displacement of the bottom plate and the water content is represented by the equation y_4, and the fitting effect of $R^2=0.99$ is significant. To sum up, the relationship between surrounding rock deformation and water content can be significantly described by exponential equation, which provides a reference for water drenching roadway support.

Evolution law of plastic zone of roadway surrounding rock

Figure 12 shows the failure evolution law of the plastic zone of the surrounding rock of the roadway under different moisture contents. The grid in the model is divided into 0.2 m. According to Figure 12A, the plastic zone failure range is 1.8 m away from the roof, and tensile failure occurs

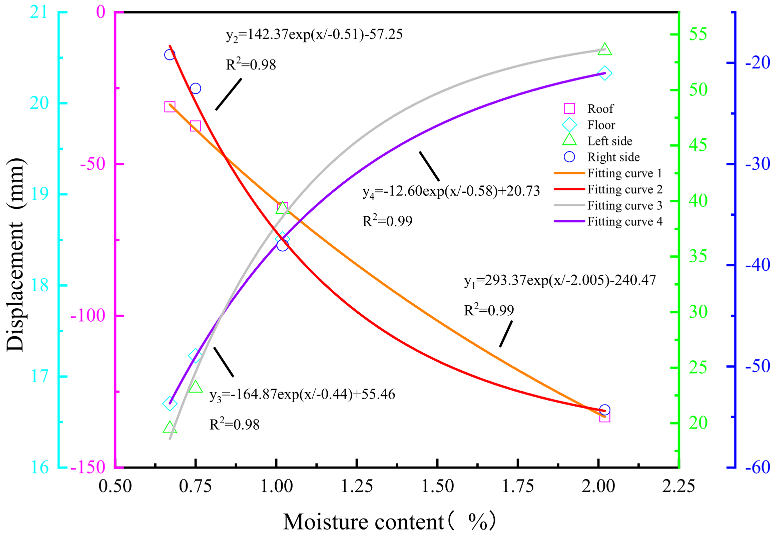

FIGURE 11
Prediction of surrounding rock displacement under different moisture contents.

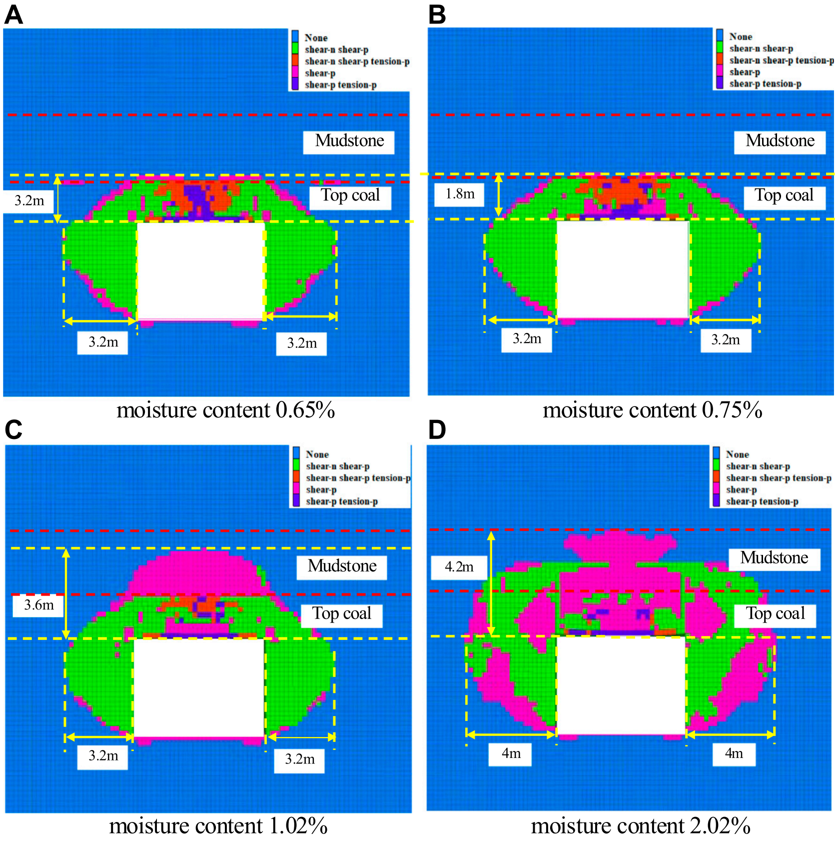

FIGURE 12
Evolution law of surrounding rock plastic zone under different water content. **(A)** Moisture content 0.65% **(B)** Moisture content 0.75% **(C)** Moisture content 1.02% **(D)** Moisture content 2.02%.

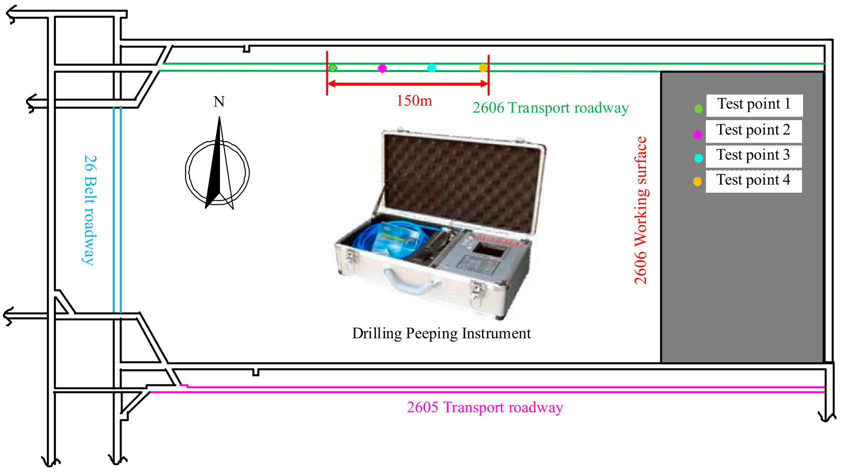

FIGURE 13
Location of roadway and test points for experimental tests.

at the coal-rock interface. As shown in Figures 12A,B, there are the same plastic zone failure ranges, but a large amount of tensile failure occurs at the coal-rock interface, and the top coal failure is more serious. The roofs in Figure 12A and Figure 12B will appear integral separation phenomenon. In this case, the supporting density of anchor cables should be increased, and the pre-tightening force should be increased. As shown in Figure 12C, the failure range of the plastic zone extends to 3.6 m from the roof. At this time, all the top coal is destroyed, and a large amount of mudstone is destroyed. The pores in the coal continuously absorb water, the strength of mechanical characteristics decreases, the lithological strength of mudstone is relatively soft, leading to the serious damage. It can be seen from Figure 12D that the failure range of the plastic zone extends to 4.2 m from the roof. The mudstone above the roof is completely destroyed, and a large number of shear failures occur. The bending failure occurs in the roof of Figure 12C and Figure 12D. At this point, the bolt should be passed through multiple separation positions and anchored deep into the stable rock formation. It can be seen from Figures 12A–D that the water drenching has a serious impact on the damage of the roadway roof, and there is no obvious change in the plastic zone of the two sides and the floor. At the coal-rock interface, tensile failure occurs, and coal-rock separation occurs. During the excavation process, due to the continuous infiltration of groundwater into the roof, the pores of the coal and rock mass themselves continuously absorb water, and the moisture content increases. As a result, the strength of the roof is reduced, and the weakening of the supporting capacity of the anchor rod and anchor cable is caused. The failure depth above the roof of the plastic zone increases, and the water drenching roadway has the most serious impact on the roof.

Field experiment of water−drenching roadway

In Zhangcun coal mine, the experimental test is located at 150 m of roadway, and 4 test points are arranged with the interval of 50 m. The borehole peeping instrument was used to conduct on-site experiments, as shown in the Figure 13.

Drilling peep in 2,606 roadway roof

The roof drilling detector was used for borehole peeping on the roof of four test points. The hole depth of each borehole is 9.6 m and the hole diameter is 30 mm, which is completely perpendicular to the roof. Figure 14 shows the drilling image of the roof fracture development. Figures 14A,B is the drilling peep results of test points1-4. As shown in Figure 14A, when the drilling depth is 0.8m and 1.1–1.3 m, there are slight local fissures, and the lithology is sandy mudstone with soft hardness, and the color of the returned water is grayish black. According to the above plastic zone distribution, the roof plastic zone failure is less than 1.8 m, and the moisture content is less than 0.65%. In Figure 14B, there is a slight fissure at the drilling depth of 2.4 m, and the lithology is sandstone with high hardness, and the color of the returned water is grayish-white. According to the above distribution law of plastic zone, the failure range of roof plastic zone is 1.8–3.6 m, and the moisture content is 0.65–1.02%. As shown in Figure 14C, when the drilling depth is 3–4.0 m, the lithology is mudstone, hard-soft rock. The hole wall is rough, pitted, and uneven, and the color of the returned water is black. According to the above distribution of plastic zone, the moisture content is less than 2.02%. In Figure 14D, at the

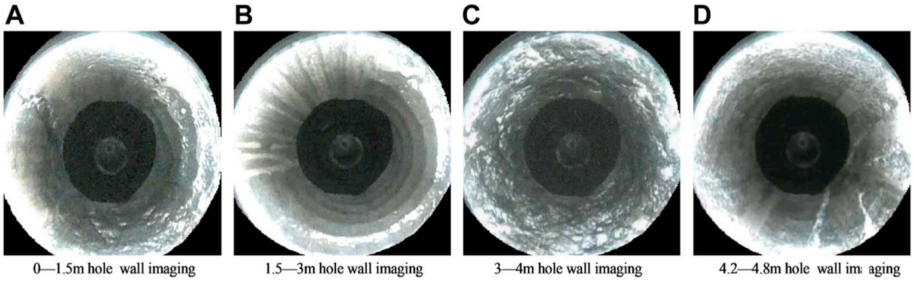

FIGURE 14
Fracture development in the roof detected by drilling image. **(A)** 0–1.5 m hole wall imaging **(B)** 1.5–3 m hole wall imaging **(C)** 3–4 m hole wall imaging **(D)** 4.2–4.8 m hole wall imaging.

drilling depth of 4.2–4.8 m, there is local breakage with slight fissures, the lithology is muddy sandstone with hard hardness, and the color of the returned water is gray and black. According to the above distribution law of plastic zone, the moisture content is greater than 2.02%.

Conclusion

1) There is a negative exponential relationship between water content and compressive strength, elastic modulus and tensile strength of coal. The instability failure law of the surrounding rocks of the roadway with different moisture contents is obtained. The influence of moisture content on the surrounding rock can be ordered as roof > two sides > floor.
2) The exponential equations of the moisture content rate and the displacement stability value of roof, floor and two sides of the roadway are obtained.
3) The water content ranges of four test points were obtained by comparing the borehole peeping results with the failure range of plastic zone. Provide theoretical guidance for roadway surrounding rock zoning support.

Data availability statement

The original contributions presented in the study are included in the article/Supplementary Material, further inquiries can be directed to the corresponding author.

Author contributions

All authors contributed to the study conception and design. Data collection and analysis were performed by CJ, SL, CF, ML, ZY, LY, and ZP. All authors read and approved the final manuscript.

Funding

This research was financially supported by the National Natural Science Foundation of China (Grant Nos. 52074146 and 51874159).

Acknowledgments

The authors would like to thank all editors and reviewers for their comments and suggestions.

Conflict of interest

ML was employed by the Company Shanxi Lu'an Chemical (Group) Co., Ltd.

The remaining authors declare that the research was conducted in the absence of any commercial or financial relationships that could be construed as a potential conflict of interest.

Publisher's note

References

Bai, Q. S., and Tu, S. H. (2016). Failure analysis of a large span longwall drift under water-rich roofs and its control techniques. *Eng. Fail. Anal.* 67, 15–32. doi:10.1016/j.engfailanal.2016.05.028

Castro-Filgueira, U., Alejano, L. R., Arzúa, J., and Ivars, D. M. (2017). Sensitivity analysis of the micro-parameters used in a PFC analysis towards the mechanical properties of rocks. *Procedia Eng.* 191, 488–495. doi:10.1016/j.proeng.2017.05.208

Chen, D. H., Chen, H. E., Zhang, W., Lou, J. Q., and Shan, B. (2021). An analytical solution of equivalent elastic modulus considering confining stress and its variables sensitivity analysis for fractured rock masses. *J. Rock Mech. Geotechnical Eng.* 14, 825–836. doi:10.1016/j.jrmge.2021.08.007

Chen, S., Wu, A., Wang, Y., Chen, X., Yan, R., and Ma, H. (2018). Study on repair control technology of soft surrounding rock roadway and its application. *Eng. Fail. Anal.* 92, 443–455. doi:10.1016/j.engfailanal.2018.06.006

Chen, Y., Li, Q., Pu, H., Liang, C., Deyu, Q., Xuyang, S., et al. (2020). Modeling and simulation of deformation mechanism of soft rock roadway considering the mine water[J]. *Geofluids* 2020. doi:10.1155/2020/8812470

Dou, Z., Tang, S. X., Zhang, X. Y., Liu, R. C., Zhuang, C., Wang, J. G., et al. (2021). Influence of shear displacement on fluid flow and solute transport in a 3D rough fracture. *Lithosphere* 2021, 1569736. doi:10.2113/2021/1569736

Fan, C., Li, S., Elsworth, D., Han, J., and Yang, Z. (2020). Experimental investigation on dynamic strength and energy dissipation characteristics of gas outburst-prone coal. *Energy Sci. Eng.* 8 (4), 1015–1028. doi:10.1002/ese3.565

Fan, C., Wen, H., Li, S., Bai, G., and Zhou, L. (2022). Coal seam gas extraction by integrated drillings and punchings from floor roadway considering hydraulic-mechanical coupling effect[J]. *Geofluids* 2022, 5198227. doi:10.1155/2022/5198227

Fan, C., Wen, H., Sun, H., Zhou, L., Zhang, X., Zhu, C., et al. (2022). Experimental investigation on the effect of loading and unloading on coal permeability with different sediment beddings[J]. *Lithosphere* 2022, 9949201. doi:10.2113/2022/9949201

Fan, C., Yang, L., Wang, G., Huang, Q., Fu, X., and Wen, H. (2021). Investigation on coal skeleton deformation in CO2 injection enhanced CH4 drainage from underground coal seam. *Front. Earth Sci. (Lausanne).* 9, 766011. doi:10.3389/feart.2021.766011

Gao, M. Z., Xie, J., Gao, Y. N., Wang, W. Y., Li, C., Yang, B. G., et al. (2021). Mechanical behavior of coal under different mining rates: A case study from laboratory experiments to field testing. *Int. J. Min. Sci. Technol.* 31 (2021), 825–841. doi:10.1016/j.ijmst.2021.06.007

He, M. C. (2014). Progress and challenges of soft rock engineering in depth[J]. *J. China Coal Soc.* 39 (8), 1409–1417. doi:10.13225/j.cnki.jccs.2014.9044

He, Q. (2021). *Instability mechanism of surrounding rock in weakly cemented roadway under force-water coupling [D].* Hebei Engineering University. doi:10.27104/d.cnki.ghbjy.2021.000571

Jia, C., Li, S., Fan, C., and Tang, J. (2021). Numerical simulation of mechanical characteristics of roadway surrounding rock under dynamic and static loading. *Shock Vib.* 2021–16. doi:10.1155/2021/1869583

Jing, H., Yin, Q., Yang, S., and Chen, W. (2021). Micro-mesoscopic creep damage evolution and failure mechanism of sandy mudstone. *Int. J. Geomech.* 21 (3), 04021010. doi:10.1061/(asce)gm.1943-5622.0001940

Li, G., Jiang, Z., Lv, C., Huang, C., Gui, C., and Li, M. (2015). Instability mechanism and control technology of soft rock roadway affected by mining and high confined water. *Int. J. Min. Sci. Technol.* 25 (04), 573–580. doi:10.1016/j.ijmst.2015.05.009

Li, S., Liu, R., Zhang, Q., and Zhang, X. (2016). Protection against water or mud inrush in tunnels by grouting: A review. *J. Rock Mech. Geotechnical Eng.* 8 (5), 753–766. doi:10.1016/j.jrmge.2016.05.002

Liu, B., Yang, H., and Karekal, S. (2020). Effect of water content on argillization of mudstone during the tunnelling process. *Rock Mech. Rock Eng.* 53 (2), 799–813. doi:10.1007/s00603-019-01947-w

Liu, C. D., Cheng, Y., Jiao, Y. Y., Zhang, G. H., Zhang, W. S., Ou, G. Z., et al. (2021). Experimental study on the effect of water on mechanical properties of swelling mudstone. *Eng. Geol.* 295, 106448. doi:10.1016/j.enggeo.2021.106448

Ma, C., Xu, J., Tan, G., Xie, W., and Lv, Z. (2021). Research on supporting method for high stressed soft rock roadway in gentle dipping strata of red shale. *Minerals* 11 (4), 423. doi:10.3390/min11040423

Su, Y. Q., Gong, F. Q., Luo, S., and Liu, Z. X. (2021). Experimental study on energy storage and dissipation characteristics of granite under two-dimensional compression with constant confining pressure. *J. Cent. South Univ.* 28 (3), 848–865. doi:10.1007/s11771-021-4649-2

Tao, Z., Cao, J., Yang, L., Guo, A., Huang, R., Yang, X., et al. (2020). Study on deformation mechanism and support measures of soft surrounding rock in muzhailing deep tunnel. *Adv. Civ. Eng.* 2020, 1–14. doi:10.1155/2020/9367916

Wang, X., Li, Y., Zhao, C., Wang, Y., and Huang, S. (2021). Study on deformation failure mechanism and control technology of surrounding rock in soft rock roadway. *Geotech. Geol. Eng. (Dordr).* 39 (8), 5931–5942. doi:10.1007/s10706-021-01977-8

Wang, Y., Yang, H. N., Han, J. Q., and Zhu, C. (2022). Effect of rock bridge length on fracture and damage modelling in granite containing hole and fissures under cyclic uniaxial increasing-amplitude decreasing-frequency (CUIADF) loads. *Int. J. Fatigue* 158, 106741. doi:10.1016/j.ijfatigue.2022.106741

Wen, W., Zhang, S., Xiao, T., Hao, Y., Li, D., and Li, H. (2021). Factors that affect the stability of roads around rocks. *Geomatics, Nat. Hazards Risk* 12 (1), 829–851. doi:10.1080/19475705.2021.1895327

Xie, H., Ju, Y., Gao, M., and Gao, F. (2018). Theories and technologies for *in-situ* fluidized mining of deep underground coal resources[J]. *J. China Coal Soc.* 43 (5), 1210–1219. doi:10.13225/j.cnki.jccs.2018.0519-cn

Yang, R., Li, Y., Guo, D., Yao, L., Yang, T., and Li, T. (2017). Failure mechanism and control technology of water-immersed roadway in high-stress and soft rock in a deep mine. *Int. J. Min. Sci. Technol.* 27 (2), 245–252. doi:10.1016/j.ijmst.2017.01.010

Yang, S. Q., Chen, M., Jing, H. W., Chen, K. F., and Meng, B. (2017). A case study on large deformation failure mechanism of deep soft rock roadway in Xin'An coal mine, China. *Eng. Geol.* 217, 89–101. doi:10.1016/j.enggeo.2016.12.012

Yang, S. Q., Tian, W. L., Jing, H. W., Huang, Y. H., Yang, X. X., and Meng, B. (2019). Deformation and damage failure behavior of mudstone specimens under single-stage and multi-stage triaxial compression. *Rock Mech. Rock Eng.* 52 (3), 673–689. doi:10.1007/s00603-018-1622-y

Yu, W., Li, K., Liu, Z., An, B., Wang, P., and Wu, H. (2021). Mechanical characteristics and deformation control of surrounding rock in weakly cemented siltstone. *Environ. Earth Sci.* 80 (9), 1–15. doi:10.1007/s12665-021-09626-2

Zhai, W., He, F., Xu, X., Lv, K., Li, L., and Song, J. (2022). Floor heave mechanism in water-rich soft rock roadways and a DS-IBA control approach. *Geomat. Nat. Hazards Risk* 13 (1), 2107–2123. doi:10.1080/19475705.2022.2107439

Zhang, Q. B., He, L., and Zhu, W. S. (2016). Displacement measurement techniques and numerical verification in 3D geomechanical model tests of an underground cavern group. *Tunn. Undergr. Space Technol.* 56, 54–64. doi:10.1016/j.tust.2016.01.029

Zhao, B., Wen, G., Nian, J., Ma, Q., Fan, C., Lv, X., et al. (2022). Numerical simulation study on the multi-physical field response to underground coal and gas outburst under high geo-stress conditions. *Minerals* 12, 151. doi:10.3390/min12020151

Zhao, K., Yang, D., Zeng, P., Huang, Z., Wu, W., Li, B., et al. (2021). Effect of water content on the failure pattern and acoustic emission characteristics of red sandstone. *Int. J. Rock Mech. Min. Sci.* 142, 104709. doi:10.1016/j.ijrmms.2021.104709

Zheng, L., Zuo, Y., Hu, Y., and Wu, W. (2021). Deformation mechanism and support technology of deep and high-stress soft rock roadway. *Adv. Civ. Eng.* 2021–14. doi:10.1155/2021/6634299

Zhu, C., Karakus, M., He, M. C., Meng, Q. X., Shang, J. L., Wang, Y., et al. (2022). Volumetric deformation and damage evolution of Tibet interbedded skarn under multistage constant-amplitude-cyclic loading. *Int. J. Rock Mech. Min. Sci.* 152, 105066. doi:10.1016/j.ijrmms.2022.105066

Zhu, Z., Wu, Y., and Han, J. (2022). A prediction method of coal burst based on analytic hierarchy process and fuzzy comprehensive evaluation. *Front. Earth Sci.* 9, 834958. doi:10.3389/feart.2021.834958

frontiers | Frontiers in Earth Science

TYPE Original Research
PUBLISHED 13 September 2022
DOI 10.3389/feart.2022.1007218

OPEN ACCESS

EDITED BY
Guangyao Si,
University of New South Wales, Australia

REVIEWED BY
Jiahao Wu,
Tsinghua University, China
Yuqing Bai,
Comenius University, Slovakia
Weisheng Du,
China Coal Research Institute (China),
China

*CORRESPONDENCE
Erhu Bai,
2283204550@qq.com

SPECIALTY SECTION
This article was submitted to Economic Geology,
a section of the journal
Frontiers in Earth Science

RECEIVED 30 July 2022
ACCEPTED 22 August 2022
PUBLISHED 13 September 2022

CITATION
Lu W, Bai E, Wei L, He C, Sun Y and Shi L (2022), Numerical simulation on spatial steering rule of directional perforation hydraulic fractures in low-permeability reservoir.
Front. Earth Sci. 10:1007218.
doi: 10.3389/feart.2022.1007218

Numerical simulation on spatial steering rule of directional perforation hydraulic fractures in low-permeability reservoir

Weiyong Lu[1,2,3,4], Erhu Bai[2,3]*, Le Wei[5], Changchun He[6,7], Yaohui Sun[1,4] and Lei Shi[1,4]

[1]Department of Mining Engineering, Lyuliang University, Shanxi, China, [2]State Key Laboratory Cultivation Base for Gas Geology and Gas Control (Henan Polytechnic University), Jiaozuo, China, [3]School of Energy Science and Engineering, Henan Polytechnical University, Jiaozuo, China, [4]Lyuliang Engineering Research Center of Intelligent Coal Mine, Shanxi, China, [5]China Coal Technology and Engineering Group Chongqing Research Institute, Chongqing, China, [6]School of Civil Engineering and Architecture, East China University of Technology, Nanchang, China, [7]State Key Laboratory of Coal Resources and Safe Mining, China University of Mining and Technology, Xuzhou, China

For purpose of clearing the spatial pattern of hydraulic fracture during directional perforation in low-permeability unconventional reservoirs, RFPA^{2D}-Flow software is used to numerically calculate their spatial steering trajectory and deflection distance. The accuracy of numerical calculation results is verified by theoretical and experimental results. Then the influences of horizontal principal stress difference, perforation length, and azimuth on the hydraulic fractures' spatial steering trajectory are studied. It is shown by the results that 1) the software can accurately predict the space steering trajectory and deflection distance of directional perforation hydraulic fractures, 2) both deflection distance and spatial steering trajectory of hydraulic fractures are quantitatively evaluation indexes, which are used to evaluate the hydraulic fractures' spatial steering effects, and 3) under different horizontal principal stress differences, perforation azimuths, and lengths, the same hydraulic fracture's propagation trajectories are presented. They initiate from the perforation end and gradually deflect along the maximum horizontal principal stress direction and finally represent curved fractures like both wings. With the increase in horizontal principal stress difference, the fractures' deflection distance decreases. However, it increases with the increase in perforation azimuth and length. Their deflection amplitude increases first and then decreases. Initiation pressure of hydraulic fracture rises with the decrease in perforation length and increase in perforation azimuth and horizontal principal stress difference.

KEYWORDS

low-permeability reservoir, directional perforation, hydraulic fracture, steering trajectory, deflection distance

1 Introduction

It is hydraulic fracturing that is considered to be one of the most effective and common methods to improve the physical properties of low-permeability reservoirs. Generally, it is conducted before an oil and gas well is put into production (Gehne and Benson, 2019; Nandlal and Weijermars, 2019; Lu et al., 2020a; Lu et al., 2020b; Lu and Huang, 2020; Ogata et al., 2020). Directional perforation hydraulic fracturing can alleviate the quick water outlet problems, enlarge the reformed reservoir volume, and poor water injection effect caused by straight line communication among fractures. It can also effectively reduce the initiation pressure, which is favorable for the formation of hydraulic fracture (Zhun et al., 2015; Liu et al., 2018; Qi et al., 2018; Hossain et al., 2020; Zhang et al., 2020). However, hydraulic fracture initiates from the perforation, which is the result of being affected by the perforating direction and far-field *in situ* stress and well-born effect. Hydraulic fracture with a certain curvature is formed, and its curvature is determined by the angle between the maximum principal stress and perforating direction (Chen et al., 2017). For directional perforation hydraulic fracturing, accurate prediction and control of hydraulic fracture propagation trajectory are the key conditions to the successful implementation of this technology. Therefore, the propagation path of hydraulic fractures must be clearly obtained before the hydraulic fracturing is conducted, so as to determine reasonable parameters of the fracture morphology and reconstruction effect of directional perforation hydraulic fracturing.

In recent years, serial physical experiments, the critical water pressure, and propagation path have been studied using the method of theoretical calculations and numerical simulations. Their impact factors of directional perforation hydraulic fracture have also been studied. The fracture initiation and propagation

TABLE 1 Summary of the existing analytical models and empirical models.

Sequence number	Research findings or results	References
1	In terms of theoretical calculation, a two-dimensional coupling model for diverting hydraulic fracturing is established. The results show that the fracture direction gradually changes toward the maximum horizontal stress direction. Fracture dynamic reorientation is greatly and obviously affected by horizontal stress difference	Zhang G. Q. et al. (Zhang and Chen, 2010a; Zhang and Chen, 2010b)
2	The governing equations of hydraulic fracture activation and steering in three-dimensional space are deduced. It indicates that along the main fracture propagation direction, fracture width dramatically narrows after re-orientation when high horizontal differential stress is subjected. Higher pump rate and higher viscosity of the fracture fluid can generate a wider fracture because higher residual energy is provided after the re-orientation	Chen M. et al. (Chen, 2013)
3	With the method of fully coupled finite element, the damage model is built on the basis of Mohr-Coulomb and maximum tensile stress criterions As a result, the larger the perforation azimuth from the maximum principal stress direction, the larger the curvature of the hydraulic fracture reorientation	Liu L. et al. (Liu et al., 2018)
4	With the characteristic length of the evolutionary fracture, a three-dimensional model of fuzzy fracture based on the incremental finite element method is proposed. It is indicated by the results that the new model is better than the standard smeared fracture. The interface obtained using the new coupling method is more efficient than the traditional model, which is built on the basis of a continuous but graded mesh	Hu Y. et al. (Hu et al., 2014)
5	A fully coupled steering fracturing model based on displacement discontinuity is established. It is shown that both fracture pacing and boundary conditions applied to the previously created fractures have influenced the path of the fracture. not only the fracture path is affected by but also by the	Sesetty V. et al. (Sesetty and Ghassemi, 2015)
6	The incremental fracture growth model by using the maximum axial strain fracture criterion is established. It is found that with the stress anisotropy coefficient decrease, initial critical water pressure increases, but the contact area with the formation increases. The perforation angle is one of the critical factors, which can have great effects on the fracturing	Dong Zhuo et al. (Dong and Tang, 2019)
7	The dynamic expansion model of directional perforation hydraulic fracturing based on a micro-element method (MEM model) is established. It is expressed by the results that by the contrast of the match degree of the micro-seismic monitoring results, the hydraulic fracture trajectory obtained using the newly proposed model is larger than that obtained through the XFE model. The deflection distance decreases negatively logarithmically with increasing horizontal *in situ* stress difference while increasing linearly with increasing the perforated angle, injection rate, and viscosity. The deflection is almost influenced by the perforation length. The research work is significant to further understand oriented perforation steering fracturing	He Feifei et al. (He et al., 2020)
8	A theoretical model of tensile and shear failure induced by water pressure based on the maximum shear strain and other fracture mechanical criteria is established. The analysis indicates that while the perforation length increases, the critical water pressure decreases	Dong and Tang Shibin (Tang et al., 2017; Dong et al., 2018)

are influenced by the prefabricated fracture dip, which is studied by Liyuan Liu and Haiyan Zhu et al. through numerical simulation and physical test (Zhun et al., 2015; Liu et al., 2018). In the same way, large-scale true triaxial hydraulic fracturing physical simulation experiment was conducted by Chen and Jiang Hu et al. It is shown that formation fracture pressure and its morphology is affected by perforation azimuth and horizontal principal stress difference (Jiang et al., 2009; Chen et al., 2010; Jiang et al., 2014). For some laboratory test methods, they take more money and time, but only limited results can be obtained at times. Theoretical calculation and numerical simulation are widely used because of their low cost and convenient operation in controlling the variation of influence parameters. The summary of the existed analytical models and empirical models can be seen in Table 1. All these analytical models and empirical models can be used to study the characteristics of the hydraulic fracture rotation rule in rock mass.

Although the theoretical method can analyze the parameter influence and provide the theoretical basis for verification for numerical calculation, they cannot intuitively show the propagation process of hydraulic fracture intuitively. That is to say, the propagation process of hydraulic fracture can be shown using numerical simulation methods. However, the accuracy of numerical calculation is affected by the selected parameters. At times, the calculation results may not be accurate. Moreover, there is a certain gap with the actual calculation results. Therefore, the selected parameters need to be verified before the numerical calculation. In general, there are two methods, the finite element method (FEM) and the extended finite element method (EFEM), which can be used to conduct numerical simulation. The FEM has been a common method to simulate the propagation progress of hydraulic fracture in recent years (Zhang and Chen, 2010a; Zhang and Chen, 2010b; Hunsweck et al., 2013; Bao et al., 2014; Bao et al., 2015). However, the fracture path needs to be set in advance before computation, which cannot reflect the turning law of the fracture and the arbitrariness of its expansion. At the end of each time step, the fractures need to be re-gridded, thus mitigating the grid accuracy and computing efficiency (Chen et al., 2017). The EFEM makes up for the FEM defects in simulating the fracture propagation (Daux et al., 2000; Sukumar et al., 2000; Moës and Belytschko, 2002). Based on the EFEM, the morphology of fracture propagation influenced by different horizontal stress differences and perforation azimuth was simulated by Sepehri et al. (2015). A solid–fluid coupling for simultaneous propagation and steering of directional perforating hydraulic fractures in vertical wells in low-permeability reservoirs was established by Shi Jihui et al. It is indicated that both the fracture turning radius and its initiation pressure are influenced by fracturing fluid injection rate, perforation azimuth, and main stress difference (Shi et al., 2020). The parameters, including perforation length and azimuth, have great influence on hydraulic fractures' initiation and propagation. The coupling model of hydraulic fracturing is established with the foundation of two criterions. One is the maximum tensile stress criterion; the other is the stress intensity factor criterion. This method is utilized to conduct the degree of influence (Chen et al., 2017). As we know, the fracture propagation deflection is affected by the parameters of fracturing fluid. The fracturing fluid is characterized with its viscosity and injection rate. So, a fluid–solid coupling model of the steering fracture was established by Wang X.L. (Wang et al., 2018a; Wang et al., 2018b).

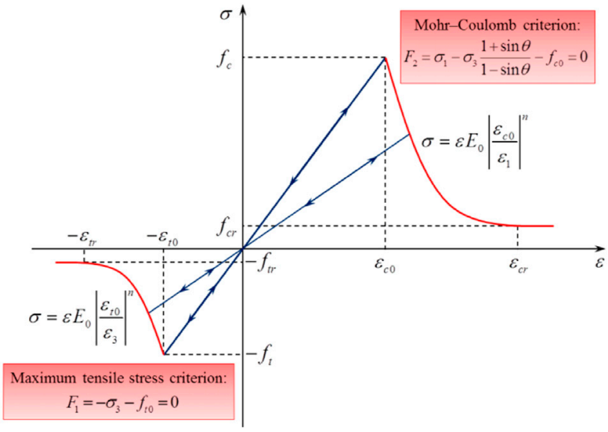

FIGURE 1
Damage constitutive law for rock under uniaxial stress condition (Liu et al., 2018).

The existing studies have played an important role in rules of the spatial turning and directional fracture propagation under different influence factors (Wang et al., 2017; Guo et al., 2018; He et al., 2018; Guo et al., 2020). However, the influencing mechanism of each factor has not been revealed, and the deflection process of the directional perforation hydraulic fracture remains unknown. In addition, there are few research studies on the deflection distance of hydraulic fracture, which is key to measuring the directional propagation effect of hydraulic fracture. Thus, it is the computer simulation software of RFPA^{2D}-Flow that is adopted to analyze the fractures' deflection process in this study. First, two indexes are put forward to quantitatively analyze and evaluate the spatial deflection of directional perforated hydraulic fracture. One index is the quantitative extraction of the deflection propagation trajectory of hydraulic fracture, and the other is deflection distance of hydraulic fracture. Then, the accuracy of the numerical calculation results of RFPA^{2D}-Flow was verified by the results obtained using the MEM model and laboratory test. Finally, regarding the two quantitative indexes as the starting point, the influence rule and the mechanism of horizontal principal stress difference,

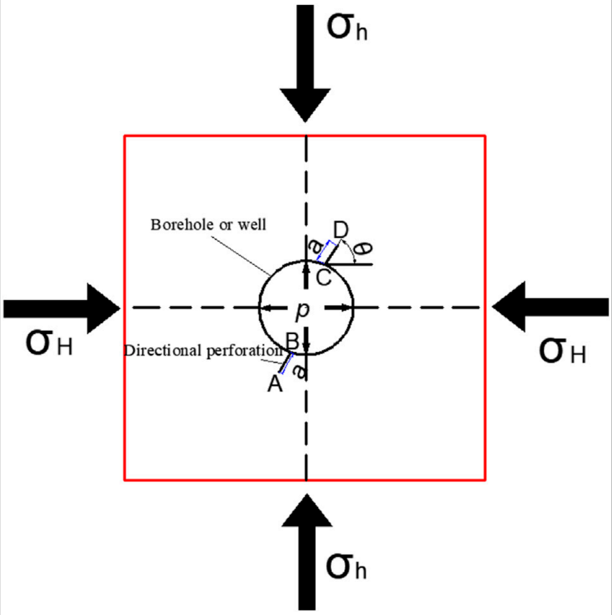

FIGURE 2
Geometric model of directional perforation hydraulic fracturing.

perforation azimuth, and length on the fractures' distances and deflection path is analyzed. The results of this study have certain reference value for further understanding the spatial steering process and the optimization of parameters of hydraulic fracturing with the help of the directional perforation.

2 Numerical simulations of the steering process of the directional perforation hydraulic fracture

2.1 Tensile and shear failure criteria of the rock of the software

In this study, a piece of computer simulation software is used. The detailed introduction about the software can be found from the literatures (Zhu and Tang, 2004; Li et al., 2011; Lu et al., 2020a). So, it has not been repeatedly introduced. But the tensile and shear failure criteria of the rock mass are introduced in detail.

As illustrated in Figure 1, rock damage in tension or shear is initiated when its state of stress (positive for compression) satisfies the maximum tensile stress criterion or the Mohr-Coulomb criterion, respectively, as $F_1 = 0$ and $F_2 = 0$. In terms of the damage constitutive law shown in Figure 1, when $F_1 < 0$ and $F_2 < 0$, the applied stress is insufficient to satisfy the maximum tensile stress criterion and the Mohr-Coulomb failure criterion, respectively. $F_1 = 0$ and $dF_1>0$ implies rock damage in the tensile mode when the stress state satisfies the maximum tensile stress criterion and the rock is still under load. $F_1 = 0$ and $dF_2>0$ implies rock damage in the shear mode when the stress state satisfies the Mohr-Coulomb failure criterion and the rock remains loaded (Liu et al., 2018).

In Figure 1, f_{t0} and f_{c0} are, respectively, uniaxial tensile and compressive strength, E and E_0 are, respectively, the Young's modulus of the damaged and the undamaged element, σ_1 and σ_3 are, respectively, the first and third principal stresses, θ is the internal frictional angle, and F_1 and F_2 are two damage threshold functions; ε_1 and ε_3 are, respectively, the major and minor principal strains, ε_{t0} and ε_{c0} are, respectively, the maximum tensile and maximum compressive principal strains when tensile and shear damage occurs, and n is a constitutive coefficient specified as 2.0.

2.2 Establishment of physical model

The size of the two-dimensional model is 300 mm × 300 mm (Figure 2). Its boundary is impermeable and constrained by surrounding pressure. There is a borehole, whose diameter is 20 mm, in the center of the model. The total cell number of the model, which is divided, is 90000. There are two pre-existing perforations. One is named AB, and the other is marked with CD. Their length, a, is 30 mm. The angle, marked with θ, between the directional perforation and the maximum horizontal principal stress σ_H, is termed as orientation angle. θ is valued as 60°. The maximum principal stress σ_H and minimum principal stress σ_h is 6 and 1 MPa in the horizontal and vertical direction, respectively. In the beginning, there is no water pressure, and its increase rate is 0.2 MPa/step.

2.3 Parameter selection

The parameters of the experimental test adopted by Jiang Hu et al. and the theoretical calculation by He Feifei et al. are seen in Table 2 (Jiang et al., 2009; He et al., 2020). The parameters, such as compressive and tension strength, can be obtained by a mechanical test, and their proportion and internal friction angle can be calculated. Then, the stress-strain curve can be obtained. Moreover, the residual strength coefficient, the maximum tension and compressive strain coefficient, the elastic modulus, and the internal friction angle are very easy to obtain. The permeability can be obtained by the laboratory experiment. Before water is poured into the borehole, there is no water pressure. Therefore, initial water pressure is 0. A piece of computer simulation software is used to calculate the fracture propagation trajectory with the similar experimental and theoretical conditions, and the results of numerical

TABLE 2 Parameters of numerical simulation.

Parameters	Value and unit	Parameters	Value and unit
Elasticity modulus	8.402 GPa	Homogeneous degree	3
Compressive strength	28.34 MPa	Damage mutation coefficient	5
Tensile strength	2.59 MPa	Poisson's ratio	0.23
Permeability coefficient	$0.1 \times 10\ \mu m^{-2}$	Coefficient of pore pressure	1
Porosity	0.0185	Coupling coefficient	0.1

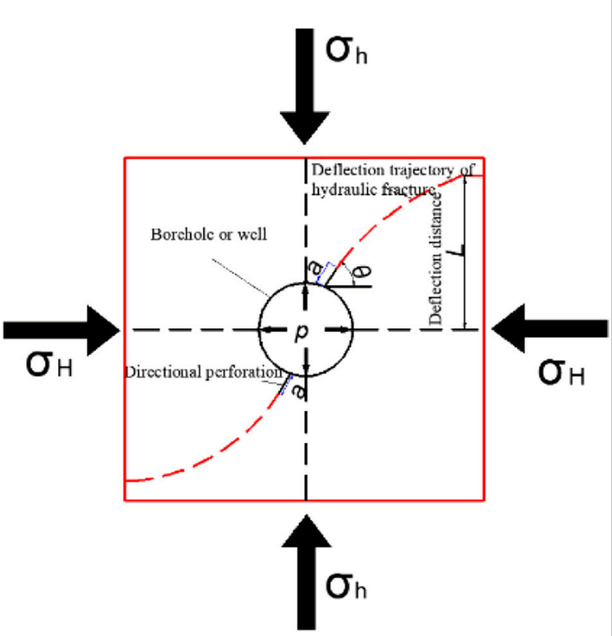

FIGURE 3
Evaluation indexes of spatial steering expansion of hydraulic fractures.

simulation were compared with the experimental and theoretical results.

2.4 Comparison of RFPA^{2D}-flow numerical calculation results with MEM model and laboratory test results

2.4.1 Evaluation index of spatial steering of directional perforation hydraulic fracture

In general, the maximum principle is along the vertical direction. During the expansion of hydraulic fracture, fracture always propagates along the direction in which the resistance is the least value. Therefore, the surface of the preferred fracture is usually along the maximum horizontal principal stress. In the far field, the hydraulic fracture expansion direction is usually perpendicular to the direction of the minimum horizontal principal stress. In this study, the distance of the deflection is marked with *L*, and the spatial turning expansion trajectory of the hydraulic fractures is shown in Figure 3. These two indexes are utilized to measure the law of spatial turning of the directional perforating hydraulic fracturing. The maximum horizontal principal stress, minimum horizontal principal stress, perforation azimuth, perforation length, water injection pressure, and fracture deflection distance is marked with σ_H, σ_h, *θ*, *a*,*p*, and *L*.

2.4.2 Accuracy of numerical calculation results calculated by RFPA^{2D}-Flow software

The result of simulation obtained by Hu et al. is shown in Figure 4. It can be indicated that the hydraulic fracture gradually biases toward the direction of σ_H after it initiates at the point of the perforation end. A steering fracture in a bent wing is formed, but the two wings of the bent fracture is not strictly symmetrical. The spatial steering expansion trajectory of the directional perforation hydraulic fracture obtained by the numerical simulation is basically identical with that of the experimental test.

Based on the micro-element method, a dynamic propagation model (MEM model) was established by He Feifei et al., which is used to quantitatively determine the expansion trajectory and deflection distance of hydraulic fractures in low-permeability unconventional oil and gas reservoirs during directional perforation steering fracturing (He et al., 2020). In this study, the results of the MEM model, physical experiment, and RFPA^{2D}-Flow calculation are quantitatively compared (Figure 5) to verify the accuracy of numerical simulation results. It can be seen from Figure 5 that 1) for the right wing ($X > 0$) of the hydraulic fracture, the results of numerical calculation are basically consistent with those obtained using laboratory tests and the MEM model. For the left wing ($X < 0$), the results of numerical calculation and indoor laboratory test and the MEM model are a little different. This can be explained by the fact that in the laboratory test, due to the impact of loading conditions and the heterogeneity of specimens themselves, the hydraulic fracture does not initiate along the predetermined direction. A two-wing steering fracture with an incomplete symmetry of the starting end of directional perforation is eventually formed. The steering asymmetry of the right wing ($X > 0$) is more obvious. 2) The distance of the fracture deflection of the left wing ($X < 0$)

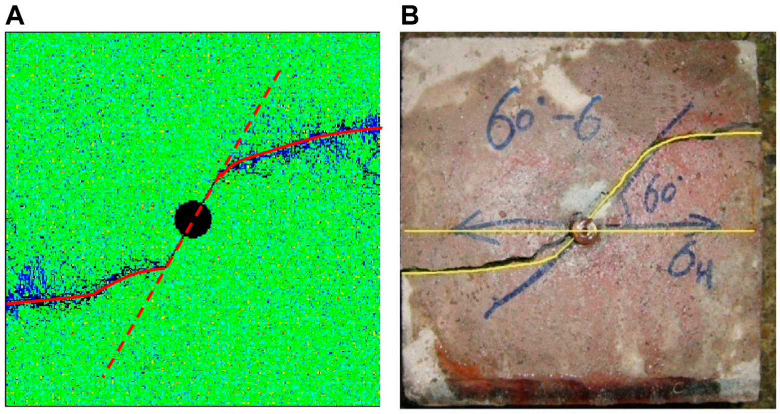

Numerical calculation

Physical experiment

FIGURE 4
Comparison of the deflection trajectory of hydraulic fracture between numerical calculation and physical experiment.

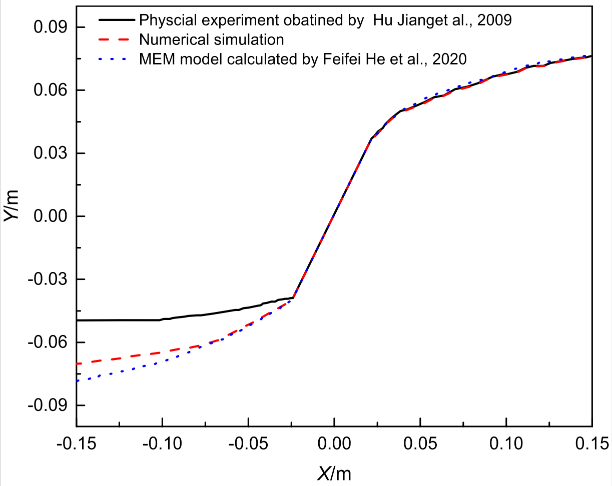

FIGURE 5
Comparison of results calculated using RFPA^{2D}-Flow software, laboratory test, and the MEM model.

calculated using physical experiment, numerical calculation and the MEM model is 0.049, 0.07, and 0.079 m, respectively. The distance of the fracture deflection calculated by numerical calculation is located between the deflection distance calculated using physical experiment and the MEM model. The results of numerical calculation are basically the same as those calculated using the MEM model. They are closer to those calculated by the physical experiment. Through the quantitative comparison of the trajectory and deflection distance of hydraulic fracturing obtained using laboratory fracturing test and the MEM model, it is proved that the results calculated using RFPA^{2D}-Flow software are accurate, feasible, and reliable.

3 The influencing factors of spatial steering process and deflection distance of hydraulic fracture

The deflection trajectory and its deflection distance of hydraulic fractures, which is shown in Figure 3, are two key indexes to evaluate the fracturing turning effect. As we know, it is very important for the design optimization of hydraulic fracture turning to figure out the fracture propagation trajectory and deflection distance under various influencing factors. RFPA^{2D}-Flow software is adopted to study the influence of parameters such as principal stress difference $\triangle\sigma(\triangle\sigma = \sigma_H\text{-}\sigma_h)$, perforation length, and azimuth on the propagation trajectory and deflection distance of directional perforation hydraulic fracture.

3.1 Influence of horizontal stress difference on spatial steering trajectory and deflection distance of hydraulic fractures

$\triangle\sigma$ is the most important factor, which affects the fracture deflection distance and propagation path. In the model, the σ_h is 1 MPa, and the σ_H is selected as 10 MPa, 8 MPa, 6 MPa, 4 MPa, and 2 MPa to determine how horizontal principal stress difference $\triangle\sigma$ influences the trajectory and deflection distance of hydraulic fractures in space.

It is water pressure, acoustic emission signal, and fracture morphology of hydraulic fractures under several different $\triangle\sigma$ that is illustrated in Figure 6. Figure 7 indicates the quantitative comparison results of deflection distance. It can be seen that the fracture propagation trace is almost consistent. From the perforation end, the hydraulic fracture initiates first. Then it

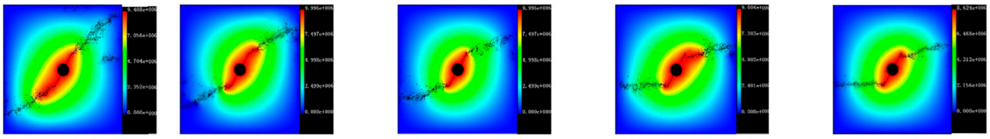

(I) The water pressure cloud map

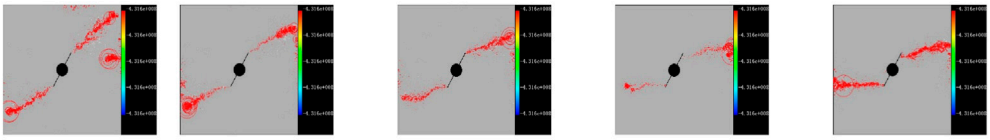

(II)The signal of acoustic emission

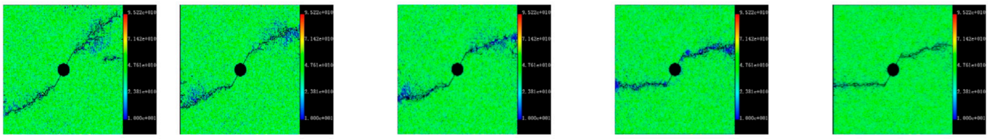

(III) Fracture propagation monograph

△σ=1 MPa △σ=3 MPa △σ=5 MPa △σ=7 MPa △σ=9 MPa

FIGURE 6
Water pressure, AE signal, and fracture deflection morphology under different △σ

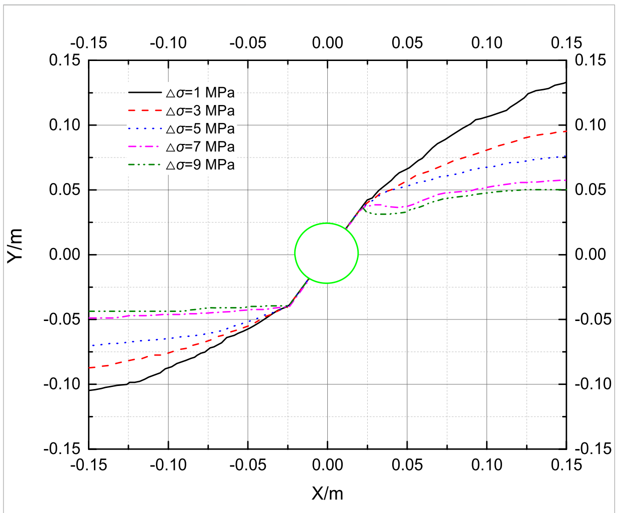

FIGURE 7
Deflection trajectory of hydraulic fracture under different principal stress difference.

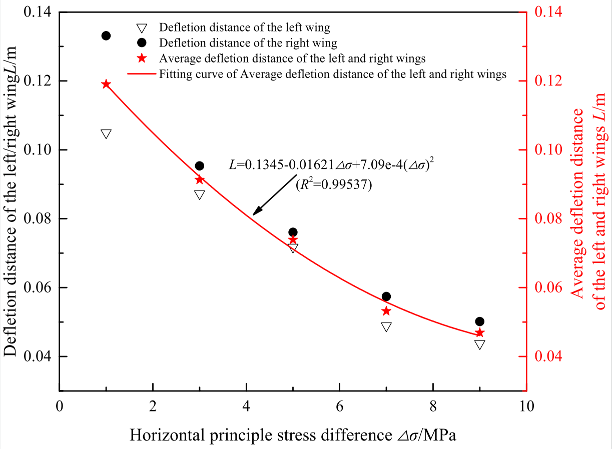

FIGURE 8
Deflection distance of hydraulic fracture under different principal stress difference.

deflects along the σ_H direction gradually. Meanwhile, the fracture deflection amplitude increases first. But it then decreases on the contrary. However, the fracture deflection distance under different $\Delta\sigma$ is different. The greater the $\Delta\sigma$, the smaller the fracture deflection distance. With the increase in the horizontal stress difference, the deflection curvature radius of the hydraulic fracture becomes smaller and smaller. This can be explained by the fact that the deflection curvature radius of the hydraulic fracture in a two-dimensional space can be calculated using the formula (Romero et al., 1995) where K is the ratio of σ_H and σ_h, R_L is the deflection curvature radius of hydraulic fracture, the stress intensity factor K_I is related to the fracture size, the geometric characteristics of fractures, and the load received. It can be seen from this formula that K being greater causes the curvature radius of hydraulic fracture to be smaller when the stress

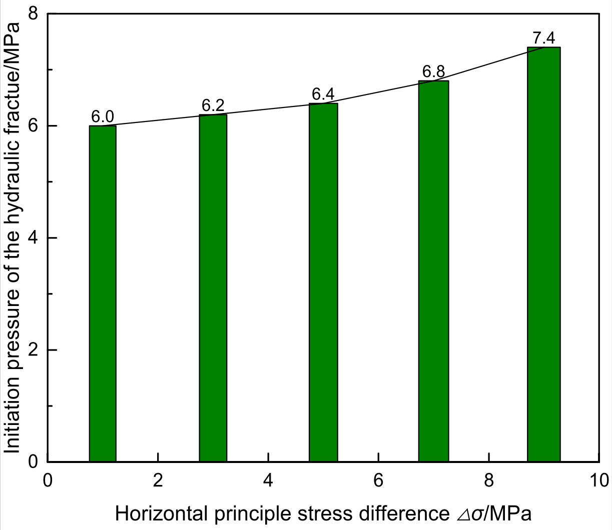

FIGURE 9
Initiation pressure of hydraulic fractures under different horizontal principal stresses.

intensity factor K_I and minimum principal stress σ_h are constant. The greater difference of $\triangle\sigma$ makes the shorter fracture turning path and the faster turning to the optimal fracture surface (Jiang et al., 2009).

During the hydraulic fracturing process of numerical simulation, the acoustic emission (AE) signal, water pressure changes, and fractures' shape change is monitored (Figure 6). The failure of the rock mass is usually caused by tensile or shear stress. For the AE signal, tensile and shear fracture is marked as circles with red and white colors, respectively. The location of the circles is the place in which the tensile or shear failure occurs. The larger the circle, the more the rupture energy releases. The shape of the AE signal can be used to track the fracture propagation. It is obvious that the tensile rupture is more than the shear rupture because the number of red circles is more than the white ones.

The relationship between L and the $\triangle\sigma$ can be further illustrated in Figure 8: 1) The deflection distance L and $\triangle\sigma$ conform to the quadratic polynomial $L = 0.1345–0.01621\triangle\sigma\text{-}4\ (\triangle\sigma)^2$, and the correlation coefficient is 0.99537. 2) When $\triangle\sigma$ decreases from 9 MPa to 7 MPa, 5 MPa, 3 MPa, and 1 MPa, respectively, the average deflection distance of hydraulic fractures increases by 0.006 meters, 0.017 meters, 0.021 meters, and 0.028 m, respectively. When $\triangle\sigma$ is less than 7 MPa, the fracture deflection distance is more visible. When $\triangle\sigma$ is greater than 7 MPa, little change happens. 3) The slope of the fitting curve decreases with the increase in $\triangle\sigma$. It is demonstrated that the fracture deflection distance variation decreases slowly.

Figure 9 manifests the initiation pressure of the hydraulic fracture corresponding to different horizontal principal stress differences. With $\triangle\sigma$ being 9 MPa, 7 MPa, 5 MPa, 3 MPa, and 1 MPa, the correspondent fracture initiation pressure is 7.4, 6.8, 6.4, 6.2, and 6.0 MPa. It makes clear that the initiation pressure decreases gradually with the decrease in $\triangle\sigma$. The reason is that the higher the normal stress on the surface of the fracture surface, the greater the water pressure that is required to open the fracture. The greater $\triangle\sigma$ produces the greater normal stress on the fracture surface, and the greater initiation pressure of hydraulic fracture. The conclusions of this study are consistent with the results of relevant physical experiments (Chen et al., 2010; Dong and Tang, 2019).

3.2 Influences of perforation parameters on the fracture's spatial turning process and deflection distance

The parameters, mainly including the azimuth and length of perforation, most directly affect the steering propagation trajectory and deflection distance of directional perforation hydraulic fracture. To a large extent, it determines the fracturing effect and deflection distance of hydraulic fracture.

3.2.1 Perforation azimuth

Several different perforation azimuths of 15°, 30°, 45°, 60°, and 75° are chosen to study its influence on the fracture deflection distance and trajectory.

It is shown in Figure 10 that AE signal, water pressure changes, and fracture deflection morphology under different perforation azimuth: 1) all hydraulic fractures under different perforation azimuths initiate at the perforation tip and then extend for a distance in the direction of the existing perforation and gradually turn toward the σ_H direction. The deflection amplitude first increases and then decreases. 2) There are differences in the deflections of hydraulic fractures under different perforation azimuths. Larger perforation azimuth produces the more obvious fracture deflection. 3) Under different perforation azimuths, the trends of the propagation trajectory of the hydraulic fractures are roughly the same, and all the final shape is presented as a two-wing bending fracture. 4) When the directional perforation azimuth is 75°, a new fracture also appears σ_H. This is because the maximum stress concentration value of around the fracturing borehole wall appears along the maximum horizontal principal stress. At this time, two hydraulic fractures simultaneously initiate along both the directional perforation and the borehole wall in the σ_H direction. This directional perforation azimuth is considered as a critical angle. At this critical angle, the first principal stress magnitude occurring at the directional perforation tip and the wall of the borehole in the σ_H direction are equal (Lu and He, 2021a). The analysis about acoustic emission signals of Figure 6II is also suitable for Figure 10II.

The hydraulic fracture deflection trajectory is well shown in Figure 11. Several perforation azimuths of 15°, 30°, 45°, 60°, and

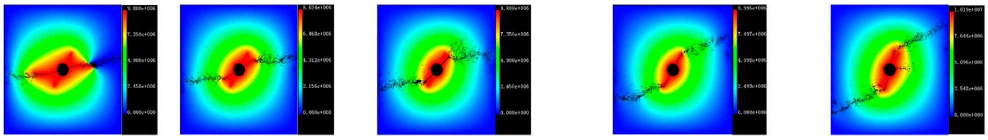

(I) The water pressure change

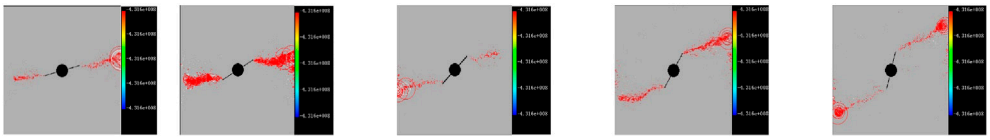

(II)The signal ofAcoustic Emission

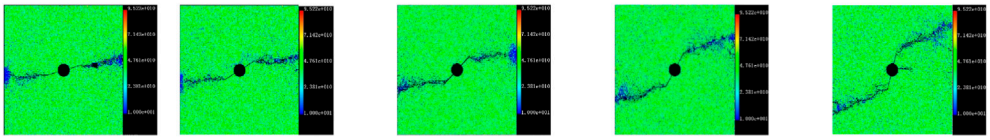

(III) Hydraulic fracture propagation process

θ=15 degrees *θ*=30 degrees *θ*=45 degrees *θ*=60 degrees *θ*=75 degrees

FIGURE 10
Water pressure, acoustic emission signal, and fracture deflection morphology under different perforation azimuths.

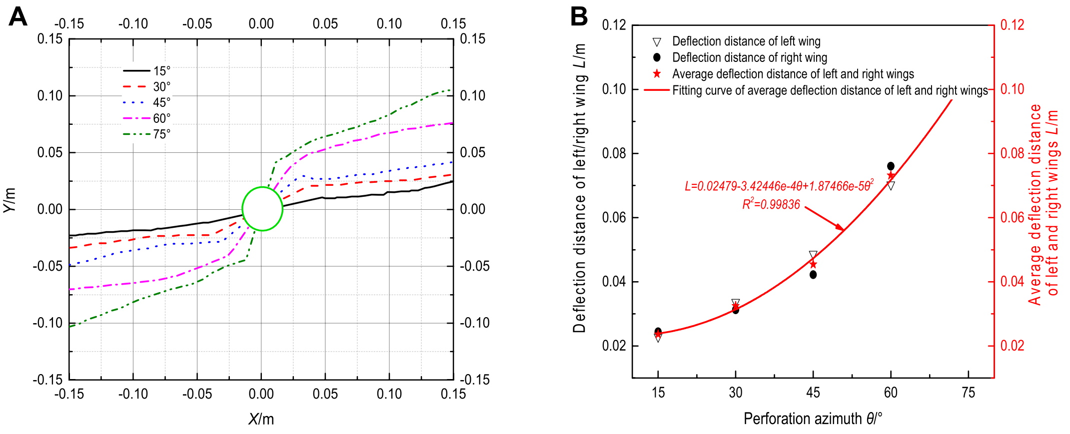

Fracture deflection trajectory

Fracture deflection distance

FIGURE 11
Hydraulic fractures' deflection trajectory and distance under different perforation azimuths.

75° are chosen to study its fluences on the fracture deflection distance. As a result, 0.024, 0.032, 0.045, 0.073, and 0.104 m are the corresponding average deflection. This indicates that smaller perforation azimuth will lead to a quicker deflection of hydraulic fracture to the σ_H direction.

That is to say, with the perforation azimuth being increased, a larger fracture initiation angle in the initial stage of fracture expansion appears. So, the fracture slowly turns to the σ_H direction. The reason is as following. When the main principal stress is fixed, the distribution of the shear and tensile stress at the perforation end will be affected by the perforation azimuth, and then the fracture initiation angle and the deflection angle of the micro-step increment in the subsequent expansion will also be affected. In the range from

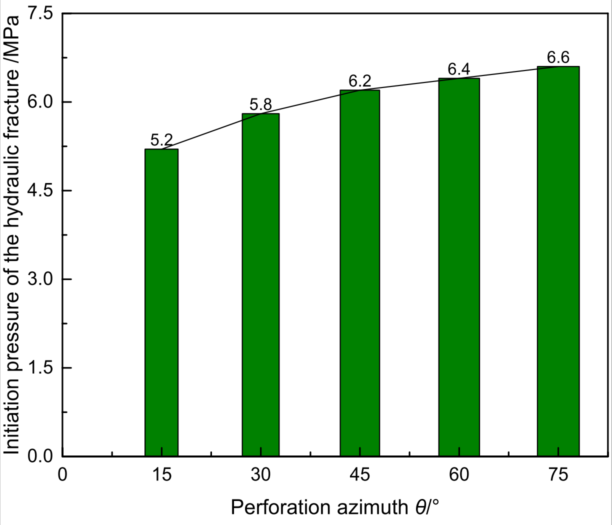

FIGURE 12
Initiation pressure of hydraulic fractures under different perforation azimuths.

0 to π/2, the larger the perforation azimuth, the more the number of the micro-step increment and deflection times, the smaller the deflection curvature of the hydraulic fracture propagation path, and the larger the deflection distance. However, there are few variation amplitudes of initial fracture angles under different values of θ. Compared with the effect of perforation azimuth on the number of deflections, the effect of perforation azimuth on the initial fracture angle can be ignored (He et al., 2020).

The relationship between L and θ appears in Figure 11B: 1) the relationship between L and θ is conformed to L = 0.02479–3.42446e-4θ+1.87466e-5θ^2, which is a quadratic polynomial, and 0.998 is the corresponding correlation coefficient. The fitting curve derivatives increase with the increase in θ. It is indicated that deflection distance of hydraulic fracture increases with the increase in perforation azimuth, which means the sensitivity between L and θ rises slowly. With the increase in perforating azimuth angle, hydraulic fractures near the well or the borehole or drilling become more twisted, and the corresponding deflection distance is greater. 2) With the perforation azimuth being 15° increment, the corresponding fracture deflection distance increases by 0.08, 0.13, 0.28, and 0.31 m, respectively. It is indicated that with the increase in θ, the variation amplitude of L is increasing slowly as well, and the reservoir that can be communicated by the hydraulic fracture is also broader.

The relationship between the fracture initiation pressure P_f and the θ is shown in Figure 12. It is characterized with nonlinearity between the P_f and θ. With θ being, respectively, 15°, 30°, 45°, 60°, and 75°, the corresponding fracture initiation pressure is, respectively, 5.2, 5.8, 6.2, 6.4, and 6.6 MPa. According to the theory of the fracture mechanics, with the maximum effective tensile stress coming to the tensile strength around the wall of the borehole strength, the rock mass is broken and the fracture occurs. P_f increases with the increase in θ as well. The initiation pressure of the perforated vertical well can be calculated using the formula $P_f = ¼\{\sigma_h [3+6\cos(2\theta)]+\sigma_H [3-6\cos(2\theta)]+2\mu(\sigma_H-\sigma_h)\cos(2\theta)-\alpha P_p+\sigma_t\}$. Here, pore pressure, tensile strength, Poisson's ratio, and the pore elastic coefficient are marked as P_p, σ_t, μ, and α, respectively (Hossain et al., 2020). Accordingly, with the increase in θ, the P_f increases gradually. In addition, the larger the θ, the more energy is needed to overcome the shear failure of the perforation tip, resulting in a high holding pressure generated by the injection of fracturing fluid that is needed to achieve the fracture initiation at the perforation tip (Shi et al., 2020).

With the increase in θ, the stress variation increases, the fracture expansion path is longer and steering radius is larger in this region (Shi et al., 2020). Consequently, the perforation in the σ_H direction can be better connected with hydraulic fracture, allowing for the fracturing fluid to flow along the path of least resistance. Perforated hole, which is consistent with the best fracture plane, can effectively reduce or eliminate the tortuous flow path or flow restrictions near the well. The two-wing fracture that is formed is characterized with the smallest tortuosity and lower injection pressure. If the perforation hole is not consistent with the σ_H direction, a complex flow path is often generated near the well. Therefore, the angle between directional perforation azimuth and the optimal fracture surface must be as small as possible to reduce the distortion of hydraulic fractures near the well.

3.2.2 Perforation length

The proper perforation length is beneficial to pass through the polluted area near the well and reduce the influence of well-born effect on the fracture initiation and propagation. Several perforation lengths a of 20, 30, 40, 50, and 60 mm are chosen to study its influence on the spatial turning expansion trajectory and deflection distance of hydraulic fracture.

From Figure 13, several rules are found: 1) although the perforation lengths are different, the fracture propagation trajectories are nearly the same as each other. The monograph of hydraulic fracture is presented like curve fractures with two wings. 2) After hydraulic fractures initiate from the perforation end, they gradually turn to the σ_H direction. The amplitude of the fracture deflection increases first, but then the opposite feature is presented. 3) For different perforation lengths, there are different fracture deflection distances, and there is a positive correlation. The analysis about acoustic emission signals of Figure 6II is also suitable for Figure 13II.

Several perforation lengths a of 60, 50, 40, 30, and 20 mm are chosen. For the left and right fracture wing, the fracture deflection distance is different. For the right fracture wing, they are 0.074, 0.073, 0.071, 0.070, and 0.053 m. However, for the right fracture wing, they are 0.086, 0.079, 0.076, 0.073, and 0.054 m. It is indicated that with

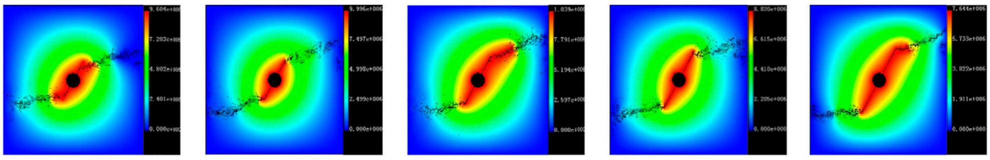

(I) Water pressure

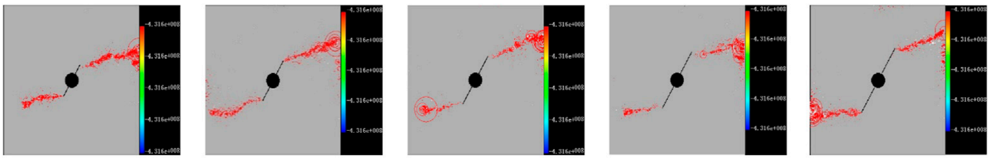

(II) AE signal

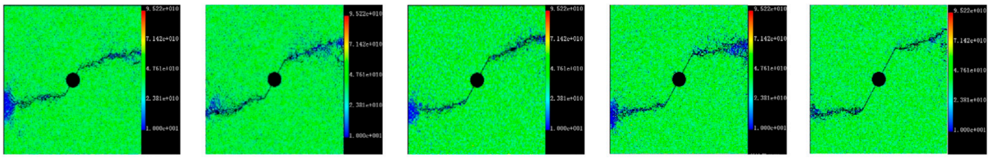

(III) Hydraulic fracture deflection morphology

a=20 millimeters *a*=30 millimeters *a*=40 millimeters *a*=50 millimeters *a*=60 millimeters

FIGURE 13
Water pressure, AE signal, and fracture deflection morphology under different perforation lengths.

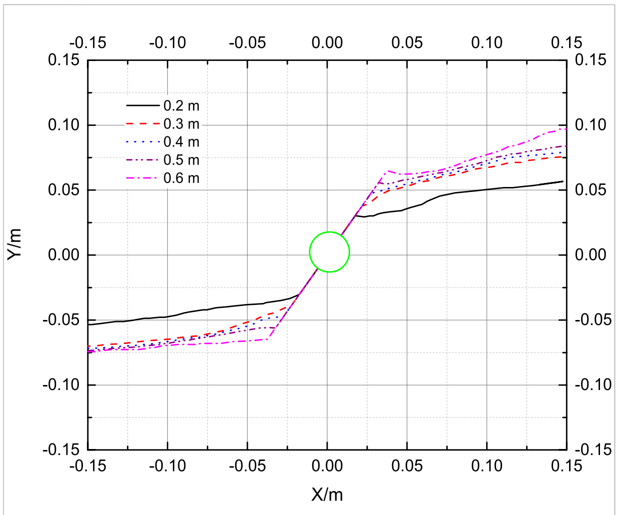

FIGURE 14
Fracture deflection trajectory with the change of perforation length.

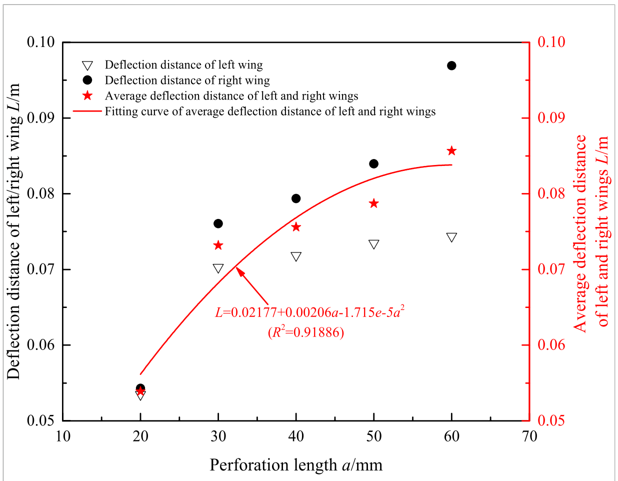

FIGURE 15
Curve line of hydraulic fracture deflection distance with the perforation length.

the increase in perforation length, the deflection distances of the left or right wing increases. So does the average deflection distance. Meanwhile, the perforation length increase is unconducive to the control of fracture deflection distance. The communicating effect of effective reservoirs is not good during the propagation process of the hydraulic fracture (Figure 14).

The relationship between the L and a is quantitatively illustrated in Figure 15: 1) the relationship is conformed to the formula $L = 0.02177 + 0.00206a\text{-}1.715\text{e-}5a^2$, which is

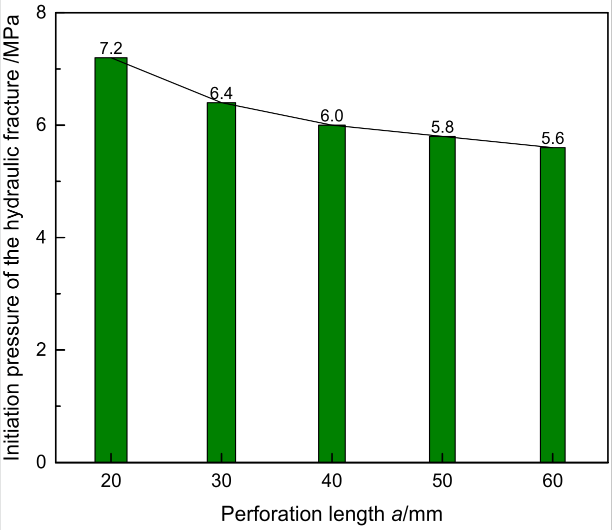

FIGURE 16
Change of hydraulic fracture initiation pressure with perforation length.

presented as a quadratic polynomial relationship. It is 0.92 that is the correlation coefficient R^2.

2) When the *a* is a fixed value, the right fracture wing deflection distance is larger than the left one. The difference of the deflection distance between the two under the same perforation length increases with the increase in the value of *a*. 3) The tangent derivative of the fitting line in Figure 15 gradually decreases. It is indicated that with the increase in the perforation length, its influence on the fracture deflection distance becomes smaller and smaller.

The curve line of hydraulic fracture deflection distance with the perforation length is shown in Figure 16. The hydraulic fracture initiation pressure increases gradually with the perforation length decrease. It is the same as the calculation results of the fracture growth increment method obtained by Dong Zhuo et al. and the numerical method by Chen Zhengrong et al. (Chen et al., 2013; Dong and Tang, 2019; Bai et al., 2020; Lu and He, 2021b). It is shown that the appropriate perforation length under the condition of relatively low injection pressure can obtain the optimal fracturing effect in the engineering practice of hydraulic fracturing.

4 Discussion

For oriented perforation steering fracturing, accurate prediction and control of the fracture propagation trajectory are the key conditions for successful implementation of this technology. Therefore, it is important to determine the fracture propagation path before the diversion fracturing operation, so as to determine the proper operation parameters and improve the post-pressure effect. Currently, the hydraulic fractures' deflection characterizations can be presented by spatial shape and initiation pressure. However, in this study, it is demonstrated that it is found that the deflection distance and angle are the other two important parameters to measure the fractures' directional propagation effect. So, it is better and fuller to use these aforementioned four parameters, which can realize the purpose of the quantitative evaluation. However, the trajectory of the hydraulic fracture is also influenced by the fluid injection parameters, formation mechanical parameters, perforation depth, aperture, and density. All the influencing effect should be studied in the following research work.

5 Conclusion

(1) The accuracy of numerical calculation results calculated using RFPA^{2D}-Flow software is verified by the experimental and theoretical results. It is demonstrated that this software can be used to predict the change of the hydraulic fractures' spatial turning trajectory and deflection distance with the principal stress differences, perforation azimuth, and lengths accurately. The results calculated using this software are not only more consistent with the experimental results than the MEM model based on the micro-element method but can also realize the visualization of the spatial steering process of hydraulic fracture.

(2) Hydraulic fractures' spatial steering trajectory and deflection distance can be two quantitative evaluation indexes to evaluate the directional perforated hydraulic fracture's spatial steering effect. Through the quantitative comparison of these two indexes obtained using laboratory fracturing test and the MEM model, it is proved that these two indexes are accurate, feasible, and reliable.

(3) The variation of the propagation path of the hydraulic fracture under different horizontal principal stress differences, perforation azimuth, and perforation length are almost identical. First, they initiate from the perforation end. Then they slowly deflect toward the direction of the maximum horizontal principal stress. At last, a curved fracture with double wings is presented. The hydraulic fracture deflection distance and its ascending amplitude increase with the decrease in horizontal principal stress difference. Larger perforation azimuth will lead to more deflection and larger deflection distance, and the deflection amplitude will increase first but then decrease. With the perforation length increase, the fracture deflection distance slowly increases, and the deflection amplitude increases first and then decreases. Initiation pressure of hydraulic fracture increases with the decreases in perforation length and the increase in horizontal principal stress difference and perforation azimuth.

Data availability statement

The original contributions presented in the study are included in the article/Supplementary Material; further inquiries can be directed to the corresponding author.

Author contributions

Conceptualization, WL and EB; methodology, WL and LW; formal analysis, WL and CH; investigation, WL and YS; data curation, WL and LS; writing—original draft preparation, WL; writing—review and editing, WL and EB; funding acquisition, WL, EB, and CH. All authors have read and agreed to the published version of the manuscript.

Funding

This work was supported by the Fundamental Research Program of Shanxi Province (No. 20210302124633), the State Key Laboratory Cultivation Base for Gas Geology and Gas Control (Henan Polytechnic University) (No. WS 2021B07), the National Natural Science Foundation of China (No. 52104127), and the Lvliang Platform base construction project (No.2021GCZX-1–46), and Funded by the Research Fund of The State Key Laboratory of Coal Resources and safe Mining, CUMT (No. SKLCRSM22KF012) and Jiangxi Provincial Natural Science Foundation (No. 20212BAB214003).

Conflict of interest

The authors declare that the research was conducted in the absence of any commercial or financial relationships that could be construed as a potential conflict of interest.

Publisher's note

References

Bai, Q. S., Liu, Z. H., Zhang, C., and Wang, F. (2020). Geometry nature of hydraulic fracture propagation from oriented perforations and implications for directional hydraulic fracturing. *Comput. Geotechnics* 125 (4), 103682. doi:10.1016/j.compgeo.2020.103682

Bao, J. Q., Fathi, E., and Ameri, S. (2014). A coupled finite element method for the numerical simulation of hydraulic fracturing with a condensation technique. *Eng. Fract. Mech.* 131, 269–281. doi:10.1016/j.engfracmech.2014.08.002

Bao, J. Q., Fathi, E., and Ameri, S. (2015). Uniform investigation of hydraulic fracturing propagation regimes in the plane strain model. *Int. J. Numer. Anal. Methods Geomech.* 39 (5), 507–523. doi:10.1002/nag.2320

Chen, M. (2013). Re-orientation and propagation of hydraulic fractures in shale gas reservoir. *J. China Univ. Petroleum Nat. Sci. Ed.* 37 (5), 88–94. doi:10.3969/j.issn.1673-5005.2013.05.013

Chen, M., Jiang, H., Zhang, G. Q., and Jin, Y. (2010). The experimental investigation of fracture propagation behavior and fracture geometry in hydraulic fracturing through oriented perforations. *Pet. Sci. Technol.* 28 (13), 1297–1306. doi:10.1080/10916466.2010.483435

Chen, Z. R., Deng, J. G., Zhu, H. Y., Dong, G., Hu, L., and Lin, H. (2013). Research on initiation of oriented perforation fracturing and perforation optimization design method. *Rock Soil Mech.* 34 (8), 2309–2315. doi:10.1007/s00345-014-1381-7

Chen, J. B., Wei, B., and Wang, H. Q. (2017). Influence of directional perforation parameters on fracture propagation. *Fault-Block Oil Gas Field* 24 (3), 391–395. doi:10.6056/dkyqt201703021

Daux, C., Moes, N., Dolbow, J., Sukumar, N., and Belytschko, T. (2000). Arbitrary branched and intersecting cracks with the extended finite element method. *Int. J. Numer. Methods Eng.* 48 (12), 1741–1760. doi:10.1002/1097-0207(20000830)48:12<1741::aid-nme956>3.0.co;2-l

Dong, Z., Tang, S. B., Gamage, R. P., and Lang, Y. (2018). A theoretical model for hydraulic fracturing through a single radial perforation emanating from a borehole. *Eng. Fract. Mech.* 196, S1016654205. doi:10.1016/j.engfracmech.2018.04.029

Dong, Z., and Tang, S. B. (2019). Oriented perforation hydraulic fracture propagation based on the maximum tangential strain criterion. *Rock Soil Mech.* 40 (11), 4543–4553. doi:10.16285/j.rsm.2018.1740

Gehne, S., and Benson, P. M. (2019). Permeability enhancement through hydraulic fracturing: Laboratory measurements combining a 3D printed jacket and pore fluid over-pressure. *Sci. Rep.* 9 (1), 12573–12611. doi:10.1038/s41598-019-49093-1

Guo, T. K., Rui, Z. H., Qu, Z. Q., and Qi, N. (2018). Experimental study of directional propagation of hydraulic fracture guided by multi-radial slim holes. *J. Petroleum Sci. Eng.* 166, 592–601. doi:10.1016/j.petrol.2018.03.102

Guo, T. K., Tang, S. J., Liu, S., Liu, X., Xu, J., Qi, N., et al. (2020). Physical simulation of hydraulic fracturing of large-sized tight sandstone outcrops. *SPE J.* 1 (26), 372–393. doi:10.2118/204210-pa

He, Y. W., Cheng, S. Q., Rui, Z. H., Qin, J., Fu, L., Shi, J., et al. (2018). An improved rate-transient analysis model of multi-fractured horizontal wells with non-uniform hydraulic fracture properties. *Energies* 11 (2), 393. doi:10.3390/en11020393

He, F., Zhang, R. X., Kang, T. H., and Zhang, X. (2020). Dynamic propagation model for oriented perforation steering fracturing cracks in low permeability reservoirs based on microelement method. *Chin. J. Rock Mech. Eng.* 39 (4), 782–792. doi:10.1016/j.jngse.2019.103105

Hossain, M. M., Rahman, M. K., and Rahman, S. S. (2020). Hydraulic fracture initiation and propagation: Roles of wellbore trajectory, perforation and stress regimes. *J. Petroleum Sci. Eng.* 27 (3), 129–149. doi:10.1016/s0920-4105(00)00056-5

Hu, Y. J., Chen, G. L., Cheng, W. P., and Yang, Z. (2014). Simulation of hydraulic fracturing in rock mass using a smeared crack model. *Comput. Struct.* 137, 72–77. doi:10.1016/j.compstruc.2013.04.011

Hunsweck, M. J., Shen, Y. X., and Lew, A. J. (2013). A finite element approach to the simulation of hydraulic fractures with lag. *Int. J. Numer. Anal. Methods Geomech.* 37 (9), 993–1015. doi:10.1002/nag.1131

Jiang, H., Chen, M., Zhang, G. Q., Jin, Y., Zhao, Z., and Zhu, G. (2009). Impact of oriented perforation on hydraulic fracture initiation and propagation. *Chin. J. Rock Mech. Eng.* 28 (7), 1321–1326. doi:10.3321/j.issn:1000-6915.2009.07.004

Jiang, H., Liu, S. J., He, B. S., Chen, M., and Zhang, G. Q. (2014). Experiments of the oriented perforating impact on the multi-fracture pattern of hydraulic fracturing treatment. *Nat. Gas. Ind.* 34 (2), 66–70. doi:10.3787/j.issn.1000-0976.2014.02.010

Li, L. C., Yang, T. H., Liang, Z. Z., Wancheng, Z., and Chunan, T. (2011). Numerical investigation of groundwater outbursts near faults in underground coal mines. *Int. J. Coal Geol.* 85 (3-4), 276–288. doi:10.1016/j.coal.2010.12.006

Liu, L. Y., Li, L. C., Elsworth, D., Zhi, S., and Yu, Y. (2018). The impact of oriented perforations on fracture propagation and complexity in hydraulic fracturing. *Processes* 6 (11), 213. doi:10.3390/pr6110213

Lu, W. Y., Wang, Y. L., and Zhang, X. (2020). Numerical simulation on the basic rules of multi-hole linear codirectional hydraulic fracturing. *Geofluids* 2020 (1), 1–14. doi:10.1155/2020/6497368

Lu, W. Y., Huang, B. X., Chen, S. L., and Huang, B. (2020). Experimental verification of the water-methane displacement effect in gassy coal. *Int. J. Oil Gas Coal Technol.* 23 (1), 126–141. doi:10.1504/ijogct.2020.10026582

Lu, W. Y., and He, C. C. (2021). Numerical simulation of the laws of fracture propagation of multi-hole linear co-directional hydraulic fracturing. *Energy Explor. Exploitation* 39 (3), 903–926. doi:10.1177/0144598721988993

Lu, W. Y., and He, C. C. (2021). Quantitative evaluation indexes of the spatial steering effect of directional perforation hydraulic fractures. *Energy Explor. Exploitation* 39 (4), 1246–1261. doi:10.1177/01445987211010266

Lu, W. Y., and Huang, B. X. (2020). Mathematical model of methane driven by hydraulic fracturing in gassy coal seams. *Adsorpt. Sci. Technol.* 38 (3-4), 127–147. doi:10.1177/0263617420919247

Moës, N., and Belytschko, T. (2002). Extended finite element method for cohesive crack growth. *Eng. Fract. Mech.* 69 (7), 813–833. doi:10.1016/s0013-7944(01)00128-x

Nandlal, K., and Weijermars, R. (2019). Impact on drained rock volume (DRV) of storativity and enhanced permeability in naturally fractured reservoirs: Upscaled field case from hydraulic fracturing test site (hfts), wolfcamp formation, midland basin, west Texas. *Energies* 12 (20), 3852. doi:10.3390/en12203852

Ogata, S., Yasuhara, H., Kinoshita, N., and Kishida, K. (2020). Coupled thermal-hydraulic-mechanical–chemical modeling for permeability evolution of rocks through fracture generation and subsequent sealing. *Comput. Geosci.* 7 (7), 1845–1864. doi:10.1007/s10596-020-09948-3

Qi, M. H., Li, M. Z., Guo, T. K., Liu, C., Gao, S., and Tang, S. (2018). Influence of oriented perforation design on refracture reorientation: Simulation and experiment. *J. Energy Resour. Technol.* 140 (8), 82903. doi:10.1115/1.4039742

Romero, J., Mack, M. G., and Elbel, J. L. (1995). “Theoretical model and numerical investigation of near-wellbore effects in hydraulic fracturing,” in SPE Annual Technical Conference and Exhibition:Drilling and Completion, Houston, USA, October 1995 (Houston, TX: Society of Petroleum Engineers).

Sepehri, J., Soliman, M. Y., and Morse, S. M. (2015). Application of extended finite element method (XFEM) to simulate hydraulic fracture propagation from oriented perforations. *Soc. Petroleum Eng.* 1 (3), 173342. doi:10.2118/SPE-173342-MS

Sesetty, V., and Ghassemi, A. (2015). A numerical study of sequential and simultaneous hydraulic fracturing in single and multi-lateral horizontal wells. *J. Pet. Sci. Eng.* 132, 65–76. doi:10.1016/j.petrol.2015.04.020

Shi, J. H., Li, Q. C., Li, Q., and Cheng, Y. F. (2020). Factors affecting reorientation of hydraulically induced fracture during fracturing by oriented perforations in shale reservoirs. *China Sci.* 15 (5), 528–536.

Sukumar, N., Moës, N., Moran, B., and Belytschko, T. (2000). Extended finite element method for three-dimensional crack modelling. *Int. J. Numer. Methods Eng.* 48 (11), 1549–1570. doi:10.1002/1097-0207(20000820)48:11<1549::aid-nme955>3.0.co;2-a

Tang, S. B., Liu, X. J., Luo, J., and Dong, Z. (2017). Theoretical model for tensile and shear crack initiation at the crack tip in rock subjected to hydraulic pressure. *Chin. J. Rock Mech. Eng.* 36 (9), 2124–2135. doi:10.13722/j.cnki.jrme.2017.0114

Wang, X. M., Chen, P., Rui, Z. H., and Jin, F. (2017). Modeling friction performance of drill string torsional oscillation using dynamic friction model. *Shock Vib.* 2017, 1–14. doi:10.1155/2017/4051541

Wang, X. L., Shi, F., Liu, C., Lu, D., Liu, H., and Wu, H. (2018). Extended finite element simulation of fracture network propagation in formation containing frictional and cemented natural fractures. *J. Nat. Gas Sci. Eng.* 15 (5), 528–536. doi:10.1016/j.jngse.2017.12.013

Wang, B., Zhou, F. J., Wang, D. B., Liang, T., Yuan, L., and Hu, J. (2018). Numerical simulation on near-wellbore temporary plugging and diverting during refracturing using XFEM-Based CZM. *J. Nat. Gas. Sci. Eng.* 55, 368–381. doi:10.1016/j.jngse.2018.05.009

Zhang, G. Q., and Chen, M. (2010). Dynamic fracture propagation in hydraulic re-fracturing. *J. Petroleum Sci. Eng.* 70 (3-4), 266–272. doi:10.1016/j.petrol.2009.11.019

Zhang, G. Q., and Chen, M. (2010). The relationship between the production rate and initiation location of new fractures in a refractured well. *Pet. Sci. Technol.* 28 (7), 655–666. doi:10.1080/10916460902804564

Zhang, R. X., Zhang, X. Y., Kang, T. H., and He, F. (2020). Dynamic fracture propagation model for oriented perforation steering fracturing in low permeability reservoir based on microelement method. *J. Nat. Gas Sci. Eng.* 74, 103105. doi:10.1016/j.jngse.2019.103105

Zhu, W. C., and Tang, C. A. (2004). Micromechanical model for simulating the fracture process of rock. *Rock Mech. Rock Eng.* 37 (1), 25–56. doi:10.1007/s00603-003-0014-z

Zhun, H. Y., Deng, J. G., Jin, X. C., Hu, L., and Luo, B. (2015). Hydraulic fracture initiation and propagation from wellbore with oriented perforation. *Rock Mech. Rock Eng.* 48 (2), 585–601. doi:10.1007/s00603-014-0608-7

frontiers | Frontiers in Earth Science

TYPE Original Research
PUBLISHED 04 January 2023
DOI 10.3389/feart.2022.1029946

OPEN ACCESS

EDITED BY
Hongtu Zhang,
Henan Polytechnic University, China

REVIEWED BY
Feng Du,
China University of Mining and Technology, Beijing, China
Zhibo Zhang,
University of Science and Technology Beijing, China
Chaojun Fan,
Liaoning Technical University, China

*CORRESPONDENCE
Yu Wang,
xhwangyu@yeah.net

SPECIALTY SECTION
This article was submitted to Economic Geology,
a section of the journal
Frontiers in Earth Science

RECEIVED 28 August 2022
ACCEPTED 22 September 2022
PUBLISHED 04 January 2023

CITATION
Yang H, Wang Y, Dai Y, Zhang J and Chen G (2023), On the acoustic attenuation characteristics of sonar detection in the salt-cavern gas storage environment.
Front. Earth Sci. 10:1029946.
doi: 10.3389/feart.2022.1029946

On the acoustic attenuation characteristics of sonar detection in the salt-cavern gas storage environment

Haiyan Yang[1], Yu Wang[1,2]*, Yao Dai[1], Junfu Zhang[1] and Gang Chen[1]

[1]School of Mechanical Engineering, Xihua University, Chengdu, Sichuan, China, [2]School of Automation Engineering, University of Electronic Science and Technology of China, Chengdu, Sichuan, China

Aiming at the acoustic attenuation in the salt-cavern environment, this paper established a theoretical relationship of the ultrasonic attenuation in the salt-cavern gas storage, based on the wave equation of the acoustic wave propagating in a non-ideal medium, and considering the specific environment of gas storage, and analyzes how the wall roughness of the gas storage affects the acoustic attenuation. The results show that the inner wall roughness of the salt-cavern gas storage has an effect on the acoustic attenuation. The inner wall surface is at the solid-liquid interface, where the change of the medium will affect the attenuation of the acoustic wave, and the effective reflection coefficient of the inner wall will cause the acoustic wave to attenuate at a lower frequency. On this basis, the characteristics of insoluble particles in the salt-cavern gas storage were also studied, and the main components of different media in salt-cavern cavities and the diameter distribution of different particles were obtained, and an experimental platform was established. According to the experimental results, the roughness of a reflective surface significantly affects the attenuation coefficient of the acoustic wave, and the acoustic wave will suffer two energy losses on a rough wall surface. In addition, the insoluble particles also affect the acoustic attenuation significantly, and scattering attenuation increases with the particle size. The research conclusions provide theoretical basis for the variation characteristics of ultrasonic attenuation with the environmental medium and ultrasonic excitation frequency of the salt-cavern gas storage.

KEYWORDS

salt-cavern gas storage, sonar detection, acoustic attenuation, wall roughness, insoluble particles

Introduction

With the world vigorously implementing strategic energy reserves, storing resources like oil or natural gas in natural or artificially modified underground storage groups or surface storage tanks should be one of the effective ways to respond to this strategy. At present, most of the underground storage groups are salt-cavern-type underground gas storages. The underground gas storages are mainly located in underground rock formations with extremely low porosity, permeability and stable mechanical properties such as salt rocks (Zhang et al. 2021). Rock salt is internationally recognized as the optimal place to stockpile energy sources (Liang, 2004), which has become an important development direction of underground natural gas storage in the future (Wu et al., 2019). The data shows that the main risks of safe operation of the gas storage are: wellhead normalization under pressure (Zhao, 2019) wellhead gas leakage (Zhao et al., 2020), internal cavity creep and collapse caused by frequent gas injection and production (Ma et al., 2021). Therefore, salt-cavern gas storage requires regular safety exploration and evaluation on the shapes of the cavities (Pfeifle et al., 1998). A salt-cavern gas storage has a complex internal environment and is located at a deep underground position, so it cannot be detected or observed with conventional detection methods. The internal environment of salt cavern gas storage is extremely complex and far from the bottom, acoustic wave is one of the best carriers for long-distance transmission in complex media, and has been proved to be an effective way to detect the shape of salt cavern gas storage. It is a challenge to obtain the shape of the salt cavern in real-time through the variation characteristics of acoustic attenuation in the gas storage medium.

Some scholars have studied the effects of reflection wall roughness on the scattering field and coherent field of acoustic waves through simulation methods, and obtained the statistical distribution information on the amplitude of the scattering field of acoustic waves (Ogilvy, 1988), but the applicability of the calculation results is limited by the valid range of Kirchhoff approximation. The propagation process of ultrasonic waves in a salt-cavern gas storage is complex, involving the interactions between ultrasonic waves and insoluble particles (Liu, 2019; Zhou et al., 2017), the reflection and transmission of vertically incident acoustic waves at the interface between the two media (Tao, 1996), and the changes in the acoustic radiation force of the particles in the liquid medium caused by the changes in the oblique incidence angle of the acoustic wave; (Wang and Zhang, 2018; Fu et al., 2010). Chen et al. (2001) also studied the ultrasonic reflection and transmission of the double rough interfaces; Hutchins et al. (2020) used piezoelectric composite transducers and pulse compression processing technology in their experiments to weaken the attenuation of acoustic signals; Tsuji et al., 2021 built a multiple echo reflection ultrasonic spectroscopy based on the ECAH scattering model; Yu et al., 2020 established the ultrasonic scattering attenuation mechanism of multiple scattering effect by measuring the particle concentration in natural gas hydrate with multi frequency ultrasound, the calculation results show that the multi frequency ultrasonic attenuation method in the range of 1–5 MHz has a good effect on the measurement of liquid concentration; Wang et al., 2020 established the acoustic attenuation expression in the tailings slurry through the acoustic wave equation, which accurately describes the propagation characteristics of the acoustic wave.

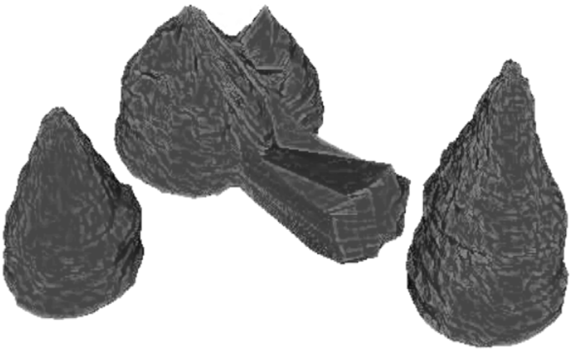

FIGURE 1
Example of multi-topology reconstructed cave in the mining area.

Through review and analysis of the above research, it can be seen that the propagation process of acoustic waves in the salt-cavern environment is relatively complex. To understand the attenuation changes of acoustic waves in this environmental medium, it is necessary to carry out specific analysis according to the actual operational environment of the acoustic wave detection equipment. There are relatively few studies on acoustic attenuation in gas storages. Therefore, it is urgent to study the effects of the topographic characteristics of salt-cavern gas storages on ultrasonic attenuation, so as to provide theoretical basis for the accuracy of sonar detection.

In this paper, based on the specific environment of the gas storage, the theoretical relationship of the ultrasonic attenuation in the salt-cavern gas storage was established, and the effects of wall roughness and insoluble particles on the acoustic attenuation were also studied in detail, and through an experiment, the characteristics of ultrasonic attenuation with the changes in the salt-cavern gas storage environment were verified.

Analysis of the complex salt-cavern environment

The cavities in salt caverns are usually built by injection of fresh water and drainage of brine, and the final salt-cavern gas storage formed is shown in Figure 1, the single volume is required

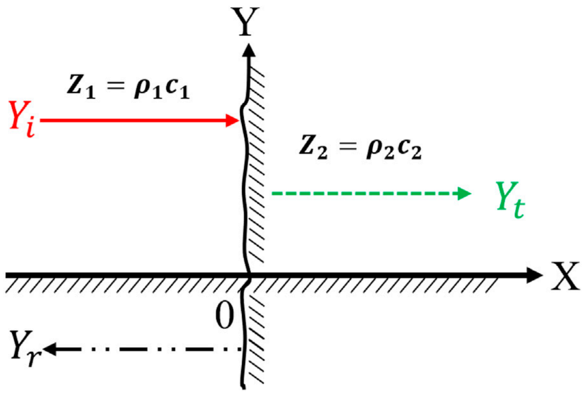

FIGURE 2
Schematic diagram of sound wave incidence under non-ideal conditions.

to be more than 80000 m^3 usually. The method will dissolve the soluble salt and other media in the cavities of the salt cavern, resulting in changes in the water-solid interface of the cavity. Generally speaking, brine contains large amount of soluble salts, which change in the vertical direction of the cavities (Jiang et al., 2014). Due to the high density of brine and its flowing, the brine often contains a large amount of insoluble particles, which leads to complexity and uncertainty in the propagation of acoustic waves in the medium, so it is necessary to carefully study and accurately understand the attenuation characteristics of the acoustic waves in the brine medium.

The detection targets inside the gas storage are mainly the walls of the gas storage and the changes in the distances between the sonar detection equipment and the walls of the gas storage. Due to the different solubility of different salt minerals in the gas storage formed by brine mining, the wall roughness of the gas storage has a great impact on the sonar detection (Wen et al., 2012).

Study on the effects of rough walls on acoustic attenuation

In this paper, the approximate three-dimensional modeling of the salt cavern was carried out using the parametric surface, and the wall surfaces of the salt cavern with different roughness were obtained. The rough surfaces of the three-dimensional model were constructed by the following double sum function:

$$f(x,y) = \sum_{m=-M}^{M} \sum_{n=-N}^{N} a(m,n) \cos\left(2\pi(mx+ny) + \phi(m,n)\right) \tag{1}$$

where, x and y are the spatial coordinates; m and n are the spatial frequencies; $a(m,n)$ is the gradually decreasing amplitude following some distribution; $\phi(m,n)$ is the phase angle function, where the phase angle ϕ will be sampled from a function with a uniform random distribution between -π/2 and π/2. $a(m,n)$ is calculated as follows:

$$a(m,n) = \frac{1}{|m^2+n^2|^{\beta}} = \frac{1}{(m^2+n^2)^{\frac{\beta}{2}}} \tag{2}$$

where, β represents the speed of high frequency attenuation, which controls the changes in the surface roughness.

When the frequency of the detected acoustic wave is high enough, on the irradiated interface of the local acoustic wave, as shown in Figure 2, the problem can be approximately regarded as a wave scattering problem with a large-scale uneven surface (Wen et al., 2012). Considering the calculation of the scattering field by Kirchhoff approximation, the concept of the effective reflection coefficient was introduced in this paper. Through the effective reflection coefficient, the walls of the salt cavern and the medium in it can form a whole, and the sound field computation model can be established by the acoustic wave transmission and reflection on the walls of the salt cavern.

Due to the concavo-convex surface boundaries of the salt-cavern cavities, the roughness is different at different positions. The sound field can be divided into two parts, with one being the most effective area participating in the formation of the reflected signal, where the acoustic wave will form the coherent component of the reflected signal, and the other being the incoherent component generated by the uneven surfaces of the sound field, which will form the acoustic scattering of the acoustic wave (Wen et al., 2012).

When the acoustic wave is vertically incident and received vertically, the received RMS sound pressure value can be expressed as follows (Wen et al., 2012):

$$\left(\overline{P^2}\right)^{1/2} = \frac{1}{2h}\left[P_0^2 V_{coh}^2 10^{-0.2\alpha h} + P_0^2 \iint_s m_s(\theta,\varphi) 10^{0.2\psi(h,\theta,\varphi)} ds\right]^{1/2} \tag{3}$$

where, P_0 is the sound pressure incident on the cavity wall; V_{coh} the coherent reflection coefficient; α the absorption coefficient; m_s the surface scattering coefficient; and h is the distance between the transducer and the cavity wall.

The maximum irradiated area of the scattering surface is determined by the directional effective half-opening angle θ_0 of the transducer, which can be obtained according to the relationship between the transmitted sound intensity and the received sound intensity:

$$P_e = \left(\frac{V_e}{2h}\right)^2 P_b 10^{0.2ah} \tag{4}$$

where, P_b is the transmitted sound intensity; P_e the received sound intensity; and V_e the effective reflection coefficient; therefore, the effective reflection coefficient can be expressed and defined as follows according to the previous analysis and assumption:

$$V_e^2 = \left[V_{coh}^2 + \iint_s m_s(\theta,\varphi) 10^{0.2\alpha\left(h-\psi(h,\theta,\varphi)\right)} ds \right] \tag{5}$$

In general, the scattering coefficient $m_s(\theta,\varphi)$ is isotropic in the horizontal direction, so the above formula can be simplified as:

$$V_e^2 = \left[V_{coh}^2 + 4\pi \int_0^{\theta_0} m_s(\theta) 10^{0.2\alpha h\left(1-\frac{1}{\cos\theta}'\right)} \cos\theta \sin\theta d\theta \right] \tag{6}$$

If the effective opening angle θ_0 of the transducer is small, there is:

$$V_e^2 = \left[V_{coh}^2 + 4\pi \int_0^{\theta_0} m_s(\theta) \cos\theta \sin\theta d\theta \right] \tag{7}$$

According to the scattering field theory:

$$V_{coh}^2 = V e^{\left(-\frac{1}{2}p^2\right)} \tag{8}$$

where, V is the interface reflection coefficient; $P = 2k\sigma\cos\theta$, where p is the Rayleigh parameter; $k = 2\pi/\lambda$; σ the variance of the surface unevenness; θ the incident angle of the wave; at this time, the unevenness distribution and its correlation coefficient are Gaussian. At normal incidence, the reflection coefficient V is:

$$V = \frac{\rho_2 C_2 - \rho_1 C_1}{\rho_2 C_2 + \rho_1 C_1} \tag{9}$$

where, ρ_1 and C_1 are the density and sound speed of medium 1, respectively; and ρ_2 and C_2 are the density and sound speed of medium 2, respectively.

When the wall surface of the salt-cavern gas storage is gently undulating, the scattering coefficient of the small-scale uneven surface can be expressed with the Kirchhoff approximation:

$$m_s(\theta) = \frac{r^2}{8\pi \tan^2\delta \cos^4\theta} e^{\left(\frac{-\tan^2\theta}{2\tan^2\delta}\right)} \tag{10}$$

where, $\tan^2\theta$ is the root mean square value of the inclination angle of the unevenness. Assuming that the unevenness of the reflecting surface is Gaussian, there is:

$$V_{incoh} = V\left[1 - e^{\left(\frac{-\tan^2\theta_0}{2\tan^2\delta}\right)}\right] \tag{11}$$

Through Eqs 10, 11, the relationship between the effective reflection coefficient and the actual one can be obtained:

$$V_e = V\left[e^{\left(-\frac{4\pi\sigma}{c_0}\right)} + \left(1 - e^{\left(\frac{-\tan^2\theta_0}{2\tan^2\delta}\right)}\right)\right]^{1/2} \tag{12}$$

It can be seen from the above formula that, the effective reflection coefficient of the acoustic wave is related to the frequency of the acoustic wave and the root mean square of the inclination angle of the rock wall unevenness. In order to study the direct relationships between the three, the effective reflection coefficient was calculated using MATLAB. Take the sonar detector parameters currently used in Jintan, Jiangsu Province, China as an example, let the frequency of the acoustic wave be 500 KHz–4 MHz, the actual reflection coefficient 1, the root mean square of the inclination angle 0.4, 0.5, 0.6 and 0.7, the sound speed 1400 m/s, 1500 m/s, 1600 m/s and 1700 m/s, the emitted sound intensity 100 dB, and the variance of the unevenness of the rock wall 10^{-3}. The calculation results of the effect of the effective reflection coefficient are shown in Figure 3.

It can be seen from Figure 3 that when the sound speed was 1400 m/s, at the acoustic wave frequency of about 500 kHz, the effective reflection coefficient decreased with the increase of frequency; at a frequency between 500 kHz and 4 MHz, the effective reflection coefficient decreased with the root mean square of the inclination angle increasing; and at a frequency above 500 kHz, the increase of the acoustic wave frequency will not affect the effective reflection coefficient, indicating that when the acoustic wave frequency increases to a certain value, the reflected energy of the acoustic wave will not be affected by the frequency. It can be seen from Figures 4, 5 that the higher the sound speed, the greater the effective reflection coefficient, and the higher the sound intensity of the acoustic echo.

Physical properties of insoluble particles

The cavities in salt caverns are usually built by injection of fresh water and drainage of brine. This method will dissolve the soluble salt and other media in the cavities of the salt cavern, resulting in changes in the water-solid interface of the cavity. Generally speaking, brine contains large amount of soluble salts, which change in the vertical direction of the cavities (Jiang et al., 2014). Due to the high density of brine and its flowing, the brine often contains a large amount of insoluble particles, which leads to complexity and uncertainty in the propagationof acoustic waves in the medium, so it is necessary to study how the insoluble particles affect the attenuation characteristics of the acoustic waves in the brine medium.

When the diameter of the insoluble particles is small, the particles are usually cubic or spherical. When the particle diameter increases to a certain value, the shape of the particles gradually becomes irregular, often with a honeycomb structure. The larger the particle diameter is, the more obvious the honeycomb structure and the rougher the particle surfaces will be, and the stronger the scattering of acoustic waves will be (Shi, 2015). The actual physical forms of insoluble

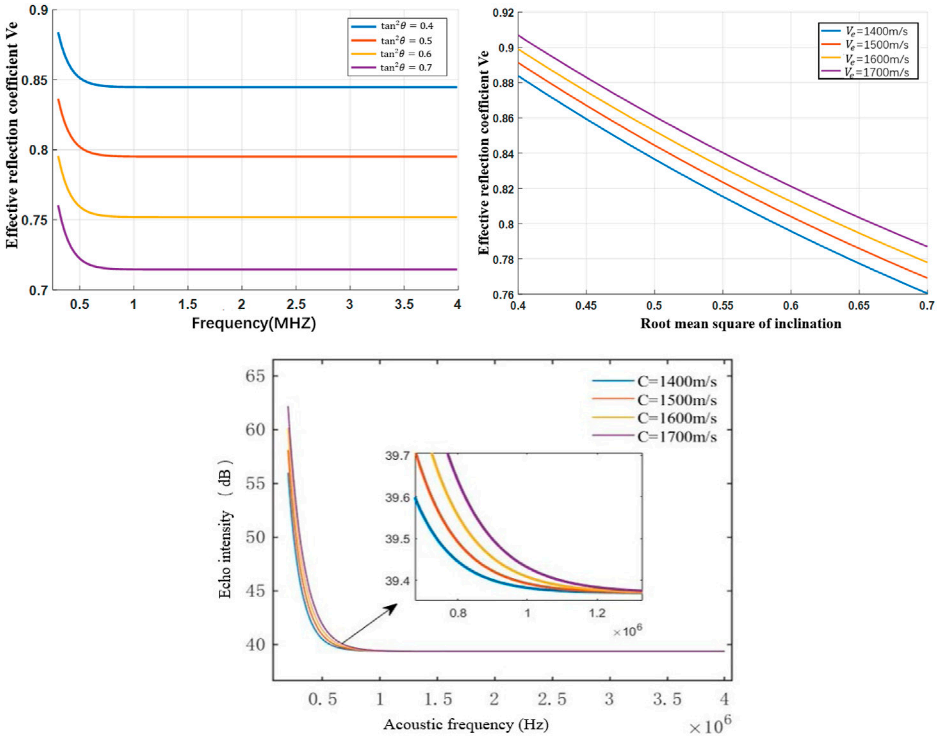

FIGURE 3
Relationship between sound frequency and echo intensity at different sound speeds.

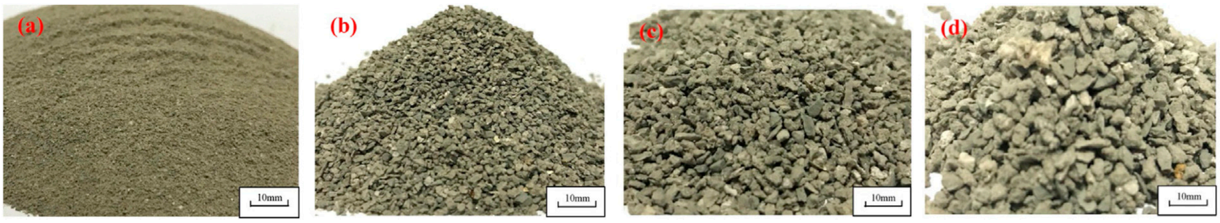

FIGURE 4
Physical images of insoluble particles in salt cavern gas storage with different diameters. **(A)** (<0.5 mm); **(B)** (0.5–1.0 mm); **(C)** (1.0–2.0 mm); **(D)** (2.0–3.0 mm).

particles in a salt-cavern gas storage are shown in Figure 4 (Li et al., 2021).

It can be seen from Table 1 that the diameters of insoluble particles are mainly concentrated between 0.25 mm and 10 mm, and the particle porosity increases with the increase of the diameter.

In this paper, Jintan gas storage in Zhejiang was taken as the object, where the related parameters of insoluble particles were investigated and analyzed. The investigation results are shown in Table 1.

Experimental study

Experimental setup and materials

In order to simulate the propagation process of acoustic waves in the complex environment of the salt-cavern gas storage, an experimental platform was built, as shown in Figure 5, which was used to drive the ultrasonic transducer to transmit and receive acoustic waves through the

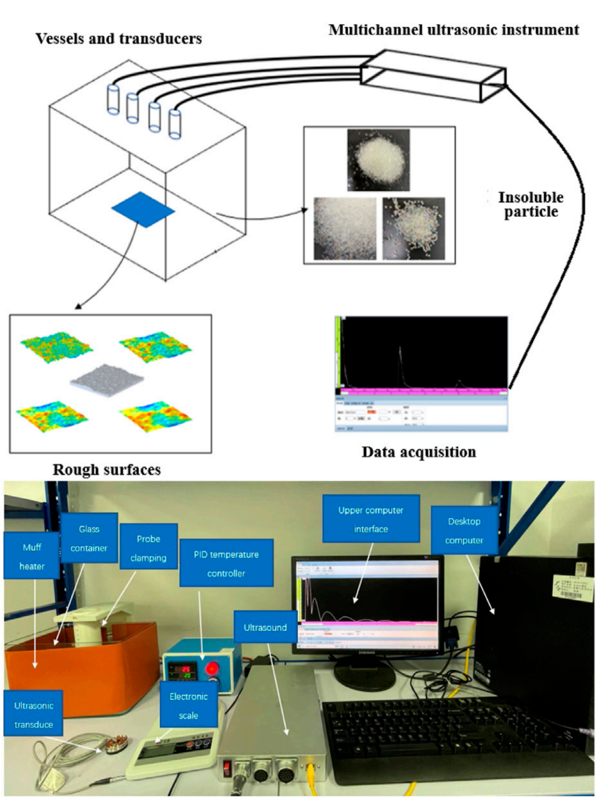

FIGURE 5
Overall experimental platform and schematic diagram.

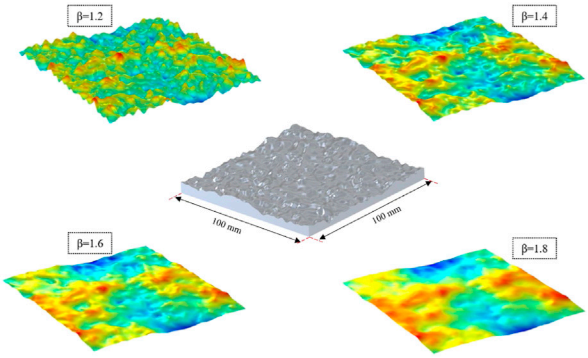

FIGURE 6
3D models of four different rough surfaces.

ultrasonic instrument. The acoustic data were obtained through external equipment. The experimental data were recorded, and finally processed. External heating equipment and foam were used to thermally insulate the container to ensure that the experimental temperature would not change near the set value, so as to study the changes in acoustic attenuation.

The measurement of the ultrasonic attenuation coefficient was obtained by calculating the relationship between the two ultrasonic wave amplitudes and the acoustic propagation distance according to the following formula:

$$\alpha = -\frac{\ln(E/E_0)}{L} \tag{13}$$

where, E_0 is the first acoustic wave amplitude (V); E the second acoustic wave amplitude (V); L the distance (m) from the ultrasonic transducer to the reflection wall, which is a fixed value; the two acoustic wave amplitudes can also be measured through experiments. With the above formula, the attenuation coefficient (V/m) of the acoustic wave can be calculated.

With Eq. 2, a 3D models with 4 different rough surfaces was established in the 3D software, as shown in Figure 6, and also 3D printed, as shown in Figure 7. The size of the experimental model was 100 mm × 100 mm × 17 mm. Since the roughness of the model surfaces cannot be accurately defined, the factor β was used in this paper to control the changes in the surface roughness.

As can be seen from Figures 6, 7, with β increasing, the surface of the model becomes smoother. In the actual environment, the acoustic wave reflection wall is almost a rough one. At present, the roughness cannot be defined by 3D

TABLE 1 Jintan insoluble particle distribution table.

Particle size/mm	Mass content/%	Cumulative content/%	Bulk density/(g/cm^3)	Porosity/%
>20	19.33	100	0.64	73.59
10–20	6.33	80.67	0.7	71.31
4.75–10	10.42	74.33	0.72	70.42
2–4.75	25.58	63.92	0.88	63.9
1–2	11.42	38.33	0.93	61.76
0.5–1	9.75	26.92	0.96	60.83
0.25–0.5	11.58	17.17	1.01	58.54
0.074–0.25	4.92	5.58	1.01	58.6
<0.074	0.67	0.67	1	59.02

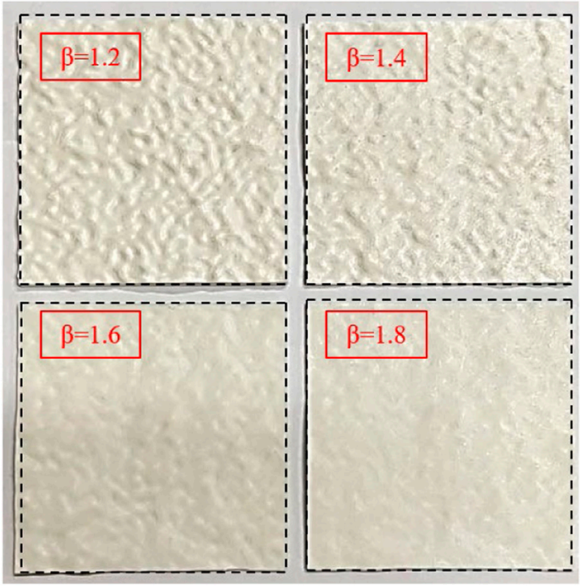

FIGURE 7
Four models of 3D printing.

modeling or accurate mathematical formulas. Therefore, in this paper, the fabricated salt-cavern acoustic reflection wall was only for qualitative research, and the 3D model was used to carry out the experiment of the rough acoustic reflection wall surface to study the general variation law of acoustic attenuation on the wall surfaces with different roughness.

According to the survey results in Table 1 above, the diameter of the insoluble particles ranges from 0.25 mm to 10 mm. In this experiment, spherical glass beads as shown in Figure 8 were used as the insoluble particles in the salt cavern, with a diameter of 1 mm, 1.5 mm and 2 mm. The related physical parameters of glass beads are shown in Table 2. As glass beads do not dissolve, whose physical parameters are close to the insoluble particles in a salt cavern, so they can be used as the substitutes in the experiment.

Experimental research on wall roughness

In the experiment, pure water was used as the acoustic propagation medium, with a height of 160 mm, and the distances between the ultrasonic transducer and the reflecting walls were 145 mm, 117 mm, 127 mm, 127 mm, 129 mm, and 114 mm, respectively. The temperature of the solution was measured to be 30°C. According to the existing sold equipment parameters, the excitation voltage of the ultrasonic transducer 150 V, the sampling frequency 2 MHz, the RPF 2 KHz, and the signal gain set according to the specific conditions in the experiment. Mean filtering was performed on the received waveforms. The excitation frequencies of the ultrasonic transducer were 0.5 MHz, 1 MHz, 2 MHz, 3.1 MHz, 4 MHz and 5 MHz, and the obtained operating frequencies of the ultrasonic transducer 0.5 MHz, 1 MHz, 2 MHz, 3.1 MHz, 4 MHz and 5 MHz, respectively. The average of multiple measurements was taken, with the measurement results shown in Figure 9.

It can be seen from Figure 9 that the roughness of the reflective surface had a great effect on the acoustic attenuation coefficient, in which the acoustic frequency was the main influencing factor. As the roughness of the reflecting surface increased, the acoustic attenuation coefficient tended to increase. The acoustic attenuation coefficient of each reflecting wall differed greatly at 1 MHz, and less at 5 MHz. The experimental measurements were carried out on reflecting surfaces with different roughness using different acoustic frequencies. In the same medium environment, the acoustic attenuation coefficients measured at different acoustic frequencies were different. Specifically, the acoustic attenuation coefficient increased with the increase of the acoustic frequency, indicating that the roughness of the reflecting surface has a great impact on the acoustic attenuation coefficient.

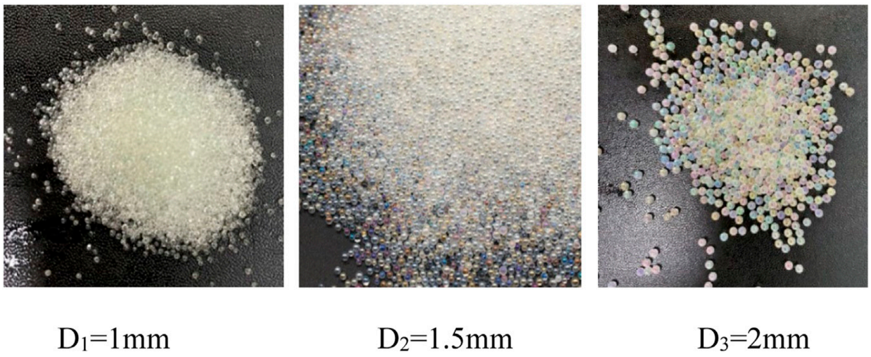

FIGURE 8
Insoluble particle diameter distribution.

TABLE 2 Physical parameters related to glass beads.

Material	Density	Melting point (°C)	Thermal conductivity	Refractive index	Specific heat
SiO_2	2.2 g/cm^3	1723	0.27 W/cm·K	1.6	966 J/Kg°C

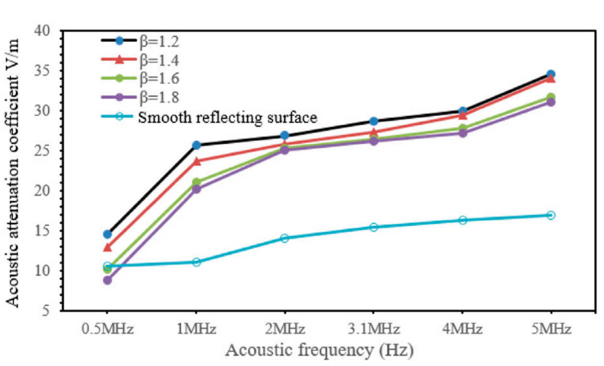

FIGURE 9
Variation of the acoustic attenuation coefficient with the roughness of the reflecting wall.

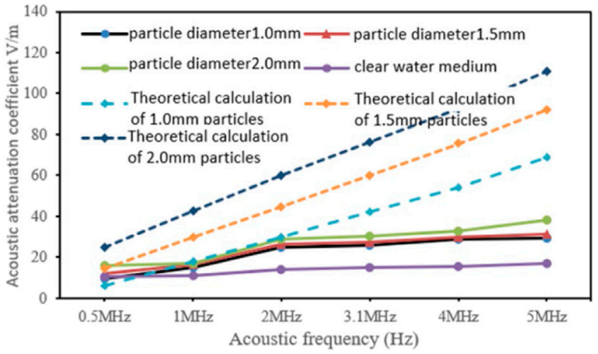

FIGURE 10
Variation of sound wave attenuation coefficient with diameter of insoluble matter.

Effect of insoluble particles on sound attenuation

Glass beads with a diameter of 0.1 mm, 0.15 mm, and 2 mm were placed in the container, and then stirred to make them evenly distributed on the bottom surface of the container. At the same time, the solution temperature was measured to make sure it was 30°C. After the solution temperature was stabilized and the glass beads evenly distributed, the experiment was carried out. The solution was sodium chloride solution with a mass fraction of 2%. In the same way, the parameters of the particles with other diameters were measured. The excitation voltage of the ultrasonic transducer was 150 V, the sampling frequency 2 MHz, and the RPF 2 KHz. The received waveforms were average filtered. The excitation frequency of the ultrasonic transducer was 0.5 MHz, 1 MHz, 2 MHz, 3.1 MHz, 4 MHz and 5 MHz, and the obtained operating frequencies of the ultrasonic transducers were 0.5 MHz, 1 MHz, 2 MHz, 3.1 MHz, 4 MHz, and 5 MHz. The heights of the ultrasonic transducers from the bottom of the containers were 145 mm, 117 mm, 127 mm, 127 mm, 129 mm, and 114 mm, respectively. The time and voltages of the echoes were measured multiple times and averaged, with the measurement results shown in Figure 10.

It can be seen from Figure 10 that, after the particles were added, the acoustic attenuation coefficient increased significantly. At the same acoustic frequency, the larger the particle diameter, the stronger the acoustic scattering, and the larger the acoustic attenuation coefficient, indicating that the particle diameter has a positive correlation with the acoustic attenuation coefficient; with the same particle diameter, the higher the acoustic frequency, the greater the acoustic attenuation coefficient, indicating that the acoustic frequency and the particle diameter have obvious effects on the acoustic attenuation coefficient of the sodium chloride solution with the same concentration and temperature. When the acoustic frequency was high, the difference between the experimental result and the theoretical calculation was large. The reason is that in the acoustic attenuation experiment of insoluble particles, the particles were distributed on the bottom surface of the container because they were heavier than the solution, and accordingly, acoustic waves only came into contact with the particles at the bottom of the container and generated the scattering effect, while in the Urick model, the calculation of the scattering attenuation was carried out on the assumption that the particles were uniformly distributed in the solution, and that the acoustic waves interacted with the insoluble particles in the process of emission and reception and generated the scattering effect multiple times instead of generating it only at the bottom of the container.

Conclusion

This paper carried out theoretical analysis on the ultrasonic attenuation in the salt-cavern cavities, focusing on the effects of propagation distance, wall roughness, and insoluble particles on the acoustic attenuation, obtained the relationships between the acoustic frequency, sound speed and effective reflection coefficient, and theoretically verified the feasibility of ground simulation experiments. The main conclusions are as follows:

(1) At the same acoustic frequency, the larger the particle diameter, the stronger the acoustic scattering, and the larger the acoustic attenuation coefficient; the same particle diameter, the higher the acoustic frequency, the greater the acoustic attenuation coefficient.
(2) The roughness of the inner wall surfaces in the salt-cavern gas storage also has an effect on the acoustic attenuation. The inner wall surfaces are at the solid-liquid interface, where the acoustic impedance changes due to the change of the propagation medium; too much difference in acoustic impedance will cause serious attenuation of acoustic waves.

Data availability statement

The original contributions presented in the study are included in the article/Supplementary Material, further inquiries can be directed to the corresponding author.

Author contributions

Al authors listed have made a substantial, direct, and intellectual contribution to the work and approved it for publication.

Conflict of interest

The authors declare that the research was conducted in the absence of any commercial or financial relationships that could be construed as a potential conflict of interest.

Publisher's note

References

Chen, Z. Q., Mei, L., Wang, Y. W., Chen, L. G., and Ni, C. L. (2001). Reflection and transmission of ultrasonic waves from double rough surfaces. *J. Mech. Strength* (01), 98–101.

Fu, W. H., Jin, T., and Tian, X. P. (2010). A finite element model of sound propagation in regions with non-uniform temperature. *J. Fudan Univ. Nat. Sci.* 49 (01), 132–136.

Hutchins, D. A., Watson, R. L., Davis, L. A. J., Akanji, L., Billson, D. R., Burrascano, P., et al. (2020). Ultrasonic propagation in highly attenuating insulation materials. *Sensors* 20 (8), 2285. doi:10.3390/s20082285

Jiang, D. Y., Yi, L., Chen, J., Ren, S., Zhang, J. W., and Li, Y. P. (2014). Similar experiment of the concentration field in layered salt-rock cavity in construction period. *J. Sichuan Univ. Eng. Sci. Ed.* 05 (033), 14–21.

Li, P., Li, Y., Shi, X., Zhao, K., Liu, X., Ma, H., et al. (2021). Prediction method for calculating the porosity of insoluble sediments for salt cavern gas storage applications. *Energy* 221 (8), 119815. doi:10.1016/j.energy.2021.119815

Li, Y. P., Shi, X. L., Liu, W., Wang, B. W., Ma, X. Q., and Yang, C. H. (2016). Motion of insoluble subsidence during leaching sump for salt cavern storage. *Chin. J. Rock Mech. Eng.* 35 (01), 23–31.

Liang, W. G. (2004). *Study on multi-field coupling theory and its application of hydraulic fracturing and solution mining for salt deposits*. Taiyuan, China: Taiyuan University of Technology.

Liu, J. (2019). *Propagation characteristics of ultrasound in non-uniform gas-solid two-phase medium*. Nanjing, China: Nanjing University of Science & Technology.

Ma, X. Q., Xu, Z. J., Chen, L. P., and Shi, X. L. (2021). Creep deformation analysis of gas storage in salt caverns. *Int. J. Rock Mech. Min. Sci.* 139, 104635. doi:10.1016/j.ijrmms.2021.104635

Ogilvy, J. A. (1988). Computer simulation of acoustic wave scattering from rough surfaces. *J.phys.d Appl.phys* 21 (2), 260–277. doi:10.1088/0022-3727/21/2/006

Pfeifle, T. W., Brodsky, N. S., Munson, D. E., and Munson, D. (1998). Experimental determination of the relationship between permeability and microfracture-induced damage in bedded salt. *Int. J. Rock Mech. Min. Sci.* 35 (4–5), 593–594. doi:10.1016/s0148-9062(98)00058-8

Shi, L. Y. (2015). *Acoustic measurements of the water column suspended particles*. Hangzhou, China: Zhejiang University.

Tao, X. D. (1996). Reflection and transmission of sound wave perpendicular to the interface between two media. *Mod. Phys. Knowl.* (S1), 55–56.

Tsuji, K., Nakanishi, H., and Norisuye, T. (2021). Viscoelastic ECAH: Scattering analysis of spherical particles in suspension with viscoelasticity. *Ultrasonics* 115, 106463. doi:10.1016/j.ultras.2021.106463

Wang, J. X., and Cheng, J. H. (2020). Research on relationship between tailings slurry concentration and ultrasonic attenuation coefficient. *Industrial Mine Automation* 6 (2), 5.

Wang, Y., and Zhang, X. F. (2018). Acoustic radiation force of a fluid cylindrical particle in obliquely incident plane wave. *J. Shaanxi Normal Univ. Sci. Ed.* 46 (5), 51–55.

Wen, W., Chen, J., and Wang, Y. (2012). Research on the technology of three-dimensional surface topological reconstruction of salt caverns supported by 3D GIS [J]. *Land Resour. Inf.*

Wu, Z. D., Zheng, D. W., Li, D. G., and Deng, X. J. (2019). Feasibility study and suggestions on constructing underground gas storage in abandoned mines in China. *Coal Econ. Res.* 39 (5), 15–19.

Yu, H., Tan, C., and Dong, F. (2020). Measurement of particle concentration by multi-frequency ultrasound attenuation in liquid-solid dispersion. *IEEE Trans. Ultrasonics Ferroelectr. Freq. Control* 68 (99), 843–853. doi:10.1109/tuffc.2020.3020361

Zhang, B., An, G. Y., and Liu, T. H. (2021). Prediction of Salt horizon distribution for Pingding salt cavern underground gas storage. *J. Salt Sci. Chem. Industry* 50 (02), 5-9-13.

Zhao, J. (2019). Desulfurization operation technology of underground gas storage containing hydrogen sulfide in North China. *Chem. Eng. oil gas* 48 (06), 1–6.

Zhao, J., Xie, J., Sun, G. H., Song, Y. N., and Zhao, Q. (2020). Operation risks and technical countermeasures of underground gas storage containing hydrogen sulfide in north China. *Storage Transp. Eng.* 39 (03), 56–63.

Zhou, Z. G., Zong, J., Wang, W. G., and Hou, M. Y. (2017). Experimental study on the influence of granular shear deformation on sound propagation. *Acta Phys. Sin.* 66 (15), 192–198.

Frontiers in Earth Science

TYPE Hypothesis and Theory
PUBLISHED 05 January 2023
DOI 10.3389/feart.2022.1026816

OPEN ACCESS

EDITED BY
Guangyao Si,
University of New South Wales, Australia

REVIEWED BY
Junxiang Zhang,
Zhongyuan University of Technology, China
Jingyu Jiang,
China University of Mining and Technology, China
Tao Yang,
North China Institute of Science and Technology, China

*CORRESPONDENCE
Yu Wang,
2471805285@qq.com

SPECIALTY SECTION
This article was submitted to Economic Geology, a section of the journal Frontiers in Earth Science

RECEIVED 24 August 2022
ACCEPTED 13 September 2022
PUBLISHED 05 January 2023

CITATION
Wang Z, Wang Y and Wang F (2023), Influence radius of pressure relief of energy-accumulating blasting and water injection in the heading face of the liangbei coal mine.
Front. Earth Sci. 10:1026816.
doi: 10.3389/feart.2022.1026816

Influence radius of pressure relief of energy-accumulating blasting and water injection in the heading face of the liangbei coal mine

Zhenfeng Wang[1,2], Yu Wang[1]* and Feng Wang[3]

[1]School of Energy Science and Engineering, Henan Polytechnic University, Jiaozuo, China, [2]Yimei Group Postdoctoral Workstation, Yima, China, [3]Henan Xuchang Xinlong Mining Coal, Xuchang, China

This study aims to reasonably determine the influence radius of pressure relief of energy-accumulating blasting and water injection in the Liangbei Coal Mine and effectively eliminate local stress concentration and coal seam outburst risk. The change in gas parameters in each test hole before and after energy-accumulating blasting and water injection is determined through ANSYS/LSDYNA numerical simulation, theoretical analysis and calculation, and the application of the gas parameter method in the 32051 heading face of the Liangbei Coal Mine. The influence radius of pressure relief technology of energy-accumulating blasting and water injection in the Liangbei Coal Mine in the direction of energy-accumulating trough is studied, which provides reliable data for the layout parameters of energy-accumulating blasting and water injection hole in the working face of the Liangbei Coal Mine. The experimental results are as follows: 1) The simulation *via* ANSYS/LSDYNA shows that a blasting cavity is formed by an explosive shock wave in the borehole. The diameter of the blasting cavity in the energy-accumulating direction is 42 cm, which is 10 times the diameter of the energy-accumulating blasting and water injection hole. The diameter of the blasting cavity in the non-energy-accumulating direction is 14 cm, which is 3.3 times the diameter of the energy-accumulating blasting and water injection hole. The stress in the energy-accumulating direction is 2.9 times larger than that in the non-energy-accumulating direction. The crack length in the energy-accumulating direction is 294 cm, and the crack length in the non-energy-accumulating direction is 80 cm. 2) Theoretical analysis and calculation present that the crushing area of shaped charge blasting is 39 cm, the fracture area is 267 cm, and the vibration area is 159 cm. 3) Comparison of the change in gas parameters of each test hole in the field experiment before and after energy-accumulating blasting and water injection indicates that the influence radius of pressure relief in the direction of energy-accumulating trough is 300 cm. 4) The layout of energy-accumulating blasting and water injection in the working face of the Liangbei Coal Mine with 550 cm borehole spacing demonstrates that the verification index of gas drilling decreases, the analytical values (Δh2) decrease from 120–140 Pa to 100–120 Pa, the drilling cutting weight (S) decreases from 3.2 to 4.6 kg/m to 3.0–3.8 kg/m, and stress is released and transferred to deep coal. This study has guiding significance for outburst elimination by local arrangement of energy-gathering blasting and water injection borehole in the working face of the Liangbei Coal Mine.

KEYWORDS

energy-accumulating blasting, water injection, energy-accumulating pipe, gas parameter meter, variation in gas parameters, radius of influence

Introduction

Energy-accumulating blasting is one kind of directional blasting, forming energy-accumulating flow in specific direction to cut coal body, creating large cracks, increasing the permeability of coal body, and eliminating local stress concentration of coal body (Zhai, 2010). Wei found that pressure relief blasting technology can reduce the degree of stress concentration in coal and rock mass and effectively avoid the occurrence of rock burst disasters (Wei et al., 2011). Cao determined that loose blasting can increase the length of pressure relief zone in front of stope (Cao et al., 2013). Dou found that the use of loose blasting in strong impact danger zone can make the peak stress transfer to the deep coal body (Dou et al., 2018). Guo discovered that the superposition effect of stress wave resulted in the formation of uniform pressure zone in the middle section of two blasting holes and its neighborhood (Guo et al., 2020; Guo et al., 2021). Yang used ANSYS/LSDYNA numerical simulation to study the cohesive blasting parameters of the surrounding hole and found that cohesive blasting can enhance the stress superposition on the connecting line of the surrounding hole, and the blasting stress is 1.4 times of that without cohesive tube blasting (Yang et al., 2019). Song used the ANSYS/LSDYNA software to study the concentrated blasting of the same segment with porous structure and found that the cracks mainly expanded along the connection line of blast holes, and the coal between adjacent blast holes was subjected to two blasting actions (Song et al., 2018). The effective influence range of cohesive blasting can be determined by comparing the change in parameters in the test hole (Gao et al., 2019; Guo et al., 2019). Blasting hole spacing has an important influence on the presplitting effect; too small will increase engineering quantity, whereas too large will alter the effect (Zhang et al., 2019). Hua found that when the charge length is fixed, the tangential maximum tensile stress decreases with the increase in hole spacing (Hua et al., 2020). Kim found that the energy transfer efficiency of hydraulic presplitting blasting was higher than that of ordinary presplitting blasting in tunnel excavation and surrounding rock vibration detection (Kim, 2007). Using a superdynamic strain test system, Zong found the advantage of hydraulic blasting by analyzing the stress and strain distribution characteristics of water and air blasting under different uncoupling coefficients (Zong and Luo, 2006). Bingxiang studied the control of water pressure to increase the amount of fracturing and found that with the increase in pressure, detonation cracks continued to expand. Under the action of detonation pressure, the propagation of coal joint cracks extended (Huang et al., 2011; Huang and Li, 2015; Li et al., 2022a; Li et al., 2022b). Wei studied the influence of hydrolyzing coupling charge structure on explosion stress fading and found that the hydrolyzing coupling coefficient of 2.57 is the best coefficient to induce cracking of gun hole (Yuan et al., 2018; Yuan et al., 2019). Low permeability of coal seam and difficult gas drainage, found that dynamic multifield coupling model of gas drainage (Zhang et al., 2021; Zhang et al., 2022). The action mechanism, influence parameters, and blasting results of concentrated energy blasting and hydraulic blasting were studied deeply by the above scholars, but most of them were about deep hole concentrated blasting. Local coal affected by mining and coal pillar will produce local stress concentration area. Few scholars have studied the energy-accumulating blasting and water injection technology, ignoring the effect of the wave energy of adjacent holes in the process of condensed energy detonation of local shallow holes.

Gas parameter meters are used to detect borehole flow, gas concentration, and borehole negative pressure. The pressure relief ring formed by explosive injection of coal, crack propagation in coal, flow rate, and gas concentration in borehole will change. Using a gas parameter meter to compare the numerical changes of borehole flow and gas purity before and after borehole cohesive energy explosion can determine whether the cracks around the borehole expand.

This study aims to reasonably determine the influence radius of energy-accumulating blasting and water injection in the direction of energy-accumulating trough in the Liangbei Coal Mine. Numerical simulation, theoretical analysis, and gas parameter method are used to carry out a field experimental study on the influence radius of energy-accumulating blasting and water injection in the direction of energy-accumulating trough. Reasonable radius parameters of energy-accumulating blasting and water injection in the direction of energy-accumulating trough provide reliable and reasonable data for the layout parameters of local energy-accumulating blasting and water injection holes in the Liangbei Coal Mine.

Engineering background

The elevation height of the 32051 intermediate base entry is -484.61–456.7 m, the buried depth is 568.3–595.5 m, the design

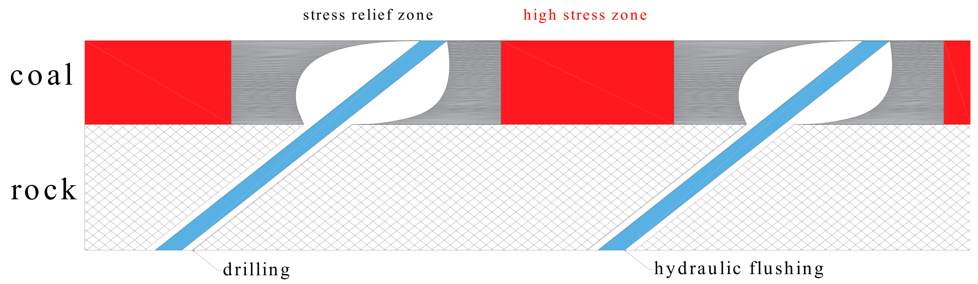

FIGURE 1
Schematic of the hydraulic flushing model.

length is 715.5 m, the average coal seam thickness is 4.5 m, the gas content is 2.41–7.57 m^3/t, the gas pressure is 0–0.8 Mpa, the damage type of coal in mining section 32 is type V, and the gas permeability coefficient of coal seam is between 0.02011 and 0.0472 $m^2/Mpa^2 \cdot d^{-1}$, which is difficult to extract. The consistent coefficient of coal is 0.151–0.33, and the coal quality is soft. The initial velocity of gas release is 16.81–36.8 mmHg. The 32,051 working face in the Liangbei Coal Mine has outburst hazard.

To solve the safety hazard of stress concentration in front of excavation work caused by a small coal pillar during water conservancy measures of the bottom roadway in the Liangbei Coal Mine, a large number of large-diameter outburst elimination boreholes should be constructed in accordance with the coal seam thickness in the excavation face. Lan found that a large number of boreholes can transfer the stress concentration area to the end of pressure relief hole and deep surrounding rock (Liu et al., 2007; Tan, 2011; Liu et al., 2012; Lan et al., 2013). Nevertheless, the amount of drilling is enormous, excessive drilling construction seriously affects the tunneling speed of the excavation face, and the effect of eliminating stress concentration is limited. Serious shortage of drill footage per month occurs, and mining and excavation replacement is seriously affected from both production and safety perspectives (Figure 1).

In consideration of the above factors, directional pressure relief technology of energy-accumulating blasting and water injection in the Liangbei Coal Mine is researched. The influence radius of energy-accumulating blasting and water injection is studied to arrange blasting holes in the working face of the Liangbei Coal Mine reasonably.

Theoretical analysis

In accordance with the failure characteristics of coal, the area affected by energy-accumulating blasting and water injection can be divided into three zones: crushing zone, fracture zone, and blasting vibration zone. Owing to the energy-accumulating effect of the energy-accumulating pipe in the direction of the energy-accumulating trough in energy-accumulating blasting and water injection, the influence range of the energy-accumulating pipe is larger than that of deep hole blasting. In the calculation, a high detonation velocity is used to replace the energy-accumulating effect of the energy-accumulating pipe. The values of each parameter in the formula are shown in the following parameter data table.

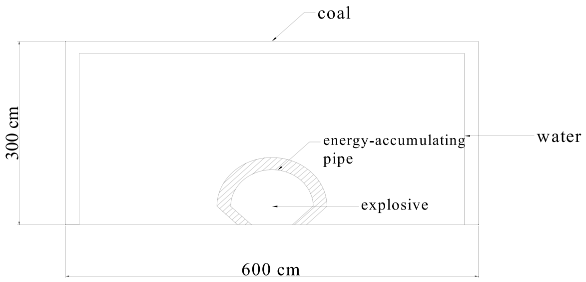

FIGURE 2
Schematic of the energy-accumulating blasting and water injection model.

Calculation of the scope of crushing zone

During energy-accumulating blasting and water injection, the blasting shock wave formed by the explosive is much larger

TABLE 1 Coal parameters.

ρ	E	μ	Compressive	Tens
$g \cdot cm^{-3}$	GPa		MPa	MPa
1.384	2.9	0.4	4.94	0.37

TABLE 2 Explosive parameters.

ρ	v	P	A	B	R_1	R_2	ω	E_0
$g\cdot cm^{-}$	$cm\cdot \mu s^{-1}$	/GPa	GPa	GPa				GPa
1.14	0.32	2.92	246.1	10.26	7.177	2.4	0.069	0.019

TABLE 3 Water parameters.

ρ	C	S_1	S_2	S_3	GAMAO	a	E_0	V_0
kg/m^3								
1,000	1.65	1.92	-0.096	0	0.350	0	0	1

TABLE 4 Parameters of the energy-gathering pipe.

ρ	E	μ	Compressive	Tens
$g\cdot cm^{-3}$	GPa		MPa	MPa
8.93	1.17	0.35	0.004	0.001

than the compressive strength of the coal body, and the coal body is broken. Given that the crushing zone is under the constraint condition of the coal body, most of the energy consumption of the shock wave is consumed in the plastic deformation, crushing, and heating of the coal body, resulting in a rapid decline in the energy of the shock wave. The shock wave energy is insufficient to crush the coal body, so the radius of the crushing zone is small. The estimation formula is

$$R_c = \left(0.2\rho_s \frac{c^2}{\sigma_c}\right)^{\frac{1}{2}} R_b. \tag{1}$$

In Eq. 1: R_c-radius of the crushing zone, m; R_b-cavity radius after blasting, m; σ_c-uniaxial compressive strength of coal, Pa; ρ_s-coal density, kg/m^3; c-P-wave velocity of coal, 1,200–1,500 m/s.

The cavity radius formed after energy-accumulating blasting and water injection is

$$R_b = \sqrt[4]{p_m/(\sigma_0 r_b)}. \tag{2}$$

In Eq. 2: r_b-blasting hole radius, cm; p_m-average detonation pressure of explosives, Pa.

$$p_m = \rho_s D^2/8. \tag{3}$$

In Eq. 3: D-explosive detonation velocity, m/s; σ_0-coal strength under multidirectional stress, Pa.

$$\sigma_0 = \sigma_c \sqrt[4]{\rho_s \frac{c}{\sigma_c}}. \tag{4}$$

Substituting the parameters into Eqs 1–4 leads to R_c=39 cm.

Calculation of the scope of fracture zone

When the shock wave passes through the crushing zone, it continues to propagate to the coal body, but its energy attenuation is insufficient to cause deformation and fracture of the coal body. At this time, the high-temperature and high-pressure gas enters the coal fracture through the crushing zone and forms tensile stress in the fracture. Given that the tensile strength of coal is considerably less than its compressive strength, the coal is easy to form tensile failure. When the tensile stress formed by gas is greater than the tensile strength of coal, coal tensile failure and crack propagation occur. According to the quasi-static pressure of detonation gas, the calculation formula for fracture zone is

$$R_a = r_b \sqrt{\frac{p_j}{\sigma_t}}. \tag{5}$$

In Eq. 5: p_j-quasi-static pressure acting on borehole wall, Pa. When the hole is not coupled, there is

$$p_j = \frac{1}{8}\rho_s D^2 \left(\frac{r_c}{r_b}\right)^6. \tag{6}$$

In Eq. 6: r_c-charge radius, cm.

Substituting the parameters into Eqs 5, 6 yields R_a=267 cm.

Calculation of the scope of blasting vibration zone

Outside the fracture zone, the stress generated by blasting shock wave and high-temperature and high-pressure gas is not enough to cause tensile and compressive failure of the coal body. It can only cause vibration of coal unit particle and local vibration of the coal body. The calculation formula for vibration zone is

$$R_s = (1.5\text{–}2.0)\sqrt[3]{q}. \tag{7}$$

In Eq. 7: R_s-radius of blasting vibration zone, cm; q-loading of coal per unit volume, 1.2 kg/m^3.

Substituting the parameters into Eq. 7 results in R_s=159 cm.

In summary, the influence range of explosion fissure in the direction of energy-accumulating blasting and water injection includes the crushing and fracture zones. The scope of influence is

$$R = R_c + R_a. \tag{8}$$

In Eq. 8: R-radius of energy-accumulating blasting and water injection, cm.

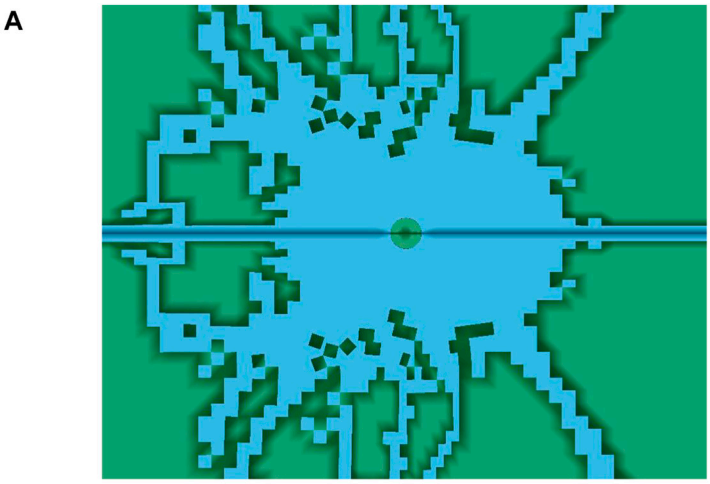

Cavity diagram of borehole blasting

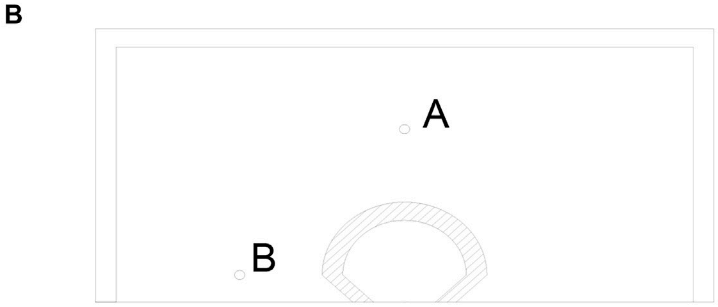

Longitudinal (A) and transverse (B) diagrams of blasting cavity

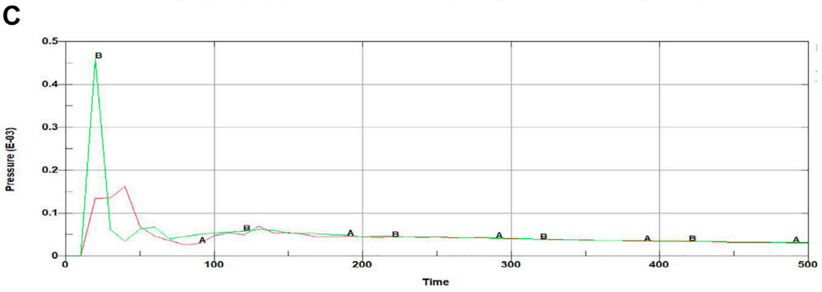

Longitudinal (A) and transverse (B) stress diagrams of blasting cavity

FIGURE 3
Cavity diagram of energy-accumulating blasting. **(A)** Cavity diagram of borehole blasting. **(B)** Longitudinal (A) and transverse (B) diagrams of blasting cavity. **(C)** Longitudinal (A) and transverse (B) stress diagrams of blasting cavity.

Substituting the parameters into Eq. 8 gives R=306 cm.

Numerical simulation

Numerical model

The influence range of directional pressure relief and increased permeability of energy-accumulating blasting and water injection in the Liangbei Coal Mine is studied. The ANSYS/LSDYNA numerical simulation software is used to establish a one-half three-dimensional calculation model. The model size is 600 cm×300 cm×1 cm. The borehole diameter is 4.2 cm, the explosive diameter is 2.4 cm, and the energy-accumulating pipe thickness is 0.2 cm (Figure 2). The model consists of coal, water, energy-accumulating pipe, and explosives. In the common joint of water, energy-accumulating pipe, and explosive, there is a gap between the explosive and borehole, which belongs to water-uncoupled charge. The calculation step is 0.9 μs. A coal failure criterion is added. Constraints are applied in

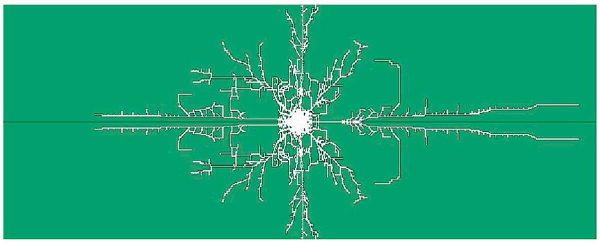

FIGURE 4
Fracture propagation diagram.

z direction to the front and rear planes of the model, unreflected boundary condition constraints on the up, right, and left boundary of the model, and in y direction to the bottom planes of the model.

Material parameters and state equations

The coal material parameters in the simulation are shown in Table 1.

For the elastic–plastic material constitutive model of coal body, the keyword MAT_PLASTIC_ KINEMATIC in LSDYNA is defined.

For the three-stage emulsified explosive, the keyword MAT_HIGH_EXPLOSIVE_BURN in LSDYNA is defined. Table 2 indicated the parameters. The explosive change is described by the JWL equation of state:

$$p = A\left(1 - \omega/VR_1\right)e^{-VR_1} + B\left(1 - \omega/VR_2\right)e^{-VR_2} + \omega E_0/V. \quad (9)$$

The MAT_NULL material model in LSDYNA is defined for air, and the equation of state is defined by LINEAR_POLYNOMIAL. Table 3 presents the parameters.

$$pk = C_0 + C_1\mu + C_2\mu^2 + C_3\mu^3 + \left(C_4 + C_5\mu + C_6\mu^2\right). \quad (10)$$

The MAT_PLASTIC_KINEMATIC material model in LSDYNA is defined for the energy-gathering pipe, and Table 4 indicates the parameters.

Analysis of numerical simulation results

Explosives explode in boreholes, forming explosion cavities around the boreholes. When the shock wave passes through the energy-accumulating pipe, it is compressed by the pipe, creating a jet in the direction of the energy-accumulating trough that penetrates the coal body and generates cracks.

Figures 3A–C depict that a blasting cavity forms rapidly around the borehole, and the area and stress of the blasting cavity

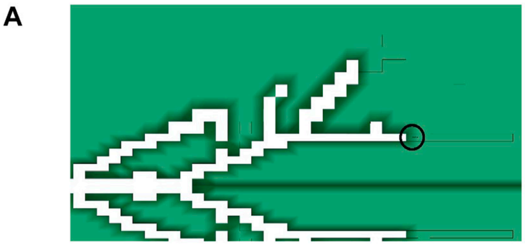

Diagram before fracture propagation

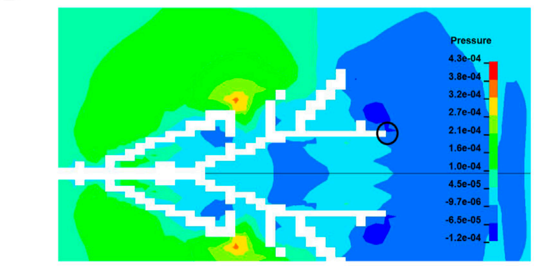

Stress diagram before fracture propagation

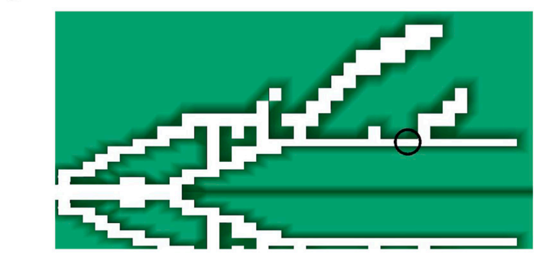

Diagram after fracture propagation

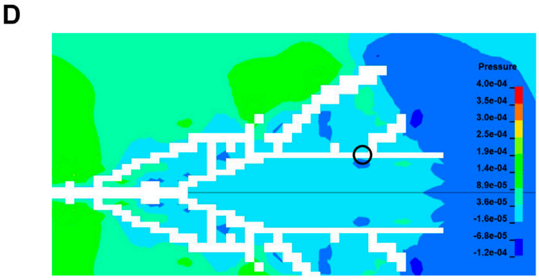

Stress diagram after fracture propagation

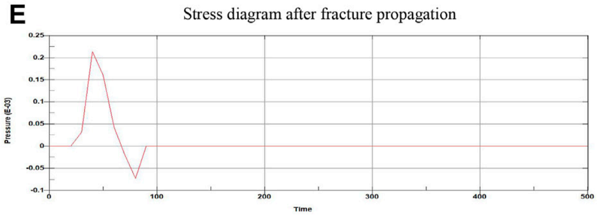

Diagram of fracture stress versus time

FIGURE 5
Variation diagram of local fracture propagation. **(A)** Diagram before fracture propagation. **(B)** Stress diagram before fracture propagation. **(C)** Diagram after fracture propagation. **(D)** Stress diagram after fracture propagation. **(E)** Diagram of fracture stress versus time.

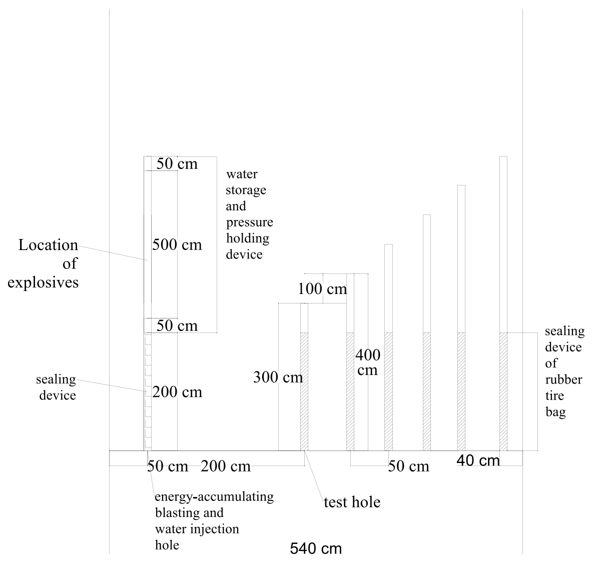

FIGURE 6
Determination of the blasting influence radius of the working face borehole layout.

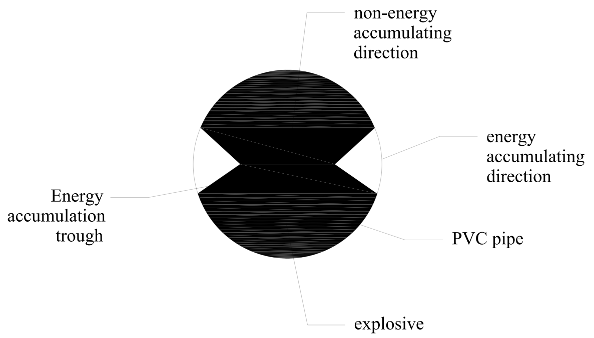

FIGURE 7
Explosive arrangement in the energy-accumulating pipe.

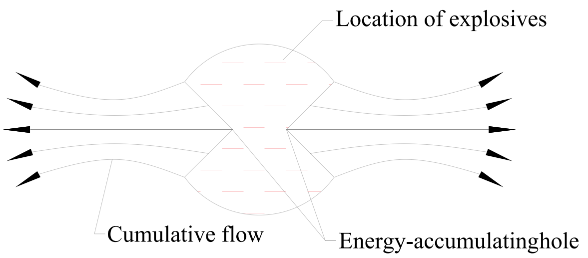

FIGURE 8
Principle of energy-accumulating blasting.

in the energy-accumulating direction are larger than those in the non-energy-accumulating direction. Measurement of the blasting cavity area by using the measure button of LSDYNA shows that the diameter of the blasting cavity in the energy-accumulating direction is 42 cm, which is 10 times the diameter of the energy-accumulating blasting and water injection hole. The diameter of the blasting cavity in the non-energy-accumulating direction is 14 cm, which is 3.3 times of the diameter of the energy-accumulating blasting and water injection hole.

Two measuring points are selected in the borehole: energy-accumulating direction (horizontal) measuring point B and non-energy-accumulating direction (vertical) measuring point A. Their stress versus time diagram is output. The stress range is 0–46 MPa in the energy-accumulating direction and 0–16 MPa in the non-energy-accumulating direction. The stress in the energy-accumulating direction is 2.9 times that in the non-energy accumulating direction. Thus, the energy-accumulating pipe can effectively gather explosive explosion energy; in this direction, the coal body has large force and obvious crack propagation.

Stress waves move mainly in the direction of the energy-accumulating trough with formation of tensile stress concentration at the crack tip. The crack tip continues to expand under tensile stress. Owing to stress wave migration, fracture propagation, and the movement of coal around the fracture, the coal forms compressive stress concentration.

Figure 4 illustrates that in the energy-accumulating direction, two jets are formed by the action of the energy-accumulating trough, and the energy is greater than that in the non-energy-accumulating direction. Fracture length is measured using the measure button of LSDYNA. The fracture length in the energy-accumulating direction is 293.6 cm, and that in the non-energy-accumulating direction is 80.2 cm. That is, the fracture length in the energy-accumulating direction is 3.7 times that in the non-energy-accumulating direction.

As shown in Figures 5A–D crack is selected in the model to observe the stress changes before and after expansion. When the explosive explodes, the explosion shock wave is transmitted in the coal body to form a blasting cavity, and then the crack is expanded by the stress wave. Given that the compressive strength of coal is much greater than the tensile strength and the pressure formed by explosion is not greater than the compressive strength of coal, the coal is not damaged. When the stress tensile wave is greater than the tensile strength of coal, the tensile failure of coal extends cracks. Figure 5E shows that before the crack propagation, coal is subjected to pressure, and the peak stress is 23 MPa, which is less than the compressive strength of the coal unit. Hence, the coal crack does not expand. Under the action of tensile force, the peak stress is 8 MPa, which is greater than the tensile strength of the coal unit. Consequently, the coal unit fails, and the fracture expands.

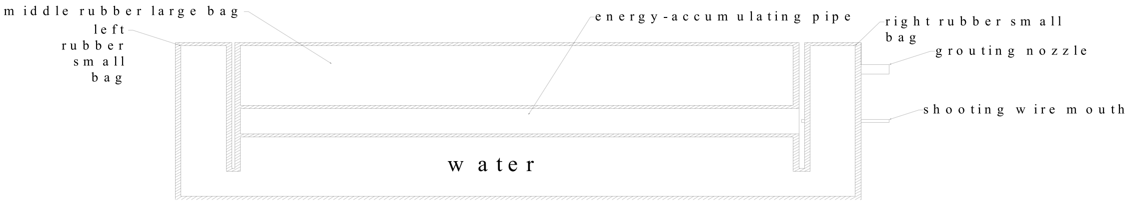

FIGURE 9
Water storage and pressure holding device.

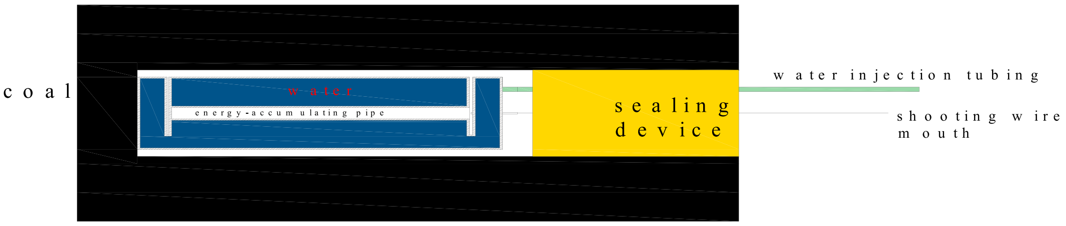

FIGURE 10
Internal schematic of the blasting hole.

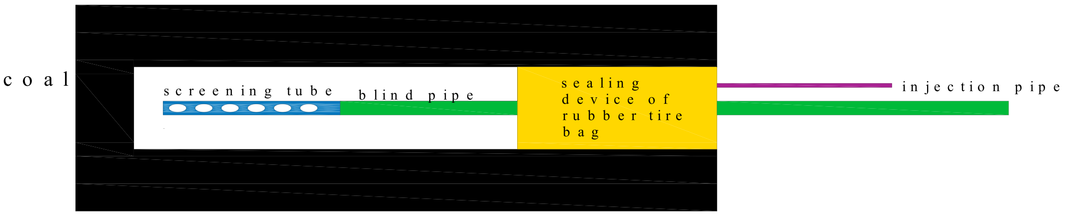

FIGURE 11
Internal schematic of the test hole.

Engineering experiment

Experimental arrangement

Energy-accumulating blasting and water injection and test holes are constructed along a coal seam at the same horizontal position of the excavation face. The interval between the blasting hole and test hole 1 is 200 cm, and the interval between each test hole and the previous test hole is 50 cm, as shown in Figure 5. To eliminate the influence of the gap in the test hole on the blasting shock wave, the depth of the latter test hole is 100 cm greater than that of the hole. The depth of the energy-accumulating blasting and water injection hole is 800 cm, that of test hole 1 is 300 cm, that of test hole 2 is 400 cm, etc. Explosives are loaded into a PVC pipe to form a "V"-shaped energy-accumulating structure, and the energy-accumulating pipe is placed horizontally (Figures 6–8).

The energy-accumulating blasting and water injection hole uses a mud sealing hole, and the length is 200 cm. The length of the energy-accumulating pipe is 500 cm, the three-grade emulsion explosive is 5 kg, and a detonator is used. According to the research and engineering experience of scholars, the charge quantity of loose blasting is

$$\mathbf{Q}_s = (\mathbf{0.33}\text{–}\mathbf{0.5})\boldsymbol{q}\boldsymbol{W}^3. \tag{11}$$

In Eq. 11: Q_s-charge quantity of loose blasting, kg; W-minimum resistance line, m.

FIGURE 12
Gas parameter meter.

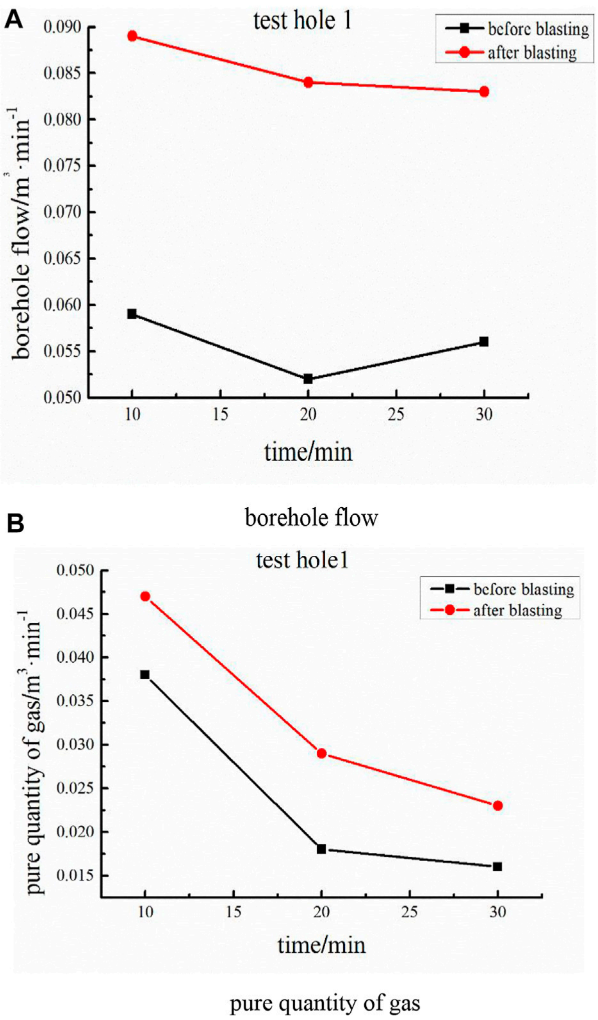

FIGURE 13
Comparison of parameters before and after blasting of test hole 1. **(A)** borehole flow. **(B)** pure quantity of gas.

The borehole wall of the test hole can be regarded as a free surface because the distance of the energy-accumulating blasting and water injection hole is 200 cm from the first test hole, so W is 200 cm.

Substituting the parameters into Eq. 11 leads to Q_s=4.8 kg. In this experiment, the charge quantity of energy-accumulating blasting and water injection is 5 kg.

In the field experiment, due to the development of fractures around the borehole, it is not effective to fill the borehole with water, and the shock wave of shaped charge will influence the sealing effect of the test hole. Therefore, a new type of rubber bag water storage and pressure keeping device for the integration of energy-accumulating blasting and water injection and a rubber tire capsule sealing device are designed (Figure 9).

The water storage and pressure holding device includes left rubber small bag, middle rubber large bag, and right rubber small bag. There is a certain thickness of through channel under the three bags for water circulation. The gap between the left small pocket and the middle pocket makes the energy-accumulating pipe far from the hole bottom. The gap between the right small bag and the middle bag is convenient for the loading of the energy-accumulating pipe, so that a certain distance exists between the energy-accumulating pipe and the sealing section. There are holes in the center position of the middle large bag for loading into the energy-accumulating pipe. A grouting nozzle and a shooting wire mouth exist on the right pocket for the connection of the grouting pipe and the shooting wire. Through the grouting pump, the water is filled in the whole device, and there is a certain water pressure under the action of the hole wall. The rubber bag is not permeable to obtain a good water storage effect and solve the problem that the development of borehole cracks does not allow to store water and maintain pressure. The external diameter of the water storage and pressure holding device is 4.2 cm, the length of the left bag is 50 cm, the length of the middle bag is 50 cm, the right bag is 50 cm, and the position diameter of the energy-accumulating tube is 2.4 cm (Figure 10).

There is only one rubber tire bag on the sealing device, which is set on the gas drainage pipe. The grouting pipe injects the flexible gel sealing material into the tire bag through the grouting nozzle on the tire bag to seal the hole. Owing to the toughness and fluidity of the sealing device and material, when the borehole is deformed, the device can seal the borehole in real time, without air leakage gap. After the experiment, the flexible gel sealing material in the sealing bag can be released, and the sealing bag can be recycled. The length of the sealing

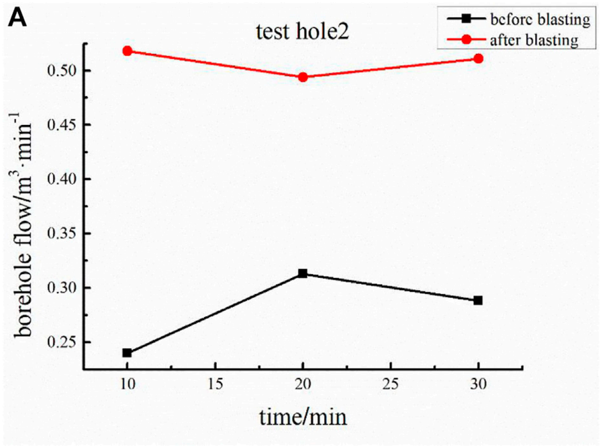

borehole flow

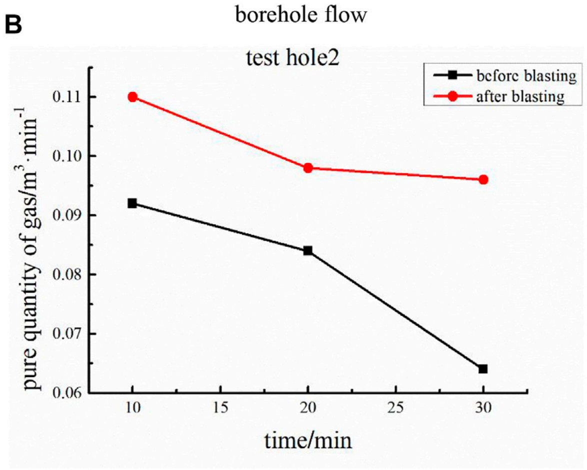

pure quantity of gas

FIGURE 14
Comparison of parameters before and after blasting of test hole 2. **(A)** borehole flow. **(B)** pure quantity of gas.

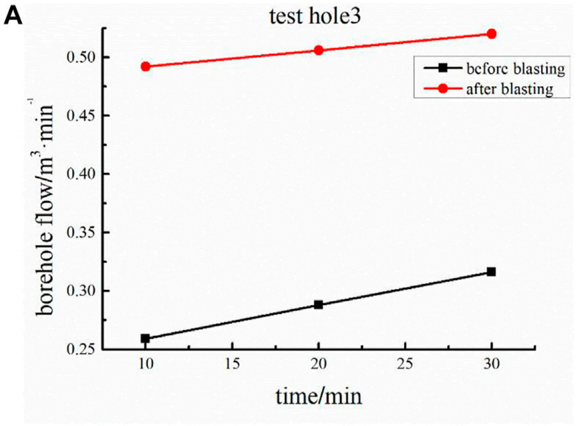

borehole flow

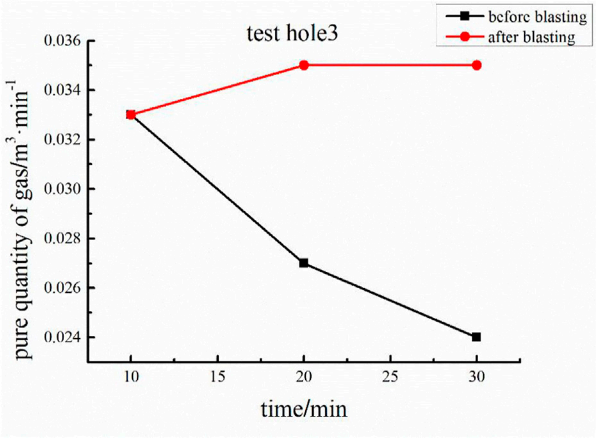

pure quantity of gas

FIGURE 15
Comparison of parameters before and after blasting of test hole 3. **(A)** borehole flow. **(B)** pure quantity of gas.

device for testing hole sealing is 200 cm, and the diameter is 4.2 cm (Figure 11).

Gas parameter methood

Changes in gas parameters occur in the borehole due to crack propagation after blasting. The influence range of blasting is determined by measuring the difference in gas parameters in the borehole before and after blasting. The stable drilling flow and gas concentration of each test hole are measured before blasting, and the pure amount is calculated. After blasting, the drilling flow and gas concentration of each test hole are measured every 10 min, and the pure amount is calculated. The gas parameter difference of the test hole before and after blasting is compared to determine whether the test hole is in the blasting influence range, as well as the size of the influence range, (Figure 12).

Result analysis

Figure 13 illustrates that before blasting of test hole 1, the borehole flow is 0.05–0.06 m^3/min, and the pure quantity of gas is 0.015–0.04 m^3/min; after blasting, the borehole flow is 0.08–0.09 m^3/min, and the pure quantity of gas is 0.023–0.047 m^3/min. Comparison of gas parameters in the borehole before and after blasting shows that the borehole flow is increased by 53.29% on average, and the pure quantity of gas is increased by 38.45% on average. With the crack propagation in test hole 1, the gas parameters change significantly.

Figure 14 depicts that before blasting of test hole 2, the borehole flow is 0.2–0.33 m^3/min, and the pure quantity of gas is 0.06–0.095 m^3/min; after blasting, the borehole flow is 0.47–0.55 m^3/min, and the pure quantity of gas is 0.095–0.11 m^3/min. Comparison of gas parameters in the

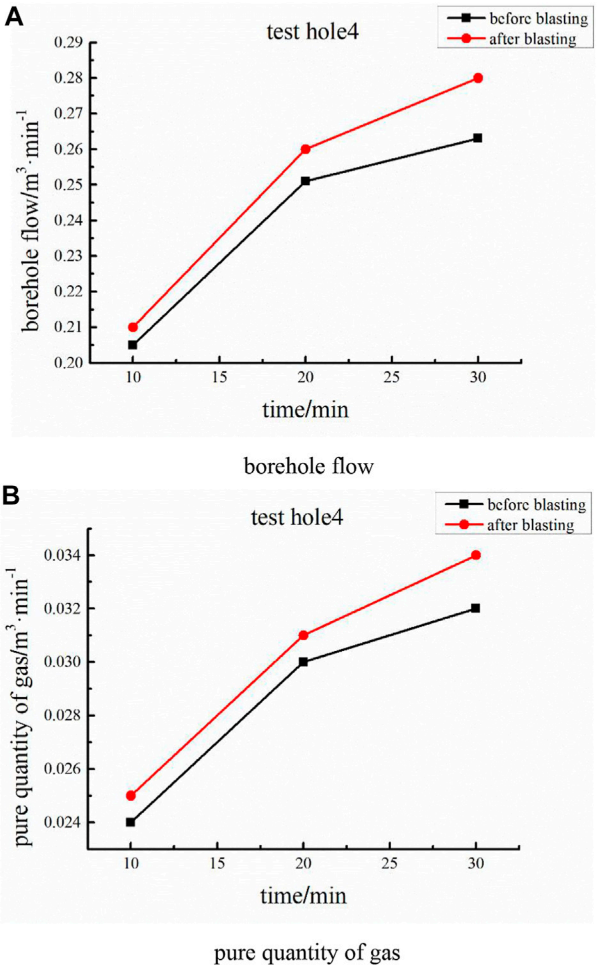

FIGURE 16
Comparison of parameters before and after blasting of test hole 4. **(A)** borehole flow. **(B)** pure quantity of gas.

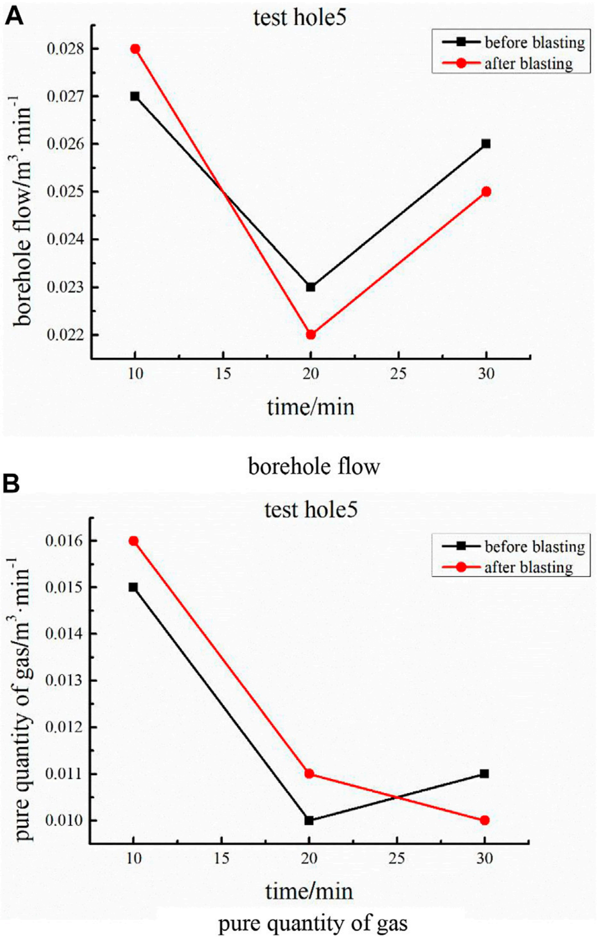

FIGURE 17
Comparison of parameters before and after blasting of test hole 5. **(A)** borehole flow. **(B)** pure quantity of gas.

borehole before and after blasting indicates that the borehole flow is increased by 81.09% on average, and the pure quantity of gas is increased by 26.44% on average. With the crack propagation in test hole 2, the gas parameters change significantly.

Figure 15 presents that before blasting of test hole 3, the borehole flow is 0.25–0.33 m^3/min, and the pure quantity of gas is 0.024–0.033 m^3/min; after blasting, the borehole flow is 0.47–0.55 m^3/min, and the pure quantity of gas is 0.033–0.035 m^3/min. Comparison of gas parameters in the borehole before and after blasting shows that the borehole flow is increased by 75.90% on average, and the pure quantity of gas is increased by 22.63% on average. With the crack propagation in test hole 3, the gas parameters change significantly.

Figure 16 demonstrates that before blasting of test hole 4, the borehole flow is 0.2–0.26 m^3/min, and the pure quantity of gas is 0.024–0.032 m^3/min; after blasting, the borehole flow is 0.21–0.28 m^3/min, and the pure quantity of gas is 0.025–0.034 m^3/min. Comparison of gas parameters in the borehole before and after blasting indicates that the borehole flow is increased by 7.69% on average, and the pure quantity of gas is increased by 6.25% on average. Test hole 4 is less affected by blasting, the crack propagation is weak, and the gas parameters change minimally.

Figure 17 illustrates that before blasting of test hole 5, the borehole flow is 0.023–0.027 m^3/min, and the pure quantity of gas is 0.01–0.015 m^3/min; after blasting, the borehole flow is 0.021–0.028 m^3/min, and the pure quantity of gas is 0.01–0.016 m^3/min. Comparison of gas parameters in the borehole before and after blasting shows that the borehole flow is increased by -1.32% on average, and the pure quantity of gas is increased by 3.37% on average. Test hole 5 under weak blasting stress wave action can only push coal, so that the cracks in coal are closed, cracks do not occur under coal expansion, and the drilling flow is decreased.

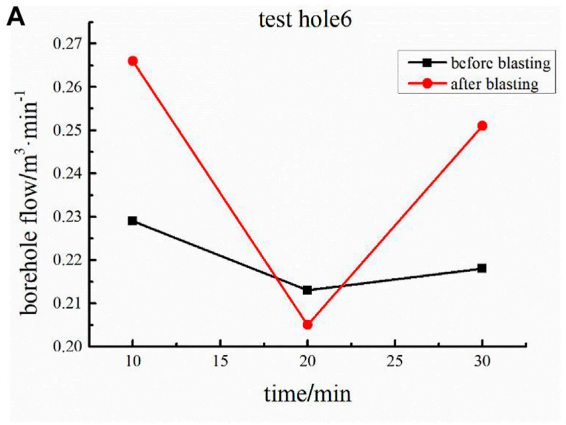

borehole flow

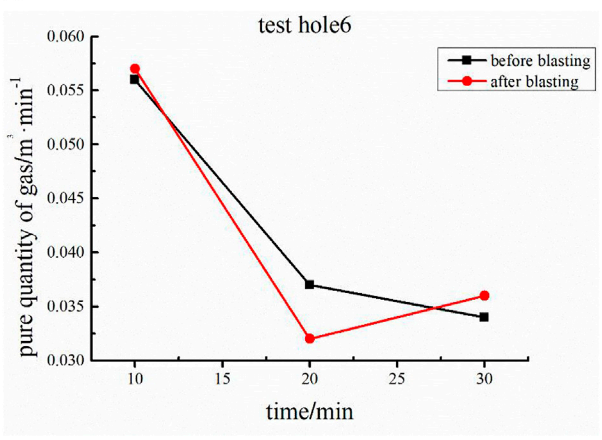

pure quantity of gas

FIGURE 18
Comparison of parameters before and after blasting of test hole 6. **(A)** borehole flow. **(B)** pure quantity of gas.

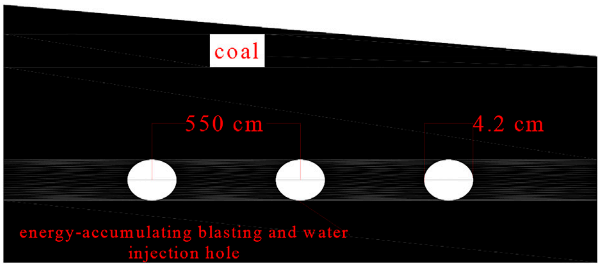

FIGURE 19
Front view of the blasting hole.

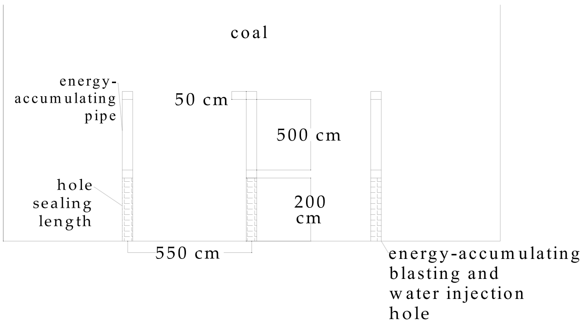

FIGURE 20
Vertical view of the blasting hole.

Figure 18 depicts that before blasting of test hole 6, the borehole flow is 0.21–0.23 m^3/min, and the pure quantity of gas is 0.033–0.056 m^3/min; after blasting, the borehole flow is 0.2–0.27 m^3/min, and the pure quantity of gas is 0.031–0.057 m^3/min. Comparison of gas parameters in the borehole before and after blasting indicates that the borehole flow is increased by 9.39% on average, and the pure quantity of gas is increased by −1.06% on average. Blasting stress wave is not transmitted to test hole 6, and the change in gas parameters before and after blasting is not obvious.

In conclusion, the gas parameters of test holes 1–3 change obviously after blasting, which are in the range of blasting influence. By contrast, the gas parameters of test holes 4–6 change minimally after blasting, which are not in the range of blasting influence. Therefore, the distance from the blasting hole to test hole 3 is the influence range of energy-accumulating blasting and water injection in the direction of the energy-accumulating trough, which is 300 cm.

Engineering application

The layout of single-row-arrangement energy-accumulating blasting and water injection holes is determined in accordance with the actual situation of the Liangbei Coal Mine. The influence radius of energy-accumulating blasting and water injection is 300 cm. To prevent a blank zone, the blasting hole spacing is 550 cm. The blasting hole depth is 800 cm, the borehole diameter is 4.2 cm, the explosion hole sealing length is 200 cm, and the energy-accumulating pipe length is 500 cm, as shown in Figures 19, 20.

After the implementation of energy-accumulating blasting and water injection in the coal mining face of the Liangbei Coal Mine, the rupture and loosening of coal form a pressure relief ring, and the validation index of gas drilling declines. Comparative analysis indicates that the computed values decrease from 120–140 Pa to 100–120 Pa, and the drilling cutting weight decreases from 3.2 to 4.6 kg/m before the test to 3.0–3.8 kg/m. The permeability of blasting coal is improved. After the test, the methane concentration in the roadway increases obviously but does not exceed the standard. The water injection volume is effectively improved, and the dust is significantly reduced during tunneling. The single hole water injection is 0.1–0.7 m^3, with an average of 0.5 m^3. Compared with the water content in the original coal seam, the water content in the blasting area is increased from 1.26%–1.45% to 2.35%–2.75%, which effectively improves the mechanical properties of coal.

Conclusion

(1) The borehole is impacted by the shock wave of explosives, forming a blasting cavity. The diameter of the blasting cavity in the energy-accumulating direction is 42 cm, which is 10 times of the diameter of the circular hole. The diameter of the blasting cavity in the non-energy-accumulating direction is 14 cm, which is 3.3 times of the diameter of the circular hole. The stress range in the energy-accumulating direction is 0–46 MPa, and that in the non-energy-accumulating direction is 0–16 MPa. That is, the stress in the energy-accumulating direction is 2.9 times that in the non-energy-accumulating direction. Hence, the energy-accumulating pipe can effectively gather explosive energy.

(2) Fracture length is measured using the measure button of LSDYNA. The fracture length in the energy-accumulating direction is 293.6 cm, and that in the non-energy-accumulating direction is 80.2 cm. That is, the fracture length in the energy-accumulating direction is 3.7 times that in the non-energy-accumulating direction.

(3) Theoretical analysis and calculation indicate that the crushing area of shaped charge blasting is 39 cm, the fracture area is 267 cm, and the vibration area is 159 cm.

(4) Comparison of gas parameters before and after blasting by using a gas parameter meter shows that the gas parameters of test holes 1–3 change obviously after blasting and are in the range of blasting influence. On the contrary, the gas parameters of test holes 4–6 change minimally after blasting and are not in the range of blasting influence. The distance between the energy-accumulating blasting and water injection hole and test hole 3 is determined as the influence radius of the energy-accumulating blasting and water injection process. Through numerical simulation, theoretical analysis, and field experiments, the influence radius of directional pressure relief of energy-accumulating blasting and water injection in the Liangbei Coal Mine is determined to be 300 cm.

Data availability statement

The original contributions presented in the study are included in the article/supplementary material, further inquiries can be directed to the corresponding author.

Author contributions

ZW proposed the research. YW prepared the figures and tables and interpreted the test and data. All authors have read and agreed to the published version of the manuscript.

Acknowledgments

The authors appreciate the comments and suggestions by the editors and reviewers. This work is supported by the State Key Laboratory Cultivation Base for Gas Geology and Gas Control (WS2021B07).

Conflict of interest

The authors declare that the research was conducted in the absence of any commercial or financial relationships that could be construed as a potential conflict of interest.

Publisher's note

References

Cao, H., Jiang, C-L., and Zang, P. (2013). Feasibility analysis of loose blasting outburst prevention mechanism based on spherical shell instability theory. *[J].Safety Coal Mines* 44 (01), 153–156.

Dou, L-M., He, X-Q., and Ren, T. (2018). Mechanism of coal-gas dynamic disasters caused by the superposition of static and dynamic loads and its control technology[J]. *J. Of China Univ. Of Min. And Technol.* 47 (01), 48–59.

Gao, X-Y., Liu, J., and Zhang, C. (2019). Experimental study on permeability Improvement of deep hole pre splitting cumulative blasting in low permeability coal seam. *J.Safety Coal Mines* 50 (04), 23–26+31.

Guo, D-Y., Zhang, C., and Li, K. (2021). Mechanism ofmillisecond-delay detonation on coal cracking under deep-hole cumulative blasting in soft and low permeability coal seam[J/ol]. *J. Of China Coal Soc.*, 1–10.

Guo, D-Y., Zhao, J-C., and Lv, P-F. (2019). Effective fracture zone under deep-hole cumulative blasting in coal seam[J]. *Chin. J. Of Eng.* 41 (05), 582–590.

Guo, D-Y., Zhao, J-C., and Zhu, T-G. (2020). Crack propagation and coalescence mechanism of double-hole cumulative blasting incoal seam[J]. *Chin. J. Of Eng.* 42 (12), 1613–1623.

Hua, X-Z., Liu, X., and Huang, Z-G. (2020). Stability mechanism of non-pillar gob-Side entry retaining by roof cutting under the coupled static-dynamic loading [J]. *J. Of China Coal Soc.* 45 (11), 3696–3708.

Huang, B., and Li, P. (2015). Experimental investigation on the basic law of the fracture spatial morphology for water pressure blasting in a drillhole under true triaxial stress. *Rock Mech. Rock Eng.* 48 (4), 1699–1709. doi:10.1007/s00603-014-0649-y

Huang, B., Liu, C., Fu, J., and Guan, H. (2011). Hydraulic fracturing after water pressure control blasting for increased fracturing. *Int. J. Of Rock Mech. And Min. Sci.* 48 (6), 976–983. doi:10.1016/j.ijrmms.2011.06.004

Kim, D-G. (2007). A study on notch bit system for controlling blast vibration and over-break in rock mass [J]. *Tunn. And Undergr. Space* 17 (3), 216–224.

Lan, Y-W., Gao, H-M., and Chen, X-H. (2013). Numerical simulation study on influence factors of borehole pressure relief effect[J]. *Min. Saf. And Environ. Prot.* 40 (03), 6–9.

Li, B., Shi, Z., Li, L., Zhang, J., Huang, L., and He, Y. (2022). Simulation study on the deflection and expansion of hydraulic fractures in coal-rock complexes. *Energy Rep.* 8, 9958–9968. doi:10.1016/j.egyr.2022.07.174

Li, B., Zhang, J., Liu, Y., Qu, L., Liu, Q., Sun, Y., et al. (2022). Interfacial porosity model and modification mechanism of broken coal grouting: A theoretical and experimental study. *Surfaces And Interfaces* 33, 102286. doi:10.1016/j.surfin.2022.102286

Liu, H-G., He, Y-N., and Xu, J-H. (2007). Numerical simulation and industrial test of boreholes destressing technology in deep coal tunnel[J]. *J. Of China Coal Soc.* (01), 33–37.

Liu, Y-K., Liu, C., and Ding, J-X. (2012). Study and application on destressing and elimination outburst technology in LargeDiameter hole[J]. *Saf. Coal Mines* 43 (02), 82–84.

Song, Y-Q., Li, X-S., and Guo, D-Y. (2018). Numerical simulation of multi-hole and same delaytime of cumulative blasting in coal seam and its application[J]. *J. Of China Coal Soc.* 43 (S2), 469–474.

Tan, D-Y. (2011). Research of heterogeneous drill rod and craft technology of construction for soft-extrude coal along level bed[J]. *Coal Mine Mach.* 32 (04), 220–222.

Wei, M-Y., Wang, E-Y., and Liu, X-F. (2011). Numerical simulation of rockburst prevention effect by blasting pressure relief in deep coal seam[J]. *Rock And Soil Mech.* 32 (08), 2539–2543+2560.

Yang, J-H., Hu, D-R., and Zhu, C-H. (2019). Study on numerical simulation on shaped charge blasting parameters of Peripheral holes[J]. *Coal Sci. And Technol.* 47 (01), 187–192.

Yuan, W., Wang, W., and Su, X. (2019). Experimental and numerical study on the effect of water-decoupling charge structure on the attenuation of blasting stress [J]. *Int. J. Of Rock Mech. And Min. Sci.* 124. doi:10.1016/j.ijrmms.2019.104133

Yuan, W., Wang, W., and Su, X. (2018). Numerical study of the impact mechanism of decoupling charge on blastingenhanced permeability in low-permeability sandstones [J]. *Int. J. Of Rock Mech. And Min. Sci.* 106 (300-10). doi:10.1016/j.ijrmms.2018.04.029

Zhai, H. (2010). An experimental study on A permeability improvement and pressure relieving technology by energy cumulative blasting in steeply inclined boreholes made upward through rock and coal seam[J]. *Chinacoal* 36 (04), 86–89.

Zhang, J., Li, B., and Liu, Y. (2022). Dynamic multifield coupling model of gas drainage and A new remedy method for borehole leakage [J]. *Acta Geotech.*, 1–17.

Zhang, J., Liu, Y., Ren, P., Han, H., and Zhang, S. (2021). A fully multifield coupling model of gas extraction and air leakage for in-seam borehole. *Energy Rep.* 7, 1293–1305. doi:10.1016/j.egyr.2021.02.037

Zhang, S., Wang, X-L., and 'Zhao, W-F. (2019). Study on application of D-type energy gathering blasting tube on gob-side entry retaining[J]. *Coal Sci. And Technol.* 47 (10), 175–182.

Zong, Q., and Luo, Q. (2006). Experimental study on distribution character of blasting stress when boreholes with water-couple charge[J]. *J. Of Exp. Mech.* 03, 393–395+78.

frontiers | Frontiers in Earth Science

TYPE Original Research
PUBLISHED 09 January 2023
DOI 10.3389/feart.2022.1089248

Study on the test of coal mass fracture grouting sealing with coal-based materials and its application

Yingjun Gao[1,2], Banghua Yao[1,2,3]*, Hongtu Zhang[1,2], Boyang Zhang[2], Jinhu Song[4], Qian Wang[4], Jinming Niu[4] and Jinhua Li[4]

[1]School of Safety Science and Engineering, Henan Polytechnic University, Jiaozuo, China, [2]Collaborative Innovation Center of Coal Work Safety and Clean High Efficiency Utilization, Jiaozuo, China, [3]State Key Laboratory of Coking Coal Exploitation and Comprehensive Utilization, Pingdingshan, China, [4]Sima Coal Industry Co., Ltd., Shanxi Lu'an Group, Changzhi, China

OPEN ACCESS

EDITED BY
Guangyao Si,
University of New South Wales, Australia

REVIEWED BY
Yinlong Lu,
China University of Mining and Technology, China
Liming Qiu,
University of Science and Technology Beijing, China

*CORRESPONDENCE
Banghua Yao,
yaobanghua@126.com

SPECIALTY SECTION
This article was submitted to Economic Geology, a section of the journal Frontiers in Earth Science

RECEIVED 04 November 2022
ACCEPTED 22 November 2022
PUBLISHED 09 January 2023

CITATION
Gao Y, Yao B, Zhang H, Zhang B, Song J, Wang Q, Niu J and Li J (2023), Study on the test of coal mass fracture grouting sealing with coal-based materials and its application.
Front. Earth Sci. 10:1089248.
doi: 10.3389/feart.2022.1089248

This study is focused on coal mass fracture grouting sealing and seepage reduction with coal-based grouting sealing materials. First, a new type of coal-based grouting sealing materials was developed and applied to the fractured coal sample in the grouting test. Then, the coal sample before and after grouting was scanned and reconstructed with the aid of industrial computed tomography (CT). Based on CT images and reconstructed data, a theoretical model of grouting sealing for fractured coal mass was constructed by taking the migration and sedimentation of grouting slurry particles into consideration. Furthermore, on the ground of the theoretical model, a numerical calculation model of grouting sealing for the fractured coal sample was established, and the mechanism of grouting sealing and seepage reduction with coal-based sealing materials was simulated. Finally, a field test of gas extraction drilling and sealing was performed using the coal-based grouting sealing technology. The results show that: 1) The new type of coal-based grouting materials is effective in sealing the coal mass fracture, as the fracture is tightly filled with slurry particles after grouting. 2) The numerical simulation reproduces the whole process of grouting slurry flow and fracture sealing. After the permeability of the grouting coal sample decreases rapidly, it gradually tends to stabilize. The permeability of the whole coal sample goes down by 96% on average, and that of the fracture drops by more than 99.9% on average. The law of slurry diffusion and permeability variation calculated by numerical simulation is in line with the test results, which verifies the reasonableness of the model. 3) The application of the coal-based grouting sealing technology achieves an excellent sealing effect, promoting the gas extraction concentration by 1.43 times. The research results provide guidance for revealing mechanism of coal mass fracture grouting sealing with coal-based materials and bolstering the effect of extraction borehole sealing.

KEYWORDS

gas extraction, coal-based materials, grouting sealing, fractured coal mass, seepage reduction mechanism, sealing test

1 Introduction

As coal mining in China extends into the deep, disasters such as coal and gas outburst are becoming increasingly severe. Since the increase in coal mining depth amplifies the *in situ* stress, the coal mass in deep coal seams is broken and soft with a weak bearing capacity (Chen et al., 2016). Under the influence of mining, a large number of fractures appear in the coal mass, causing changes in its stress state and inducing its instability and failure. Ultimately, disasters such as coal and gas outburst are likely to occur (Huang et al., 2019; Hao et al., 2021; Bao et al., 2022). Gas extraction is an important technical method to develop and utilize gas resources and prevent gas disasters in coal mines (Yu et al., 2015; Zhang et al., 2022a; Bi et al., 2022; Zhang et al., 2022b; Gao and Ren, 2022). However, under the influence of the excavation and mining of the roadway and borehole, the coal layer could be damaged by different degrees of deformation, so there are a large number of fractures and leakage channels around the extraction borehole (Liu et al., 2020; Wang et al., 2021; Li et al., 2022a). And seriously impacts the gas extraction effect (Zhou et al., 2016; Zhang et al., 2022c; Yao et al., 2022), the average concentration of coal mine gas extraction is merely 30% (Wang and Cheng, 2012; Wang et al., 2020).

In order to improve the efficiency of gas extraction scholars proposed cement mortar sealing technology (Zhang et al., 2022d), the polyurethane sealing technology, the sealing technology of “two plugs and one injection” and the bag sealing technology (Sun et al., 2022). Among them, “two plugs and one injection” is a common method to sealing boreholes in Chinese coal mines. The principle is to create a grouting space in the boreholes through the “two plugs” materials and then inject the sealing slurry under pressure (Yang et al., 2019). This method can promote the combination of slurry and fractures on the borehole wall in the coal seam, pertinently strengthen the sealing, and effectively enhance the gas extraction effect.

Under practical working conditions, sealing materials and sealing parameters are often selected according to experience, which lacks a scientific theoretical basis. This restricts the optimization of sealing effect for gas extraction boreholes (Li et al., 2016). Other scholars also have important reference significance for the test of sealing materials in this paper (Liu et al., 2020a). Therefore, in-depth study on the property of grouting materials and the mechanism of coal seam fracture sealing is of great engineering significance for enhancing the sealing effect of extraction boreholes and improving the efficiency of gas extraction.

Currently, scholars at home and abroad have carried out a series of research on grouting materials, characteristics of slurry flow inside coal rock fractures and mechanism of grouting sealing and seepage reduction with slurry (Li et al., 2022b). At present, the major object of research on grouting sealing materials is cement-based sealing materials. In terms of relevant research on slurry materials, primary consideration is given to the influence of slurry properties on bearing capacity and durability (Ge et al., 2014; Di et al., 2021; Guo et al., 2021). In order to utilize coal resources efficiently, scholars use coal debris as slurry material, on the ground of cement-based sealing materials, the addition of a certain concentration of coal fly ash. Research shows that compared to cement-based sealing materials, they not only enhance the mechanical strength and behavior of slurry, but also enhance the durability of sealing materials (Chindaprasirt et al., 2003; Liu et al., 2010; Nath and Sarker, 2011). Coal debris has the benefit of obtaining materials locally and low cost, utilizing waste resources rationally. Meanwhile, developed a new type of green sealing materials with borehole coal debris as the base material (Li et al., 2015). The property of slurry flow inside coal rock fractures plays an important role in investigating fracture evolution during the grouting process, and taking into account the time-varying concentration in the midst of slurry flow can more faithfully reflect the influence of sedimentation during solid particle migration (Yang et al., 2011; Zhang et al., 2015).

Some scholars have explored the sealing performance of grouting slurry for fractured rock mass. For instance, through engineering tests, Kang (Kang, 2021) proved the variation process of organic polymer materials in the field of grouting sealing and seepage reduction, and found that under the same grouting pressure, such materials boast a larger diffusion range and a better bonding effect in roadway surrounding rock. Based on the engineering practice of high-pressure grouting in mine roadways. Zhang et al. (2020) revealed the mechanism of grouting sealing and seepage reduction of coal mass, i.e., the slurry, as a semi-fluid, entered into the coal fractures under pressure, which restricts the entrance of gas and liquid. Yang et al. (2016) analyzed the fracture changes in mudstone samples before and after grouting under laboratory conditions with the aid of the computerized tomography CT scanning technology, and evaluated the fracture sealing performance using the fractal dimension method. Wei et al. (2020) investigated the grouting sealing and seepage reduction characteristics of fractured coal mass by means of industrial CT and numerical simulation. Liu et al. (2020b) studied the permeability evolution characteristics of rock mass before and after grouting through tests. Xu et al. (2019) explored the effect of grouting sealing and seepage reduction for deep fractured rock on a self-developed grouting physical simulation platform.

In the above research, scholars have conducted many useful explorations in grouting sealing materials, slurry flow models as

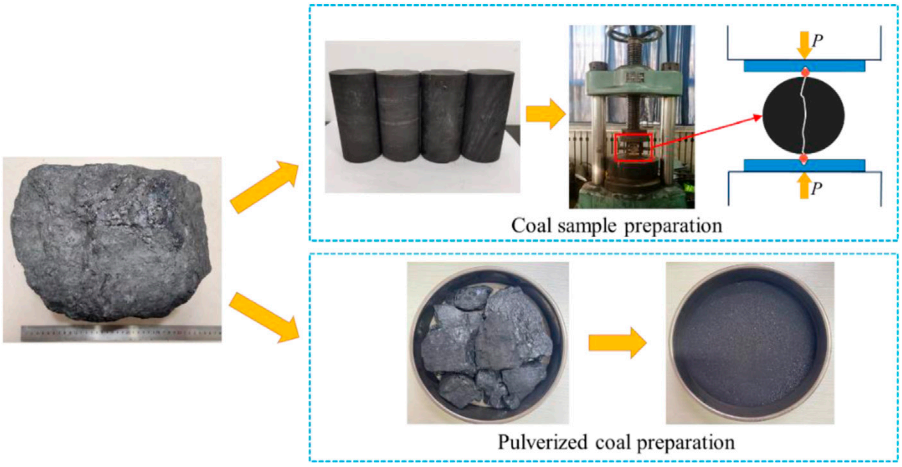

FIGURE 1
Coal sample and pulverized coal preparation.

well as grouting sealing and seepage reduction for fractured coal mass. However, the existing theoretical models rarely consider the coupling between slurry flow and coal deformation, and fail to investigate the fracture evolution under the combined effect of stress and slurry particle sedimentation. In this study, the fracture distribution of coal mass was reconstructed by adopting advanced experimental methods such as CT scanning, and the model of grouting sealing and seepage reduction for fractured coal mass was constructed. Besides, the fracture sealing mechanism of a new type of grouting slurry was quantitatively analyzed. Finally, the model of grouting sealing for gas extraction boreholes was established. The research results can lay a foundation for optimizing the grouting and sealing process of gas extraction boreholes and is of great theoretical and practical significance.

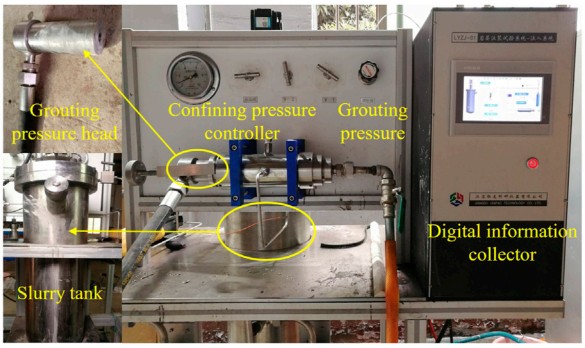

FIGURE 2
Rock strata grouting test device.

2 Grouting test on fractured coal mass

2.1 Test system

Bituminous coal from the 360803 working face of a mine in Huainan City, China, was selected and processed into a standard coal sample of 50 mm × 100 mm. Then, the sample was split with the Brazilian splitting method by the NY-60 pressure tester. Afterwards, a penetrating fracture would emerge in the coal sample. Next, the residual broken coal blocks were crushed and a 100-mesh sieve was used to screen pulverized coal (Figure 1). Finally, a new type of coal-based sealing materials was prepared with pulverized coal. The slurry was comprised of water, curing agent, expansion agent and pulverized coal whose particle size was less than 100 meshes at the water-solid ratio of 1.5. Configured a new coal-based sealing material using coal debris with a slurry water-solid ratio of 1.5, consisting of 500 g coal debris with particle size less than 100 mesh, 2 g curing agent, 400 g expansive agent, and 1,353 g water.

The grouting test on fractured coal mass adopted the “rock strata grouting test system-pour into system” independently developed and designed by Henan Polytechnic University. The test system mainly comprises six parts: a grouting pressure controller, a confining pressure controller, a digital collector, a slurry tank, a grouting pressure head and a coal sample holder. The photo and schematic diagram of the rock strata grouting test system are presented in Figures 2, 3, respectively. The test method are as follows: 1) The fractured coal sample was wrapped with sealing ring and then loaded into the grouting chamber. Grouting chamber left side connected to the grouting

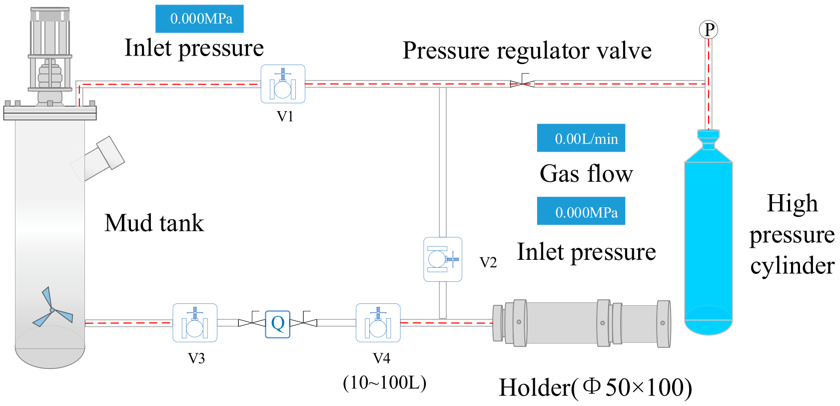

FIGURE 3
Rock strata grouting test system.

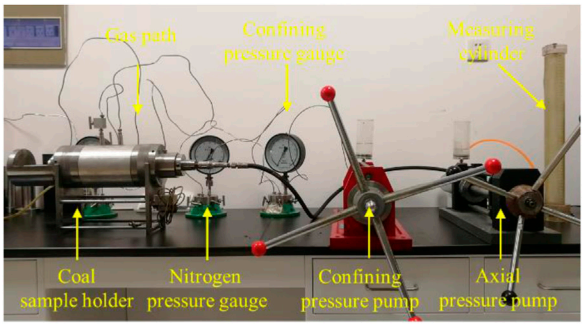

FIGURE 4
Nitrogen seepage test system.

pressure head, right side connected to the slurry outlet and valve, and closed all the valves in the system, keeping the coal sample in an airtight environment. 2) Adjust confining pressure to 0.8 MPa through confining pressure controller. 3) Prepared slurry according to the slurry water-solid ratio of 1.5, and put into the slurry tank. 4) The coal-based grouting materials were poured into the fractured coal sample by the booster pump under the grouting pressure of 0.2 MPa for 30–40 min. The upper and lower valves of the grouting chamber were opened to keep the grouting circuit unblocked. 5) The grouting valves were closed and the coal sample was taken out for tests, after which the grouting pipeline and the booster pump were cleaned.

2.2 Permeability test on grouting coal samples

The permeability test was performed using the self-designed nitrogen seepage test system (Figure 4). The test system mainly consists of a gas path, a coal sample holder, a pressure gauge, a confining pressure controller and a measuring cylinder. Among them, the coal sample holder includes a confining pressure chamber, a permeability test pressure head and other components. Meanwhile, the confining pressure chamber is connected with the confining pressure controller to control the confining pressure that the coal sample is subject to. The permeability test pressure head is linked to the gas pipeline so as to test the permeability of the coal sample in the holder. The main parameters of the nitrogen seepage test system are as follows:

1) Coal sample size: Φ50 mm × 100 mm, precision ± 2 mm;
2) Confining pressure: 0–50 MPa, precision ± 0.1 MPa;
3) Gas pressure: 0–15 MPa, precision ± 0.05 MPa.

Before carrying out the permeability test, the following assumptions were made: 1) Nitrogen flows in the coal sample fracture as laminar flow, and gas seepage conforms to Darcy's law; 2) Gas permeability is irrelevant to seepage pressure. The volume of gas seepage per unit time is measured by means of the water drainage method and substituted into the permeability calculation formula (Li et al., 2021):

$$k = \frac{2QP_0\mu B}{\left(P^2 - P_0^2\right)A} \tag{1}$$

where k is the permeability of the coal sample, mD; Q is the volume flow rate of nitrogen at the outlet under standard atmospheric pressure, m^3/s; P_0 is the standard atmospheric pressure, 101.325 kPa; μ is the dynamic viscosity of nitrogen, 1.66×10^{-5} Pa•s; B is the length of the coal sample, cm; P is the pressure of nitrogen at the inlet, MPa; A is the cross-sectional area of the coal sample, m^2.

Under a confining pressure of 0.8 MPa, and measured the coal sample permeability before fracturing k_1, the permeability

TABLE 1 Permeability measurement results.

P/MPa	Confining pressure/MPa	k_1/mD	k_2/mD	k_3/mD
0.6	0.8	1.9	53.8	2.6

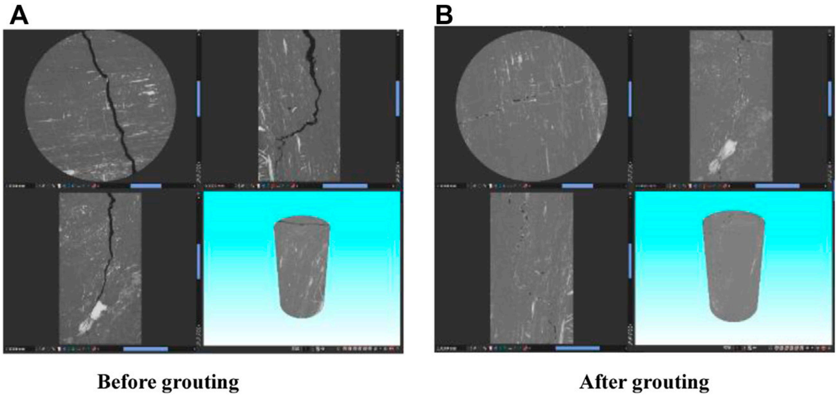

FIGURE 5
CT scan of coal sample before and after grouting. **(A)** Before grouting. **(B)** After grouting.

after splitting k_2 and the permeability after grouting k_3 respectively, and listed in Table 1.

The permeability after grouting k_3 is greatly reduced compared with the permeability after splitting k_2. Indicating that the grouting of fractured coal mass would produce a better grouting effect and achieve the leakage sealing performance. However, the permeability after grouting k_3 is little higher than the permeability before fracturing k_1, the reason is that the slurry failed to completely sealing the detailed fractures in the coal sample, resulting in higher permeability.

2.3 CT scanning and reconstruction of fractured coal samples

The industrial CT equipment was used to scan the coal samples before and after grouting to obtain the CT images in Figure 5. Figure 5A displays the CT images before grouting, from which it can be seen that the fracture penetrates the coal sample and is of simple distribution overall. As the fracture extends from the top to the middle of the coal sample, it gradually narrows and tilts to the right, and the main fracture is found in the upper 2/3 of the coal sample. When stretching to 2/3 of the coal sample, the fracture begins to extend horizontally to the lower left, during which the fracture width changes insignificantly. Subsequently, it further extends downward, during which it becomes comparatively twisted, serrated and narrow. Finally, it turns into a crack at the bottom of the coal sample.

Figure 5B gives the CT images of fracture distribution of the reconstructed coal sample after grouting. As can be observed from the top view, the slurry has filled the fracture. As can be seen from the front view, the main fracture is filled with the slurry, except for the upper part. According to the side view, the filling effect is remarkable on the whole, but the slurry fails to fill the upper part of the coal sample sufficiently, probably because the fracture has such a large twist angle that the slurry cannot stay at the corner. Besides, the fracture at the bottom of the coal sample is not completely filled. The is attributed to the fact that this part of fracture is too narrow and too far from the top of the coal sample; consequently, the slurry whose pressure decreases gradually in the filling process fails to open up and fill the fracture at the bottom.

3 Numerical simulation on grouting sealing and seepage reduction for fractured coal mass

3.1 Model of grouting sealing and seepage reduction for fractured coal mass

3.3.1 Equation of mass conservation

The coal mass is a pore-fracture dual-porosity medium. The grouting slurry mainly seeps into the coal mass alongside the fracture structure. The particles in the grouting slurry experience sedimentation while flowing under the influence of gravity. As a result, the pores and fractures of the coal mass become narrow or even blocked, thus affecting the porosity and permeability of the coal mass (Si et al., 2021a; Si et al., 2021b).

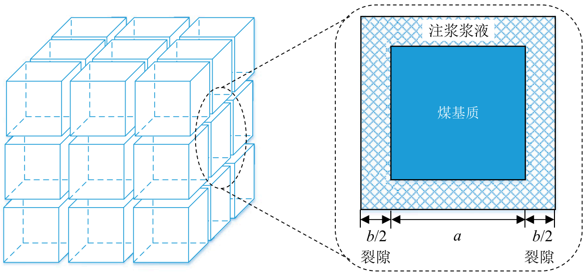

FIGURE 6
Fracture structure model of fractured coal.

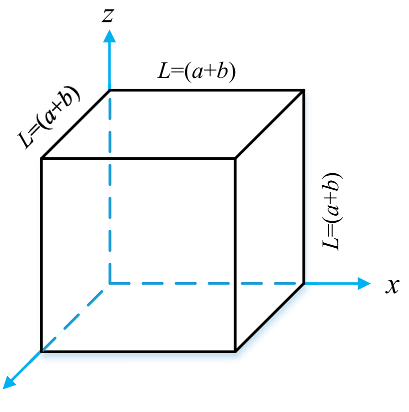

FIGURE 7
Microelement sketch.

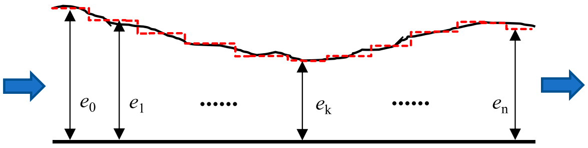

FIGURE 8
Rough single fracture model.

For the convenience of modeling research, the following assumptions were made:

1) In the pore-fracture dual-porosity structure of fractured coal mass, the fracture variation plays a major role in seepage, and the influence of pores in the coal matrix is ignored;
2) The solid particles in the grouting slurry are incompressible, and the grouting concentration is stable and invariant;
3) The grouting slurry can be regarded as a Newtonian fluid;
4) The sedimentation of suspended particles in the grouting slurry is an irreversible process.

The fracture structure model of fractured coal mass is established (Figure 6). In the model, the coal matrix blocks are cubes with a side length of a; the width of the fracture is b; the volumes of the micro-unit of the coal matrix are $V=(a+b)$ (Huang et al., 2019) and $V_1=a$ (Huang et al., 2019), respectively. The fracture rate φ of the micro-unit can be expressed as:

$$\varphi = \frac{(a+b)^3 - a^3}{(a+b)^3} \tag{2}$$

Figure 7 presents the micro-unit. By adopting the Euler description method, the equation of mass conservation for fractured coal mass during grouting is established as (Zhu et al., 2020):

$$\frac{\partial (D\varphi)}{\partial t} = -\nabla (D\varphi v)L + K_{\text{dep}} D\varphi \tag{3}$$

where D is the volume fraction of particles in the fracture; φ is the fracture rate of fractured coal mass; K_{dep} is the sedimentation coefficient of particles; L is the length of the whole fracture, m; v is the absolute velocity when the particles migrate in the fractured coal mass, m/s.

3.3.2 Equation of slurry flow

The process of slurry flow in the micro-unit fractures is shown in Figure 8. The micro-unit method is adopted to divide the rough fracture into several smooth sections along the slurry flow direction, and each section is of relatively small lengths and different widths. In this way, the rough fracture can be replaced by a series of smooth sections.

Eq. 4 is the equation of permeability coefficient when the slurry flows in the coal mass that bears a single fracture (Li et al., 2017):

$$K_f = \frac{\rho g}{12u}\left(\frac{n}{\sum 1/ek^3}\right)^{\frac{2}{3}} \tag{4}$$

where K_f is the permeability coefficient of the coal fracture; ρ is the density of the slurry; g is the gravity of the slurry; n is the number of micro-unit fracture sections; and e_k is the width of each section.

3.3.3 Equation of permeability evolution

The grouting slurry seeps into the coal mass alongside the fracture and gradually migrates to the deep part of the fracture. In this process, it experiences sedimentation as a result of seepage velocity reduction and gravity. Under the impact of sedimentation, the particles gradually seal the coal fracture, which will inevitably lead to the decline of coal mass

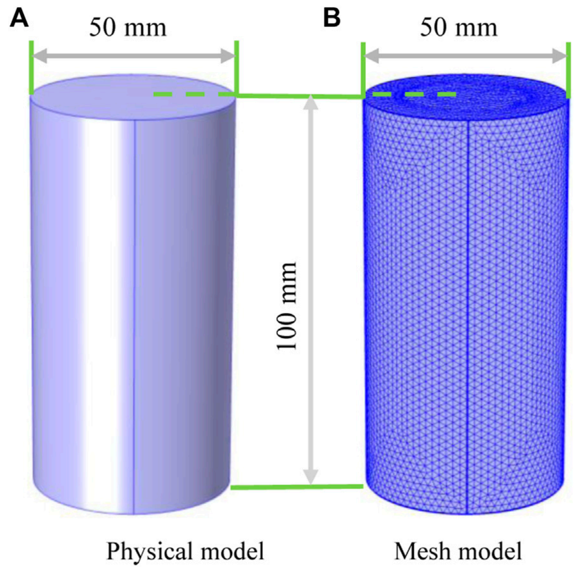

FIGURE 9
Schematic diagram of the model. **(A)** Physical model. **(B)** Mesh model.

permeability. Eq. 5 is the equation of permeability variation (Wei et al., 2020):

$$\frac{\rho_s^2}{\varphi_0(\rho_s - S)}\frac{\partial S}{\partial t} - \rho_s\frac{\partial S}{\partial t} = K_{\mathrm{dep}}C \tag{5}$$

where φ_0 is the initial fracture rate of fractured coal mass; ρ_s is the density of suspended particles, g/cm^3; S is the concentration of sedimented particles, g/cm^3; C is the concentration of suspended particles in the fracture, g/cm^3.

The above equations of mass conservation (3), slurry flow (4) and permeability evolution (5) together constitute the slurry flow coupling theoretical model.

3.2 Establishment of a numerical model of grouting for fractured coal mass

In the above tests, industrial CT was used to scan the coal sample after splitting to obtain its internal fracture distribution. In this section, the multi-physics coupling software COMSOL Multiphysic was adopted to establish a numerical calculation model that shared the same size (50 mm in diameter and 100 mm in height) as the tested coal sample (Figure 9). CT images contain pore and frame information in each pixel, and the smaller the gray value of the image pixel, the higher porosity of the sample at that location. By selecting a reasonable threshold value, the porosity of the sample can be effectively described. Using a self-written Matlab program to extract and arrange the pixels of the CT scanned coal samples, and then import the reconstructed 3D pixel values of the coal samples into COMSOL by difference method, and refined mesh division was conducted.

The boundary conditions and initial conditions of the numerical calculation model were set up based on the test conditions. Since the coal-based sealing materials were injected from one end of the coal sample, the upper boundary of the model served as the slurry injection end, with the grouting pressure being 0.2 MPa and the model confining pressure being 0.8 MPa. The remaining boundaries were all impermeable ones, that is, the slurry would not overflow from these boundaries. The initial slurry concentration of the numerical calculation model was 0. Major parameters of numerical simulation are shown in Table 2.

3.3 Analysis on grouting pressure on fractured coal mass

As can be known in Figure 10, the grouting pressure on the fractured coal sample varies as time goes by. Specifically, the diffusion range of grouting pressure increases from the top to the bottom alongside the fracture. When the grouting time is 1,000 s, the grouting pressure basically runs through the whole coal sample, after which it remains basically stable. Moreover, the grouting pressure diffuses faster in the upper part of the coal sample and relatively slowly in the local area at the bottom. At 2,000 s, the grouting pressure in part of the fracture at the bottom is still rising. From the CT images, it can be known that the slurry diffuses fast in the upper part because the fracture is well developed and the permeability is high there, while it diffuses slowly in the lower part because the fracture is poorly developed there.

3.4 Variation of coal permeability

The time-varying cloud map of coal permeability during grouting is exhibited in Figure 11 where the parts with a wide fracture and a high permeability are red and orange while those with a narrower fracture and a low permeability are light blue and dark blue. A penetrating fracture can be observed at 2/3 of the model. Before grouting, the permeability of the fracture is much higher than that of the unfractured area.

As the grouting time passes by, the grouting slurry seeps into the coal mass along the fracture and gradually migrates and settles to the deep part of the fracture, resulting in the continuous narrowing and even sealing of the fracture. Ultimately, the permeability of the model decreases. When the grouting time is 100 s, the permeability in the upper part of the coal sample changes from reddish orange to light blue, which indicates that the permeability begins to drop as the slurry begins to enter the

TABLE 2 Main parameters of numerical simulation.

Slurry density/kg·m^{-3}	Grouting pressure/MPa	Water-solid ratio	Viscosity/Pa·s	Grouting time/s
1,340	0.2	1.5	$\eta=154.55e^{0.0254t}$	2000

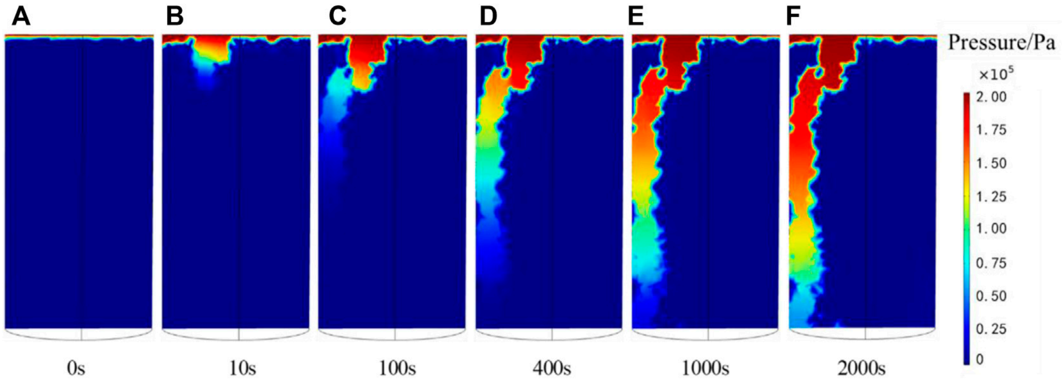

FIGURE 10
Cloud map of grouting pressure variation with time. **(A–F)** refers to the grouting pressure clouds at different times, in accordance with the numerical simulation specification.

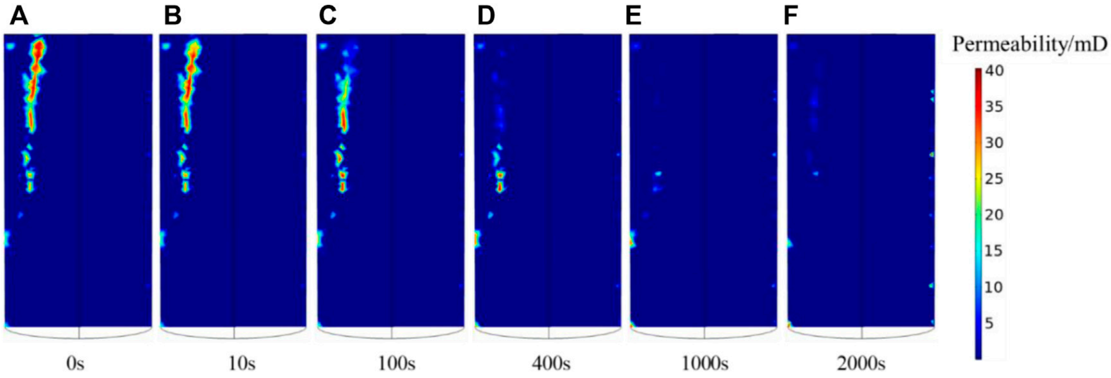

FIGURE 11
Cloud map of permeability variation with time. **(A–F)** refers to the permeability clouds at different times, in accordance with the numerical simulation specification.

coal mass from the top. The permeability falls significantly in the early stage of grouting (before 400 s). With the passage of grouting time, the sealing effect gradually weakens. When the grouting time is 1,000 s, the permeability of the upper 2/3 of the coal sample gradually turns into dark blue, and slurry only fails to reach the left boundary. When the grouting time is 2,000 s, the coal sample changes into dark blue as a whole, which means that the slurry has basically filled the entire fracture. From the permeability variation in the grouting process, it can be found that the upper part of the fracture is sealed by the slurry first. As the grouting proceeds, the slurry continues to diffuse and seal the fracture downward until it finally seals the fracture. The reason is that the upper part of the fracture, which is developed, is conducive to slurry flow and sealing, while the lower part of the fracture, which is poorly developed, is unfavorable for slurry flow and sealing.

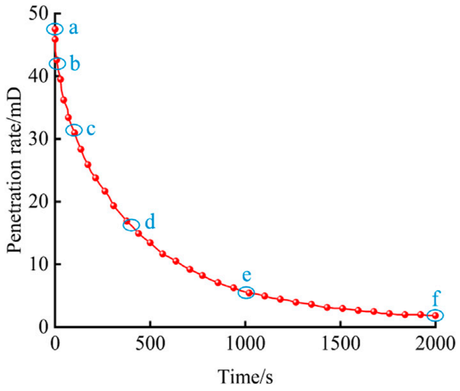

FIGURE 12
Permeability of grouting coal sample with time.

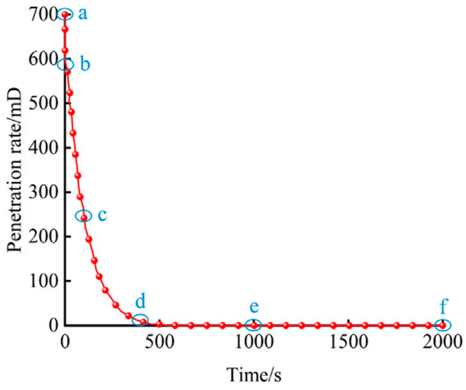

FIGURE 13
Permeability of coal sample fracture with time.

The curve of permeability of the grouting coal sample with time obtained by numerical simulation is shown in Figure 12. The numbers therein correspond to the permeabilities of the model at 0 s, 10 s, 100 s, 400 s, 1,000 s and 2,000 s, respectively. Overall, the permeability gradually goes down with time, by 93.5% on average. The permeability after splitting of the coal sample is 47.4 mD, stabilizes after around 1,000 s, and eventually reaches about 1.86 mD at 2,000 s, a decrease of 96.0%. In the test, the measured values of the permeability before and after grouting are 53.8 mD and 2.6 mD, respectively. The numerical simulation results are consistent with the test results, yet some errors still exist, because the permeability test was carried out after the grouting slurry inside the coal sample was dried. As can be seen from the permeability curve, after the grouting time exceeds 1,500 s, the permeability curve starts to decline slowly, barely affecting the overall permeability value of the model. Figure 13 presents the curve of permeability of the fracture with time in the grouting process obtained by numerical simulation. Clearly, the permeability of the fracture varies in the same trend as the overall permeability of the coal sample. The difference lies in that the fracture is of a higher initial permeability and a greater decrease range (more than 99.9%). The above numerical simulation results of fractured coal sample during grouting are basically the same as the measured results, which confirms the reasonableness of the theoretical model.

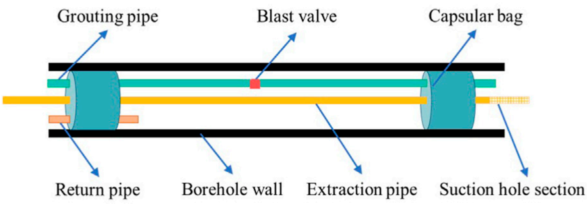

FIGURE 14
Schematic diagram of two plugs and one injection for coal-based grouting material.

4 Field application

4.1 Coal-based grouting sealing technology

The above research shows that the coal-based grouting materials can tightly seal the coal mass fracture. On this basis, the borehole sealing device of “two plugs and one injection” was employed to seal the gas extraction borehole on site. The schematic diagram of the technology and relevant device coal-based grouting sealing for a gas extraction borehole is depicted in Figure 14. The borehole device is mainly composed of two 1-m-long capsular bags, two grouting pipes and a blast valve. One capsular bag is about 1 m away from the borehole outlet, and the other is about 1 m from the suction hole section. A slurry outlet containing a blast valve is set between the two capsular bags. During grouting, as the grouting pressure inside the capsular bags and the grouting pipelines rise, the blast valve will blast and open up to realize the sealing and filling the surrounding rock fracture between the capsular bags. In this way, the gas extraction borehole is sealed.

4.2 Sealing effect of coal-based grouting

The coal-based grouting sealing technology was adopted to seal the gas extraction borehole in the coal seam of a track roadway in Zhaogu No. 2 Coal Mine. After the completion of gas

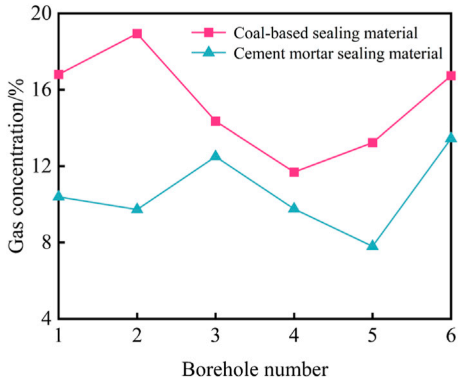

FIGURE 15
Comparison of sealing effect of two materials.

extraction borehole construction, the sealing device of "two plugs and one injection" was fixed on the gas extraction pipe line and then transferred to the borehole. According to the water-solid ratio of 1.5, an appropriate number of additives was added into the slurry to configure the coal-based slurry which was then injected into the sealing device of "two plugs and one injection" by using the grouting pump. As the grouting process continued, the two capsular bags were gradually filled with the coal-based slurry, and the grouting pressure also rose accordingly. Subsequently, the grouting pressure opened up the bast valve. At this time, the grouting pressure would plunge. As the slurry filled the fracture in the surrounding rock, the grouting pressure went up again, and finally reached 1 MPa or so, which marks the completion of gas extraction borehole sealing. After the sealing, the gas extraction data were recorded with the average concentration of a single borehole within 3 months as the evaluation index (Figure 15). According to the recorded data, the gas extraction concentration after ordinary cement mortar borehole sealing ranges from 7.8% to 13.5% with an average of 10.7%, while the average gas extraction concentration after coal-based grouting sealing ranges from 11.6% to 18.9% with an average of 15.3%. The gas extraction concentration is promoted by 1.43 times, which suggests that the coal-based grouting sealing technology can achieve a better sealing effect.

5 Conclusion

In this paper, a new type of coal-based grouting sealing materials was developed and applied to the fractured coal sample in the grouting test. Furthermore, the coal sample before and after grouting was scanned and reconstructed by means of industrial CT. On this basis, the numerical calculation model of grouting sealing for the fractured coal sample was established, and the mechanism of grouting sealing and seepage reduction with coal-based sealing materials was simulated. Finally, the field test on gas extraction borehole sealing was performed using the coal-based grouting sealing technology. The main conclusions are listed as follows.

1) Through the permeability test on the fractured coal sample before and after grouting, it is found that the coal-based grouting materials can fill the fracture tightly, and the permeability plunges after grouting, which means that the coal-based grouting materials exert an excellent sealing effect on the coal sample. The numerical simulation results are basically the same as the measured results, which confirms the correctness of the theoretical model.
2) By constructing the fracture structure model, established a slurry flow coupling theoretical model of mass conservation, slurry flow and permeability evolution equation. On the ground of the real-time fracture industrial CT scanning reconstruction model, the whole process of coal sample fracture sealing by coal-based slurry was simulated by importing the reconstructed CT images into COMSOL numerical simulation software with the self-compiled Matlab program. By doing so, the variation of coal sample permeability with time was concluded. The research results provide guidance for exploring the mechanism of grouting sealing and seepage reduction and strengthening the sealing effect for gas extraction boreholes.
3) The gas extraction concentration after ordinary cement mortar borehole sealing ranges from 7.8% to 13.5% with an average of 10.7%, while the average gas extraction concentration after coal-based grouting sealing ranges from 11.6% to 18.9% with an average of 15.3%. The gas extraction concentration is promoted by 1.43 times, which indicates that the coal-based grouting sealing technology can achieve a better sealing effect.

Data availability statement

The original contributions presented in the study are included in the article/Supplementary Material, further inquiries can be directed to the corresponding author.

Author contributions

YGwas responsible for writing and framing articles; BY offered a great deal of guidance and advice on writing articles; HZ assisted in completing the simulation part; BZ assisted in completing the experimental part; JS, QW, JN, and JL assisted in completing the field test part. All authors have read and agreed to the published version of the manuscript.

Funding

This study was supported by the National Natural Science Foundation of China (Grant Nos 52274193 and 52274192), promotion projects in Henan Province (Grant No. NSFRF220205) and the Innovative Scientific Research Team of Henan Polytechnic University in China (T2022-1). Natural Science Foundation of Henan (Grant No. 202300410182).

Acknowledgments

We thank the State Key Laboratory Cultivation Base for Gas Geology and Gas Control. We would like to express our gratitude to engineers of Zhaogu No. 2 Mine of Jiaozuo Coal Industry (Group) Co., Ltd. for their help in the field tests.

Conflict of interest

JS, QW, JN, and JL were empolyed by the Sima Coal Industry Co., Ltd., Shanxi Lu'an Group.

The remaining authors declare that the research was conducted in the absence of any commercial or financial relationships that could be construed as a potential conflict of interest.

Publisher's note

References

Bao, R. Y., Shi, B., and Zhang, C. (2022). Research and application of concentric ring reinforcement and sealing technology for gas drainage boreholes in soft-coal seams. *ACS omega* 7, 34763–34769. doi:10.1021/ACSOMEGA.2C01388

Bi, R. Q., Chen, X. X., Zhang, L., Wang, S. Y., Liu, X. H., and Hua, S. (2022). Refinement study on pressure relief zone of gas extraction borehole considering roughness. *Sustainability* 14, 9541. doi:10.3390/SU14159541

Chen, J. T., Guo, W. J., Yin, L. M., Lu, C., Chang, X. K., Zhang, S. C., et al. (2016). Experimental study of floor cracking under deep mining. *Chin. J. Rock Mech. Eng.* 35, 2298–2306. doi:10.13722/j.cnki.jrme.2015.1557

Chindaprasirt, P., Homwuttiwong, S., and Sirivivatnanon, V. (2003). Influence of fly ash fineness on strength, drying shrinkage and sulfate resistance of blended cement mortar. *Cem. Concr. Res.* 34, 1087–1092. doi:10.1016/j.cemconres.2003.11.021

Di, H. F., Zhang, H. B., Hou, C. Y., Zheng, D. D., Chai, H. C., Liu, L., et al. (2021). Effect of pre-curing stress on strength and micro structure of sulphoaluminate grouting materials. *J. Henan Polytech. Univ. Nat. Sci.* 40 (03), 163–168. doi:10.16186/j.cnki.1673-9787.2019120053

Gao, Y. B., and Ren, J. (2022). Study on the effect of borehole size on gas extraction borehole strength and failure mode. *ACS omega* 7, 25635–25643. doi:10.1021/ACSOMEGA.2C02834

Ge, Z. L., Mei, X. D., Lu, Y. Y., Xia, B. W., and Chen, J. F. (2014). Mechanical model and test study of sealed drilling for hydraulic fracturing in underground coal mines. *Rock Soil Mech.* 35 (07), 1907–1913. doi:10.16285/j.rsm.2014.07.019

Guo, X., Xue, S., Zheng, C. S., and Li, Y. B. (2021). Experimental research on performance of new gas drainage borehole sealing material with high fluidity. *Adv. Mater. Sci. Eng.* 2021, 1–12. doi:10.1155/2021/6645425

Hao, J., Li, X., Song, Y., Zhang, P., and Liu, H. (2021). Analysis of mining roadway with large deformation of broken soft coal and research on supporting technology: A case study in xin'an coal mine, China. *Eng. Fail. Anal.* 130, 105761. doi:10.1016/J.ENGFAILANAL.2021.105761

Huang, M. Q., Zhang, L., Zhang, C., and Chen, S. (2019). Characteristics of permeability changes in bituminous coal under conditions of stress variation due to repeated mining activities. *Nat. Resour. Res.* 29, 1687–1704. doi:10.1007/s11053-019-09542-0

Kang, H. P. (2021). Seventy years development and prospects of strata control technologies for coal mine roadways in China. *Chin. J. Rock Mech. Eng.* 40, 1–30. doi:10.13722/j.cnki.jrme.2020.0072

Li, B., Zhang, J. X., Liu, Y. W., Qu, L. N., Liu, Q., Sun, Y. X., et al. (2022). Interfacial porosity model and modification mechanism of broken coal grouting: A theoretical and experimental study. *Surf. Interfaces* 33, 102286. doi:10.1016/J.SURFIN.2022.102286

Li, H., Guo, S. S., and Li, C. (2015). Research and application of drilling cuttings backfill hole sealing technology. *Saf. Coal Mines* 46 (11), 14–20. doi:10.13347/j.cnki.mkaq.2015.11.004

Li, S. C., Liu, R. T., Zhang, Q. S., and Zhang, X. (2016). Protection against water or mud inrush in tunnels by grouting: A review. *J. Rock Mech. Geotechnical Eng.* 8, 753–766. doi:10.1016/j.jrmge.2016.05.002

Li, S. C., Zheng, Z., Liu, R. T., Wang, X. C., Zhang, L. Z., and Wang, H. B. (2017). Analysis on fracture grouting mechanism considering grout-rock coupling effect. *Chin. J. Rock Mech. Eng.* 36, 812–820. doi:10.13722/j.cnki.jrme.2016.0765

Li, T., Yao, B. H., Liu, Y., and Wang, D. K. (2021). Grouting fractured coal permeability evolution based on industrial CT scanning. *Geofluids* 2021, 1–12. doi:10.1155/2021/5564786

Li, X., Si, G. Y., Oh, J., Canbulat, I., Xiang, Z. Z., and Li, T. B. (2022). A pre-peak elastoplastic damage model of gosford sandstone based on acoustic emission and ultrasonic wave measurement. *Rock Mech. Rock Eng.* 55 (8), 4819–4838. doi:10.1007/s00603-022-02908-6

Liu, J. W., Wu, N., Si, G. Y., and Zhao, M. X. (2020). Experimental study on mechanical properties and failure behaviour of the pre-cracked coal-rock combination. *Bull. Eng. Geol. Environ.* 80, 2307–2321. doi:10.1007/s10064-020-02049-6

Liu, J. Z., Sun, W., Miao, C. W., and Liu, J. P. (2010). Research on the hydration heat of paste in ultra high strength concrete at low water-binder ratio. *J. Build. Mat. (Shanghai, China.* 13, 139–142. doi:10.3969/j.issn.1007-9629.2010.02.002

Liu, Q., Chen, W. Z., Yuan, J. Q., Wang, Y. X., and Wan, H. (2020). Evaluation of grouting reinforcement effect for karst filling medium based on seepage-erosion theory. *Chin. J. Rock Mech. Eng.* 39 (3), 1–9. doi:10.13722/j.cnki.jrme.2019.1112

Liu, Y., Zhang, J., Wei, J. P., and Liu, X. T. (2020). Optimum structure of a Laval nozzle for an abrasive air jet based on nozzle pressure ratio. *Powder Technol.* 364, 343–362. doi:10.1016/j.powtec.2020.01.086

Nath, P., and Sarker, P. (2011). Effect of fly ash on the durability properties of high strength concrete. *Procedia Eng.* 14, 1149–1156. doi:10.1016/j.proeng.2011.07.144

Si, L. L., Wei, J. P., Xi, Y. J., Wang, H. Y., Wen, Z. H., Li, B., et al. (2021). The influence of long-time water intrusion on the mineral and pore structure of coal. *Fuel* 290, 119848. doi:10.1016/J.FUEL.2020.119848

Si, L. L., Zhang, H. T., Wei, J. P., Li, Bo., and Han, H. K. (2021). Modeling and experiment for effective diffusion coefficient of gas in water-saturated coal. *Fuel* 284, 118887. doi:10.1016/j.fuel.2020.118887

Sun, X. Y., Li, K., and Wang, X. (2022). Capsule-bag-type sealing technology for gas drainage boreholes and its application. *Geofluids* 2022, 1–14. doi:10.1155/2022/1671859

Wang, C. B., Si, G. Y., Zhang, C. G., Cao, A. Y., and Canbulat, I. (2021). Location error based seismic cluster analysis and its application to burst damage assessment in underground coal mines. *Int. J. Rock Mech. Min. Sci. (1997).* 143, 104784. doi:10.1016/j.ijrmms.2021.104784

Wang, L., and Cheng, Y. P. (2012). Drainage and utilization of Chinese coal mine methane with a coal-methane co-exploitation model: Analysis and projections. *Resour. Policy* 37, 315–321. doi:10.1016/j.resourpol.2012.06.013

Wang, W., Li, H., Liu, Y., Liu, M., Wang, H., and Li, W. (2020). Addressing the gas emission problem of the world's largest coal producer and consumer: Lessons from the sihe coalfield, China. *Energy Rep.* 6, 3264–3277. doi:10.1016/J.EGYR.2020.11.199

Wei, J. P., Yao, B. H., Liu, Y., Wang, D. K., Cui, P. F., and Yao, S. (2020). Grouting fluid diffusion law and variable mass seepage model for fractured coal. *J. China Coal Soc.* 45 (01), 204–212. doi:10.13225/j.cnki.jccs.YG19.1526

Xu, Z. P., Liu, C. W., Zhou, X. W., Gao, G. R., and Feng, X. H. (2019). Full-scale physical modelling of fissure grouting in deep underground rocks. *Tunn. Undergr. Space Technol.* 89, 249–261. doi:10.1016/j.tust.2019.04.008

Yang, H. M., Ren, F. K., Wang, Z. F., Chen, S. W., and Pei, G. Z. (2019). Quality inspection and quantitative evaluation method for borehole sealing in gas drainage. *J. China Coal Soc.* 44 (S1), 164–170. doi:10.13225/j.cnki.jccs.2018.1176

Yang, R. S., Xue, H. J., Guo, D. M., He, T. Y., Li, T. T., Zhao, P. F., et al. (2016). Laboratory grouting experiment based CT analysis of grouted soft rocks in deep mines. *J. China Coal Soc.* 41 (2), 345–351. doi:10.13225/j.cnki.jccs.2015.0328

Yang, Z. Q., Hou, K. P., and Guo, T. T., and , M. Q. (2011). Study of column-hemispherical penetration grouting mechanism based on Bingham fluid of time-dependent behavior of viscosity. *Rock Soil Mech.* 32, 2697–2703. doi:10.16285/j.rsm.2011.09.037

Yao, B. H., Yao, S., Wei, J. P., Wen, Z. H., Liu, Y., and Si, L. L. (2022). A new method for determining the sealing depth of extraction borehole based on the constant-pressure gas injection and its applications. *Rock Mech. Rock Eng.* 55, 3703–3717. doi:10.1007/S00603-022-02844-5

Yu, B. H., Su, C., and Wang, D. (2015). Study of the features of outburst caused by rock cross-cut coal uncovering and the law of gas dilatation energy release. *Int. J. Min. Sci. Technol.* 25, 453–458. doi:10.1016/j.ijmst.2015.03.020

Zhang, H. D., Liu, Y., Tang, J. R., Liu, W. C., and Chen, C. J. (2022). Investigation on the fluctuation characteristics and its influence on impact force of supercritical carbon dioxide jet. *Energy* 253, 124125. doi:10.1016/J.ENERGY.2022.124125

Zhang, J. F., Lin, H. F., Li, S. G., Yang, E. H., Yang, D., Yang, B., et al. (2022). Accurate gas extraction(age) under the dual-carbon background: Green low-carbon development pathway and prospect. *J. Clean. Prod.* 377, 134372. doi:10.1016/J.JCLEPRO.2022.134372

Zhang, J. X., Li, B., Liu, Y., Li, P., Fu, J. W., Chen, L., et al. (2022). Dynamic multifield coupling model of gas drainage and a new remedy method for borehole leakage. *Acta Geotech.* 17, 4699–4715. doi:10.1007/S11440-021-01444-X

Zhang, Q. S., Zhang, L. Z., Zhang, X., Liu, R. T., Zhu, M. T., and Zheng, D. Z. (2015). Grouting diffusion in a horizontal crack considering temporal and spatial variation of viscosity. *Chin. J. Rock Mech. Eng.* 34 (6), 1198–1210. doi:10.13722/j.cnki.jrme.2014.0958

Zhang, X. B., Gao, J. L., Jia, G. N., and Zhang, J. W. (2022). Study on the influence mechanism of air leakage on gas extraction in extraction boreholes. *Energy Explor. Exploitation* 40, 1344–1359. doi:10.1177/01445987211070664

Zhang, Z. F., Kang, H. P., Jiang, Z. Y., Li, W. Z., Jiang, P. F., Cai, R. C., et al. (2020). Study and application of high-pressure splitting grouting modification technology in coalmine with depth more than 1 000 m. *J. China Coal Soc.* 45, 972–981. doi:10.13225/j.cnki.jccs.SJ19.1545

Zhou, F. b., Sun, Y. N., Li, H. J., and Yu, G. F. (2016). Research on theoretical model and engineering technology of the coal seam gas drainage hole sealing. *J. China Univ. Min. Technol. Engl. Ed.* . 45 (03), 433–439. doi:10.13247/j.cnki.jcumt.000498

Zhu, G. X., Zhang, Q. S., Feng, X., Liu, R. T., Zhang, L. Z., Liu, S. Q., et al. (2020). Study on the filtration mechanism in permeation grouting using the particle deposition probability model. *Adv. Eng. Sci.* 52, 125–135. doi:10.15961/j.jsuese.201900802

frontiers | Frontiers in Earth Science

TYPE Original Research
PUBLISHED 10 January 2023
DOI 10.3389/feart.2022.1054896

OPEN ACCESS

EDITED BY
Yihuai Zhang,
Imperial College London,
United Kingdom

REVIEWED BY
Muhammad Arif,
Khalifa University, United Arab Emirates
Danqing Song,
Tsinghua University, China

*CORRESPONDENCE
Bo Li,
✉ anquanlibo@hpu.edu.cn

SPECIALTY SECTION
This article was submitted to
Economic Geology,
a section of the journal
Frontiers in Earth Science

RECEIVED 27 September 2022
ACCEPTED 30 November 2022
PUBLISHED 10 January 2023

CITATION
Zhang J, Xu B, Zhang P, Cai M and Li B (2023), Effects of surface roughness on wettability and surface energy of coal. *Front. Earth Sci.* 10:1054896.
doi: 10.3389/feart.2022.1054896

Effects of surface roughness on wettability and surface energy of coal

Jian Zhang[1,2,3], Bo Xu[1], Pengyan Zhang[1], Maolin Cai[1] and Bo Li[1,2,3]*

[1]School of Safety Science and Engineering, Henan Polytechnic University, Jiaozuo, China, [2]State Key Laboratory Cultivation Base for Gas Geology and Gas Control, Henan Polytechnic University, Jiaozuo, China, [3]The Collaborative Innovation Center of Coal Safety Production of Henan, Jiaozuo, China

Surface roughness has an important effect on the wettability and surface energy of coal. Although the predecessors had studied the effect of surface roughness on the wettability of coal, there were few researches on the effect of surface energy of coal, and the relationship between wettability and surface energy had not been thoroughly studied. This paper aimed to study the effect of surface roughness on the wettability and surface energy of coal, and revealed the relationship between the wettability and surface energy of coal. Based on the surface roughness of coal, this paper selected Hami lignite, Anyang coking coal and Zhaogu anthracite as the research objects, used the experimental methods to measure the surface roughness and experimental contact angle of coal under different conditions to study the effect of surface roughness on the wettability, and then applied the OWRK method to calculate the surface energy of coal to study the effect of surface roughness on the surface energy. The experimental results showed that the wettability of hydrophilic coal became better and the surface energy increased with the increase of surface roughness, while the results of hydrophobic coal were opposite. There was a positive correlation between the wettability and surface energy of coal, and the wettability of coal could be analyzed from the perspective of surface energy. Surfactant could change the wettability of coal, but unchanged the law of wettability with surface roughness.

KEYWORDS

coal dust, surface roughness, wettability, surface energy, surfactant

1 Introduction

As an important energy source in China, coal will still play a dominant role in the coming decades (Wei et al., 2019; Du et al., 2020; Yang and He, 2020; Du and Song, 2022). In recent years, coal mining technology is tending to be more automated and intelligent, and production rate of coal is therefore gradually increasing. However, with the increase operation of coal mining, mine dust production is also growing, and meanwhile the harm of mine dust is increasingly serious. As one of the seven major disasters in coal mines, the harm of mine dust is multifaceted, mainly including pneumoconiosis (Wu, 2019) and coal dust explosion (Chen et al., 2018). Effective treatment of mine dust is one of the important measures to improve the working environment, provide safe operating conditions and ensure the safety of coal mine workers. Wet dust removal is one of the effective measures to control mine dust. Studies have shown that increasing the water content of coal can greatly reduce the amount of dust generated during coal mining (Wang, 2011). Injecting aqueous solutions containing surfactants into coal seams can also achieve the effect of dust removal (Wang, 2020). Chen (Chen et al., 2019) analyzed the wettability of low rank coal based on the development of bedding samples and pore characteristics of coal, and found that the wettability of coal was related to the direction of bedding. The better the pore size sorting of coal, the better the wettblity of coal. In the study of micro-wettability characteristics of coal dust, Zhang (Zhang et al., 2021) analyzed the influence of surface characteristics of coal dust on the wettability of coal dust, and found that the wettability of coal dust was positively correlated with the specific surface area of coal dust. The better the wettability of coal dust, the faster the settling rate of coal dust. Xia (Xia et al., 2016; Xia, 2017) used the experimental method to determine the surface roughness and contact angle of ultra-low ash coal to study the effect of surface roughness on the wettability of coal, and found that the wettability of coal first increased, second decreased, and then slightly increased with the surface roughness increased. Li (Li et al., 2021) used the phase field interfacial tracking method to simulate the wetting of droplets on the surface of coal samples. The simulation results showed that the contact angle of hydrophilic coal samples decreased and the wettability increased with the increase of surface roughness, and the results of hydrophobic coal samples were opposite. Li (Li et al., 2015) measured the surface tension of surfactants at different concentrations by capillary rise method, and found that surfactants effectively reduced the surface tension of pure water and improved the wetting effect of pure water on coal. Huang (Huang et al., 2010) studied the wetting ability of different surfactants by sedimentation method, and found that the type and concentration of surfactants had different effects on the wettability of coal.

Based on the effect of coal surface morphology and surfactant on the wettability of coal, the above studies had made an important contribution to improving the efficiency of mine wet dust removal. However, they did not analyze the surface energy of coal and study the relationship between wettability and surface energy. Therefore, this paper studied the wettability and surface energy of coal based on surface roughness, analyzed the experimental contact angle under different surface roughness to reflect the effect on the wettability, then used OWRK method to calculate the surface energy of coal, studied the effect of surface roughness on the surface energy, and finally revealed the relationship between the wettability and surface energy.

2 Experimental coal samples and roughness measurement

Surface roughness is the unevenness of the machined surface with smaller spacing and tiny peaks and valleys (Wang X. G., 2011), which generally occurs on the cutting surface during solid machining or the structural surface damaged by external shear forces. The smaller the surface roughness, the smoother the surface. According to the calculation method and sampling method, the classification of roughness is divided into arithmetic roughness, mean square roughness and maximum profile roughness. Since the calculation of mean square roughness is faster and more accurate, it is used to characterize the surface roughness in this study.

2.1 Experimental coal samples

Based on the surface roughness of coal samples, this study selected three coal samples with different ranks as the research objects, which were Hami lignite, Anyang coking coal and Zhaogu anthracite. Proximate analysis of the three coal samples are shown in Table 1.

2.2 Roughness measurement

Roughness measurement methods can be divided into contact and non-contact for solid matters. Contact measurement refers to the contact between the probing instrument and the solid part to be measured, which can directly obtain the surface roughness of the part to be measured. It can be divided into comparison method, impression method and probe contact method (Puttkamer and Jiang, 1984; Sherrington and Smith, 1992). Non-contact measurement refers to the feedback of roughness information of the measured surface by indirect means without contact with the measured surface. It can be divided into ultrasonic technology (Coker and Shin, 1996; Bui et al., 2015), laser triangulation method (Lu and Huang, 2004; Wang et al., 2004), machine vision technology (Tsai, 1987; Zhang et al., 2012), speckle method (Gao, 2009) and scattering method (Ni and Chen, 2001). The contact measurement method is slow, low accuracy, less applicable occasions, and the measured surface is easy to cause damage in the measurement process. Therefore, this study chooses the non-contact measurement method, which can quickly, accurately and stably detect the surface roughness of the objects online. The optical contact angle topography instrument was used to measure the surface roughness of coal samples, as is shown in Figure 1.

TABLE 1 Proximate analysis of the coal samples.

Coal sample	Moisture (M_{ad}/%)	Ash (A_{ad}/%)	Volatile (V_{adf}/%)
Hami lignite	5.94	10.05	33.61
Anyang coking coal	0.57	12.23	23.17
Zhaogu anthracite	2.98	15.55	7.98

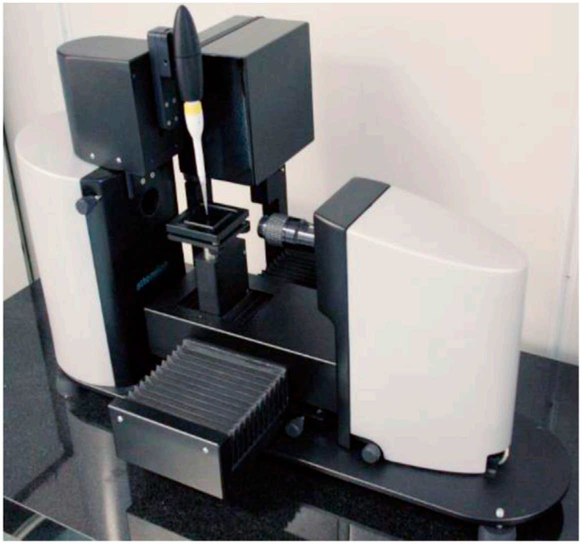

FIGURE 1
Optical contact angle topography instrument.

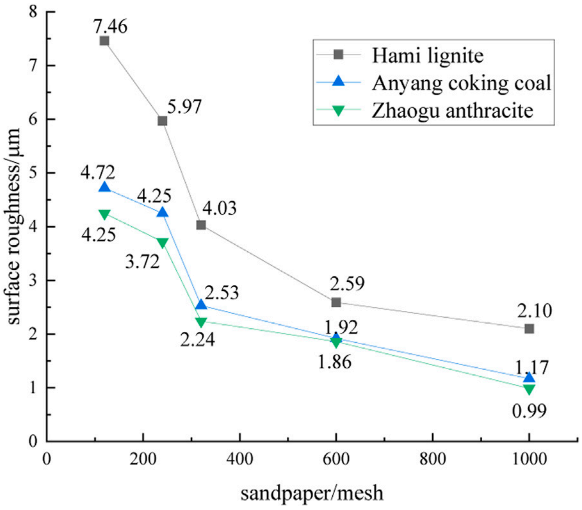

FIGURE 2
Surface roughness of three coal samples.

2.3 Measurement results

The surface of coal samples was directly polished by 120 mesh, 240 mesh, 320 mesh, 600 mesh and 1,000 mesh sand paper, respectively. Then the coal samples were cleaned with distilled water. Finally, the coal samples were dried for measurement. Three surfaces were selected for each coal sample, and each surface was measured five times. The measurement results were shown in Figure 2.

3 Effect of surface roughness on wettability of coal

The concept of contact angle was proposed to quantitatively characterize the hydrophilicity and hydrophobicity of solid substance (Good, 2012). Solid surface with contact angle values less than 90° is considered to be hydrophilic, and it is deemed more hydrophilic against the contact angle. In contrast, the values greater than 90° have hydrophobic properties, and the larger the value, the worse the wettability. When the droplet is in a stable state on the solid surface, a tangent line of the vapor-liquid contact line was made at a point on the solid-liquid-vapor three-phase contact line. The angle formed between the tangent line and the solid-liquid contact line is the contact angle, as shown in Figure 3 γ_{lv}, γ_{sl} and γ_{sv} represent the surface tension or surface energy between liquid-vapor, solid-liquid and solid-vapor, respectively.

3.1 Contact angle measurement

The optical contact angle topography instrument was used to measure the contact angle of coal samples in this study. The measurement principle was shown in Figure 4. The droplet was suspended in the dropper, and the LED light source was provided on the side to illuminate where the droplets come into contact with the solid surface. The contour of the droplet and the solid surface was recorded by the camera. Then the angle between the tangent line of the three-phase contact line and the phase interface was calculated by the Young–Laplace

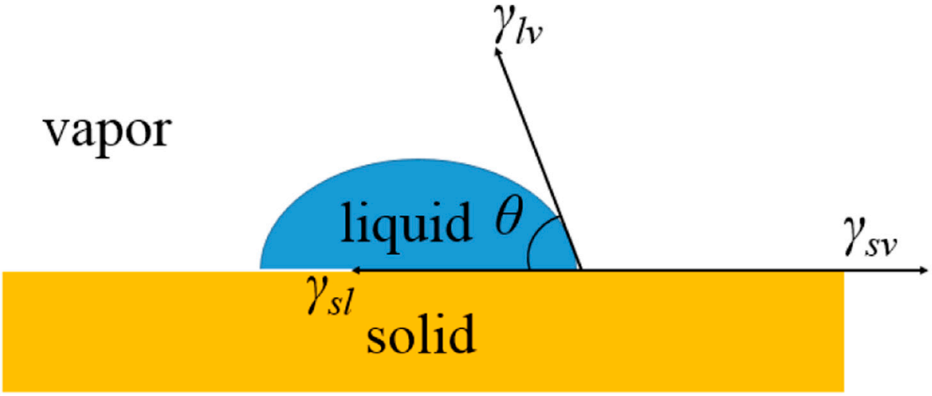

FIGURE 3
Diagram of contact angle.

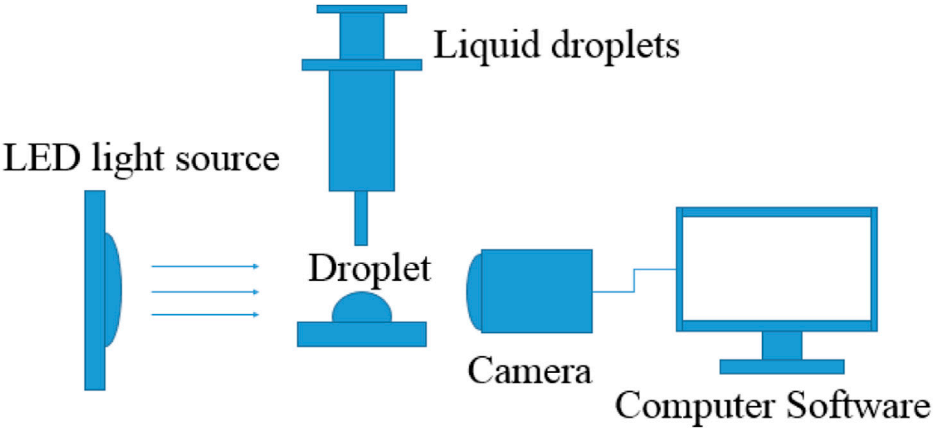

FIGURE 4
Principle of contact angle measurement.

method (Rior and Neumann, 1997) to obtain the value of the contact angle.

The dropper was filled with deionized water and glycerol, respectively. The coal samples were placed on the loaded platform. The dropper was set to drop 10 μL of liquid, and automatically descend to make the droplet contact with the surface of the coal sample. The process and images of the contact angle measurement were recorded by the camera automatically. The contact angle value was obtained by software processing. The roughness of each coal sample was measured at 5 to 6 points, and the average value is taken. From the experimental point of view, the liquid itself has a certain surface tension, and in the case of small size, it mostly exists in a nearly spherical state. In order to reduce the measurement error of the experiment, this experiment was conducted on the surface of the coal sample without cracks.

3.2 Experimental results and analysis

The experimental contact angles of the coal samples surfaces after wetting by deionized water and glycerol under different roughness were measured respectively. The former contact angle can characterize the intuitive influence of the surface roughness on the wettability of coal. The latter contact angle was used to calculate the surface energy of coal under different surface roughness, which can further explain the influence of the change of surface energy on the wettability change of the former. The test results are shown in Figure 5, where 1 represents deionized water and 2 represents glycerol.

It can be seen from Figure 5 that the experimental contact angle values of the three coal samples are different, and their wettability is also different. After the surface of the three coal

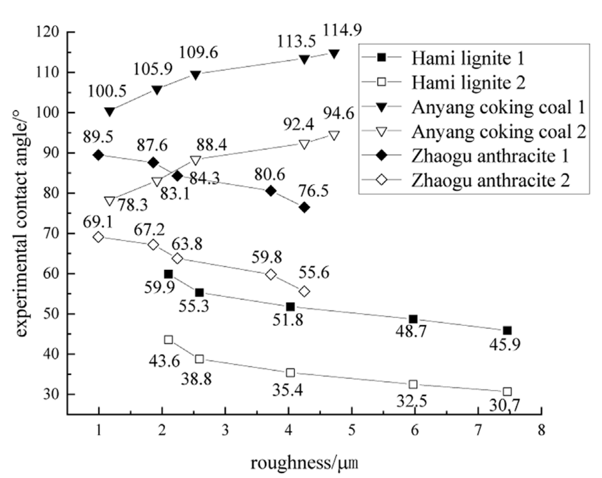

FIGURE 5
Experimental contact angles of three coal samples.

samples was wetted by deionized water, the experimental contact angle values of Hami lignite were all less than 60°, showing hydrophilicity. The experimental contact angle values of Anyang coking coal were all greater than 100°, showing hydrophobicity. The experimental contact angle values of Zhaogu anthracite were all greater than 76° and less than 90°, showing weak hydrophilicity. The result is the same as the conclusion obtained by Li (Li and Li, 2016) that lignite has the best hydrophilicity, coking coal has the worst hydrophilicity, and anthracite is in between. It is found from Figure 5 that with the increase of coal surface roughness, the experimental contact angle values of Hami lignite and Zhaogu anthracite gradually decrease, and their wettability becomes better, while the experimental contact angle value of Anyang coking coal gradually increase, and its wettability becomes worse. This is because of the different degrees of coal metamorphism, resulting in different components of coal. Lignite has the most oxygen-containing functional groups, followed by anthracite, and the least in coking coal. Coking coal has the most aromatic hydrocarbons and aliphatic hydrocarbons, followed by anthracite, and lignite has the least. The different ranges of variation in contact angle values for the three coal samples are also due to the differences in the surface structural properties of coal caused by the different degrees of coal metamorphism. At the same time, it was also found that after the surfaces of the three coal samples were wetted by glycerol, the contact angle values decreased, which showed that the hydrophilicity of lignite was increased, the hydrophobicity of coking coal was decreased, and the hydrophilicity of anthracite was improved. This is because glycerol reduces the surface tension of the liquid, which in turn improves the wettability of the coal samples.

4 Effect of surface roughness on surface energy of coal

The surface energy of coal is caused by the balanced intermolecular forces on the interior and the unbalanced forces on the surface. Coal is a complex polymer structure with carbon as the skeleton, and the forces among internal carbon elements and between carbon elements and other elements are balanced. When coal is destroyed by external forces, the force balance is broken and the coal will produce a new surface. The surface molecules of coal are attracted by the internal forces, and this force is the surface energy (force).

4.1 Surface force parameters

The surface force parameters of deionized water and glycerol include surface tension, dispersion force and polarity force. The results are shown in Table 2.

4.2 Surface energy calculation

The calculation method of coal surface energy is divided into gas adsorption method (Nie et al., 2000) and contact angle calculation method. The gas adsorption method usually takes a long time, while the contact angle calculation method takes a short time and several mature calculation models can be used for contact angle calculation method. The contact angle calculation methods include the Fowkes method (Fowkes, 1963), the Wu average method (Wu, 1971) and the OWRK method. In this paper, the OWRK method is used to calculate the surface energy of coal.

The OWRK method is an improvement of the Fowkes method. Owens and Wendt (Owens and Wendt, 1969) considered the effect of polarity force on the surface energy and obtained a new Eq. 1. Equation 1 combines with the Young's equation and the surface force parameters of the two liquids, and the Eqs 2, 3 of the dispersion force and the polarity force are obtained.

$$\gamma_{sl} = \gamma_{sv} + \gamma_{lv} - 2\left(\sqrt{\gamma_{sv}^{d}\gamma_{lv}^{d}} + \sqrt{\gamma_{sv}^{p}\gamma_{lv}^{p}}\right) \tag{1}$$

$$\sqrt{\gamma_{sv}^{d}} = \frac{\gamma_{lv2}\left(1+\cos\theta_2\right)\sqrt{\gamma_{lv1}^{p}} - \gamma_{lv1}\left(1+\cos\theta_1\right)\sqrt{\gamma_{lv2}^{p}}}{2\sqrt{\gamma_{lv1}^{p}\gamma_{lv2}^{d}} - 2\sqrt{\gamma_{lv1}^{d}\gamma_{lv2}^{p}}} \tag{2}$$

$$\sqrt{\gamma_{sv}^{p}} = \frac{\gamma_{lv2}\left(1+\cos\theta_2\right)\sqrt{\gamma_{lv1}^{d}} - \gamma_{lv1}\left(1+\cos\theta_1\right)\sqrt{\gamma_{lv2}^{d}}}{2\sqrt{\gamma_{lv1}^{d}\gamma_{lv2}^{p}} - 2\sqrt{\gamma_{lv1}^{p}\gamma_{lv2}^{d}}} \tag{3}$$

Where γ_{sl} γ_{sv} and γ_{lv} represent the surface tension of coal between solid-liquid, solid-vapor and liquid-vapor, $\gamma_{sv,d}$ and $\gamma_{sv,p}$ represent the dispersion force and polarity force between solid

TABLE 2 Surface force parameters of liquid (Unit: mJ/m2).

Liquid	Surface tension γ_l	Dispersion force $\gamma_{l,d}$	Polarity force $\gamma_{l,p}$
deionized water	72	21	51
glycerol	64	34	30

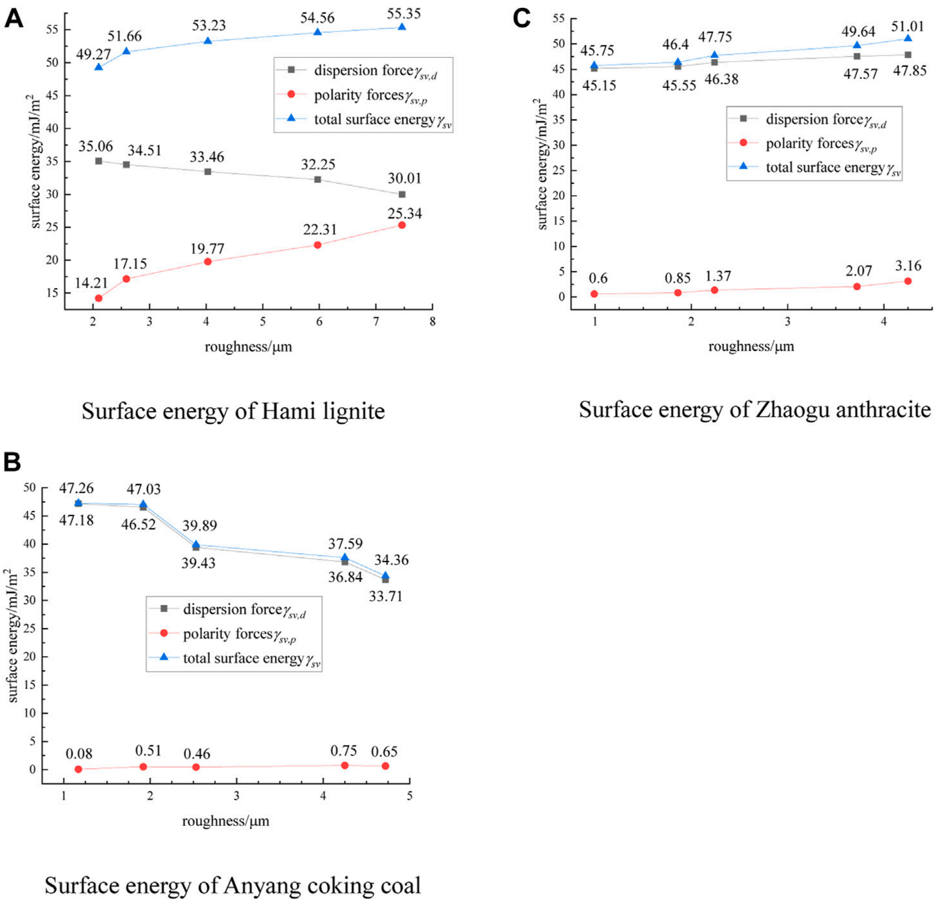

Surface energy of Hami lignite

Surface energy of Zhaogu anthracite

Surface energy of Anyang coking coal

FIGURE 6
Surface energy of three coal samples **(A)** Hami lignite, **(B)** Anyang coking coal, **(C)** Zhaogu anthracite.

and vapor, $\gamma_{lv,d}$ and $\gamma_{lv,p}$ represent the dispersion force and polarity force between liquid and vapor. The unit is mJ/m^2. Where the subscript 1 represents deionized water, the subscript 2 represents glycerol, and θ represents the experimental contact angle of the two liquids.

4.3 Calculation results and analysis

The contact angle values measured by the experiment were brought into the above equation. The surface energies of Hami lignite, Anyang coking coal and Zhaogu anthracite at different roughness were obtained. The calculation results are shown in Figure 6.

It is found from Figure 6 that the surface energy of lignite is provided by both dispersion force and polarity force, while that of coking coal and anthracite is mainly provided by dispersion force. This is related to the degree of metamorphism of the coal samples. Lignite has lower degree of metamorphism and more polar components, while coking coal and anthracite have higher degree of metamorphism and less polar components. The surface energy of coal samples with different hydrophilicity and hydrophobicity is different under the action of roughness,

TABLE 3 Introduction of surfactants.

Type	Name	Abbreviation	Chemical formula
Anionic	sodium dodecyl sulfate	SDS	$C_{12}H_{25}OSO_3Na$
Cationic	cetyl trimethyl ammonium chloride	CTAC	$C_{19}H_{42}ClN$

and the trend of change with roughness is also different. With the surface roughness of lignite increases, the dispersion force decreases, the polarity force increases, and the total surface energy tends to increase. With the surface roughness of coking coal increases, the dispersion force decreases, the polarity force does not change significantly, and the total surface energy tends to decrease. With the increase of anthracite surface roughness, the dispersion force and the polarity force increase, and the total surface energy tends to increase. Combined with the analysis in Figure 5 again, it was found that the surface energy of the three coal samples showed a negative correlation with the contact angle values of the coal samples. With the increase of coal surface energy, the contact angle values of the three coal samples gradually decreased, the wettability of lignite and anthracite increased, and the hydrophobicity of coking coal decreased. The surface energy and wettability of the three coal samples showd the same trend with the change of surface roughness. The influence of surface roughness on the wettability of coal samples can be analyzed from the perspective of coal surface energy.

5 Effect of surfactant on wettability of coal

Surfactants are usually added to liquids to change its properties. At present, surfactants are widely used in modern coal mining. Such as coal seam water injection, which is injected into the coal seam containing a certain concentration of surfactant water solution to improve the water content of the coal seam. It is conducive to the control of coal dust and gas in the underground.

5.1 Selection of surfactant

There are thousands of surfactants, and they can be divided into anionic surfactants, cationic surfactants and non-ionic surfactants according to the type. When anionic/cationic surfactants are dissolved in deionized water, negative/positive charges are ionized, giving the solution a negative/positive nature. The non-ionic surfactants do not ionize when dissolved in deionized water, and the solution becomes electrically neutral. This paper selected two different types of surfactants, namely Sodium Dodecyl Sulfate (SDS) and Cetyl Trimethyl Ammonium Chloride (CTAC). Their introduction are shown in Table 3.

5.2 Surfactant formulation

Because of its high efficiency, the surfactants can be added in small amounts to obtain good results and save the cost of raw materials. Combined with the previous experience of using surfactants, the surfactant solutions with mass concentrations (wt%) of 0.1%, 0.2% and 0.3% were prepared by using experimental instruments, such as balance, beaker, glass rod, distilled water and liquid storage bottles. The solutions were filled into the liquid storage bottles and labeled for convenient experimental use.

5.3 Experimental results and analysis

The prepared surfactant solutions were drawn into the dropper, and the contact angles of the coal samples were measured according to the above experimental procedure. The results are shown in Figure 7.

It can be seen from Figure 7 that the same surfactant has the same trend of change in the contact angle values of the three coal samples. With the increase of CTAC concentration, the contact angle values are decreasing gradually and the wettability becomes better. However, with the increase of SDS concentration, the contact angle values first decreases and then increases. When SDS concentration is 0.2%, the contact angle values is the smallest and the wettability is the best. The contact angle variation trend of the same coal sample under different surfactants is different. This is because the solid-liquid interfaces within different solutions have an optimal number of active molecules adsorbed. Before the optimum adsorption number is reached, with the surfactant concentration increases, the more number of active molecules adsorbed at the interface, the better stability of the interface and the better wettability of the coal sample. After the optimum adsorption number is exceeded, if the surfactant concentration continues to increase, the repulsive force between the surfactant molecules will increase, which will decrease the stability of the interface. When the repulsive force increases to a certain value, the surfactant molecules at the interface will be squeezed out of the adsorption layer, which increases the solid-

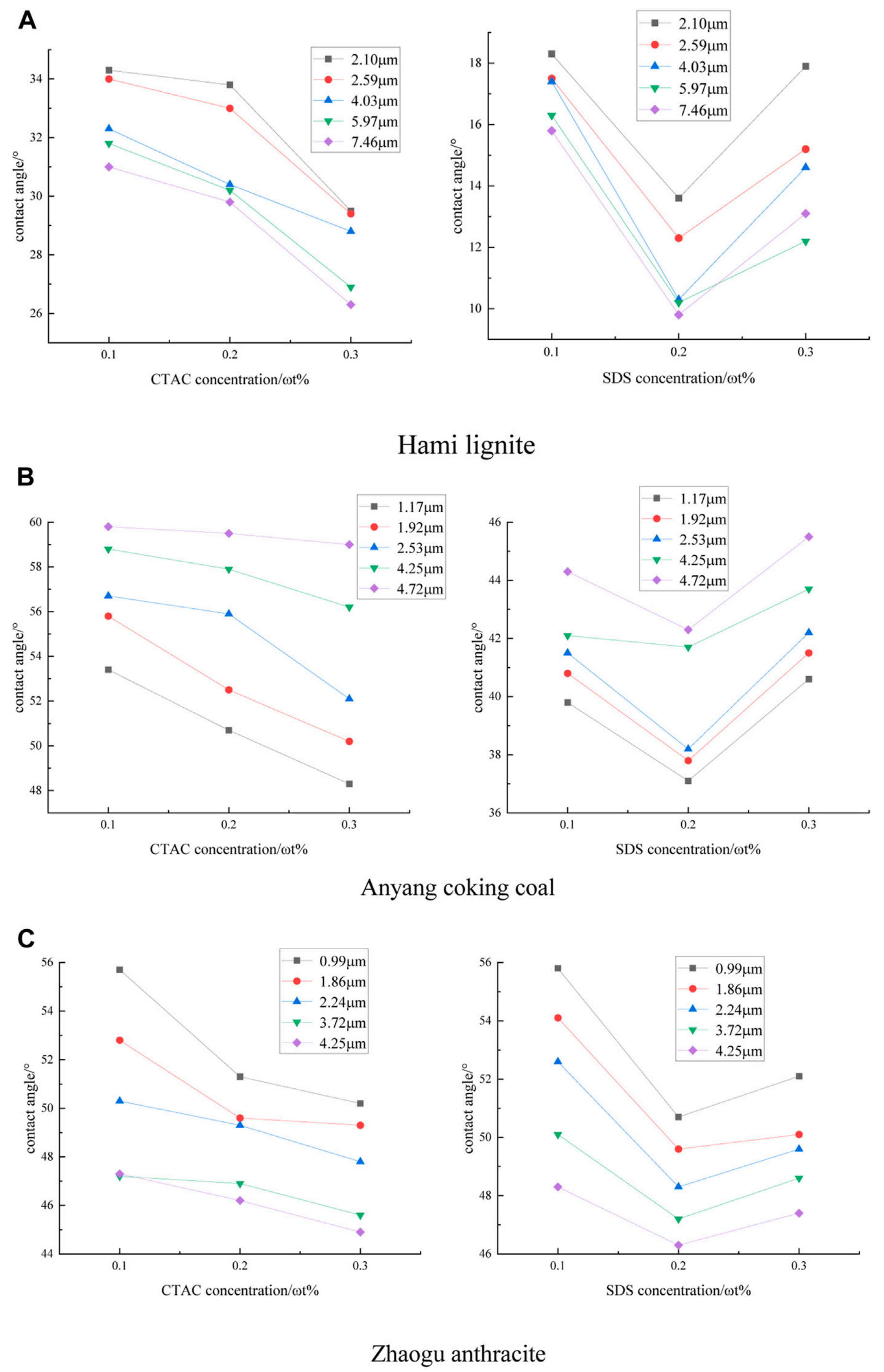

FIGURE 7
Experimental contact angle of three coal samples. **(A)** Hami lignite **(B)** Anyang coking coal **(C)** Zhaogu anthracite.

liquid interfacial tension and thus reduces the wettability of the coal sample. It is also found that the presence of surfactant did not change the variation law of wettability with surface roughness of the three coal samples.

6 Conclusion

Through the above experiments, the effect of surface roughness on the wettability and surface energy of coal was studied, and the relationship between the wettability and surface energy was revealed. The following conclusions were obtained:

1) The degree of coal metamorphism affected both wettability and surface energy properties. The three coals had different degree of metamorphism, which resulted in different components. Lignite had a low degree of metamorphism, more oxygen-containing functional groups, better wettability, more polar components, and the surface energy was provided by both dispersion force and polarity force. However, coking coal and anthracite had a high degree of metamorphism, more aromatic hydrocarbons and aliphatic hydrocarbons, less wettability, less polar components, and the surface energy was mainly provided by dispersion force.
2) There was a positive correlation between the wettability and surface energy of coal, and the wettability of coal could be analyzed from the perspective of surface energy. For the coal with the same properties, the surface energy and wettability had a same variation trend as the surface roughness. With the surface roughness of coal increased, the surface energy of lignite and anthracite increased, the experimental contact angle decreased, and the wettability became better. While the surface energy of coking coal decreased, the experimental contact angle increased, and the wettability became worse.
3) Surfactant could change the wettability of coal, but unchanged the law of wettability with surface roughness. With the increase of CTAC surfactant concentration, the experimental contact angle of coal decreased and the wettability became better. With the increase of SDS surfactant concentration, the experimental contact angle of coal first decreased and then increased, the wettability first became better and then worse. They unchanged the law of wettability with surface roughness.

There are some shortcomings in the experiments and research process. 1) The experimental coal samples polished by hand will cause errors in the determination results. In order to reduce the errors, the subsequent research should try to use mechanical devices to polish coal samples. 2) There are two surfactants used in the experiments, and a variety of different surfactants can be used in the subsequent experiments for comparison and analysis to summarize the rules.

Data availability statement

The original contributions presented in the study are included in the article/Supplementary Material, further inquiries can be directed to the corresponding author.

Author contributions

All authors contributed to the study conception and design. Data collection and analysis were performed by JZ, BX, PZ, MC, and BL. All authors read and approved the final manuscript.

Funding

The study is mainly supported by National Nature Science Foundation of China (Grant No. 52174171). The authors also acknowledge the support by Henan Province Key Scientific Research Projects of Institution of Higher Education (22A440012) and Outstanding Youth Fund of Henan Polytechnic University.

Acknowledgments

The authors would like to thank all editors and reviewers for their comments and suggestions.

Conflict of interest

The authors declare that the research was conducted in the absence of any commercial or financial relationships that could be construed as a potential conflict of interest.

Publisher's note

References

Bui, G. T., Chen, Y. Z., and Pang, D. C. (2015). Polymer-based capacity micromachined ultrasonic transducer for surface roughness measurement. *Key Eng. Mater.* 661 (4145), 22–28. doi:10.4028/www.scientific.net/kem.661.22

Chen, H. H., Shi, S. L., and Zheng, M. L. (2018). Analysis on coal dust explosion based on fuzzy fault tree. *Coal Technol.* 37 (08), 180–182. doi:10.13301/j.cnki.ct.2018.08.068

Chen, Y., Ma, D. M., Xia, Y. C., Guo, C., Yang, P., and Shao, K. (2019). Study on wettability and influencing factors of different macroscopic components in low rank coal. *Coal Sci. Technol.* 47 (09), 97–104. doi:10.13199/j.cnki.cst.2019.09.009

Coker, S. A., and Shin, Y. C. (1996). In-process control of surface roughness due to tool wear using a new ultrasonic system. *Int. J. Mach. Tools Manuf.* 36 (3), 411–422. doi:10.1016/0890-6955(95)00057-7

Du, H., Song, D. Q., Chen, Z., and Guo, Z. Z. (2020). Experimental study of the influence of structural planes on the mechanical properties of sandstone specimens under cyclic dynamic disturbance. *Energy Sci. Eng.* 8 (11), 4043–4063. doi:10.1002/ese3.794

Du, H., and Song, D. Q. (2022). Investigation of failure prediction of open-pit coal mine landslides containing complex geological structures using the inverse velocity method. *Nat. Hazards* 111, 2819–2854. doi:10.1007/s11069-021-05159-w

Fowkes, F. M. (1963). Additivity of intermolecular forces at interfaces. I. Determination of the contribution to surface and interfacial tensions of dispersion forces in various liquids. *J. Phys. Chem.* 67 (12), 2538–2541. doi:10.1021/j100806a008

Gao, Z. (2009). *Study of spatial-average-based surface roughness measurement techniques using static and dynamic speckle patterns*. Harbin, China: Harbin Institute of Technology.

Good, R. J. (2012). Contact angle, wetting, and adhesion: A critical review. *J. Adhesion Sci. Technol.* 6 (12), 1269–1302. doi:10.1163/156856192x00629

Huang, W. G., Hu, F., and Liu, N. Q. (2010). Study on surfactant wettability for coal dust. *Min. Saf. Environ. Prot.* 37 (3), 4–6. doi:10.3969/j.issn.1008-4495.2010.03.002

Li, J., Zhou, F., and Liu, H. (2015). The selection and application of a compound wetting agent to the coal seam water infusion for dust control. *Int. J. Coal Prep. Util.* 36 (4), 192–206. doi:10.1080/19392699.2015.1088529

Li, J. Y., and Li, K. Q. (2016). Influence factors of coal surface wettability. *J. China Coal Soc.* 41 (S2), 448–453. doi:10.13225/j.cnki.jccs.2015.1656

Li, C., Zhang, J., Han, J., and Yao, B. H. (2021). A numerical solution to the effects of surface roughness on water-coal contact angle. *Sci. Rep.* 11 (1), 459. doi:10.1038/s41598-020-80729-9

Lu, J. R., and Huang, Y. Q. (2004). Laser triangulation method for surface measurement. *J. Xiamen Univ. Sci.* 43 (01), 50–53. doi:10.3321/j.issn:0438-0479.2004.01.013

Ni, Q. L., and Chen, B. (2001). Measurement of surface roughness by scattering method. *Opt. Precis. Eng.* 9 (02), 151–154. doi:10.3321/j.issn:1004-924X.2001.02.012

Nie, B. S., He, X. Q., and Wang, E. Y. (2000). Surface free energy of coal and its calculation. *J. Taiyuan Univ. Technol.* 31 (04), 346–348. doi:10.16355/j.cnki.issn1007-9432tyut.2000.04.002

Owens, D. K., and Wendt, R. C. (1969). Estimation of the surface free energy of polymers. *J. Appl. Polym. Sci.* 13 (8), 1741–1747. doi:10.1002/app.1969.070130815

Puttkamer, H. V., and Jiang, Z. Q. (1984). *The surface roughness was measured with electric stylus profile status-the current situation and problems of surface roughness measurement*. China: China Inspection Body & Laboratory, 16–17. CNKI:SUN:XDJL.0.1984-06-005.06

Rior, D., and Neumann, A. W. (1997). Axisymmetric drop shape analysis: Computational methods for the measurement of interfacial properties from the shape and dimensions of pendant and sessile drops. *J. Colloid Interface Sci.* 196 (2), 136–147. doi:10.1006/jcis.1997.5214

Sherrington, I., and Smith, E. H. (1992). Performance assessment of stylus based areal roughness measurement systems. *Int. J. Mach. Tools Manuf.* 32 (1-2), 219–226. doi:10.1016/0890-6955(92)90081-Q

Tsai, R. Y. (1987). A versatile camera calibration technique for high-accuracy 3D machine vision metrology using off-the-shelf TV cameras and lenses. *IEEE J. Robot. Autom.* 3 (4), 323–344. doi:10.1109/JRA.1987.1087109

Wang, X. J., Gao, J., and Wang, L. (2004). Survey on the laser triangulation. *Chin. J. Sci. Instrum.* 25 (S2), 601–604+608. doi:10.19650/j.cnki.cjsi.2004.s2.185

Wang, W. H. (2011). Appliation present status and outlook of seam water injection dust control technology. *Coal Sci. Technol.* 39 (01), 57–60. doi:10.13199/j.cst.2011.01.63.wangwh.021

Wang, X. G. (2011). The measurement method of surface roughness and the correct application of parameters. *Shanghai Meas. Test.* 38 (05), 48–49+52. doi:10.3969/j.issn.1673-2235.2011.05.016

Wang, X. N. (2020). *Study on synergistic effect of surfactant compounding on wettability of coal dust*. Huainan, China: AnHui University of Science and Technology. doi:10.26918/d.cnki.ghngc.2020.000038

Wei, X. F., Wang, J. G., and Ding, Y. J. (2019). Progress and development trend of clean and efficient coal utilization technology. *Bull. Chin. Acad. Sci.* 34 (04), 409–416. doi:10.16418/j.issn.1000-3045.2019.04.005

Wu, S. (1971). Calculation of interfacial tension in polymer systems. *J. Polym. Sci. C. Polym. Symp.* 34 (1), 19–30. doi:10.1002/polc.5070340105

Wu, X. J. (2019). The mortality rate of pneumoconiosis is as high as 22.04% and the prevention and control work in coal field is urgent. *Saf. Health* 457 (01), 45–47. CNKI:SUN:LDAQ.0.2019-01-026.

Xia, W. C., Ni, C., and Xie, G. Y. (2016). The influence of surface roughness on wettability of natural/gold-coated ultra-low ash coal particles. *Powder Technol.* 288, 286–290. doi:10.1016/j.powtec.2015.11.029

Xia, W. C. (2017). Role of surface roughness in the attachment time between air bubble and flat ultra-low-ash coal surface. *Int. J. Mineral Process.* 168, 19–24. doi:10.1016/j.minpro.2017.09.006

Yang, Y., and He, Z. (2020). China's overseas oil and gas dependence: Situation, geographical risks, and countermeasures. *Resour. Sci.* 42 (08), 1614–1629. doi:10.18402/resci.2020.08.15

Zhang, J. G., Li, H. M., Liu, Y. T., Li, X. Y., Xie, J., Dai, Z. X., et al. (2021). Micro-wetting characteristics of coal dust and preliminary study on the development of dust suppressant in Pingdingshan mining area. *J. China Coal Soc.* 46 (03), 812–825. doi:10.13225/j.cnki.jccs.YT21.0140

Zhang, N., Chang, L., and Xu, X. P. (2012). Research on the technology of three-dimensional reconstruction based on machine vision. *Laser & Optoelectron. Prog.* 49 (05), 66–72. doi:10.3788/LOP49.051001

frontiers | Frontiers in Earth Science

TYPE Original Research
PUBLISHED 11 January 2023
DOI 10.3389/feart.2022.1037985

Check for updates

OPEN ACCESS

EDITED BY
Hongtu Zhang,
Henan Polytechnic University, China

REVIEWED BY
Xing Yi,
Nagaoka University of Technology,
Japan
Zhu Li,
Taiyuan University of Technology, China

*CORRESPONDENCE
Jinkui Ma,
289005557@qq.com

SPECIALTY SECTION
This article was submitted to Economic Geology, a section of the journal Frontiers in Earth Science

RECEIVED 06 September 2022
ACCEPTED 26 October 2022
PUBLISHED 11 January 2023

CITATION
Dong Q, Wang S, Ma J, Lyu S and Lu W (2023), Methane emission characteristics and model of CBM wells. *Front. Earth Sci.* 10:1037985.
doi: 10.3389/feart.2022.1037985

Methane emission characteristics and model of CBM wells

Qingxiang Dong[1], Shengwei Wang[1,2], Jinkui Ma[3]*, Shuaifeng Lyu[1] and Weiyong Lu[4]

[1]School of Earth Resources, China University of Geosciences, Wuhan, China, [2]State Key Laboratory of Coal and CBM Co-mining, Jincheng, China, [3]State Key Laboratory of Coal Mine Safety Technology, China Coal Technology & Engineering Group Shenyang Research Institute, Shenyang, China, [4]School of Mining Engineering, Lyuliang University, Lyuliang, China

CBM (CBM) development in coal mining area has good safety, economic and energy benefits, but methane emission is common in surface well sites. In view of this, taking the CBM wells in Qinshui County of Shanxi Province as an example, the methane emission location and emission volume of CBM wells are obtained, and the prediction model of methane emission volume is established through field investigation and multiple regression analysis. The results show that 81% of CBM wells have methane emission. Wellhead and drainage outlet are the two main positions of methane emission. The proportion of wells with emission volume between 0 and 10 m^3/d is 59%. On the whole, the emission accounts for 1.53% of the gas well production. There is almost no methane emission in the single liquid phase flow stage. The methane emission in the gas-liquid two-phase flow stage is positively correlated with the bottom hole flow pressure, times of stroke and gas production, and negatively correlated with the pump embedment and water production. The bottom hole flow pressure and the pump embedment have the greatest impact on the methane emission. In the single-phase gas flow stage, methane emission is positively correlated with gas production and casing pressure, and negatively correlated with stroke frequency and water production.

KEYWORDS

coalbed methane well, methane emission, gas-liquid two-phase flow, single gas phase flow, multiple linear regression

Introduction

CBM is a clean energy with methane as the main component. The development of CBM resources has three attributes: coal mine safety, energy utilization and environmental protection. China's CBM industry has taken shape, and the amount of CBM resources within 2000 m burial depth is 30.05×10^{12} m^3, ranking third in the world. Qinshui Basin in Shanxi Province has the most successful CBM development (Jia and Zhou, 2013; Shang et al., 2020; Xue et al., 2020; Sun et al., 2021; Zhu et al., 2021). The development process of CBM includes drilling, reservoir reconstruction and drainage gas production (Lyu et al., 2020a; Lyu et al., 2020b; Shen et al., 2020). The methane content in CBM is generally greater than 96.5%. Its ability to absorb infrared rays, greenhouse effect and radiation efficiency are 25 times, 26 times and 27 times that of carbon dioxide respectively, and its average life in the air is as high as 8 years (Tang and Li, 1990; Tang et al., 2006; Wu et al., 2014). The increase of the volume fraction of methane in the atmosphere causes the weakening of the atmospheric circulation, which is not conducive to the flow of solid particles, and significantly increases the greenhouse effect and urban heat island effect. Therefore, methane emission not only wastes clean energy, but also causes serious damage to the environment (Li et al., 2019). In addition, when the volume fraction of methane in the air reaches 5%–16%, it will explode in case of open fire. When the volume fraction of methane in the environment reaches 25%–30%, it may cause physical discomfort of operators, such as headache, fatigue, accelerated heartbeat and even suffocation (Zhang, 2011). It can be seen that when the methane volume fraction reaches the critical value under the condition of methane emission in the CBM well site, there are potential safety hazards for the well site equipment and personnel. Domestic and foreign scholars have carried out research on the monitoring and prevention methods of gas emission in natural gas transportation pipelines, but there are few studies on the methane emission mode, location, rate, emission amount and other parameters and evaluation methods of natural gas production wells, especially CBM emission wells (Zhang, 2011; Hou and Zeng, 2013; Li, 2014; Zhou et al., 2016; Kong and Wang, 2019). Therefore, it is of great significance to reveal the characteristics of methane emission and establish the prediction model of methane emission for formulating the production system of CBM and preventing methane emission. It will play a positive role in promoting the ecological civilization construction goal of striving to achieve carbon peak by 2030 and carbon neutrality by 2060. Therefore, taking the surface CBM wells in Qinshui Coal Mine Area as the research object, the methane emission and operating parameters of 204 CBM wells were tested and investigated on the spot. According to the multi factor analysis method (Luo et al., 2019; Meng and Zhu, 2019; Zheng, 2020), a methane emission model applicable to this area is established, which provides a basis for the formulation of control measures for methane emission of CBM wells.

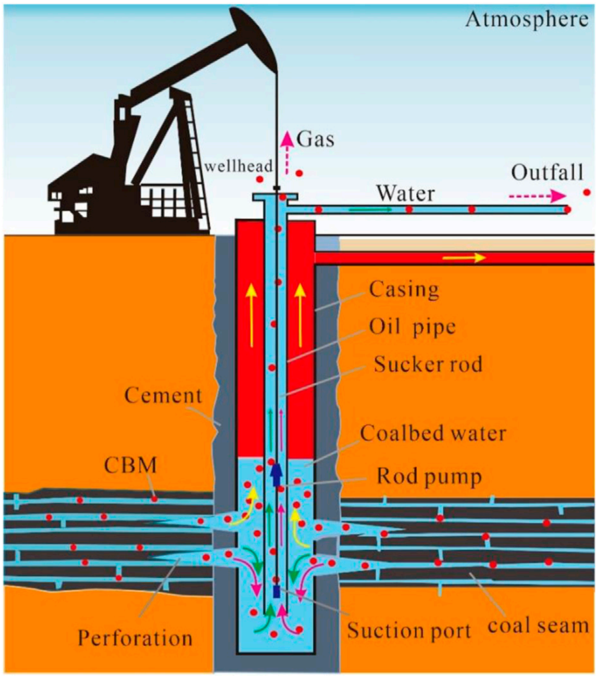

FIGURE 1
Principle of methane emission in CBM well.

Principle and measurement method of methane emission in CBM well

Methane emission principle

Figure 1 shows the principle of methane emission from CBM wells. After the completion of the drilling of the CBM well, the well is completed by running the casing-well cementation-perforating-fracturing. The purpose of fracturing is to produce artificial fractures in the coal seam, improve the permeability of the coal reservoir and improve the gas water flow channel. The oil pipe and drainage pump are installed in the casing to discharge the liquid in the wellbore to the surface through the oil pipe. As the bottom hole flow pressure decreases to the CBM desorption pressure, the adsorbed CBM begins to desorb and enters the casing along the fracturing fracture and perforation hole after diffusion and seepage. Due to the difference of gas and water, the CBM enters the annulus between the casing and the oil pipe and migrates to the low-pressure wellhead, thus entering the gas transmission pipeline for gathering and utilization. However, under the action of fluid entrainment, part of methane escapes into the oil pipe, and mainly escapes directly into the atmosphere from the drainage outlet on the ground. At the same time, as the pumping unit drives the pumping rod to rise and fall back and forth, the wellhead will be eccentric worn, the seal will be damaged, and the CBM will also overflow from the wellhead. Therefore, the direct cause of CBM emission is that the methane gas in the formation enters the oil pipe through gas channeling, and the poor sealing quality of the wellhead will also cause methane emission. Through theoretical analysis and a lot of field verification, the methane emission points of CBM wells are mainly at wellhead and sucker rod annulus and water outlet. Methane emission also occurs at the flange connection of a few CBM wells.

Determination method

The selected CBM wells are located in 6 CBM working areas in Qinshui County, Shanxi Province, mainly

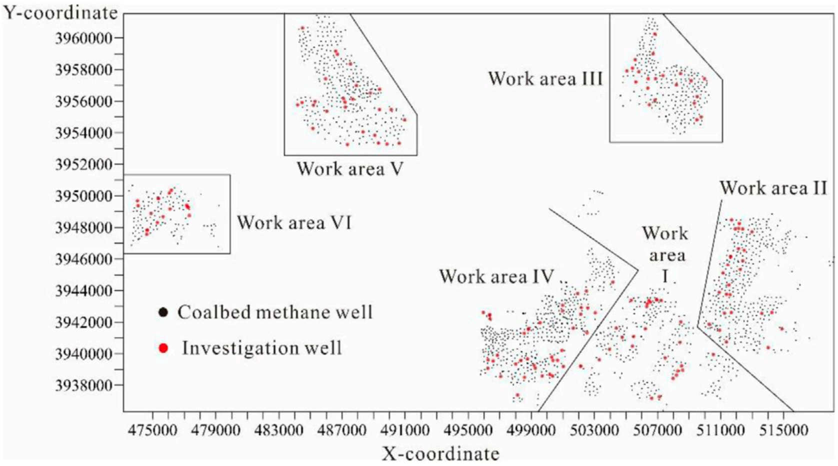

FIGURE 2
Distribution map of CBM wells in the study area.

distributed on both sides of Qinhe river. The distribution map of CBM wells in the study area of Qinshui county is shown in Figure 2.

The methane emission parameters of CBM wells are measured on site. First of all, the location, process flow, production equipment parameters, output, energy consumption and other data of CBM wells are recorded. The explosion-proof infrared thermal imager is used to detect the gas emission, and the emission position of the measuring point is determined according to the infrared imaging. When there is no wind in the well pad, the temperature of the emission point is measured by the hand-held infrared thermometer, and the volume fraction of methane is measured by the inhaled methane gas detector. Use impeller anemometer or thermal flowmeter to test the gas flow rate and obtain the atmospheric pressure at the measuring point. The calculation formula of methane emission is as follows:

$$Q = qS\varphi \tag{1}$$

Where: Q is methane emission under site environmental conditions, m^3/h; q is the gas flow rate at the measuring point, m/h; S is the emission area, m^2; φ is the measured methane volume fraction, %.

For CBM wells with large liquid and gas output at the drainage outlet, the gas-liquid separation device is used to measure the gas flow in conjunction with the gas bag, and then the methane volume fraction is measured to obtain the methane emission.

Due to the influence of temperature and pressure under environmental conditions, and the output of CBM wells is the gas volume under standard conditions, the measured methane emission is converted into the emission under standard conditions according to the conservation of matter. That is:

$$Q_0 = \frac{QpT_0}{p_0T} \tag{2}$$

Where: Q_0 is methane emission under standard conditions, m^3/h; p is the field measured atmospheric pressure, kPa; T_0 is the temperature under standard conditions, taking 273.15 K; p_0 is the atmospheric pressure under standard conditions, taking 101.325 kPa; T is the field measured temperature, K.

Simultaneous Eq. 1, 2 can be obtained:

$$Q_0 = \frac{pT_0qS\varphi}{(p_0T)} \tag{3}$$

In the actual measurement, it was found that the methane volume fraction at the measuring point also changed periodically because the pumping unit and other drainage and production equipment operated repeatedly under a certain number of impulses. The change curve of methane volume fraction at the outlet of CBM well is shown in Figure 3. After the methane detector is close to the measuring point, the volume fraction starts to rise after the methane gas is sucked into the instrument and touched by the detector. After 25 s, the volume fraction of methane is stable at about 20% and fluctuates up and down regularly, and the fluctuation period is about 12 s. This fluctuation period is consistent with the pumping unit stroke of the well (5 times/min). When the methane detector was removed, the methane volume fraction decreased to 0. It is worth noting that due to the rapid diffusion of methane in the air and the influence of

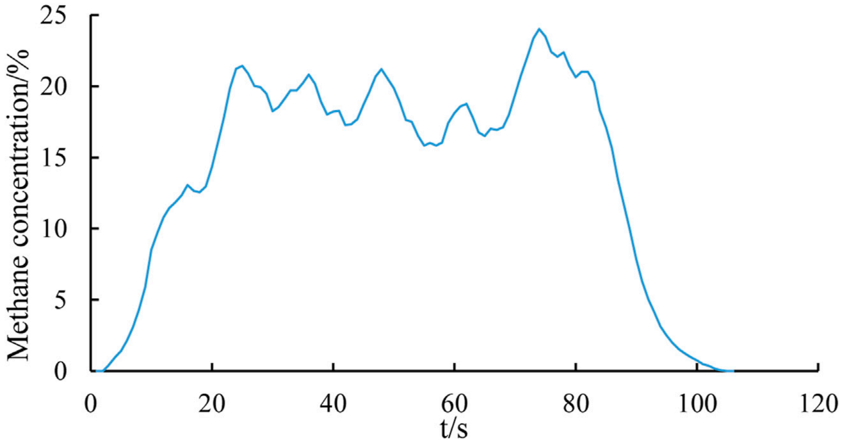

FIGURE 3
Change curve of methane volume fraction at drainage outlet of CBM well.

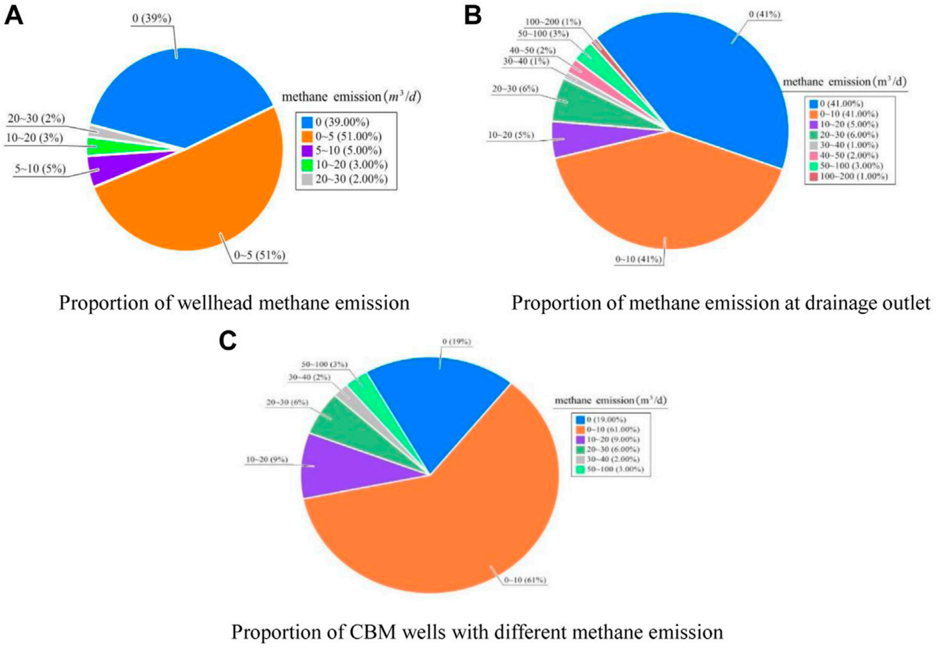

FIGURE 4
Proportion of CBM wells with methane emission in different parts **(A)** Proportion of wellhead methane emission **(B)** Proportion of methane emission at drainage outlet **(C)** Proportion of CBM wells with different methane emission.

surrounding wind speed, the methane volume fraction can hardly be detected about 0.5 m away from the methane emission point. Therefore, the safety risk caused by methane emission in the well pad is small. In order to make the determination of methane volume fraction more accurate and eliminate the error caused by unbalanced emission of methane, the rising and falling sections at both ends of the methane volume fraction curve are cut off during calculation, and the average volume fraction in the middle period is taken as the volume fraction of methane emission.

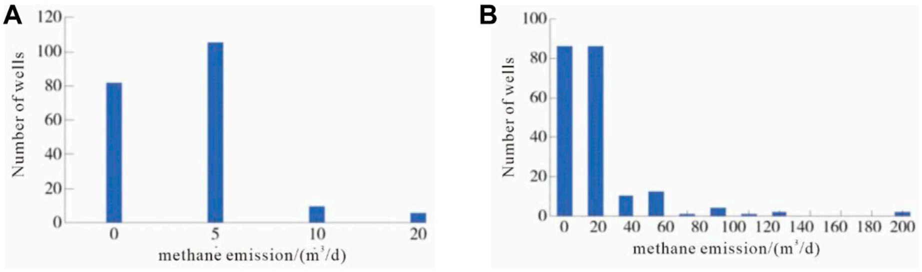

Number of CBM wells with wellhead methane emission

Number of CBM wells with methane emission at drainage outlet

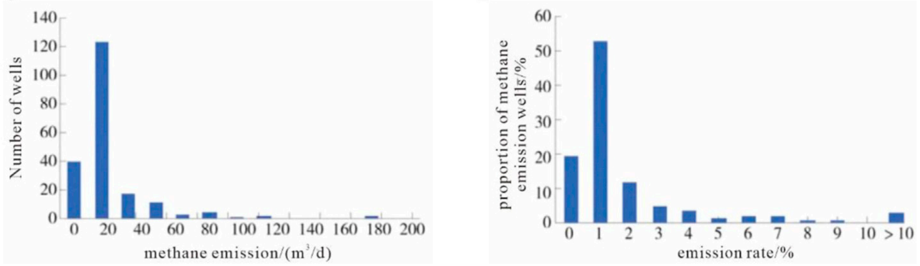

Number of CBM wells with different methane emission

Proportion of CBM wells with different methane emission rate

FIGURE 5
Statistics of CBM wells with different methane emission and emission rates **(A)** Number of CBM wells with wellhead methane emission **(B)** Number of CBM wells with methane emission at drainage outlet **(C)** Number of CBM wells with different methane emission **(D)** Proportion of CBM wells with different methane emission rate.

Results and discussion

Methane emission characteristics

Among the 204 investigated CBM wells, the methane emission at the wellhead is between 0 and 20 m^3/d, of which 39% of CBM wells have no methane emission detected at the wellhead. There are 116 CBM wells with methane emission at the wellhead and the emission is less than 10 m^3/d, accounting for 56% of the total number of wells. Therefore, more than 1/2 CBM wells have wellhead methane emission, but the emission is generally low. Figure 4 shows the proportion of CBM wells with different methane emission. The statistical chart of the number of CBM wells with different methane emission and emission rate is shown in Figure 5.

It can be seen from Figure 4 and Figure 5 that the methane emission at the drainage outlet is between 0 and 200 m^3/d, and 41% of the wells have not detected methane emission. There are 86 CBM wells with emission less than 10 m^3/d, accounting for 41% of the total number of wells. There are 32 CBM wells with emission greater than 10 m^3/d, accounting for 18% of the total number of wells. In contrast, the methane emission at the drainage outlet is generally higher than that at the wellhead, and the number of emission wells also accounts for a large proportion. In general, 19%, 59% and 22% of CBM Wells have no emission, 0–10 m^3/d emission and more than 10 m^3/d emission, respectively. It is worth noting that all the emission sites with methane emission greater than 20 m^3/d are located at the drainage outlets.

In order to characterize the degree of methane emission, the methane emission rate of CBM gas wells is defined as the percentage of methane emission in CBM production. Statistics show that 52% of the wells have a methane leak rate of less than 1%, 26% of the wells have a methane leak rate between 2% and 10%, and 3% of the wells have a methane leak rate greater than 10%. The average emission rate is 1.53%. The methane emission rate may be small for a single well, but when the average CBM well produces 2000 m^3/d of gas, the methane emission rate is 30 m^3/d, which is enough methane to run a household for a month every day. Therefore, effective control of methane emission can effectively improve the resource utilization rate.

Multi factor analysis of methane emission

In order to reveal the relationship between methane emission and CBM production parameters and find out the main control factors, a single factor analysis of methane emission is carried out

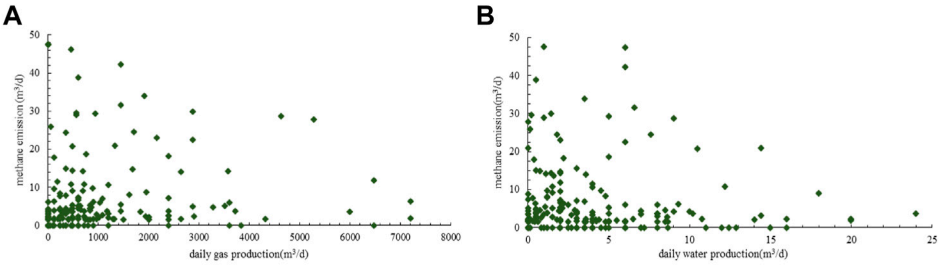

Relationship between daily gas production and methane emission

Relationship between daily water production and methane emission

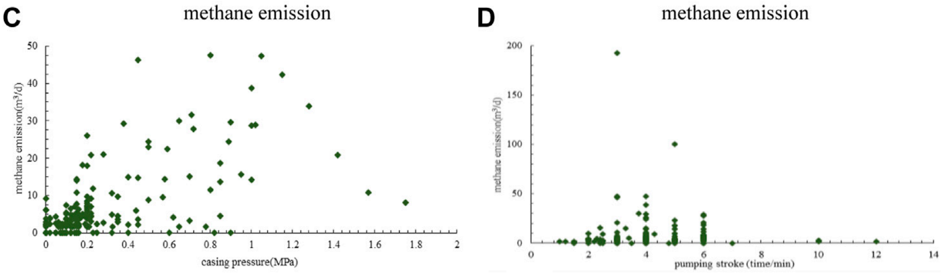

Relationship between casing pressure and methane emission

Relationship between pumping stroke and methane emission

FIGURE 6
Single factor analysis of methane emission in CBM wells **(A)** Relationship between daily gas production and methane emission **(B)** Relationship between daily water production and methane emission **(C)** Relationship between casing pressure and methane emission **(D)** Relationship between pumping stroke and methane emission.

first. Theoretically, the more and denser the methane bubbles under the well, the greater the probability of bubbles entering the water inlet. That is, the higher the gas production, the higher the methane emission. CBM is transported to the surface through casing and tubing annulus, and casing pressure often has a positive correlation with gas production. Due to the pumping unit and liquid lifting, the liquid discharge also directly affects the methane emission. The single factor analysis chart of methane emission of CBM wells is shown in Figure 6.

In fact, it can be seen from Figure 6 that there is no significant linear relationship between the methane emission of the investigated well and the daily gas production, casing pressure and daily gas production. Therefore, for the running CBM drainage and production wells, methane emission is controlled by a variety of factors. There are obvious limitations in using single factor method to analyze methane emission.

In addition to daily gas production, casing pressure, daily water production and other factors, the depth from the pump suction port to the liquid surface, the number of strokes, the bottom hole flow pressure and other factors will also affect the methane emission. The closer to the moving liquid surface, the more bubbles in the water, and the depth from the pump suction port to the liquid surface affects the volume of gas entering the suction port. When the impulse of the oil well pump is large, the liquid flow speed in the well is accelerated, and the liquid is easy to pull the bubbles downward, making it easier for the gas to enter the pump with the liquid. The greater the bottom hole flow pressure is, the greater the pressure difference is between the fluid and the outside world. In the case of constant pump suction port cross-sectional area, the fluid flow rate will be faster.

TABLE 1 Statistical table of model parameters (the gas-liquid two-phase flow stage).

Model	R	R^2	Adjusted R^2	Significance
Logistic	0.544	0.296	0.186	0.38

Methane emission model of CBM well

According to the gas water saturation or fluid production characteristics of the coal reservoir, the process of CBM drainage and production is generally divided into three stages: single-phase water flow, gas-liquid two-phase flow and unidirectional gas flow. Among them, in the single-phase water flow stage, which is also the initial stage of drainage, the reservoir pressure has not yet fallen to the critical desorption pressure. The adsorbed gas in the coal reservoir has not yet been desorbed, and the CBM well only discharges water without producing gas, or only a small amount of free gas is produced. At this time, the

TABLE 2 Table of regression coefficients of various factors (the gas-liquid two-phase flow stage).

Model	Non standardized coefficient		Normalization coefficient	T	Relevance
	B	Standard error	Beta		
constant	0.593	3.181	-	0.186	0.853
X_1	−0.122	0.54	−0.47	2.244	0.032
X_2	10.145	3.483	0.62	2.913	0.006
X_3	0.602	0.481	0.19	1,252	0.220
X_4	−0.242	0.269	−0.14	−0.900	0.375
X_5	0.001	0.001	0.19	1.233	0.227

methane emission is lack of material source, and the methane emission of CBM wells detected at this stage is mostly zero. In fact, only one well has methane emission, which can be ignored. Therefore, the methane emission function at this stage is constant, that is Q_0=0.

In the gas-liquid two-phase flow stage, the casing pressure starts to appear, the liquid level drops steadily, and the pump suction port remains below the liquid level. At this time, the gas at the bottom of the well flows into the tubing in the form of bubbles, and the flow pressure at the bottom of the well at this stage is the sum of the casing pressure and the hydrostatic column pressure. Five factors including the depth X_1 of the pump suction port under the dynamic liquid surface, the bottom hole flow pressure X_2, the times of flushing X_3, the daily water production X_4 and the daily gas production X_5 are taken as independent variables, and the SPSS software is used to conduct multiple linear regression. The model of methane emission in gas-liquid two-phase flow stage is obtained.

$$Q_0 = 0.593 - 0.122X_1 + 10.145X_2 + 0.602X_3 - 0.242X_4 + 0.001X_5 \tag{4}$$

The significance of the regression equation of this model is 0.38 (Table 1), which is significantly higher than that of single factor analysis. In the functional relationship, the standardized regression coefficients of the independent variables X_1, X_2, X_3, X_4, X_5 are -0.47, 0.62, 0.19, -0.14, 0.19 respectively (Table 2).

It can be seen that methane emission is positively correlated with bottom hole flow pressure, flushing times and daily gas production. These three factors promote bottom hole methane gas to enter the tubing and rise to the surface. Among them, the standardized regression coefficient of bottom hole flow pressure is 0.62, accounting for the largest weight, indicating that the bottom hole flow pressure has the largest impact on methane emission in the gas-liquid two-phase flow stage. The second is impulse times and daily air flow. The normalized regression coefficients of pump embedment and daily water output are −0.47 and −0.14 respectively, so methane emission is negatively correlated with these two factors. The greater the depth of the pump suction port under the liquid surface, the longer the methane bubble migration distance, so the slower the methane emission stall rate and the smaller the emission.

TABLE 3 Statistical table of model parameters (the single-phase gas flow stage).

Model	R	R^2	Adjusted R^2	Significance
Logistic	0.647	0.418	0.289	0.36

After entering the single-phase gas flow stage, the pressure drop funnel expands to the limit, and the liquid level decreases to the buried depth of the coal reservoir. Part of the time, the coal seam is exposed above the liquid surface, and the water production is very small. CBM mainly enters the wellbore freely under the action of casing pressure in the form of single-phase gas flow. At this stage, because the hydrostatic column pressure is very small, the casing pressure is approximately equal to the bottom hole flow pressure. Therefore, daily water production, stroke times, daily gas production and casing pressure are selected as independent variables. Through multiple linear regression, the methane emission model in single-phase gas flow stage was obtained.

$$Q_0 = 3.144 - 0.686Y_1 - 0.288\,Y_2 + 0.001\,Y_3 + 20.433\,Y_4 \tag{5}$$

The significance of the regression equation of this model is 0.36, lower than 0.5, and the significance is good (Table 3). The standardized regression coefficients of the independent variables Y_1, Y_2, Y_3 and Y_4 in the functional relationship are −0.21, −0.08, 0.12, and 0.62 respectively (Table 4).

Methane emission is positively correlated with daily gas production and casing pressure. These two factors have a promoting effect on methane emission, of which the standardized regression coefficient of casing pressure is 0.62, accounting for the largest weight. It indicates that the casing pressure has the greatest influence on the bottom hole methane entering the tubing at this stage. The methane emission is

TABLE 4 Table of regression coefficients of various factors (the single-phase gas flow stage).

Model	Non standardized coefficient		Normalization coefficient	T	Relevance
	B	Standard error	Beta		
constant	3.144	4.568	-	-	0.500
Y1	−0.686	0.582	−0.21	0.688	0.254
Y2	−0.288	0.650	−0.08	−0.444	0.662
Y3	0.001	0.001	0.12	0.650	0.524
Y4	20.433	6.110	0.62	3.344	0.004

TABLE 5 Calculation results of methane emission model (the gas-liquid two-phase flow stage).

Well number	X_1/ m	X_2/ MPa	X_3/ time/min	X_4/ m^3/d	X_5/ m^3/d	Measured value/ m^3/d	Calculated value/m^3/d	Absolute error	Relative error (%)
CZ-303	30.74	0.16	4	7	1833.84	2.319	1.014	1.305	56.27
ZH-54	40.44	0.604	6	1.2	432	3.047	5.545	2.498	81.98
Z-14-10	22.9	0.429	2.3	1.9	600	3.748	3.676	0.072	1.92
CZ-185	11.04	0.140	5	3	1,080	4.480	4.030	0.45	10.04
CZ-216	18.49	0.150	6	3.6	2,640	16.371	5.240	11.131	67.99

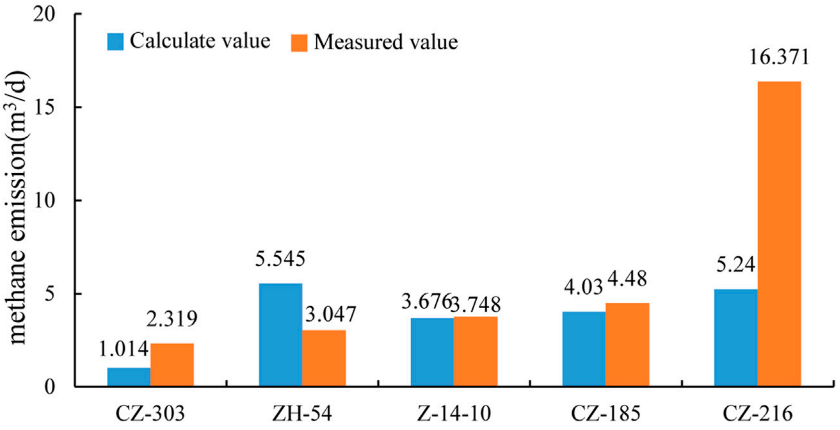

FIGURE 7
Comparison of measured and calculated (the gas-liquid two-phase flow stage).

negatively correlated with the times of flushing and water production. Although the water production at this stage is very small, the liquid column in the wellbore prevents the methane gas flow from rising to the surface to a certain extent. The greater the number of strokes, the disturbance effect on the methane gas flow that has entered the oil pipe through the pump suction port, and on the contrary, it is unfavorable for the methane gas to enter the oil pipe and migrate to the surface. Therefore, in different stages of CBM gas well drainage and production process, the influence of various operating parameters on methane emission is quite different.

TABLE 6 Calculation results of methane emission model (the single-phase gas flow stage).

Well number	Y_1/ m^3/d	Y_2/ time/min	Y_3/ m^3/d	Y_4/ MPa	Measured value/ m^3/d	Calculated value/m^3/d	Absolute error	Relative error (%)
CZ-028	0.80	5	2,400	0.05	4.276	4.577	0.301	7.04
CZ-270	0.50	6	864	0.12	4.142	4.389	0.247	5.96
CZ-313	0.46	4	120	0.16	5.426	5.069	0.357	6.58
ZH-39	0.30	4	240	0.15	5.164	5.091	0.073	1.41
ZH-175	0.72	4	360	0.40	11.282	10.031	1.251	11.09

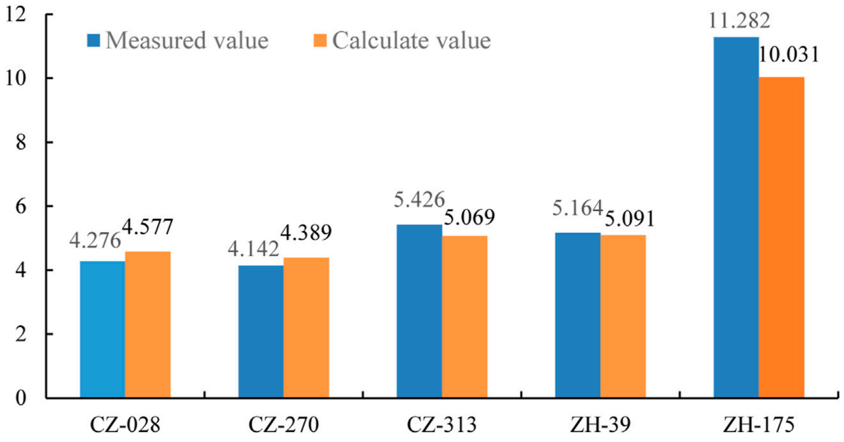

FIGURE 8
Comparison of measured and predicted (the single-phase gas flow stage).

Example verification

Five CBM drainage wells in the gas-liquid two-phase flow stage are selected as the control wells. Table 5 and Figure 7 show the comparison between the measured value and the predicted value of methane emission from CBM wells.

The measured methane emission of well CZ-303, ZH-54, Z-14-10, CZ-185 and CZ-216 are 2.319, 3.047, 3.748, 4.48, and 16.371 m^3/d respectively. The calculated values of methane emission obtained by the model are 1.014, 5.545, 3.676, 4.03, and 5.24 m^3/d respectively. Compared with the predicted value, the relative error of the measured value is 1.92%–81.98%, and the absolute error is 0.072–11.131 m^3/d.

The absolute error of 4 wells is less than 2.5 m^3/d. Among the 204 coal-bed gas wells investigated in the early stage, the number of wells with methane emission between 0 and 2.5 m^3/d accounted for 6.37%. At the same time, in the gas water two-phase flow stage, due to the instability of water production and gas production, it is greatly affected by many factors. Therefore, there are some errors in the field measurement results. This is also the reason why the actual measurement and calculation errors are large when the methane emission is large. However, the proportion of CBM wells with emission exceeding 20 m^3/d is less than 20%. Therefore, this prediction model has high accuracy for most CBM wells.

Five CBM drainage wells in the single-phase gas flow stage are selected as the control wells. Table 6 and Figure 8 show the comparison between the measured value and the predicted value of methane emission from CBM wells.

The measured methane emission of well CZ-028, CZ-270, CZ-313, ZH-39, and ZH-175 are 4.276, 4.142, 5.426, 5.164, and 11.282 m^3/d respectively. The calculated values of methane emission obtained by the model are 4.577, 4.389, 5.069, 5.091, and 10.031 m^3/d respectively. Compared with the predicted value, the relative error of the measured value is 1.41%~11.09%, and the absolute error is 0.073~1.251 m^3/d.

Conclusion

1) Methane emission is common in the drainage process of coal-bed methane wells, and the wellhead and drainage outlet are

the two main points of methane emission. Among the 204 CBM wells investigated, 19%, 61% and 20% are CBM wells with no methane emission, emission between 0 and 10 m^3/d and emission greater than 10 m^3/d, respectively. Overall, methane emission accounts for 1.53% of the production of production wells.

2) In the process of coal-bed gas well drainage and production, the methane emission in the single-phase water flow stage is almost zero. In the gas-liquid two-phase flow stage, methane emission is positively correlated with bottom hole flow pressure, flushing times and daily gas production, and negatively correlated with pump embedment and daily water production. Among them, bottom hole flow pressure and pump embedment have the greatest impact on methane emission. In the single-phase gas flow stage, methane emission is positively related to daily gas production and casing pressure, and negatively related to the number of strokes and daily water production. Among them, casing pressure and daily water production have the greatest impact on methane emission.
3) A model of methane emission in CBM wells at different stages is established by using multiple factor regression analysis. Through the example verification, the absolute error of the prediction model for the gas water two-phase flow stage is 0.072–11.131 m^3/d. Due to the complexity of the measurement in each stage, and the number of emission exceeds 20 m^3/d is less, this prediction model has high accuracy for most CBM wells. Prediction model for the single-phase gas flow stage, the relative error of the measured value is 1.41%–11.09%, and the absolute error is 0.073–1.251 m^3/d, the results meet the requirements of industrial calculation.
4) Methane emission from CBM well not only causes the loss of gas production, reduces economic benefits, but also increases the potential safety hazards of the well site. More importantly, it also increases the greenhouse effect, which is not conducive to environmental protection. According to the main control factor model of methane emission, targeted measures are taken to actively prevent and control methane emission.

Data availability statement

The original contributions presented in the study are included in the article/Supplementary Material, further inquiries can be directed to the corresponding author.

Author contributions

QD: Conceptualization, Investigation, Data curation, Methodology, Writing-original draft. SW: Conceptualization, Funding acquisition, Project administration. JM: Conceptualization, Formal analysis, Methodology, Writing-review, Editing, Supervision. SL: Data curation, Investigation. WL: Investigation, Software, Validation.

Funding

This work was financially supported by the National Natural Science Foundation of China (Grant No.52174230), Postdoctoral Science Foundation of China (CN) (Grant No. 2021MD703848) and Fundamental Research Program of Shanxi Province (20210302124633).

Conflict of interest

Publisher’s note

References

Hou, J., and Zeng, Y. (2013). Regulation and oversight of the venting and leaking of methane in the natural gas development: A comparative study. *Nat. Gas. Ind.* 33 (09), 126–130. doi:10.3787/j.issn.1000-0976.2013.09.022

Jia, X., and Zhou, H. (2013). Present situation and countermeasure research for the exploitation and utilization of coal bed methane in China taking Jincheng City as an example. *Saf. Environ. Eng.* 20 (6), 12.

Kong, Y., and Wang, J. (2019). Research on security assessment of CBM emission with diverse leaking radius. *Energy Technol. Manag.* 44 (06), 120–122.

Li, J. (2014). *Study on simulation and risk assessment of emission and diffusion of CBM field gathering and transportation*. Xuzhou: China University of Mining and Technology, 25–34.

Li, Y., Ge, J., and Weng, W., (2019). Stoichiometry ratio of CO_2 and CH_4 emissions in dajiuhu peat wetlang of shennongjia. *Saf. Environ. Eng.* 26 (4), 21–28. doi:10.13578/j.cnki.issn.1671-1556.2019.04.004

Luo, K., Li, Y., and Wang, Z. (2019). Research on safety thickness of overlying strata in goaf under multi-factor coupling. *Saf. Coal Mines* 50 (12), 223–226. doi:10.13347/j.cnki.mkaq.2019.12.049

Lyu, S., Wang, S., Hongtai, L., Wang, T., and Shi, X., (2020a). Analysis of the influence of natural fracture system on hydraulic fracture propagation morphology in coal reservoir [J]. *J. China Coal Soc.* 45 (7), 2590–2601. doi:10.13225/j.cnki.jccs.DZ20.0859

Lyu, S., Wang, S., Chen, X., Wang, T., and Shi, X., (2020b). Natural fractures in soft coal seams and their effect on hydraulic fracture propagation: A field study. *J. Petroleum Sci. Eng.* 192, 1–16. doi:10.1016/j.petrol.2020.107255

Meng, S., and Zhu, S. (2019). Comparison between linear regression and nonlinear regression of Langmuir equation parameters. *Saf. Coal Mines* 50 (1), 188–191. doi:10.13347/j.cnki.mkaq.2019.01.046

Shang, J., Liu, H., and Sang, S., (2020). Coupling analysis on permeability and pore fracture development in high rank coal reservoirs of southern Qinshui Basin. *Saf. Coal Mines* 51 (6), 184–190. doi:10.13225/j.cnki.jccs.dz20.0830

Shen, P., Bai, J., and Guishan, L. I., (2020). Integrated geosteering technology of logging and orientation in deep CBM horizontal well. *J. China Coal Soc.* 45 (7), 2491–2499. doi:10.13225/j.cnki.jccs.dz20.0830

Sun, Q., Zhao, Q., and Jiang, X., (2021). Prospects and strategies of CBM exploration and development in China under the new situation. *J. China Coal Soc.* 46 (1), 65–76. doi:10.13225/j.cnki.jccs.2020.1579

Tang, J., Wu, X., and Bao, Z. H., (2006). Effect of geogenic emission of methane on the atmosphere. *Geol. Sci. Technol. Inf.* 25 (2), 75–82.

Tang, X. Y., and Li, J. L. (1990). *Atmospheric enviromental chemistry*, 48-51. Beijing: Higher Education Press, 305–306.

Wu, T., Ming, W. E. I., and Guang, L. I., (2014). Mechanism analysis of the influence of methane content on the atmospheric structure and rainstorm. *Sci. Technol. Eng.* 14 (23), 153–157. doi:10.3969/j.issn.1671-1815.2014.23.028

Xue, C., Xue, Y., and Ji, X. (2020). Study on dynamic evolution of social ecological system risk in CBM development based on Choquet–Brusselato. *Min. Saf. Environ. Prot.* 47 (4), 116–121. doi:10.19835/j.issn.1008-4495.2020.04.023

Zhang, Y. (2011). *Diffusion law and security-related issues research of the coal bed methane leaking from the well*. Qingdao: China University of Petroleum East China, 45.

Zheng, Q. (2020). The geological characteristics of coal seam and controls on coal gas in Yongju Coal Mine, Shanxi Province. *Sci. Technol. Eng.* 20 (24), 9830–9834.

Zhou, G., Lin, R., and Sun, D., (2016). Study on greenhouse gas emission factors of wellhead casing. *Chem. Eng. Equip.* 12 (4), 126–128.

Zhu, J., Ling, L. I., and Yang, S. (2021). Research on discrimination of mine water bursting source based on factor analysis. *Min. Saf. Environ. Prot.* 48 (2), 87–91. doi:10.19835/j.issn.1008-4495.2021.02.017

frontiers | Frontiers in Earth Science

TYPE Original Research
PUBLISHED 11 January 2023
DOI 10.3389/feart.2022.1034332

EDITED BY
Leilei Si,
Henan Polytechnic University, China

REVIEWED BY
Yanchao Xue,
Northeastern University, China
Jinpeng Zhang,
Shandong Agricultural University, China

*CORRESPONDENCE
Rong Liu,
qianxunsen@163.com

SPECIALTY SECTION
This article was submitted to Economic Geology,
a section of the journal
Frontiers in Earth Science

RECEIVED 01 September 2022
ACCEPTED 27 September 2022
PUBLISHED 11 January 2023

CITATION
Kong P, Liu R, Xing L, Li Z, Xu C and Zhang Z (2023), Study on the dynamic response and the hazard of rock burst under the influence of fault slip.
Front. Earth Sci. 10:1034332.
doi: 10.3389/feart.2022.1034332

Study on the dynamic response and the hazard of rock burst under the influence of fault slip

Peng Kong[1,2], Rong Liu[1,2]*, Luyi Xing[3], Zhihong Li[4], Chuanwei Xu[5] and Zhongteng Zhang[6]

[1]School of Mining Engineering, Anhui University of Science and Technology, Huainan, China, [2]Coal Mine Safety Mining Equipment Innovation Center of Anhui Province, Huainan, China, [3]School of Civil Engineering, Shandong Jianzhu University, Jinan, China, [4]Yankuang Energy Group Company Limited, Jining No. 2 Coal Mine, Jining, China, [5]Jinan Urban Construction Group, Jinan, China, [6]Yankuang Energy Group Company Limited, Baodian Coal Mine, Jining, China

In the process of coal mine production, rock burst accidents near faults occur frequently. In order to further reveal the induced mechanism of fault slip rock burst, a numerical simulation method for dynamic calculation of fault slip under the influence of mining is proposed, and the law of fault slip and dynamic response characteristics of the stope are studied. The study shows that with the working face getting closer to the fault, the fault activity and the number of high-energy microseismic events increase significantly, and the fault slip dynamic load has a significant impact on the vibration velocity and abutment stress of coal and rock mass near the stope. Under the effect of a strong fault slip dynamic load, the coal and rock mass in the area with peak abutment stress undergo plastic failure and release a large amount of energy, and the potential of fault slip rock burst is high. The evaluation index I_{cd} of rock burst hazard under fault slip dynamic load is proposed, and the rock burst hazard of working face passing through the fault is analyzed. The research results provide a theoretical basis for further revealing the induced mechanism and hazard assessment of fault slip rock bursts.

KEYWORDS

rock burst, fault, dynamic response, microseismic, hazard assessment

Introduction

Rock burst is the sudden release of elastic energy accumulated in coal and rock mass under certain conditions. When a rock burst occurs, it is often accompanied by loud noise, strong instantaneous vibration, and shock waves, resulting in the throwing out of coal and rock mass, the instantaneous sinking of the roof, or the sudden bulging of the floor. It can destroy the equipment and cause severe deformation or even closure of the roadway in serious cases (Jiang et al., 2020; Xue et al., 2020; Li et al., 2021a; Li et al., 2021b). According to the different inducing factors of rock burst, Ortlepp and Stacey (1994) divided rock burst into three categories: the strain rock burst, the coal pillar rock burst, and the fault slip rock burst. Ortlepp's classification of rock burst and corresponding shock source and magnitude is given in Table 1. The strain rock burst often occurs in the area with peak

TABLE 1 Rock burst classification, source, and magnitude.

Type of rock burst	Inducing factors	Magnitude (M_L)
Strain rock burst	Flaking and ejection of rock	−0.2–1.5
Coal pillar rock burst	Sudden instability of coal pillar	1.0–2.5
Fault slip rock burst	Fault slip	2.0–5.0

abutment stress or at the elastic–plastic interface of coal and rock mass. The strain rock burst causes large-scale expansion of the plastic failure area of coal and rock mass and the ejection of coal and rock mass. The coal pillar rock burst is mainly caused by sudden instability and failure of the coal pillar, which is induced by the concentrated static load of the coal pillar exceeding the bearing capacity of coal and rock mass. The main sources of high static load are the stress of primary rock and mining-induced stress. The main failure form caused by a coal pillar rock burst is the pressure failure of the coal pillar or the instantaneous bulging of the floor. Compared with the other two types of rock bursts, the fault slip rock burst has higher source energy and a larger damage range. Fault slip rock burst is caused by the instability and failure of coal and rock mass near the mining space due to the dynamic disturbance of fault slip microseismicity, and the severity of rock burst is closely related to the size of fault slip microseismic event. Moreover, the location of microseismic source–induced dynamic load disturbance may be far away from the rock burst appearance location.

With the gradual depletion of coal resources in shallow and easily mined coal seam areas, the geological situation of coal mining in China is deteriorating. In particular, coal mines in the eastern and northeast regions are generally affected by complex geological conditions, and the fault structure is one of the most common geological structures in the process of coal mine production. The wide distribution of fault structures has a significant impact on the distribution of abutment stress (Xue et al., 2021; Li et al., 2022; Si et al., 2022) and the characteristics of overburden movement (Wang et al., 2018; Wang et al., 2019). Lai et al. (2016) studied the influence range of dynamic pressure during mining in fault fracture areas through the field monitoring method. The result indicated that the roadway deformation shows obvious asymmetric change characteristics during the working face passing through the fault, the roadway deformation near the fault side was greater, and the bolt stress and surrounding rock stress concentration increased significantly. Luo et al. (2014) and Wang et al. (2014) carried out a similar material simulation test for a mining panel near the F16 reverse fault in Yuejin Coal Mine. The research result showed that with the increase of mining depth of the working face and the decrease of the fault coal pillar size, the degree of coal pillar stress concentration increased significantly. In addition, the dynamic load provided by the fault slip is one of the main factors that induce rock burst. Zhu et al. (2016) studied the law of fault activation in the mining of deep and extra-thick coal seam through on-site microseismic analysis and numerical simulation; they divided the whole process of mining-induced fault activation into three stages: stress manifestation, energy storage, and structural activation.

The continuous disturbance to the fault during mining the panel is likely to cause fault slip, and the process of fault slip is often accompanied by strong microseismic events. The strong microseismicity causes severe dynamic load disturbance to the coal and rock mass in the stope, and the rock burst hazard of the stope increases significantly. Affected by complex geological conditions, more than 50 rock burst accidents occurred during mining in the Longfeng Coal Mine, Guizhou Province. A total of 36 rock bursts were related to the fault structure, and 31 occurred in the roadway near the fault (Li et al., 2018). From 2008 to 2014, a total of 20 rock bursts occurred in Qianqiu Coal Mine and Yuejin Coal Mine affected by the F16 reverse fault. The accidents caused dozens of deaths, and the length of the roadway damaged by the rock bursts reached more than 1,000 m (Cai et al., 2021). On 22 February 2020, when mining Panel 2305S through the FD8 fault, a serious rock burst occurred in Xinjulong Coal Mine. The accident caused four deaths and severely damaged about 500 m of the roadway. The source of the fault slip microseismic event which induced the rock burst was 160 m above the coal seam, and the source energy reached 4.2×10^7 J. Therefore, a microseismic event with large energy released by the fault slip is one of the important factors causing the violent appearance of mine pressure and even inducing rock burst disaster.

In the research on the mechanism of fault slip activation–induced microseismic events, Brace and Byerlee put forward the hypothesis of seismic stick slip by analyzing the results of rock shear tests, and they believed that the unstable slip of stress reduction on the fault was caused by the existence of large normal stress on the fault (Brace and Byerlee, 1966). Compared with the joints with weak fillings, the frequency and energy released during the shear process of clean joints are higher (Meng et al., 2017). In addition, the roughness of joints is also an important factor affecting fault activation–induced microseismic events (Zhou et al., 2016; Si et al., 2021a; Wang et al., 2021). The higher the roughness of joints, the greater the potential of fault slip releasing strong microseismicity. In terms of numerical simulation research, Zhu studied the focal characteristics of the fault under the influence of mining. The

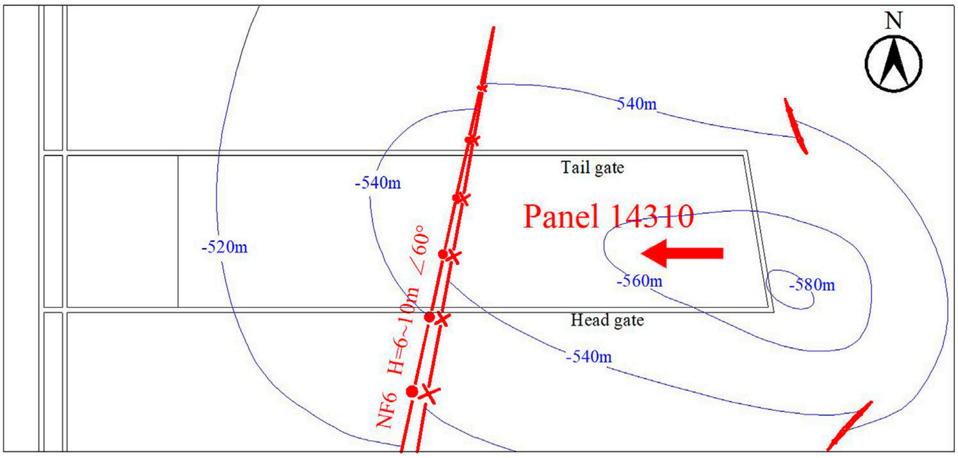

FIGURE 1
Layout of panel 14310 in Dongtan Coal Mine.

research results showed that the greater the mining depth, the greater the seismic moment of fault slip induced by mining.

Scholars have carried out a lot of research on the effect of fault mining action and have achieved fruitful results. However, at present, the understanding of the induced mechanism of fault slip rock burst is not clear, especially, the research on the shear slip law of fault induced by mining, the fault slip microseismic characteristics, and the dynamic response of surrounding rock under fault slip dynamic load is not enough. Based on the engineering background of mining the panel through the fault, the research methods, including field investigation, laboratory test, theoretical analysis, and numerical simulation, were applied in this study. A systematic study was carried out on the evolution of microseismic events induced by fault slip under the influence of mining, the dynamic response characteristics of stope under fault slip dynamic load, the mechanism of fault slip rock burst, and the rock burst hazard. The research results can provide theoretical guidance for understanding the induced mechanism of fault slip rock bursts and provide a certain reference for hazard assessment and prevention of fault slip rock bursts.

Case study

Engineering background

The average thickness of the coal seam in the Dongtan Coal Mine 14310 Panel is 8 m. The mining technology is comprehensive mechanized top coal caving mining, and the retreating full caving method is used to manage the roof. The direct roof of the coal seam is mudstone with an average thickness of about 4 m. The basic roof is mainly composed of siltstone and sandstone. The roof of the coal seam is relatively hard, especially since the average uniaxial compressive strength of sandstone in the roof reaches 102 MPa. The coal seam and roof of the panel have a weak rock burst tendency. The working face has a buried depth of 540 m, a width of 230 m, and a strike length of 1000 m. The geological structure of the working face is complex, in which the NF6 normal fault crosses through the panel, with a fault dip of 60° and a drop of 6–10 m. In the actual mining process, the working face crosses through the footwall of the NF6 normal fault. NF6 normal fault has a great impact on mining. The layout of Panel 14310 and fault location are shown in Figure 1.

The distribution of microseismic events when mining the panel through the fault

The distribution of microseismic events during Panel 14310 of the Dongtan Coal Mine mined through the fault is shown in Figure 2 (Kong et al., 2022). It can be seen that there was a concentrated area of microseismic events near the fault when mining the panel through the fault. Moreover, the number and energy level of microseismic events near the roof fault were much greater than those near the floor fault, indicating that the roof fault was more active than the floor fault affected by mining. The distribution height of microseismic events near the fault was larger than that of the complete roof area, and the energy level was high. Microseismic events with energy greater than 5×10^3 J had mostly occurred near the roof fault plane and were induced by fault slip.

In order to analyze the occurrence law of microseismic events and fault activity when mining Panel 14310 through the fault of

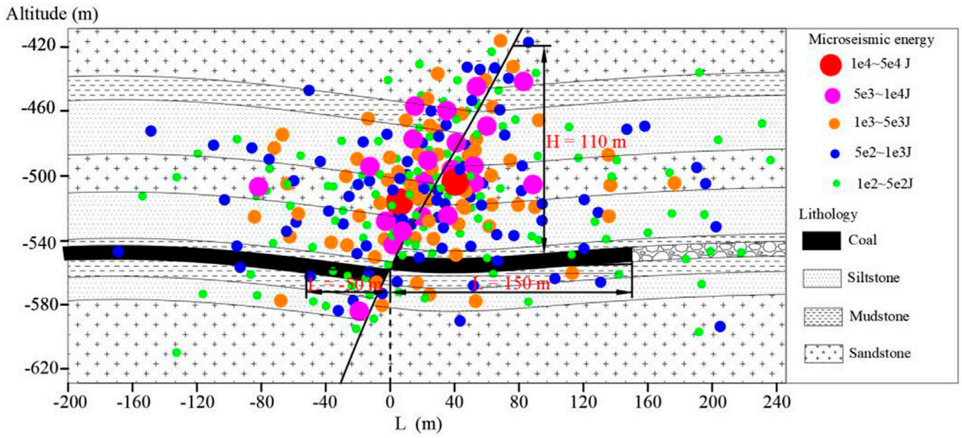

FIGURE 2
Distribution of microseismic events when mining the panel through the fault.

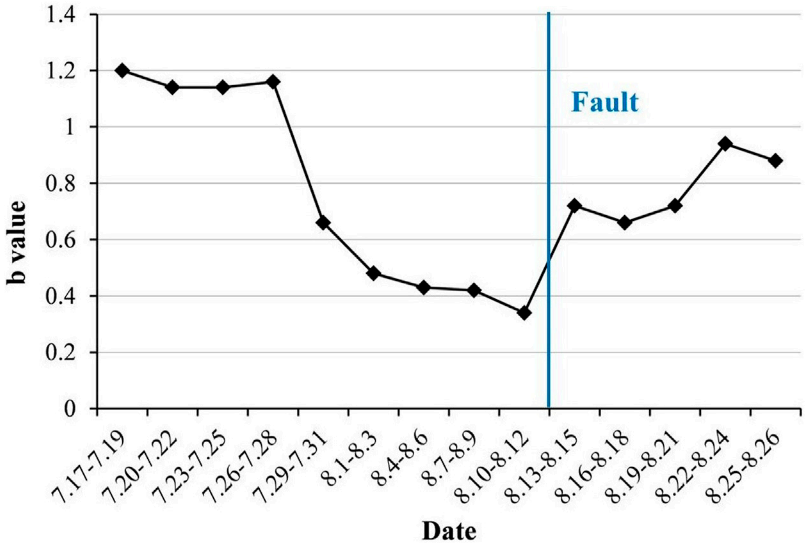

FIGURE 3
b Value of microseismic event when mining the panel through the fault.

Dongtan Coal Mine, the microseismic events during the mining period in Dongtan Coal Mine from July 17 to August 26 (the working face was 108 m away from the fault to 56 m across the fault) were statistically processed, and the b value of microseismic events was calculated.

Gutenberg and Richter have conducted long-term research on natural seismicity and found that the relationship between earthquake occurrence frequency (lg$N$) and earthquake magnitude (M) met the power–law relationship. They put forward the relationship between earthquake magnitude and earthquake frequency, namely, the G-R relationship (Scholz, 1968; Wang, 2012):

$$\lg N(\geq M) = a - bM, \tag{1}$$

where M is the earthquake magnitude, $N\geq(M)$ represents the number of earthquakes with a magnitude greater than or equal to M, and a and b are constants. The value of b represents the magnitude of earthquake intensity. The larger the value of b, the larger the proportion of low-energy earthquakes, and the earthquake intensity is low. The smaller the value of b, the

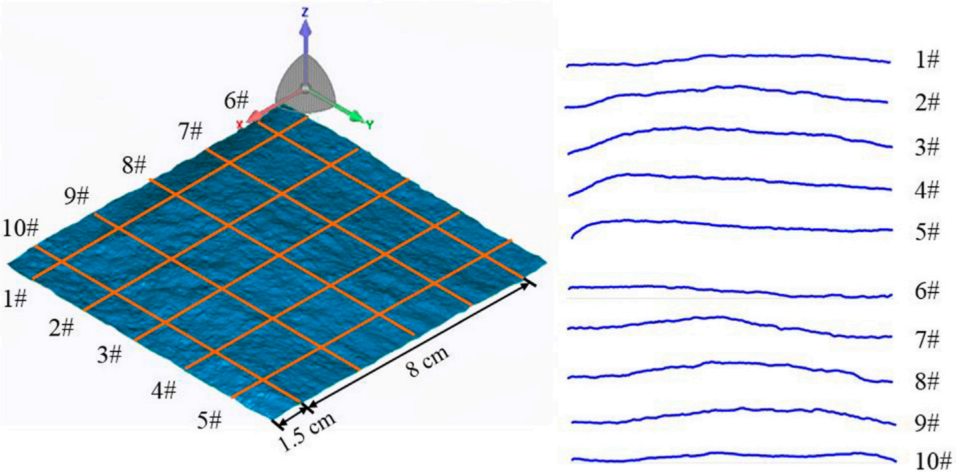

FIGURE 4
Point cloud data of the rough structural plane and layout of survey line.

TABLE 2 Division of energy levels for microseismic events.

Level	Energy(J)	lg$E$
1	$\geq 1 \times 10^2$	2
2	$\geq 2.5 \times 10^2$	2.4
3	$\geq 5 \times 10^2$	2.7
4	$\geq 7.5 \times 10^2$	2.9
5	$\geq 1 \times 10^3$	3
6	$\geq 2.5 \times 10^3$	3.4
7	$\geq 5 \times 10^3$	3.7
8	$\geq 7.5 \times 10^3$	3.9
9	$\geq 1 \times 10^4$	4

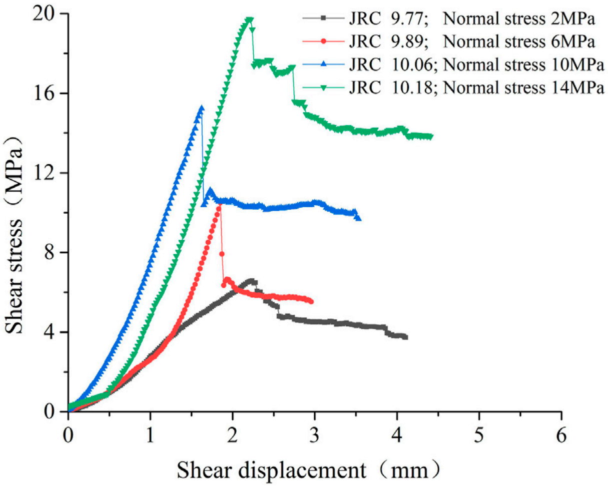

FIGURE 5
Shear stress-strain curves of the structural plane under different normal stress and JRC conditions.

larger the proportion of high-energy earthquakes, and there is a high possibility of strong earthquakes or rock bursts. Therefore, the *b* value can be used as an index to evaluate the strength level of an earthquake somewhere. The research showed that the occurrence law of mine microseismic events also followed the same law. The smaller the b value, the greater the potential of a strong mine microseismic event or rock burst.

When calculating the *G-R* relationship of microseismic events when mining the panel through the fault, the energy level *lgE* was used instead of the magnitude *M*, so Eq. 1 can be expressed as

$$\lg N\left(\geq lgE\right) = a - b\lg \mathrm{E}. \tag{2}$$

The *b* value was calculated with three days as the time interval. The microseismic events and energy levels within three days were counted, and the microseismic events were classified according to the energy. In order to ensure the accuracy of the calculation, the microseismic events were divided into nine levels. The energy level division and the setting of *M*(*lgE*) are shown in Table 2. After dividing the energy level according to the table, the number *N* of microseismic events at each energy level was counted, and the value of *lgN* was calculated. Linear fitting was performed on the corresponding data of *lgE* and *lgN*, and the *b* value of the working face at different mining positions was obtained.

The *b* value of microseismic event when the working face advanced to different positions is shown in Figure 3. It can be seen that the *b* value varied greatly when the working face was at different positions. From July 17 to July 28, the distance from the working face to the fault was 108–64 m, and the *b* values were 1.2, 1.14, 1.14, and 1.16, respectively. The *b* value generally showed a slightly decreasing trend, but the decreasing range was very small, and the *b* value had been maintained at a high level. It illustrated that there were few microseismic events with high energy in this mining stage. From July 29 to July 31, the distance from the working face to the fault was 64–52 m, and the *b* value decreased sharply from 1.16 to 0.66, indicating that the frequency of high-energy microseismic events increased significantly.

From August 1 to August 12, the distance from the working face to the fault was 52–4 m, and the *b* values were 0.48, 0.43, and 0.34, respectively. The *b* value was kept at a low level. As the working face got close to the fault, the *b* value decreased gradually. It showed that with the working face getting closer to the fault, the frequency of high-energy microseismic events increased significantly. According to Figure 2, large energy microseismic events were mostly concentrated near the fault. It can be seen that when the working face advanced near the area, the fault activity was intense under the influence of mining. Microseismic events with large energy released by fault slip dislocation occurred frequently. Microseismic events with large energy may induce rock burst accidents easily, and the hazard of rock bursts is high.

From August 13 to August 26, the working face advanced from 4 m away from the fault to 56 m across the fault, and the *b* values were 0.66, 0.72, 0.94, and 0.88, respectively. The value *b* showed a gradually increasing trend basically. It showed that the frequency of large energy microseismic events released by fault slip decreased, the degree of disturbance to the working face decreased, and the hazard of fault slip rock burst decreased.

Shear characteristics of fault structural plane

The fault zone is cut by widely distributed structural planes, and their mechanical behavior is significantly affected by structural planes. In engineering practice, the fault structural plane is not straight and often shows rough characteristics. The mechanical properties and shear slip characteristics of the rough structural surface are quite different from those of the flat and smooth structural surface. Especially during the stick slip process of the hard rough structural surface, the energy level released by the shear wear of the bulge is higher (Zhou et al., 2016; Si et al., 2021a; Wang et al., 2021). Therefore, an in-depth study of the mechanical properties of rough structural planes is of great significance for revealing the law of fault slip.

The hard sandstone in the roof of Dongtan Coal Mine played an important role in roof movement and fault slip, so the direct shear test was carried out on the sandstone structural plane in the hard roof of Dongtan Coal Mine to test the law of fault shear slip and determine the weakening parameters of fault shear slip. The test specimen was a cuboid with a size of 100 mm high by 110 mm wide by 110 mm long. First, the complete cuboid rock specimens were split to form a rough structural plane to simulate that in a natural state. Then, the randomly generated structural plane was scanned using a 3D laser scanner to obtain the coordinate point cloud data of the rough structural plane. 3D laser scanning was carried out at Qingdao Research Institute of Xi'an Jiaotong University. The measurement speed of the scanner is 18000 measurements/second, the measurement accuracy reaches 0.05 metrological level, the volume accuracy is 0.02 mm + 0.2 mm/m, and the resolution is 0.1 mm. The point cloud data of rough structural surface obtained by 3D laser scanning is shown in Figure 4. The measurement accuracy can meet the requirements for calculating the roughness of structural surfaces. Finally, the structural plane roughness was calculated, and the roughness of the structural plane was obtained based on Eqs 3 and 4 (Tse and Cruden, 1979).

$$\mathrm{JRC} = 32.2 + 32.47 \log Z_2, \tag{3}$$

$$Z_2 = \left[\frac{1}{M\,(D_x)^2}\sum_{i=1}^{M}\left(y_{i+1} - y_i\right)^2\right]^{\frac{1}{2}}, \tag{4}$$

where JRC is the joint roughness coefficient, Z_2 is the root mean square of the average slope of the joint contour line, D_x is the spacing between two points, and M is the number of D_x on the whole rough line.

The direct shear test under different normal stress conditions was carried out on the rough structural surface, and four tests were carried out. The normal stress was 2, 4, 10, and 14 MPa, respectively. The roughness of the four rough structural surfaces was 9.77, 9.89, 10.06, and 10.18, respectively. The structural plane roughness of the four specimens had little difference, and the roughness of the specimens can be considered the same. The direct shear test adopts the deep soft rock nonlinear test system of the China University of Mining and Technology, and the direct shear rate during the test is 0.004 mm/s.

Figure 5 shows the shear stress-strain curve of the rough structural plane under different normal stress conditions. It can be seen that the shear strength of the structural plane increased along with the normal stress. When the normal stress in the process of direct shear was 2, 6, 10, and 14 MPa, the shear strength of the structural plane was 6.6, 10.5, 15.2, and 19.7 MPa, respectively. It showed that under the condition of the same roughness, the larger the normal stress was, the less likely the rough structural plane was to

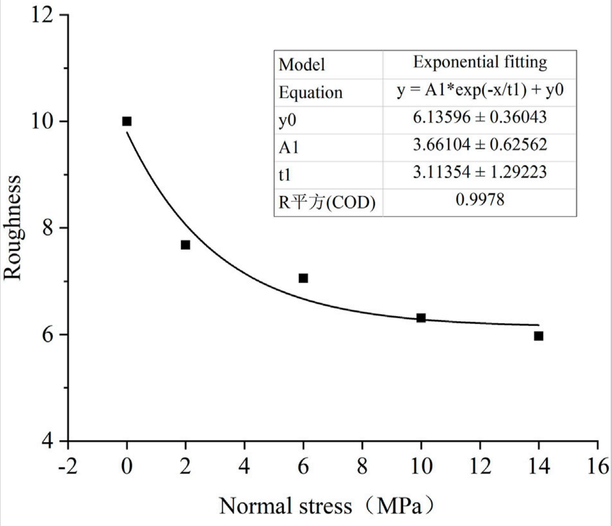

FIGURE 6
JRC value of the structural plane after shear under different normal stress.

shear failure. The difference between the peak shear stress and the shear stress after shear failure was defined as the shear stress drop. When the normal stress was 2, 6, 10, and 14 MPa, the shear stress drop was 2.9, 4.9, 5.5, and 5.9 MPa, respectively. Therefore, the shear strength and shear stress drop of the structural plane increased with the increase of normal stress in the process of direct shear of the rough structural plane. The higher the normal stress, the more obvious the stick slip characteristics in the shear slip process of the structural plane.

The structural plane roughness after direct shear was scanned using a three-dimensional laser again, and the structural plane roughness after direct shear was calculated to study the slip weakening characteristics of the rough structural plane. The roughness after direct shear of the rough structural plane under different normal stress conditions is shown in Figure 6. It can be seen that the higher the normal stress, the greater the reduction value of structural surface roughness after direct shear. When the normal stress was 2 MPa, the reduction value of roughness after direct shear was 2.09. When the normal stress was 14 MPa, the roughness reduction after direct shear was 4.21. The roughness of the structural plane decreased exponentially with the increase of normal stress. The decrease of roughness after direct shear of the rough structural plane meant that the physical and mechanical properties of the structural plane would decay in varying degrees after direct shear. The significant reduction of roughness after direct shear was the main reason why the structural plane showed stick slip characteristics and released a lot of energy in the shear process. The higher the normal stress of the structural plane, the more obvious the slip weakening characteristics and the higher the released energy level in the direct shear process.

Simulation methodology

Model establishment

The FLAC3D numerical simulation model of Panel 14310 in Dongtan Coal Mine was established, as shown in Figure 7. The model was 710 m long, 450 m wide, and 180 m high. There are 316,664 gridpoints and 301,995 zones in the model, and the mesh size meets the accuracy requirements of numerical calculation. According to the actual occurrence characteristics of NF6 normal fault, the dip angle of the interruption layer in the numerical model was set as 60°, and the drop was set as 8 m. The mining situation of the working face passing through the fault from the footwall was simulated. In order to eliminate the influence of the boundary effect in the process of numerical calculation, the distance between the panel and the model boundary should be not less than 100 m; the buried depth of the simulated coal seam was 540 m, and the unit weight of the unsimulated rock above the model was assumed to be 25 KN/m^3 (Kong et al., 2019; Si et al., 2021b). It was calculated that the equivalent load of the unsimulated rock stratum was 10.8 MPa, and the load was applied to the upper boundary of the model. According to the *in-situ* stress test results, the lateral pressure coefficient of the model along the fault inclination direction was set as 0.6, and the lateral pressure coefficient along the fault strike direction was set as 0.8.

Mohr–Coulomb strain softening model was adopted for coal and rock mass in the numerical simulation. In the Mohr–Coulomb strain softening model, the strength parameters show a linear attenuation trend with the increase of equivalent plastic strain and finally attenuate to the residual value after the plastic failure of coal and rock mass. The research shows that the ratio of residual cohesion to initial cohesion of coal and rock mass generally ranges from 1/2 (Zhang et al., 2015) to 1/40 (Yan et al., 2013), so the ratio of residual cohesion to initial cohesion was taken as 1/5 in this study. Table 3 shows the mechanical parameters of coal and rock mass in the process of numerical simulation. The fault is simulated by an improved ubiquitous-joint model, and the model can take the slip weakening characteristics in the process of fault slip into consideration and reduce the roughness value after fault slip under different normal stress conditions. The parameters of the rock mass in the fault zone were taken as 1/5 of the sandstone parameters in the coal seam roof, the joint dilatancy angle was taken as 0, the initial roughness (JRC) was taken as 10, and the rock wall strength of the structural plane (JCS) was 102 MPa. The roughness value of

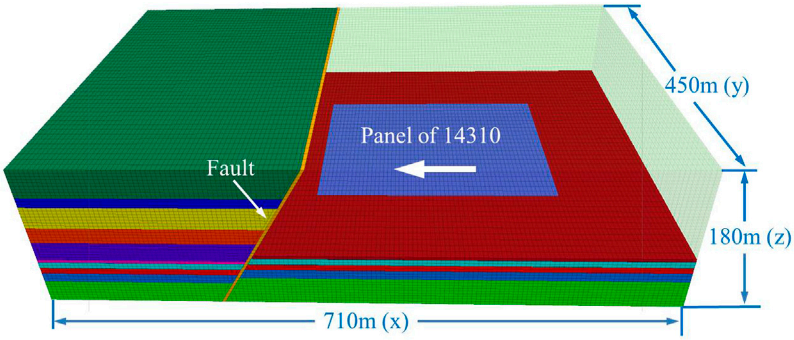

FIGURE 7
Numerical simulation model.

TABLE 3 Coal and rock mass properties in numerical simulation.

Lithology	E_m (GPa)	υ	C (MPa)	σ_{rm} (MPa)	φ (deg.)	c_r (MPa)	ε_p (%)
Sandstone	10.5	0.22	3	0.62	34.5	0.6	0.01
Siltstone	6.7	0.24	2.1	0.37	31	0.42	0.01
Mudstone	2.9	0.28	1.2	0.2	29	0.24	0.01
Coal	1.1	0.34	0.9	0.12	26	0.18	0.01

the rough structural plane after sliding under different normal stress conditions can be referred to in Figure 9.

Dynamic calculation of mining-induced fault slip

In this simulation, the fault slip law and dynamic response characteristics of 14,310 working faces in the Dongtan Coal Mine were numerically simulated. The numerical simulation process can be mainly divided into two parts. The first part was the excavation process of the panel. The numerical simulation calculation of the excavation process of the panel adopted static analysis, and the length of the panel excavated each time was determined as 10 m. During the static calculation, the boundary of the model is fixed.

The second part of the numerical simulation after the excavation of the panel was the dynamic analysis of fault slip. In order to eliminate the reflection and refraction of waves by the model boundary, the boundary condition of the model changed into a viscous boundary in the process of dynamic calculation. Based on the first step, the fault slip source M_0 after the excavation of the working face can be obtained, and the calculation of fault slip seismic moment M_0 is shown in Eq. 5. In Eq. 5, G is the stiffness of the fault plane, A is the area of fault shear slip, and D is the shear displacement of the fault. The fault slip seismic moment M_0 was applied to the element near the corresponding fault in the form of a couple so as to carry out dynamic analysis and study the dynamic response characteristics of the surrounding rock of the stope under the dynamic load of fault slip (Domański and Gibowicz, 2008; Wang and Cai, 2017). The research shows that using local damping to simulate the dynamic analysis of rock mechanics can achieve ideal results, and the local damping of rock is generally 2%–5%, so the local damping is selected as 5% in the dynamic calculation (Jiang et al., 2020). The next cycle would be carried out after the dynamic calculation was completed; another 10 m working face was excavated for the next round of static calculation to obtain the corresponding fault slip source M_0, and then the dynamic analysis was carried out until the working face was mined through the fault. The whole process of numerical simulation is shown in Figure 8. The numerical simulation method can be used to analyze the dynamic response characteristics of coal and rock mass under the dynamic load of fault slip so as to provide a basis for studying the rock burst hazard under the dynamic load of fault slip.

$$M_0 = GAD. \tag{5}$$

Reliability verification of numerical calculation method

Figure 9 shows the comparison between the fault slip seismic moment M_0 in the actual mining process of the working face and the

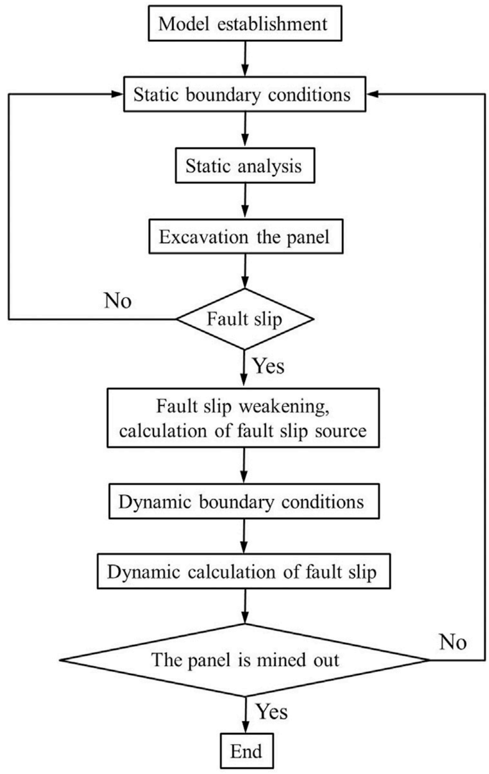

FIGURE 8
Flow chart of dynamic calculation.

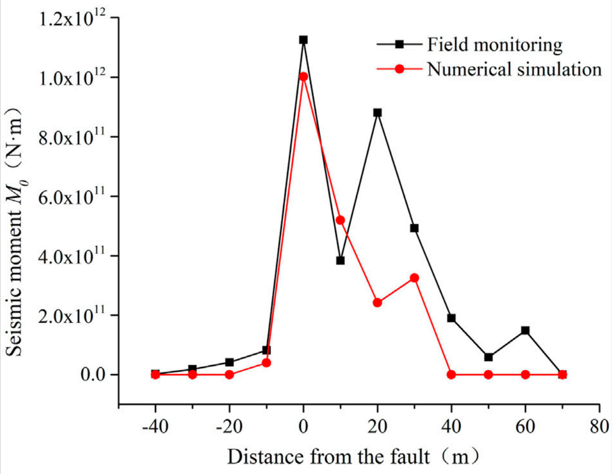

FIGURE 9
Comparison of fault slip seismic moment (M_0) between field monitoring and numerical simulation.

value calculated by numerical simulation. The mining situation and fault stress state of the working face in the process of the numerical simulation were consistent with the actual situation on site. The fault slip source M_0 monitored on site was obtained by converting the energy of microseismic event near the fault and by empirical Eqs 6 and 7 (Mutke et al., 2009), where E is the energy of microseismic event and M_L is Richter magnitude. Considering the complexity of mining conditions in the actual production process and many factors affecting the fault slip microseismicity, although the numerical simulation results were different from the specific values of the field monitoring results, the general trend of the two was highly consistent. The correlation coefficient of seismic moment between the numerical simulation results and the field monitoring results is 0.86, which proves that the numerical simulation method has certain reliability and application value for the rock burst hazard assessment and mining design of the panel.

$$\log E = 1.8 + 1.9M_L, \tag{6}$$

$$\log M_0 = 10.42 + 1.009M_L. \tag{7}$$

Simulation results

Fault slip law under the influence of mining

Figure 10 shows the cloud map of fault shear stress and shear displacement when the working face advanced to different positions. It can be found that when the working face gradually advanced from the footwall of the fault to 30 m away from the fault, the fault began to slip under the influence of mining, the shear stress in the fault slip area decreased and released energy, and the fault slip area was 52–68 m above the coal seam. The fault area close to the coal seam maintained good stability, and the shear stress level was high, which accumulated a lot of elastic properties. With the continuous advancement of the working face near the fault, the degree of mining disturbance to the fault was increasing, and the range of fault slip area extended from the high fault plane to the fault plane near the roof of the coal seam. When the working face advanced to 10 and 0 m away from the fault, the fault slip range and fault slip displacement increased sharply, affected by mining, and the shear stress in the fault slip area close to the coal seam dropped suddenly, releasing a lot of energy. The fault slip microseismic event was large, and the rock burst hazard was significantly increased under the influence of a strong fault slip dynamic load.

Influence of fault slip dynamic load on vibration velocity of coal and rock mass

The propagation of fault slip dynamic load can cause vibration and even damage coal and rock mass. Therefore, the influence of fault slip dynamic load on coal and rock mass near

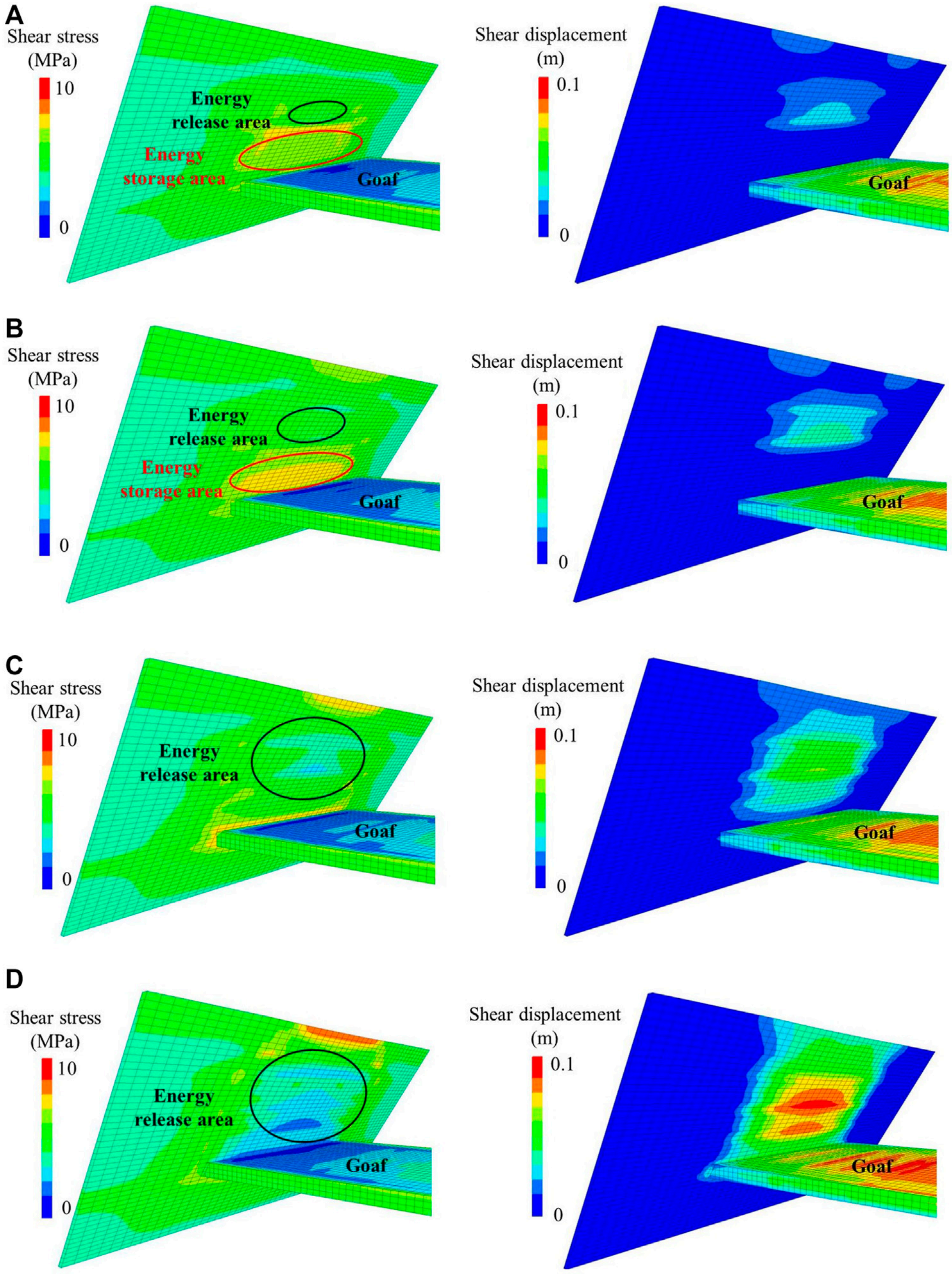

FIGURE 10
Shear stress and shear slip of the fault when mining the panel to different positions. **(A)** The working face is 30 m away from the fault. **(B)** The working face is 20 m away from the fault. **(C)** The working face is 10 m away from the fault. **(D)** The working face is 0 m away from the fault.

the stope can be judged by studying the vibration velocity when the working face advanced to different positions. Figure 11 shows the nephogram of vibration velocity when the working face advanced to 30 and 10 m away from the fault (the nephogram of vibration velocity was taken from the middle part of the panel at y = 225 m). It can be observed from the figure that during the advancement of the working face, fault slip first caused the vibration of the coal and rock mass near the fault; the closer it was to the fault, the greater the vibration velocity of the coal and rock mass. Over time, the seismic waves travel from the source position of the fault to all around after the shear slip of the fault. The energy of seismic waves decreased during transmission, so the vibration velocity of coal and rock mass farther away from the source of fault slip was smaller. However, when the source of fault

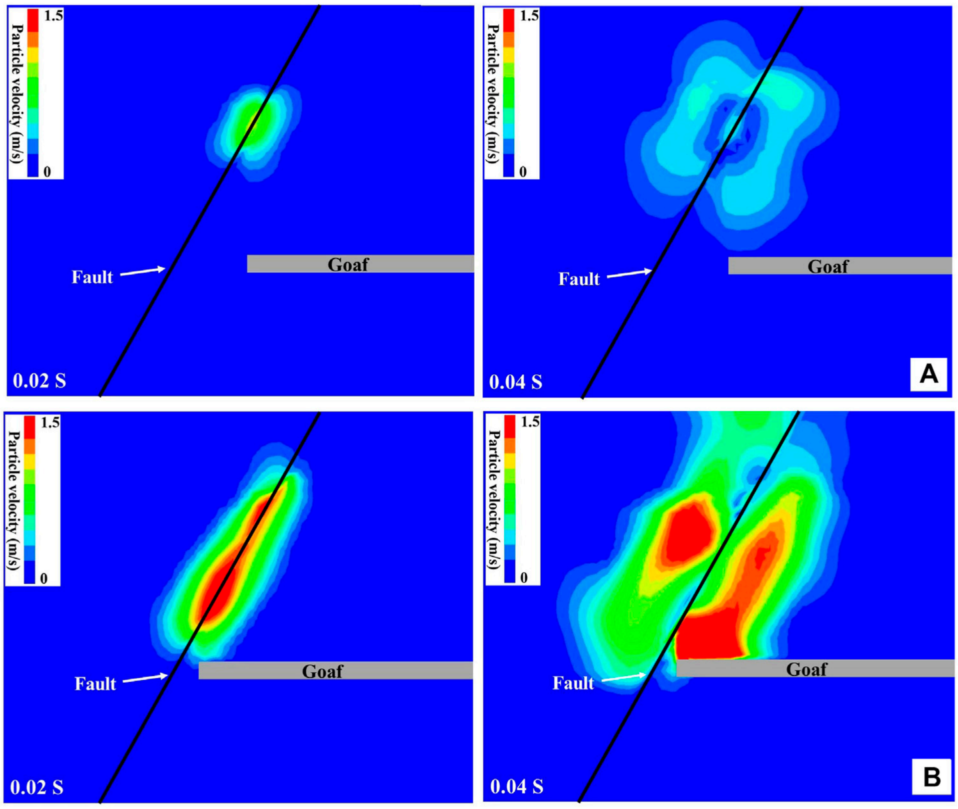

FIGURE 11
Particle velocity nephogram of the working face at different positions. **(A)** The working face is 30 m away from the fault. **(B)** The working face is 10 m away from the fault.

slip was large enough, the dynamic load released by fault slip would still cause large vibration of coal and rock mass near the working face.

Figure 12 shows the peak particle vibration velocity (PPV) in the area with peak advance abutment pressure at different advancing positions of the working face. It can be seen from Figures 11 and 12 that when the working face advanced to 30 and 20 m away from the fault, the PPV of the coal and rock mass at this location were 0.55 and 0.48 m/s, respectively. When the fault slip dynamic load propagated to the coal and rock mass in the area with peak abutment pressure, the fault slip source was small, and the dynamic load disturbance to the coal and rock mass in the area with peak abutment pressure was small. When the working face advanced to 10 m away from the fault, a large area slip occurred in the fault, the fault slip source increased obviously, and the PPV of coal and rock mass in the area with peak abutment pressure increased to 0.68 m/s. When the working face advanced to the fault position, the fault lost the support of the coal pillar completely, and the slip range extended from the high fault

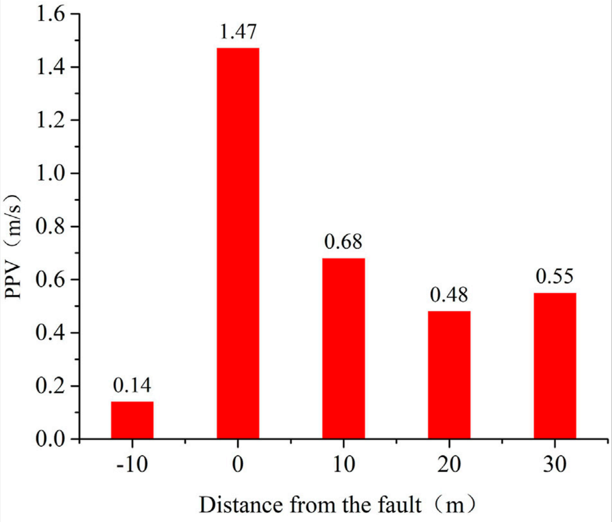

FIGURE 12
PPV evolution with retreat mining.

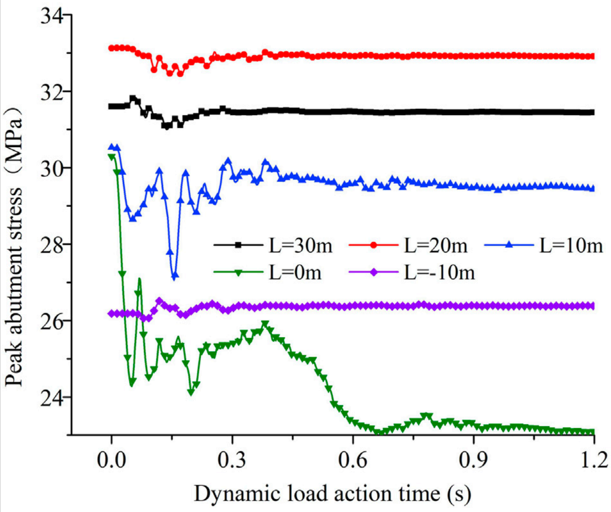

FIGURE 13
Variation of peak abutment stress under dynamic load.

plane to the fault plane at the basic top. The fault slip source increased further, and the fault slip source was close to the coal seam. The PPV of coal and rock mass in the area with peak abutment pressure reached 1.47 m/s. According to previous studies (Mutke et al., 2009; Mutke et al., 2015; Wang et al., 2022), a PPV of about 1 m/s was enough to induce rock burst, which would cause severe deformation of the roadway or rock fall, thus, the rock burst hazard would be greatly increased. When the working face crossed through the fault, the influence degree of mining on the fault decreased, and the PPV of coal and rock mass in the area with peak abutment pressure decreased significantly to 0.14 m/s. When the working face advanced to 20 m across the fault, the mining would have little effect on the fault, and the mining would not be affected by the dynamic load of the fault slip anymore.

Influence of fault slip dynamic load on abutment stress

The dynamic load released by fault slip has a significant influence on the coal and rock mass near the mining space. In severe cases, it may result in great damage to coal and rock mass in a high static load stress area near the working face with the release of a large amount of elastic energy, which may induce a fault slip–type rock burst. Therefore, it is of great significance to study the dynamic response of coal and rock mass in the area with peak advance abutment stress of working face under dynamic load to evaluate the hazard of rock burst. Figure 13 shows the variation of the coal and rock mass under dynamic load. It can be seen that the dynamic response characteristics of the peak abutment stress varied greatly when the working face advanced to different positions. The peak abutment stress vibrated to varying degrees under the fault slip load and gradually tended to be stable after the action of dynamic load. Especially when the working face was 10 m away from the fault and advanced to the fault position, the abutment stress oscillated violently after being loaded by the fault slip and then decreased significantly.

Figure 14 shows the dynamic response of advanced abutment stress when the working face advanced to different positions. It can be seen from Figures 13, 14 and 16 that when the working face advanced to 20 m away from the fault, before the action of dynamic load, the peak value of abutment stress was located 15 m in front of the working face. Affected by the fault stress barrier, the stress concentration of the coal pillar was high, and the peak abutment stress was 33.1 MPa. The fault slip dynamic load caused stress reduction of coal and rock mass about 20 m ahead of the working face. Because the fault slip dynamic load was small so the degree of stress reduction was small, and the stress reduction value of coal and rock mass in the area with peak abutment stress was only 0.2 MPa. When the working face advanced 10 m away from the fault, the peak value of advance abutment stress occurred in the coal and rock mass area of the hanging wall of the fault before the action of dynamic load, and the peak abutment stress decreased to 30.5 MPa. After the action of dynamic load, the area where the advance abutment stress decreased extended to about 45 m in front of the working face, and the reduction of the peak value for the abutment stress was 1.1 MPa. It indicated that the disturbance range and degree of dynamic load of fault slip on coal and rock mass in front of working face after the plastic failure of fault coal pillar significantly increased compared with that when fault coal pillar remained stable. When the working face advanced to 0 m away from the fault, the disturbance range and degree of dynamic load on coal and rock mass near the working face increased further. The area where the abutment stress decreased after dynamic loading extended to the range of 50 m ahead of the working face, while the coal and rock mass in the area with peak abutment pressure occurred severe plastic failure under the influence of strong fault slip dynamic load, and the stress decreased to 5.5 MPa. The rock burst hazard increased significantly. When the working face mined through the fault, the peak abutment stress before the action of fault slip dynamic load decreased to 26.2 MPa, and the disturbance of fault slip dynamic load on coal and rock mass near the working face was small. The dynamic load of fault slip only caused stress reduction of a small part of coal and rock mass in the plastic area and caused a slight stress increase of coal and rock mass in the area with peak abutment stress. The hazard of fault slip rock burst decreased significantly.

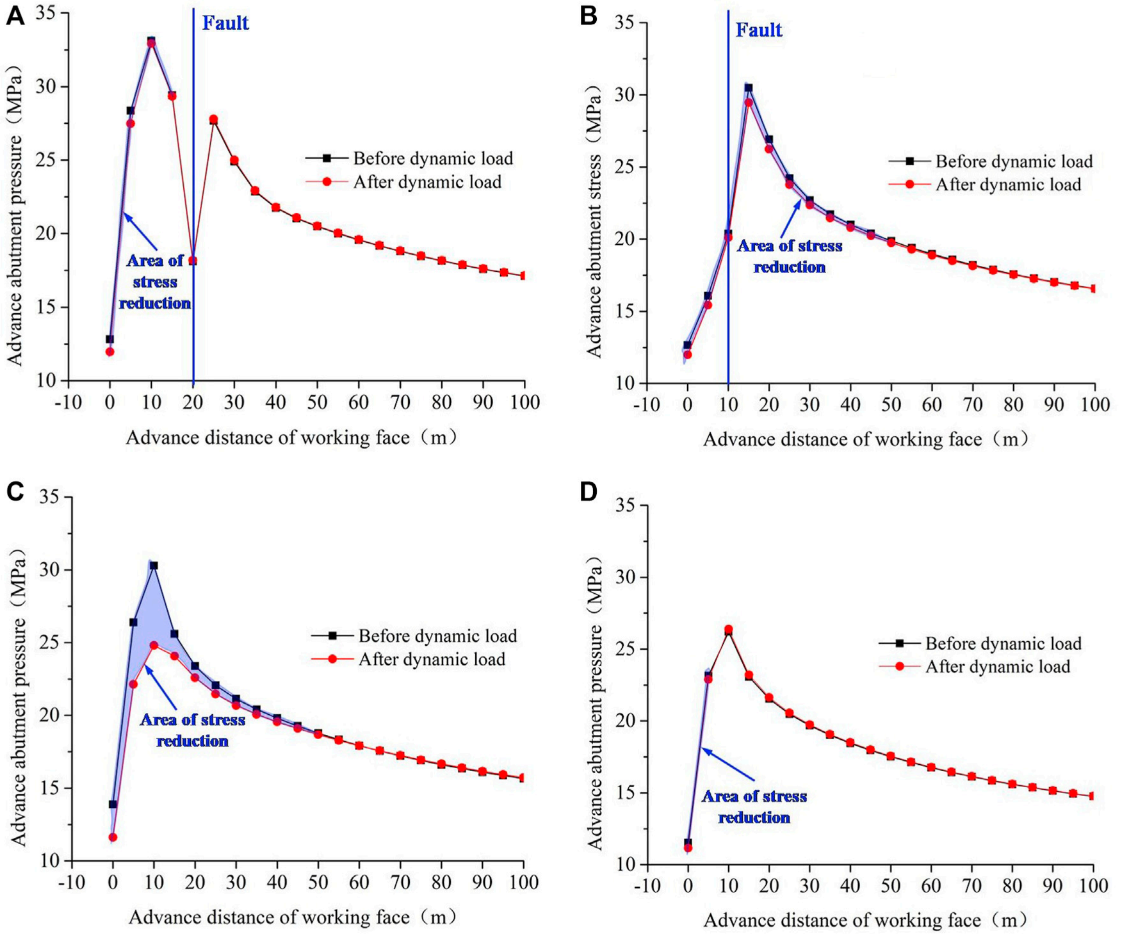

FIGURE 14
Dynamic response of advanced abutment stress. **(A)** The working face is 20 m away from the fault. **(B)** The working face is 10 m away from the fault. **(C)** The working face is 0 m away from the fault. **(D)** The working face mined through the fault for 10 m.

Analysis of rock burst hazard under fault slip dynamic load

Based on the stress superposition principle (Jiang et al., 2015), some scholars superimposed the self-weight stress, mining stress, and tectonic stress in the mining process to obtain the total stress of the coal body σ_s. The ratio of total stress to uniaxial compressive strength $[\sigma_c]$ of the coal body was used as the judgment index to divide the rock burst hazard. The formula of judgment index I_c for rock burst hazard was expressed as

$$I_c = \frac{\sigma_s}{[\sigma_c]}. \tag{8}$$

According to the rock burst hazard judgment index I_c, the rock burst hazard was divided into four levels: no hazard, slight hazard, moderate hazard, and severe hazard. The classification of rock burst hazard is shown in Table 4.

TABLE 4 Classification of rock burst danger levels.

0–1.5	1.5–2.0	2.0–2.5	>2.5
No hazard	Slight hazard	Moderate hazard	Severe hazard

The field detection and numerical simulation results showed that when mining near the fault, the fault slip source induced by mining produced a dynamic load on the coal and rock mass near the working face. When the disturbance degree of fault slip dynamic load was large enough, that is, the sum of the maximum fault slip dynamic load and the static load of coal in the limit equilibrium area was greater than the strength of coal, the superposition of dynamic and static loads resulted in damage to the coal body, and, in severe cases, the coal body was severely damaged, and a large amount of elastic energy was released which

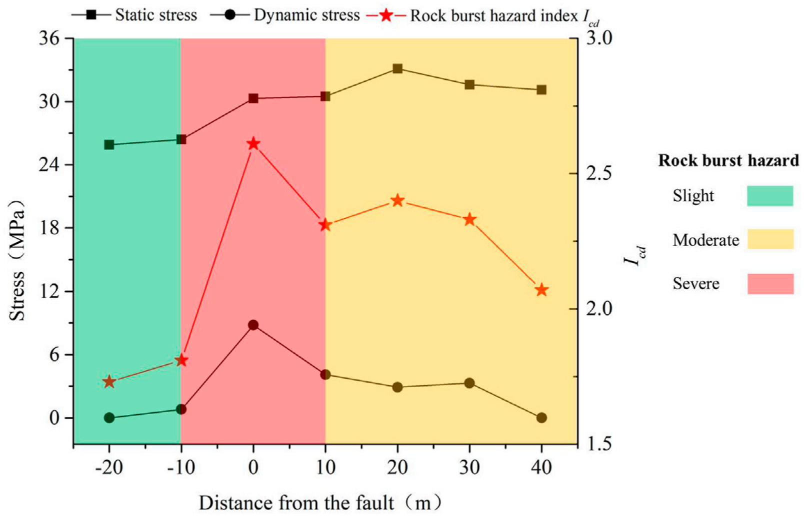

FIGURE 15
Classification of rock burst hazard.

would induce fault slip rock burst. The dynamic load stress disturbance generated by transmission of fault slip source to coal mass near the working face was closely related to the vibration velocity of coal. Considering that the vibration velocity near the coal and rock mass in the mining space can be not only obtained by the numerical simulation method but also monitored on-site by a microseismic system, the vibration velocity of the coal and rock mass near the mining space can be used as an index parameter to study the disturbance degree of fault slip source to the coal and rock mass near the working face. The maximum vertical dynamic load stress due to slip load of fault in the area with peak abutment pressure σ_d can be expressed as

$$\sigma_d = \rho C v_0, \tag{9}$$

where, ρ is the density of coal, C is the propagation velocity of wave, and v_0 is the peak vibration velocity in the vertical direction of coal.

Because the dynamic load of fault slip had a great influence on the coal and rock mass near the working face, the static load stress and the dynamic load stress of fault slip should be considered when evaluating the rock burst hazard of the working face near the fault. Combining Eq. 8 and Eq. 9, I_{cd} can be expressed as Eq. 10 for judging rock burst hazard under fault slip dynamic load, and the classification of rock burst hazard is still as shown in Table 4.

$$\mathrm{I}_{cd} = \frac{\sigma_s + \sigma_d}{[\sigma_c]} = \frac{\sigma_s + \rho C v_0}{[\sigma_c]}. \tag{10}$$

Based on index I_{cd}, the rock burst hazard was analyzed through the static load stress and the vibration velocity of coal and rock mass in the area with peak abutment stress under fault slip dynamic load. Considering that there was little difference between the peak vertical vibration velocity of coal and rock mass in the area with peak abutment pressure and the peak particle vibration velocity (PPV) of coal and rock mass, so the peak vertical vibration velocity of coal and rock mass in the area with peak abutment pressure was taken as the value of PPV. The propagation speed of the longitudinal wave was 4300 m/s, and the coal density and compressive strength were 1400 kg/m^3 and 15 MPa, respectively, based on the test results. The division of rock burst hazard degree during the working face mining through the fault is shown in Figure 15.

It can be seen from Figure 15 that the fault blocked the distribution of the static load stress to a certain extent. The static load stress before the working face crossed the fault was larger than that after the working face crossed the fault, but the variation of the static load stress at the working face was smaller than that of the dynamic load stress of the fault slip. Fault slip type rock burst was affected by both static load stress level and fault slip dynamic load. When the working face was passing through the fault (10 m away from the fault to 10 m across the fault), the hazard of rock burst was the highest due to the superposition of high static load and strong fault slip dynamic load. The hazard of rock burst assessment result was consistent with the actual production situation on site, which proved that the rock burst hazard assessment method had certain reliability.

Conclusion

During the mining period, with the working face getting closer to the fault, the number of high-energy microseismic events released by fault slip increases significantly, and the fault slip rock burst hazard is high. After the working face is mined through the fault, the disturbance degree of mining to the fault decreases, the occurrence frequency and energy level of microseismic events decrease, and the hazard of fault slip rock burst is small. The b value representing microseismic intensity gradually decreases as the working face gets closer to the fault. The *b* value gradually increases after the working face crosses through the fault. The *b* value of a microseismic event can be used as an index to evaluate fault activity and early warning of fault slip rock bursts.

The dynamic calculation of fault slip and its dynamic response under the influence of mining was carried out by FLAC3D numerical simulation software, and the whole process of numerical simulation of “mining–fault slip release dynamic load–mining spatial dynamic response” was realized. Mining induces fault slip and weakens and releases dynamic load, which has a significant impact on the vibration velocity and abutment stress of coal and rock mass near mining space. The vibration velocity and the reduction value of peak abutment stress both reach the highest when the working face advances near the fault. Under the effect of strong fault slip dynamic load, the coal and rock mass in the area with peak abutment stress undergo plastic failure and release large amounts of elastic energies, and the hazard of fault slip rock burst is high.

Considering the stress disturbance caused by the fault slip dynamic load on the coal and rock mass near the working face, the hazard of rock burst judgment index I_{cd} was proposed. The hazard of rock burst when the working face mined through the fault was analyzed, and the rock burst hazard when the working face passed through the fault was divided, which provided a new idea for the rock burst hazard assessment under the influence of fault.

Data availability statement

The original contributions presented in the study are included in the article/Supplementary Material; further inquiries can be directed to the corresponding author.

Author contributions

Conceptualization: PK and RL; methodology: PK; software: PK; validation: LX, ZL, and ZZ; formal analysis: CX; resources: CX; data curation: ZZ; writing—original draft preparation: PK; writing—review and editing: RL; visualization: LX and ZL; project administration: RL.

Funding

The research of this study was sponsored by the Natural Science Foundation of Anhui Province (2208085QE144), the National Natural Science Foundation of China (U21A20110), the National Natural Science Foundation of China (52104073), and Start-up Fund for Introducing Talents and Scientific Research of Anhui University of Science and Technology (13210151).

Conflict of interest

Author ZL and ZZ were employed by Yankuang Energy Group Company Limited. Author CX was employed by Jinan Urban Construction Group.

The remaining authors declare that the research was conducted in the absence of any commercial or financial relationships that could be construed as a potential conflict of interest.

Publisher’s note

References

Brace, W. F., and Byerlee, J. D. (1966). Stick-slip as a mechanism for earthquakes. *Science* 153 (3739), 990–992. doi:10.1126/science.153.3739.990

Cai, W., Dou, L., Si, G., and Hu, Y. (2021). Fault-induced coal burst mechanism under mining-induced static and dynamic stresses. *Engineering* 7 (5), 687–700. doi:10.1016/j.eng.2020.03.017

Domański, B., and Gibowicz, S. J. (2008). Comparison of source parameters estimated in the frequency and time domains for seismic events at the Rudna copper mine, Poland. *Acta Geophys.* 56 (2), 324–343. doi:10.2478/s11600-008-0014-1

Jiang, F., Shu, C., and Wang, C. (2015). Impact risk appraisal of stope working faces based on stress superimposition. *Chin. J. Rock Mech. Eng.* 34 (12), 2428–2435.

Jiang, L., Kong, P., Zhang, P., Shu, J., Wang, Q., Chen, L., et al. (2020). Dynamic analysis of the rock burst potential of a longwall panel intersecting with a fault. *Rock Mech. Rock Eng.* 53 (4), 1737–1754. doi:10.1007/s00603-019-02004-2

Kong, P., Jiang, L., Jiang, J., Wu, Y., Chen, L., and Ning, J. (2019). Numerical analysis of roadway rock-burst hazard under superposed dynamic and static loads. *Energies* 12 (19), 3761. doi:10.3390/en12193761

Kong, P., Yuan, A., Liu, Y., and Li, Z. (2022). Study on fault slip dynamic response and rock burst potential under the influence of different horizontal stresses. *Geomatics, Nat. Hazards Risk* 13 (1), 1321–1341. doi:10.1080/19475705.2022.2073831

Lai, X., Zheng, J., and Jiang, X. (2016). Influential range assessment of dynamic pressure in fault zone with broken rock masses[J]. *J. Min. Saf. Eng.* 33 (02), 361–366.

Li, D., Li, Y., Masoumi, H., and Chen, J. (2021). An analytical model for axial performance of rock bolts under constant confining pressure based on continuously yielding criterion. *Tunn. Undergr. Space Technol.* 113, 103955. doi:10.1016/j.tust.2021.103955

Li, D., Masoumi, H., and Ming, C. (2021). A constitutive model for cable bolts exhibiting cone shaped failure mode. *Int. J. Rock Mech. Min. Sci.* 145, 104855.

Li, D., Shirani Faradonbeh, R., Lv, A., Wang, X., and Roshan, H. (2022). A data-driven field-scale approach to estimate the permeability of fractured rocks. *Int. J. Min. Reclam. Environ.*, 1–17. doi:10.1080/17480930.2022.2086769

Li, P., Cai, M., and Guo, Q. (2018). Research situations and development tendencies of fault slip rockburst in coal mine. *Harbin Gongye Daxue Xuebao/Journal Harbin Inst. Technol.* 50 (3), 1–17.

Luo, H., Li, Z., and Wang, A. (2014). Study on the evolution law of stress field when approaching fault in deep mining[J]. *J. China coal Soc.* 32 (02), 322–327.

Meng, F., Zhou, H., Wang, Z., Zhang, L., Kong, L., Li, S., et al. (2017). Influences of shear history and infilling on the mechanical characteristics and acoustic emissions of joints. *Rock Mech. Rock Eng.* 50 (8), 2039–2057. doi:10.1007/s00603-017-1207-1

Mutke, G., Dubiński, J., and Lurka, A. (2015). New criteria to assess seismic and rock burst hazard in coal mines/nowe kryteria dla oceny zagrożenia sejsmicznego I tąpaniami W kopalniach węgla kamiennego. *Archives Min. Sci.* 60 (3), 743–760. doi:10.1515/amsc-2015-0049

Mutke, G., Lurka, A., and Dubiński, J. (2009). "Seismic monitoring and rock burst hazard assessment in deep polish coal mines-case study of rock burst on April 16, 2008 in Wujek-Slask coal mine[C]," in 7th International Symposium on Rockburst and Seismicity in Mines (RASiM 7): Controlling Seismic Hazard and Sustainable Development of Deep Mines. Editors C. A. Tang (Rinton Press), 1413–1424.

Ortlepp, W. D., and Stacey, T. R. (1994). Rockburst mechanisms in tunnels and shafts. *Tunn. Undergr. Space Technol.* 9 (1), 59–65. doi:10.1016/0886-7798(94)90010-8

Scholz, C. (1968). The frequency-magnitude relation of microfracturing in rock and its relation to earthquakes. *Bull. Seismol. Soc. Am.* 58 (1), 399–415. doi:10.1785/bssa0580010399

Si, L., Zhang, H., Wei, J., and Hongkai, H. (2021). Modeling and experiment for effective diffusion coefficient of gas in water-saturated coal. *Fuel* 284. 118887, doi:10.1016/j.fuel.2020.118887

Si, S., Wei, J., Xi, Y., Wang, H., Wen, Z., Li, B., et al. (2021). The influence of long-time water intrusion on the mineral and pore structure of coal. *Fuel* 290, 119848. doi:10.1016/j.fuel.2020.119848

Si, L., Xi, Y., Wei, J., Wang, H., Zhang, H., Xu, G., et al. (2022). The influence of inorganic salt on coal-water wetting angle and its mechanism on eliminating water blocking effect. *J. Nat. Gas. Sci. Eng.* 103, 104618. doi:10.1016/j.jngse.2022.104618

Tse, R., and Cruden, D. M. (1979). Estimating joint roughness coefficients. *Int. J. Rock Mech. Min. Sci. Geomechanics Abstr.* 16 (5), 303–307. doi:10.1016/0148-9062(79)90241-9

Wang, A., Pan, Y., Li, Z. H., Liu, C. S., Han, R. J., Xiang, F., et al. (2014). Similar experimental study of rockburst induced by mining deep coal seam under fault action[J]. *Rock Soil Mech.* 35 (9), 2486–2492.

Wang, H., Jiang, Y., and Jiang, C. (2019). Characteristics of overlying strata movement in double fault area under the dynamic pressure[J]. *J. Min. Saf. Eng.* 36 (03), 513–518.

Wang, P., Jiang, L., Jiang, J., Zheng, P., and Li, W. (2018). Strata behaviors and rock burst–inducing mechanism under the coupling effect of a hard, thick stratum and a normal fault. *Int. J. Geomech.* 18 (2), 04017135. doi:10.1061/(asce)gm.1943-5622.0001044

Wang, S. (2012). *The horstfault mine quake's mechanism and monitoring analysis in Dong Tan Colliery [D]*. fuxin china: Liao Ning Technical University.

Wang, X., and Cai, M. (2017). Numerical modeling of seismic wave propagation and ground motion in underground mines. *Tunn. Undergr. Space Technol.* 68, 211–230. doi:10.1016/j.tust.2017.05.019

Wang, Z., Linlin, G., Qingzhao, Z., and Bo-An, J. (2021). Influence of initial stress and deformation states on the shear creep behavior of rock discontinuities with different joint roughness coefficients[J]. *Rock Mech. Rock Eng.* 54 (11), 1–14. doi:10.1007/s00603-021-02633-6

Wang, X., Li, J., Zhao, X., and Liang, Y. (2022). Propagation characteristics and prediction of blast-induced vibration on closely spaced rock tunnels. *Tunn. Undergr. Space Technol.* 123, 104416. doi:10.1016/j.tust.2022.104416

Xue, Y., Xu, T., Wasantha, P. L. P., Yang, T. h., and Fu, T. f. (2020). Dynamic disaster control of backfill mining under thick magmatic rock in one side goaf: A case study. *J. Cent. South Univ.* 27, 3103–3117. doi:10.1007/s11771-020-4532-6

Xue, Y., Xu, T., Zhu, W., Heap, M. J., Heng, Z., and Wang, X. (2021). Full-field quantification of time-dependent and -independent deformation and fracturing of double-notch flawed rock using digital image correlation. *Geomech. Geophys. Geo-energ. Geo-resour.* 7, 100. doi:10.1007/s40948-021-00302-0

Yan, S., Bai, J., Wang, X., and Huo, L. (2013). An innovative approach for gateroad layout in highly gassy longwall top coal caving. *Int. J. Rock Mech. Min. Sci.* 59, 33–41. doi:10.1016/j.ijrmms.2012.11.007

Zhang, K., Zhang, G., Hou, R., Wu, Y., and Zhou, H. (2015). Stress evolution in roadway rock bolts during mining in a fully mechanized longwall face, and an evaluation of rock bolt support design. *Rock Mech. Rock Eng.* 48, 333–344. doi:10.1007/s00603-014-0546-4

Zhou, H., Meng, F., Zhang, C., Hu, D., Lu, J., and Xu, R. (2016). Investigation of the acoustic emission characteristics of artificial saw-tooth joints under shearing condition. *Acta Geotech.* 11 (4), 925–939. doi:10.1007/s11440-014-0359-3

Zhu, S., Jiang, F., Kouame, K. J. A., Li, X., Tan, W., Zhang, B., et al. (2016). Fault activation of fully mechanized caving face in extra-thick coal seam of deep shaft[J]. *Chin. J. Rock Mech. Eng.* 35 (01), 50–58. doi:10.13722/j.cnki.jrme.2014.1574

frontiers | Frontiers in Earth Science

TYPE Original Research
PUBLISHED 12 January 2023
DOI 10.3389/feart.2022.1054040

OPEN ACCESS

EDITED BY
Hongtu Zhang,
Henan Polytechnic University, China

REVIEWED BY
Chenchen Wang,
China University of Mining and Technology, Beijing, China
Bai Xin,
University of South China, China
Anhu Wang,
University of Science and Technology Beijing, China

*CORRESPONDENCE
Guangxue Cao,
cao-gx@hfut.edu.cn

SPECIALTY SECTION
This article was submitted to Economic Geology,
a section of the journal
Frontiers in Earth Science

RECEIVED 26 September 2022
ACCEPTED 31 October 2022
PUBLISHED 12 January 2023

CITATION
Chen P, Cheng T, Wang J and Cao G (2023), Accumulation and evolution of ice jams influenced by different ice discharge: An experimental analysis.
Front. Earth Sci. 10:1054040.
doi: 10.3389/feart.2022.1054040

Accumulation and evolution of ice jams influenced by different ice discharge: An experimental analysis

Pangpang Chen, Tiejie Cheng, Jun Wang and Guangxue Cao*

School of Civil and Hydraulic Engineering, Hefei University of Technology, Hefei, China

Ice jam, a unique hydrological phenomenon of rivers in cold regions, is a major cause of ice flooding. There are many different kinds of damage that can result from ice jams: e.g., blockage of the water flow, rising water levels that can flood farmland and dwellings, damage to hydraulic structures, and interruptions to shipping. The formation of an ice jam is influenced by various factors associated with different fields of study. The accumulation of an ice jam is thus a complex process worth investigating. However, previous studies seldom take account of ice discharge factors. This study carries out 29 tests on the accumulation of an ice jam, and discovers four kinds of phenomena: inlet ice that fails to submerge (case 1); thickening ice from upstream to downstream (case 2); thickening ice from downstream to upstream (case 3); and failure to form an ice jam (case 4). Two typical examples are used to detail cases 2 and 3. The authors suggest differentiating between the two cases using the longitudinal boundary line running through the point of the Froude number (Fr) = 0.119. Furthermore, the authors analyze the phenomena that make it difficult for an ice jam to form and suggest using the critical discriminant line to distinguish between cases 3 and 4. Combined with the longitudinal boundary line, a partition result diagram of the different accumulation features of ice jams is presented to differentiate between the four modes of accumulation of ice jams.

KEYWORDS

ice jam, ice cover, experimental study, specific phenomena, fr, longitudinal boundary, critical discriminant

Introduction

River ice, a typical hydrological feature of rivers in cold regions, has considerable impact on the global hydrological system, especially in the northern hemisphere (Yang et al., 2020). When river ice is submerged in front of the ice cover, ice jams and ice dams are easily formed and can induce ice floods (Becket et al., 2021), which can in turn cause extensive damage to infrastructure, shipping, and hydropower production, and can also harm river ecology and water quality (White, 2003; Beltaos and Burrell, 2015; Frolova et al., 2015; Lindenschmidt et al., 2016).

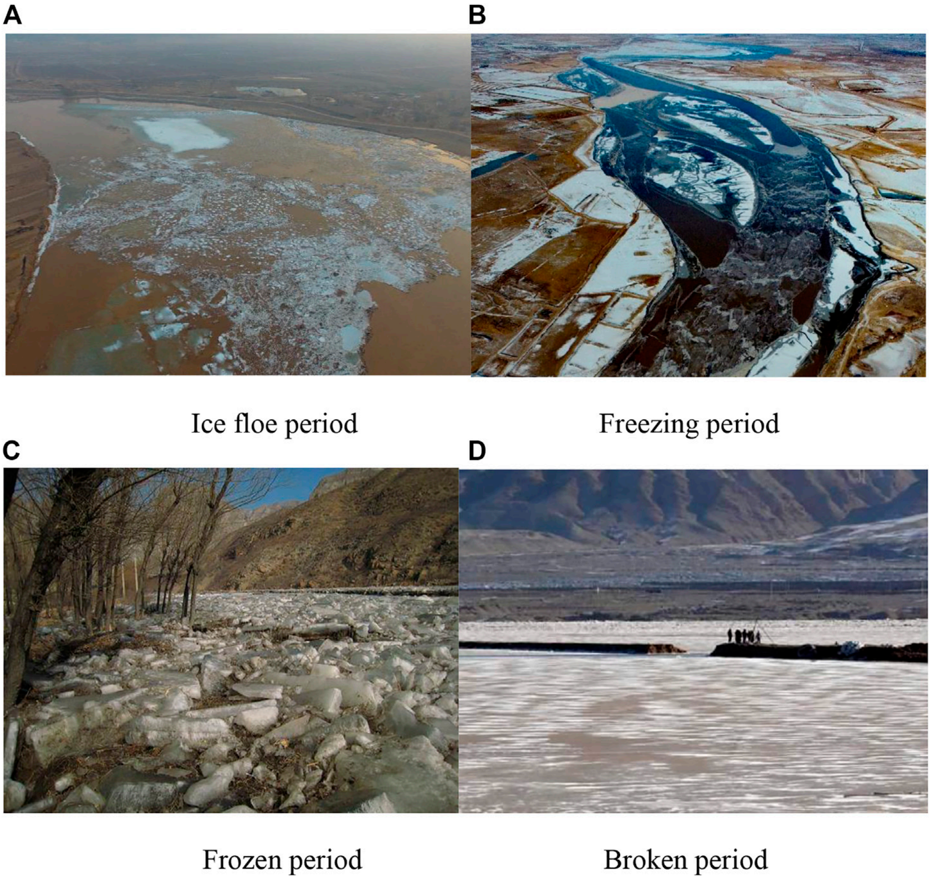

FIGURE 1
Ice jam during the stable sealing period of the Yellow River in China. **(A)** Ice pans (floe) floating period, **(B)** Freeze-up period, **(C)** Ice-covered/jammed period, and **(D)** River break-up period.

There are many potential kinds of damage resulting from ice jams: e.g., blockage to the water flow section, rising water levels that can flood farmland and dwellings, damage to hydraulic structures, interruptions to shipping, and disruptions to hydropower generation. Ice jams can also block the water inlet of water plants, thereby interrupting the water supply. The scouring effect of an ice jam can erode riverbanks and riverbeds, threatening the living environment of fish and other wild species, and can expose the biological mechanisms buried beneath the riverbed. According to the ice jam database of the U.S. Army Corps of Engineers (with historical records since 1780), more than 22,500 ice jams have occurred in the United States alone, about 10% of which led to some degree of flooding. Taking, for example, the local reach of the Athabasca River, about 60 km from Fort McMurry in Canada, in 1997 ice flooding caused direct economic losses worth millions of dollars.

The Yellow River in China also faces serious ice disasters (Figure 1) (Sui et al., 2008). Located at 96°–119°E and 32°–42°N, the Yellow River Basin has a particular geography that favors the generation of ice in its upper, middle, and lower reaches in winter. The winding pattern of the river makes it easy for ice floods to form during the annual freeze-up and break-up periods. In March 1996, the river burst its banks in Wulan Township and Jiefangtan Township, Dalat Banner, resulting in direct economic losses of CNY 70 million. On 1 March 1999, an ice jam formed in the Hohhot and Qingshuihe sections of the river, and the ensuing rising water levels had a direct economic cost of CNY 12.623 million. On the morning of 17 December 2001, an ice flood occurred in the Wuhai section of the river in Inner Mongolia. The embankment burst for nearly 80m, and the ice water destroyed five villages, three farms, and two schools in Wuda District. In total, over 900 farmers and 4,000 villagers were affected by the ice flood.

Domestic and foreign research into ice hydraulics mainly focuses on ice jams. The formation and accumulation mechanisms of ice jams have been explored extensively through prototype observation (Sui et al., 2002; Beltaos and Carter, 2009; Deng et al., 2019; Wolfe et al., 2020), experimental study (Healy and Hicks, 2006; Wang et al., 2019), theoretical analysis (Daly and Axelson, 1990; Hicks and

Healy, 2003; Wang et al., 2012), and numerical simulation (Beltaos, 2008; Wang et al., 2009; Wang et al., 2011; Beltaos, 2019). The data observed show that, in winter, river ice generally goes through several stages, namely, ice pans (floe) floating period, freeze-up period, ice-covered/jammed period and river break-up period.

During the ice pans (floe) floating period, the water surface loses too much heat due to the continuous low temperature. The turbulence of the water body then causes a heat exchange between the water surface and the water body. In various places, the water cools down very quickly, and ice particles form rapidly. Ice floes with high-flow ice density then gradually form, accumulate, and move downstream. The ice floe period mainly means that after the initial freezing, ice floes continue to move in the river channel and either dive beneath or collide with other hydraulic structures (Hayakawa et al., 2001).

During the freeze-up period, the ice cover initially appears in relatively narrow river sections. The ice floe in front of the ice cover will stop or become submerged under the ice jam, at a place with a high water gradient or strong turbulence. During the formation and accumulation of the ice jam, the head of the jam advances continuously downstream or upstream, and the ice grows thicker or thinner beneath the jam. When the movement of floating ice in rivers is blocked, it will accumulate, and the effect of low temperatures will be the freezing phenomenon. The flow and ice condition tends to be stable after the end of the freezing period, which then becomes the ice-covered/jammed period.

During the ice-covered/jammed period, the river flow develops from an open flow with a free surface to an undercurrent covered over with ice. The presence of ice complicates the river hydraulic process, and sometimes determines the hydrodynamic features of the river (Wu et al., 2014; Amroune et al., 2020). From the perspective of hydraulics, the existence of the ice cover creates additional flow boundaries, thus increasing the wet perimeter (Lindenschmidt and Rokaya, 2019; Namaee and Sui, 2019). In addition, the ice cover increases the river's resistance, and reduces the discharge downstream. The hydraulic radius of the flow section is hence significantly reduced. Studies have shown that, in the presence of the ice cover, the flow is very sensitive to the friction coefficient. Compared with the open flow condition, the hydraulic radius will reduce to 46% and the water flow will lower to 60%. The ice jam will push up the water level much higher than the complete and static ice floe or open flow. Rokaya et al. (2020) have demonstrated that, compared with the open flow, an ice jam will increase the water depth of a river two to three times, under the same or even lower flow discharge. When the flow discharge is fixed, the water level will rise abnormally, due to the existence of ice jam.

At the end of winter the temperature turns positive, and the river gradually enters the River break-up period. The ice situation at this stage is manifest in the rupture of the ice cover and the re-obstruction of large ice floes in the narrow river sections (Chang et al., 2022). This stage is the main period for ice flood disaster, although the ice jam in the opening period is also harmful to the hydrological conditions of rivers. Due to difficulties obtaining field observation data, a numerical simulation method is chiefly used to research the break-up period of ice jams.

The formation of an ice jam is affected by various factors, as reflected in different disciplines such as thermodynamics, solid mechanics, hydrology, hydraulics, and river dynamics. As the ice jam accumulates and evolves, different types of ice jams will be formed depending on the conditions. Putting thermodynamic factors aside, ice jam accumulation is already a complex process, even if only mechanical action is taken into account (Shen and Wang, 1995). Through experimental studies, this study explores the influence of the hydraulic conditions and ice discharge on the accumulation of ice jams and identifies and investigates four different kinds of ice jam accumulation. The internal mechanism of each phenomenon is studied in detail, before a discrimination method and a partition result diagram designed to differentiate between the four different features of ice jams accumulations are presented.

Experimental method

The experimental analysis was carried out in the straight test water channel of the Ice Research Lab, Institute of Water Science, Hefei University of Technology. Figure 2 shows the layout plan of the 26.68-m-long, 40-cm-wide channel. From upstream to downstream, there are 22 sections with a spacing of 1.2 m. An automatic ice feeder is set at the four sections upstream, and a one-meter-long ice cover model of light polystyrene foam board is placed in the 20th to the 21st sections downstream. The measuring points of all stacking tests are mainly the 16 sections from the 5th to the 20th.

The ice particle model is made of polyethylene particles, the most commonly used material in international river ice tests (Ambtman et al., 2011; Peters et al., 2017). Because the density is 0.917 g/cm^3, which is close to natural river ice, this material can also reduce the influence of surface tension once the model ice is soaked. In terms of shape, the model is mainly composed of 3.5 mm oblate ellipsoid particles, with a porosity of about 0.4. The initial hydraulic conditions include water flow, water depth of the control section in the upstream, and ice discharges. On this basis, different hydraulic conditions are combined. In each experiment, the water discharge is kept constant and uniform. The automatic ice feeder then starts to add ice, and the ice discharge rate is maintained as constant. To monitor the complete process of ice jam accumulation, real-time data, including pressure head and ice thickness, are recorded every 30 min at each measuring point. Each experiment is terminated when the water discharge conditions and ice jam thickness reaches the state of equilibrium (i.e., no hydraulic parameters change with time). In general, each experiment lasts from 4 h to 20 h.

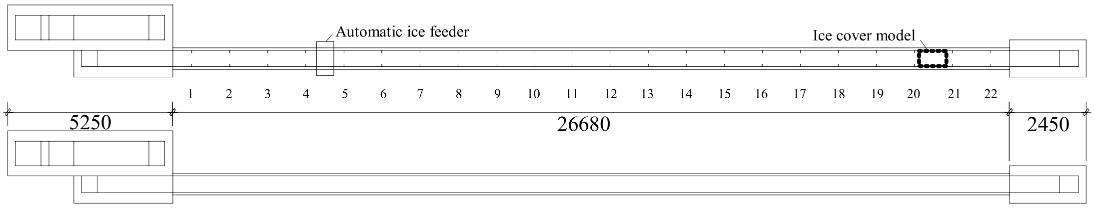

FIGURE 2
Layout plan of the straight channel.

TABLE 1 Initial date, stable data, and accumulation of 29 ice jam experiments under different test conditions.

Serial number	Initial flow depth (cm)	Discharge (L/s)	Initial section velocity (m/s)	Ice discharge (L/s)	Stable Fr	Leading edge section number	Type of accumulation
1	10	4.008	0.1	0.01429	—	—	First case
2	10	4.802	0.12	0.01354	—	—	First case
3	10	5.606	0.14	0.01299	0.109	5	Second case
4	10	6.4023	0.16	0.006249	0.145	5	Third case
5	10	6.4023	0.16	0.0105	0.145	5	Third case
6	10	7.2039	0.18	0.01054	0.151	18	Third case
7	10	10	8	0.0274	0.173	17	Third case
8	10	10	8	0.01360	0.202	20	Fourth case
9	15	7.796	0.13	0.02882	—	—	First case
10	15	8.9975	0.15	0.02177	0.106	5	Second case
11	15	9.6021	0.16	0.00993	0.121	5	Second case
12	15	10.8071	0.18	0.0367	0.116	5	Second case
13	15	10.8071	0.18	0.006132	0.132	15	Third case
14	15	12.0177	0.2	0.03699	0.133	5	Third case
15	15	13.1994	0.22	0.02365	0.161	14	Third case
16	20	8.0154	0.1	0.03373	—	—	First case
17	20	10.4144	0.13	0.03351	—	—	First case
18	20	12.0177	0.15	0.03558	—	—	First case
19	20	14.4258	0.18	0.03694	0.114	5	Second case
20	20	15.2024	0.19	0.04025	0.12	5	Second case
21	20	15.2024	0.19	0.00743	0.124	17	Third case
22	20	16.0276	0.2	0.0259	0.132	15	Third case
23	25	14.0024	0.14	0.01269	—	—	First case
24	25	16.0036	0.16	0.01599	0.096	5	Second case
25	25	18.0129	0.18	0.01327	0.111	6	Second case
26	25	20.0018	0.2	0.02034	0.122	5	Third case
27	25	20.4978	0.205	0.01298	0.124	16	Third case
28	25	21.0011	0.21	0.01327	0.125	18	Third case
29	25	22.0009	0.22	0.02579	0.130	19	Third case

The flow discharge is controlled through the opening of the upstream valve and is calculated by water head from the piezometer and a triangular weir flow formula. The flow depth of the 4th section is controlled by the opening angle of the tail gate at the end of the water flume. Each section is equipped with a piezometer to measure the piezometric water

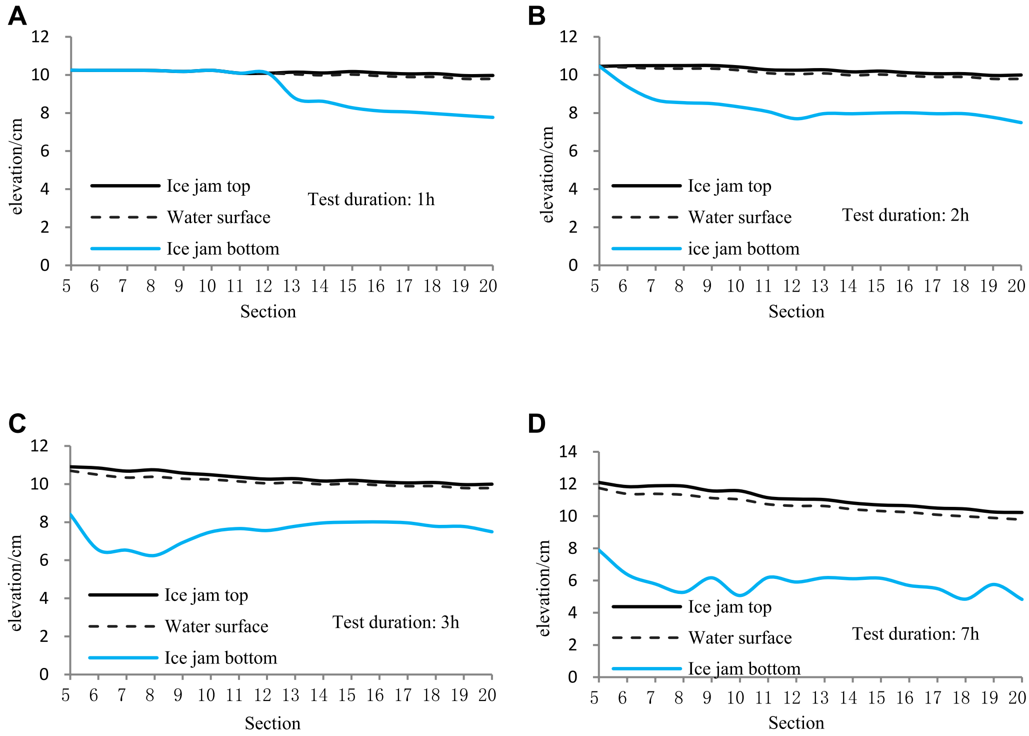

FIGURE 3
Specific phenomena of the second case (third experiment).

head. The dynamic ice thickness is measured with a graduated scale. The measurement accuracy of all lengths is within mms. The volume method is used for estimating ice discharge.

Experimental results

The initial data and test records of the ice jam experiments are recorded in Table 1, including the stable Froude number (Fr) in the upstream, the leading edge section number of front of the ice jam, and the sequence of ice jam accumulation during 29 experiments under different experimental conditions. It can be seen from the results that the ice jam accumulation fell into four cases.

In case 1, the ice particles did not submerge during the experiment. The ice jam was juxtaposed at the flow surface and developed on to the upstream flow.

In case 2, the ice particles did not submerge initially, but all submerged when the ice jam developed at a certain section in the upstream section. Initially, the ice jam accumulated and thickened from upstream to downstream. Eventually, the ice jam of the entire channel reached the state of equilibrium.

In case 3, some part of the ice particles did not submerge in front of the initial ice cover (at section 20). The initial ice jam accumulated and thickened from downstream to upstream, until the ice jam of the entire channel reached the state of equilibrium.

In case 4, all ice particles submerged in front of the initial ice jam (at section 20). Finally, the length of the ice jam accumulation was almost invisible or the ice jam was unable to form.

Among the four cases, the experiment was terminated in the first case, and the ice jam did not reach the state of equilibrium in the channel.

In the second and third cases, the ice jam accumulation followed different sequences: the initial ice jam thickened from upstream to downstream, and from downstream to upstream, respectively. The difference stemmed from whether or not the initial ice particles would partially submerge at section 20. If no ice particles submerged, the ice jam would thicken from upstream to downstream. If some ice particles submerged, the ice jam would thicken from downstream to upstream. If all ice particles submerged, the ice jam would not form in the channel. The specific phenomena of the two cases are described in the subsequent section.

In the fourth case, the initial hydraulic conditions were equivalent to stable hydraulic conditions, indicating that all the ice particles from upstream were submerged under these conditions.

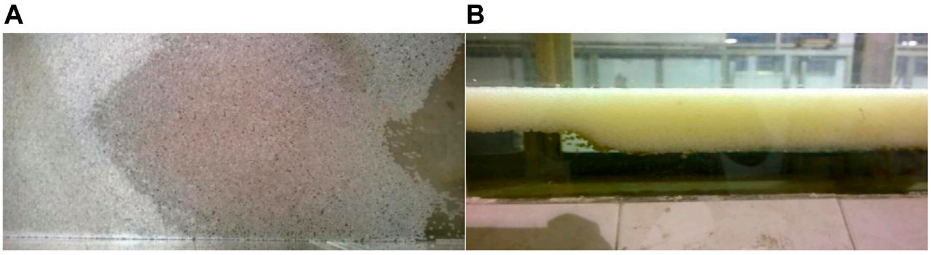

FIGURE 4
Head of the ice jam in the second case [flow direction is from **(B)** to **(A)**].

Details of case 2

Figure 3 shows the details of the phenomenon in case 2, with the third experiment as an example. The water surface elevation was calculated by measured ice thickness and the porosity of ice jam, which is same for the Figure 5. In this case, the accumulation sequence was from upstream to downstream. The initial water depth of section 4 (h_0) was 10 cm, the mean velocity of the section (v_0) was 0.14 m/s, the flow discharge (Q) was 5.6 L/s, and the ice discharge Q_i was 0.01299L/s. The experiment lasted about 7 h.

Figures 3A–D show the ice thickness measured along the channel at 1 h, 2 h, 3 h, and 7 h after adding model ice particles. It can be seen that when the particles were added by the automatic ice feeder to the upstream section 5, no particles were submerged at section 20. This means no ice particles flowed out of the test area. At this point, the accumulation process of the ice jam became the first stage, a sign of the juxtaposition-upward phenomenon (Figures 3A,B). It is noteworthy that the ice jam was not as thick as a single layer of model ice particles but was approximately 2.5 cm (about 7–8 times of a layer). The ice jam advanced upstream under the hydraulic action.

When the front of ice jam reached the upstream section 4, the inlet ice particles were all submerged at the bottom of the ice jam. Hence, the accumulation of the ice jam entered the second stage, i.e., the main stage for the ice jam to thicken (Figure 3C).

As described previously, the head of the ice jam of a certain thickness formed under the bottom front of the ice jam at section 5 (Figure 4). The head would move to the downstream with a hydraulic limit thickness when the flow intensity was sufficient to carry the inlet ice particles downward. The hydraulic limit thickness of the head of the ice jam is referred to as the initial ice jam thickness (Figure 3C). In this case, the initial ice jam thickness was about 4.5 cm.

The head of the ice jam advanced continuously downstream until reaching section 20. Then the ice particles would begin to flow out of the test area. In the beginning, the inlet ice discharge was not equal to the outlet ice discharge, and the ice jam entered the third and final stage of accumulation, i.e., the thickening stage. The overall thickness of the ice jam would grow slightly until the ice discharge at the inlet equaled that of the outlet. Finally, the hydraulic parameters and ice conditions tended to become stable (Figure 3D). Similarly, the ice jam thickness after stabilization is called the ice jam thickness equilibrium. Comparing Figures 3C,D, it can be seen that the initial ice jam thickness was slightly smaller than the ice jam thickness equilibrium.

Details of case 3

Figure 5 shows the details of the phenomenon in case 3, with the fifth experiment as an example. In this case, the accumulation sequence is from downstream to upstream. The initial water depth of section 4 (h_0) was 10cm, the mean velocity of the section (v_0) was 0.16 m/s, the flow discharge (Q) was 6.4L/s, and the ice discharge Q_i was 0.0105L/s. The experiment lasted about 4 h.

Figures 5A–D show the ice thickness measured along the channel at 1 h, 2 h, 3 h, and 4 h after adding model ice particles. The sequence of ice jam accumulation was completely difference from that in Figure 3.

After the addition of ice particles, some particles were submerged at section 20. Thus, some of the inlet ice particles flowed directly out of the test area, while the rest were detained and accumulated, resulting in the thickening of the ice jam. Compared with case 2 in Figure 3, no juxtaposition upward occurred in case 3. The head of the ice jam movement kept pace with the front of the ice jam, and the ice jam accumulated from downstream to upstream, reaching the initial ice jam thickness (Figures 5A–C). When the front of the ice jam reached the upstream section 5, it entered the final thickening stage, where the inlet and outlet ice discharges became equal. The accumulation phenomenon after stabilization is illustrated in Figure 5D, which presents the equilibrium ice jam thickness of each section.

In other words, the difference between the two cases depends on whether the upstream ice jam head (Figure 4) formed during the ice jam evolution. For case 3, no upstream ice jam head formed and there was no secondary thickening process throughout the entire experiment.

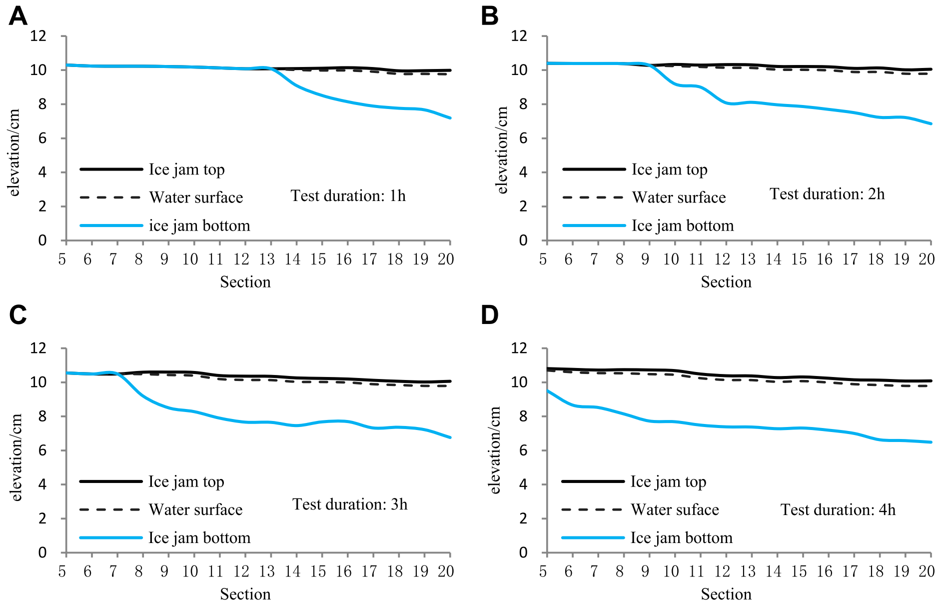

FIGURE 5
Specific phenomena of the third case (fifth experiment).

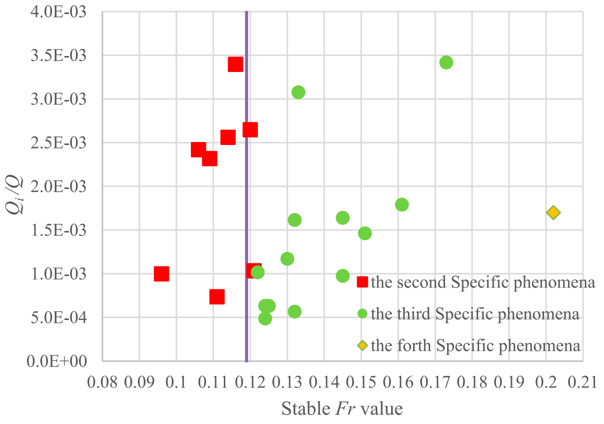

FIGURE 6
Specific phenomena of different stable Fr and ice flow discharge ratios.

Discussion

In terms of the thickening phenomena, the accumulation of the ice jam could be divided into two categories: accumulation from upstream to downstream, and accumulation from downstream to upstream. The fundamental reason for different accumulation phenomena lies in whether the initial hydraulic conditions result in the inlet ice particles being partially submerged at the front of the initial ice cover model (section 20).

According to the experimental data in Table 1, the different ice jam accumulation processes under different hydraulic conditions (stable Fr) and the discharge ratio (ice to flow discharge ratio) are illustrated in Figure 6.

The straight line parallel to the *Y* axis in Figure 6 indicates that the stable Fr was 0.119. Taking this line as a boundary, the left side of the line stands for the second case of ice jam accumulation, and the right side of the line represents the third and fourth cases.

During the experiments, the water level kept rising with the ice jam accumulation. Thus, the Fr in front of the ice jam continued to fall as the water level rise. As shown in Figure 6, when the stable Fr surpassed 0.119, the ice jam accumulation was accompanied by the continuous submersion and transport of inlet ice, and case 3 of ice jam accumulation occurred. When the opposite condition appeared, the ice particles in front of the ice jam did not submerge until the hydraulic condition was sufficient to carry the ice out of the test area, and then case 2 or case 1 occurred.

In other words, if the stable Fr in front of the ice jam was greater than or equal to 0.119, the accumulation would obey case 3 or case 4; by contrast, if the stable Fr dropped to less than 0.119, and if the ice particles did not submerge, the accumulation would follow case 2. If the ice discharge was large, case 1 would be more likely.

TABLE 2 Results of nine tests.

Serial number	Initial flow depth (cm)	Discharge (L/s)	Initial section velocity (m/s)	Ice discharge (L/s)	Stable Fr	Leading edge section number	Type of accumulation
6	10	7.2039	0.18	0.01054	0.151	18	Third case
7	10	10	8	0.0274	0.173	17	Third case
8	10	10	8	0.01360	0.202	20	Fourth case
13	15	10.8071	0.18	0.006132	0.132	15	Third case
15	15	13.1994	0.22	0.02365	0.161	14	Third case
21	20	15.2024	0.19	0.00743	0.124	17	Third case
22	20	16.0276	0.2	0.0259	0.132	15	Third case
27	25	20.4978	0.205	0.01298	0.124	16	Third case
28	25	21.0011	0.21	0.01327	0.125	18	Third case
29	25	22.0009	0.22	0.02579	0.130	19	Third case

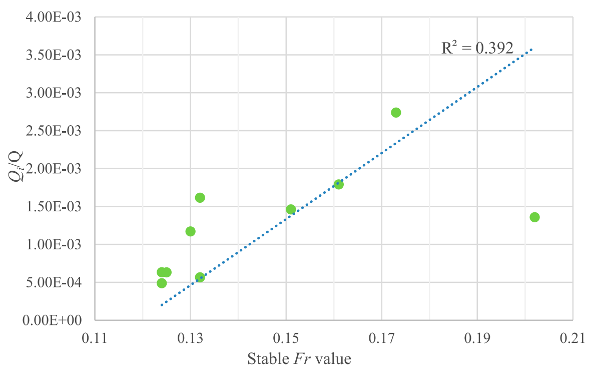

FIGURE 7
Critical conditions for failure to form ice jams.

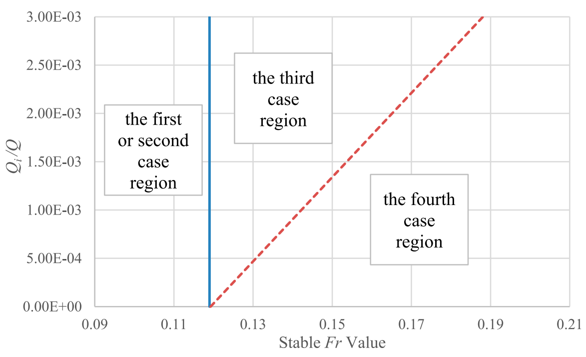

FIGURE 8
Partition result diagram of ice jam accumulation with different features.

Along with the experiment data, the results suggest that the relationship between the stable Fr and 0.119 provides an important reference for judging the specific phenomena of ice jam accumulations.

In case 4, most or all of the ice particles submerged in front of the initial ice jam (section 20), and the final ice jam was very short, or no ice jam ultimately formed. In this case, the channel failed to form any ice jam. By contrast, ice jams formed in cases 1–3.

Among the 29 tests in Table 1, only test 8th fully conformed to the accumulation phenomenon in case 4. Table 2 reports the nine tests, in which inlet ice particles mostly submerged at the initial ice cover (section 20), and where the final lengths of the ice jams were very short (i.e., the test phenomena were close to case 4). These were tests No. 6, 7, 13, 15, 21, 22, 27, 28, and 29. The initial conditions of these tests and the Fr numbers in front of the head of the ice jam are summarized in Table 2.

Based on the data in Table 2, the ratio of ice discharge Q_i to flow discharge Q (hereinafter referred to as discharge ratio Q_i/Q) was taken as the abscissa, and the stable Fr in front of the ice jams as the ordinate, to create the critical conditions for failure to form ice jams (Figure 7). It can be learned from the trend line in Figure 7 that the stable F was basically positively proportional to the discharge ratio Q_i/Q.

In fact, Figure 7 reports the limiting critical conditions for the formation of ice jams. The ice jams could not form with the growing Fr value under a certain ice flow discharge ratio. Therefore, the trend line in Figure 7 (hereinafter referred to as the critical discriminant line for the formation of an ice jam) helps in judging whether the ice jams could form in the channel. If Fr and Q_i/Q were on the right side of that line, the ice jam could not form in the channel. If the two values appeared on the left side of that line, the ice jam would eventually form.

Through regression analysis, the critical discriminant line in Figure 7 can be described by the following linear equation:

$$\frac{Q_i}{Q} = 0.0436Fr - 0.0052. \tag{1}$$

Suppose the discharge ratio Q_i/Q is equal to 0. The following can be derived from Eq. 1:

$$Fr \approx 0.119. \tag{2}$$

Based on the data in Table 1, 2, the stable Fr was taken as the abscissa, Q_i/Q was taken as the ordinate, and Fr=0.119 (when $Q_i/Q=0$) was taken as the center point to draw the longitudinal boundary line of Figure 6 and the critical discriminant line of Figure 7. The two lines divide the first quadrant of the Cartesian coordinate system into three parts. Figure 8 summarizes the ice jam accumulation features in each quadrant.

Combining the experimental study results and the hydraulic features of ice jam accumulation, the following can be inferred: if the hydraulic parameter falls after stabilization in the regions of cases 1 and 2 (the rectangular area in Figure 8), the experimental data suggest that the inlet ice does not submerge at section 20 but is juxtaposed upward until submergence at the head of the ice jam under a certain hydraulic condition, or that it continues to be juxtaposed with the rising water level. If the parameter falls in the region of case 3 (i.e., the inverted right triangular area in Figure 8), the experimental data show that the inlet ice partially submerges at section 20. After that, partial submergence occurs as the ice cover moves upward. This process continues until all of the inlet ice particles submerge under a certain hydraulic condition. If the parameter falls in the region of case 4 (the right triangular area in Figure 8), the experimental data indicate that all inlet ice particles submerge at section 20.

Conclusion

The formation of an ice jam is affected by various factors drawn from different disciplines, e.g., thermodynamics, solid mechanics, hydrology, hydraulics, and river dynamics. Different types of ice jams can form under different conditions, even if only mechanical action is taken into account (without considering thermodynamics). Previous studies have mainly focused on the mechanical characteristics of stable ice jams, while this study focuses on changes to the hydraulic characteristics during the evolution of ice jam under different ice discharge. Experiments and analyses were carried out to study how hydraulic conditions and ice discharge affect the accumulation of ice jams. Through 29 tests, four different accumulation patterns of ice jams were detected and are discussed in detail.

Based on the third and fifth experiments, cases 2 and 3 in the experiments were analyzed in detail. It was discovered that, if Fr was greater than 0.119, the inlet ice particles may submerge at the head of the ice jam. Hence, the longitudinal boundary line through Fr = 0.119 was suggested as a way to distinguish the two cases. Further analysis was carried out to analyze those tests where it was difficult to form an ice jam. The results show that the critical discriminant line helps to distinguish between cases 3 and 4. Combined with the longitudinal boundary line, a partition result diagram was developed for ice jam accumulations with different features and used to differentiate between the four kinds of accumulations.

Due to an insufficient number of experimental studies, the conclusions may be a little simple in this paper, and more model tests or prototype observation results are needed to enrich the conclusions. In addition, the value of stable Fr is not the initial condition of the test. Thus the relationship between the initial Fr and the stable Fr value needs to be studied to obtain the ice jam mechanical equilibrium equation under different hydraulic and ice discharge conditions.

Data availability statement

The original contributions presented in the study are included in the article/Supplementary Material; further inquiries can be directed to the corresponding author.

Author contributions

PC: measured data analysis and manuscript writing; TC: experimental test development and measured data collation; JW: research guidance and revision suggestions; GC: test program development and research plan.

Funding

This research was supported by the National Natural Science Foundation of China (NSFC) under grant nos. 51879065 and 51379054.

Conflict of interest

The authors declare that the research was conducted in the absence of any commercial or financial relationships that could be construed as a potential conflict of interest.

Publisher's note

References

Ambtman, K. E. D., Steffler, P. M., and Hicks, F. E. (2011). Analysis of the stability of floating ice blocks. *J. Hydraul. Eng.* 137 (4), 412–422. doi:10.1061/(ASCE)HY.1943-7900.0000316

Amroune, A., Mihoub, R., Enrico, G., and Carlos, U. (2020). Groundwater flow dynamics and distribution of hydrochemical facies using GIS in Hodna Plain, M'Sila, Southeastern Algeria. *Int. J. Sustain. Dev. Plan.* 15 (6), 789–800. doi:10.18280/ijsdp.150601

Becket, M. A., Dow, K. E., and Clark, S. P. (2021). Development of an ice jam database and prediction tool for the Lower Red River. *Can. Water Resour. J./Revue Can. des ressources hydriques* 46 (1-2), 73–86. doi:10.1080/07011784.2021.1898479

Beltaos, S., and Burrell, B. C. (2015). Hydrotechnical advances in Canadian river ice science and engineering during the past 35 years. *Can. J. Civ. Eng.* 42 (9), 583–591. doi:10.1139/cjce-2014-0540

Beltaos, S., and Carter, T. (2009). Field studies of ice breakup and jamming in lower Peace River, Canada. *Cold Regions Sci. Technol.* 56 (2-3), 102–114. doi:10.1016/j.coldregions.2008.11.002

Beltaos, S. (2019). Numerical prediction of ice-jam profiles in lower Athabasca River. *Can. J. Civ. Eng.* 46 (8), 722–731. doi:10.1139/cjce-2018-0542

Beltaos, S. (2008). Progress in the study and management of river ice jams. *Cold regions Sci. Technol.* 51 (1), 2–19. doi:10.1016/j.coldregions.2007.09.001

Cheng, T. J., Wang, J., Chen, P. P., and Sui, J. (2022). Simulation of ice accumulation around bridge piers during river breakup periods using a discrete element model. *J. Hydrodyn.* 34 (1), 94–105. doi:10.1007/s42241-022-0010-y

Daly, S. F., and Axelson, K. D. (1990). Stability of floating and submerged blocks. *J. Hydraulic Res.* 28 (6), 737–752. doi:10.1080/00221689009499023

Deng, Y., Li, Z., Wang, J., and Xu, L. (2019). The microstructure of yellow river ice in the freezing period. *Crystals* 9 (9), 484. doi:10.3390/cryst9090484

Frolova, N. L., Agafonova, S. A., Krylenko, I. N., and Zavadsky, A. S. (2015). An assessment of danger during spring floods and ice jams in the north of European Russia. *Proc. IAHS.* 369, 37–41. doi:10.5194/piahs-369-37-2015

Hayakawa, T., Yamamoto, Y., and Kawai, K. (2001). Ice floe impact interaction with pile structures on vertical breakwaters. Proceedings of the . Int. Conf. Port Ocean Eng. Under Arct. Cond. Ottawa, Canada.

Healy, D., and Hicks, F. E. 2006. Experimental study of ice jam formation dynamics. *J. Cold Reg. Eng.* 20 (4), 117–139. doi:10.1061/(asce)0887-381x(2006)20:4(117)

Hicks, F. E., and Healy, D. (2003). Determining winter discharge based on hydraulic modeling. *Can. J. Civ. Eng.* 30 (1), 101–112. doi:10.1139/l02-031

Lindenschmidt, K. E., Das, A., Rokaya, P., and Chu, T. (2016). Ice-jam flood risk assessment and mapping. *Hydrol. Process.* 30 (21), 3754–3769. doi:10.1002/hyp.10853

Lindenschmidt, K. E., and Rokaya, P. (2019). A stochastic hydraulic modelling approach to determining the probable maximum staging of ice-jam floods. *J. Environ. Inf.* 34 (1). doi:10.3808/jei.201900416

Namaee, M. R., and Sui, J. (2019). Effects of ice cover on the incipient motion of bed material and shear stress around side-by-side bridge piers. *Cold Regions Sci. Technol.* 165, 102811. doi:10.1016/j.coldregions.2019.102811

Peters, M., Dow, K., Clark, S. P., Malenchak, J., and Danielson, D. (2017). Experimental investigation of the flow characteristics beneath partial ice covers. *Cold Regions Sci. Technol.* 142, 69–78. doi:10.1016/j.coldregions.2017.07.007

Rokaya, P., Peters, D. L., Elshamy, M., Budhathoki, S., and Lindenschmidt, K. E. (2020). Impacts of future climate on the hydrology of a northern headwaters basin and its implications for a downstream deltaic ecosystem. *Hydrol. Process.* 34 (7), 1630–1646. doi:10.1002/hyp.13687

Shen, H. T., and Wang, D. S. (1995). Under cover transport and accumulation of frazil granules. *J. Hydraul. Eng.* 121 (2), 184–195. doi:10.1061/(asce)0733-9429(1995)121:2(184)

Sui, J., Karney, B. W., Sun, Z., and Wang, D. (2002). Field investigation of frazil jam evolution: A case study. *J. Hydraul. Eng.* 128 (8), 781–787. doi:10.1061/(asce)0733-9429(2002)128:8(781)

Sui, J., Wang, J., Balachandar, R., Sun, Z., and Wang, D. (2008). Accumulation of frazil ice along a river bend. *Can. J. Civ. Eng.* 35 (2), 158–169. doi:10.1139/L07-093

Wang, J., Chen, P. P., and Sui, J. Y. (2011). Progress in studies in ICE accumulation in river bends. *J. Hydrodyn.* 23 (6), 737–744. doi:10.1016/S1001-6058(10)60171-0

Wang, J., Hua, J., Chen, P. P., Sui, J., Wu, P., and Whitcombe, T. (2019). Initiation of ice jam in front of bridge piers—an experimental study. *J. Hydrodyn.* 31 (1), 117–123. doi:10.1007/s42241-019-0017-1

Wang, J., Sui, J., and Chen, P. (2009). Numerical simulations of ice accumulation under ice cover along a river bend. *Int. J. Environ. Sci. Technol. (Tehran).* 6 (1), 1–12. doi:10.1007/BF03326055

Wang, J., Sui, J. Y., Zhang, H. Y., Chen, P. P., and Hirshfield, F. (2012). Mechanisms of ice accumulation in a river bend–an experimental study. *Int. J. Sediment Res.* 27 (4), 521–537. doi:10.1016/S1001-6279(13)60010-4

White, K. D. (2003). Review of prediction methods for breakup ice jams. *Can. J. Civ. Eng.* 30 (1), 89–100. doi:10.1139/l02-047

Wolfe, B. B., Hall, R. I., Wiklund, J. A., and Kay, M. L. (2020). Past variation in Lower Peace River ice-jam flood frequency. *Environ. Rev.* 28 (3), 209–217. doi:10.1139/er-2019-0047

Wu, P., Hirshfield, F., Sui, J., Wang, J., and Chen, P. P. (2014). Impacts of ice cover on local scour around semi-circular bridge abutment. *J. Hydrodyn.* 26 (1), 10–18. doi:10.1016/S1001-6058(14)60002-0

Yang, X., Pavelsky, T. M., and Allen, G. H. (2020). The past and future of global river ice. *Nature* 577 (7788), 69–73. doi:10.1038/s41586-019-1848-1

frontiers | Frontiers in Earth Science

TYPE Original Research
PUBLISHED 12 January 2023
DOI 10.3389/feart.2022.1059832

Studies of natural gas production prediction and risk assessment for tight gas in Sichuan Basin

Haitao Li[1], Guo Yu[2], Yizhu Fang[1], Yu Chen[3] and Dongming Zhang[3]*

[1]Exploration and Development Research Institute of PetroChina Southwest Oil and Gas Field Company, Chengdu, China, [2]PetroChina Southwest Oil and Gas Field Company Planning Department, Chengdu, Sichuan, China, [3]College of Resources and Security, Chongqing University, Chongqing, China

OPEN ACCESS

EDITED BY
Guangyao Si,
University of New South Wales, Australia

REVIEWED BY
Yingke Liu,
China University of Mining and Technology, China
Jiadong Qiu,
University of South China, China
Mingzhong Gao,
Sichuan University, China

*CORRESPONDENCE
Dongming Zhang,
zhangdm@cqu.edu.cn

SPECIALTY SECTION
This article was submitted to Economic Geology,
a section of the journal
Frontiers in Earth Science

RECEIVED 02 October 2022
ACCEPTED 31 October 2022
PUBLISHED 12 January 2023

CITATION
Li H, Yu G, Fang Y, Chen Y and Zhang D (2023), Studies of natural gas production prediction and risk assessment for tight gas in Sichuan Basin.
Front. Earth Sci. 10:1059832.
doi: 10.3389/feart.2022.1059832

After a new round of tight gas geological evaluation was launched in 2018, a new chapter of tight gas exploration and development has been opened in the Sichuan Basin. In order to make better planning work, it is very important to study the variation rule and risk assessment of tight gas production. In this paper, the peak production is predicted by Ward model. Based on the prediction results, Hubbert and Gauss models were established to study the variation law of tight gas production, and the accuracy and prediction results of the models were determined by the degree of fitting and correlation coefficient. By studying the relationship between *URR* and production, it is concluded that the production increases in a step, and the future production of tight gas is simulated from the perspective of realization probability. Finally, the risk assessment matrix is established to study the difficulty degree of achieving the production target. The results are as follows: 1) Hubbert model has higher accuracy in predicting tight gas production change. The peak year of tight gas is 2042, the peak production is $(86 - 106) \times 10^8 m^3/a$, and the final *URR* recovery degree is about 60%. 2) The realization probability of production is calculated, and the possibility of reaching the target value is evaluated from the perspective of risk, so as to guide the production of tight gas, and finally promote the formulation of tight gas development planning in the Sichuan Basin.

KEYWORDS

tight gas, natural gas production prediction, risk quantification, life cycle model, production realization probability, risk level evaluation matrix

1 Introduction

The breakthroughs made by the natural gas industry have improved the energy structure and promoted the development of a low-carbon economy. Current international development trend is basically green energy, advocating energy saving and carbon reduction, the oil and gas field has turned to natural gas as the focus. Therefore, the efficient development of natural gas is extremely important (Chengzao et al., 2014; Jia, 2018). In natural gas development planning, it is necessary to carry out peak production prediction and risk quantitative analysis. Through peak production prediction and risk quantitative analysis, a judgment mechanism that is coordinated with accuracy and rationality is formed, so as to achieve the purpose of optimizing development benefits. Only by establishing a prediction method that accurately describes the law of production growth and reasonably predicting the change trend of natural gas production can the basin exploration planning work be better formulated, and risk quantification research can be carried out based on the production prediction results (WANG et al., 2016; TONG et al., 2018).

In recent years, the exploration potential of tight gas has been explored and gradually been paid attention to, becoming a new force of natural gas in our country, with large-scale production in Sichuan, Ordos, Songliao and other basins, and has become a key area for increasing oil and gas reserves and production in China. In order to continue to promote the exploration and development of tight gas in the Sichuan Basin, a new round of evaluation of tight gas geological conditions was launched in 2018. The Jinhua-Qilin area in central Sichuan was selected as a pilot area for the integration of tight gas exploration and development, and technical research and management model innovation were carried out. Especially in 2020, the tight gas resource potential of the Sichuan Basin was re-evaluated, and the central Sichuan area was selected as the core production area for tight gas. New drilling and testing of natural gas production have repeatedly hit new highs, opening a new chapter for tight gas exploration and development in the Sichuan Basin (Wu. et al., 2021; Huang. et al., 2022). The development of tight gas in the Sichuan Basin is still in the early stage of exploration, and the proved rate is even less than 20%. There is a huge amount of tight gas exploration, and it is also the focus of development in the Sichuan Basin in the future, which plays a crucial role in the development of natural gas production and economy (DAI et al., 2021; Lin et al., 2021).

However, tight gas reservoirs have the characteristics of strong heterogeneity, small pore size, low permeability, and strong stress sensitivity, which require fracturing development. The particularity of reservoirs, fluid seepage characteristics and the multiple complexity of fracturing stimulation measures make it difficult to predict the productivity of tight gas, it is difficult to obtain the variation law of tight gas production and the actual production value that can be achieved (Zheng et al., 2021). Therefore, it is necessary to predict the growth trend of tight gas production in this area, analyze the realization probability of its peak production, and guide the planning of tight gas based on production prediction and risk assessment.

At present, there are many researches on natural gas production prediction models, such as peak prediction method, grey system method, neural network method, etc (Mohr and Evans, 2011; Zeng. et al., 2020). Comparing these methods, it can be seen that the peak prediction method is more suitable for the study of production variation law (Zheng et al., 2020). For natural gas fields that are still in the early stage of development or production, the peak prediction method is more accurate and more practical for medium and long-term prediction (Ravnik et al., 2021; Wang. et al., 2022). Lao. and Sun. (2022) combined with the dispersion coefficient, established the Bernoulli model with nonlinear distribution, which is also the representative model of grey prediction. The model can accurately analyze those predictions to a certain extent. Finally, the model is used to prediction natural gas consumption and production in China, and corresponding suggestions are given based on the prediction results. The Hubbert model established by Sun et al. (2021) can better predict the change of production, and this model has multiple life cycles, and *URR* is introduced to participate in the prediction of production. Then, through grey relational analysis, the best consumption curve corresponding to different *URR* scenarios is selected. Empirical results show that natural gas production of China cannot meet the growing consumption. Therefore, policy measures must be taken to alleviate this situation. Accurate prediction of natural gas production and consumption can inform decision-making and help governments formulate new major policies. Wang et al. (2018) introduced the ultimate recoverable reserves as a boundary condition into the multi-cycle Gauss model to predict the trend of natural gas production (Guo et al., 2021). JamesWard. et al. (2012) used a newly developed model to prediction growth in fossil fuel production. The prediction of the Ward model only needs to combine the production data in recent years and the historical cumulative production. This prediction method is worthy of reference.

At present, there are many research methods for risk quantification of natural gas reserves and production, including probability method, neural network method, fuzzy clustering method, etc (Ward et al., 2018; Yiping et al., 2021). Compared with these methods, it can be seen that the probability method is more suitable for risk assessment, especially for the calculation of the risk level of tight gas in the Sichuan Basin. Probabilistic method can be used to determine the degree of difficulty to achieve the target production, so as to guide the planning of exploration and development. Based on the generalized Weng's model commonly used in the life cycle model method, Chong et al. (2021) established an improved multi-cycle generalized Weng's model to determine the number of cycles in oil and gas field production prediction, so as to improve the prediction effect of the model. The improved model is applied to the production prediction of Daqing Oilfield, and it is fitting effect on annual production is obviously better than that of the single-cycle model and the multi-cycle model. Shih-Chi et al. (2005) combined a Bayesian approach with a Monte Carlo approach to quantify and update uncertainty in life cycle assessment results. Flouri et al. (2015) investigated how gas supply disruptions in Algeria, the EU's third-largest supplier, affect gas security in Europe. Using Monte Carlo simulations, results were analyzed for the most affected countries, emphasizing the importance of supply diversification, reserves and production to enhance gas security.

In order to develop a better tight gas planning scheme, production targets should be studied from multiple perspectives. Among them, it is very important to predict the change rule and peak range of production, calculate the realization probability of target production, and evaluate the risk of production. This paper is based on the actual situation of tight gas core production areas in central Sichuan. First, the Ward model was used to predict the peak production and peak year, and then the ultimate recoverable reserves *URR* was introduced into the Hubbert and Gauss prediction model as a boundary condition. The accuracy of the two prediction models was compared and analyzed, and the production prediction results of tight gas in the Sichuan Basin were obtained. Then, according to the principle of Monte Carlo method, the realization probability of production in different stages is calculated and analyzed, and compared with the change rule of peak production and model parameters with *URR*, and the risk assessment of target production in different stages is carried out combined with the degree of dispersion. Through the self-built production grade evaluation matrix, a systematic quantitative research on the production risk of natural gas is carried out. The Figure 1 shows the flow chart of the research work.

2 Tight gas production prediction and risk quantification theory

2.1 Tight gas production prediction theory

2.1.1 Ward predictive model

Tight gas is currently in the initial stage of development, especially in the core production area of tight gas in Sichuan, where production data is scarce and cannot be fitted with conventional prediction models. Therefore, this paper adopts Ward's research idea (JamesWard. et al., 2012), takes *URR* as the qualification, and predicts the future production results according to the specified initial growth rate. The production value of a certain year is used as the initial production for the start of the growth curve, that is, at the beginning of the prediction, an initial production value is specified, and then the trend of production change is studied and the peak production is estimated. The Ward model equations are as follows.

$$Q = Q_0 e^{kt}\left(1 - \frac{Q(t)}{URR}\right). \tag{1}$$

In the formula, Q is the annual production, the unit is $10^8 m^3/a$; Q_0 is the initial production; k is the growth rate; t is the time; $Q(t)$ is the annual cumulative production;URR is the ultimate recoverable reserves.

The Ward predictive model is an asymmetric growth curve of production from a given point, which is a left-biased curve. Compared with the symmetrical curve and the right-biased curve, the left-biased curve allows the production to maintain a longer production growth period and a higher peak production. Therefore, tight gas can be developed as quickly as possible, and the driving effect of tight gas on total natural gas production can be maximized.

2.1.2 Hubbert predictive model

Hubbert model is very suitable for the study of tight gas production trend. After the production of a gas field starts, the production will increase continuously with the increase of time. After experiencing the rapid growth stage and slow growth stage, the production begins to stabilize and reach a stable period, and then the production begins to decline. And the area between the production curve and the time axis is equal to the ultimate recoverable reserves *URR* (Tilton, 2018). The Hubbert model equations are as follows (Guo et al., 2021).

$$P = \frac{URR}{1 + e^{-b(t-t_m)}}. \tag{2}$$

In the formula, P represents the cumulative production, the unit is $10^8 m^3/a$; URR is the ultimate recoverable reserve, the unit is $10^8 m^3$; t is the production mining time; t_m is the production peak time; b is the model parameter.

Equation 2 can be derived from t to get the formula for calculating annual production:

$$Q = \frac{dP}{dt} = \frac{b \times URR \times e^{-b(t-t_m)}}{\left[1 + e^{-b(t-t_m)}\right]^2}. \tag{3}$$

In the formula, Q represents the annual production, the unit is $10^8 m^3/a$.

When $t = t_m$, the production growth peaks. At this time, the rate of change of the cumulative production P is the largest, that is, the dP/dt is the largest. At this time:

$$Q_m = b \times \frac{URR}{4}. \tag{4}$$

In the formula, Q_m is the peak annual production, the unit is $10^8 m^3/a$.

Transform Eq. 4 into $URR = 4Q_m/b$, and substitute it into Eq. 3. The annual production calculation formula of the Hubbert model can be obtained (Wang et al., 2016).

$$Q = \frac{2Q_m}{1 + cosh[b(t - t_m)]} \tag{5}$$

The curve trend predicted by using the Hubbert model is a gradual increase, and changes from a rapid increase to a slow increase, forming a stable phase around the peak production, and then gradually decreasing.

2.1.3 Gauss predictive model

Gauss model is also suitable for tight gas production prediction. The change trend curve is usually slighter and taller when Gauss model is used for prediction, but the overall change trend is consistent with Hubbert model from a macro perspective, and both of them are symmetrical with the peak yield as the axis of symmetry. Therefore, two models should be used in the study and the more accurate model should be selected (Hu et al., 2020; Luz-Sant'Ana. Patricia Roman-Roman. et al., 2017). The Gauss model equations are as follows.

$$f(t) = \frac{1}{s\sqrt{2\pi}} e^{-(t-\mu)^2/2s^2} \tag{6}$$

In the formula, μ is the mean; s is the standard deviation.

In the process of tight gas mining, the cumulative production of mining time in the interval $(0-\infty)$ is regarded as the ultimate recoverable reserves (URR). Multiply the distribution density function $f(t)$ by the ultimate recoverable reserves to obtain the formula for calculating the annual production Q (Zhang and Zhao, 2021).

$$Q = \frac{URR}{s\sqrt{2\pi}} e^{-(t-\mu)^2/2s^2} \tag{7}$$

Eq. 7 is derived with respect to the mining time.

$$\frac{dQ}{dt} = \frac{URR}{s\sqrt{2\pi}} e^{-(t-\mu)^2/2s^2} \left(-\frac{t-\mu}{s^2}\right) \tag{8}$$

When the production change reaches its highest value, annual rate of change in production is $dQ/dt = 0$. At this time, the peak time of annual production.

$$t_m = \mu \tag{9}$$

Substitute $t_m = \mu$ into Eq. 7 to obtain the peak annual production Q_m.

$$Q_m = \frac{URR}{s\sqrt{2\pi}}. \tag{10}$$

Substituting Eqs 9, 10 into Eq. 7, the annual production calculation formula of the Gauss model can be obtained.

$$Q = Q_m e^{-(t-t_m)^2/2s^2}. \tag{11}$$

In the formula, the model parameter s can characterize the fluctuation of the peak to a certain extent.

2.2 Production risk quantification theory

2.2.1 Monte Carlo probability method

Monte Carlo probability method is based on probability theory and mathematical statistics theory. The basic idea of this method is to establish a probability calculation model, and then obtain the statistical characteristics of the probability through sampling experiments, so as to obtain the approximate result of the realization probability. Monte Carlo method can describe the characteristics of things with random nature more realistically, and it is less limited in calculation. Therefore, this method is suitable for the probability estimation of production and plays an important role in the risk assessment of production in this paper.

When estimating the production probability according to the principle of Monte Carlo method, the problem to be solved should be transformed into the expected value of a probability model, and then the model should be randomly sampled. Finally, a simulation experiment is carried out on the computer, enough random numbers are drawn and statistical analysis is carried out on the problem to be solved (Krupenev. et al., 2020).

Assuming that the distribution density of the known random variable $f(x)$ is $\psi(x)$, the mathematical expectation of the variable $f(x)$ is:

$$E = \int_{x_0}^{x_1} f(x)\psi(x)\mathrm{d}x. \tag{12}$$

According to the distribution density function $\psi(x)$, N sample points x_i are randomly selected, and the arithmetic mean value of the function value $f(x_i)$ corresponding to the sample points is used as the integral estimation value.

$$\overline{E_N} = \frac{1}{N}\sum_{i=1}^{N} f(x_i). \tag{13}$$

According to the probability distribution density function of the variable, the variable values are randomly selected in turn, and the probability density distribution of the objective function can be obtained after a large number of repeated independent simulations of the variable values. Monte Carlo simulation can realize the calculation process of random sampling of variables (Gabriel et al., 2021).

The premise of applying Monte Carlo simulation is to determine the mathematical model of the objective function and the probability distribution of the variables in the model. Each parameter generates a large number of random sample points according to the given probability distribution, which is substituted into the model to calculate the probability density distribution curve of the objective function. The specific steps are shown in Figure 2.

2.2.2 Risk level evaluation matrix

Assessing the risk level of production requires two indicators, the realization probability P and the degree of dispersion of production C. The dispersion degree of production represents the degree of difference between a certain production and other production values, that is, the corresponding production value will also change due to the change of risk. The degree of dispersion also indicates the

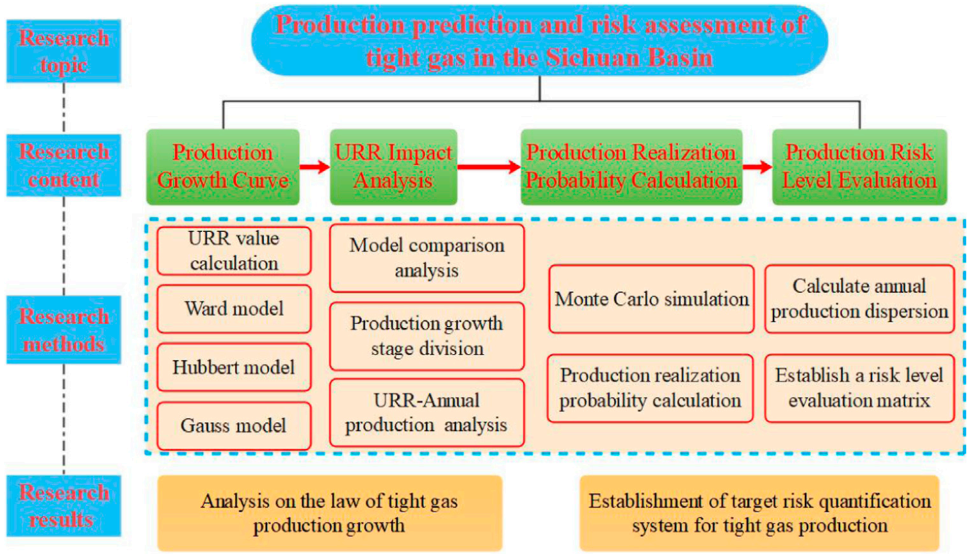

FIGURE 1
Flow chart of tight gas production prediction and risk assessment.

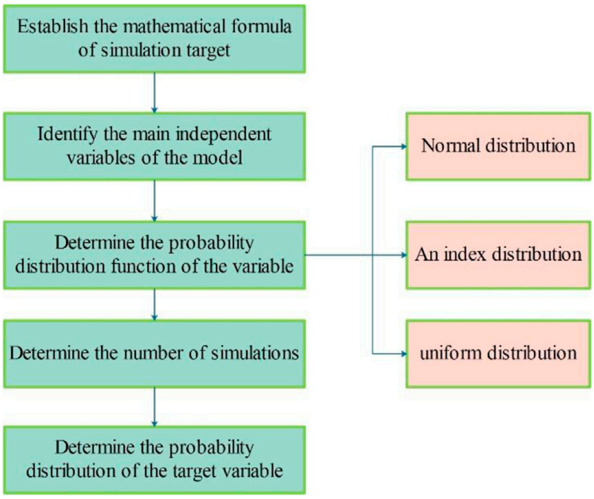

FIGURE 2
Specific steps of Monte Carlo simulation method.

degree of stability of production, that is, the smaller the degree of dispersion of production, the higher its stability (Gutierrez et al., 2016).

The formula for calculating the degree of dispersion is as follows.

$$C = 1 - \frac{\mu}{s}. \tag{14}$$

In the formula, μ is the mean and s is the standard deviation.

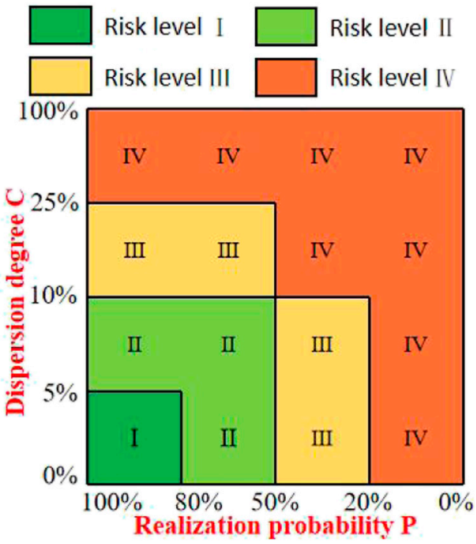

FIGURE 3
Quantitative matrix of production risk level.

Taking into account the two evaluation indicators of production realization probability P and dispersion degree C, a risk assessment matrix is established. The production risk is divided into four levels (Figure 3), and the production risk can be comprehensively quantified according to the tight gas production prediction results.

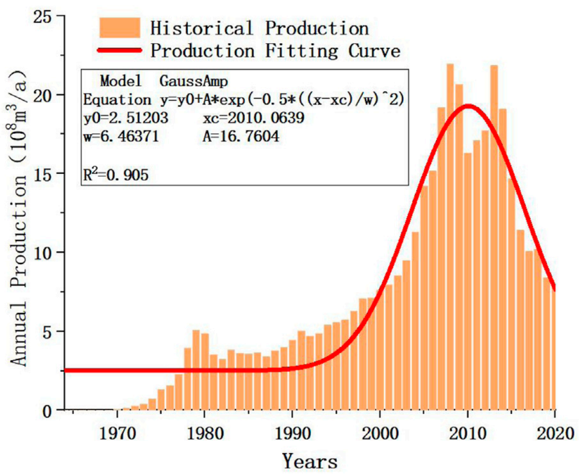

FIGURE 4
Fitting curve of tight gas historical production.

The division of the production risk level is mainly determined by the dispersion degree and the realization probability, which is determined by the specific situation of tight gas production. The probability of 80%, 50% and 20% is the most meaningful for the planning. Therefore, these three probabilities are selected as the standard, and the dispersion degree is also divided according to the actual calculation results. The relationship between the grade division principle of risk assessment of production and its corresponding risk matrix is as follows (Guo et al., 2022):

Risk Level I (dark green area in Figure 3): Production targets are very easy to achieve. Division principle: the probability of production realization is $P > 80\%$, and the degree of dispersion $C \leq 5\%$.

Risk Level II (light green area in Figure 3): Production targets are easy to achieve. Division principle: the probability of production realization is $50\% \leq P \leq 80\%$, and the degree of dispersion is $C \leq 10\%$; or the probability of production realization is $P > 80\%$, and the degree of dispersion is $5\% < C \leq 10\%$.

Risk Level III (yellow area in Figure 3): Production targets are relatively easy to achieve. Division principle: the probability of production realization is $20\% \leq P < 50\%$, and the degree of dispersion is $C \leq 10\%$; or the probability of production realization is $P > 50\%$, and the degree of dispersion is $10\% < C \leq 25\%$.

Risk Level IV (orange area in Figure 3): Production targets are not easy to achieve. Division principle: the probability of production realization is $P < 20\%$; or the probability of production realization is $20\% \leq P < 50\%$, and the degree of dispersion is $C > 10\%$; or the degree of dispersion is $C > 25\%$.

TABLE 1 Corresponding *URR* values under different proven rates.

Tight gas proven rate	**10%**	**12.5%**	**15%**	**17.5%**	**20%**
URR ($10^8 m^3$)	1,380	1725	2070	2,415	2,760

3 Tight gas production prediction

3.1 Estimation of *URR* and peak production

The production curve of tight gas started in 1964 (Figure 4). The fitting curve of tight gas production maintains a trend of increasing first and then decreasing, and the increasing and decreasing periods are almost symmetrical about the peak value. This is consistent with the prediction curves of the Hubbert and Gauss models, and therefore, the study of tight gas production trend can refer to these two models.

As can be seen from the curve, one cycle of mining work has been completed from 1964 to 2020. However, in 2020, the potential of tight gas resources in the Sichuan Basin was re-evaluated, and the central Sichuan area was selected as the core production area for further exploration. At this time, only the production in 2021 and the historical production of the previous cycle are used as a reference. Therefore, the Ward model is used to predict the production peak and peak year of tight gas, and then the models are established to predict the change trend of tight gas production.

Before carrying out tight gas production predestining work, it is necessary to first estimate the numerical range of the ultimate recoverable reserves *URR*. Through geological exploration, it is found that the current resource of tight gas in the Sichuan Basin is $6.9 \times 10^{12} m^3$. By analyzing the exploration and development laws of many gas reservoirs in the Sichuan Basin, the range of the proven rate and recovery rate of tight gas is selected. According to the current tight gas exploration and mining technical conditions in the Sichuan Basin, the proven rate of tight gas is in the range of 10%–20%, That is, the range of cumulative proven reserves at the end of the life cycle is $(0.69 - 1.38) \times 10^{12} m^3$. At present, the recovery factor of tight gas in the Sichuan Basin is about 20%, so the estimated *URR* range is $(1380 - 2760) \times 10^8 m^3$. After determining the range of *URR*, using it as the boundary condition, according to the principle of Ward model, the variation trend of tight gas production is predicted.

Select the proven rates of 10%, 12.5%, 15%, 17.5%, and 20%, respectively, and calculate the *URR* values corresponding to each proven rate (Table 1). The growth trend of tight gas production under these five scenarios with different proven rates is studied.

Substitute different *URR* values into Eq. 1 respectively, initial production and historical cumulative production data are known. The growth rate remains at 10% initially, and then gradually decreases (Höök et al., 2012), without considering

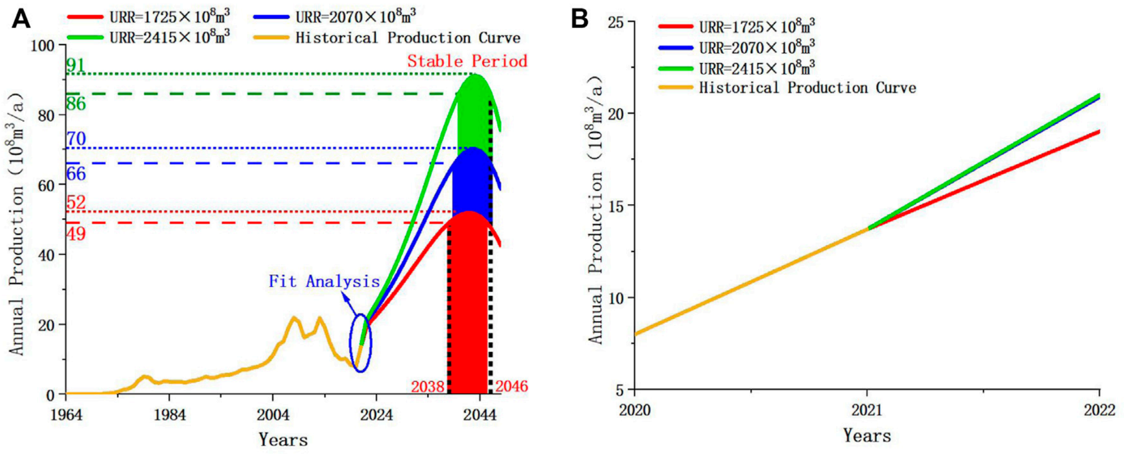

Production prediction curve

Fit analysis plot

FIGURE 5
Prediction results of tight gas production based on Ward model.

the extreme cases of the proven rate, when $URR = (1725 - 2415) \times 10^8 m^3$, the production prediction curve and fitting analysis curve are shown in Figure 5.

In Figure 5A, the stable production period is roughly between 2038 and 2046 (between the black dotted lines), with peak production occurring in 2042 or 2043. In Figure 5B, for the prediction results under different *URR*, the best fit with historical production is $URR = (2070 - 2415) \times 10^8 m^3$, the higher the degree of fit, the higher the accuracy of the prediction. The final peak production result should choose the prediction value with a high degree of fit. Therefore, the predicted peak production is $(70 - 91) \times 10^8 m^3/\text{a}$, the predicted results can be used as reference values for the predictions of the Hubbert and Gauss models. Next, based on the above work, the production trend of tight gas is predicted under five different *URR*s, and different stages are analyzed.

3.2 Prediction and fitting analysis of tight gas production

Using the Hubbert and Gauss model, the peak production of tight gas is predicted and its variation trend is studied. The five *URR*s were respectively substituted into Eqs 5, 11 to establish the tight gas production-time relationship of Hubbert and Gauss model (Eqs 15, 16) and tight gas production prediction results based on the Hubbert and Gauss models (Figures 6A, 7A). Among them, Eq. 15 is the production-time relation of Hubbert model, and Eq. 16 is the production-time relation of Gauss model. The model parameters covered by these formulas are: annual peak production Q_m, peak production time t_m, peak slope *b* and standard deviation *s*. Eq. 15 corresponds to Figures 6A, and Eq. 16 corresponds to Figures 7A.

$$Q = \begin{cases} \dfrac{2 \times 33.02}{1 + cosh\left[0.0957\,(t - 2042)\right]}, & URR = 1380 \times 10^8 m^3 \\ \dfrac{2 \times 49.29}{1 + cosh\left[0.1143\,(t - 2042)\right]}, & URR = 1725 \times 10^8 m^3 \\ \dfrac{2 \times 68.00}{1 + cosh\left[0.1314\,(t - 2042)\right]}, & URR = 2070 \times 10^8 m^3 \\ \dfrac{2 \times 86.03}{1 + cosh\left[0.1425\,(t - 2042)\right]}, & URR = 2415 \times 10^8 m^3 \\ \dfrac{2 \times 105.98}{1 + cosh\left[0.1536\,(t - 2042)\right]}, & URR = 2760 \times 10^8 m^3 \end{cases}, \tag{15}$$

$$Q = \begin{cases} 38.01 \times e^{-(t-2042)^2 \big/ \left(2\times 14.48^2\right)}, & URR = 1380 \times 10^8 m^3 \\ 54.43 \times e^{-(t-2042)^2 \big/ \left(2\times 12.64^2\right)}, & URR = 1725 \times 10^8 m^3 \\ 71.00 \times e^{-(t-2042)^2 \big/ \left(2\times 11.63^2\right)}, & URR = 2070 \times 10^8 m^3 \\ 88.00 \times e^{-(t-2042)^2 \big/ \left(2\times 10.95^2\right)}, & URR = 2415 \times 10^8 m^3 \\ 105.0 \times e^{-(t-2042)^2 \big/ \left(2\times 10.49^2\right)}, & URR = 2760 \times 10^8 m^3 \end{cases} \cdot \tag{16}$$

In order to deeply analyze the growth law of tight gas production with *URR*, it is necessary to study the relationship between the above model parameters and *URR*. Therefore, one hundred different *URR* values were uniformly sampled within the estimated range of $URR = (1380 - 2760) \times 10^8 m^3$ (Section 3.1). Substitute these *URR* values into Eqs 5–11 to calculate different production prediction results (Figures 6A, 7A).

It can be seen that the production prediction results in Figures 6A, 7A are highly similar. Therefore, both production prediction results can be analyzed simultaneously. The value of peak production is positively proportional to the value of *URR*, that is, the greater the *URR* is, and the greater the peak

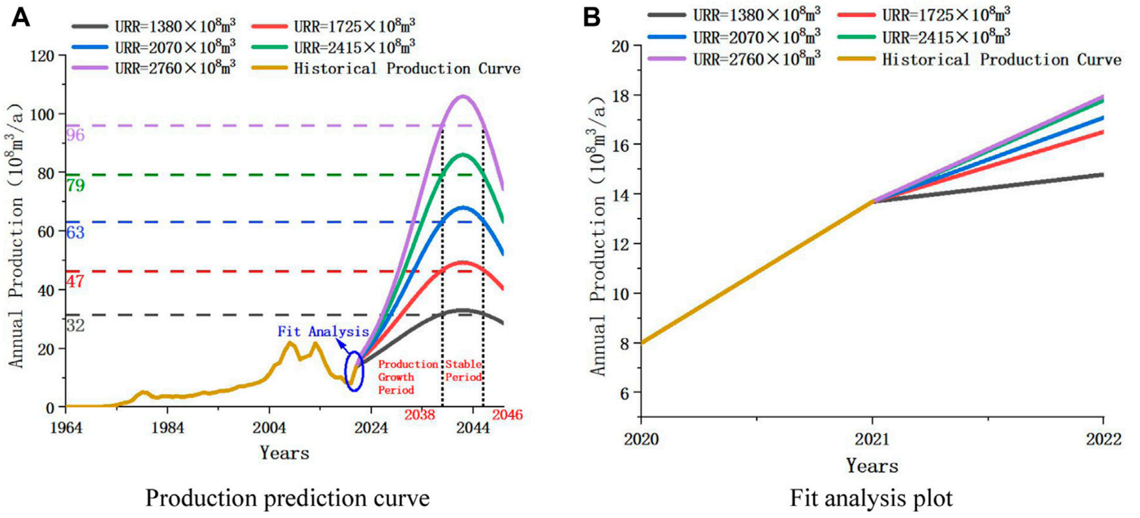

Production prediction curve

Fit analysis plot

FIGURE 6
Prediction results of tight gas production based on Hubbert model.

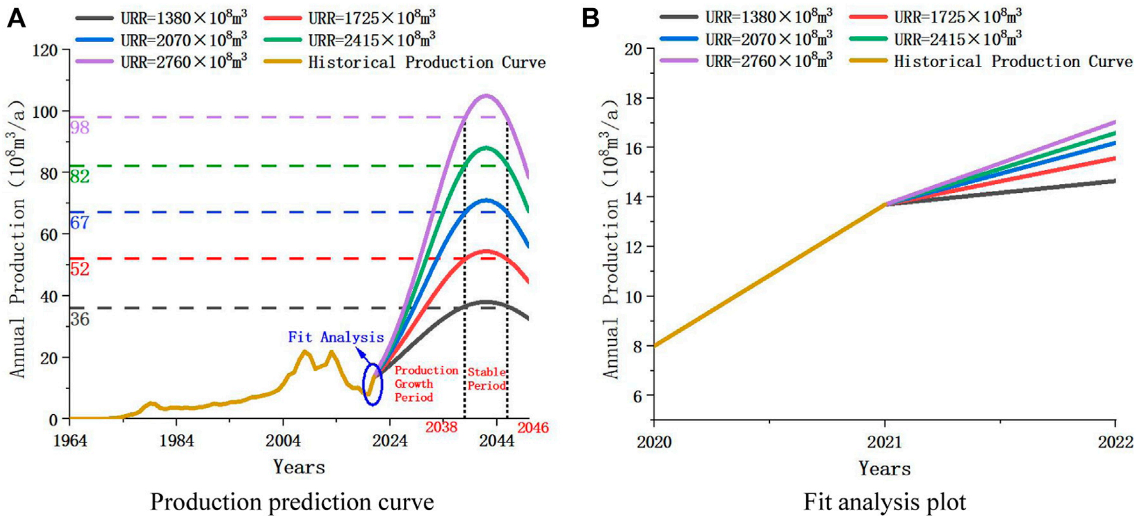

Production prediction curve

Fit analysis plot

FIGURE 7
Prediction results of tight gas production based on Gauss model.

production is. The peak production always occurs in 2042, that is, $t_m \equiv 2042$, and the production growth curve is axisymmetric about $t = 2042$.

According to the increase amplitude of tight gas production, the future production trend can be divided into two stages, that is, the production rising stage (2022–2038) and the production stable stage (2038–2046). In 2022–2038, production rises rapidly as the year increases. In 2038–2042, the production maintains steady growth and reaches the peak production Q_m in 2042. In 2042–2046, production remains in a steady decline.

In order to compare the accuracy of production prediction results under the two different models, correlation analysis is required. This paper makes a fitting analysis diagram for the results in the early stage of prediction (Figures 6B, 7B). The fitting result represents the coincidence degree of predicted prediction and historical prediction. It can be intuitively observed from the

TABLE 2 Correlation coefficient of production prediction results.

URR ($10^8 m^3$)		1,380	1725	2070	2,415	2,760
correlation coefficient	Hubbert model	0.9315	0.9811	0.9895	0.9956	0.9962
	Gauss model	0.9245	0.9599	0.9755	0.9828	0.9884

figure that the better the fitting degree is, the closer the prediction is to the real situation, and that is, the more accurate the prediction result is.

As can be seen from the figure, for the Hubbert model, the best fit with historical production is $URR = (2415 - 2760) \times 10^8 m^3$, for the Gauss model, the best fit with historical production is $URR = 2760 \times 10^8 m^3$. And from the figure, the Hubbert model fits better than the Gauss model. After comparing the fitted graphs, this paper also calculates the correlation coefficient to determine the accuracy of the model from the perspective of data. The calculation formula is:

$$r = \frac{n\sum_{i=1}^{n} x_i y_i - \sum_{i=1}^{n} x_i \sum_{i=1}^{n} y_i}{\sqrt{n\sum_{i=1}^{n} x_i^2 - \left(\sum_{i=1}^{n} x_i\right)^2}\sqrt{n\sum_{i=1}^{n} y_i^2 - \left(\sum_{i=1}^{n} y_i\right)^2}}. \qquad (17)$$

In the formula, r is the correlation coefficient, n is the number of data points, and x_i and y_i are the coordinate values of each point.

The correlation coefficient method can directly reflect the correlation degree between two groups of variables, which can be used as one of the judgment criteria for the accuracy of prediction results. The correlation coefficients of the production prediction results of the two models under different *URR*s are shown in Table 2. It can be seen from the table that the correlation coefficients of the two models are very close to 1, and the corresponding production prediction results are very accurate. However, the correlation coefficients of the predicted results of the Hubbert model under each *URR* are higher than those of the Gauss model. The higher the correlation coefficient is, the more accurate and representative the prediction result is. Therefore, the prediction data of the Hubbert model is selected as the prediction result of tight gas production. In addition, since the Hubbert model has the highest fitting degree under $URR = (2415 - 2760) \times 10^8 m^3$, the final peak range should also correspond to it.

3.3 Overview

The low degree of exploration and development of tight gas leads to many unknown factors. Therefore, the ultimate recoverable reserves *URR* is introduced into the study of production change trend as a main factor. The final range of peak production was calculated by defining the value range of *URR*, and Hubbert and Gauss model were established to realize the calculation. The accuracy of the results was judged by comparing the results of the correlation coefficients and referring to the degree of fitting of the predictions. Establishing a prediction model for the growth trend of tight gas production under different proven rates can provide a theoretical basis for tight gas exploration and development planning. The production results predicted by the Hubbert model are shown in Table 3.

Preliminary prediction results show that tight gas production in the Sichuan Basin will continue to maintain a rapid growth trend in the next 20 years. According to the fitting degree and correlation analysis between the predicted results and historical production, the production of tight gas will reach the peak range of $(86 - 106) \times 10^8 m^3/a$ in 2042. At the end of the stable production period, the *URR* recovery was about 60%.

4 Tight gas production risk quantification

4.1 Realization probability analysis combined with Monte Carlo principle

As described in Section 3.2, the production growth process for future time periods is divided into two stages. That is, the production rising stage (2022–2038) and the production stable stage (2038–2046). Therefore, it is necessary to calculate and analyze the production realization probability for different production growth stages.

In order to clearly describe the influence of *URR* on production prediction results, the variation trend of peak production and model parameters under different *URR*s was first analyzed and studied. As shown in Figure 8, with the increase of *URR*, the peak production Q_m and the model parameter b both keep increasing trend on the whole. However, in a certain area where the *URR* does not change significantly, Q_m and b show a negative correlation trend, that is, when Q_m increases, b decreases. This law corresponds to Eq. 4. Then zoom in on the prediction results of the two production growth stages in Figures 6A, and change the abscissa of these figures from year to *URR*. The *URR*-production prediction results of each stage and year can be obtained (Figure 9).

It can be seen from Figure 9 that the change trend of annual production with *URR* is consistent with the change trend of peak production in Figure 8, regardless of whether it is a rising stage or

TABLE 3 Prediction results of tight gas production under different *URR* conditions.

URR/10^8m^3	Q_m/t_m	**Stable production stage**			
	10^8m^3/year	**Time/year**	**Minimum production/10^8m^3**	**Cumulative production/10^8m^3**	***URR* recovery degree (%)**
1,380	33/2042	2038–2046	32	728	52.75
1725	50/2042	2038–2046	47	981	56.87
2070	68/2042	2038–2046	63	1,232	59.52
2,415	86/2042	2038–2046	79	1,480	61.28
2,760	106/2042	2038–2046	96	1725	62.50

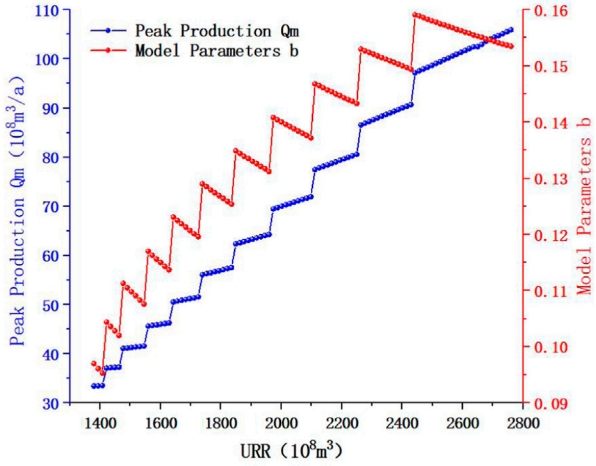

FIGURE 8
Peak production *versus* model parameters.

a stable stage. This law corresponds to Eq. 4. Therefore, it can be considered that with the increase of *URR*, the annual production shows a step-like growth trend. At the same time, with the increase of *URR*, the interval between the production curves of different years is larger, which shows that the increase of *URR* also leads to the increase of annual production growth rate. This also explains that in Figure 6, the larger the *URR*, the greater the slope of the production prediction curve, and the greater the production increase.

To calculate the different production realization probabilities for each year of the two production growth stages, the Monte Carlo method described in Section 2.2.1 was applied. Take 2030 as an example to introduce the probability analysis process of tight gas production. Taking the Hubbert production calculation equation of Eq. 5 as the mathematical model of probability simulation, *URR* is the main independent variable affecting production. Since the value of *URR* is obtained by uniform sampling (Section 3.2). Therefore, uniformly distributed *URR* values are directly drawn at random multiple times. Set the number of *URR* extractions to 10,000 times. For each *URR* value extracted, calculate the corresponding Q_m and t_m values, and substitute them into Eq. 5 together with $t = 2030$ to obtain the production Q in 2030.

The production of a certain year is repeatedly calculated by cycle. After 10,000 cycles, the distribution probability of the target production can be achieved is obtained, and then the cumulative probability is calculated according to the distribution probability. That is, the probability at the minimum point of annual production is 1, the probability at the next point of production is equal to 1 minus the sum of the distribution probabilities of all previous production, and so on up to the maximum point of annual production. The distribution probability is the average probability of each production value point under the normal distribution, the sum is 1, and the cumulative probability is the realization probability of annual production.

Since the *URR* is uniformly distributed, the accuracy of the production probability statistics can be guaranteed. Figure 10 shows the production realization probability results for representative years in the 2 phases. As can be seen from Figure 10, for the distribution probability, its changing trend is similar to the normal distribution. That is, in the same year, the closer the production is to the extreme value, the lower the probability, and the closer to the middle value, the higher the probability. For cumulative probability, the lower the production value, the higher the realization probability.

Figure 11A is a graph of the production realization probability of each year during the stable production period. It can be seen from the figure that with the increase of the annual production prediction value, the realization probability gradually decreases. At the same time, the production corresponding to the realization probability of 10%–20% is the ideal production, and the ideal production in the stable production period under the prediction model is stable between $(80-90)\times 10^8m^3$/a. Figure 11B shows the prediction of annual production under different probabilities (realization probability 10%–90%), where

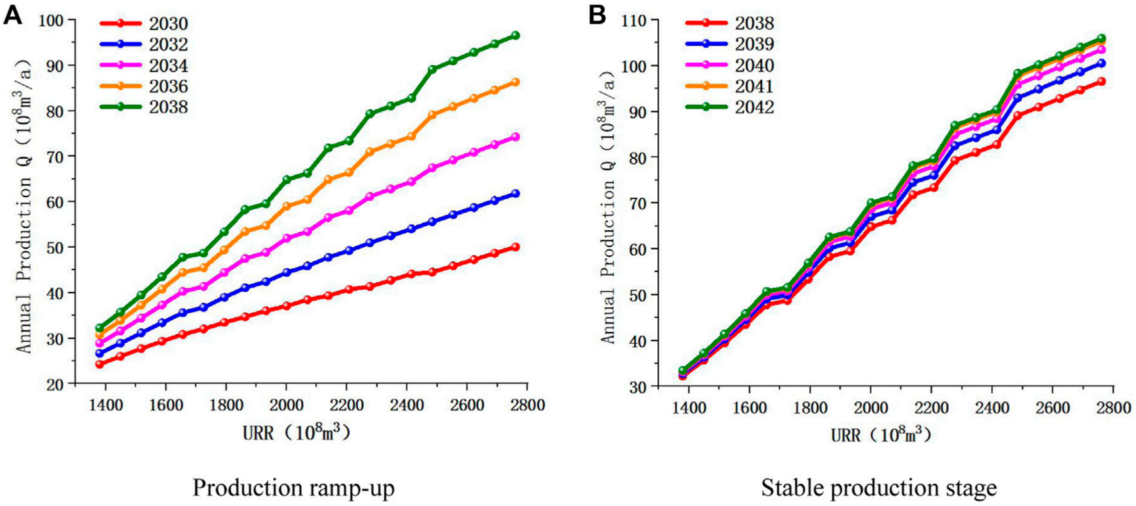

Production ramp-up

Stable production stage

FIGURE 9
URR-production prediction result graph.

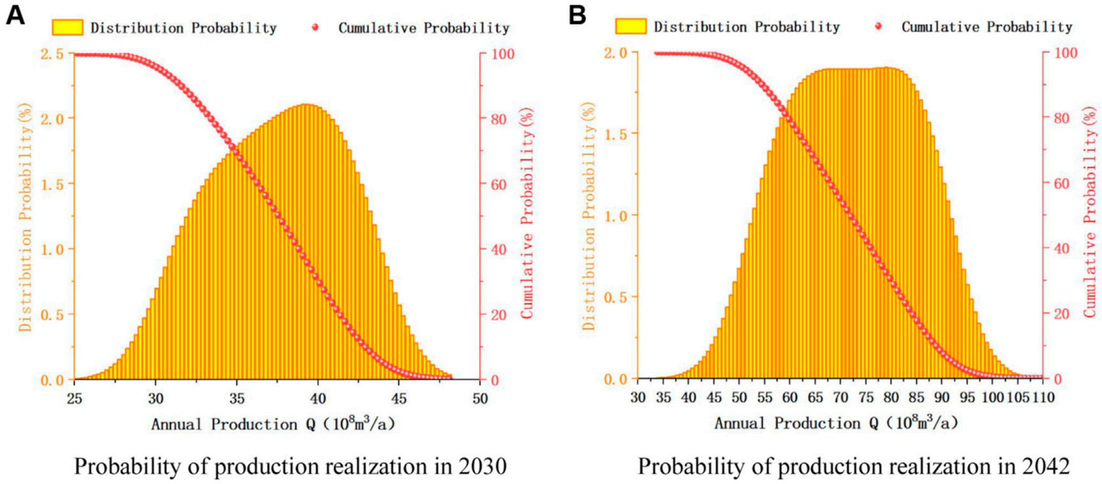

Probability of production realization in 2030

Probability of production realization in 2042

FIGURE 10
Production-realization probability plot in different years.

P90 indicates that the probability is 90%. It can be seen from the figure that the change trend of annual production under different probabilities is basically the same, and the production values of adjacent probabilities are also roughly the same. This indicates that the production change trend under the prediction model is relatively stable, and the prediction results are more accurate.

Table 4 represents the production values that can be achieved in several major years under different probability scenarios. The probability is the cumulative probability, so cumulative probability is also realization probability. In 2042, P20 = 96.89× $10^8 m^3$/a means that the probability of production reaching 96.89× $10^8 m^3$/a is 20%. In this paper, the production of tight gas is calculated in the probability interval of 0%–100%, and the risk quantification of production in different probability intervals. Among them, the production corresponding to P80 is the guaranteed production, the production corresponding to P50 is the average production, and the production corresponding to P20 is the ideal production. The probability values calculated by Monte Carlo method represent the

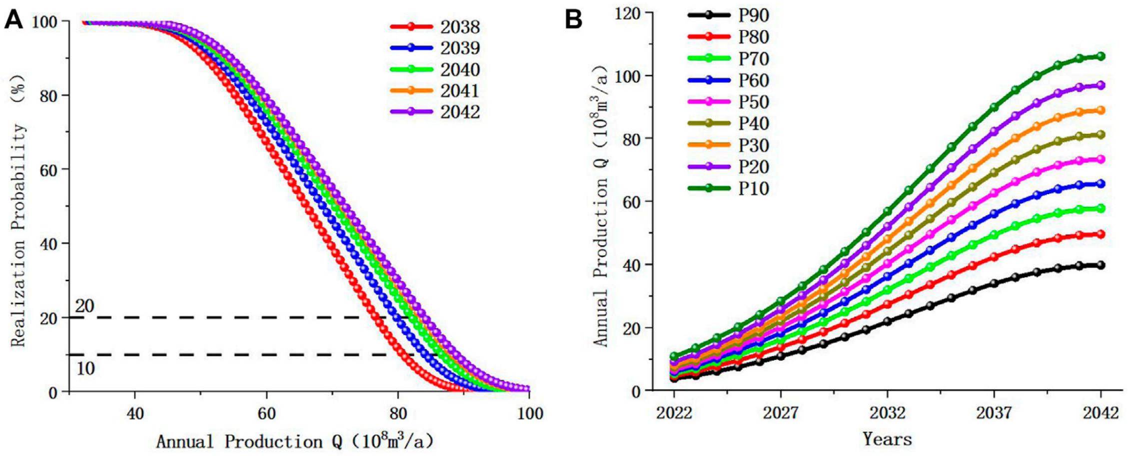

Probability of realization in different years

Annual production with different probabilities

FIGURE 11
Production - realization probability trend chart.

TABLE 4 Calculation results of production realization probability in different stages and years.

Annual production Q/($(10^8 m^3/a)$	P90	P80	P70	P60	P50	P40	P30	P20	P10
2030	17.05	21.41	25.03	28.33	31.42	34.38	37.31	40.39	44.15
2035	29.42	36.73	42.84	48.59	54.19	59.68	65.11	70.70	77.25
2040	38.82	48.35	56.36	63.99	71.56	79.12	86.64	94.33	103.25
2042	39.83	49.61	57.82	65.65	73.43	81.22	88.97	96.89	106.07

possibility of achieving tight gas production in different periods. This feasibility study has an important guiding role for the planning of tight gas production in the future.

4.2 Production risk level evaluation based on matrix analysis

In order to conduct risk quantification research on tight gas production, the risk matrix (Figure 3) in Section 2.2.2 needs to be introduced to evaluate the production risk level. According to the probability calculation method in Section 2.2, the production distribution probability and realization probability curve of each year in the two stages were obtained respectively. According to the distribution probability curve, the mean value μ and the standard deviation s of the annual production are obtained, so as to obtain the dispersion degree C of the annual production according to Eq. 14.

In the rising stage of production, $5\% < C \leq 10\%$. At this time, the annual production corresponding to $P > 50\%$ is a risk level II, the annual production corresponding to $20\% \leq P < 50\%$ is a risk level III, and the annual production corresponding to $P < 20\%$ is a risk level IV.

In the stable production stage, $10\% < C \leq 25\%$. At this time, the annual production corresponding to $P > 50\%$ is a risk level III, and the annual production corresponding to $P \leq 50\%$ is a risk level IV.

Since the dispersion degree is different in different stages, the risk level of production target in different stages and years can be obtained by combining the dispersion degree and realization probability. (Figure 12) (Guo et al., 2022).

It can be known from Figure 11 that the higher the target production is, the lower the corresponding realization probability value is, and the production -probability curve is also in the region with higher risk level. According to the production risk quantification results of different stages in Figure 12, the

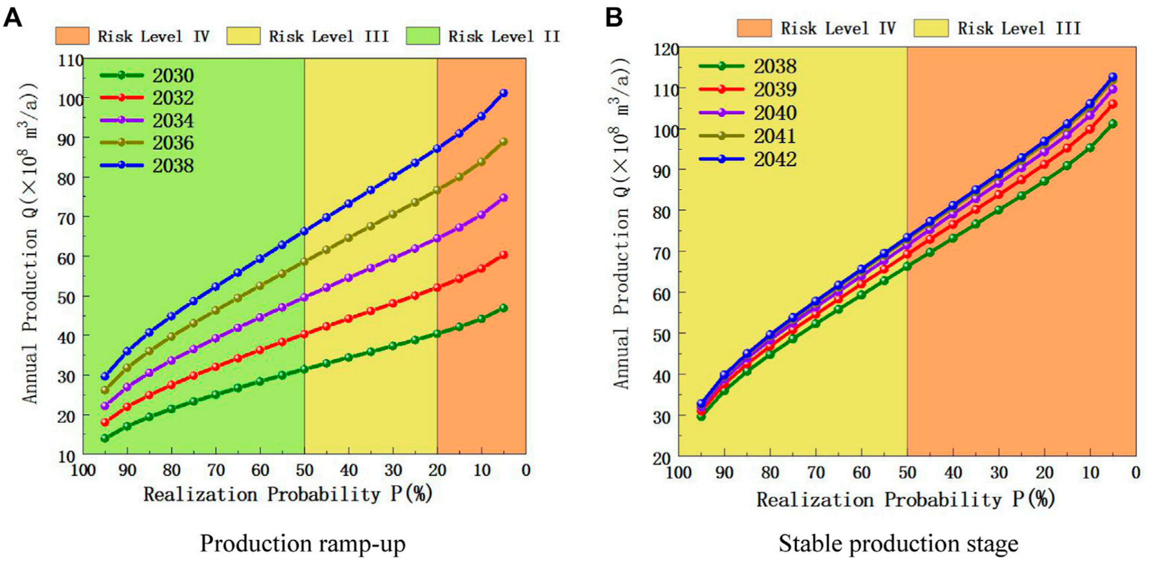

Production ramp-up

Stable production stage

FIGURE 12
Production risk level assessment.

realization probability and risk level of different productions in each year can be directly obtained. Production risk level indicates how easy it is to achieve the production target, therefore, combined with the realization probability calculation and risk level evaluation, the risk quantification of production can be well studied, and the realization probability of tight gas target production can be calculated, which provides data support for feasibility analysis.

4.3 Overview

The quantitative research on tight gas production risk is based on the production prediction results. According to the uniformly distributed proved rate, *URR* of different degrees is calculated, and the probability of achieving the target production in different stages is studied to obtain the possibility of achieving the tight gas production in different years. Combined with the realization probability and the degree of dispersion, the risk grade analysis was used to evaluate the annual production in different stages of production growth. The target risk of tight gas production is comprehensively analyzed.

At present, the exploitation of tight gas in the Sichuan Basin is still in its early stage, and the production prediction and risk quantification of tight gas are also in the shallow stage. In this paper, *URR* was introduced as the influencing factor of production change trend by using the proved rate as the medium, without more comprehensive quantitative research considering other factors. Risk assessment is based on the results of production prediction and studies the degree of difficulty to achieve the target production. Therefore, the production prediction and risk assessment of tight gas need to carry out more research work, so as to provide a better reliable basis for tight gas production planning.

5 Conclusion

1) According to the uniformly distributed proved rate, *URR* was introduced as the main factor, and Hubbert and Gauss models were respectively used to predict the variation trend of tight gas production. According to the curve fitting results and correlation size, the accuracy of Hubbert model is higher, and the predicted results of this model are finally adopted. According to the amplitude of production change, the process of production increase is divided into two stages, namely, production increase stage and production stability stage. The production prediction results show that the tight gas production will reach the peak range of $(86-106)\times 10^8 m^3$/a in 2042. And the production will be stable from 2038 to 3046, and the *URR* recovery degree will be about 60% at the end of the stable production period.
2) Based on the results of tight gas production prediction and risk assessment combined with the realization probability and dispersion degree, the possibility of achieving different target production can be intuitively obtained, and finally provides a basis for the planning of tight gas production. According to the Monte Carlo method, the production change curve is analyzed, and the production realization probability of different years in each stage is calculated, and then the risk assessment of tight gas

production is carried out based on the dispersion degree. Finally, the establishment of the target risk quantification system for tight gas production in the Sichuan Basin was promoted.

3) Sun et al. (2021), Wang et al. (2018), JamesWard et al. (2012) and others all predicted natural gas production from the perspective of single prediction. In this paper, according to the actual situation of Sichuan Basin and the lack of historical tight gas data, Word model was first used to predict the peak production and the range of peak time, and then Hubbert model and Gauss model were combined to predict. Combining with the degree of fitting and the calculation of correlation coefficient of prediction results, a more accurate model was determined. Based on the Monte Carlo method and the risk matrix principle, the realization probability of future production was predicted, and the risk assessment of tight gas production was carried out by combining the realization probability and dispersion degree. In this paper, a new idea was adopted on the combination and progression of the methods, which can provide a reference for the prediction of gas reservoirs with few historical data.

Data availability statement

The raw data supporting the conclusion of this article will be made available by the authors, without undue reservation.

Author contributions

HL and GY provide technical support, theoretical basis and on-site guidance; YF provides data basis and algorithm process; YC processes data and writes papers; and DZ reviews and modifies them.

Funding

This study was financially supported by the Scientific Research Foundation of State Key Laboratory of Coal Mine Disaster Dynamics and Control (2011DA105287-zd201804).

Conflict of interest

HL and YF were employed by Exploration and Development Research Institute of PetroChina Southwest Oil and Gas Field Company. GY was employed by PetroChina Southwest Oil and Gas Field Company Planning Department.

The remaining authors declare that the research was conducted in the absence of any commercial or financial relationships that could be construed as a potential conflict of interest.

Publisher's note

References

Chengzao, J., Yongfeng, Z., and Xia, Z. (2014). Prospects of and challenges to natural gas industry development in China. *Nat. Gas. Ind. B* 1, 1–13. doi:10.1016/j.ngib.2014.10.001

Chong, L., Wu., W.Z., Xie., W., Zhang, T., and Zhang, J. (2021). Forecasting natural gas consumption of China by using a novel fractional grey model with time power term. *Energy Rep.* 7, 788–797. doi:10.1016/j.egyr.2021.01.082

Dai, Jinxing., Ni, Yunyan., Liu, Quanyou., Wu, X., Gong, D., Hong, F., et al. (2021). Sichuan super gas basin in southwest China. *Petroleum Explor. Dev.* 48 (2), 1251–1259. doi:10.1016/s1876-3804(21)60284-7

Flouri., M., Karakosta., C., Kladouchou., C., and Psarras, J. (2015). How does a natural gas supply interruption affect the EU gas security? A Monte Carlo simulation. *Renew. Sustain. Energy Rev.* 44, 785–796. doi:10.1016/j.rser.2014.12.029

Gabriel, M. P., Bruno, F., Josiane, S. C., Flávia, M., Fabio, O., João, J. R., et al. (2021). Evaluation of characteristic diameter on barite settling in drilling fluids by Monte Carlo method. *J. Petroleum Sci. Eng.*

Guo, Y., Chen, Y., Li, H., Liu, L., Wang, C., Chen, Y., et al. (2022). Studies on natural gas production prediction and risk quantification of Sinian gas reservoir in Sichuan Basin. *J. Pet. Explor. Prod. Technol.* 12 (4), 1109–1120. doi:10.1007/s13202-021-01368-y

Guo, Y., Fang, Y., Li, H., Wang, C., and Zhang, D. (2021). Establishment and application of prediction model of natural gas reserve and production in Sichuan Basin. *J. Pet. Explor. Prod. Technol.* 11 (6), 2679–2689. doi:10.1007/s13202-021-01189-z

Gutierrez, J. P., Benitez, L. A., Ruiz, E. A., and Erdmann, E. (2016). A sensitivity analysis and a comparison of two simulators performance for the process of natural gas sweetening. *J. Nat. Gas Sci. Eng.* 31 (11), 800–807. doi:10.1016/j.jngse.2016.04.015

Höök, M., Li, J., Johansson, K., and Snowden, S. (2012). Growth rates of global energy systems and future outlooks. *Nat. Resour. Res.* 21 (1), 23–41. doi:10.1007/s11053-011-9162-0

Hu, Yong., Wenxiang, He., and Guo, Bincheng. (2020). Combining sedimentary forward modeling with sequential Gauss simulation for fine prediction of tight sandstone reservoir. *Mar. Petroleum Geol.* 112, 104044. doi:10.1016/j.marpetgeo.2019.104044

Huang., Y., Ai, W., Xiao., K., Lin, T., and Jin, W. (2022). Types and Genesis of sweet spots in the tight sandstone gas reservoirs:Insights from the Xujiahe Formation, northern Sichuan Basin, China. *Energy Geosci.* 3, 270–281. doi:10.1016/j.engeos.2022.03.007

JamesWard., D., Mohr., Steve H., Myers., Baden R., and Nel, W. P. (2012). High estimates of supply constrained emissions scenarios for long-term climate risk assessment. *Energy Policy* 51, 598–604. doi:10.1016/j.enpol.2012.09.003

Jia, Ailin (2018). Progress and prospects of natural gas development technologies in China. *Nat. Gas. Ind. B* 5, 547–557. doi:10.1016/j.ngib.2018.11.002

Krupenev., Dmitry, Denis, Boyarkin., and Iakubovskii., Dmitrii (2020). Improvement in the computational efficiency of a technique for assessing the reliability of electric power systems based on the Monte Carlo method. *Reliab. Eng. Syst. Saf.* 204, 107171. doi:10.1016/j.ress.2020.107171

Lao., Tongfei, and Sun., Yanrui (2022). Predicting the production and consumption of natural gas in China by using a new grey forecasting method. *Math. Comput. Simul.* 202, 295–315. doi:10.1016/j.matcom.2022.05.023

Lin, Jiang., Wen, Zhao., Yang, Fan., Hong, F., Gong, Y., and Hao, J. (2021). Effects of micro-fracture and micro-coal line on tight gas accumulation, Triassic Xujiahe Formation, Sichuan Basin, China. *Energy Rep.* 7, 7913–7924. doi:10.1016/j.egyr.2021.08.185

Luz-Sant'Ana, P., Roman-Roman, I., Torres-Ruiz., F, and Torres Ruiz, F. (2017). Modeling oil production and its peak by means of a stochastic diffusion process based on the Hubbert curve. *Energy* 133, 455–470. doi:10.1016/j.energy.2017.05.125

Mohr, S. H., and Evans, G. M. (2011). Long term forecasting of natural gas production. *Energy Policy* 39, 5550–5560. doi:10.1016/j.enpol.2011.04.066

Ravnik, J., Jovanovac, J., Trupej, A., Vistica, N., and Hribersek, M. (2021). A sigmoid regression and artificial neural network models for day-ahead natural gas usage forecasting. *Clean. Responsible Consum.* 3, 100040. doi:10.1016/j.clrc.2021.100040

Shih-Chi, Lo., Ma, Hwong-wen, and Lo, Shang-Lien (2005). Quantifying and reducing uncertainty in life cycle assessment using the Bayesian Monte Carlo method. *Sci. Total Environ.* 340, 23–33. doi:10.1016/j.scitotenv.2004.08.020

Sun, Y., Rahmani, A., Saeed, T., Zarringhalam, M., Ibrahim, M., and Toghraie, D. (2021). Simulation of deformation and decomposition of droplets exposed to electro-hydrodynamic flow in a porous media by lattice Boltzmann method. *Alexandria Eng. J.*

Tilton, J. E. (2018). The Hubbert peak model and assessing the threat of mineral depletion. *Resour. Conservation Recycl.* 13 (9), 280–286. doi:10.1016/j.resconrec.2018.08.026

Tong, Xiaoguang., Zhang, Guangya., Wang, Zhaoming., Wen, Z., Tian, Z., Wang, H., et al. (2018). Distribution and potential of global oil and gas resources. *Petroleum Explor. Dev.* 45, 779–789. doi:10.1016/s1876-3804(18)30081-8

Wang, H., Ma, F., Tong, X., Liu, Z., Zhang, X., Wu, Z., et al. (2016a). Assessment of global unconventional oil and gas resources. *Petroleum Explor. Dev.* 43, 925–940. doi:10.1016/s1876-3804(16)30111-2

Wang, J., Jiang, H., Zhou, Q., Wu, J., and Qin, S. (2016b). China's natural gas production and consumption analysis based on the multicycle Hubbert model and rolling Grey model. *Renew. Sustain. Energy Rev.* 53 (11), 1149–1167. doi:10.1016/j.rser.2015.09.067

Wang, Q., Li, S., Li, R., and Ma, M. (2018). Forecasting U.S. shale gas monthly production using a hybrid ARIMA and metabolic nonlinear grey model. *Energy* 16 (10), 378–387. doi:10.1016/j.energy.2018.07.047

Wang., J., Lian., S., Lei., B., Li, B., and Lei, S. (2022). Co-training neural network-based infrared sensor array for natural gas monitoring. *Sensors Actuators A Phys.* 335, 113392. doi:10.1016/j.sna.2022.113392

Ward, P. G., Thaw Tar, T. Z., Wang., M., Dauwels, J., and Ukil, A. (2018). Leak detection in low-pressure gas distribution networks by probabilistic methods. *J. Nat. Gas Sci. Eng.* 58, 69–79. doi:10.1016/j.jngse.2018.07.012

Wu, X., Chen, Y., Wang, Y., Zeng, H., Jiang, X., and Hu, Y. (2021b). Geochemical characteristics of natural gas in tight sandstone of the Chengdu large gas field, Western Sichuan Depression, Sichuan Basin, China. *J. Nat. Gas Geoscience* 6, 279–287. doi:10.1016/j.jnggs.2021.09.003

Yiping, W., Buqing, S., Jianjun, W., Qing, W., Haowu, L., Zhanxiang, L., et al. (2021a). An improved multi-view collaborative fuzzy C-means clustering algorithm and its application in overseas oil and gas exploration. *J. Petroleum Sci. Eng.* 197, 108093. doi:10.1016/j.petrol.2020.108093

Zeng., B., Xin, M., and Meng, Z. (2020). A new-structure grey Verhulst model for China's tight gas production forecasting. *Appl. Soft Comput.* 96, 106600. doi:10.1016/j.asoc.2020.106600

Zhang, K., and Zhao, Y. (2021). Modeling dynamic dependence between crude oil and natural gas return rates: A time-varying geometric copula approach. *J. Comput. Appl. Math.* 386 (4), 113243. doi:10.1016/j.cam.2020.113243

Zheng, C., Wu, W., Xie, W., and Li, Q. (2020). A MFO-based conformable fractional nonhomogeneous grey Bernoulli model for natural gas production and consumption forecasting. *Appl. Soft Comput.* 11 (6), 106891. doi:10.1016/j.asoc.2020.106891

Zheng, Y., Han, Xu., Zeng, Ji., Zhou, C., Zhou, L., and Chen, W. (2021). Practice of high-intensity volume fracturing in the Shaximiao Formation tight sandstone gas reservoirs of the Qiulin Block, central Sichuan Basin. *Nat. Gas. Ind. B* 8, 367–375. doi:10.1016/j.ngib.2021.07.007

frontiers | Frontiers in Earth Science

TYPE Original Research
PUBLISHED 16 January 2023
DOI 10.3389/feart.2022.1083689

OPEN ACCESS

EDITED BY
Leilei Si,
Henan Polytechnic University, China

REVIEWED BY
Geng Jiabo,
Jiangxi University of Science and Technology, China
Guofa Ji,
Yangtze University, China

*CORRESPONDENCE
Ning Jiang,
jiangning@sdust.edu.cn
Ke Lv,
lk970313@163.com

SPECIALTY SECTION
This article was submitted to Economic Geology,
a section of the journal
Frontiers in Earth Science

RECEIVED 29 October 2022
ACCEPTED 28 November 2022
PUBLISHED 16 January 2023

CITATION
Jiang N, Lv K, Gao Z, Jia C, Ye L, Meng S and Su Q (2023), Experimental study on mechanical properties of single fracture-hole red sandstone.
Front. Earth Sci. 10:1083689.
doi: 10.3389/feart.2022.1083689

Experimental study on mechanical properties of single fracture-hole red sandstone

Ning Jiang[1,2,3]*, Ke Lv[1,2]*, Zhiyou Gao[1,2,4], Chuanbao Jia[1,2,5], Lei Ye[1,2], Shuyu Meng[1,2] and Quanbao Su[1,2]

[1]State Key Laboratory of Mine Disaster Prevention and Control, Shandong University of Science and Technology, Qingdao, China, [2]College of Energy and Mining Engineering, Ministry of Education, Shandong University of Science and Technology, Qingdao, China, [3]General Institute of Exploration and Research of China National Administration of Coal Geology, Beijing, China, [4]Shandong Geology and Mineral Resources Engineering Group Co., Ltd., Jinan, China, [5]Department of Mining Engineering, Lvliang College, Lvliang, China

Various fractures and holes in the natural rock mass affected the mechanical properties of the rock mass and the safety construction of engineering. In this study, we investigated the mechanical properties of a single fracture-hole rock specimen using particle flow code 2D (PFC2D) numerical simulation software and through laboratory tests. We analysed the failure behaviours and mechanical properties of the rock specimen with a single fracture-hole specimen under different fracture angles. The failure modes of single fractured rock samples with different fracture angles were revealed. The fracture propagation and stress evolution of the rock specimen with a single fracture-hole under different fracture angles were investigated. The experimental results shown that the peak strength, peak strain, elastic modulus, initial fracture stress, and damage stress of the single fracture-hole rock specimen with different fracture angles were significantly less than those of the intact rock specimen. Moreover, fracture hole defects accelerated the generation of fractures and promote the failure of the rock specimen. The failure modes were divided into Y, inverted Y, and V types. Before the rock specimen fractures, the stress concentration area was mainly distributed at both ends of the fracture. The stress concentration area at both ends of the fracture gradually decreased, and the stress concentration area near the hole gradually increased as the fracture angle increased. By experiments, the acoustic emission of the model had gone through three stages: initial, steady growth, and rapid decline. The size of the inclination angle affected the number of acoustic emission hits and the generation of acoustic emission signals. Failure behaviours of the rock specimen with a single fracture-hole were systematically investigated, which could promoted the development of fracture rock mechanics and improved the understanding of instability failure mechanism in rock engineering, such as nuclear wasted treatment engineering and deep underground engineering.

KEYWORDS

uniaxial compression, mode of failure, laboratory test, mechanical property, PFC 2D

1 Introduction

Rocks were affected by a series of geological actions due to long-term geological movement, resulted in the occurrence of various types of defects inside and on the surface of rocks (Wang et al., 2018; Pan et al., 2019; Zhao et al., 2019; Yin et al., 2021; Qi XH, 2022). The mechanical properties of rocks with different types of defects vary greatly compared with intact rocks (Zhang and Wong, 2012; Wu et al., 2016; Yang et al., 2016; Zhang et al., 2019; Zhou et al., 2019; Chen et al., 2021). In recent years, with the development of various underground projects, such as water conservancy projects, bridge and tunnel projects, and mining projects, several fractures and holes were generated in rocks, leading to changes in the mechanical properties of rock mass (Brantut et al., 2013; Zhang et al., 2016; Sqy et al., 2017; Zhang et al., 2020). Therefore, it was of great significance to study the failure characteristics and mechanical properties of rock with a single fracture-hole for effective operations of various underground projects.

At present, there were increasingly the experimental studies and numerical simulations reported on defective rock. Specifically, the failure characteristics and mechanical properties of rocks with different types of defects were analysed in terms of pore morphology and fracture length. Based on the existing literature, many researchers obtained successful results regarding conventional holes, fractures, and pore-fracture combinations. Lin et al. (2020a) (Zhang and Yin, 2014) used acoustic emission (AE) and digital image correlation (DIC) techniques to analyse the results of a series of uniaxial compression tests on defective rocks with double circular holes, and fully realized the mechanical properties and fracture mechanism of holes in defective rocks. Yang et al. (2016) (Lin et al., 2020a) conducted uniaxial compression tests of brittle sandstone samples with a single fracture using rock mechanics servo control test system, and the influence of fracture penetration on strength and deformation failure behaviour of brittle sandstone samples with single fracture was analysed. Ma et al. (2021) (Yang and Jing, 2011) studied the experimental results of a square rock containing two parallel discontinuous rough fractures under uniaxial compression load. The results shown that the initiation and propagation of this type of fracture reduced the mechanical properties of the specimen before reaching its peak strength. The interaction of fracture parameters had a significant indigenous effect on the compressive strength and deformation modulus. Lin et al. (2020b) (Asadizadeh et al., 2018) studied the mechanical properties of a double circular fracture-hole rock under uniaxial compression using the discrete element method. The experimental results shown that the existence of holes and fractures would reduce the mechanical properties of rock. Chen et al. (2020a) (Lin et al., 2020b) performed uniaxial compression tests of rock with 10 different types of hole defects using PFC2D, and the failure behaviour and mechanical properties were analysed. The results shown that the hole shape had an influence on the stress distribution around the hole, and the hole defects reduce the damage degree of the rock. Ma et al. (2021) (Chen et al., 2020a) conducted uniaxial compression tests using PFC2D to study the failure mechanism of sandstone samples with double-hole and double-fracture combination defects. Wu et al. (2019)) studied the effect of the interaction between holes and fractures on the coalescence behaviour of fractures around holes based on the uniaxial compression test and particle flow code (PFC).

For other types of defective rocks, various relevant studies had also been conducted. Lu et al. (2021) proposed that the dip angle had a significant influence on the strength anisotropy of the columnar jointed rock by analysing the failure mode and failure mechanism of the columnar jointed rock under different load conditions. Liu et al. (2017) (Lu et al., 2021) studied the influence of the number of cross-fractures, fracture angle, and fracture spacing on the defective rock by PFC3D and revealed the damage and fracture mechanism of the fractured rock under uniaxial compression. Asadizadeh et al. (2019) (Liu et al., 2017) conducted experiments on artificial fractured rocks with several discontinuous rough fractures under uniaxial compression. Through the multivariate statistical analysis, the effects of the four parameters, such as fracture roughness coefficient, bridge length, bridge angle, and fracture angle, on uniaxial compressive strength, deformation modulus, and fracture coalescence stress of fractured rocks were studied. Bahaaddini et al. (2013) (Asadizadeh et al., 2019) modelled SRM using the discrete element software PFC3D and studied the influence of fracture geometry parameters on the rock failure mechanism, unconfined compressive strength, and deformation modulus. The results shown that the fracture direction and step angle were the main factors that determine the failure mode of rock, and the fracture direction relative to the principal stress direction was the most important parameter that affects rock properties. Huang and Yang (2016) (Bahaaddini et al., 2013) carried out a series of PFC2D numerical simulations on sandstone samples with three parallel fractures under uniaxial compression. The influence of fracture dip angle on stress-strain curve, strength and deformation parameters, and fracture evolution characteristics in sandstone with three fractures were analysed in detail. Dai et al. (2019) (Huang and Yang, 2016) conducted a numerical simulation by using the parallel bond particle model containing two intersecting fractures. The intersection angle of the two fractures was used to perform the numerical simulation. Moreover, they studied the effects of the intersection and inclination angles on the peak stress, fracture initiation stress and fracture coalescence stress. Cheng et al. (2019) (Dai et al., 2019) numerically simulated the plate fracture model and performed laboratory tests on specimens with various shape echelon defects, compared the variation trend of fracture initiation stress and peak stress in the simulation and experiment, and explained the influence of the fracture array angle on fracture initiation stress and peak stress.

The research materials of the aforementioned studies were specimens with only simple defects or those with simple superposition of different defects. There were few studies on the mechanical properties and failure process of some rocks with complex defect, while the rock defects in the actual geotechnical engineering were mostly complex combined defects. With the above problems of pre-fabricated rock defects, in this study, we used the single fracture-hole composite defect specimen with a more complex defect combination as the research object. We conducted uniaxial compression tests on a single fracture-hole rock specimen in the laboratory.

2 Methodology

Due to the complex operation and large workload, it was difficult to analyse the influence of different fracture angles on the mechanical properties and failure characteristics of a single fracture-hole rock specimen *via* experiments. Compared with physical tests, numerical analysis was simple, convenient, and cheap, had high repeatability, and could address the problem of an insufficient number of experiments. Therefore, in this study, we used the particle flow numerical simulation software to analyse the mechanical properties and failure characteristics of a single fracture-hole rock specimen.

2.1 Overview of particle flow code

The PFC was based on the discrete element method proposed by Cundall in 1979 (Cheng et al., 2019), which simulates the motion and interaction of circular granular media through the discrete element method. The composite material of the PFC model consisted of solid particles, which interacted with each other to illustrate their behaviour. The PFC model represents the independent motion and interaction between different particles in internal force contact. In the PFC software, the particle shape could be described in the form of a two-dimensional disk or three-dimensional sphere, and the characteristics and particle parameters of particles in a discontinuous environment could be analysed.

In PFC2D, contact and parallel connections could be used to simulate the connection between rock particles. A contact connection could only transfer force between units, while a parallel connection could transfer both force and torque. Parallel keys in parallel links could be regarded as a set of elastic springs with constant normal and shear stiffness, uniformly distributed on the cross-section of the contact plane (two-dimensional rectangular and three-dimensional disc) and centred on the contact point. These springs act parallel to the springs of the linear component. The relative motion occured at the contact after the parallel bond was formed, resulting in both force and torque in the bonding material. This force and torque acted on two contact blocks was related to the maximum normal and shear stresses of the bonding material around the bonding. If any of these maximum stresses exceed the corresponding bond strength, the bond material, along with its associated force, moment, and stiffness, was removed from the model. In this study, the uniaxial compression test of rock specimen was simulated using parallel keys (Figure 1).

2.2 Model and boundary condition

It was necessary to determine the mechanical parameters and bond properties of microscopic particles in rock when simulating the rock specimen with PFC2D. However, these parameters could not be obtained directly through laboratory tests. Therefore, it was necessary to select and validate microscopic parameters before performing numerical simulations. Many numerical simulations were conducted to ensure that the simulation test conditions were consistent with the laboratory test. Then, the numerical simulation results were compared with the laboratory test results, and the microscopic mechanical parameters of the particles were adjusted repeatedly through trial and error (Holt et al., 2005) until the simulation test requirements were met.

Figure 2 shown the comparison of the final calibration results between the laboratory and numerical tests. Based on the figure, the stress-strain curve was similar in shape and the failure mode was in good agreement. Table 1 shown that the determined final microscopic parameters.

The mechanical properties and failure characteristics of single fracture-hole rock specimen with different fracture angles were studied using PFC2D, and the numerical models of a single fracture-hole rock specimen with different fracture angles were established. The width and height of the model specimen were 50 and 100 mm, respectively. The circular hole had a radius of 5 mm. The lower and right boundaries of the circular distance were 20 and 20 mm, which were located in the centre below the model. The fracture width and length were 0.5 and 10 mm, respectively. The angles between the fracture centre and the horizontal direction of the rock specimen were set to 0°, 15°, 30°, 45°, 60°, 75°, and 90°. The geometric parameters and numerical model of the specimen were shown in Figure 3. The plane stress model was adopted, which was loaded by the displacement loading at a rate of 0.01 mm/s.

2.3 Analysis of the numerical simulation results

2.3.1 Stress evolution law

To increase the efficiency of the experimental data, the subsequent data changes would had no significant effect on

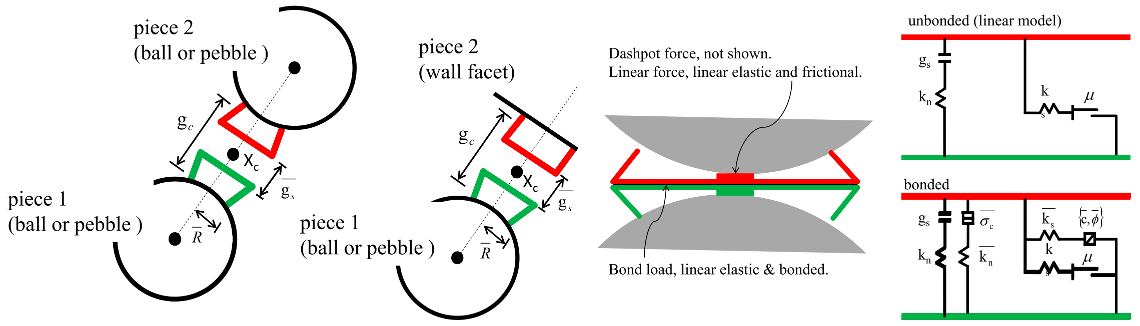

FIGURE 1
Parallel bond model (Cundall and Strack, 1979).

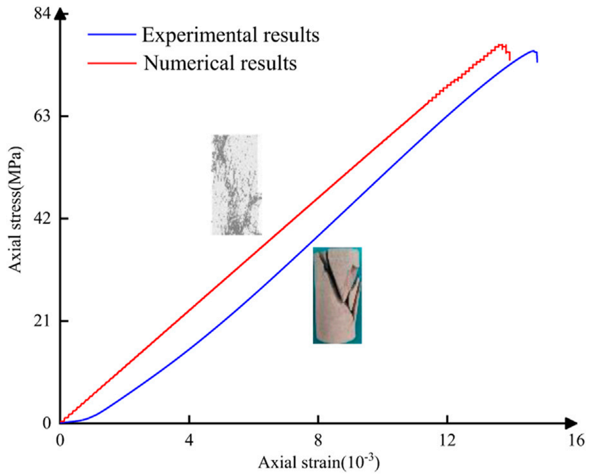

FIGURE 2
Comparison of calibration numerical and experimental results.

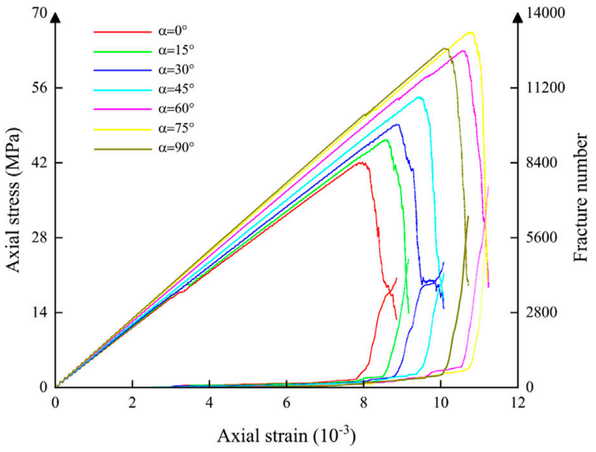

FIGURE 3
Stress-strain curve and fracture number-strain curve of a single fracture-hole rock specimen.

TABLE 1 Micro-parameters of the model in the numerical simulation.

Parameter	Value	Parameter	Value
Porosity	0.1	Minimum particle diameter	0.2
Parallel bond cohesive force (MPa)	47	Particle density (kg/m^3)	2500
Particle size ratio	1.4	Particle contact modulus (GPa)	3.3
Parallel bond tensile strength (MPa)	20	Friction angle of parallel bond (o)	50

this simulation when the stress decreased to 30% of the peak stress. Thus, we did not calculate it. Compared with the stress-strain law of the intact rock, the fracture angle had no significant effect on the stress-strain law of a single fracture-hole rock specimen. In addition, they had experienced the initial fracture compaction stage, linear elastic deformation stage, non-linear deformation stage, and post-peak softening stage.

The strain-stress curves of the intact rock and single fracture-hole rock specimen with different fracture angles were shown in Figures 3, 4, and the stress-strain curve and the number of the

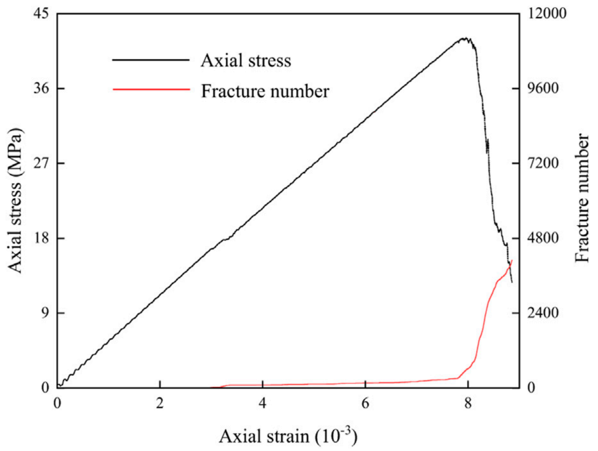

FIGURE 4
Complete rock stress-strain curve and fracture number-strain curve.

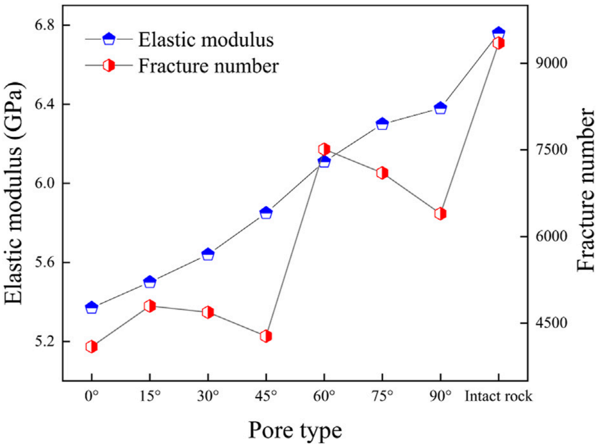

FIGURE 5
Relationship between elastic modulus and fracture number of single fracture-hole rock model with different fracture angles.

fractures-strain curve with the same fracture angle were in the same colour.

In Figure 3, the peak strength of the single fracture-hole rock model and the time to reach the peak strength gradually increase as the fracture angle increases. This was because the hole and fracture defects weaken the brittleness of the rock and increase its ductility, verifying the accuracy of the laboratory test. In Figure 3, the stress-strain curve divided the deformation of the single fracture-hole rock model into four stages: pore fracture compaction, elastic deformation, plastic deformation, and post-fracture. The stress decreased rapidly when the stress exceeded the peak stress.

In Figure 4, the strain-stress curve of the intact rock model was similar to that of the single fracture-hole rock model. Before reaching the peak, the rock model shown plastic deformation, and the image shown linear growth at this stage. After reaching the peak strength, the stress decreased rapidly, indicated that the rock had a typical brittle failure, which was related to the laboratory test material of red sandstone. The above conclusions were consistent with the numerical simulation results of other scholars (Chen et al., 2020b).

2.3.2 Elastic modulus and number of fractures

The relationship between elastic modulus and fracture number of the intact rock model and single fracture-hole rock model with different fracture angles was shown in Figure 5. Based on the figure, with the increasing fracture angle of the single fracture-hole rock model, the elastic modulus gradually increases, and there was no huge fluctuation. When fracture angle changed from 0° to 90°, the growth rate at each stage was small, and the maximum was not more than 1.5 GPa. In addition, the number of fractures increased and decreased in stages as the fracture angle of the single fracture-hole rock model increased. When the fracture angle was 0°–45°, the number of fractures was significantly lower than that when the fracture angle was 60°–90°. With the increase of the fracture angle, the number of fractures increases periodically, the elastic modulus increases, and the bearing capacity of the single fracture-hole rock model decreases. The number of fractures in the intact rock model was much larger than that in the single fracture-hole rock model with different fracture angles. In addition, the total number of fractures in the rock model decreased as the fracture angle decreases. In practical geotechnical engineering, pre-fabricated horizontal fractures and holes could was considered to reduce the number of fractures generated during rock failure to control the degree of rock failure.

2.3.3 Peak stress and peak strain

Peak stress was the maximum stress value of rock during uniaxial compression. It represented the maximum strength and beared capacity of rock and was an important parameter to study the mechanical properties of rock. In Figure 6, the peak stress values of the intact rock model and single fracture-hole rock model shown an increasing trend, and the growth trend of peak stress was consistent with the growing trend of peak strain. With the increase of fracture angle, the values of peak stress and peak strain of single fracture-hole rock model gradually increased. Based on Figure 6, the peak stress and peak strain values of the single fracture-hole rock model and the complete rock model were different.

2.4 Failure analysis of the rock model

2.4.1 Initiation stress and damage stress of the rock model

In the uniaxial compression test of the rock model, the rock model bore the axial loading stress. Under its action, the contact

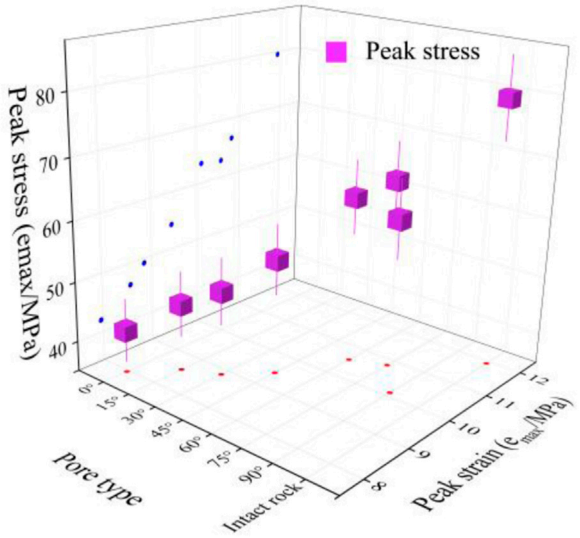

FIGURE 6
Peak stress and peak strain model diagram of the single fracture-hole rock model with different angles of the intact rock and fracture.

force between the particles of the rock model was greater than the cohesive force such that the stress concentration occurs in a certain area of the rock model, and local damage occurred, resulted in micro-fractures. The axial stress corresponding to the first occurrence of micro-fractures was the initiation stress. The fracture gradually extended, and the number of fractures increased as the axial stress of the rock model increased. When the axial stress increases to a peak value, the growth rate of the fracture reaches the peak value, and the axial stress of the rock model was called the damage stress.

Fracture initiation stress σ_{ci} and damage stress σ_{cb} were not only important characteristic values of the rock mass strength but also the boundary points of different stages in the process of fracture propagation. Table 2 shown the fracturing and damage stresses of the complete rock and single fracture-hole rock model and their relationship to the uniaxial compressive strength.

The fracture initiation stress and damage stress of the intact rock model and single fracture-hole rock model with different fracture angles were shown in Figure 7. Based on the figure, the initiation and damage stresses of the single fracture-hole rock model with different fracture angles were smaller than those of the intact rock model, and their values were 26.60 and 79.09 MPa, respectively. The fracture initiation stress of the single fracture-hole rock model shown a decreasing trend at 0°–45° and an increasing trend in 60°–90°. The damage stress of a single fracture-hole rock model shown an increasing trend, and the growth rate was close. The above phenomena shown that the change of the fracture angle of a single fracture-hole rock model intensifies the failure process of rock model.

2.4.2 Failure characteristics and stress evolution of the rock model

The initiation, damage, peak value, and final failure time of the rock model were used as the characteristic moments for comparison to study the failure characteristics of the rock model and the development process of fractures in the uniaxial compression process of the single fracture-hole rock model and intact rock model with different fracture angles. Figure 8 shown the macroscopic failure process of the single fracture-hole rock model and intact rock model with different fracture angles. It was apparent that the complete rock model and the single fracture-hole rock model with different fracture angles were mainly tensile fractures. The shear fractures were relatively small (red was tensile fractures, blue was compressive shear fractures, and green was tensile shear fractures) compared than that in the single fracture-hole rock model.

Based on Figure 8A, when the uniaxial compressive stress of the rock model with a fracture angle of 0° increases to 27.04 MPa, it did not fracture at the tip of the fracture but produces a tensile fracture in the upper and lower parts of the pre-fabricated fracture along the direction of the axial stress. Then, it broken at the upper right corner of the rock model as the axial stress gradually increases. The propagation path of the fracture extended from the initial to the unilateral, and then to the bilateral. When the fracture runs from the bottom to the upper left corner, a short slip deformation occurs, forming many tensile-shear fractures and a V-shaped fracture morphology. The failure mode was a tensile-main shear failure. In Figures 8B,C, the fracture propagation of the rock model with fracture angles of 15° and 30° was consistent with that of the model.

It could be easily obtained from Figures 8D,E that, when the fracture angles of the single fracture-hole rock model were 45° and 60°, a tensile fracture was generated on both sides of the fracture in the fracturing stage, and the fracture in the failure process was mainly concentrated in the upper left end of the rock model. The fracture propagation path changed from a fracture at one end to a fracture at both ends, and gradually concentrated in the hole direction as the axial loading stress increases. Finally, the fracture ran through the rock model, and the failure model was a tension-dominated local shear failure.

As shown in Figure 8F, the length of the tensile fractures generated on both sides of the fracture in the single fracture-hole rock model at the fracturing stage was significantly shorter than that of the rock model at other angles when the fracture angles α of the single fracture-hole rock model were 75° and 90°. Based on Figure 8G, no tensile fractures were generated on both ends of the fracture, but tensile fractures were generated in the axial direction of the hole. Fractures in the process of failure were mainly concentrated in the left and right lower ends of the rock model. With the increased of axial loading stress, the fracture propagation path gradually extended along the hole direction until it ran through the entire rock model, and finally formed an inverted y-shaped fracture morphology. The failure model was a shear-dominated and tensile failure.

TABLE 2 Relationship between initiation stress, damage stress, fracture number, and uniaxial compressive strength of the rock model.

Category	σ_{ci}/MPa	σ_{cb}/MPa	σ_{ci}/σ	σ_{cb}/σ	Number of fractureds
α = 0°	16.38	41.93	0.3891	0.9960	4093
α = 15°	15.33	46.27	0.3314	0.9978	4797
α = 30°	11.14	48.96	0.2265	0.9953	4689
α = 45°	10.22	54.21	0.1882	0.9983	4276
α = 60°	14.33	62.90	0.2276	0.9989	7511
α = 75°	24.20	66.22	0.3642	0.9965	7102
α = 90°	25.29	63.20	0.3988	0.9967	6397
Intact rock	26.60	79.09	0.3346	0.9948	9352

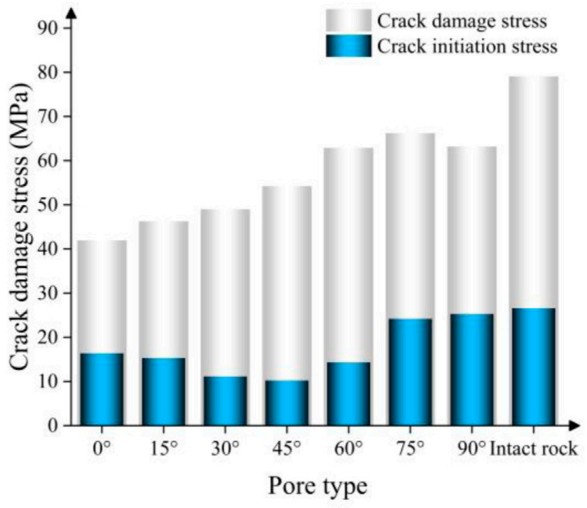

FIGURE 7
Relationship between initiation stress and damage stress of the intact rock model and single fracture-hole rock with different fracture angles.

Based on Figure 8H, the failure of the intact rock model in the failure process was mainly concentrated in the lower end of the rock model. The propagation path of the fracture extended from the initial to the unilateral, and then to the bilateral as the axial loading stress increased. When the fracture ran from the bottom to the upper left corner, a short slip deformation occurs, formed many tensile-shear fractures and a V-shaped fracture morphology. The failure mode was a tensile-main shear failure.

2.5 Fracture propagation and stress evolution of the rock model

The contact force chain and stress evolution results of the four stages of initiation, damage, peak, and failure of each model were selected to investigate the stress distribution and evolution results of the intact rock model and single fracture-hole rock model with different fracture angles. In the contact force chain diagram, the red and blue regions represented the compressive stress region and tensile stress region, respectively. In the stress evolution results, the tensile stress was positive and the compressive stress was negative. The contact force chain and stress evolution results of the single fracture-hole rock model with different fracture angles were shown in Figure 8.

Based on Figure 9, the complete rock model and the single fracture-hole rock model with different fracture angles were dominated by compressive stress in the failure process. In addition, the failure of the complete rock model and the single fracture-hole rock model was due to the loss of the bearing capacity in the middle of the rock model, which was because the fracture was in the middle position of the upper part of the rock model. The rock model begins to fracture when the axial stress was 27.04 MPa and the fracture angle $\alpha = 0°$. Local stress concentration occurred at both ends of the fractures, resulted in four tensile stress regions and six compressive stress regions. Two tensile stress regions were generated near the hole. The compressive stress region in the rock model reached the maximum when the axial stress was 41.81 MPa as the axial stress increases, as shown in Figure 9. Moreover, there was no stress concentration at both ends of the fracture when the fracture angle was 90°. Until the axial stress reaches the peak value of 60.76 MPa and the rock model was damaged, there was no stress concentration at both ends of the fracture because the direction of the fracture was consistent with the direction of the axial stress, and most of the stress was transferred to the vicinity of the hole. The local stress concentration near the fracture was gradually weakened, and the local stress concentration near the hole was more apparent as the fracture angle increased. The peak stress of the rock model with different fracture angles was less than that of the intact rock model. The ratio of the peak stress of the single fracture-hole rock model to the peak stress of the intact rock model increased from 52.7% to 85.42%. This indicated that the peak stress of the single fracture-hole rock model was gradually increasing as the fracture angle increases. When the fracture angles were 15°, 30°, 45°, 60°, and 75°, there were six

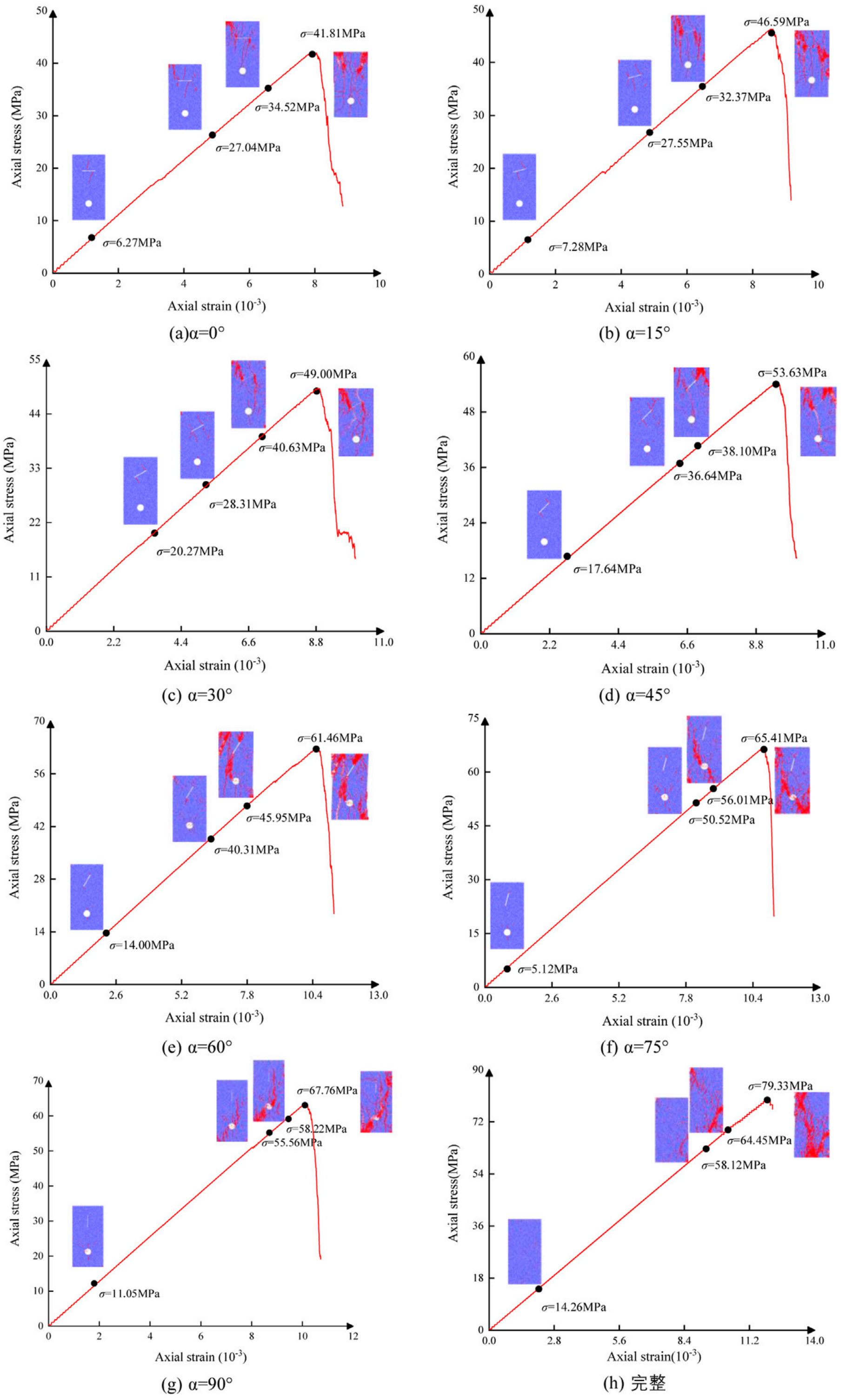

FIGURE 8
Complete rock model and failure mode of single fracture-hole rock model with different fracture angles. **(A–H)**, the damage mode images of the fracture at 0-90° and intact are indicated.

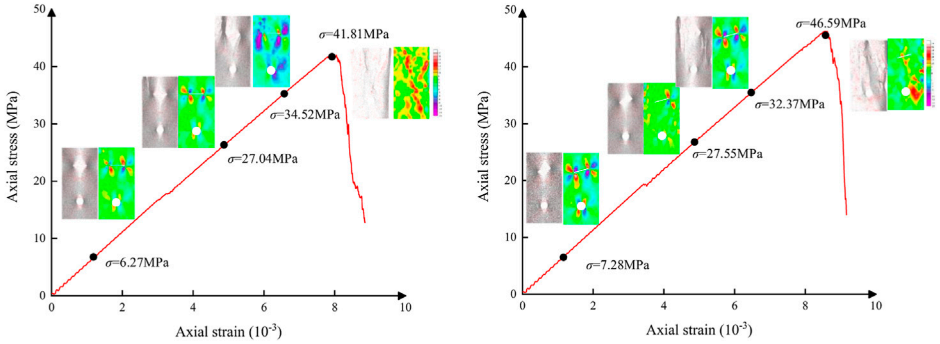

(a) α=0°

(b) α=15°

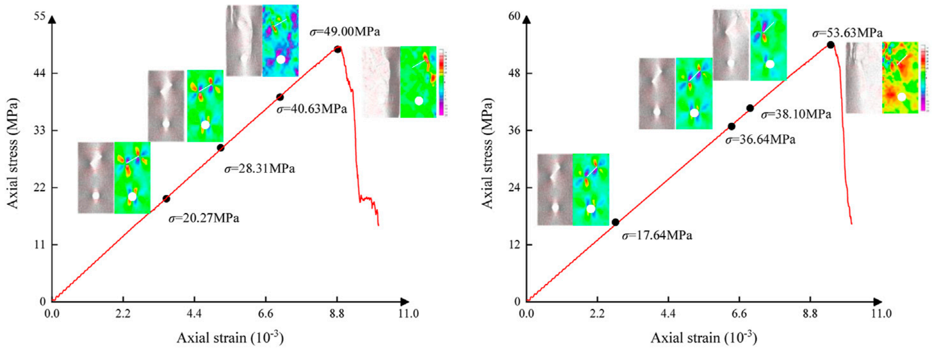

(c) α=30°

(d) α=45°

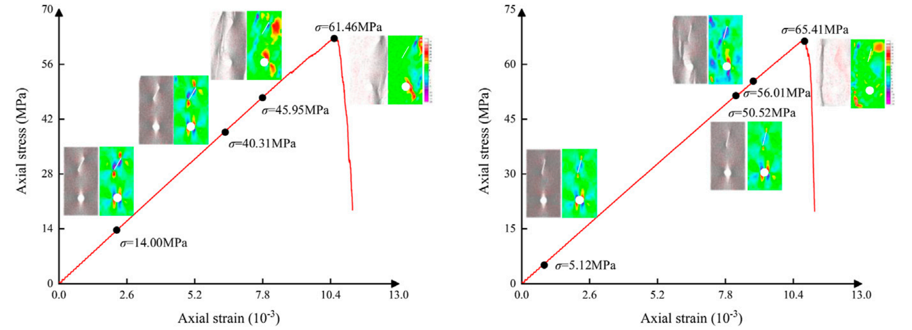

(e) α =60°

(f) α =75°

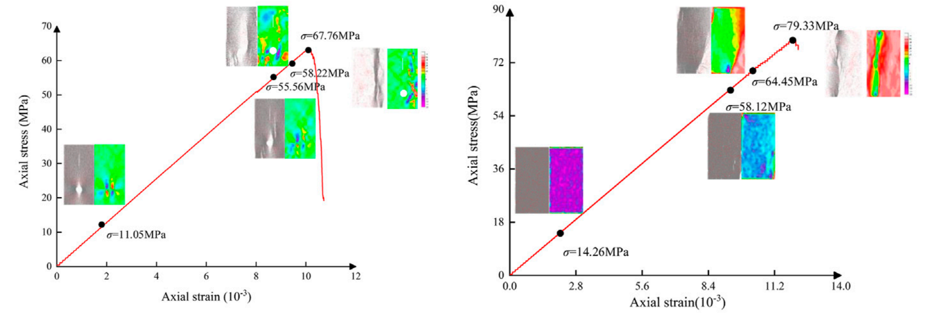

(g) α =90

(h) Intact rock

FIGURE 9
Contact force chain and stress evolution results of intact rock model and fractured rock model with different angles. **(A)** α = 0°, **(B)** α = 15°, **(C)** α = 30°, **(D)** α = 45°, **(E)** α = 60°, **(F)** α = 75°, **(G)** α = 90, **(H)** Intact rock.

compressive stress concentration areas and six tensile stress concentration areas during the initiation period, and the distribution of stress concentration areas was the same.

3 Experimental study on the mechanical properties of single fracture-hole rock specimen

Field sampling was difficult and costly due to the uncertainty and complexity of the natural rock internal structure. However, artificial specimen preparation was convenient, low cost, and could accurately determined the fracture angle and hole size of a single fracture-hole rock specimen. Therefore, artificial specimens were selected in this experiment, and acoustic emission and DIC were used to study the fracture propagation and stress evolution characteristics of a single fracture-hole rock specimen.

3.1 Specimen preparation

The specimen material used in this test was red sandstone from a quarry in Hubei. Red sandstone was composed of granular clastic structure and argillaceous cementation structure. The strength of red sandstone varied greatly due to the difference in the cementing material and weathering degree, made the sample preparation difficult. Therefore, only single fracture-hole rock specimen with fracture angles of 30° and 45° were prepared for experiments, and the relationship between acoustic emission characteristics, rock fracture propagation and digital speckle and different fracture angles were studied. Specimens were taken from the same intact rock specimen and cut into a length of 100 mm, width of 50 mm, and thickness of 20 mm to reduce the difference between specimens. The high-pressure water jet cutting machine was used to cut the sample, as shown in Figure 10.

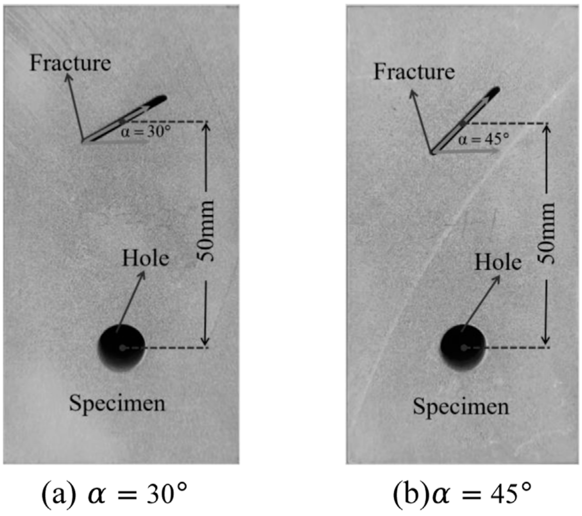

FIGURE 10
Geometric shape of single fracture-hole rock specimen in laboratory test. **(A)** $\alpha = 30°$, **(B)** $\alpha = 45°$.

3.2 Test scheme

The specimens were placed on the AG-X rock mechanics electronic universal testing machine, and uniaxial compression tests were conducted on each specimen. The axial stress was applied on the surface of the rock specimen until it was damaged. In the displacement control test, the uniaxial compression test was carried out on the red sandstone specimens prepared at a fixed displacement speed of 0.01 mm/s. During the test, AE signals and DIC digital characteristics in the deformation process of the red sandstone were monitored in real-time by acoustic emission and digital speckle (Figure 11).

3.3 Test result analysis

3.3.1 Stress-strain image analysis

As shown in Figure 12A, the OA section was the internal pore compaction stage of the rock specimen when the fracture angle was 30°. Due to the existence of small fractures in natural rock, the early stage of uniaxial compression was a process of compaction of small fractures, formed early non-linear deformation. In this stage, the lateral expansion of the specimen was small, and the volume of the rock specimen decreases as the load increases. The AC section was the stage from the elastic deformation of rock specimen to the stable development of micro-elastic fractures, and the stress-strain curve at this stage was approximately linear. The rock specimen in the AB and BC sections was in the elastic deformation stage and the stable development stage of micro-fracture, respectively. At this stage, the acoustic emission energy value changed slightly due to the high brittleness of sandstone. CD section was the unstable fracture development stage of rock specimen. The rock specimen changed from elastic deformation to plastic deformation at point C with the continuous loading of axial stress. In this stage, the internal fracture condition of the rock specimen had undergone a qualitative change, and the internal fractures of rock specimen gradually increased. The stress-strain curve reach the peak at this stage, and the acoustic emission energy value also reached the peak. In the stage after point D, although the bearing capacity of the rock specimen reached its peak strength, and its internal structure was also destroyed, the entire rock specimen remains, and the stress-strain curve shown a rapid decline.

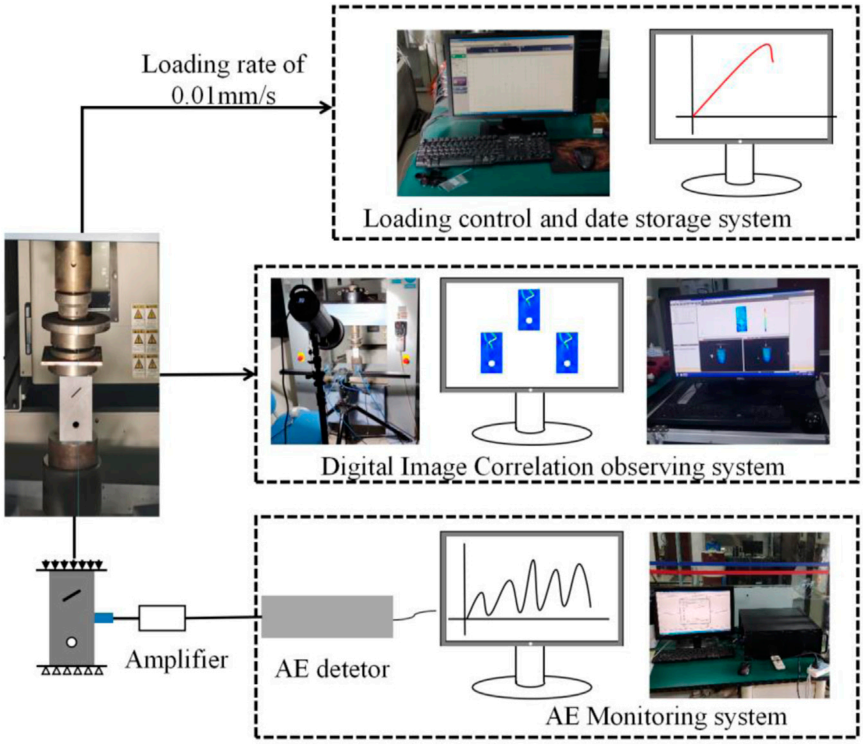

FIGURE 11
Test control and monitoring system.

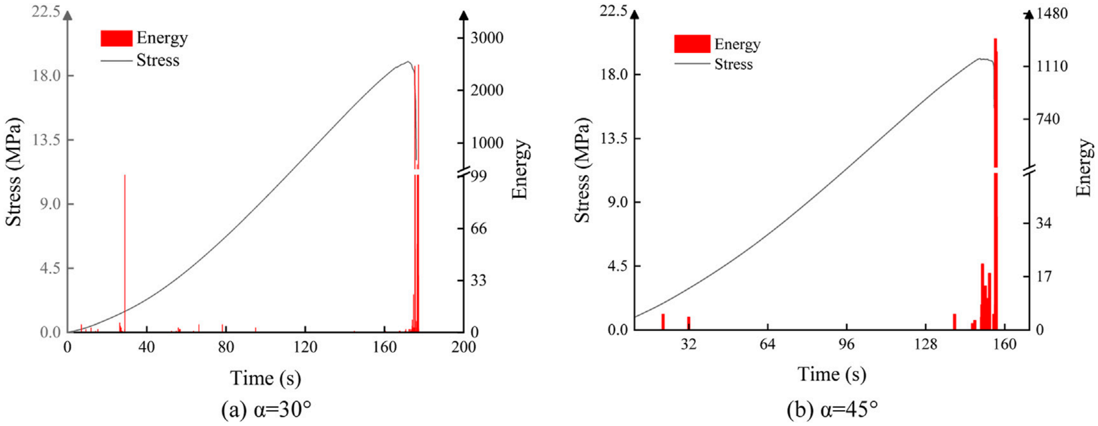

(a) α=30°

(b) α=45°

FIGURE 12
Relationship between axial stress-strain curve, acoustic emission times and time of a single fracture-hole rock specimen. **(A)** α = 30°, **(B)** α = 45°.

As shown in Figure 12B, when the fracture angle α was 45°, the peak stress of the rock specimen in the CD section was higher than that in Figure 12A, and the time for the rock specimen to reach the peak strength was also longer than that in Figure 12A under the continuous loading of axial pressure.

3.3.2 Digital image correlation image analysis

When the fracture angle of single fracture-hole rock specimen was 30°, the DIC characteristic diagram of the laboratory test was shown in Figure 13. Combined with Figure 12, the failure characteristics of the rock specimen with fracture angles were as follows.

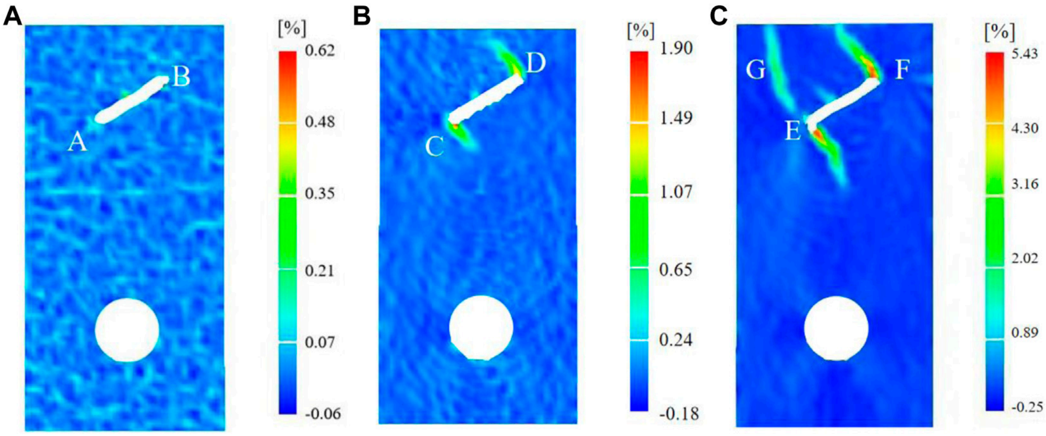

FIGURE 13
$\alpha = 30^{\circ}$ DIC feature map. **(A-C)**, the three stages of compression and densification, crack initiation, and damage are indicated, respectively.

As shown in Figure 13A, the stress concentration occurred at the fracture tip AB at the initial loading stage of the rock specimen, and the microfracture first occurs here, accompanied by a small amount of acoustic emission energy. With the continuous loaded of axial stress, as shown in Figure 13B, the fractures at both ends of the fracture extended in the opposite direction, the fractures at CD shown a trend of penetrating through the rock specimen, and the stress at both ends of the fracture was significantly increased compared with Figure 13A. With the continuous loading of the axial stress of the rock specimen, as shown in Figure 13C, the fractures at EF at both ends of the fracture gradually developed, and the trend of penetrating the rock specimen was more apparent. In addition, the fractures that penetrate rock specimen occurred at G, and the stress increases significantly. Based on the uniaxial compression test, the internal microfracture expanded rapidly and penetrated each other, and the energy value rose to about 2,500 in an instant.

When the fracture angle of a single fracture-hole rock specimen was 45°, the DIC characteristic diagram of the laboratory test was shown in Figure 14. As shown in Figure 14A, the stress concentration occurred at the fracture tip AB at the initial loading stage of the rock specimen, and the microfracture occurred here first, accompanied by a small amount of acoustic emission energy. With the continuous loading of axial stress, as shown in Figure 14B, the fractures at both ends of the fracture extended in the opposite direction, the fractures at CD shown a trend of the penetration through the rock

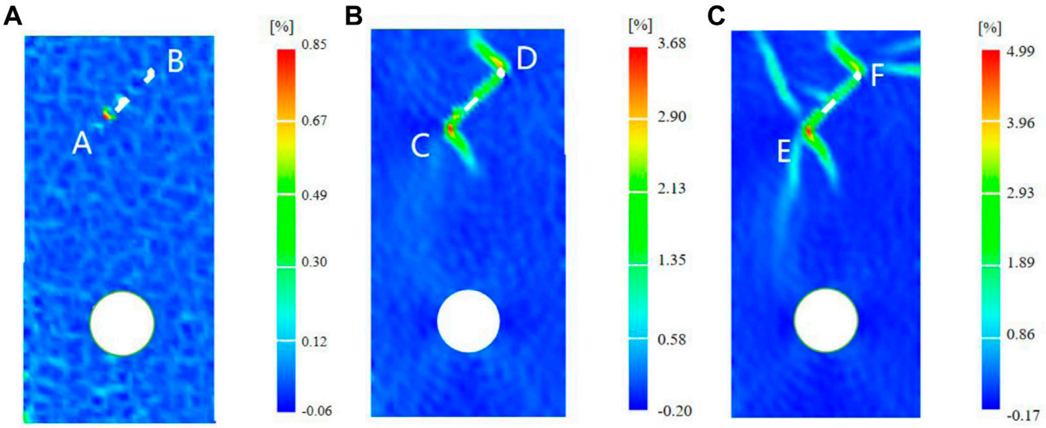

FIGURE 14
$\alpha = 45^{\circ}$ DIC feature diagram. **(A-C)**, the three stages of compression and densification, crack initiation, and damage are indicated, respectively.

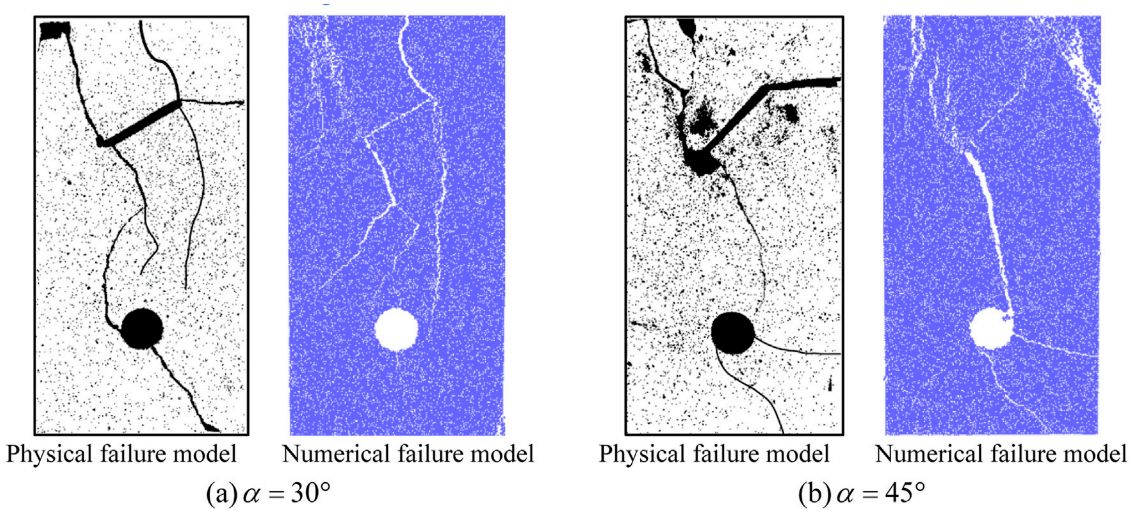

FIGURE 15
Failure diagram of a test and numerical model with fracture angles of 30° and 45°. **(A)** α = 30°, **(B)** α = 45°.

specimen, and the stress at both ends of the fracture was significantly increased compared to that in Figure 14A. On the other hand, with the continuous loaded of the axial stress of the rock specimen, as shown in Figure 14C, the fractures at EF at both ends of the fracture gradually developed and increased, the trend of penetrating the rock specimen became more apparent, and the stress increased significantly. With the uniaxial compression test, the internal microfracture expanded rapidly and penetrated each other, and the energy value increased to approximately 1,300 in an instant.

3.4 Comparison between the numerical simulation and laboratory tests

Combined with the results of the numerical simulation analysis in Section 2 and the laboratory test analysis in Section 3, the fracture angles of 30° and 45° in the numerical simulation were selected for the analysis. Figure 15 shown the comparison of the failure diagram of the laboratory test and the numerical model when the fracture angles were 30° and 45°. Based on Figure 15, the fracture development in the laboratory test and numerical simulation test started from the vicinity of the fracture. Then, the fracture gradually extended to both sides of the rock specimen as the axial loading pressure increases. The macroscopic failure characteristics of the laboratory test specimens with fracture angles of 30° and 45° were similar to those of the numerical simulation of the single fracture-hole rock model, as shown Figure 15.

4 Conclusion

In this study, we performed the uniaxial compression test of a single fracture-hole rock specimen with different fracture angles. Laboratory tests were analysed using acoustic emission and digital speckle. Simultaneously, PFC2D was used to establish a numerical model to analyse the mechanical properties, fracture propagation, and stress field evolution of a single fracture-hole rock specimen with different fracture angles. The major conclusion were as follows:

(1) In the laboratory test, a single fracture-hole rock specimen with fracture angles of 30° and 45° was selected for the test. The rock specimen experienced the compaction, elastic deformation, and plastic deformation stages after the auxiliary analysis of the acoustic emission and DIC until complete failure.
(2) Fractures with different angles had a great influence on the mechanical properties of the rock specimen. The peak strength, peak strain, elastic modulus, fracture initiation stress, and damage stress of the single fracture-hole rock specimen with different fracture angles were significantly smaller compared to those of the intact rock specimen.
(3) The results of the laboratory test and numerical simulations were good, and the macroscopic failure characteristics of the rock specimen were similar.
(4) The research on defect combination of different fracture angles around the hole could provided theoretical guidance for practical geotechnical engineering, such as prefabricated fractures in geotechnical engineering and pressure relief in coal mine drilling.

Data availability statement

The original contributions presented in the study are included in the article/Supplementary Material, further inquiries can be directed to the corresponding author.

Author contributions

NJ: conceptualization, methodology, investigation, formal Analysis, writing—original draft, laboratory test; KL: conceptualization, funding acquisition, resources, supervision, writing—review and editing, numerical simulation; ZG: resources, supervision; CJ: visualization, investigation; LY: visualization, writing—review and editing; SM: visualization; QS: writing—review and editing.

Funding

This work was supported by the Natural Science Foundation of China (Nos. 52004146, 52074169 and 52174159), the Shandong Provincial Natural Science Foundation (Nos. ZR2020QE102), the China Postdoctoral Science Foundation (2022M713386).

Conflict of interest

Author ZG was employed by Shandong Geology and Mineral Resources Engineering Group Co., Ltd.

The remaining authors declare that the research was conducted in the absence of any commercial or financial relationships that could be construed as a potential conflict of interest.

Publisher's note

References

Asadizadeh, M., Hossaini, M. F., Moosavi, M., Masoumi, H., and Ranjith, P. G. Mechanical characterisation of jointed rock-like material with non-persistent rough joints subjected to uniaxial compression. *Eng. Geol.*, 2019; 260:105224–105224. doi:10.1016/j.enggeo.2019.105224

Asadizadeh, M., Moosavi, M., and Hossaini, M. F. Investigation of mechanical behaviour of non-persistent jointed blocks under uniaxial compression. *Geomechanics Eng.*, 2018; 14(1):29–42. doi:10.12989/gae.2018.14.1.029

Bahaaddini, M., Sharrock, G., and Hebblewhite, B. K. Numerical investigation of the effect of joint geometrical parameters on the mechanical properties of a non-persistent jointed rock mass under uniaxial compression. *Comput. Geotechnics*, 2013; 49(20):206–225. doi:10.1016/j.compgeo.2012.10.012

Brantut, N., Heap, M. J., Meredith, P. G., and Baud, P. Time-dependent cracking and brittle creep in crustal rocks: A review. *J. Struct. Geol.*, 2013; 52(5):17–43. doi:10.1016/j.jsg.2013.03.007

Chen, M., Liu, J., Xie, Z., Liu, J., Cen, Y., Li, B., et al. Discrete element modeling on mechanical behavior of heterogeneous rock containing x-shaped fissure under uniaxial compression. *Geofluids*, 2020b; 2020(4):1–14. doi:10.1155/2020/8828199

Chen, S. J., Xia, Z. G., Feng, F., and Yin, D. W. Numerical study on strength and failure characteristics of rock samples with different hole defects. *Bull. Eng. Geol. Environ.*, 2020a; 80(7):1523–1540. doi:10.1007/s10064-020-01964-y

Chen, S. J., Zhang, J. C., Yin, D. W., Cheng, X. Z., and Ning, J. Relative permeability measurement of coal microchannels using advanced microchip technology. *Fuel*, 2021; 312:122633–633. doi:10.1016/j.fuel.2021.122633

Cheng, Y., Jiao, Y. Y., and Tan, F. Numerical and experimental study on the cracking behavior of marble with en-echelon flaws. *Rock Mech. Rock Eng.*, 2019; 52(11):4319–4338, doi:10.1007/s00603-019-01849-x

Cundall, P. A., and Strack, O. D. Discussion: A discrete numerical model for granular assemblies. *Geotechnique*, 1979; 29(1):331–336. doi:10.1680/geot.1980.30.3.331

Dai, B., Chen, Y., Zhao, G. Y., Liang, W. Z., and Wu, H. A numerical study on the crack development behavior of rock-like material containing two intersecting flaws. *Mathematics*, 2019; 7(12):1223. doi:10.3390/math7121223

Holt, R. M., Laas, J., Larsen, I., Li, L., Pillitteri, A. G., and Snsteb, E. F. Comparison between controlled laboratory experiments and discrete particle simulations of the mechanical behaviour of rock. *Int. J. Rock Mech. Min. Sci.*, 2005; 42(7-8):985–995. doi:10.1016/j.ijrmms.2005.05.006

Huang, Y., and Yang, S. Particle flow analysis on crack coalescence behavior of sandstone specimen containing three pre-existing fissures under uniaxial compression. *J. Basic Sci. Eng.*, 2016; 24(6):1232–1247. doi:10.16058/j.issn.1005-0930.2016.06.014

Lin, Q., Cao, P., Cao, R., Lin, H., and Meng, J. J. Mechanical behavior around double circular openings in a jointed rock mass under uniaxial compression. *Arch. Civ. Mech. Eng.*, 2020; 20(1):19–18. doi:10.1007/s43452-020-00027-z

Lin, Q., Cao, P., Meng, J. J., Cao, R. H., and Zhao, Z. Y. Strength and failure characteristics of jointed rock mass with double circular holes under uniaxial compression: Insights from discrete element method modelling. *Theor. Appl. Fract. Mech.*, 2020; 109:102692. doi:10.1016/j.tafmec.2020.102692

Lisjak, A., and Grasselli, G. A review of discrete modeling techniques for fracturing processes in discontinuous rock masses. *J. Rock Mech. Geotechnical Eng.*, 2014; 6(4):301–314. doi:10.1016/j.jrmge.2013.12.007

Liu, J. M., Sun, S. R., Yue, L., Wei, J. H., and Wu, J. M. Mechanical and failure characteristics of rock-like material with multiple crossed joint sets under uniaxial compression. *Adv. Mech. Eng.*, 2017; 9(7):168781401770871. doi:10.1177/1687814017708710

Lu, W. B., Zhu, Z. D., He, Y. X., and Que, X. C. Strength characteristics and failure mechanism of a columnar jointed rock mass under uniaxial, triaxial, and true triaxial confinement. *Rock Mech. Rock Eng.*, 2021; 54, 2425, 2439(3). doi:10.1007/s00603-021-02400-7

Ma, J. B., Jiang, N., Wang, X., Wang, X. J., Jia, X. D., and Yao, D. H. Numerical study of the strength and characteristics of sandstone samples with combined double hole and double fissure defects. *Sustainability*, 2021; 13, 7090(13). doi:10.3390/su13137090

Pan, X., Guo, W., Wu, S., and Chu, J. An experimental approach for determination of the weibull homogeneity index of rock or rock-like materials. *Acta Geotech.*, 2019; 15(2):375–391. doi:10.1007/s11440-019-00803-z

Qi, X. H., Wang, H., Chu, J, and Chiam, K. Two-dimensional prediction of the interface of geological formations: A comparative study. *Tunnelling And Underground Space Technology*, 2022;104329 121. doi:10.1016/j.tust.2021.104329

Sqy, A., Pgra, B., Hwj, A., Wlt, A., and Yang, J. A. An experimental investigation on thermal damage and failure mechanical behavior of granite after exposure to different high temperature treatments. *Geothermics*, 2017; 65:180–197. doi:10.1016/j.geothermics.2016.09.008

Wang, Y. T., Zhou, X. P., and Kou, M. M. Three-dimensional numerical study on the failure characteristics of intermittent fissures under compressive-shear loads. *Acta Geotech.*, 2018; 101:1161–1193. doi:10.1007/s11440-018-0709-7

Wu, H., Chen, Y., Zhao, G., and Liang, W. A numerical study on the crack development behavior of rock-like material containing two intersecting flaws. *Mathematics*, 2019; 7(12):1223. doi:10.3390/math7121223

Wu, Z., Fan, L., Liu, Q., and Ma, G. Micro-mechanical modeling of the macro-mechanical response and fracture behavior of rock using the numerical manifold method. *Eng. Geol.*, 2016; 225. 49, 60, doi:10.1016/j.enggeo.2016.08.018

Yang, S. Q., and Jing, H. W. Strength failure and crack coalescence behavior of brittle sandstone samples containing a single fissure under uniaxial compression. *Int. J. Fract.*, 2011; 168(2):227–250. doi:10.1007/s10704-010-9576-4

Yang, Y. T., Tang, X. H., Zheng, H., Liu, Q. S., and He, L. Three-dimensional fracture propagation with numerical manifold method. *Eng. Analysis Bound. Elem.*, 2016; 72:65–77. doi:10.1016/j.enganabound.2016.08.008

Yin, D. W., Wang, F., Zhang, J. C., Li, F. X., Zhu, C., and Feng, F. Experimental study on the short-term uniaxial creep characteristics of sandstone-coal composite samples. *Minerals*, 2021; 11, 1398(12). doi:10.3390/min11121398

Zhang, D., Ranjith, P. G., and Perera, M. The brittleness indices used in rock mechanics and their application in shale hydraulic fracturing: A review. *J. Petroleum Sci. Eng.*, 2016; 143:158–170. doi:10.1016/j.petrol.2016.02.011

Zhang, J. C., Si, L. L., Chen, J. G., Kizil, M. S., Wang, C. G., and Chen, Z. W. Stimulation techniques of coalbed methane reservoirs. *Geofluids*, 2020, 2020; (3): 1–23. doi:10.1155/2020/5152646

Zhang, J. C., and Yin, S. X. Some technologies of rock mechanics applications and hydraulic fracturing in shale oilshale gas and coalbed methane. *Meitan Xuebao/Journal China Coal Soc.*, 2014; 39(8):1691–1699(9). doi:10.13225/j.cnki.jccs.2014.9004

Zhang, S., Li, Y., Shen, B., Sun, X., and Gao, L. Effective evaluation of pressure relief drilling for reducing rock bursts and its application in underground coal mines. *Int. J. Rock Mech. Min. Sci.*, 2019; 114:7–16. doi:10.1016/j.ijrmms.2018.12.010

Zhang, X. P., and Wong, L. N. Y. Cracking processes in rock-like material containing a single flaw under uniaxial compression: A numerical study based on parallel bonded-particle model approach. *Rock Mech. Rock Eng.*, 2012; 45(5): 711–737. doi:10.1007/s00603-011-0176-z

Zhao, Y. L., Wang, Y. X., Wang, W. J., Tang, L. M., Liu, Q., and Cheng, G. M. Modeling of rheological fracture behavior of rock cracks subjected to hydraulic pressure and far field stresses. *Theor. Appl. Fract. Mech.*, 2019; 101:59–66. doi:10.1016/j.tafmec.2019.01.026

Zhou, S. W., Zhuang, X. Y., and Rabczuk, T. Phase field modeling of brittle compressive-shear fractures in rock-like materials: A new driving force and a hybrid formulation. *Comput. Methods Appl. Mech. Eng.*, 2019; 355(1):729–752. doi:10.1016/j.cma.2019.06.021

frontiers | Frontiers in Earth Science

TYPE Original Research
PUBLISHED 17 January 2023
DOI 10.3389/feart.2022.1089957

A comprehensive insight into the effects of acidification on varied-sized pores in different rank coals

Peiwen Jiang[1], Chengtao Yang[2]*, Feng Chen[1], Bing Li[1], Jiangang Ren[1], Jianbao Liu[1] and Zhimin Song[1,3]*

[1]School of Environmental and Bioengineering, Henan University of Engineering, Zhengzhou, China, [2]Institute of Henan Energy and Chemical Industry Group Co, Ltd, Zhengzhou, China, [3]School of Geosciences and Engineering, North China University of Water Resources and Electric Power, Zhengzhou, China

Elucidating the evolution law of coal pore structure under acidification is crucial for guiding the practical application of acidizing technology and improving the production of coalbed methane. To comprehensively investigate the influence of acidification on varied-sized pores in different rank coals, in this study, fat coal, meagre coal and anthracite coal were collected and acidified with a mixed solution composed of hydrochloric acid (9 wt%) and hydrofluoric acid (3 wt%). An approach integrating low-pressure CO_2 adsorption (LPGA-CO_2), low-temperature N_2 adsorption (LTGA-N_2) and Mercury intrusion porosimetry (MIP) was adopted to fully characterize the varied-sized pore structure before and after acidification to eliminate the limitations of single method. The results demonstrated that acid treatment improved the pore opening degree and connectivity in coal, but had essentially no effect on the pore shape. After acidification, all the coal samples showed significant increases in the porosity and total pore volume, which was mainly contributed by the numerous newly formed large mesopores and macropores, especially the macropores (with an average contribution rate of 74.59%). Taken as a whole, acid treatment had the largest impact on macropores, followed by mesopores, and the smallest impact on micropores. In addition, the variation trend of total specific surface area (SSA) under acidification was primarily determined by micropores. For the three different rank coals selected in this study, the total SSA of fat coal (PM) was more easily affected by acidification and had the largest percentage increase after acid treatment, followed by anthracite coal (YM), while that of meagre coal (LA) decreased slightly. This difference was driven primarily by the different variation trend of micropore SSA in different rank coals. After acidification, the SSA of ultra-micropores and super-micropores all increased in fat coal (PM) and anthracite coal (YM), whereas for meagre coal (LA), although ultra-micropores SSA increased, super-micropores SSA decreased, which ultimately led to the slight decrease of its micropore SSA. Moreover, the total pore volume increment of coal was closely related to the macropore volume increment under acidification, but not significantly related to the coal maturity,which might indicate that, compared with coal rank, the mineral content in coal might be a more important consideration when measuring the applicability of acidification technology.

EDITED BY
Hongtu Zhang,
Henan Polytechnic University, China

REVIEWED BY
Gang Xu,
Xi'an University of Science and Technology, China
Quangui Li,
Chongqing University, China

*CORRESPONDENCE
Chengtao Yang,
byctat@163.com
Zhimin Song,
songzhimin1961@hotmail.com

SPECIALTY SECTION
This article was submitted to Economic Geology, a section of the journal Frontiers in Earth Science

RECEIVED 04 November 2022
ACCEPTED 24 November 2022
PUBLISHED 17 January 2023

CITATION
Jiang P, Yang C, Chen F, Li B, Ren J, Liu J and Song Z (2023), A comprehensive insight into the effects of acidification on varied-sized pores in different rank coals.
Front. Earth Sci. 10:1089957.
doi: 10.3389/feart.2022.1089957

KEYWORDS

acidification, different rank coals, varied-sized pores, pore structure evolution, gas adsorption, mercury intrusion porosimetry

1 Introduction

Coal-bed methane (CBM) drainage is an effective technical means by which to prevent coal and gas outbursts, and it is also the practical demand for China to establish a new energy system under the goal of "double carbon" (Wang et al., 2014; Jiang et al., 2022). The exploitation of CBM is a continuous dynamic process, including desorption of CBM from the pore surface, diffusion from pores to fractures, and then seepage from fractures to the rockshaft (Tan et al., 2018; Li L. et al., 2020). Therefore, well-developed pore and fracture network is essential for the fast and efficient gas extraction (Liu et al., 2023). However, for coal seams with high mineral content, the pores and fractures are often blocked by minerals (such as calcite, kaolinite and pyrite), which seriously hampers the desorption and migration of CBM (Chen S. et al., 2021). Aiming at this problem, many studies have demonstrated that acidizing treatment can effectively remove the minerals and link the blocked channels (Turner and Steel, 2016; Wang et al., 2020; Chen Q. et al., 2021; Guo et al., 2021). Therefore, it is crucial to elucidate the pore structure evolution characteristics of coal under acidification for guiding the practical application of acidification technology and improving the production of CBM.

In recent years, many scholars have performed studies on the variation of coal pore structure under acidification. In these studies, the pore structure was commonly characterized by nuclear magnetic resonance (NMR), scanning electron microscopy (SEM), gas adsorption method (GA), and high-pressure Mercury intrusion (MIP) (Zhang et al., 2016; Zhao et al., 2018; Li S. et al., 2020; Ni et al., 2020; Wang et al., 2020; Liu et al., 2021; Xie et al., 2021; Yi et al., 2021). For example, Ni et al. explored the changes in pore structure under nitric acid treatment by SEM and LTGA-N_2. They found that nitric acid treatment could enlarge the pores in coal and increase the pore openness (Ni et al., 2020). Zhang et al. launched the acidification experiment of coal with acetic acid and hydrochloric acid, and characterized the pore structure by LTGA-N_2. The results showed that acid treatment made pores more complicated, and less aliphatic structure and more aromatic structure predicted more micropores (Zhang et al., 2016). In the work reported by Xie et al., SEM was used to qualitatively evaluate the changes in surface morphological characteristics caused by acetic acid acidification, and the combination of MIP and LTGA-N_2 methods was used to quantitatively analyze the overall evolution characteristics of pore structure. They found that acidification helped to form cylinders pores and parallel plates pores, thus improving the pore connectivity (Xie et al., 2021). Taking acid solution with different components as treatment agents, Li et al. carried out NMR and SEM tests on the raw and acidified coal samples and explored the pore evolution characteristics, showing that different acid solutions affected macropores (1–100 μm), mesopores (0.1–1 μm) and micropores (<0.1 μm) differently (Li S. et al., 2020). Zhao et al. analyzed the change of pore structure under the treatment of hydrofluoric acid and hydrochloric acid using LTGA-N_2, finding that acidification had a more pronounced effect on pores below 10 nm (Zhao et al., 2018). Yi et al. treated coal samples with hydrochloric acid, and used LTGA-N_2 and LPGA-CO_2 to characterize the pore structure. The results showed that, with increasing acid concentration, the volume of small mesopores and macropores showed a consistently increasing trend. However, the volume of large mesopores showed first a decrease and then an increase, and the variation trend of micropore volume was uncertain (Yi et al., 2021).

From previous relevant researches, we can see that various advanced techniques have been employed to analyze the changes of coal pore structure under acidification. Nevertheless, due to the limitation of the testing principle, these studies can only detect pore structure characteristics within a specific range of pore size (Zhang et al., 2017; Liu X. et al., 2019; Wei et al., 2019; Qin et al., 2020; Lu et al., 2021; Mou et al., 2021). For example, neither LTGA-N_2 nor MIP can accurately characterize pores with diameters below 2 nm, which is attributed to the extremely slow nitrogen diffusion rate under low pressure and the limitation of the maximum mercury intrusion pressure (Mou et al., 2021). The approach combining LTGA-N_2 and LPGA-CO_2 enables the accurate characterization of micropores and mesopores, but not micron-sized macropores (Jagiello et al., 2019; Yi et al., 2021). However, pores with different sizes all play an important role in methane migration, among which micropores exert a great influence on methane adsorption capacity, and mesopores and macropores provide channels for methane diffusion and seepage (Tan et al., 2018). Thus, a characterization of full-sized coal pore structure before and after acid treatment is necessary to accurately reveal the mechanism of enhanced CBM production and improve the CBM extraction efficiency. Moreover, few studies have involved the differences in pore structure evolution between different coal ranks under acidification.

Based on the above analysis, in this study, different rank coals were acidified with hydrochloric acid and hydrofluoric acid. In order to eliminate the limitations of single method, an approach integrating LPGA-CO_2, LTGA-N_2 and MIP was performed to analyze the pore structure of raw and acidified coal samples. First, the pore structure of raw and acidified coals was respectively characterized using the three methods mentioned above. Then, the accurate full-sized pore structure parameters were obtained by intercepting the data of the three test methods in their optimal performance intervals, and the full-sized pore distribution curves were plotted. On this basis, the varied-sized pore evolution characteristics of different rank coals under acidification was investigated by comparing and analyzing the variation of micro-, meso-, and macropore structure characteristics, such as specific surface area (SSA), pore size distribution, as well as pore volume. At the same time, changes in pore morphological characteristics such as pore shape and pore connectivity caused by acidification were also discussed. This work aimed to provide a useful theoretical reference for the application of acidizing technology, which is of great practical significance for guiding the efficient exploitation of CBM and preventing gas outburst disasters.

2 Materials and methods

2.1 Samples and acidification

The three experimental coal samples with different ranks were respectively fat coal from Mine No.11 of Pingdingshan coal mine (PM), meagre coal from Lu'an coal mine (LA), and anthracite coal from Mine Chensilou of Yongcheng coal mine (YM). The first two kinds of coal belonged to middle-rank coal, and the last one belonged to high-rank coal. The samples came from the same coal seam and area to minimize the extrinsic effects of coal heterogeneity. The three types of coal samples were pulverized and sieved into two particle sizes: 0.18–0.25 mm for the LPGA-CO_2 and LTGA-N_2 tests, and 3–6 mm for the MIP test. Half of the grinded samples were soaked in acid solution for 24 h at room temperature, and then filtered. Next, the acidified coal samples were repeatedly washed until the pH was close to neutral, and then dried at 105°C for 12 h. The untreated coal samples were marked as PM-0, LA-0 and YM-0, and the corresponding acidified samples were marked as PM-1, LA-1 and YM-1, respectively.

In this research, an acid solution consisting of hydrochloric acid (9 wt%), hydrofluoric acid (3 wt%) and potassium chloride (2 wt%) was used for acid treatment. In this solution, the hydrochloric acid was used to dissolve carbonate minerals, hydrofluoric acid to remove silicate minerals, and potassium chloride to prevent pore plugging caused by swelling of clay minerals in water.

2.2 Test apparatus and methods

The low-pressure CO_2 adsorption test (LPGA-CO_2) was conducted on a Micromeritics ASAP 2020 instrument. The theoretical basis of this method was that CO_2 can be physically adsorbed on the solid surface at saturation temperature. The coal's micropore structure parameters, including pore size distribution, SSA, and pore volume were deduced and analyzed from the CO_2 adsorption isotherms obtained at 273.15 K, using density functional theory (DFT). The low-temperature N_2 adsorption test (LTGA-N_2) was carried out on a surface area analyzer (Micromeritics ASAP 2460) to characterize the mesopore structure. The LTGA-N_2 measurement took nitrogen as the probe molecule, and its testing principle was similar to that of LPGA-CO_2. The N_2 adsorption isotherms were recorded at 77 K. Then, the adsorption branch data of isotherms were processed using Barrett–Joyner–Halenda (BJH) theory, and the structural parameters of mesopore were calculated and analyzed. The Mercury intrusion porosimetry (MIP) test was conducted on an automatic mercury injection apparatus (Microactive Auto Pore V9600, United States). The range of mercury intrusion pressure was 0.1–60000 psia, and the test range of aperture was 3.5 nm to 1,000 μm. During the testing process, mercury injection volumes at different pressures were recorded to acquire the intrusion curves and extrusion curves. The pore size distribution, pore volumes, SSA, and porosities were calculated according to the correspondence between the pore diameter and the injection pressure. In this study, the pores in coal were classified following the relevant scheme recommended by International Union of Pure and Applied Chemistry (IUPAC), which divided pores into macropores (above 50 nm), mesopores (2–50 nm), and micropores (below 2 nm), with the micropores further divided into ultra-micropores (below 0.7 nm) and super-micropores (0.7–2.0 nm) (Thommes and Cychosz, 2014; Thommes et al., 2015).

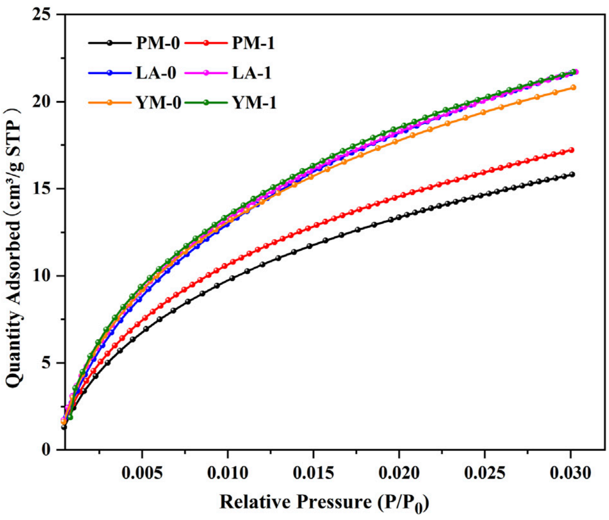

FIGURE 1
LPGA-CO_2 adsorption isotherms of the raw and acidified coal samples.

TABLE 1 Micropore structural parameters of the raw and acidified coal samples from the LPGA-CO_2 measurement[a].

Sample	Acidification	Pore volume (10^{-3} cm^3/g)			Pore specific surface area (m^2/g)		
		V_{ultra}	V_{super}	V_{mic}	S_{ultra}	S_{super}	S_{mic}
PM-0	pre-	15.14	5.99	21.13	54.12	14.70	68.82
PM-1	post-	17.05	7.60	24.65	61.67	15.77	77.44
LA-0	pre-	20.62	10.42	31.04	74.39	25.25	99.64
LA-1	post-	21.59	8.58	30.17	78.31	20.04	98.35
YM-0	pre-	22.59	9.75	32.34	76.99	22.18	99.17
YM-1	post-	23.91	10.46	34.37	82.55	24.89	107.44

[a]Note: According to the IUPAC classification, V_{mic}, V_{ultra}, and V_{super} refer to the volume of total micropores (below 2 nm), ultra-micropores (below 0.7 nm), and super-micropores (0.7–2 nm), respectively. S_{mic}, S_{ultra}, and S_{super} refer to the specific surface area of total micropores (below 2 nm), ultra-micropores (below 0.7 nm), and super-micropores (0.7–2 nm), respectively.

3 Results and discussion

3.1 Micropore evolution characteristics (<2 nm)

The LPGA-CO_2 isotherms of the raw and acidified coal samples are presented in Figure 1. We can see that the shapes of the CO_2 adsorption curves were similar to the low-pressure region of Langmuir isotherm, indicating the existence of abundant open micropores. With increasing adsorption pressure, the CO_2 adsorption quantity increased rapidly at P/P_0 of 0–0.01, then slowed down when the relative pressure was greater than 0.01. The respective maximum CO_2 adsorption quantities of PM-0, LA-0, and YM-0 were 15.81, 21.63, and 20.81 cm^3/g, which showed an overall upward trend with increasing metamorphism. After acidification, the maximum CO_2 adsorption quantities of PM and YM increased significantly, while that of LA showed little change. To explore the possible reasons for this difference, the changes of ultra-micropores (below 0.7 nm) and super-micropores (0.7-2.0 nm) were discussed in more detail below.

Table 1 shows the corresponding micropore structural parameters. We can see that for PM and YM, the volumes and areas of ultra-micropore and super-micropore all showed an increasing trend after acidification. However, for LA, the volume and area of ultra-micropore increased while that of super-micropore decreased. These two opposite changes caused the total micropore volume and total micropore SSA of LA to slightly decreased. It can be seen from the analysis of Figure 1 and Table 1 that for coal samples of different ranks, the volume and SSA of ultra-micropores after acidification all increased, while that of super-micropores might increase or decrease. In other words, acid treatment can facilitate the development of ultra-micropores, but it had a two-sided effect on the change of super-micropores. Based on this analysis, it can be inferred that the simultaneous effect of acidification on ultra-micropore and super-micropore changes might lead to an increase in the total micropore volume and total micropore SSA in different coals, or no obvious change, or even decrease.

Figure 2 illustrates the micropore volume distribution and micropore area distribution of the raw and acidified coal samples. In this study, the actual pore size range tested by LPGA-CO_2 was 0.33–1.1 nm, which was determined by the kinetic diameter of CO_2 and the maximum relative pressure limit of CO_2 in this method (Thommes and Cychosz, 2014). We can see that these two types of distribution curves were highly similar in morphology, which was attributed to the micropore filling mechanism in the carbon dioxide adsorption process. All the curves appeared to be bimodal distribution and can be divided into ultra-micropore region and super-micropore region with 0.7 nm as the demarcation point. The pores with a diameter of 0.55 and 0.85 nm were the most probable ones, which meant that pores with these two diameters had the largest contribution to the micropore SSA and volume. After acidification, for the medium rank coals (PM and LA), the multiple peaks in the ultra-micropore range of raw coal samples tended to merge into a broad peak, suggesting a more uniform distribution of ultra-micropores in acidified coal samples. Contrarily, for high rank coal (YM), the two peaks in the ultra-micropore range were clearly separated after acidification, accompanied by an increase in peak value and a decrease in peak width, and the peak at 0.55 nm obviously moved to the left. These phenomena indicated that acid treatment reduced the ultra-micropore diversity of high rank coal and produced numerous smaller ultra-micropores. In other words, after acid treatment, the ultra-micropore structure of high rank coal was more regular. For pores in the super-micropore range, the main peak of all the raw and acidified samples was located at 0.85 nm, suggesting that acid treatment only changed the number of super-micropores without altering the super-micropore diameter.

3.2 Mesopore evolution characteristics (2–50 nm)

Figure 3 gives the N_2 adsorption isotherms obtained from the LTGA-N_2 measurement. According to the latest classification

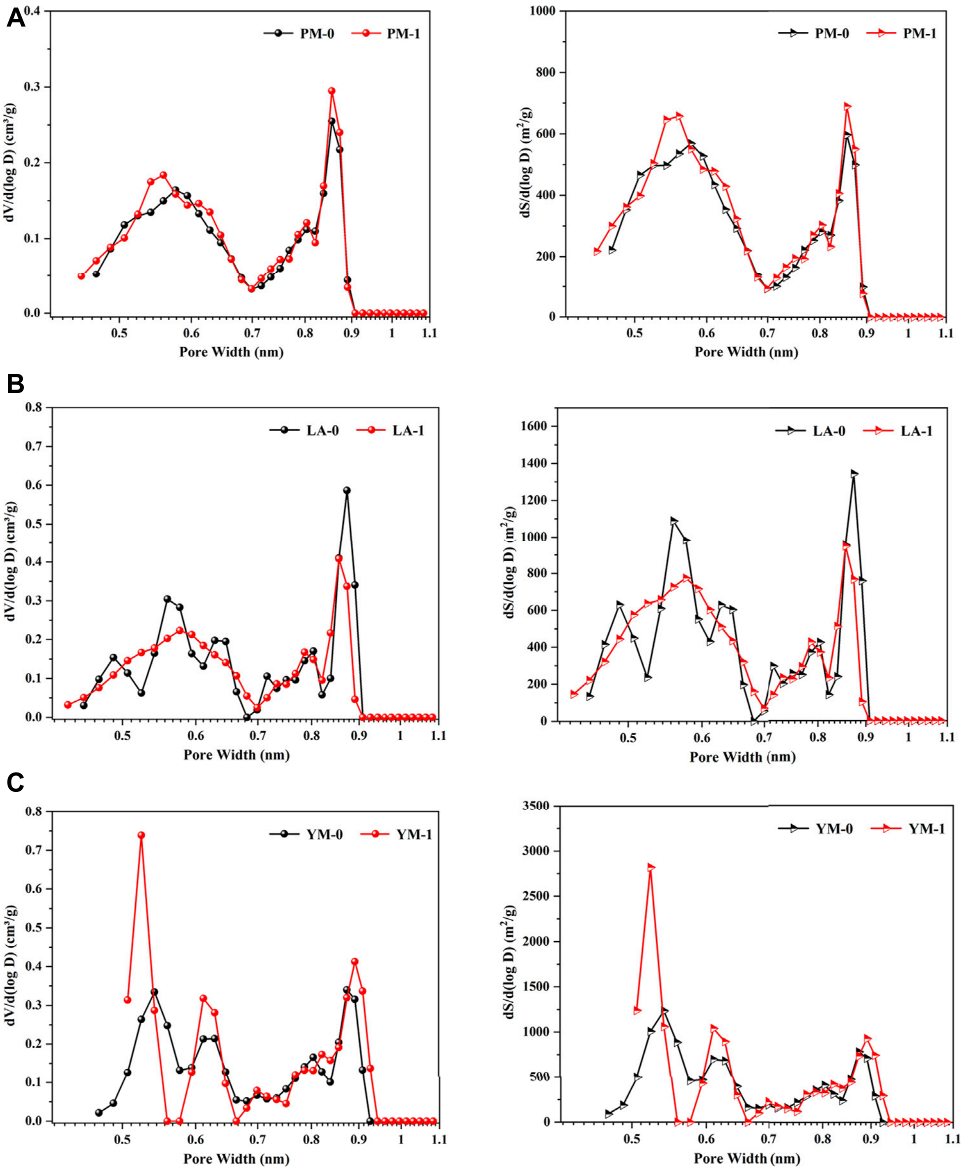

FIGURE 2
Micropore volume distribution curves and micropore area distribution curves from the LPGA-CO_2 measurement: **(A)** PM; **(B)** LA; **(C)** YM.

method of adsorption isotherm recommended by IUPAC, all the curves presented features as follows: type IV (a) in the low relative pressure interval and type II in the high relative pressure interval, which indicated that the studied coal samples were multi-scale porous aggregates with micropores, mesopores and macropores (Jin et al., 2016). After the acid treatment, the adsorption curves of LA-1 and YM-1 showed a sharp rise when the relative pressure was greater than 0.8, which corresponded to the multilayer adsorption process of macropores, indicating that acidification significantly contributed to the generation of larger pores (Guo et al., 2019). Moreover, it was considered that the type and size of hysteresis loops could provide information about the shape and openness of pores in coal (Ni et al., 2020). Based on the classification criteria of hysteresis loop type of the IUPAC, all the raw coal samples presented the hysteresis loop of type H3, suggesting the presence of quantities of narrow slit-shaped mesopores. In addition, the size of hysteresis loops in raw coal samples were relatively small, which meant the existence of numerous semi-closed or closed pores with poor connectivity. After acidification, the size of the hysteresis loop obviously increased while the shape remained basically the same, which suggested that acid treatment could improve the pore opening degree significantly, but not affect the pore type.

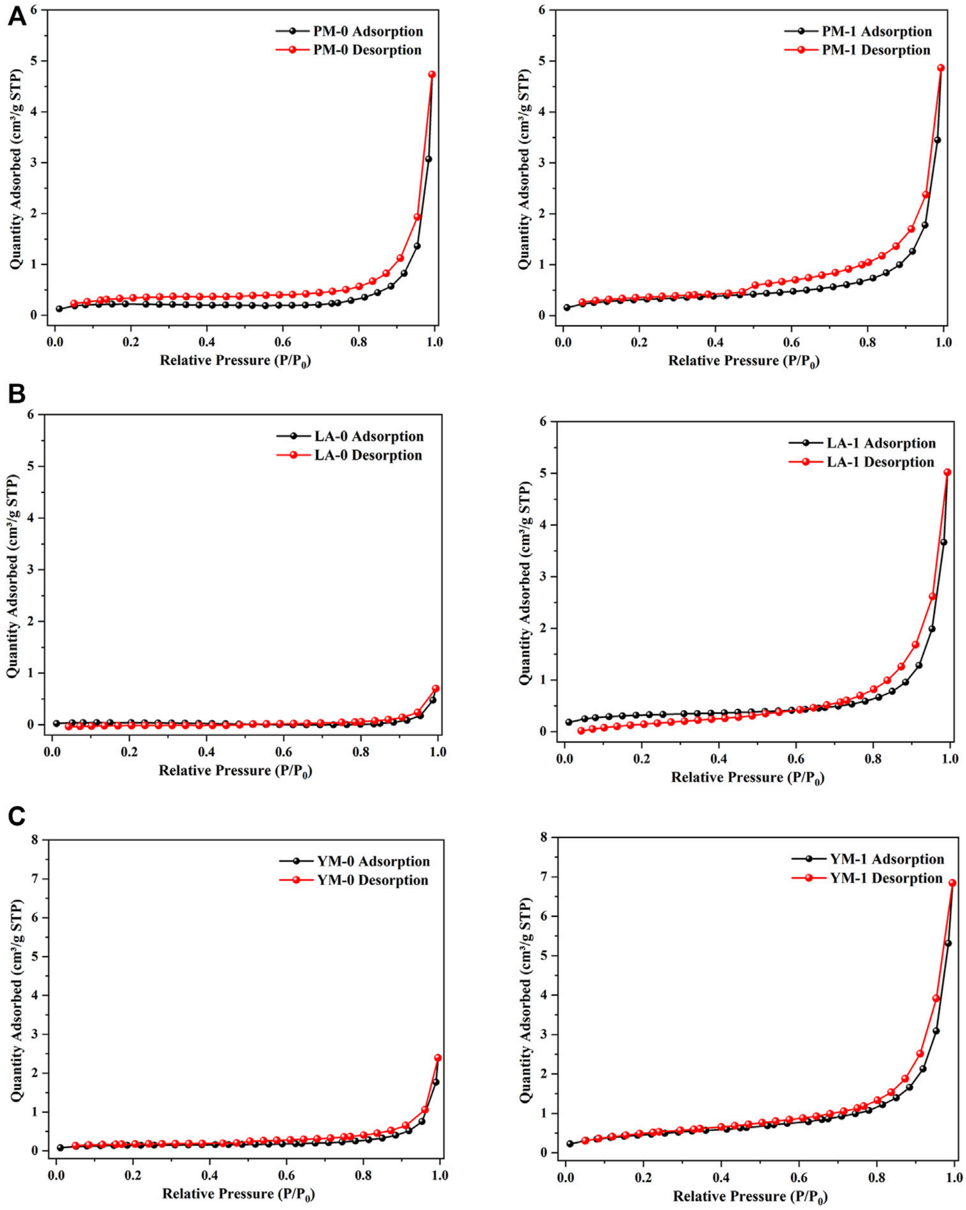

FIGURE 3
LTGA-N_2 adsorption isotherms of the raw and acidified coal samples: **(A)** PM; **(B)** LA; **(C)** YM.

The maximum N_2 adsorption quantities of LA-1 and YM-1 were 5.02 and 6.85 cm^3/g, respectively, which showed a notable increase compared with that of the corresponding raw coal. In contrast, the N_2 adsorption quantity of PM-1 was only a little higher than that of the raw coal. These findings suggested that acidification can significantly improve the nitrogen adsorption capacity of meagre coal and anthracite coal, but had little effect on that of fat coal. The mesopore structural parameters obtained by the LTGA-N_2 measurement are listed in Table 2. After being treated with acid, the mesopore volume of all the experimental samples increased, especially for LA and YM. Specifically, the mesopore volumes of PM, LA, and YM increased from 0.00724, 0.00108, and 0.00265 cm^3/g to 0.00803, 0.00763, and 0.01054 cm^3/g, respectively. The SSA of mesopores also showed an increasing trend after acidification. From the above analysis, we can see that acid treatment helped to enrich the pores in coal and improve the pore openness, which played a reinforcing role for the diffusion and migration of CBM.

Figure 4 gives the mesopore volume distribution curves and mesopore area distribution curves of the raw and acidified samples. It was clear that for raw meagre coal (LA-0) and raw anthracite coal

TABLE 2 Mesopore structural parameters of the raw and acidified coal samples from the LTGA-N_2 measurement.

Sample	Acidification	Mesopore volume (10^{-3} cm^3/g)	Mesopore specific surface area (m^2/g)
PM-0	pre-	7.24	0.83
PM-1	post-	8.03	1.09
LA-0	pre-	1.08	0.17
LA-1	post-	7.63	1.17
YM-0	pre-	2.65	0.51
YM-1	post-	10.54	1.69

(YM-0), the mesopore volume distribution curves were largely coincided with the baseline in the range of less than 10 nm, and then showed a slowly rising trend with the increase of pore diameter. This phenomenon indicated that the mesopores of these two raw coal samples were poorly developed, with only a few large mesopores with diameters greater than 10 nm. After being treated with acid, the pore volume distribution density (dV/d (log D)) increased rapidly with increasing pore diameter in the range of greater than 10 nm, and several small peaks presented within diameters less than 10 nm. From an overall perspective, the increase of the pore volume distribution density of large mesopores was more significant under acid treatment, which suggested that the expansion of mesopores in meagre coal and anthracite coal by acidification was primarily reflected in the increase of large mesopores. Additionally, although the pore volume distribution of PM was largely unchanged during the acid treatment, the peak value increased. The above phenomena indicated that substantial mesopores, especially large mesopores, were generated or exposed during the acid treatment. From the pore area distribution curves, we can see that the large mesopores contributed most of the SSA of mesopores, which further confirmed the significant promotion of acid treatment on the development of the large mesopores.

3.3 Macropore evolution characteristics (>50 nm)

The MIP intrusive and extrusive curves of the untreated and acid-treated coal samples are shown in Figure 5. As a comprehensive reflection of the pore structure, the shape of the curve contains features of the pore type and pore connectivity. The cumulative intrusion volume represents the volume of effective pores, including the semi-closed pores and open pores (Wang et al., 2015). The volume of semi-closed pores is considered equal to the cumulative extrusion volume. That is, the volume difference obtained by subtracting the cumulative extrusion volume from the cumulative intrusion volume can be considered as the volume of open pores (Wang et al., 2020). Additionally, pore type and connectivity can be determined according to the hysteresis loop characteristics. Coal with abundant open pores would have an obvious hysteresis loop, while that with few open pores would not (Guo et al., 2019). Generally, large hysteresis loops and great differences between the volume of Mercury intrusion and Mercury extrusion suggest a high fraction of open pores and excellent pore connectivity (Chen et al., 2012). From Figure 5, we can see that all the coal samples had hysteresis loops, suggesting that there were both open pores and semi-closed pores in coal. After acidification, the cumulative intrusion volume of all the coal samples increased significantly while the cumulative extrusion volume changed little. This indicated that a large number of effective pores, mainly open pores, were produced during the acidification process. The more pronounced hysteresis loops of the three acid-treated coal samples further proved a higher proportion of open pores and a better pore connectivity after acidification. This conclusion was consistent with that obtained by LTGA-N_2 measurement. These findings all suggested that many invalid pores were transferred into open pores or semi-closed pores under the action of acid etching, which favored the diffusion and migration of CBM.

Table 3 lists the pore structural parameters obtained from the MIP measurement. We can see that the mesopore data from MIP measurement was significantly larger compared to that from LTGA-N_2 measurement, which might be due to the coal compression effect under high pressure (Li et al., 2021). This finding further proved the limitation of MIP method in the characterization of mesopores. Besides, the interparticle pores effect under low pressure may lead to overestimation of the macropore size and volume in MIP measurement. For the sake of accuracy, we focused analysis on the pore characteristics with aperture between 50 nm and 60 μm, and the data below 50 nm were for reference only (Li et al., 2021). It can be seen from Table 3 that, for the raw coal samples, the macropore volumes ranged from 0.02087 to 0.02386 cm^3/g, accounting for 51.64%–53.68% of the total volumes. After being treated with acid, the volumes of mesopore and macropore all showed an increasing trend, but the increased amplitudes of macropore volume was obviously larger than that of mesopore volume. Specifically, the mesopore volumes of PM, LA, and YM increased by 21.15%, 2.01%, and 0.27%, respectively, while the macropore volumes increased by 63.11%, 197.74%, and 54.82%, respectively. This indicated that the effect of acidification on macropores was far

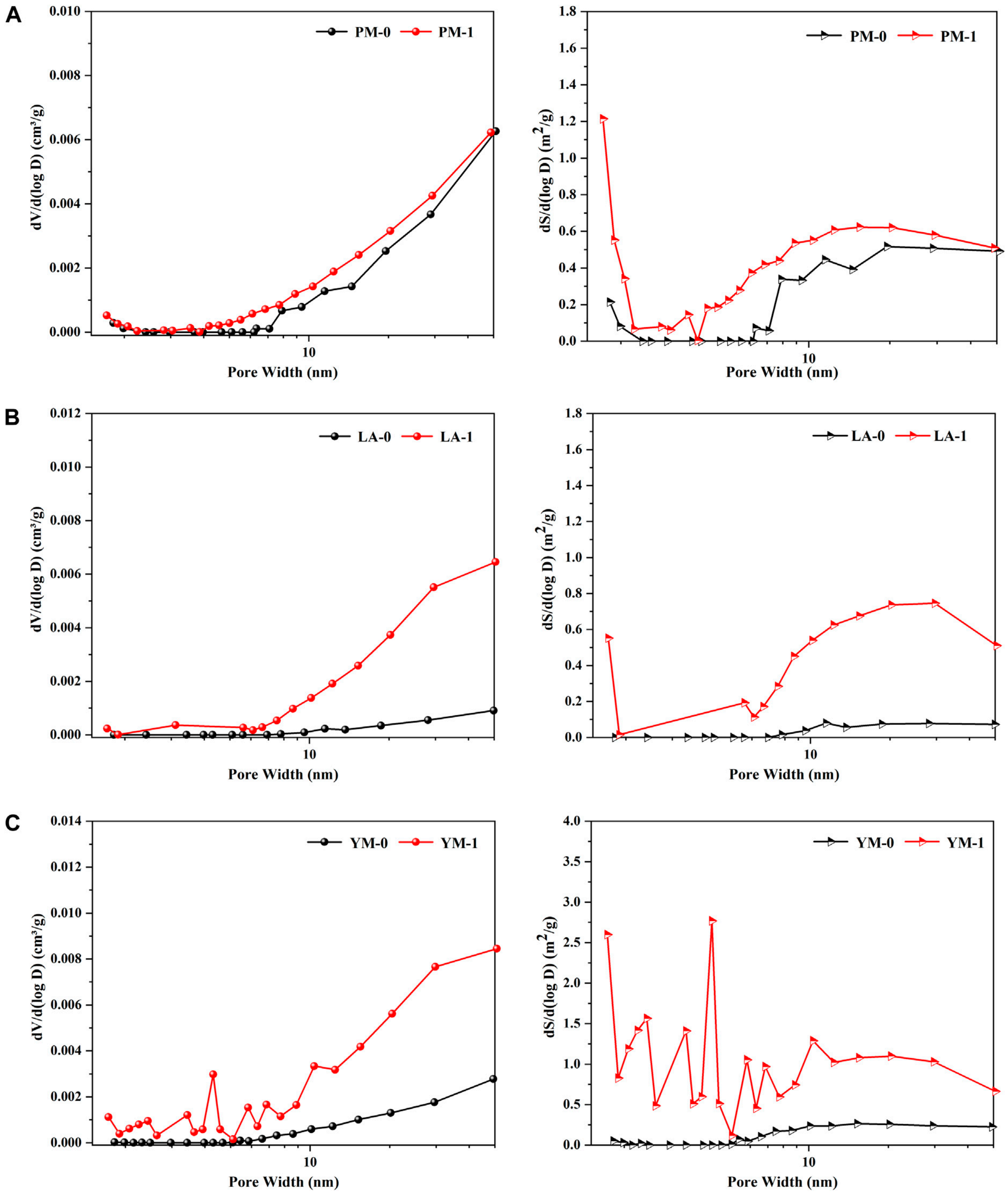

FIGURE 4
Mesopore volume distribution curves and mesopore area distribution curves from the LTGA-N_2 measurement: **(A)** PM; **(B)** LA; **(C)** YM.

more significant than that on mesopores. Additionally, due to the negligible role of macropores in contributing total SSA, although macropores were obviously developed under acidification, the total SSA changed little.

Figure 6 exhibits the pore volume distribution curves and the pore area distribution curves obtained from Mercury injection test. For the three raw coals, peaks in the macropore interval were mainly concentrated in diameters over 10 μm, illustrating that macropores

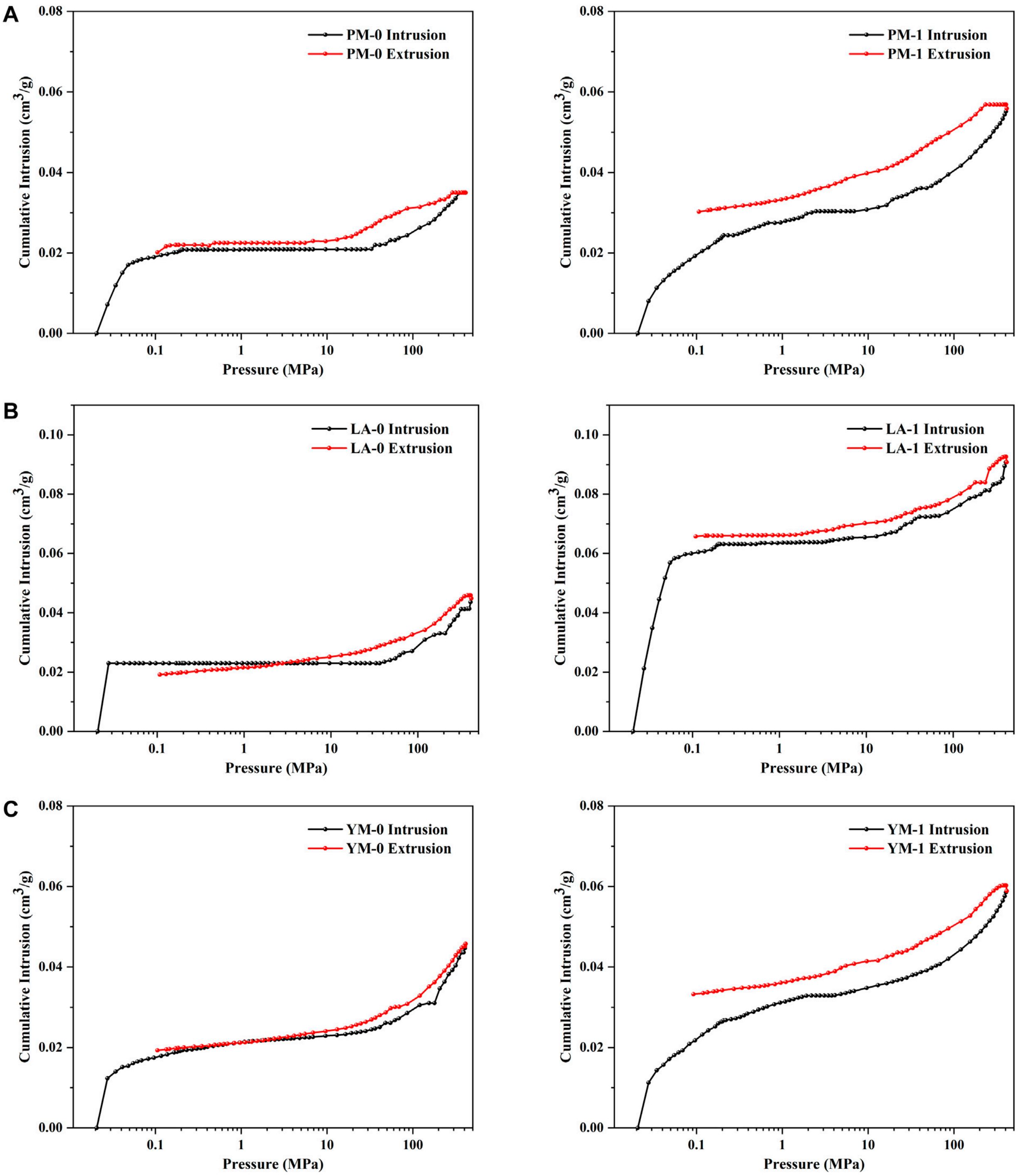

FIGURE 5
The MIP intrusive and extrusive curves of the raw and acidified coal samples: **(A)** PM; **(B)** LA; **(C)** YM.

in the raw coal samples were primarily ultra-macropores with a diameter greater than 10 μm. After being treated with acid solution, multiple broad peaks appeared between 50 nm and 10 μm, with the peak area of the original ultra-macropores showed a substantial increase, indicating that the primary macropores further expanded during the acidification process, and a variety of varied-sized macropores were formed at the same time. Moreover, it was also observed that compared with mesopores, the contribution of

TABLE 3 Pore structural parameters of the raw and acidified coal samples from the MIP measurement[a].

Sample	Acidification	Pore volume (10^{-3} cm^3/g)			Pore specific surface area (m^2/g)		
		V_{mes}	V_{mac}	V_{total}	S_{mes}	S_{mac}	S_{total}
PM-0	pre-	18.01	20.87	38.88	12.43	0.03	12.46
PM-1	post-	21.82	34.04	55.86	13.60	0.23	13.83
LA-0	pre-	21.84	23.01	44.85	12.80	0.07	12.87
LA-1	post-	22.28	68.51	90.79	14.33	0.16	14.49
YM-0	pre-	21.88	23.86	45.74	14.92	0.09	15.01
YM-1	post-	21.94	36.94	58.88	14.02	0.11	14.13

[a]Note: According to the IUPAC classification, V_{total}, V_{mes}, and V_{mac} refer to the volume of total pores, mesopores (2–50 nm), and macropores (above 50 nm), respectively. S_{total}, S_{mes} and S_{mac} refer to the specific surface area of total pores, mesopores (2–50 nm), and macropores (above 50 nm), respectively.

macropores to the total SSA were negligible. After acidification, the contribution of mesopores with diameters of about 10 nm increased, suggesting the formation of larger mesopores during acid treatment.

3.4 Comprehensive analysis of varied-sized pore evolution characteristics under acidification

According to the discussion above, the acid treatment exerted a significant influence on coal's micropores, mesopores and macropores. However, neither LPGA-CO_2, LTGA-N_2 or MIP can independently elucidate the complicate pore structure characteristics, which was limited by the test principle. Previous studies have demonstrated that the above three test methods have different optimal performance intervals: LPGA-CO_2 can accurately characterize micropores, LTGA-N_2 is suitable for characterizing mesopores, and MIP is more accurate for characterizing macropores (Wang et al., 2019; Wei et al., 2019; Lu et al., 2021; Wei et al., 2021). Referring to previous studies, the pore size distribution data of micropores (below 2 nm) from LPGA-CO_2, mesopores (2–50 nm) from LTGA-N_2, and macropores (above 50 nm) from MIP were directly combined and respectively connected at 2 nm and 50 nm to obtain the full-sized pore size distribution dataset. On this basis, the full-sized pore volume distribution curves and full-sized pore area distribution curves were plotted (Figures 7, 8). Although there was aperture interval that could not be detected by both LPGA-CO_2 and LTGA-N_2, this integrated method can reflect the relative changes of pores in coal to the greatest extent. Table 4 summarizes and lists the pore volumes and SSA measured by the three test methods in their best performance intervals, as well as the porosities obtained from Mercury intrusion measurement. It is important to note that it is not very rigorous to directly combine the pore structure data obtained from test methods based on completely different theories. There may be still differences between the pore structure parameters obtained in this study and the real pore structure characteristics of coal, but compared with single methods, they can more accurately reflect the relative changes in the varied-sized pore evolution characteristics under acidification.

From Table 4, the micropores of PM-0, LA-0 and YM-0 respectively contributed to 42.91%, 56.30% and 54.95% of the total pore volume, and the macropores respectively contributed to 42.38%, 41.74% and 40.54% of the total pore volume, while the contribution of mesopores was less than 15%, which indicated that the studied raw coals were mainly composed of micropores and macropores. With increasing coal rank, the total pore specific areas and total pore volumes showed an overall increase, which was mainly contributed by the obviously development of micropores. In addition, micropores contributed more than 98% to the raw coals' total SSA, which illustrated the dominant role of micropore in determining the adsorption capacity. After the treatment with acid, the total pore volumes of all the samples showed a significant increase. Specifically, the total pore volumes of PM, LA, and YM increased from 0.04924, 0.05513, and 0.05885 cm^3/g to 0.06672, 0.10631, and 0.08185 cm^3/g, respectively. At the same time, the porosity increased from 2.73%, 3.36%, and 3.59%–3.39%, 6.07%, and 4.54%, respectively. Comparing the variation of pore volume in different aperture intervals after acidification, we can see that the increase of total volume mainly came from macropores (with an average contribution rate of 74.59%), while the changes of mesopore volume and micropore volume were relatively small, especially that of micropores. This phenomenon indicated that acidification exhibited the greatest impact on macropores, followed by mesopores, and the smallest effect on micropores.

Based on above analysis, we can see that the improvement of the permeability of coal under acid treatment was mainly achieved by promoting the formation of mesopores and macropores, especially macropores. The newly formed mesopores and macropores linked the flow channel of CBM, thus promoting the migration and extraction of CBM. Comparing the increment of total pore volume of the three

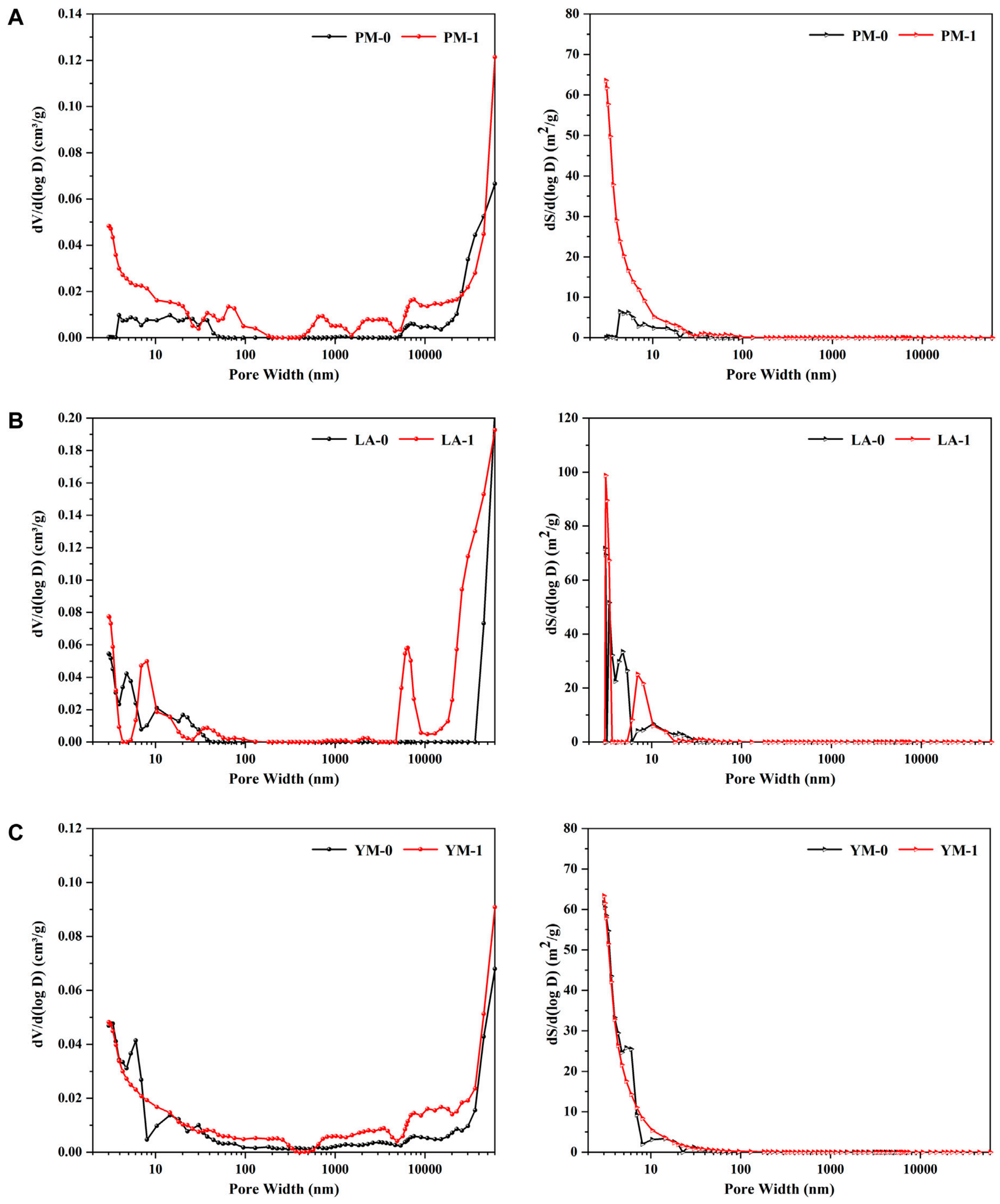

FIGURE 6
Pore volume distribution curves and pore area distribution curves from the MIP measurement: **(A)** PM; **(B)** LA; **(C)** YM.

different rank coals under acidification, it was found that there was no obvious correlation between total pore volume increment and coal maturity. This might be due to that the increase of total pore volume under acidification was mainly derived from macropores, the development of which was strongly related to the removal of minerals in coal, yet the mineral content was

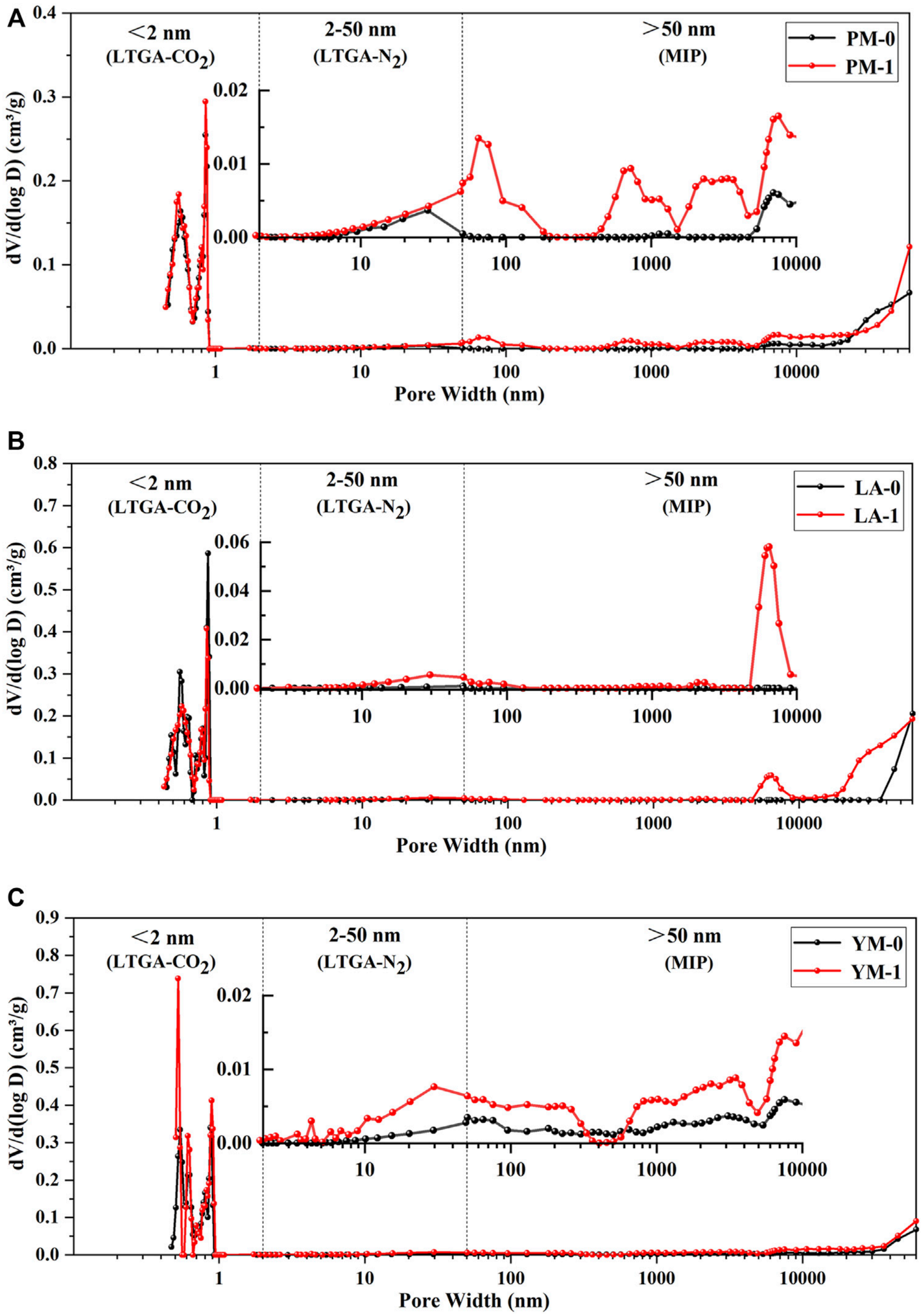

FIGURE 7
Full-sized pore volume distribution curves of the raw and acidified coal samples, and the inserts were the partial enlargement curves: **(A)** PM; **(B)** LA; **(C)** YM.

affected by the coal sedimentary environment rather than coalification (Liu S. et al., 2018; Wang et al., 2019; Mou et al., 2021; Yi et al., 2021). Previous studies have indicated that the effect of acidification on improving permeability was closely related to the mineral content in coal. The higher the mineral content, the better the permeability enhancement effect (Li et al., 2017). Based on previous studies and our preliminary results, we inferred that compared with coal rank, the mineral content in coal may be a more important consideration when measuring the applicability of acidification technology.

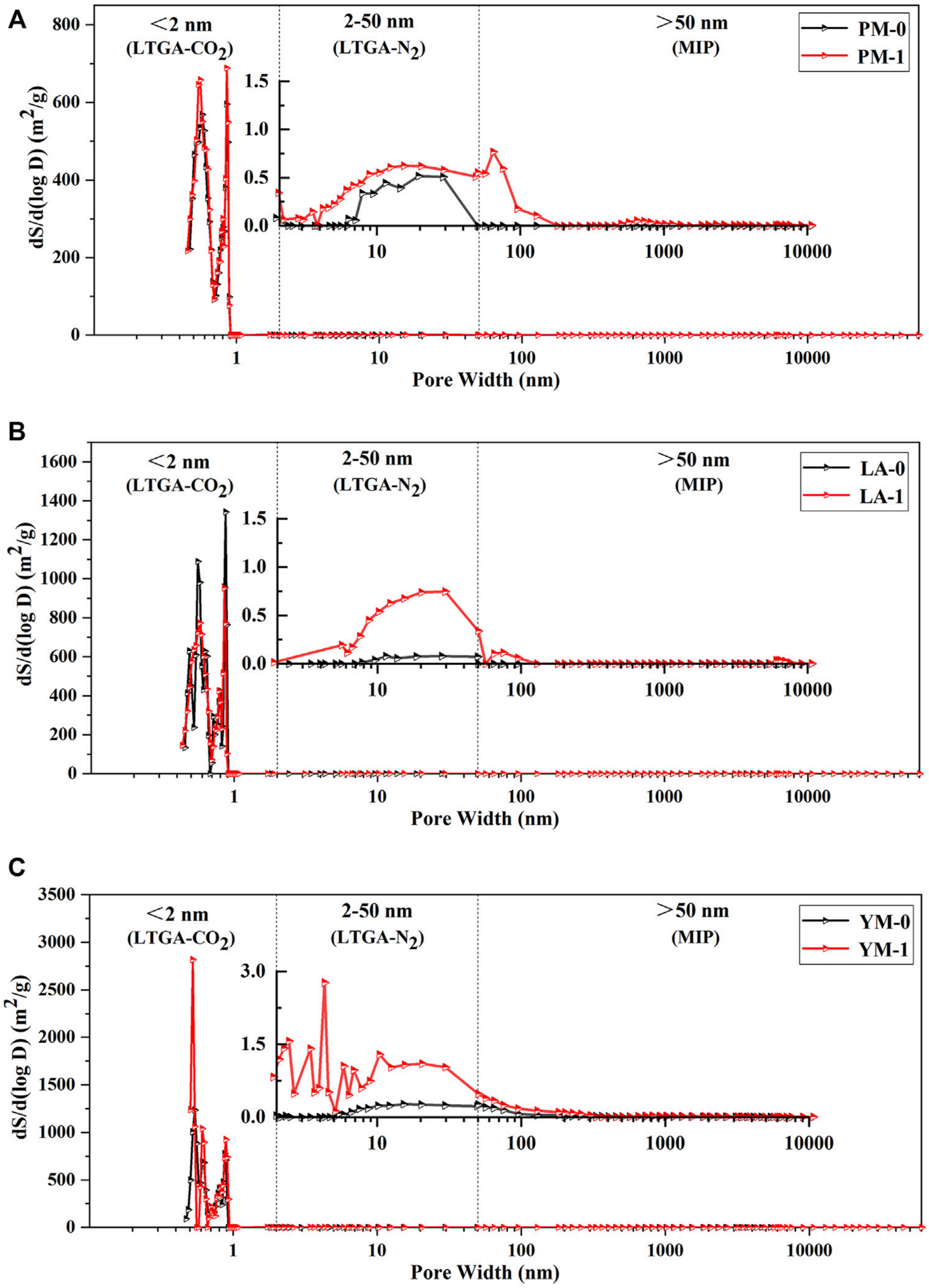

FIGURE 8
Full-sized pore area distribution curves of the raw and acidified coal samples, and the inserts were the partial enlargement curves: **(A)** PM; **(B)** LA; **(C)** YM.

Additionally, according to the specific surface area data shown in Table 4, the variation of meso- and macropores SSA after acidification could be ignored, and the increase or decrease of total SSA was mainly determined by micropores. Moreover, it also can be seen from Table 4 that, the total SSA of fat coal (PM) was more easily affected by acidification and had the largest percentage increase after acid treatment, followed by anthracite coal (YM), while that of meagre coal (LA) decreased slightly. This difference was driven primarily by the different variation trend of micropore SSA in different rank coals discussed in section 3.1.

From Figure 7, we can see that the peaks of the three raw coal samples were concentrated in the range of diameters below

TABLE 4 Full-sized pore structural parameters of the raw and acidified coal samples.

Sample	Porosity (%)	V_{total} (10^{-3} cm^3/g)	Pore volume/(10^{-3} cm^3/g) Proportion of volume/%			S_{total} (m^2/g)	Pore specific surface area/(m^2/g) Proportion of pore specific surface area/%		
			V_{mic}	V_{mes}	V_{mac}		S_{mic}	S_{mes}	S_{mac}
PM-0	2.73	49.24	21.13	7.24	20.87	69.68	68.82	0.83	0.03
		100	42.91	14.70	42.38	100	98.77	1.19	0.04
PM-1	3.39	66.72	24.65	8.03	34.04	78.76	77.44	1.09	0.23
		100	36.95	12.04	51.02	100	98.32	1.38	0.29
LA-0	3.36	55.13	31.04	1.08	23.01	99.88	99.64	0.17	0.07
		100	56.30	1.96	41.74	100	99.76	0.17	0.07
LA-1	6.07	106.31	30.17	7.63	68.51	99.68	98.35	1.17	0.16
		100	28.38	7.18	64.44	100	98.67	1.17	0.16
YM-0	3.59	58.85	32.34	2.65	23.86	99.77	99.17	0.51	0.09
		100	54.95	4.50	40.54	100	99.40	0.51	0.09
YM-1	4.54	81.85	34.37	10.54	36.94	109.24	107.44	1.69	0.11
		100	41.99	12.88	45.13	100	98.35	1.55	0.10

[a]According to the IUPAC classification, V_{total}, V_{mac}, V_{mes}, and V_{mic} refer to the volume of total pores, macropores (above 50 nm), mesopores (2–50 nm), and micropores (below 2 nm), respectively. S_{total}, S_{mac}, S_{mes} and S_{mic} refer to the specific surface area of total pores, macropores (above 50 nm), mesopores (2–50 nm), and micropores (below 2 nm), respectively.

0.9 nm and above 10 μm, and the main peaks were located at about 0.55, 0.85 nm, and tens of microns, suggesting that the pore systems were primarily composed of ultra-micropores with diameters of about 0.55 nm, super-micropores with diameters of about 0.85 nm, and ultra-macropores with diameters of tens of microns. After the acid treatment, the pores were still dominated by micropores and macropores, but the pore size distribution changed significantly.

For the ultra-micropore in coal, as analyzed in section 3.1, acid treatment made the ultra-micropore structure in medium rank coal more uniform, while that in high rank coal more regular. This might be due to that acidification caused the alkyl structure to fall off, thereby further increasing the proportion of aromatic structure in high rank coal, making the coal macromolecules more orderly arranged, thus producing smaller and more regular ultra-micropores (Liu et al., 2017; Liu Y. et al., 2018; Liu Y. et al., 2019; Li Y. et al., 2020). As for the super-micropores in coal, the main peak position of acidified coal samples stayed the same, yet the peak value of PM and YM here increased after acid treatment, while that of LA decreased. It is considered that super-micropores are the intermolecular spaces in coal, and the removal of volatiles (such as the functional groups or weak side chains of coal macromolecules) can increase the number of super-micropores (Liu Y. et al., 2019). Therefore, the development of super-micropores in PM and YM may have been due to the intermolecular spaces formed by the removal of functional groups or unstable side chains under acidification, and the decrease of super-micropores in LA may have been due to the further transformation of newly formed super-micropores into small mesopores.

From the partial enlarged curves shown in Figure 7, it was obvious that several broad new peaks occurred between diameters of 10 nm and 10 μm, and the main peaks located at 50 nm, 100 nm, 1 μm, 3 μm, and 8 μm. This might be attributed to the dissolution and removal of minerals (such as pyrite, calcite, and kaolinite) in coal after acidification, the size of which ranged from tens of nanometers to hundreds of microns (Brown et al., 2011; Liu S. et al., 2018; Wu et al., 2018). Pores that were partially blocked or occupied by minerals exposed and connected after acidification, thus significantly increasing the volume of large mesopores and macropores. This was consistent with the phenomenon observed during the acid treatment that numerous bubbles emerged from the acid solution, which might be carbon dioxide, hydrogen sulfide or other gases produced by the reaction of minerals with acid. Moreover, Figure 8 shows that 0.55 and 0.85 nm sized micropores played a dominant role in pore area distribution of raw coal samples, which suggested that these two types of pores provided most adsorption sites for CBM. After acidification, the SSA of mesopores and macropores all showed a tendency of increasing. However, compared with micropores, mesopores and macropores contributed a negligibly small portion to the increase of total SSA.

Therefore, micropores were still the main contributor to the total SSA of acidified coal samples.

4 Conclusion

In this study, fat coal (PM), meagre coal (LA) and anthracite coal (YM) were collected and acidified with a mixed solution composed of hydrofluoric acid and hydrochloric acid. The structure of micropores, mesopores, and macropores were respectively characterized by LPGA-CO_2, LTGA-N_2, and MIP methods. Combined with the data corresponding to the best performance interval of the three test methods, the evolution characteristics of varied-sized pore structure under acidification were comprehensively investigated. The following conclusions are drawn:

1) Acid treatment had little effect on the pore shape of the three selected coal samples, but could obviously enhance the pore opening degree, thus improving the pore connectivity. Acid treatment helped to improve the pore diameter diversity, which was mainly attributed to the formation of numerous large mesopores and micron sized macropores.
2) After acidification, the total pore volume and porosity of the three different rank coals all increased significantly, which were mainly contributed by the newly formed large mesopores and macropores, especially the macropores (with an average contribution rate of 74.59%). Acid treatment exhibited the greatest impact on macropores, followed by mesopores, and the smallest on micropores.
3) The change trend of total SSA under acidification was mainly determined by micropores. After acidification, for the coal samples selected in this study, the total SSA of fat coal (PM) was more easily affected by acidification and had the largest percentage increase after acid treatment, followed by anthracite coal (YM), while that of meagre coal (LA) decreased slightly.
4) The total pore volume increment of different rank coals was closely related to the macropore volume increment under acidification, but not obviously related to the coal maturity. Therefore, compared with coal rank, the mineral content in coal might be a more important consideration when measuring the applicability of acidification technology.

Data availability statement

The original contributions presented in the study are included in the article/supplementary material, further inquiries can be directed to the corresponding authors.

Author contributions

Conceptualization, ZS, CY, and PJ; methodology, PJ and FC; validation, JL and JR; data curation, JL and FC; writing—original draft preparation, PJ; writing—review and editing, CY and ZS; supervision, BL; funding acquisition, JL and JR. All authors have read and agreed to the published version of the manuscript.

Funding

This research was financially supported by the National Natural Science Foundation of China (Grant Nos. 41972177 and 42172189); the Doctoral Cultivation Fund Project of Henan University of Engineering (Grant No. Dkj2018013); the Key Scientific Research Projects of Henan Colleges and Universities (Grant No. 22A170007); and the Natural Science Foundation of Henan province (Grant No. 222300420134).

Conflict of interest

Author CY was employed by Institute of Henan Energy and Chemical Industry Group Co., Ltd.

The remaining authors declare that the research was conducted in the absence of any commercial or financial relationships that could be construed as a potential conflict of interest.

Publisher's note

References

Brown, P., Jones, T., and BeruBe, K. (2011). The internal microstructure and fibrous mineralogy of fly ash from coal-burning power stations. *Environ. Pollut.* 159 (12), 3324–3333. doi:10.1016/j.envpol.2011.08.041

Chen, Q., Wang, Q., and Liang, Y. (2021a). Permeability enhancement via acetic acid (CH3COOH) acidizing in coals containing fracture-filling calcite. *Energy fuels.* 35 (21), 17396–17409. doi:10.1021/acs.energyfuels.1c02199

Chen, S., Xie, K., Shi, Y., Li, Z., Yang, X., and Cai, J. (2021b). Chelating agent-introduced unconventional compound acid for enhancing coal permeability. *J. Pet. Sci. Eng.* 199, 108270. doi:10.1016/j.petrol.2020.108270

Chen, S., Zhu, Y., Li, W., and Wang, H. (2012). Influence of magma intrusion on gas outburst in a low rank coal mine. *Int. J. Min. Sci. Technol.* 22 (2), 259–266. doi:10.1016/j.ijmst.2012.03.004

Guo, H., Yuan, L., Cheng, Y., Wang, K., and Xu, C. (2019). Experimental investigation on coal pore and fracture characteristics based on fractal theory. *Powder Technol.* 346, 341–349. doi:10.1016/j.powtec.2019.02.026

Guo, Z., Cao, Y., Dong, S., and Zhang, Z. (2021). Experimental studies on the enhancement of permeability of anthracite by acidizing: A case study in the daning block, southern qinshui basin. *ACS Omega* 6 (46), 31112–31121. doi:10.1021/acsomega.1c04539

Jagiello, J., Kenvin, J., Celzard, A., and Fierro, V. (2019). Enhanced resolution of ultra micropore size determination of biochars and activated carbons by dual gas analysis using N2 and CO2 with 2D-NLDFT adsorption models. *Carbon* 144, 206–215. doi:10.1016/j.carbon.2018.12.028

Jiang, T., Yu, Y., Jahanger, A., and Balsalobre-Lorente, D. (2022). Structural emissions reduction of China's power and heating industry under the goal of "double carbon": A perspective from input-output analysis. *Sustain. Prod. Consum.* 31, 346–356. doi:10.1016/j.spc.2022.03.003

Jin, K., Cheng, Y., Liu, Q., Zhao, W., Wang, L., Wang, F., et al. (2016). Experimental investigation of pore structure damage in pulverized coal: Implications for methane adsorption and diffusion characteristics. *Energy fuels.* 30 (12), 10383–10395. doi:10.1021/acs.energyfuels.6b02530

Li, L., Liu, D., Cai, Y., Wang, Y., and Jia, Q. (2020a). Coal structure and its implications for coalbed methane exploitation: A review. *Energy fuels.* 35 (1), 86–110. doi:10.1021/acs.energyfuels.0c03309

Li, S., Luo, M., Fan, C., Bi, H., and Ren, Y. (2017). Quantitative characterization of the effect of acidification in coals by NM and low-temperature nitrogen adsorption. *J. China Coal Soc.* 42 (7), 1748–1756. doi:10.13225/j.cnki.jccs.2016.0929

Li, S., Ni, G., Wang, H., Xun, M., and Xu, Y. (2020b). Effects of acid solution of different components on the pore structure and mechanical properties of coal. *Adv. Powder Technol.* 31 (4), 1736–1747. doi:10.1016/j.apt.2020.02.009

Li, Y., Song, D., Liu, S., Ji, X., and Hao, H. (2021). Evaluation of pore properties in coal through compressibility correction based on mercury intrusion porosimetry: A practical approach. *Fuel* 291, 120130. doi:10.1016/j.fuel.2021.120130

Li, Y., Song, D., Liu, S., and Pan, J. (2020c). Characterization of ultramicropores and analysis of their evolution in tectonically deformed coals by low-pressure CO2 adsorption, XRD, and HRTEM techniques. *Energy fuels.* 34 (8), 9436–9449. doi:10.1021/acs.energyfuels.0c01403

Liu, P., Nie, B., Zhao, Z., Zhao, Y., and Li, Q. (2023). Characterization of ultrasonic induced damage on multi-scale pore/fracture in coal using gas sorption and μ-CT 3D reconstruction. *Fuel* 332, 126178. doi:10.1016/j.fuel.2022.126178

Liu, S., Ma, J., Sang, S., Wang, T., Du, Y., and Fang, H. (2018a). The effects of supercritical CO2 on mesopore and macropore structure in bituminous and anthracite coal. *Fuel* 223, 32–43. doi:10.1016/j.fuel.2018.03.036

Liu, X., Song, D., He, X., Wang, Z., Zeng, M., and Deng, K. (2019a). Nanopore structure of deep-burial coals explored by AFM. *Fuel* 246, 9–17. doi:10.1016/j.fuel.2019.02.090

Liu, Y., Zhu, Y., and Chen, S. (2019b). Effects of chemical composition, disorder degree and crystallite structure of coal macromolecule on nanopores (0.4–150 nm) in different rank naturally-matured coals. *Fuel* 242, 553–561. doi:10.1016/j.fuel.2019.01.095

Liu, Y., Zhu, Y., Li, W., Zhang, C., and Wang, Y. (2017). Ultra micropores in macromolecular structure of subbituminous coal vitrinite. *Fuel* 210, 298–306. doi:10.1016/j.fuel.2017.08.069

Liu, Y., Zhu, Y., Liu, S., Chen, S., Li, W., and Wang, Y. (2018b). Molecular structure controls on micropore evolution in coal vitrinite during coalification. *Int. J. Coal Geol.* 199, 19–30. doi:10.1016/j.coal.2018.09.012

Liu, Z., Liu, D., Cai, Y., and Qiu, Y. (2021). Permeability, mineral and pore characteristics of coals response to acid treatment by NMR and QEMSCAN: Insights into acid sensitivity mechanism. *J. Pet. Sci. Eng.* 198, 108205. doi:10.1016/j.petrol.2020.108205

Lu, J., Fu, X., Kang, J., Cheng, M., and Wang, Z. (2021). Characterization of full pore and stress compression response of reservoirs with different coal ranks. *Front. Earth Sci. (Lausanne).* 9. doi:10.3389/feart.2021.764853

Mou, P., Pan, J., Niu, Q., Wang, Z., Li, Y., and Song, D. (2021). Coal pores: Methods, types, and characteristics. *Energy fuels.* 35 (9), 7467–7484. doi:10.1021/acs.energyfuels.1c00344

Ni, G., Li, S., Rahman, S., Xun, M., Wang, H., Xu, Y., et al. (2020). Effect of nitric acid on the pore structure and fractal characteristics of coal based on the low-temperature nitrogen adsorption method. *Powder Technol.* 367, 506–516. doi:10.1016/j.powtec.2020.04.011

Qin, L., Li, S., Zhai, C., Lin, H., Zhao, P., Yan, M., et al. (2020). Joint analysis of pores in low, intermediate, and high rank coals using mercury intrusion, nitrogen adsorption, and nuclear magnetic resonance. *Powder Technol.* 362, 615–627. doi:10.1016/j.powtec.2019.12.019

Tan, Y., Pan, Z., Liu, J., Kang, J., Zhou, F., Connell, L. D., et al. (2018). Experimental study of impact of anisotropy and heterogeneity on gas flow in coal. Part I: Diffusion and adsorption. *Fuel* 232, 444–453. doi:10.1016/j.fuel.2018.05.173

Thommes, M., and Cychosz, K. A. (2014). Physical adsorption characterization of nanoporous materials: Progress and challenges. *Adsorption* 20 (2-3), 233–250. doi:10.1007/s10450-014-9606-z

Thommes, M., Kaneko, K., Neimark, A. V., Olivier, J. P., Rodriguez-Reinoso, F., Rouquerol, J., et al. (2015). Physisorption of gases, with special reference to the evaluation of surface area and pore size distribution (IUPAC Technical Report). *Pure Appl. Chem.* 87 (9-10), 1051–1069. doi:10.1515/pac-2014-1117

Turner, L. G., and Steel, K. M. (2016). A study into the effect of cleat demineralisation by hydrochloric acid on the permeability of coal. *J. Nat. Gas. Sci. Eng.* 36, 931–942. doi:10.1016/j.jngse.2016.11.003

Wang, H., Cheng, X., Tian, J., Li, T., Wang, W., Pan, J., et al. (2020). Permeability enhancement of low rank coal through acidization using H2S solution: An experimental study in the Kuqa-Bay Coalfield, Xinjiang, China. *J. Pet. Sci. Eng.* 185, 106476. doi:10.1016/j.petrol.2019.106476

Wang, H., Cheng, Y., Wang, W., and Xu, R. (2014). Research on comprehensive CBM extraction technology and its applications in China's coal mines. *J. Nat. Gas. Sci. Eng.* 20, 200–207. doi:10.1016/j.jngse.2014.05.025

Wang, H., Fu, X., Jian, K., Li, T., and Luo, P. (2015). Changes in coal pore structure and permeability during N 2 injection. *J. Nat. Gas. Sci. Eng.* 27, 1234–1241. doi:10.1016/j.jngse.2015.09.068

Wang, Y., Liu, L., Zheng, S., Luo, Z., Sheng, Y., and Wang, X. (2019). Full-scale pore structure and its controlling factors of the Wufeng-Longmaxi shale, southern Sichuan Basin, China: Implications for pore evolution of highly overmature marine shale. *J. Nat. Gas. Sci. Eng.* 67, 134–146. doi:10.1016/j.jngse.2019.04.020

Wei, Q., Li, X., Zhang, J., Hu, B., Zhu, W., Liang, W., et al. (2019). Full-size pore structure characterization of deep-buried coals and its impact on methane adsorption capacity: A case study of the shihezi formation coals from the panji deep area in huainan coalfield, southern north China. *J. Pet. Sci. Eng.* 173, 975–989. doi:10.1016/j.petrol.2018.10.100

Wei, Q., Zheng, K., Hu, B., Li, X., Feng, S., Jiang, W., et al. (2021). Methane adsorption capacity of deep-buried coals based on pore structure in the panji deep area of huainan coalfield, China. *Energy fuels.* 35 (6), 4775–4790. doi:10.1021/acs.energyfuels.0c03800

Wu, H., Gao, X., Wee, H., Ngu, L.-N., Ninomiya, Y., and Wang, Q. (2018). Occurrence and characteristics of abundant fine included mineral particles in Collie coal of Western Australia. *Fuel* 216, 53–60. doi:10.1016/j.fuel.2017.11.118

Xie, J., Du, H., Chen, S., Sun, X., and Xin, L. (2021). Chemical modification effect of compound solutions of surfactants with acetic acid on coal pores. *ACS Omega* 6 (51), 35342–35354. doi:10.1021/acsomega.1c04430

Yi, M., Cheng, Y., Wang, C., Wang, Z., Hu, B., and He, X. (2021). Effects of composition changes of coal treated with hydrochloric acid on pore structure and fractal characteristics. *Fuel* 294, 120506. doi:10.1016/j.fuel.2021.120506

Zhang, J., Li, X., Wei, Q., Sun, K., Zhang, G., and Wang, F. (2017). Characterization of full-sized pore structure and fractal characteristics of marine–continental transitional longtan formation shale of sichuan basin, south China. *Energy fuels.* 31 (10), 10490–10504. doi:10.1021/acs.energyfuels.7b01456

Zhang, L., Li, Z., Yang, Y., Zhou, Y., Kong, B., Li, J., et al. (2016). Effect of acid treatment on the characteristics and structures of high-sulfur bituminous coal. *Fuel* 184, 418–429. doi:10.1016/j.fuel.2016.07.002

Zhao, B., Wen, G., Sun, H., and Zhao, X. (2018). Experimental study of the pore structure and permeability of coal by acidizing. *Energies* 11 (5), 1162. doi:10.3390/en11051162

frontiers | Frontiers in Earth Science

TYPE Original Research
PUBLISHED 17 January 2023
DOI 10.3389/feart.2022.1071250

OPEN ACCESS

EDITED BY
Leilei Si,
Henan Polytechnic University, China

REVIEWED BY
Chinedu J. Okere,
Texas Tech University, United States
Dazhao Song,
University of Science and Technology Beijing, China
Yubing Gao,
China University of Mining and Technology, China
Zhenghe Liu,
Taiyuan University of Technology, China

*CORRESPONDENCE
Linfeng Guo,
linf_g@163.com

SPECIALTY SECTION
This article was submitted to Economic Geology, a section of the journal Frontiers in Earth Science

RECEIVED 16 October 2022
ACCEPTED 22 November 2022
PUBLISHED 17 January 2023

CITATION
Liu H, Hao C, Wang Z, Li C, Guo L, Liang J and Wang H (2023), Study on stability of underlying room and pillar old goaf in close coal seam and mining of the upper coal seam.
Front. Earth Sci. 10:1071250.
doi: 10.3389/feart.2022.1071250

Study on stability of underlying room and pillar old goaf in close coal seam and mining of the upper coal seam

Hongtao Liu[1], Cheng Hao[1], Zhiwen Wang[2], Chong Li[3], Linfeng Guo[1]*, Jialu Liang[1] and Haozhu Wang[1]

[1]School of Energy and Mining Engineering, China University of Mining and Technology, Beijing, China, [2]Zuoyun Hanjiawa Coal Industry Co., Ltd., Shanxi Coal Imp. & Exp. Group, Datong, China, [3]China CAMC Engineering Co., Ltd., Beijing, China

Possible issues during mining of the upper coal seam in old goaf of nearby coal seams, including step subsidence, gas overflow in goaf, and roadway around rock fragmentation. Using the Hanjiawa Coal Mine's upper coal seam mining, which takes place 28 m above the working face of the lower coal seam, as the research's focal point. The paper focuses on the self-stability of the coal pillar in the old goaf, the failure form of the upper coal seam mining floor, the roof caving rule of the old goaf in the lower coal seam mining of the upper coal seam, and the bearing capacity of the interlayer rock strata using the pillar goaf stability evaluation system, field geological borehole electrical logging and borehole peeping, finite element difference numerical calculation, and other methods. The conclusion that the old goaf's coal pillar can be completely stable and that the interlayer rock strata can bear the stress of upper coal seam mining is reached. The results show that the failure depth of the coal pillar in the lower coal seam old goaf is 1–3 m, the maximum failure depth accounting for 15% of the width of the coal pillar, and the failure depth of the roof in the old goaf is 0–3 m; After the mining of the upper coal seam, the floor above the coal pillar of the lower coal seam is plastic failure, and the failure depth is 1–10 m, and the failure depth of the roof of the old goaf of the lower coal seam is 3–15 m, which is 4 times greater than that before the mining. The maximum failure depth of the interlayer rock strata is 22 m, accounting for 78.6% of the rock strata spacing. The interlayer rock strata can bear the mining disturbance of the upper coal seam. The plastic zone of the floor of the upper coal seam is not connected with the plastic zone of the roof of the lower coal seam.

KEYWORDS

close coal seams, upper coal seam mining, stability of old goaf, stress distribution, evolution of plastic zone

Introduction

Since the 1990s, coal enterprises have actively or passively selected to mine the lower coal seam first due to the limitations of coal economic form, the pursuit of reasonable economic benefits, the insufficient accuracy of geological exploration in the mining area, poor production technical conditions and other reasons. With the continuous progress of mining technology and the improvement of economic situation, upward mining measures can be taken to recover the remaining coal seams, so as to improve the recovery rate of coal resources and increase production and efficiency for coal enterprises (Wang and Li, 1994; Singh et al., 2002; Du and Meng, 2009; Han et al., 2013).

Many scholars have done a lot of research on the problem of coal mining in the upper part of goaf. Sun et al. (2021) put forward the concepts of "partially balanced structure horizon" and "balanced structure horizon," and established a method for judging the feasibility of upward mining under the condition of large mining height fully mechanized goaf. By means of theoretical analysis and similar simulation test, Feng (2009), Feng et al. (2009), Feng et al. (2010), Feng et al. (2011a), Feng et al. (2011b), Feng et al. (2019), and Bai et al. (2018) analyzed the evolution law of abutment pressure of upward mining in caving goaf and knife pillar goaf, established the stress-strain model, and put forward the theory and method for judging the feasibility in the technical conditions of upward fully mechanized mining in caving goaf and knife pillar goaf.

Ma (2021) studied the creep failure law of coal pillars in room pillar goaf under overburden load, determined the critical instability state in the dynamic instability process of coal pillars, and established the stability evaluation system of pillar goaf with multiple indexes based on fuzzy comprehensive evaluation method. Leilei et al. (2021a) and Leilei et al. (2021b) studied the influence of water content on coal strength from the perspective of long-time water intrusion into coal, which is conducive to the study of long-term stability of coal pillars in the old goaf of the lower coal seam. Li et al. (2019) analyzed the feasibility of upward mining of coal seam under multi-layer goaf, put forward comprehensive discriminant indexes for upward mining, and established quantitative discriminant and evaluation system for "feasibility" of upward coordinated mining. Pan et al. (2022) and Yao et al. (2022) conducted compression tests on rocks with cracks of different angles around the hole by means of numerical simulation and laboratory tests, revealed the failure mode of defective rocks, studied the crack propagation and stress evolution mode of defective rocks, which can reflect the morphological evolution and stress evolution rules of the lower coal seam goaf.

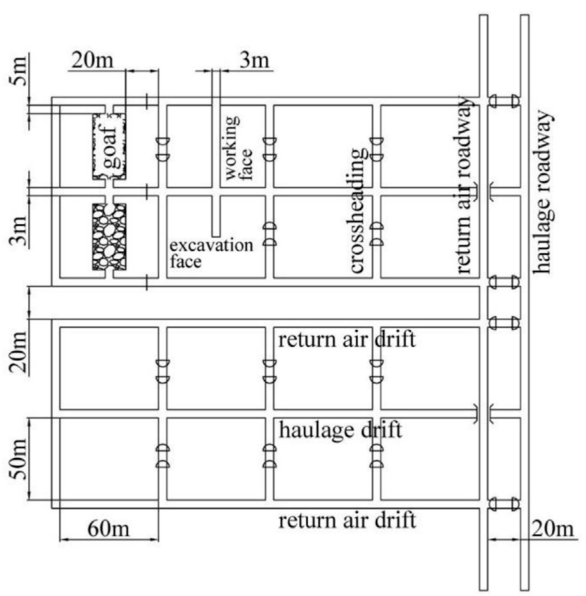

FIGURE 1
The No. 22 coal mining layout.

Han et al. (2011) studied the case of upward mining in Kailuan mining area, divided the damage degree of the upper coal seam after the mining of the lower coal seam into five grades, and established the feasibility criterion of upward mining of the close coal seam group based on multiple regression analysis. Zhang et al. (2013) studied the continuity and integrity of the upper coal seam in the upward mining of the close coal seam group in Qinghemen Mine, Fuxin Mining Area, and determined the structural change characteristics of the upper coal seam after the mining of the lower coal seam. Han et al. (1998), Ma et al. (2007), and Ma et al. (2008) studied Pingsi Coal Mine and Suanlagou Coal Mine by using the traditional discrimination method for upward mining of coal seams. Based on the limitations of the traditional discrimination method, they revealed the upward mining mechanism of close coal seams, expounded the relationship between the overlying rock status of upper seams and upward mining, and analyzed the influence of overlying rock lithology and structure of upper seams on upward mining. Qu et al. (2008) analyzed and studied the feasibility of upward mining of coal seam affected by multiple uneven mining in the lower part, and drilled holes to explore the development height of fracture zone after mining of lower coal seams, so as to provide basis for upward mining. Cheng (2004) observed and summarized the upward mining of the middle group coal in Haizi Coal Mine, and pointed out that the upward mining of the coal mine has increased the mine output and removed the gas hazard of the middle group coal mining, which has significant technical and economic benefits.

Okere et al. (2020), He et al. (2021), Zhang et al. (2021), and Tao et al. (2022) improves the accuracy of stress estimation and clarifies the impact of different test methods on the evaluation of working fluid damage. A mathematical model that can quantitatively analyze the interbed interference of coalbed

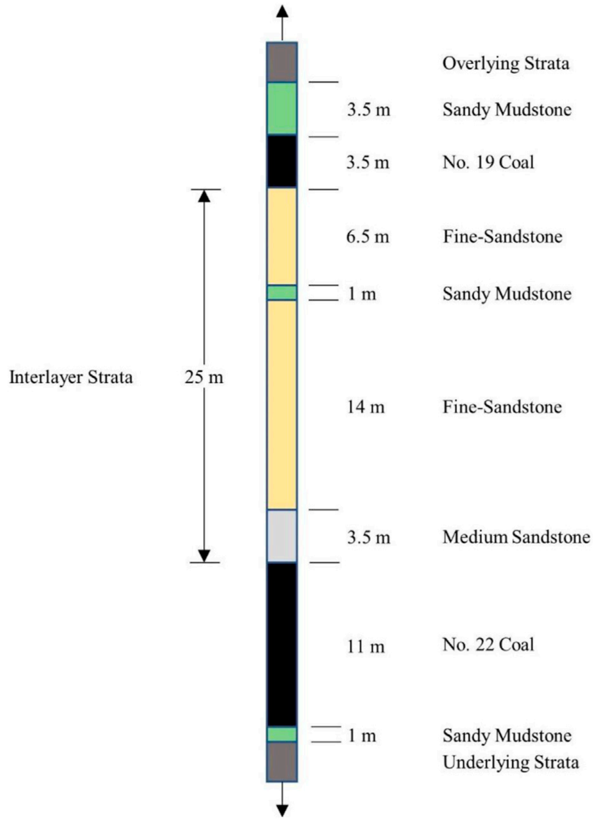

FIGURE 2
ZK-7 borehole column.

methane mining is established by the author. This mathematical model also establishes a foundation for understanding the interbed interference of close coal seams and the evaluation of mine *in situ* stress test.

Few studies have been done on the cross-goaf mining of the upper coal seam in the old goaf under the low mechanization room pillar mining conditions in the early mine. Earlier studies were mostly focused on the upward mining of the goaf in the fully mechanized face. The upper coal seam mining in the room pillar old goaf is not suited for the conventional upward mining discrimination method. In this paper, the stability discrimination method of the pillar goaf is used to determine the goaf left over by the mine, and the mining impact of the upper coal seam is simulated, providing a solid foundation for the mining of the upper coal seam under comparable circumstances.

Background

No. 22 coal seam was mined before 2009, the room and pillar mining method was adopted, with single mining means and low mechanization degree of mining work. And the coal produced by roadway mining was used instead of working face mining. The mining layout is shown in Figure 1.

Three roadways are excavated at one side of the return air roadway. The roadway width is 3 m, with an interval of 50 m. The roadway in the middle is the haulage drift, and the roadways on both sides are the return air drift. The crossheading is dug out every 60 m during the roadway excavation process, and the working face is dug out between the two crossheadings from the haulage drift to the return air drift. The side of the working face is then expanded using a rake mining machine, and the top and bottom coal are recovered using blasting to create a mine-out area. The size of the mine-out area is 20 m × 8 m.

A single mining unit shall reserve 20 m coal pillar from the crossheading on both sides, and 5 m coal pillar from the haulage drift and the return air drift. Three drifts are excavated in a single mining area, and 20 m coal pillars are reserved in two adjacent mining areas.

With the improvement of production technology, the requirements for mining the No. 19 coal seam overlying the goaf have been met. As shown in Figure 2, it can be obtained from the ZK-7 borehole column, the average interval between two coal seams is 25 m, the mining height of No. 22 coal seam is 8 m, the interval between coal seams is small and the mining height is large. According to the ratio discrimination method, “Three Zone” discrimination method and surrounding rock balance discrimination method and so on, it is difficult to mining the overlying coal seam. However, the traditional discrimination method is suitable for the determination of conventional wall mining conditions. Under the situation of room and pillar mining, the thick sandstone roof of NO. 22 coal seam will not fall after mining, and will play a role in the balanced rock stratum, so that No. 19 coal seam is above the balanced rock stratum.

Materials and methods

In this study, the stability evaluation of pillar goaf, field geological borehole survey and finite element difference numerical simulation were used.

Stability evaluation of pillar goaf

As a complex system, the stability of pillar mining goaf is affected by many factors. Ma (2021) developed a stability evaluation model for pillar goaf based on the findings of earlier studies, ranked the four primary influencing factors and their evaluation indices for pillar goaf stability according to weight scale, and concluded that the influence of geological factors, mining factors, strength factors, and environmental factors on the stability of the pillar goaf was gradually reduced.

TABLE 1 Classification standard of evaluation indexes Ma (2021).

Evaluation indexes		Class I	Class II	Class III
C1	Burial depth of coal seam	<150 m	150–300 m	>300 m
C2	Dip Angle of coal seam	$<5^\circ$	5°–25°	$>25^\circ$
C3	Geological structure	No (a)	Undeveloped (b)	Developed (c)
C4	Thickness of the roof	>15 m	5–15 m	<5 m
C5	Aspect ratio of coal pillar	>3	1–3	<1
C6	Mining ratio	>0.5	0.5–1.5	<1.5
C7	Distribution of coal pillar	Dense and uniform (a)	In-between (b)	Scattered and sparse (c)
C8	Area of goaf	<1 km^2	1~2 km^2	>2 km^2
C9	Remaining time	<5a	5–15a	>15a
C10	Compressive strength of pillar	>30 MPa	10–30 MPa	<10 MPa
C11	Compressive strength of roof	>50 MPa	20–50 MPa	<20 MPa
C12	Tensile strength of roof	>3 MPa	1~3 MPa	<1 MPa
C13	Mining disturbance	No (a)	Minor (b)	Massive (c)
C14	Groundwater	No (a)	Minor (b)	Massive (c)
C15	Weathering	No (a)	Weak (b)	Strong (c)

In the table, evaluation indexes C1, C2, C4, C5, C6, C8, C9, C10, C11, and C12 are quantitative indexes, and C3, C7, C13, C14, and C15 are qualitative indexes.

The evaluation system of this evaluation model includes evaluation set U (Class I, Class II, Class III), factor set B (geological factors, mining factors, strength factors, environmental factors), and index set C (coal seam burial depth, dip angle, geological structure, etc.).

> Class I stability of goaf is good: Goaf is stable and can resist certain external interference;
> Class II stability of goaf is general: Goaf is stable, but it is easy to lose stability due to external interference
> Class III stability of goaf is poor: Goaf cannot maintain its own stability.

Only when the stability of goaf is Class I or II, the overlying coal seam mining can be carried out. When the stability of goaf is Class III, it is difficult to carry out the overlying coal seam mining on the premise that the goaf detection and No. 19 coal seam detection are not done well.

The stability evaluation model of pillar goaf has established the classification standard and membership function calculation formula for 15 evaluation indexes. The classification standard of evaluation indexes is shown in Table 1.

For quantitative indexes of positive gain of numerical value, the membership function is calculated as follows (Ma, 2021):

$$\text{Class I: } r_1(x) = \begin{cases} 0, & x \le c_2 \\ -\dfrac{c_2 - x}{c_1 - c_2}, & c_2 < x \le c_1 \\ 1, & x > c_1 \end{cases} \tag{1}$$

$$\text{Class II: } r_2(x) = \begin{cases} 0, & x \le c_3; \quad x > c_1 \\ \dfrac{c_3 - x}{c_3 - c_2}, & c_3 < x \le c_2 \\ \dfrac{c_1 - x}{c_1 - c_2}, & c_2 < x \le c_1 \end{cases} \tag{2}$$

$$\text{Class III: } r_3(x) = \begin{cases} 1, & x \le c_3 \\ \dfrac{c_2 - x}{c_2 - c_3}, & c_3 < x \le c_2 \\ 0, & x > c_2 \end{cases} \tag{3}$$

For quantitative indexes of negative gain of numerical value, the membership function is calculated as follows (Ma, 2021):

$$\text{Class I: } r_1(x) = \begin{cases} 1, & x \le c_1 \\ \dfrac{c_2 - x}{c_2 - c_1}, & c_1 < x \le c_2 \\ 0, & x > c_2 \end{cases} \tag{4}$$

$$\text{Class II: } r_2(x) = \begin{cases} 0, & x \le c_1; \quad x > c_3 \\ -\dfrac{c_1 - x}{c_2 - c_1}, & c_1 < x \le c_2 \\ \dfrac{c_3 - x}{c_3 - c_2}, & c_2 < x \le c_3 \end{cases} \tag{5}$$

$$\text{Class III: } r_3(x) = \begin{cases} 0, & x \le c_2 \\ -\dfrac{c_2 - x}{c_3 - c_2}, & c_2 < x \le c_3 \\ 1, & x > c_3 \end{cases} \tag{6}$$

Where, x is the specific value of quantitative indexes, and c_1, c_2, and c_3 are the dividing lines of grading threshold of evaluation indexes.

TABLE 2 Membership relationship of qualitative indexes Ma (2021).

Evaluation indexes	Categories	Class I	Class II	Class III
C3 Geological structure	a	0.7	0.2	0.1
	b	0.25	0.6	0.15
	c	0.05	0.2	0.75
C7 Distribution of coal pillar	a	0.8	0.15	0.05
	b	0.2	0.65	0.15
	c	0.1	0.15	0.75
C13 Mining disturbance	a	0.8	0.15	0.05
	b	0.25	0.65	0.1
	c	0.05	0.1	0.85
C14 Groundwater	a	0.85	0.1	0.05
	b	0.25	0.65	0.1
	c	0.05	0.1	0.85
C15 Weathering	a	0.7	0.25	0.05
	b	0.3	0.6	0.1
	c	0.1	0.25	0.65

For qualitative indexes, the expert scoring method is adopted to divide them into three categories: a, b and c, and the corresponding membership relationship is shown in Table 2.

Firstly, the single-factor first-level fuzzy matrix R_n is established by the membership degree of each index:

$$R_n = \begin{pmatrix} r_{11} & r_{12} & r_{13} \\ r_{21} & r_{22} & r_{23} \\ \vdots & \vdots & \vdots \\ r_{m1} & r_{m2} & r_{m3} \end{pmatrix} \tag{7}$$

Establish the single-factor fuzzy comprehensive evaluation model:

$$\begin{aligned} A_1 &= X_1 \circ R_1 \\ A_2 &= X_2 \circ R_2 \\ A_3 &= X_3 \circ R_3 \\ A_4 &= X_4 \circ R_4 \end{aligned} \tag{8}$$

Secondly, the four-factor second-level fuzzy comprehensive evaluation model is synthesized by weight vector X and matrix R:

$$A = X \circ R \tag{9}$$

Field observation

Based on the goaf stability evaluation, ground borehole detection was done for goaf of the lower coal seam in order to confirm the accuracy of goaf stability evaluation, and the stability of the goaf roof was thoroughly assessed through borehole core breakage degree, borehole electrical measurement, and borehole peeping. In order to eliminate the impact of drilling technology on the core breakage degree, two sites above the goaf and adjacent solid coal were selected for detection.

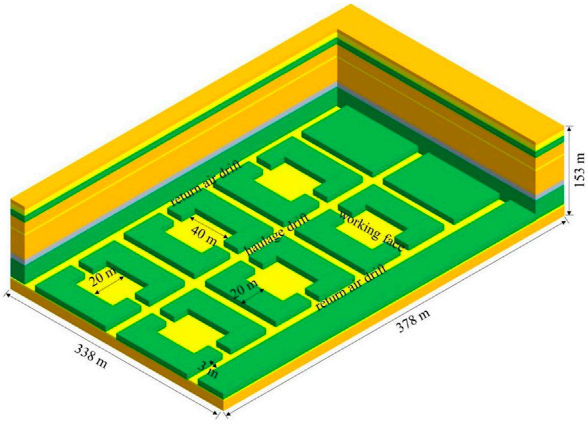

FIGURE 3
Diagram of numerical simulation model.

Numerical modeling

FLAC3D is a finite element difference numerical simulation software, which is mostly used for geotechnical engineering simulation. Combined with the ZK-7 borehole column and rock mechanics parameters, the simulation calculation was carried out for the mining of No. 19 coal seam. The length × width × height of the model was 378 m × 338 m × 153 m, as shown in Figure 3, boundary constraints were imposed on the

TABLE 3 Rock mechanics parameters.

Lithology	Thickness/ m	Tensile strength/MPa	Elastic modulus/GPa	Friction angle/(°)	Cohesion/ MPa	Poisson's ratio
Fine-sandstone 13	6	1.93	4.3	33	5.5	0.19
Sandy mudstone 9	3	2.38	6.5	30	4.1	0.13
Medium sandstone 3	11	3.12	9.2	35	6.4	0.26
Fine-sandstone 12	5	1.93	4.3	33	5.5	0.19
Sandy mudstone 8	3	2.38	6.5	30	4.1	0.13
Fine-sandstone 11	3	1.93	4.3	33	5.5	0.19
Sandy mudstone 7	3	2.38	6.5	30	4.1	0.13
Fine-sandstone 10	3	1.93	4.3	33	5.5	0.19
Sandy mudstone 6	6.5	2.38	6.5	30	4.1	0.13
Fine-sandstone 9	5	1.93	4.3	33	5.5	0.19
Sandy mudstone 5	1	2.38	6.5	30	4.1	0.13
Fine-sandstone 8	2	1.93	4.3	33	5.5	0.19
Sandy mudstone 4	3.5	2.38	6.5	30	4.1	0.13
No. 19 coal	3.5	1.21	5.7	29	2.4	0.13
Fine-sandstone 7	6.5	1.93	4.3	33	5.5	0.19
Sandy mudstone 3	1	2.38	6.5	30	4.1	0.13
Fine-sandstone 6	14	1.93	4.3	33	5.5	0.19
Medium sandstone 2	3.5	3.12	9.2	35	6.4	0.26
No. 22 coal	11	1.21	5.7	29	2.4	0.13
Sandy mudstone 2	1	2.38	6.5	30	4.1	0.13
Fine-sandstone 5	6	1.93	4.3	33	5.5	0.19
Coal line 2	1	1.21	5.7	29	2.4	0.13
Fine-sandstone 4	6	1.93	4.3	33	5.5	0.19
Coal line 1	1	1.21	5.7	29	2.4	0.13
Fine-sandstone 3	6	1.93	4.3	33	5.5	0.19
No. 25 coal	8	1.21	5.7	29	2.4	0.13
Fine-sandstone 2	13	1.93	4.3	33	5.5	0.19
Medium sandstone 1	3	3.12	9.2	35	6.4	0.26
Sandy mudstone 1	3	2.38	6.5	30	4.1	0.13
Fine-sandstone 1	10.5	1.93	4.3	33	5.5	0.19

side and bottom of the model, and a vertical stress of 3 MPa was applied to the upper surface of the model. The Mohr Coulomb criterion was selected for the model, and the side pressure coefficient was taken as 1. See Table 3 for rock mechanical parameters.

The occurrence state diagram of No. 22 coal old goaf is shown in Figure 3. At present, the mining of No. 19 coal seam has not been carried out. The conventional wall mining method is used to carry out the simulation research on the mining of No. 19 coal seam. On the base of No. 22 coal seam mining, the mining of the overlying No. 19 coal seam is simulated. The working face length is 200 m, and the mining is pushed forward by 120 m. The mining is carried out 12 times by the way of gradual excavation, and the final mining position is located above the section-pillar center of the No. 22 coal seam.

Results

Stability evaluation of the old goaf

According to the evaluation model, the stability of pillar goaf of No. 22 coal seam is evaluated as follows:

The geological structure of the room and pillar mining area is simple, there is no fault, and there is an aquifer in the overlying strata of the coal seam, which is the direct source of water filling for the goaf after mining. The parameters of various evaluation indexes can be obtained from the measured data and the existing geological data, as shown in Table 4.

Substituting the numerical values of each index into the calculation formula of membership function, the fuzzy relation matrix of each influencing factor can be obtained as follows:

TABLE 4 Specific index parameters of goaf.

Evaluation factors	Evaluation indexes	Specific parameters
B1 Geological factors	C1 Burial depth of coal seam	200 m
	C2 Dip Angle of coal seam	3°
	C3 Geological structure	Undeveloped (b)
	C4 Thickness of the roof	3
B2 Mining factors	C5 Aspect ratio of coal pillar	2.5
	C6 Mining ratio	0.5
	C7 Distribution of coal pillar	Dense and uniform (a)
	C8 Area of goaf	0.14 km^2
	C9 Remaining time	13a
B3 Strength factors	C10 Compressive strength of pillar	16 MPa
	C11 Compressive strength of roof	16 MPa
	C12 Tensile strength of roof	1.21 MPa
B4 Environmental factors	C13 Mining disturbance	No (a)
	C14 Groundwater	Minor (b)
	C15 Weathering	Weak (b)

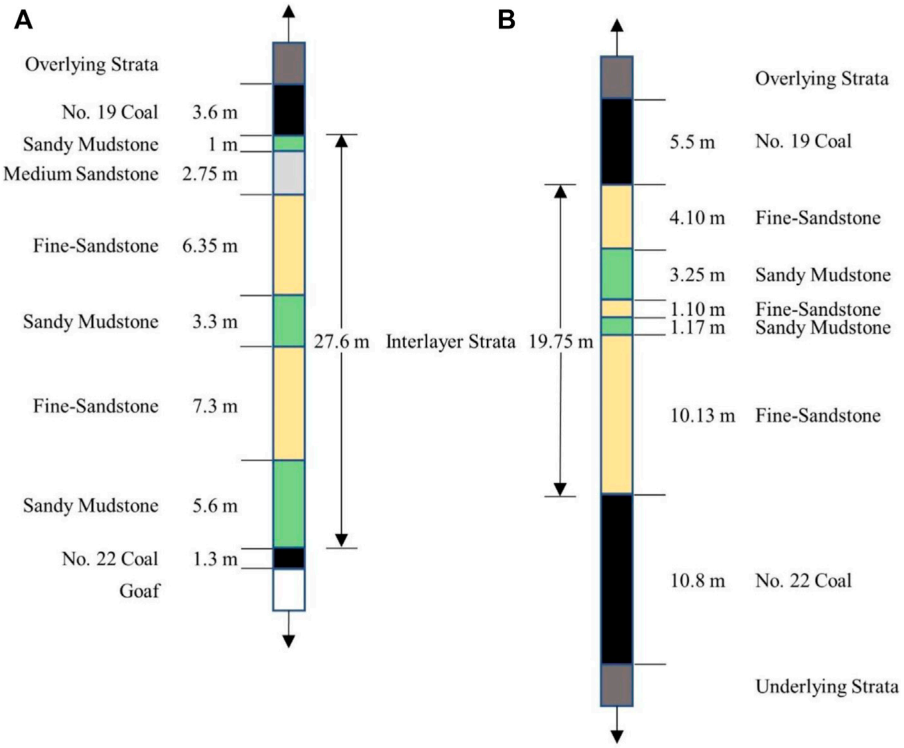

FIGURE 4
Column of boreholes in goaf and solid coal. **(A)** Goaf borehole Column; **(B)** Solid coal borehole column.

$$R_1 = \begin{pmatrix} 0 & 0.67 & 0.33 \\ 0.4 & 0.6 & 0 \\ 0.25 & 0.6 & 0.15 \\ 0 & 0.6 & 0.4 \end{pmatrix}$$

$$R_2 = \begin{pmatrix} 0.75 & 0.25 & 0 \\ 1 & 0 & 0 \\ 0.8 & 0.15 & 0.05 \\ 0.86 & 0.14 & 0 \\ 0 & 0.2 & 0.8 \end{pmatrix}$$

$$R_3 = \begin{pmatrix} 0.3 & 0.7 & 0 \\ 0 & 0.8 & 0.2 \\ 0.11 & 0.89 & 0 \end{pmatrix}$$

$$R_4 = \begin{pmatrix} 0.8 & 0.15 & 0.05 \\ 0.25 & 0.65 & 0.1 \\ 0.3 & 0.6 & 0.1 \end{pmatrix}$$

Substituting the weight and membership degree of each index into Eq. 8, the single factor first-level fuzzy comprehensive evaluation vector is obtained as follows:

$$A_1 = X_1 \circ R_1 = (0.058, 0.13, 0.604, 0.209) \circ \begin{pmatrix} 0 & 0.67 & 0.33 \\ 0.4 & 0.6 & 0 \\ 0.25 & 0.6 & 0.15 \\ 0 & 0.6 & 0.4 \end{pmatrix}$$
$$= (0.203, 0.604, 0.193)$$

$$A_2 = X_2 \circ R_2 = (0.314, 0.38, 0.172, 0.095, 0.039) \circ \begin{pmatrix} 0.75 & 0.25 & 0 \\ 1 & 0 & 0 \\ 0.8 & 0.15 & 0.05 \\ 0.86 & 0.14 & 0 \\ 0 & 0.2 & 0.8 \end{pmatrix}$$
$$= (0.835, 0.125, 0.04)$$

$$A_3 = X_3 \circ R_3 = (0.582, 0.109, 0.309) \circ \begin{pmatrix} 0.3 & 0.7 & 0 \\ 0 & 0.8 & 0.2 \\ 0.11 & 0.89 & 0 \end{pmatrix}$$
$$= (0.208, 0.77, 0.022)$$

$$A_4 = X_4 \circ R_4 = (0.731, 0.188, 0.081) \circ \begin{pmatrix} 0.8 & 0.15 & 0.05 \\ 0.25 & 0.65 & 0.1 \\ 0.3 & 0.6 & 0.1 \end{pmatrix}$$
$$= (0.656, 0.28, 0.064)$$

Based on the above calculation, the four-factor second-level fuzzy comprehensive evaluation matrix can be obtained. According to the weight vector of the four factors, the second-level fuzzy comprehensive evaluation vector can be calculated as:

$$A = X \circ R = (0.408, 0.353, 0.06, 0.179) \circ \begin{pmatrix} 0.203 & 0.604 & 0.193 \\ 0.835 & 0.125 & 0.04 \\ 0.208 & 0.77 & 0.022 \\ 0.656 & 0.28 & 0.064 \end{pmatrix}$$
$$= (0.507, 0.387, 0.106)$$

According to the calculation results of second-level fuzzy comprehensive evaluation, the membership degree of the stability class of the goaf to the stability class of I, II, and III is 0.507, 0.387, and 0.106 respectively. Obviously, the membership degree of the stability class of Class I is the highest, so the stability evaluation of goaf is good, that is, the goaf can be stable by itself at present. And can resist certain external interference.

Borehole exploration

In order to clarify the stability of the roof in the goaf of No. 22 coal seam and the integrity of No. 19 coal seam, coring was started from 30 m above No. 19 coal seam. Among them, the core recovery rate of borehole above solid coal is 85.95%, and the core recovery rate of borehole above goaf is 84.73%. The electrical survey results of the borehole above the goaf show that there is still 1.3 m of top coal in the goaf roof that has not collapsed, indicating that the roof of goaf in No. 22 coal seam has good integrity. The overburden of the No. 22 coal seam has good integrity, and no visible fissures are created, according to the borehole peep. The column of two boreholes is shown in Figure 4.

Stability analysis of the goaf

According to the numerical calculation results, the main stress distribution cloud diagram of coal pillar of No. 22 coal seam is shown in Figure 5. It can be seen from Figure 5 that the principal stress of the crossheading-pillar is concentrated. Among them, the maximum principal stress P_1 shows an obvious decreasing trend towards the center of the crossheading-pillar at the shoulder angle and bottom angle of the goaf, the minimum principal stress P_3 has the maximum stress at the center of the crossheading-pillar, and the stress decreases towards goaf and roadway.

In order to clarify the influence of mining stress distribution on the plastic zone of coal pillar, a 60 m × 60 m × 1 m working face model and a 43 m × 43 m × 1 m roadway model are established respectively. The rock mechanics parameters are shown in Table 4. The stresses above the working face and roadway are extracted for numerical simulation calculation. The results are shown in Figure 6.

It can be seen from Figure 6 that the plastic failure depth of coal pillar at the side of goaf is 0.5–2.5 m, that of coal pillar at the side of roadway is 0.5 m, so the elastic zone in the middle of coal pillar is 17 m, and the plastic failure degree of a single coal pillar is 15%. Namely, the stripping degree of coal pillar is 15%, and it can remain stable.

It can be seen from Figure 7 that after the mining of No. 22 coal, the stress concentration occurred on both sides of the working face and on both sides of the roadway, with the maximum peak principal stress of 12.19 MPa and the stress concentration factor of 2.47. The stress of the overlying strata above the working face decreases, and the maximum and minimum principal stresses are distributed in an arch shape.

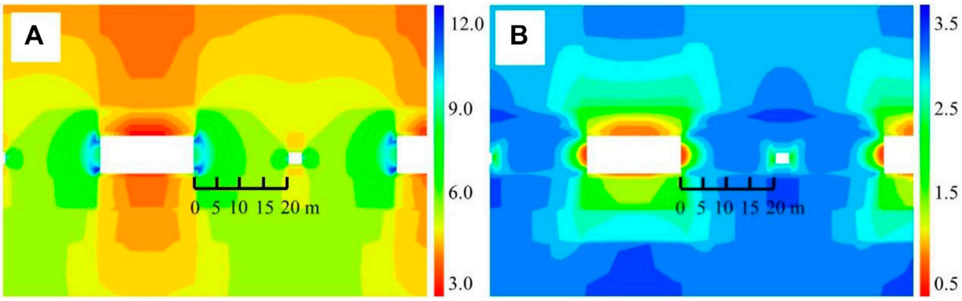

FIGURE 5
Distribution cloud diagram of principal stress in No. 22 coal pillar. **(A)** Maximum principal stress distribution cloud diagram; **(B)** Minimum principal stress distribution cloud diagram.

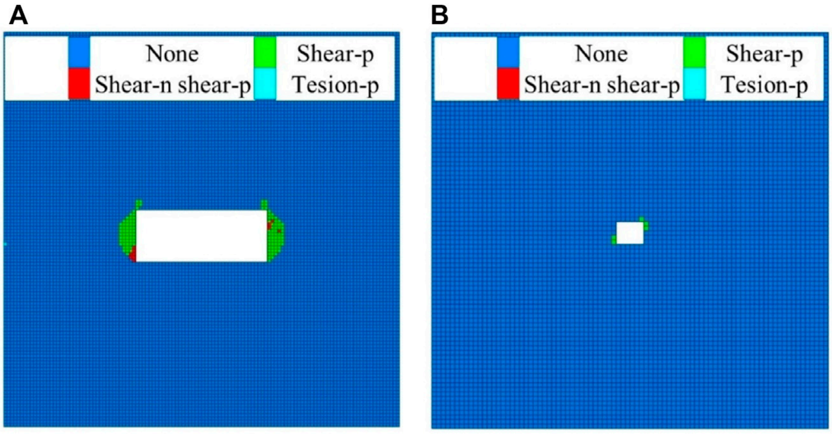

FIGURE 6
Plastic zone development pattern of single mining unit. **(A)** Plastic zone of goaf; **(B)** Plastic zone of roadway.

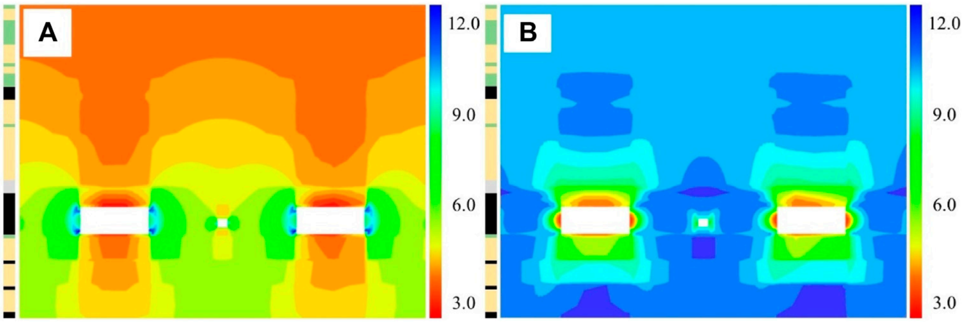

FIGURE 7
Principal stress distribution diagram of roof strata of No. 22 coal. **(A)** Maximum principal stress distribution diagram; **(B)** Minimum principal stress distribution diagram; In the figure, the lithology of each roof layer is shown in ZK-7 borehole column.

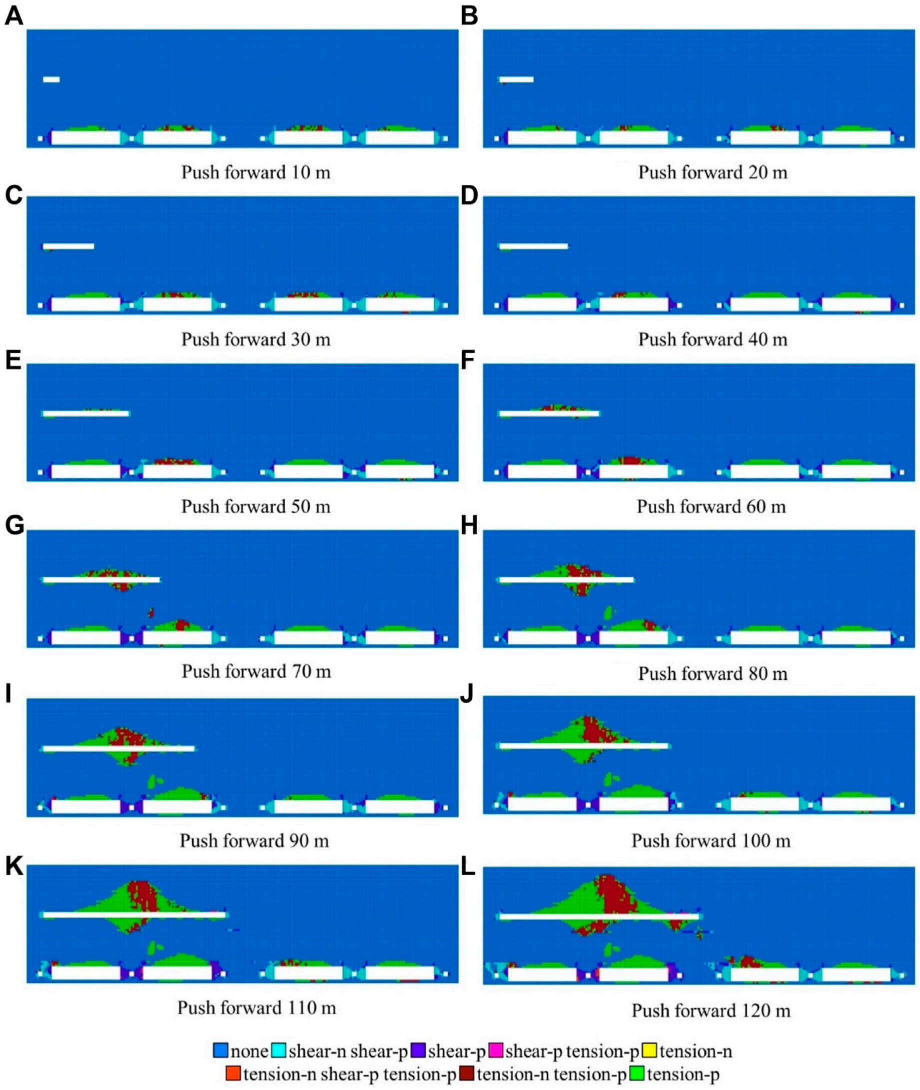

FIGURE 8
Plastic failure law diagram of No. 19 coal mining. **(A)** Push forward 10 m; **(B)** Push forward 20 m; **(C)** Push forward 30 m; **(D)** Push forward 40 m; **(E)** Push forward 50 m; **(F)** Push forward 60 m; **(G)** Push forward 70 m; **(H)** Push forward 80 m; **(I)** Push forward 90 m; **(J)** Push forward 100 m; **(K)** Push forward 110 m; **(L)** Push forward 120 m.

The principal stress gradient of the thick fine-sandstone layer above the roof is large. Under its support, the overlying strata are less affected by goaf of the lower coal seam. The location of Coal Seam No. 19 is close to the original rock stress state. Except that there are some plastic zones in the top coal of No. 22 coal seam, there is no obvious plastic state in the overlying strata.

Study on upper coal mining

The size of the crossheading-pillar between the two mining units in the room pillar mining of No. 22 coal seam is large, but the size of the drift-pillar between the mining unit and the haulage drift and the return air drift is only 5 m, so the plastic failure is relatively serious in the direction of the No. 22 coal seam mining unit excavating. The distribution of the plastic zone of No. 19 coal seam mining step by step is shown in Figure 8.

After the No. 22 coal is mined, the part of drift-pillar near the cut-hole is plastic failure, and the part of drift-pillar near the crossheading-pillar is still in the elastic state. The crossheading-pillar and the section-pillar are less affected by mining.

According to Figure 8, when the No. 19 coal seam starts mining, the surrounding rock stress is redistributed, which has a

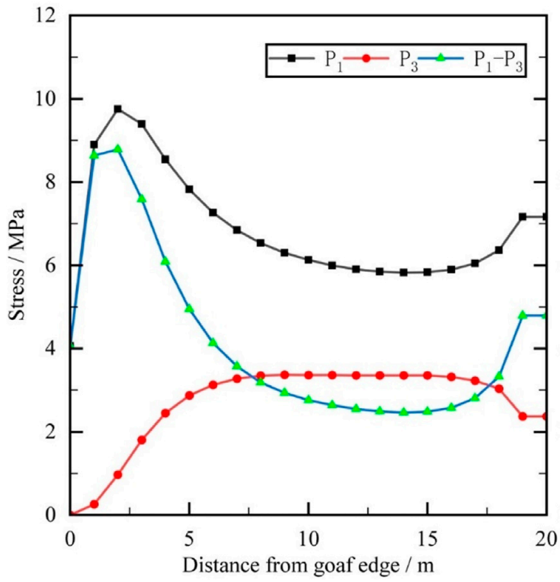

FIGURE 9
Principal stress curve of coal pillar.

mining influence on the roof and floor and the No. 22 coal seam goaf. When the No. 19 coal seam faces push forward within 40 m, the plastic failure depth of the No. 22 coal seam roof is 3 m, and the total lateral failure range is 62 m. When the working face of the No. 19 coal seam is pushed forward 50 m, the No. 19 coal seam is located above the drift-pillar of No. 22 coal seam, and the No. 19 coal roof appears plastic failure with the failure depth of 1 m and the failure width of 22 m. The plastic failure depth of the No. 22 coal goaf roof in front of the working face remains unchanged, and the lateral failure range increases to 64 m.

When the No. 19 coal face continues to push forward, plastic failure occurs on the floor of No. 19 coal working face above the drift-pillar of No. 22 coal seam and gradually increases with the advance of the working face, with the maximum failure depth of 8 m; When the No. 19 coal face is pushed to the upper part of the next mining unit of the No. 22 coal seam, due to the influence of the overburden rotary stress, the roof of goaf is failure more deeply, with the maximum failure depth of 8 m, and there is a certain failure area in the interlayer strata. The failure area is located at the side of the roof of the second mining unit of the No. 22 coal seam close to the drift-pillar; When the No. 19 coal face is pushed to the top of the section-pillar in the No. 22 coal seam, the floor of the No. 19 coal face witch above the section-pillar has plastic failure, the maximum depth of plastic failure is 10 m, and the plastic failure of the roof of the goaf on the other side of the coal pillar in the No. 22 coal seam mining area has intensified, the maximum depth of failure is 8 m. There is no plastic failure in front of the No. 19 coal seam, and the plastic zone of the No. 19 coal seam is not connected with the plastic zone of the No. 22 coal seam.

Discussion

The stress curve of coal pillar can well reflect the current stress state of coal pillar. The principal stress curve of coal pillar in the old goaf is shown in Figure 9.

It can be seen from Figure 9 that due to the roof subsidence of the goaf, the stress of the coal pillar is concentrated, and the principal stress of the coal pillar at 0–2 m on the side of the goaf increases sharply; At the position of 2–15 m, the principal stress of coal pillar decreases and tends to be stable; The principal stress of 15–20 m coal pillar increases again, which is caused by the stress concentration of roadway surrounding rock. The maximum principal stress P_1 reaches the peak value in the range of 2–4 m due to the influence of the roof subsidence and rotation in the goaf, and reaches the peak value again in the range of 18–20 m due to the influence of the stress concentration in the surrounding rock of the roadway. The minimum principal stress P_3 is small due to the goaf on both sides of the coal pillar. The abutment pressure of coal pillars in two adjacent crossheading are symmetrical to each other.

The principal stress curves of the roof strata on both sides of the crossheading-pillar of the No. 22 coal seam are shown in Figure 10. It can be seen from Figures (a) and (b) that after the mining of the No. 22 coal seam, the stress balance of the surrounding rock is destroyed. The top coal of the No. 22 coal seam is not mined as the direct roof, and its stress concentration is the largest. The top thick fine-sandstone layer is used as the control layer to isolate the impact of the old goaf on the overburden. The No. 19 coal seam has stress changes only at the corresponding position above the No. 22 coal seam old goaf, and the corresponding position above the coal pillar is close to the original rock stress state. The occurrence of the old goaf of No. 22 coal seam has little impact on No. 19 coal seam. This result is consistent with the result of the old goaf stability evaluation, that is, the goaf itself can remain stable.

Figure 11 shows the plastic failure pattern expansion diagram of the upper coal seam at different advancing positions.

It can be seen from Figure 8 that before No. 19 coal seam is mined, the failure depth of No. 22 coal seam old goaf is 0–3 m, that is, the top coal of No. 22 coal seam is partially collapsed, which is consistent with the results of drilling detection. The results of drilling detection in the goaf show that there is still 1.3 m of top coal on the roof of old goaf.

As shown in Figure 11, when the No. 19 coal face advances to the 60 m position, the failure depth of the No. 19 coal face roof is 4 m and the failure area is 85 m^2. From the 70 m position, the plastic failure depth increases by 80%, 10%, 40%, 55%, 12%, 26%, and the plastic failure area increases by 70%, 60%, 50%, 55%, 34%, 39% compared with the previous position; When the No. 19 coal face advances to the 70 m position, the failure depth of the floor of the No. 19 coal face is 6 m, and the failure area is 66 m^2. From the 80 m position, the plastic failure depth increases by 33%, 13%, 0%, 11%, 20%, and the plastic failure

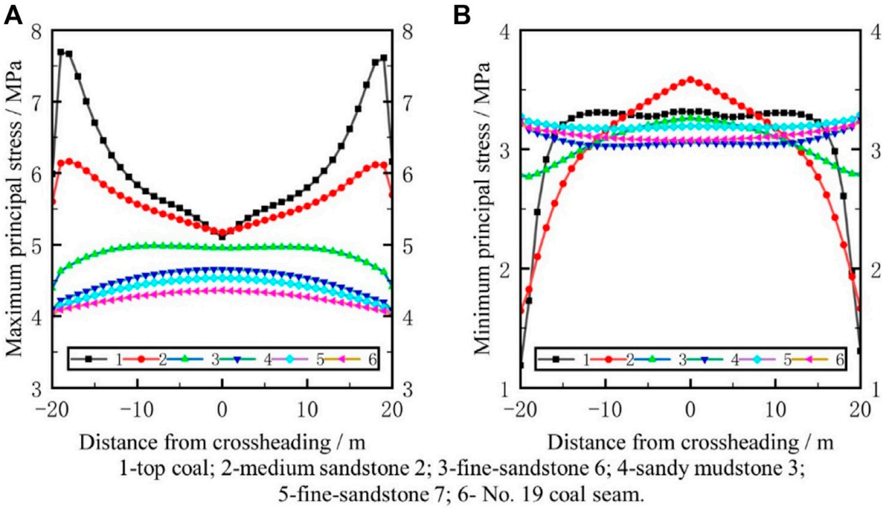

FIGURE 10
Principal stress distribution diagram of roof strata of No. 22 coal. **(A)** Maximum principal stress distribution curve of roof strata of No. 22 coal; **(B)** Minimum principal stress distribution curve of roof strata of No. 22 coal.

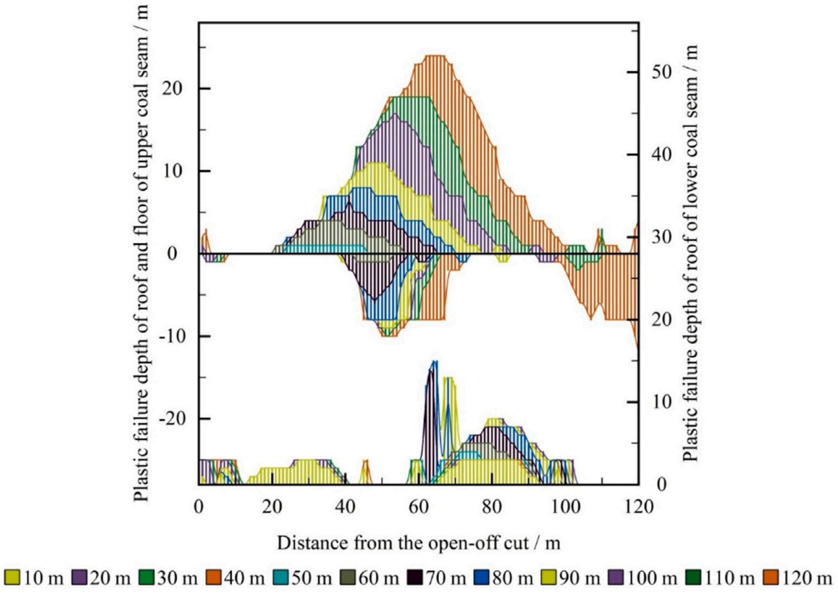

FIGURE 11
Expansion diagram of plastic failure patterns at different advancing positions in upper coal seam.

area increases by 71%, 25%, 11%, 21%, 103% compared with the previous position; Within 40 m of No. 19 coal working face advancing, the failure depth of No. 22 coal goaf roof is 3 m, the failure depth does not change, and the failure area increases by 11%. When No. 19 coal working face advancing to 50 m position, the failure depth of No. 22 coal goaf roof is 4 m, and the failure area is 167 m^2. Compared with the previous position, the plastic failure depth increases by 33%, 25%, 180%, 7%, and the failure area of plastic zone increases by 9%, 14%, 36%, 22% in the 50–80 m position. In the 90–120 m position, the plastic failure depth of No. 22 coal roof does not increase, and the failure area increases by 24%.

In the process of upper coal seam mining, the interlayer strata are failure in different positions and degrees. The maximum failure depth of interlayer strata is 22 m, accounting for 78.6% of the total thickness of interlayer strata.

Based on the above research, it can be concluded that the old goaf itself can remain stable before the mining of the upper coal seam, the top coal above the old goaf has partially collapsed, and there is no collapse of the interlayer rock strata. When the upper coal seam starts to be mined, the old goaf of the lower coal seam can bear certain mining influence, and the interlayer rock stratum remains stable.

The key to the mining of the upper coal seam is the stability of the interlayer strata. When the interlayer strata are intact, the upper coal seam can be mined normally. When there are cracks in the interlayer strata, the upper coal seam will be affected by the overflow of gas and water in the lower goaf. When the coal pillar and wall of the current coal seam goaf are stripped and the roof falls, the thickness of the interlayer strata decreases and the bearing capacity weakens. There may be some problems such as broken surrounding rock and difficult support in the upper coal seam mining.

Based on the above research and mine geological data, the following control measures are taken for the hazards in the mining process of upper coal seam:

(1) When mining upper coal seam, reasonable length of working face should be selected, the size of working face should be appropriately reduced, and the support strength of roadway and working face should be increased to reduce the bearing pressure of interlayer strata and reduce the probability of the formation of through cracks.
(2) Due to the advance of the working face, the increase of the abutment pressure will lead to the surrounding rock breaking in the advance roadway. The “anchor mesh cable” combined support can be adopted, and materials such as lengthened anchor bolts and grouting anchor bolts can be selected. If more support is required, the surrounding rock can be strengthened by grouting or increasing the support density.

Conclusion

(1) The pillar goaf stability evaluation method is adopted to calculate the stability of the lower coal seam old goaf, and the membership degree of the goaf to Class I stability is 0.507. Therefore, the stability of the old goaf is evaluated as good, and the goaf can stabilize itself and resist certain external interference.
(2) The numerical analysis shows that the plastic failure depth of the crossheading-pillar in the room and pillar mining of the lower coal seam is 15%, and the overlying thick fine-sandstone is used as the control layer, which insulates the influence of the lower mining and stress redistribution, and makes the upper coal seam stable.
(3) The conventional wall mining method is used to simulate and analyze the mining of upper coal seam. It is concluded that with the advance of the mining, the failure depth of interlayer strata will gradually increase due to the influence of the overburden rotary stress and coal pillar stress concentration in the lower coal seam. The maximum failure depth accounted for 78.6% of the interlayer spacing. The interlayer rock strata can bear the mining disturbance of the upper coal seam.
(4) Based on the above research, targeted control measures are proposed for hazards in the upper coal seam mining process.

Data availability statement

The original contributions presented in the study are included in the article/Supplementary Material, further inquiries can be directed to the corresponding author.

Author contributions

HL: Writing, methodology. CH: Data curation, writing—original draft. ZW: Investigation. CL: Numerical simulation. LG: Numerical simulation. JL: Data curation. HW: Methodology.

Funding

This work was partially supported by the National Natural Science Foundation of China (Grant No. 51574224), the National Natural Science Foundation of China (Grant No. 52004289) and the Fundamental Research Funds for the Central Universities (Grant No. 2022XJNY01).

Acknowledgments

The authors wish to sincerely thank various organizations for their financial support.

Conflict of interest

ZW was employed by Zuoyun Hanjiawa Coal Industry Co., Ltd., Shanxi Coal Imp. & Exp. Group. CL was employed by China CAMC Engineering Co., Ltd.

The remaining authors declare that the research was conducted in the absence of any commercial or financial relationships that could be construed as a potential conflict of interest.

Publisher's note

References

Bai, J., Feng, G., Wang, S., Qi, T., Yang, J., Guo, J., et al. (2018). Vertical stress and stability of interburden over an abandoned pillar working before upward mining: A case study. *R. Soc. open Sci.* 5 (8), 180346. doi:10.1098/rsos.180346

Cheng, X. (2004). Research and practice on ascending mining under complicated geological conditions. *Coal Sci. Technol.* (1), 44–46. doi:10.13199/j.cst.2004.01.46.chengxm.013

Du, J. P., and Meng, X. R. (2009). *Mining technology*. Xuzhou, China: China University of Mining and Technology Press. (In Chinese).

Feng, G. (2009). *Study on the theory and its application of upward mining of left-over coal.* Taiyuan: Taiyuan University of Technology.

Feng, G., Yan, X., Wang, X., Kang, L., and Zhai, Y. (2009). Determination of key positions of strata controlling in rocks between coal seams for upward mining. *Chin. J. Rock Mech. Eng.* 28 (S2), 3721–3726. doi:10.3321/j.issn:1000-6915.2009.z2.061

Feng, G., Zheng, J., Ren, Y., Wang, X., Kang, L., and Liu, H. (2010). Decision theory and method on feasibility on the upward fully mechanized mining of the left-over coal above gob area mined with caving method. *J. China Coal Soc.* 35 (11), 1863–1867. doi:10.13225/j.cnki.jccs.2010.11.018

Feng, G., Ren, Y., Wang, X., Li, J., and Kang, L. (2011). Experimental study on the upward mining of the left-over coal above gob area mined with caving method in Baijiazhuang Coal Mine. *J. China Coal Soc.* 36 (4), 544–550. doi:10.13225/j.cnki.jccs.2011.04.015

Feng, G., Ren, Y., Wang, X., Li, J., Kang, L., et al. (2011). Experimental study on the movement and deformation of rock strata berween coal seams in the coal mining above gob area. *J. Min. Saf. Eng.* 28 (3), 430–435. doi:10.3969/j.issn.1673-3363.2011.03.018

Feng, G., Yang, C., Zhang, Y., Bai, J., Guo, J., Du, Y., et al. (2019). Temporal and spatial evolution law of abutment pressure during upward long-wall mining in the wedge residual pillar mining area. *J. Min. Saf. Eng.* 36 (5), 857–866. doi:10.13545/j.cnki.jmse.2019.05.001

Han, W., Wang, L., and Zhou, J. (1998). Observation and investigation of ascending mining of seams in pindingshan No. 4 mine. *J. China Coal Soc.* 3, 45–48.

Han, J., Zhang, H., Zhang, P., and Li, T. (2011). Feasibility study on upward mining in seam group with short distance to each other in kailuan mining area. *Coal Sci. Technol.* 39 (10), 14–17. doi:10.13199/j.cst.2011.10.19.hanj.011

Han, J., Song, W. H., and Zhu, Z. J. (2013). *Upward mining technology of close coal seams*. Beijing, China: China Coal Industry Publishing House. (In Chinese).

He, J., Okere, C. J., Su, G., Hu, P., Zhang, L., Xiong, W., et al. (2021). Formation damage mitigation mechanism for coalbed methane wells via refracturing with fuzzy-ball fluid as temporary blocking agents. *J. Nat. Gas Sci. Eng.* 90, 103956. doi:10.1016/j.jngse.2021.103956

Leilei, S., Zhang, H., Jianping, W., Li, B., and Han, H. (2021). Modeling and experiment for effective diffusion coefficient of gas in water-saturated coal. *Fuel* 284, 118887. doi:10.1016/j.fuel.2020.118887

Leilei, S., Jianping, W., Xi, Y., Wang, H., Wen, Z., Li, B., et al. (2021). The influence of long-time water intrusion on the mineral and pore structure of coal. *Fuel* 290, 119848. doi:10.1016/j.fuel.2020.119848

Li, Y., Lei, M., Zheng, Q., Liu, S., Lv, H., Liu, L., et al. (2019). Quantitative criterion on coordinated ascending mining in close multiple" thin-medium-thick" coal seams. *J. China Coal Soc.* 44 (S2), 410–418. doi:10.13225/j.cnki.jccs.2019.0794

Ma, H. (2021). *Coupling effect of coal pillar-roof and stability evaluation of pillar goaf.* Xuzhou: China University of Mining and Technology.

Ma, L., Wang, L., Zhang, D., Liu, Y., Liu, J., Zhang, T., et al. (2007). Applicationg and study on feasibility of near distance coal seam group Ascending mining. *J. Hunan Univ. Sci. Technol. Nat. Sci. Ed.* (4), 1–5. doi:10.3969/j.issn.1672-9102.2007.04.001

Ma, L., Wang, L., Qiao, J., Wang, S., et al. (2008). Study of ascending mining of short-range-seams in pingdingshan no. 4 coal mine. *J. Min. Saf. Eng.* (3), 357–360. doi:10.3969/j.issn.1673-3363.2008.03.023

Okere, C. J., Su, G., Zheng, L., Cai, Y., Li, Z., and Liu, H. (2020). Experimental, algorithmic, and theoretical analyses for selecting an optimal laboratory method to evaluate working fluid damage in coal bed methane reservoirs. *Fuel* 282, 118513. doi:10.1016/j.fuel.2020.118513

Pan, H., Jiang, N., Gao, Z., Liang, X., and Yin, D. (2022). Simulation study on the mechanical properties and failure characteristics of rocks with double holes and fractures. *Geomechanics Eng.* 30 (1), 93–105. doi:10.12989/GAE.2022.30.1.093

Qu, G., Lin, D., and Wang, B. (2008). Technology on ascending mining affected by mining action of non-equipoise time after time. *J. Min. Saf. Eng.* (2), 217–221. doi:10.3969/j.issn.1673-3363.2008.02.020

Singh, A. K., Singh, R., Sarkar, M., Mandal, P. K., and Sharma, D. (2002). Inclined slicing of a thick coal seam in ascending order - a case study. *Cim. Bull.* 95 (1095), 124–128.

Sun, C., Yan, S., Xu, N., Liu, Y., et al. (2021). Key problems of upward mining under the condition of fully mechanized goaf with large mining height. *J. Min. Saf. Eng.* 38 (3), 449–457. doi:10.13545/j.cnki.jmse.2020.0086

Tao, X., Okere, C. J., Su, G., and Zheng, L. (2022). Experimental and theoretical evaluation of interlayer interference in multi-layer commingled gas production of tight gas reservoirs. *J. Petroleum Sci. Eng.* 208, 109731. doi:10.1016/j.petrol.2021.109731

Wang, L. Q., and Li, Z. H. (1994). *Ascending mining technology of coal seams.* Beijing, China: China Coal Industry Publishing House. (In Chinese).

Yao, D. H., Jiang, N., Wang, X., Jia, X., and Lv, K. (2022). Mechanical behaviour and failure characteristics of rocks with composite defects of different angle fissures around hole. *Bull. Eng. Geol. Environ.* 81 (7), 290. doi:10.1007/s10064-022-02783-z

Zhang, H., Han, J., Hai, L., Li, M., and Qiao, H. (2013). Study on closed multiple-seam in the ascending mining technology. *J. Min. Saf. Eng.* 30 (1), 63–67.

Zhang, Y., Okere, C. J., and Su, G. (2021). Effect of loading rates on accurate *in-situ* stress determination in different lithologies via Kaiser effect. *Arab. J. Geosci.* 14, 1304. doi:10.1007/s12517-021-07674-3

frontiers | Frontiers in Earth Science

TYPE Original Research
PUBLISHED 18 January 2023
DOI 10.3389/feart.2022.1069924

EDITED BY
Hongtu Zhang,
Henan Polytechnic University, China

REVIEWED BY
Tong Yang,
China University of Mining and Technology, Beijing, China
Botao Li,
Xi'an University of Science and Technology, China
Weiyong Lu,
Luliang University, China

*CORRESPONDENCE
Wei Wang,
0215051@ccit.edu.cn

SPECIALTY SECTION
This article was submitted to Economic Geology,
a section of the journal
Frontiers in Earth Science

RECEIVED 14 October 2022
ACCEPTED 07 November 2022
PUBLISHED 18 January 2023

CITATION
Wang M, Zhao D, Lv Y, Wang W and Wang X (2023), Prediction method of shield tunneling parameters in pebble stratum formed by weathered granite and quartzite.
Front. Earth Sci. 10:1069924.
doi: 10.3389/feart.2022.1069924

Prediction method of shield tunneling parameters in pebble stratum formed by weathered granite and quartzite

Meiyan Wang[1,2], Dajun Zhao[1], Yan Lv[1], Wei Wang[3]* and Xing Wang[3]

[1]Country College of Construction Engineering, Jilin University, Changchun, China, [2]Department of Civil Engineering, Shandong Vocational College of Science and Technology, Weifang, China, [3]School of Civil Engineering, Changchun Institute of Technology, Changchun, China

The pebble formation formed by weathered quartzite and granite is usually of high strength, strong permeability and poor self stability, which brings great difficulties to shield tunneling. It is necessary to adjust the tunneling parameters at any time to prevent the consequences of instability of the tunnel face, loss of stratum and surface settlement caused by the imbalance of the soil bin pressure. GA algorithm is embedded into PSO algorithm for parameter optimization, and grey theory is combined to establish the prediction model of soil chamber pressure based on grey least square support vector machine, which can solve the problem of difficult control of tunneling parameters in pebble stratum formed by weathered quartzite and granite. Research indicates: GA-PSO-GLSSVM chamber Earth pressure prediction model enhances the EPB chamber Earth pressure forecast accuracy in complicated strata by integrating the global search capability of the GA algorithm, the quick convergence of the PSO algorithm, and the anti-disturbance capability of the GM model. The GA-PSO-GLSSVM model has high goodness-of-fit and accuracy compared with other prediction models. This model can successfully prevent the a series of undesirable consequences such as destabilization of the palm surface, missing strata and settlement due to ground surface due to pressure imbalance in the soil chamber pressure. The research results can provide reference for EPB shield tunneling parameter control in Grade V surrounding rock.

KEYWORDS

sandy cobble stratum, weathered quartzite and granite, grade V surrounding rock, earth pressure balance shield, in chamber earth pressure, grey least square support vector machine, particle swarm optimization, genetic algorithm

Introduction

Because of its broad applications and little influence on the environment, Earth Pressure Balance shield (EPB) is frequently utilized in the building of subway tunnels. The operational status of the shield technique must frequently be reflected by the tunneling parameters since it is a closed process. In order to successfully manage ground settlement,

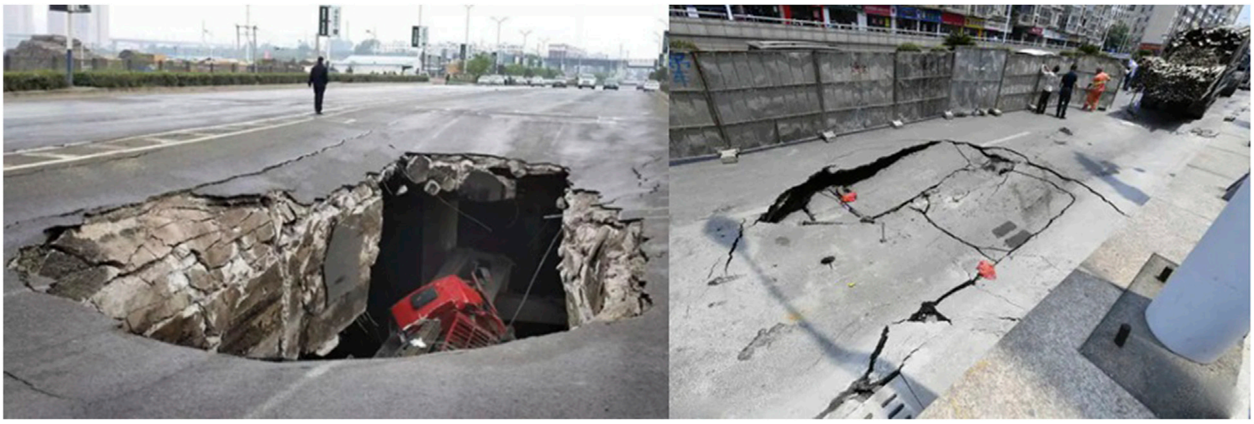

FIGURE 1
Ground subsidence caused by shield construction.

ensure the stability of the tunnel face, reduce cutting tool loss, and keep the shield in a favorable position, it is important to choose the right tunneling parameters. The shield tunneling parameters must also be modified and optimized in real time when geological conditions change during the tunneling process in order to guarantee the shield is tunneled securely and effectively. Once the tunneling parameters are improperly controlled, it is very easy to cause accidents such as ground subsidence and building collapse, as illustrated in Figure 1. Therefore, how to accurately predict and control the tunneling parameters has always been the research focus in the field of shield tunnel construction technology (Pan et al., 2022). At present, many scholars have studied the variation laws and theoretical calculations of cutter head torque, shield thrust, grouting pressure, tunneling speed and other parameters under different geological conditions during EPB shield tunneling, and established mathematical and physical models to predict tunneling parameters according to Hooke's law (Jie et al., 2017; Wei et al., 2017; Yang et al., 2017; Zhao et al., 2017; Boukhari, 2020; Cao et al., 2020; Gao et al., 2020; Al-Habahbeh, 2022; Lu et al., 2022; Lyu et al., 2022). Although these models can reflect the analytical relationship between tunneling parameters, shield tunneling is a complex and changing process, and the stratum it crosses is actually a non-uniform and discontinuous non-linear elastomer. Therefore, this kind of prediction model has certain limitations in engineering applicability.

With the rapid development of big data and artificial intelligence technology in recent years, deep learning algorithms such as big data statistical analysis (Sekiya et al., 2022; Wu et al., 2022), BP neural network (Zhou et al., 2015; Cachim and Bezuijen, 2019; Wang et al., 2022a), genetic algorithm (GA) (Ahangari et al., 2015), support vector machine (SVM) (Wang et al., 2013; Wang et al., 2022b), random forest (RF) (Zhou et al., 2017; Ge et al., 2022), particle swarm optimization (PSO) (Liu et al., 2018; Elbaz et al., 2022) have been applied in the prediction of shield tunneling parameters. The rudiment of the concept of deep learning is the deep belief network (DBN) proposed by Hinton in 2006. This method adopts unsupervised layer by layer training to improve the depth of network training, and has achieved good application results. It is considered to be one of the most potential deep learning algorithms after unsupervised learning. The research above shows that the accuracy of the prediction model established by these intelligent algorithms is significantly higher than that of the mathematical physical model, which has important application value for EPB shield tunneling under different geological conditions. The most crucial factor in ensuring the normal tunneling of the EPB shield machine is the Earth pressure inside the chamber. There have been studies done on the prediction model of the Earth pressure within the chamber, and Shangguan (2011) established the mapping link between the Earth pressure inside the chamber and controllable elements such propulsion speed. Based on a genetic algorithm, Li and Cao (2012) projected the pressure of the soil. There are currently two basic approaches for building a prediction model for the Earth pressure within a chamber using tunneling parameters. According to Hooke's rule of conservation of excavation and dumping volume of soil, one is to develop a mathematical model of the Earth pressure in chamber prediction (Liu et al., 2022). The alternative way is to construct a prediction model of the Earth pressure in a chamber based on tunneling characteristics identified during the tunneling process using neural networks and other more intelligent methods (Shi et al., 2008; Liu et al., 2011). The instability of the tunnel

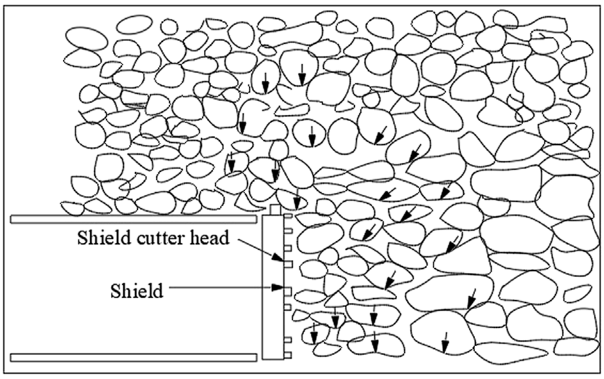

FIGURE 2
Mechanism of stratum loss during shield excavation.

face and loss of strata caused by the imbalance of Earth pressure in the chamber will have a number of unfavorable effects, including the elevation and settling of the ground surface. The coupling action of tunneling parameters such as cutter head torque, screw conveyor speed, shield thrust, grouting pressure, etc. Results in the dumping efficiency of the shield machine during the tunneling process. The dumping efficiency is influenced by the mechanical and physical parameters of the formation, which change over time.

Sandy pebble stratum usually has high permeability, loose structure, and extremely low cohesion, and its overall stability is generally poor. During shield tunneling, it is bound to change the stress state of the stratum near the excavation face, causing stratum loss, and in serious cases, it will lead to large ground subsidence and building damage, causing great difficulty to shield construction. Because the Earth pressure in chamber of EPB shield is often a nonlinear mapping relationship with other tunneling parameters, it is difficult to determine the functional relationship between the Earth pressure in chamber and other tunneling parameters by polynomial fitting. In view of this, this study integrated the GA algorithm into the PSO algorithm for parameter optimization, thoroughly examined the characteristics of large interaction and strong coupling effect between shield tunneling parameters combined with Grey theory, established a prediction model of soil pressure based on Grey Least Square Support Vector Machine (GLSSVM), the validity and reliability of the prediction model are confirmed through the sand gravel shield tunnel section project of Chengdu metro line 17, using the actual monitoring data as the training and test samples of the prediction model, which serves as a reference for the EPB shield tunneling parameter control in sandy gravel stratum.

Materials and methods

Mechanism and influencing factors of surface subsidence in sandy pebble stratum

During shield construction in sandy pebble stratum, due to the jacking and extrusion of shield machine and the shear friction between shield shell and soil, the equilibrium state of stratum is disturbed and destroyed, the soil particles move, and the initial stress of stratum changes and redistributes, causing stratum loss. The ground loss V_s is calculated as follows:

$$Vs = V_{s'}\pi r_0^2 \tag{1}$$

where, V_s is ground loss in m^2, $V_{s'}$ is ground loss ratio in % and r_0 is outer diameter in m.

The loss of sandy gravel stratum caused by shield tunneling is usually the sum of the loss of excavation face, the periphery of shield machine and the tail of shield. When the shield top thrust is extruded during shield tunneling, the soil moves sideways and loosens up in a specific area in front of the excavation face, which is what causes the formation loss at the excavation face, as illustrated in Figure 2. Because the sand pebble stratum contains a lot of pebbles and they are strong, the cutter head and shield machine's props frequently sustain significant wear. Additionally, when the cutter is replaced or the machine pauses when it runs into significant frontal obstructions, stratum loss occurs. During tunneling, the shield machine will produce varying degrees of friction, shear and extrusion with the surrounding sand pebbles, and a certain thickness of shear disturbance area will be formed around the shield, within which the soil mass will move and cause formation loss, as shown in Figure 3. Additionally, the gap between the outer diameter of the cutter head and the outside circumference of the shield shell and the overbreak of the shield brought on by the attitude adjustment during the tunneling of the shield machine would both result in the loss of the sandy gravel layer. At the shield's tail, there is a small opening between the segment lining ring and the tunnel excavation wall. Deep soil disturbance and formation loss will result from the soil disturbed by friction shear moving to this gap. Because the sandy gravel stratum has such wide pores and a high permeability coefficient, grouting cannot be done effectively, which will impact the stability of the sandy gravel stratum tunnel later on.

According to the settlement mechanism, the stress state of the excavation surface, the gap between the soil and the shield shell, the over break caused by deviation correction, the grouting pressure at the tail of the shield and other influencing factors are related to the control of the shield construction parameters, mainly including the pressure of the Earth bunker, the tunneling speed, the total thrust of the shield, the torque and speed of the cutter head, the grouting pressure and amount in the

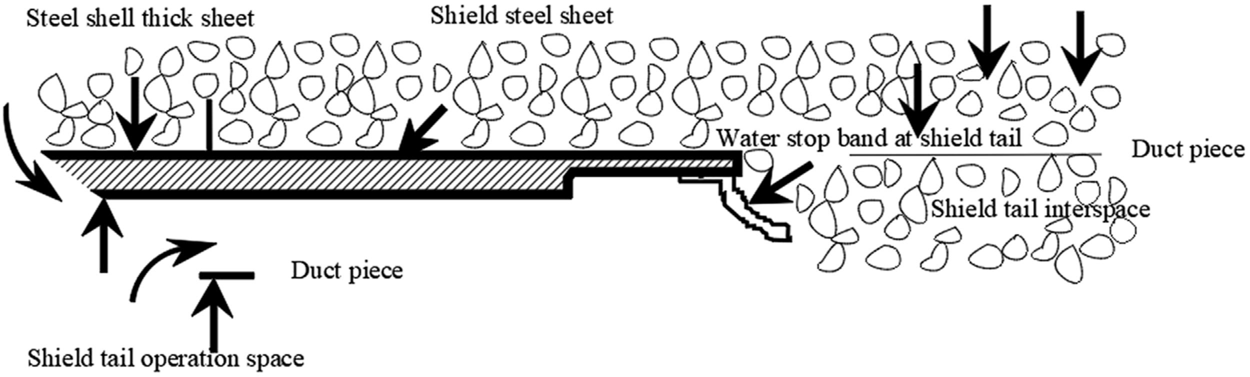

FIGURE 3
Mechanism of stratum loss around shield shell.

same step, and the posture offset of the shield. The working pressure in the soil bin is not always consistent with the real situation due to the weak flow plasticity of sand and gravel, which will impair the stability of the excavation surface and, in severe circumstances, cause surface settlement and collapse. Large stones can easily remain in the soil bin during slag discharge or migrate about, which can impact the shield machine's ability to maintain its position and attitude. The shield machine's inability to go forward once obstructed will have an impact on the stability of the excavation surface. Another important aspect impacting surface settlement is the shield tunnel's depth, which influences whether or not a pressure arch can be built on top of the tunnel to limit soil particle movement and minimize disturbance.

GA-PSO-GLSSVM prediction model for the Earth pressure in chamber in sandy pebble stratum

Based on deep learning algorithm based on statistical learning theory, LSSVM replaces quadratic programming optimization in support vector machine by solving linear equations. LSSVM model is an adaptive model, which can change the empirical risk from the first power to the second power, and replace inequality constraints with equality constraints (Lin et al., 2014; Zhang et al., 2022). Compared with the traditional support vector machine, its advantage is to improve the solution speed and simplify the complex calculation. GLSSVM model is based on LSSVM and Grey theory GM (1.1) to accumulate the original data, and then get new sequence data that is less affected by disturbance factors and has stronger regularity. The specific modeling process is as follows:

1) Original data sequence:

$$x_i^0 = \{x_1^0, x_2^0, \cdots, x_l^0\} \tag{2}$$

Where, x_i^0 is ground settlement in mm, l =1, 2, 3 ...

2) Cumulative preprocessing data sequence by GM(1.1):

$$\bar{x}_0 = \{x_1^1, x_2^1, \cdots, x_l^1\} \tag{3}$$

3) The high-dimensional feature space description of the data sequence obtained from the previous learning sample set in the LSSVM model:

$$\min J(\boldsymbol{w}, b, e) = \frac{1}{2}\boldsymbol{w}^{\mathrm{T}}\boldsymbol{w} + \frac{\gamma}{2}\sum_{i=1}^{n} e_i^2 \tag{4}$$

4) Linear functional relationship:

$$y(x) = \boldsymbol{w}^{\mathrm{T}}\varphi(x) + b \tag{5}$$

Where, $\boldsymbol{A}$ (x_i, y_i) $(i$ =1, 2, . . . , $n)$ is learning sample set, $x_i \in \boldsymbol{R}^n$ is learning sample, $y_i \in \boldsymbol{R}$ is corresponding output prediction sample, $\boldsymbol{w}$ is weight vector, J (w, b, e) is loss function, γ is fault tolerant coefficient, e_i is error, $\varphi(x)$ is mapping function and b is offset.

The Lagrangian operator is applied to optimize $\boldsymbol{w}$ and e, and the Lagrangian function is established:

$$L(\boldsymbol{w}, b, e, \boldsymbol{\alpha}) = J(\boldsymbol{w}, e) - \sum_{i=1}^{n}\alpha_i\{\boldsymbol{w}^{\mathrm{T}}\varphi(x_i) + b + e_i - y_i\} \tag{6}$$

Where, α_i is Lagrange multiplier, and the differential solution of Eq.4 is carried out. The linear equations are obtained according to the optimal conditions of KKT (Karush Kuhn Tucker):

$$\begin{bmatrix} 0 & \boldsymbol{E}^{\mathrm{T}} \\ \boldsymbol{E} & Q + \boldsymbol{I}/\gamma \end{bmatrix}\begin{bmatrix} b \\ \boldsymbol{\alpha} \end{bmatrix} = \begin{bmatrix} 0 \\ \boldsymbol{y} \end{bmatrix} \tag{7}$$

Where, $\boldsymbol{y} = [y_1, y_2, \ldots, y_i]^{\mathrm{T}}$, $\boldsymbol{E} = [1, 1, \ldots, 1]^{\mathrm{T}}$, $\boldsymbol{\alpha} = [\alpha_1, \alpha_2, \ldots, \alpha_i]^{\mathrm{T}}$, Q is kernel function for nonlinear mapping, which $Q_{ij} = K(x_i, x_j)$, $i, j = (1, 2, \ldots, n)$, and $\boldsymbol{I}$ is identity matrix. The regression model of LSSVM is obtained by solving the equations:

$$f(x) = \sum_{i=1}^{n} \alpha_i y_i K(x_i, x_j) + b \tag{8}$$

Through calculation, the predicted value of the cumulative sequence is obtained: y_{n+k} $(k = 1, 2, \ldots, n)$. The prediction model of the original data sequence is obtained by progressive reduction:

$$\bar{x}_1 = y_{n+k+1} - y_{n+k} \tag{9}$$

Parameter optimization by PSO-GA

The choice of kernel function has an important impact on the accuracy and accuracy of the prediction results of GLSSVM regression model. GLSSVM regression model usually uses Gaussian radial basis kernel function K (x_i, x_j) to analyze nonlinear sample data, as follow:

$$K(x_i, x_j) = \exp\left[-\frac{1}{\sigma^2}\left\|x_i - x_j\right\|^2\right] \tag{10}$$

In order to correctly predict unknown data without *a priori* reference value, the fault-tolerant penalty coefficient of kernel function must be γ and kernel parameters σ^2 adjust the two parameters. At present, GA and PSO algorithms are commonly used for parameter optimization, but neither of them can guarantee the optimal solution. If the operator of GA algorithm is embedded into PSO algorithm, and the GA algorithm with excellent change ability is added to the memory ability of PSO algorithm, the whole population can converge rapidly towards the global optimization (Huang et al., 2022). Suppose a group of particles in D-dimensional space, each particle corresponds to a position X and velocity V that can characterize its attributes. When the dth particle swarm iteration is updated, the iteration of motion velocity V_i and motion position X_i of particle i is updated as follows:

$$V_i^d = \omega V_i^{d-1} + c_1 r_1\left(pBest_i - X_i^{d-1}\right) + c_2 r_2\left(gBest_i - X_i^{d-1}\right) \tag{11}$$

$$X_i^d = X_i^{d-1} + V_i^d \tag{12}$$

Where, ω is inertia weight, $i = (1, 2, \ldots, m)$, $d = (1, 2, \ldots, D)$, and m is number of particles, D is search dimension, c_1 and c_2 are acceleration factors, and their values determine the optimization time, which is usually positive, $pBest_i$ is optimal position of particle i, r_1 and r_2 are random constants between [0, 1].

The value of the inertia weight ω has a direct impact on both the global and local optimization outcomes. The inertia weight is determined as follows to better balance the local and global search capabilities:

$$\omega = \omega_{\max} - t \cdot \frac{\omega_{\max} - \omega_{\min}}{t_{\max}} \tag{13}$$

Where, $\omega_{\max}$ is maximum inertia weight, $\omega_{\min}$ is minimum inertia weight, $\omega_{\min}$ is maximum iterations, t is current iterations. It can be seen that the combination of PSO and GA for parameter optimization has the advantages of global convergence of GA algorithm and rapid convergence of PSO algorithm. The topological structure diagram of prediction model for the Earth pressure in chamber is shown in Figure 4, and the prediction process is shown in Figure 5.

Performance evaluation of prediction model

The key to build the GA-PSO-GLSSVM bunker pressure prediction model is to choose which tunneling parameters are the input variables to predict the bunker pressure. According to the EPB shield's affecting elements, there is a strong correlation between Earth bunker pressure and the total thrust, cutter head torque, cutter head speed, propulsion speed, screw machine speed, grouting volume, and grouting pressure (Liu et al., 2010; Yu et al., 2020; Shen et al., 2022). However, under different geological conditions, the relationship between bunker pressure and tunneling parameters is also quite different. It is necessary to determine the tunneling parameters as input variables through correlation analysis according to the actual engineering conditions, and build the bunker pressure prediction model. The correlation between the soil pressure within the chamber and different tunneling parameters is quantitatively described in this study using the Pearson correlation coefficient (PCC):

$$v = \frac{\sum_{f=1}^{p}\left(Y_f - \bar{Y}\right)\left(Z_f - \bar{Z}\right)}{\sqrt{\sum_{f=1}^{p}\left(Y_f - \bar{Y}\right)^2}\sqrt{\sum_{f=1}^{p}\left(Z_f - \bar{Z}\right)^2}} \tag{14}$$

where, v is Pearson correlation coefficient, Y and Z are parameters to be analyzed and p is number of data groups.

The mean absolute error (MAE), root mean square error (RMSE), coefficient of determination (R^2), and relative error (MAPE) can be used to calculate the discrepancy data and the actual monitoring data in order to assess the accuracy of the prediction model. The prediction result of the prediction model is more accurate and the prediction impact is stronger if the value of the two error indicators approaches 0. The Earth pressure in chamber prediction model's topological structure, prediction method, and model validity test are as follows:

$$\mathrm{MAE} = \frac{1}{p}\sum_{f=1}^{p}\left|q_f - z_f\right| \tag{15}$$

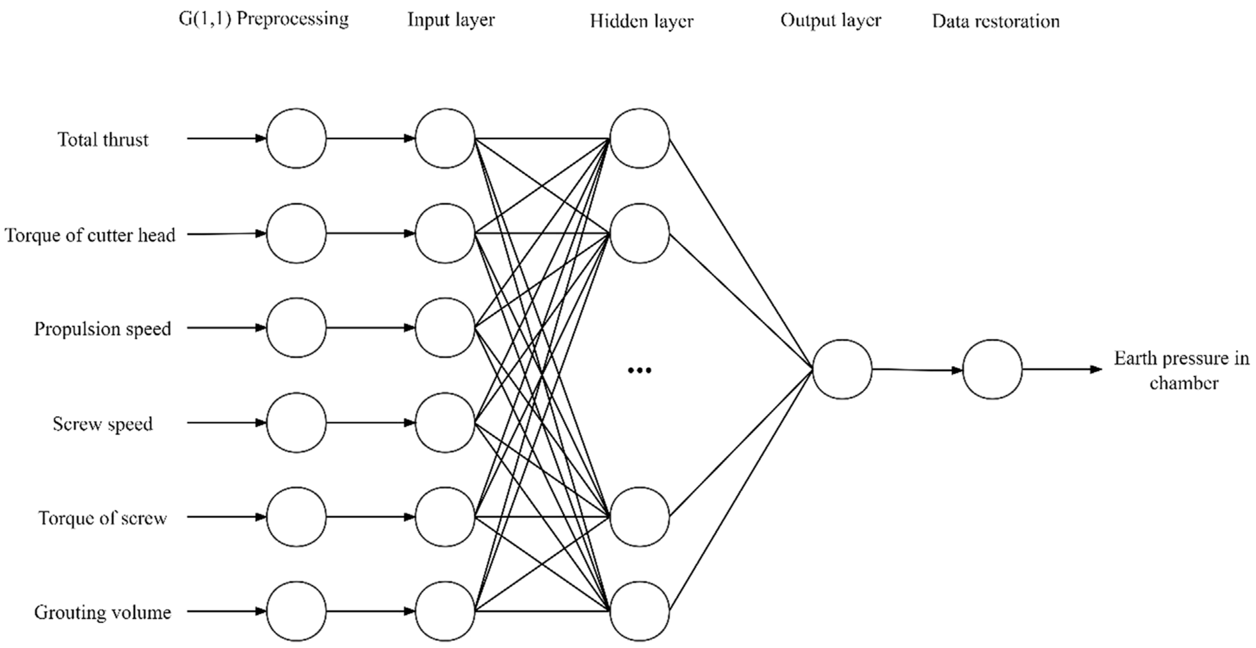

FIGURE 4
Topological structure diagram of prediction model for the Earth pressure in chamber.

$$\mathrm{RMSE} = \sqrt{\frac{1}{p}\sum_{f=1}^{p}\left(q_f - z_f\right)^2} \tag{16}$$

$$\mathrm{R}^2 = 1 - \frac{\sum_{f=1}^{p}\left(q_f - z_f\right)^2}{\sum_{f=1}^{p}\left(z_f - \bar{z}\right)^2} \tag{17}$$

$$\mathrm{MAPE} = \frac{1}{p}\sum_{f=1}^{p}\left(\frac{\left|q_f - z_f\right|}{\bar{z}}\right) \times 100 \tag{18}$$

where, q_f is parameter prediction value of group f data, z_f measured values of parameters of group f data and $\bar{z}$ is average of all measured values.

Results and discussion

Project overview

The starting point of the tunnel between the fifth municipal hospital station and Fengxi station in Chengdu Metro Line 17 is located at the intersection of the north section of Fengxi Avenue and Xifeng street. It is arranged along the north-south direction of Fengxi Avenue, and double track tunneling is accomplished using an Earth pressure balancing shield machine. The left line tunnel is 1610.186 m long, the right line tunnel is 1611.485 m long, and each of the left and right lines uses a separate EPB shield machine. In this segment, the tunnel mostly travels through dense pebble soil layer. The tunnel's minimum plane curve radius is 450 m, and its longitudinal slope gradient is 10.063‰. The tunnel's inner diameter is 7500 mm, its outer diameter is 8300 mm, the top of the tunnel is buried at a minimum depth of approximately 9.5 m and a maximum depth of about 20 m in this section. The mechanical properties of the sandy gravel strata are exceedingly complicated, and it exhibits low cohesion and a big gap between its particles. Shield machine tunneling disturbs the stratum significantly, hence it is important to precisely manage the tunneling parameters. During shield tunneling, one set of monitoring data can be obtained for each ring of excavation. The data set is composed of total thrust, cutter head torque, propulsion speed, screw machine speed, screw machine torque, grouting volume and soil pressure. According to the actual monitoring data, there are 1033 groups of data in this section, and a total of 900 groups of data from 101–1000 rings are taken for statistical analysis. In Table 1, the statistical distribution is displayed.

A total of 635 groups of data from 220 to 855 rings are selected for research. Because the shield parameters do not reflect the general conditions of normal tunneling due to the fact that the shield attitude has not yet been adjusted to the normal position at the beginning of shield tunneling, and also during the shield exit., as shown in Figure 6, and the distribution of the Earth pressure in chamber is shown in Figure 7.

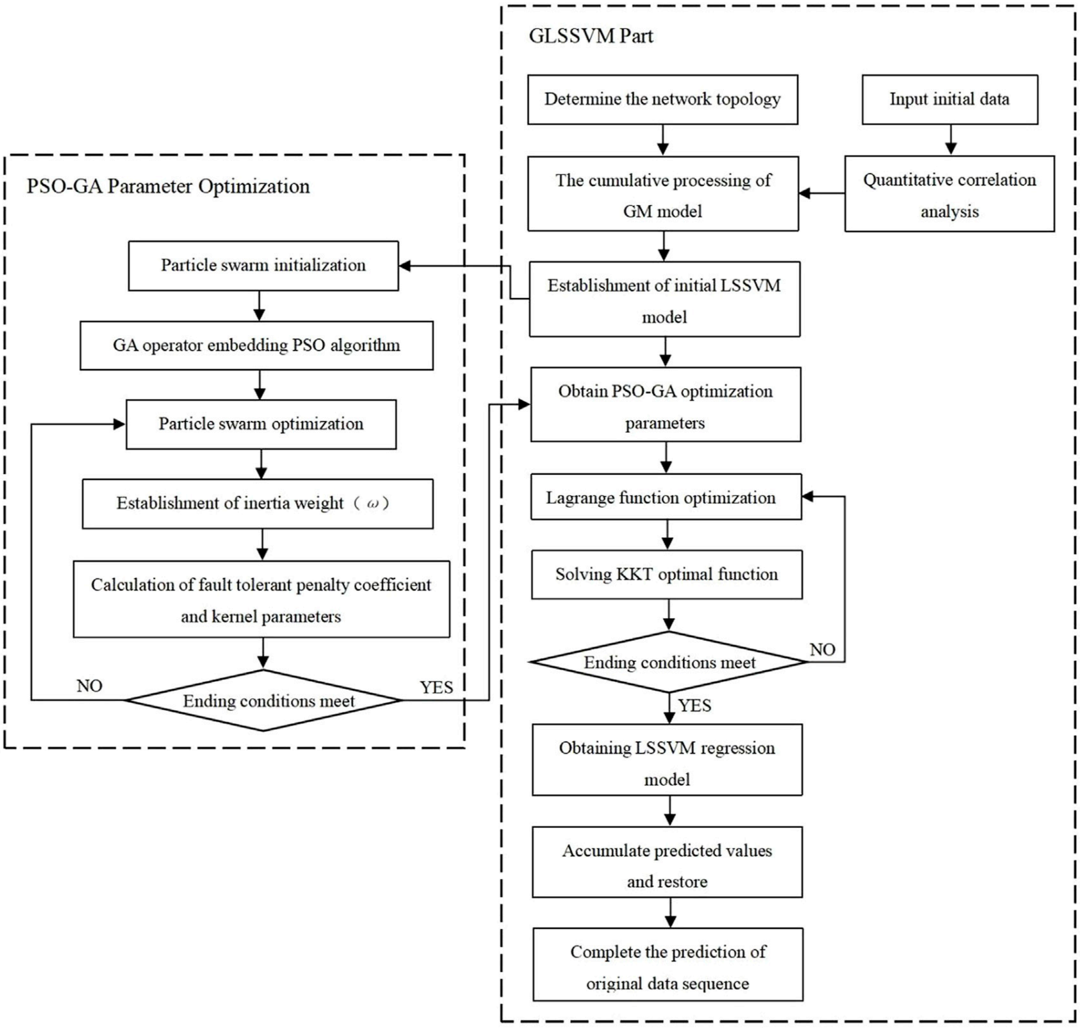

FIGURE 5
Prediction process of GLSSVM-PSO-GA prediction model.

TABLE 1 Statistical distribution of shield machine parameters in shield section.

Tunneling parameters	Number of samples	Maximum value	Minimum value	Average value	Standard deviation
Total thrust (kN)	900	51,517	10,772	31,953	4172
Torque of cutter head (kN·m)	900	22,541	1729	12,187	2366
Speed of cutter head (rpm)	900	1.50	0.86	1.39	0.08
Propulsion speed (mm/min)	900	80	13	69	9
Screw speed (rpm)	900	10.88	1.09	6.37	1.56
Torque of screw (kN·m)	900	97	6	38	12
Grouting volume (m3)	900	22.77	1.50	11.52	2.45
Earth pressure in chamber (bar)	900	2.171	0.141	0.825	0.483

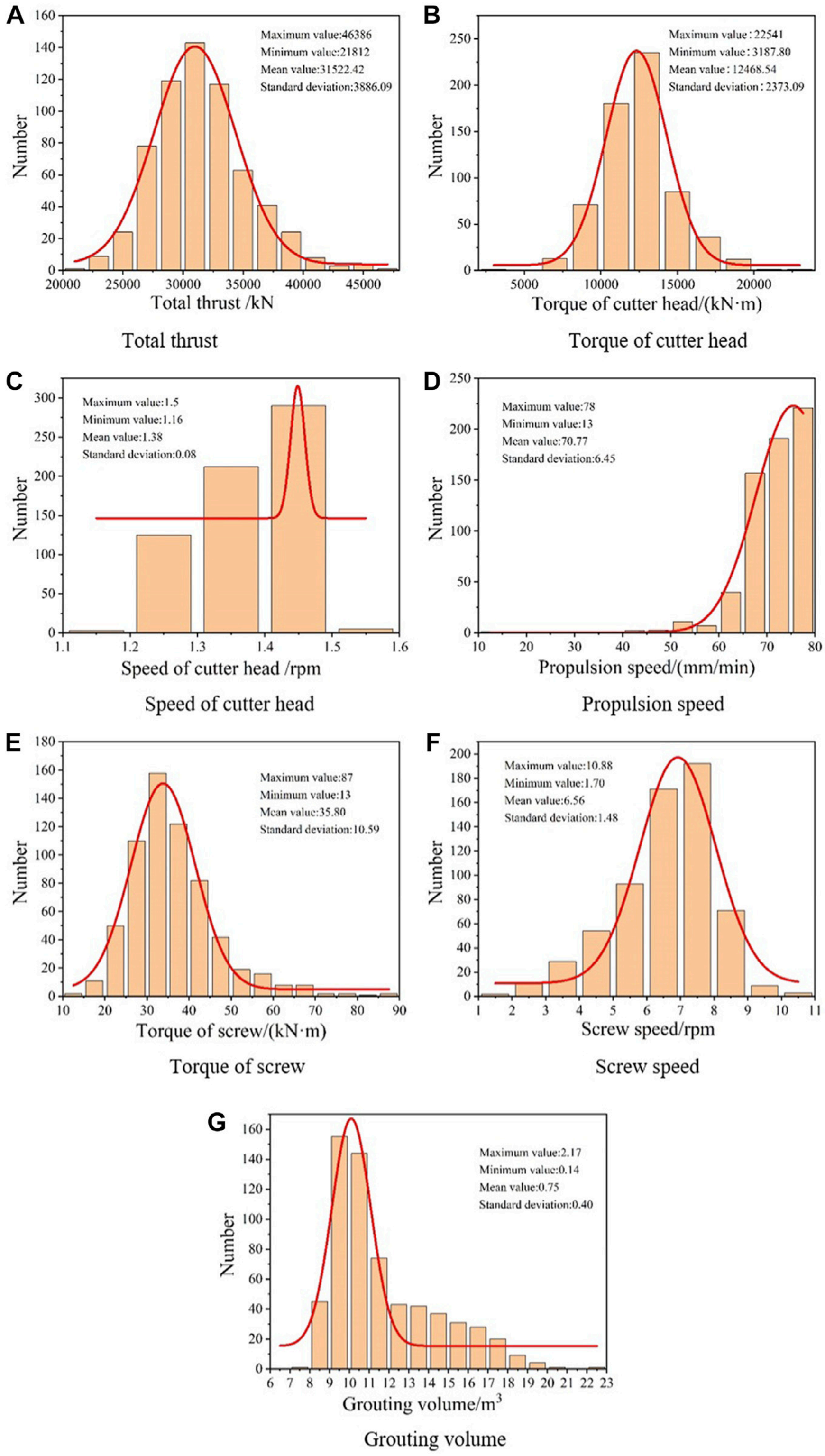

FIGURE 6
Normal distribution of shield machine parameters.

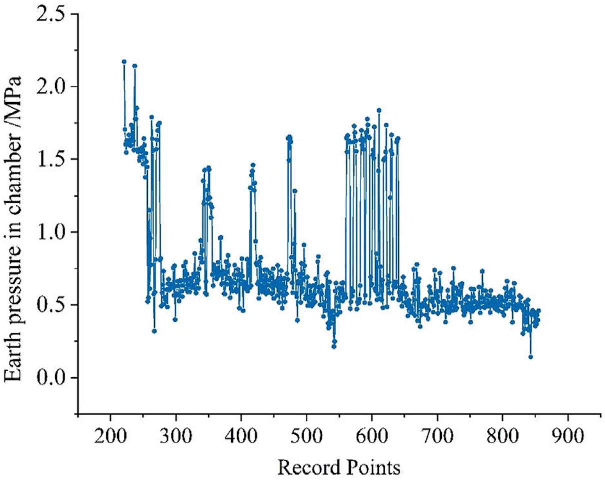

FIGURE 7
Distribution of the Earth pressure in chamber in sample data.

Correlation analysis of tunneling parameters

The association between the soil pressure inside the chamber and different tunneling parameters is expressed by the Pearson correlation coefficient, and the results of Pearson correlation coefficient is shown in Table 2. The calculations show that the Earth pressure within the chamber is positively correlated with the speed of the cutter head, the propulsion speed, the torque of the screw, and the grouting volume and negatively correlated with the total thrust, the cutter head torque, and the screw speed.

Test the calculated correlation coefficient according to requirement that the two factors are at the confidence level α when $|r| \geq r_{\alpha}$. The following correlation shows that screw speed, torque, and cutter head speed are all significantly correlated with Earth pressure in the chamber at the level of 0.01, while total thrust, propulsion speed, and grouting volume are significantly correlated at the level of 0.1, and the correlation between screw torque and Earth pressure in the chamber is negligible. Therefore, the cutter head torque, speed, screw speed, grouting volume, propulsion speed, and total thrust are the input variables for the prediction model for the Earth pressure in the chamber.

Establishment of prediction model

The training set consists of the first 535 of the 635 groups of data, while the test set consists of the last 100. GM (1.1) model accumulation preprocessing is performed on the learning sample set data, and GLSSVM model is established. The crossover operator and genetic operator of GA algorithm are embedded in PSO algorithm, and the fault-tolerant penalty coefficient of GLSSVM model kernel function is calculated γ and kernel parameters σ^2 optimize. The population size is 30, the number of iterations is 300, the crossover rate is 0.6, the variation rate is 0.1, the value range for the two optimization parameters is [0.01, 1000], and the maximum and lowest values of the inertia weight are 0.9 and 0.4, respectively. Local search capability and global search capability c_1=c_2 =1.49445. GA-GLSSVM, PSO-GLSSVM and GA-PSO-LSSVM are used to predict and analyze the data set respectively. The change law of fitness MSE is shown in Figure 8.

According to the fitness curves of each model, GA-GLSSVM model has stronger global search ability and PSO-GLSSVM model has faster convergence speed. Embedding GA operator into PSO algorithm can not only realize the global optimization advantage of GA algorithm, but also give play to the advantage of PSO to accelerate the convergence speed and improve the goodness of fit of the model. When calculating the fitness, the Grey theory GM (1,1) is used to accumulate the original data, and the new sequence data with less influence of disturbance factors and stronger regularity can be obtained. Gray superposition can significantly increase the model's prediction accuracy when compared to GA-PSO-LSSVM and GA-PSO-GLSSVM. The optimal parameter combinations of different models is shown in Table 3.

Analysis and comparison of prediction results

The optimized parameters of each model are brought into LSSVM model for prediction and analysis. The data accumulated by GM (1,1) model will get the accumulated sequence prediction

TABLE 2 Pearson correlation coefficient between chamber Earth pressure and excavation parameters.

	Total thrust	Torque of cutter head	Speed of cutter head	Propulsion speed	Screw speed	Torque of screw	Grouting volume
Earth pressure in chamber	-0.059	-0.211	0.192	0.061	-0.092	0.041	0.062

The critical values of the correlation coefficient r_{α} are 0.055, 0.065 and 0.086 at the three confidence levels of 0.1, 0.05 and 0.01 respectively.

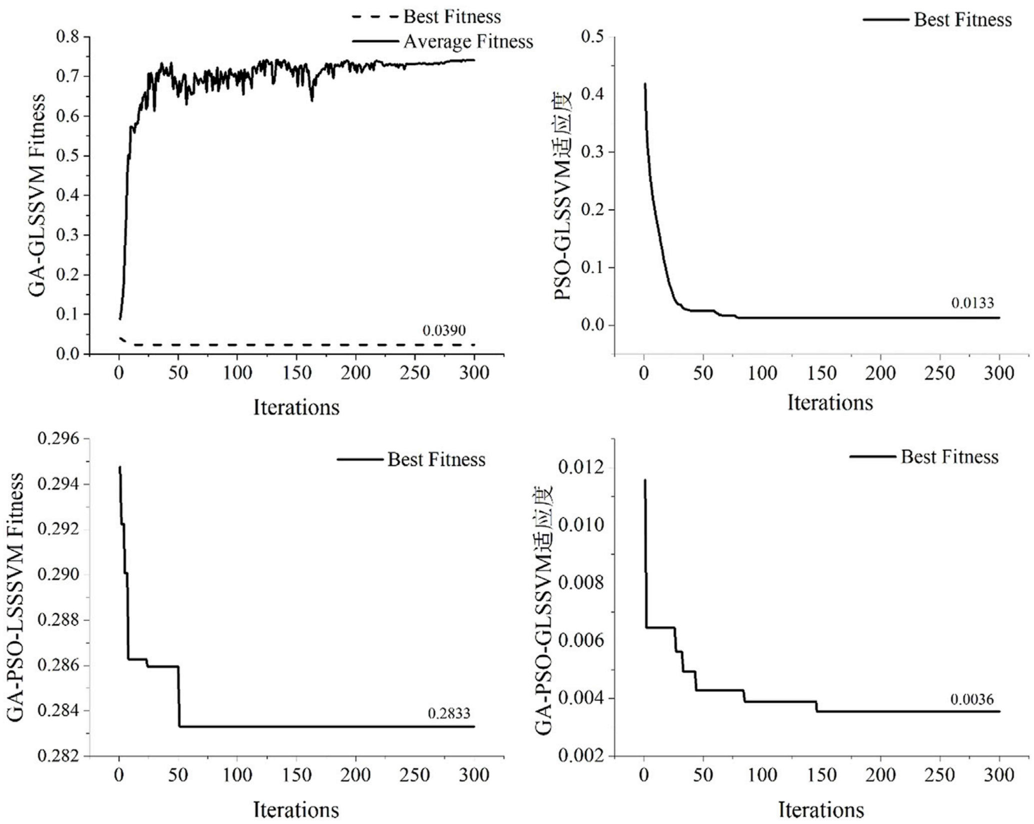

FIGURE 8
The fitness changes of different algorithms.

TABLE 3 Optimal parameter combinations of different models.

Model	γ	σ2
GA-GLSSVM	92.8865	92.8865
PSO-GLSSVM	33.9511	35.2236
GA-PSO-LSSVM	0.1476	10.7545
GA-PSO-GLSSVM	8.8016	61.1870

value, and the prediction value is restored, that is, the original data and the prediction data. The predictions' outcomes are displayed in Figure 9.

When compared, it can be seen that the PSO-GLSSVM model's prediction data is comparatively steady and fluctuates only little, although the predicted result is lower than the actual value. The GA -GLSSVM prediction results fluctuate relatively large in the late stage, and the prediction results are larger than the actual value. The benefits of the aforementioned two models are taken into consideration in the GA-PSO-GLSSVM model, and the forecast outcomes are quite similar to the actual values. The GA-PSO-LSSVM model's predictions have low accuracy and great volatility. After removing certain huge data points from the learning sample set, the distribution of the remaining 524 data is displayed in Figure 10 to demonstrate the model's correctness.

In order to further verify the effectiveness of the anti-volatility capability of the GA-PSO-GLSSVM model and to illustrate the shortcomings of the GA-PSO-LSSVM model with weak anti-volatility capability, the prediction results of the GA-PSO-LSSVM model before and after removing the volatile data are compared here. Make the model parameters unchanged, take the first 424 data as the training set and the last 100 data as the test samples for GA-PSO-LSSVM prediction, and the results are shown in Figure 11.

After excluding certain big values, the model's prediction data have less fluctuation and are more accurate when compared to the GA-PSO-LSSVM prediction results in Figure 9. For the original data samples, GM (1.1) accumulation processing of the sample data in GA-PSO- GLSSVM model can effectively reduce the impact of the fluctuation of the original data and improve the prediction accuracy.

Due to its strong water permeability and poor self stability, sandy pebble stratum is easy to cause stratum loss when

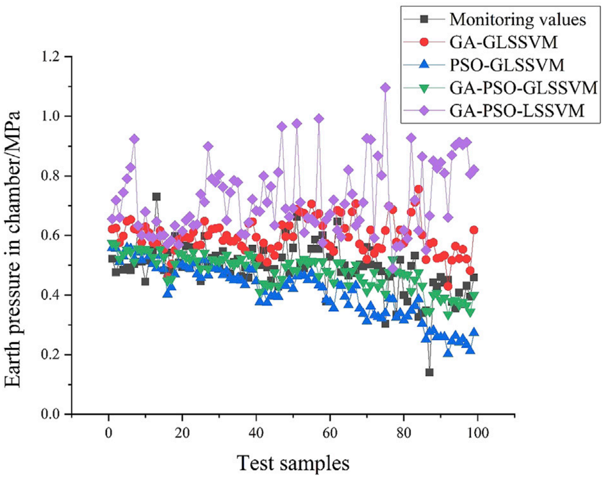

FIGURE 9
Comparison of prediction effects of different models.

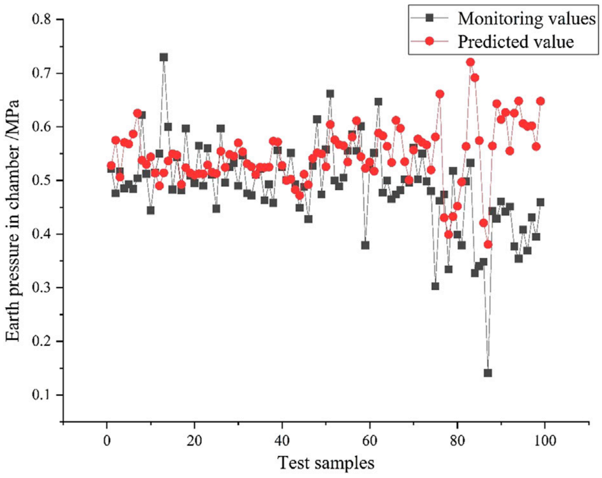

FIGURE 11
The prediction effect of GA-PSO-LSSVM model after eliminating the data with large fluctuation.

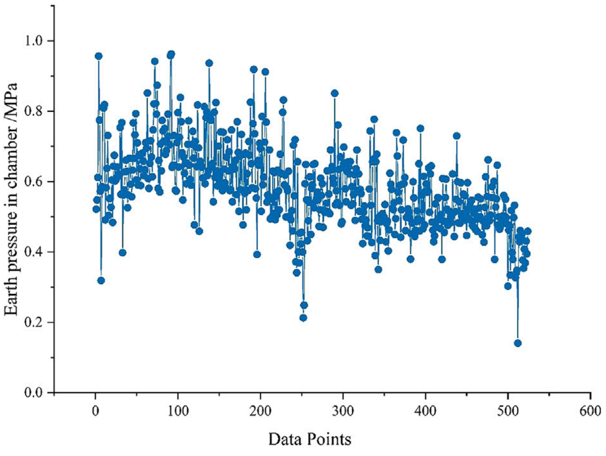

FIGURE 10
Excluding the data with large fluctuations of chamber Earth pressure.

disturbed. Therefore, there are many factors affecting the pressure of the soil during the excavation process, especially when encountering large-size pebbles or poor slag discharge, it is easy to cause abnormal fluctuations in the pressure of the soil. Through comparison study, it can be found that the GA-GLSSVM, PSO-GLSSVM, and GA-PSO-LSSVM initial prediction accuracy and effect are all rather excellent. The difference between the projected value of the soil pressure in the chamber and the observed value is significant when encountering fluctuating data. As can be observed, the prediction model's learning effect is negatively impacted by the quick shift in the tunneling scenario, which significantly reduces forecast accuracy. The GA-PSO-GLSSVM model weakens the influence of data fluctuation on the prediction model, and it has significant applicability to predict the pressure parameters of EPB shield in complex strata such as sand and gravel.

Error analysis

The root mean square error (RMSE), mean absolute error (MAE), mean absolute percentage error (MAPE), and the coefficient of decision (R^2) are used as assessment indicators to assess the accuracy of the prediction model in order to further examine the model's dependability and accuracy. Table 4 displays a comparison of each model's prediction accuracy. The GA-PSO-GLSSVM model has superior stability, fitting accuracy, and result accuracy than other models. As can be shown, the GA-PSO-GLSSVM algorithm predicts the Earth pressure in the EPB shield chamber accurately, and the effect of the prediction after GM (1.1) pretreatment is superior to that of the conventional prediction model.

Conclusion

The GA operator is embedded into the PSO model to optimize the parameter optimization process of the data. This approach combines the GA algorithm's global search capability with the PSO algorithm's benefits of quick convergence, avoids the parameter optimization falling into the local optimal solution, and speeds up the operation efficiency. At the same

TABLE 4 Comparison of prediction accuracy of each model.

Prediction model	RMSE	MRE	MAPE	R2
GA-GLSSVM	0.0390	0.0901	0.1730	0.8066
PSO-GLSSVM	0.0133	0.0935	0.1539	0.8067
GA-PSO-LSSVM	0.2833	0.2348	0.5441	-0.1469
GA-PSO-LSSVM (After removing fluctuation data)	0.2938	0.0804	0.1946	0.8197
GA-PSO-GLSSVM	0.0036	0.0565	0.1253	0.9238

time, GM (1,1) model is introduced into LSSVM model to eliminate the impact of data fluctuation on the prediction model and improve the accuracy of prediction model for the Earth pressure in chamber by GA-PSO-GLSSVM.

Compared with the prediction results of GA-GLSSVM, PSO-GLSSVM, GA-PSO-LSSVM and GA-PSO-GLSSVM, the prediction results of GA-PSO-GLSSVM model are more stable. Compared with the other three models, the root mean square error, average relative error, average absolute percentage error and resolvable coefficient are significantly better than other models, and the prediction accuracy is higher.

Through six tunneling parameters including total thrust, torque of cutter head, propulsion speed, speed of screw, torque of screw and grouting volume, the Earth pressure in chamber of shield tunneling is predicted by using GA-PSO-GLSSVM model. The actual monitoring data is used as the training and test samples of the prediction model to confirm its efficacy and dependability. This model can successfully prevent the instability of the tunnel face and the loss of stratum caused by the imbalance of soil pressure, which in turn cause a series of adverse consequences such as surface settlement, and serves as a reference for the control of EPB shield tunneling parameters in sandy gravel stratum.

Data availability statement

The original contributions presented in the study are included in the article/supplementary materials, further inquiries can be directed to the corresponding author.

Author contributions

MW is the writer and makes most of all the analysis. DZ is the tutor of MW. YL is the project leader. WW makes the monitor analysis. XW edits program.

Funding

This article is supported by: “2022 Project of Science and Technology Development Plan of Jilin Province” Research on safety early warning and settlement sensitivity classification and division of subway sections based on Remote sensing and GIS (No.20220203058SF).

Conflict of interest

The authors declare that the research was conducted in the absence of any commercial or financial relationships that could be construed as a potential conflict of interest.

Publisher’s note

References

Ahangari, K., Moeinossadat, S. R., and Behnia, D. (2015). Estimation of tunnelling-induced settlement by modern intelligent methods. *Soils Found.* 55 (4), 737–748. doi:10.1016/j.sandf.2015.06.006

Al-Habahbeh, O. M. (2022). Sustainable design of an artificial lake in Jafer basin based on gravity flow. *Math. Model. Eng. Problems* 9 (1), 101–110. doi:10.18280/mmep.090113

Boukhari, Y. (2020). Application and comparison of machine learning algorithms for predicting mass loss of cement raw materials due to decarbonation process. *Rev. d'Intelligence Artif.* 34 (4), 403–411. doi:10.18280/ria.340404

Cachim, P., and Bezuijen, A. (2019). Modelling the torque with artificial neural networks on a tunnel boring machine. *KSCE J. Civ. Eng.* 23 (10), 4529–4537. doi:10.1007/s12205-019-0302-0

Cao, X. P., Zhang, Y. P., and Zhang, Y. R. (2020). Anti-seismic effect of the shock absorption layer in tunnel. *Int. J. Saf. Secur. Eng.* 10 (1), 41–47. doi:10.18280/ijsse.100106

Elbaz, K., Yan, T., Zhou, A., and Shen, S. L. (2022). Deep learning analysis for energy consumption of shield tunneling machine drive system. *Tunn. Undergr. Space Technol.* 123, 104405. Article ID 104405. doi:10.1016/j.tust.2022.104405

Gao, F., Lv, S., Zhang, C. Y., Zhang, P., Guo, Z. G., Ma, Q. Y., et al. (2020). Discrete- and finite-element analysis on the tunneling safety of pipe jacking machine in coal rock formation. *Int. J. Heat Technol.* 38 (4), 801–807. doi:10.18280/ijht.380405

Ge, S., Gao, W., Cui, S., Chen, X., and Wang, S. (2022). Safety prediction of shield tunnel construction using deep belief network and whale optimization algorithm. *Automation Constr.* 142, 104488. Article ID 104488. doi:10.1016/j.autcon.2022.104488

Huang, H., Chang, J., Zhang, D., Zhang, J., Wu, H., and Li, G. (2022). Machine learning-based automatic control of tunneling posture of shield machine. *J. Rock Mech. Geotechnical Eng.* 14 (4), 1153–1164. doi:10.1016/j.jrmge.2022.06.001

Jie, L., Fu, K., Guo, J., Zhang, Z., and Xu, M. (2017). Establishment and optimization of a driving speed model for shield tunnelling in mixed ground. *Mod. Tunn. Technol.* 54 (3), 142–147. doi:10.13807/j.cnki.mtt.2017.03.020

Li, S. J., and Cao, L. J. (2012). Pressure control model on soil chamber of shield machine and its parameter identification. *J. China Coal Soc.* 37 (2), 206–210. doi:10.13225/j.cnki.jccs.2012.02.006

Lin, N., Li, W. D., Zhang, W. C., and Yang, J. J. (2014). Deformation prediction of deep foundation pit with least square support vector machine. *J. Liaoning Tech. Univ. Nat. Sci.* 33 (11), 1471–1474. doi:10.3969/j.issn.1008-0562.2014.11.007

Liu, J., Shi, C., Gong, C., Lei, M., Wang, Z., Peng, Z., et al. (2022). Investigation of ultimate bearing capacity of shield tunnel based on concrete damage model. *Tunn. Undergr. Space Technol.* 125, 104510. Article ID 104510. doi:10.1016/j.tust.2022.104510

Liu, X. Y., Cheng, S., and Liu, R. X. (2010). Modeling and simulation on Earth pressure control for shield tunnelling. *J. China Coal Soc.* 35 (4), 575–579. doi:10.13225/j.cnki.jccs.2010.04.033

Liu, X. Y., Shao, C., Ma, H. F., and Liu, R. (2011). Optimal Earth pressure balance control for shield tunneling based on LS-SVM and PSO. *Automation Constr.* 20 (4), 321–327. doi:10.1016/j.autcon.2010.11.002

Liu, X. Y., Xu, S., Zhang, K. J., and Cao, Y. M. (2018). Optimization control for soil pressure balance of shield based on heuristic dynamic programming. *J. Dalian Univ. Technol.* 58 (5), 526–532. doi:10.7511/dllgxb201805013

Lu, P., Yuan, D., Jin, D., Luo, W., and Liu, M. (2022). Centrifugal model tests on the structural response of the shield tunnel when constructing cross passages by mechanical methods. *Tunn. Undergr. Space Technol.* 128, 104621. Article ID 104621. doi:10.1016/j.tust.2022.104621

Lyu, H. M., Shen, S. L., Zhou, A., and Yin, Z. Y. (2022). Assessment of safety status of shield tunnelling using operational parameters with enhanced SPA. *Tunn. Undergr. Space Technol.* 123, 104428. Article ID 104428. doi:10.1016/j.tust.2022.104428

Pan, H., Tong, L., Wang, Z., and Yang, T. (2022). Effects of deep soil mixing on existing shield tunnels in soft soil ground. *Undergr. Space* 7 (4), 724–733. doi:10.1016/j.undsp.2021.12.004

Sekiya, H., Masuda, K., Nagakura, S., and Inuzuka, S. (2022). Determination of shield tunnel deformation under train load using MEMS accelerometers. *Tunn. Undergr. Space Technol.* 126, 104535. Article ID 104535. doi:10.1016/j.tust.2022.104535

Shangguan, Z. C. (2011). *Mechanism model and experimental investigation of chamber Pressure control for earth pressure balance shield*. Dalian: Dalian University of Technology, 19–30.

Shen, Y., Ling, J., Wang, W., Zhu, H., and Yan, Z. (2022). 3D numerical investigation on response of shield tunnel under combined effects of fire and structural loading. *Tunn. Undergr. Space Technol.* 128, 104659. Article ID 104659. doi:10.1016/j.tust.2022.104659

Shi, H., Gong, G. F., Yang, H. Y., and Su, J. X. (2008). Control model of Earth pressure balance for shield tunnelling. *J. China Coal Soc.* 33 (3), 343–346. doi:10.3321/j.issn:0253-9993.2008.03.024

Wang, F., Gou, B. C., and Qin, Y. W. (2013). Modeling tunneling-induced ground surface settlement development using a wavelet smooth relevance vector machine. *Comput. Geotechnics* 54, 125–132. doi:10.1016/j.compgeo.2013.07.004

Wang, S., Wang, Y., Lin, Z., Song, Z., Wang, X., and Peng, X. (2022a). Analysis of the influence of the thickness insufficiency in secondary lining on the mechanical properties of double-layer lining of shield tunnel. *Eng. Fail. Anal.* 141, 106663. Article ID 106663. doi:10.1016/j.engfailanal.2022.106663

Wang, S., Zhou, Z., Liu, P., Yang, Z., Pan, Q., and Chen, W. (2022b). On the critical particle size of soil with clogging potential in shield tunneling. *J. Rock Mech. Geotechnical Eng.* Available online 11 June 2022. doi:10.1016/j.jrmge.2022.05.010

Wei, X. J., Wang, F. Y., and Ding, Z. (2017). Analysis of torque of shield cutter head and its influence on surface deformation in soft soil region. *J. Cent. South Univ. Sci. Technol.* 49, 1491–1497. doi:10.11817/j.issn.1672-7207.2018.06.023

Wu, T., Gao, Y., and Zhou, Y. (2022). Application of a novel grouting material for prereinforcement of shield tunnelling adjacent to existing piles in a soft soil area. *Tunn. Undergr. Space Technol.* 128, 104646. Article ID 104646. doi:10.1016/j.tust.2022.104646

Yang, Y., Tan, Z. S., Peng, B., Li, J. P., and Wang, G. (2017). Study on optimization boring parameters of Earth pressure balance shield in water-soaked round gravel strata. *China Civ. Eng. J.* 50 (S1), 94–98. doi:10.15951/j.tmgcxb.2017.s1.017

Yu, H. J., Mooney, M., and Bezuijen, A. (2020). A simplified excavation chamber pressure model for EPBM tunneling. *Tunn. Undergr. Space Technol.* 103, 103457. Article ID 103457. doi:10.1016/j.tust.2020.103457

Zhang, S., Cheng, X., Qi, L., and Zhou, X. (2022). Face stability analysis of large diameter shield tunnel in soft clay considering high water pressure seepage. *Ocean. Eng.* 253, 111283. Article ID 111283. doi:10.1016/j.oceaneng.2022.111283

Zhao, B. J., Zhou, J. J., Tan, Z. S., and Li, T. (2017). Variation of shield boring parameters and correlation analysis in mixed ground. *Chin. Civ. Eng. J.* 50 (S1), 140–144. doi:10.15951/j.tmgcxb.2017.s1.025

Zhou, C. Z., Yang, J. S., and Mou, Y. T. (2015). BP Neural network prediction method for ground surface settlement caused by shield tunneling in soft layer down laid on hard layer in Nanchang. *J. Disaster Prev. Mitig. Eng.* 35 (4), 556. doi:10.13409/j.cnki.jdpme.2015.04.023

Zhou, J., Shi, X. Z., Du, K., Qiu, X. Y., Li, X. B., and Mitri, H. S. (2017). Feasibility of random-forest approach for prediction of ground settlements induced by the construction of a shield-driven tunnel. *Int. J. Geomech.* 17 (6), 04016129. Article ID. doi:10.1061/(ASCE)GM.1943-5622.0000817

Frontiers in Earth Science

TYPE Original Research
PUBLISHED 26 January 2023
DOI 10.3389/feart.2023.1112441

*CORRESPONDENCE
He Yuan Wang,
✉ 17719148589@163.com

SPECIALTY SECTION
This article was submitted to Economic Geology, a section of the journal Frontiers in Earth Science

RECEIVED 30 November 2022
ACCEPTED 06 January 2023
PUBLISHED 26 January 2023

CITATION
Li H, Wang Q, Zhang K, Zhang QH, Song T, Zhang C, Zhuo LB, Hao C, Feng FP, Wang HY and Zhang YQ (2023), The invasion law of drilling fluid along bedding fractures of shale.
Front. Earth Sci. 11:1112441.
doi: 10.3389/feart.2023.1112441

The invasion law of drilling fluid along bedding fractures of shale

Hong Li[1], Qing Wang[1], Kun Zhang[2], Qing Hui Zhang[3], Tao Song[2], Chuang Zhang[4], Lu Bin Zhuo[1], Chen Hao[1], Fu Ping Feng[5], He Yuan Wang[5]* and Yin Quan Zhang[5]

[1]CNPC Engineering Technology Research Institute Co., Ltd., Beijing, China, [2]Petrochina Daqing Oilfield Company Limited, Daqing, China, [3]PetroChina Qinghai Oilfield Third Oil Production Factory, Mangai, China, [4]PetroChina Qinghai Oilfield Drilling and Production Technology Research Institute, Dunhuang, China, [5]Key Laboratory of Ministry of Education of China on Enhanced Oil and Gas Recovery, Institute of Petroleum Engineering, Northeast Petroleum University, Daqing, China

In the process of drilling, the drilling fluid will invade into the bedding plane of shale under the action of pressure difference that will cause hydration collapse and wellbore instability. In order to ensure the wellbore stability during shale oil and gas drilling, it is necessary to clarify the invasion law of drilling fluid along bedding fractures during the drilling process. The immersion experiment method is often used to study the invasion law of drilling fluid, which is quite different from the actual invasion process of drilling fluid underground. In this paper, the depth of drilling fluid invasion into shale under different confining pressures and displacement times is intuitively and accurately determined by the displacement experiment and NMR scanning first. Also, then the mathematical relationships between drilling fluid invasion depth and invasion time, invasion pressure difference, confining pressure, bedding angle, and drilling fluid viscosity were established. The errors between the calculated values of the drilling fluid invasion depth and the experimental values were less than 15%, and the calculation accuracy was high. In addition to the influence of invasion time, formation pressure difference and confining pressure on invasion depth were researched through the method of numerical simulation. The results showed that the liquid invasion depth increased logarithmically with the increase of invasion time and formation pressure difference, but it grew slowly in the later period and tended to be stable; the invasion depth decreased exponentially with the increase of confining pressure, bedding plane angle, and drilling fluid viscosity. The results in the paper provide a basis for the subsequent determination of the collapse pressure and collapse period of bedding shale.

KEYWORDS

shale, bedding fractures, drilling fluid invasion, wellbore stability, numerical simulation

1 Introduction

Shale oil and gas are important unconventional resources and are becoming more and more important in oil and gas production. At present, there are more and more serious wellbore instability problems in the drilling process of shale oil and gas wells (Chen et al., 2003; Akbarpour and Abdideh, 2020; Aslannezhad et al., 2020), and the instability proportion is as high as 90% (Chen et al., 2014; Liu, 2014; Liu et al., 2021). Many factors will lead to wellbore instability, such as wellbore stress concentration caused by wellbore formation, vibration of the drilling tool assembly during drilling, and changes in formation rock properties caused by invasion of drilling fluid into the formation. The wellbore stress concentration caused by the formation of the wellbore and the vibration of the BHA during drilling are mainly related to the actual working conditions on site. The rules of drilling fluid invasion into the formation were mainly studied, and the basic data for the study of wellbore stability were provided in this paper. In the process of overbalanced drilling, the liquid column pressure is greater than the formation pressure. Under the action of pressure difference, the drilling fluid filtrate will invade the formation, especially the shale with well-developed bedding fractures, which will cause hydration expansion, crushing and disintegration of shale, and then lead to the reduction of rock strength and wellbore instability (Mody and Hale, 1993; Shi and Xia, 2011). Such phenomena of rock strength deterioration and wellbore instability caused by drilling fluid intrusion are quite common. Therefore, in order to solve the problem of shale wellbore instability, it is necessary to clarify the deterioration law of the shale strength after drilling fluid intrusions into bedding shale so as to provide a basis for determining the collapse pressure, the collapse period of bedding shale, the selection of drilling fluid density, and the determination of control measures. Laboratory experiments are usually adopted by the researchers in order to study the process of drilling fluid invasion into shale. In a laboratory experiment, the immersion method is usually adopted, in which the shale samples are immersed in the drilling fluid and then the drilling fluid filtrate invades the shale sample in all directions under the action of capillary force (Lin et al., 2022; Liu et al., 2022). However, the drilling fluid invades the shale reservoir only from the wall of the well along the radial axis of the wellbore in the actual drilling process. Therefore, there is a great difference between the immersion method and the actual underground invasion process in the study of drilling fluid invasion into shale. So, the accuracy of the shale strength deterioration law obtained from this experiment also needs to be discussed.

Therefore, in Section 2, the displacement experiment and nuclear magnetic resonance experiment were carried out to explore the change of invasion depth under different displacement times, displacement pressure, and confining pressure. In Section 3, the physical model was established for numerical simulation, the accuracy of the model was verified according to the comparison of the results of the simulation pre-experiment, and the single-factor influence law of drilling fluid invasion was analyzed. Finally, the content of this paper is summarized in Section 4. The method of displacement experiment and numerical simulation were adopted in this paper in order to study the law of drilling fluid invasion along the shale bedding fractures. The influence factors of drilling fluid invasion depth were confirmed, and the mathematical relationships between the invasion depth and a variety of factors were established at last, which provided the basis of accurate data for subsequent studies to determine the degradation law of the borehole strength at different positions around the borehole. The displacement experiment method adopted in the study could realize the one-way invasion of drilling fluid into shale along the end face of the core column under a certain pressure difference, which was more consistent with the actual working conditions than that with the immersion method.

2 Experiment of drilling fluid invasion

2.1 Materials

The composition of the drilling fluid was diesel oil + 3% main emulsion + 1% auxiliary emulsion + 3% organic soil + 3% fluid loss reducer + 2% calcium oxide + 2% superfine calcium carbonate + 1% film forming and blocking agent + 0.7% nano-polymer. The standard core column size is φ25 × 50 mm, which was obtained from shale reservoir at 2550 m depth (Figure 1), and the bedding fracture size obtained from the CT experiment is 160.94 μm (Figure 2).

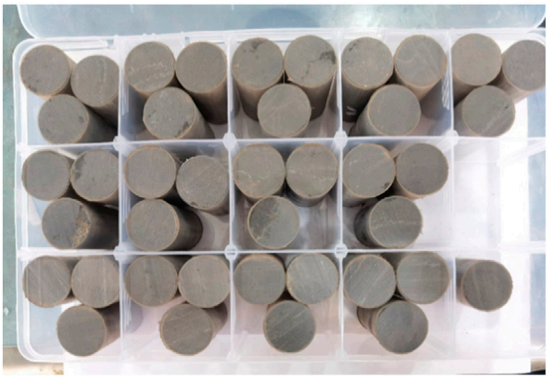

FIGURE 1
Core samples.

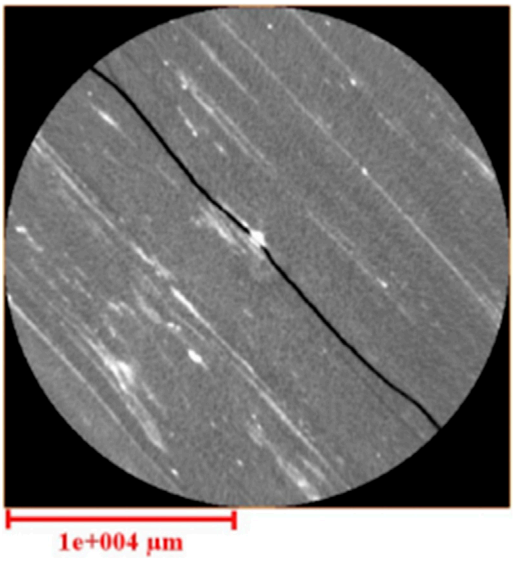

FIGURE 2
CT scanning results.

The experimental equipment used in this paper includes a WCS-FCJ non-isothermal steam oil displacement thermostat, Nantong Zhongjing Machinery Co., Ltd.; an HAS-100HSB constant pressure constant speed pump, Beijing Satellite Manufacturing Factory; a core gripper [4.5 × 4.5 × 30/50/80 (cm)], ZR-3 intermediate vessel, back pressure valve, differential pressure transmitter, and data acquisition system, Hai'an County Petroleum Scientific Research Instrument Co., Ltd.; and a MesoMR low-field nuclear magnetic resonance scanner, Nerl Miay Company (Figure 3).

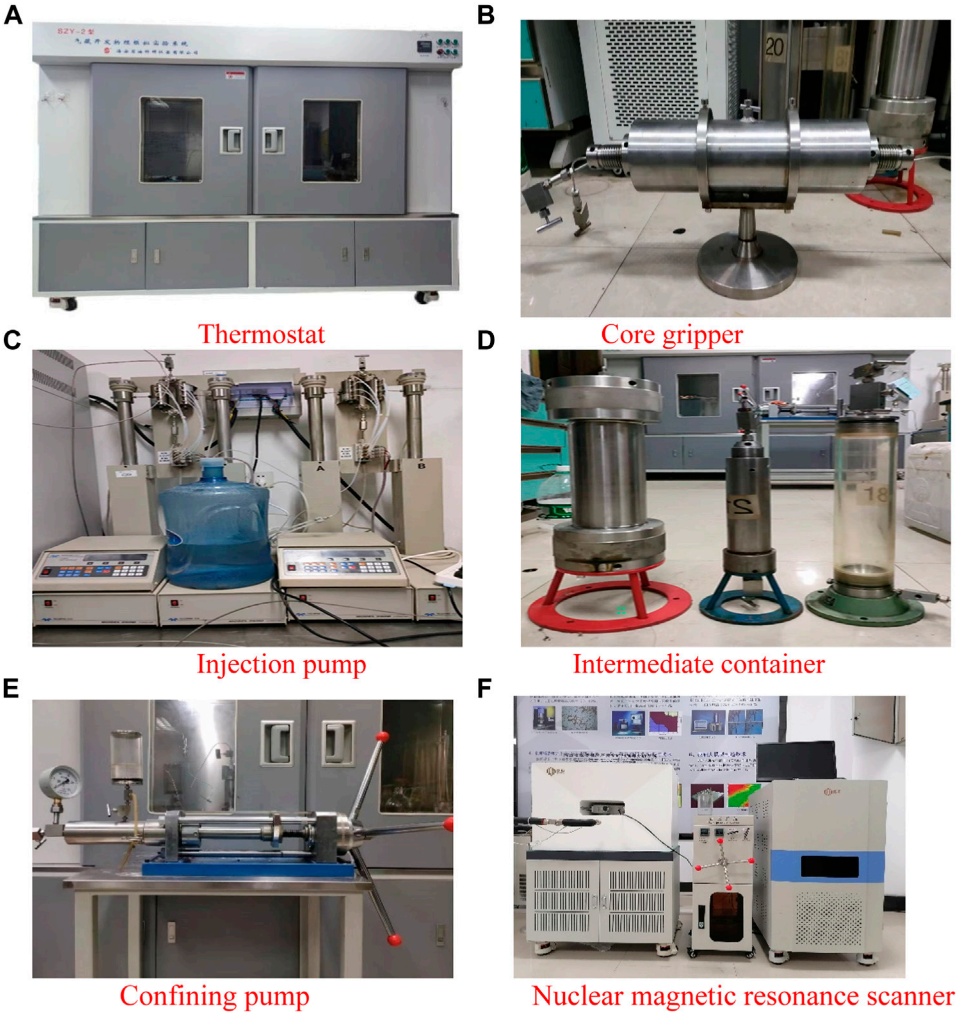

FIGURE 3
Experimental apparatus, **(A)** thermostat, **(B)** core gripper, **(C)** injection pump **(D)** intermediate container, **(E)** confining pump, and **(F)** nuclear magnetic resonance scanner.

2.2 Methods

2.2.1 Drilling fluid invasion experiment

The drilling fluid invasion experiment was carried out with the displacement experimental device. First, the standard core column (φ25 × 50 mm) was dried, and then, it was inserted into the middle container and was vacuumized using a vacuum pump; then, it was saturated with fluorine oil by connecting to a liquid tank. Then, the standard core column saturated with fluorine oil was taken out and put into the core holder. Next, the drilling fluid invaded into the standard core column using a high-voltage drive device along one end face, and the whole process was carried out at a constant temperature. In the aforementioned experiments, the invasion pressure difference is the pressure difference of the formation borehole, and the confining pressure is larger than the invasion pressure difference by 2–3 MPa. In fact, the invasion time, invasion pressure, and the invasion temperature could be changed according to the actual formation conditions. In this paper, the specific conditions of the invasion experiment are shown, as in Table 1.

2.2.2 Determination of drilling fluid invasion depth

The core column samples obtained under different invasion conditions in Section 2.2.1 were sealed to prevent the volatilization of the invading liquid, and then, they were placed in the low-field NMR scanner (Nerl Miay) for hydrogen atom signal scanning and detection. The core column has been saturated with fluorine oil before drilling fluid invasion, so there was no hydrogen atom in the core column. Therefore, the hydrogen atom signals captured by NMR scanning were all from the invading drilling fluid. Along the invasion direction of drilling fluid in NMR imaging, the distance between the farthest imaging point of the hydrogen atom signal and the starting point of invasion is the invasion depth of the drilling fluid. It could be observed from the NMR T2 spectrum, the smaller the pore, the greater the relaxation time, and the larger the pore, the smaller the relaxation time. According to the comparison of hydrogen atom signal peaks with different relaxation times, the intrusion of hydrogen atoms into rocks along the matrix and bedding fractures could be judged. It is also found that the drilling fluid invaded less along small pores and more along

TABLE 1 Drilling fluid invasion test conditions.

No.	Sample number	Angle to the bedding plane β/°	Invasion pressure/MPa	Confining pressure/MPa	Invasion time/d	Invasion temperature/℃	Viscosity of the drilling fluid/mPa·s
1	1, 2, 3, 4, and 5	0	5	7	4, 6, 8, 10, and 12	125.8	18
2	6, 7, 8, and 9	0	6, 7, 8, and 9	8, 9, 10, and 11	12	125.8	18
3	10, 11, 12, and 13	30, 45, 60, and 90	5	7	12	125.8	18
4	14, 15, 16, and 17	0	5	7	12	125.8	18, 21, 24, 27, and 30

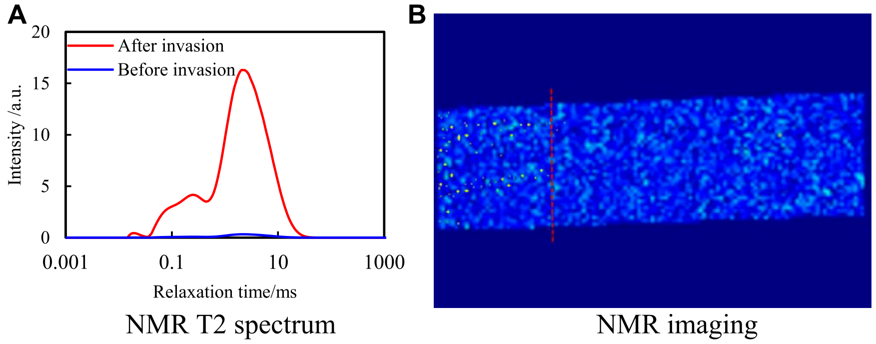

FIGURE 4
NMR spectrum. **(A)** NMR T2 spectrum. **(B)** NMR imaging.

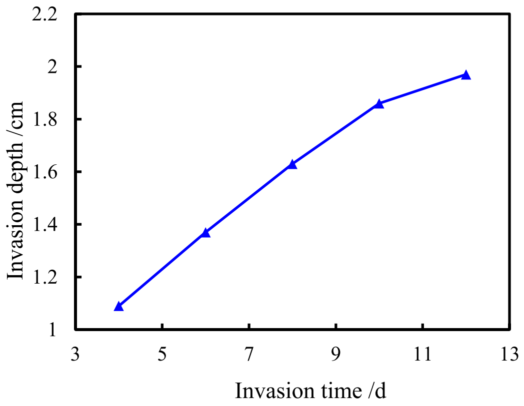

FIGURE 5
Invasion depth of the drilling fluid at different invasion times.

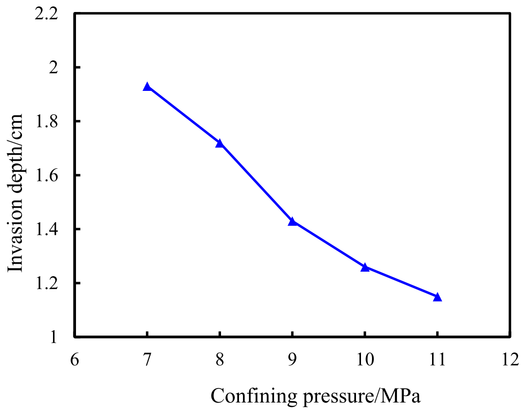

FIGURE 6
Variation of drilling fluid invasion depth with confining pressure.

bedding fractures (Figure 4A). As can be observed from NMR imaging, the yellow bright spot in the figure is the signal of the hydrogen atom from the invading drilling fluid (Figure 4B). The invasion depth of the drilling fluid in shale core can be calculated according to the ratio of the distance between the farthest imaging point of the hydrogen atom signal and the beginning of invasion in the overall core image.

2.3 Experimental results

2.3.1 Variation of invasion depth under different invasion times

The invasion depth of drilling fluid under different invasion times was tested under the conditions of invasion pressure, 5 MPa; confining pressure, 7 MPa; invasion temperature, 125.8°C; angle to the bedding

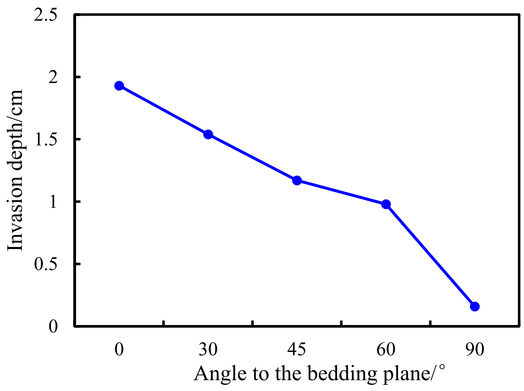

FIGURE 7
Invasion depth of the drilling fluid at different angles to the bedding plane.

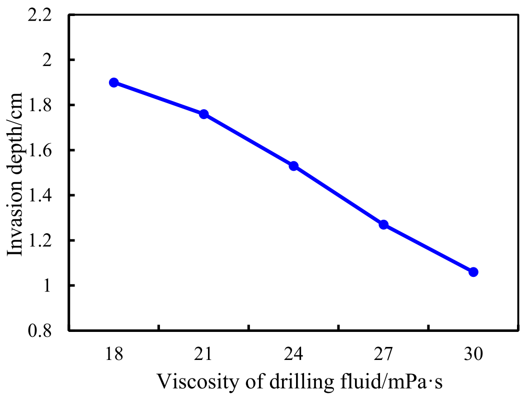

FIGURE 8
Invasion depth of the drilling fluid at different viscosities of the drilling fluid.

plane, 0°; and the viscosity of the drilling fluid, 18 mPa·s. The results are shown in Figure 5.

Clearly, the invasion depth increases apparently first but gives modest growth with the increase of invasion time. When the invasion pressure difference is constant, the contacting surface between the drilling fluid and shale pore and fracture increases with the increase of invasion time, and then, the friction resistance increases, which results in the invasion pressure difference being gradually consumed, so the invasion depth decreases.

2.3.2 Variation of invasion depth under different confining pressures

The invasion depth of the drilling fluid under different confining pressures was tested, when the invasion temperature was fixed at 125.8°C, the invasion time was 12 days, the angle to the bedding plane was 0°, and the viscosity of the drilling fluid was 18 mPa·s. The results are shown in Figure 6.

As can be observed, with the increase of confining pressure, the invasion depth of the drilling fluid gradually decreases. This is because with the increase of confining pressure, the pore structure of the rock is gradually compressed and the pore size of shale fracture is gradually closed, which leads to the gradual decrease in core permeability and porosity. The invasion resistance becomes bigger and bigger, which decreases the invasion depth of the drilling fluid along the bedding fracture.

2.3.3 Variation of invasion depth under different angles to the bedding plane

The invasion depth of the drilling fluid under different angles to the bedding plane was tested under the conditions of the invasion pressure of 5 MPa, confining pressure of 7 MPa, invasion temperature of 125.8°C, invasion time of 12 days, and the viscosity of drilling fluid of 18 mPa·s. The results are shown in Figure 7.

As shown in Figure 7, the invasion depth of the drilling fluid gradually decreases with the increase of the angle to the bedding plane. This is because with the increase of the angle to the bedding plane, the resistance of the drilling fluid to intrusion along the bedding joint gradually increases, which results in the gradual decrease in the intrusion depth of the drilling fluid along the bedding joint. When the angle to the bedding plane is 90°, the drilling fluid cannot invade along the bedding plane but can only invade along the rock matrix. Due to the small porosity of the matrix, the invasion depth is basically unchanged.

2.3.4 Variation of invasion depth under different viscosities of the drilling fluid

The invasion depth of drilling fluid under different viscosities of the drilling fluid was tested under the conditions of invasion pressure of 5 MPa, confining pressure of 7 MPa, invasion temperature of 125.8°C, invasion time of 12 days, and angle to the bedding plane of 0°. The results are shown in Figure 8.

As can be observed, with the increase of drilling fluid viscosity, the invasion depth of drilling fluid gradually decreases. This is because as the viscosity of drilling fluid increases, the resistance of drilling fluid invading along the bedding joints gradually increases, which results in the gradual decrease in the depth of drilling fluid invading along the bedding joints.

3 Numerical simulation of drilling fluid invading the bedding shale

The law of drilling fluid invasion into the shale bedding fracture can be examined intuitively and accurately by using the invasion experiment. However, due to the limited indoor conditions and cost problems, the indoor experiment cannot provide all the real mechanical and environmental conditions of the underground shale reservoir. Therefore, it is necessary to use the numerical simulation method to further study the process of drilling fluid invasion on the basis of experimental study results. The drilling fluid invasion model was established based on Darcy's law and fracture opening model, and then, the law of drilling fluid invasion of shale was further comprehensively explored using the finite element method.

3.1 Physical model

In order to simulate the process of drilling fluid invasion into bedding shale under different conditions, a physical model should be established first. In this paper, the finite element software COMSOL

TABLE 2 Parameters.

	Parameter	Dates	Unit
Invasion pressure	P_1	5, 6, 7, 8, and 9	MPa
Confining pressure	P_2	7, 8, 9, 10, and 11	MPa
Invasion time	T	4, 6, 8, 10, and 12	d
Permeability	K	1.304, 1.015, 0.740, 0.623, and 0.512	mD
Porosity	W	6.1, 4.6, 3.4, 2.8, and 2.5	%
Pore size	R	0.078, 0.061, 0.044, 0.037, and 0.031	μm

was used to construct a layered shale physical model, in which the Darcy flow and fracture flow were selected as the physical fields. The cylindrical model was established according to the core size (Figure 9A). The bedding fracture pore size, porosity, and permeability of shale in the physical model were set according to the performance parameters of shale (Figure 9B). The injection end and pressure of the injection end were marked, and the invasion depth of drilling fluid along bedding fractures was simulated and analyzed at different invasion times under the action of specified invasion pressure. Unstructured grids are used to divide the computing domain. The number of grids is 113545.

In the physical model, there were many parameters, such as invasion pressure, confining pressure, core permeability, porosity, and pore size of bedding fractures. The multiple variables were solved simultaneously by parametric scanning so as to obtain the influence of each parameter on the model results. Specific parameters are shown in Table 2.

The seepage velocity of the fluid can be expressed by Darcy's law (Yang et al., 2022) as follows:

$$v = -\frac{k}{\mu} \cdot \frac{dp}{dr}. \tag{1}$$

1 v——velocity of the fluid flow, m/s.
2 μ——fluid viscosity, mPas.
$3r$——invasion depth from the wellbore center to fracture, m.
4 p——the liquid column pressure at m from the fracture in the center of the wellbore, MPa.

Considering that the fracture opening of a single bedding fracture changes with the change of fluid pressure, the opening of bedding fracture when drilling fluid invades into the fracture at depth r is (Cao, 2016)

$$b = b_0 + \frac{p(r) - p_0}{k_n}. \tag{2}$$

1 b——the opening of the bedding fracture at any section, m.
2 b_0——the opening of the bedding fracture at fluid pressure p_0, m.
3 $p(r)$ ——the liquid column pressure at r distance from the center fracture of the wellbore, MPa.
4 p_0——original formation pressure, MPa.
5 K_n——stiffness coefficient of the bedding fracture, MPa/m.

The change of the opening of bedding fracture with pressure drop when the drilling fluid intrusion depth is r could be calculated as follows:

$$b(r) = \sqrt{\left(b_0 + \frac{p_i - p_0}{k_n}\right)^2 + \frac{\mu q}{\pi k k_n \ln r/r_i}}. \tag{3}$$

1 p_i——well fluid column pressure, MPa.
2 r_i——wellbore radius, m.

The average flow velocity equation of the fluid in the bedding fracture was applied to the horizontal radial flow model, and then, the flow velocity formula of the drilling fluid through the fracture surface was obtained as follows (Yang et al., 2022):

$$v_i = -\frac{nb^{n+1/n}}{(2n+1)^{2(n+1)/n} k_{ci}} \cdot \left|\frac{\partial p}{\partial r}\right|^{\frac{(1-n)}{n} \cdot \partial p/\partial r}. \tag{4}$$

1 n——power–law index of the drilling fluid.
2 K_{ci}——consistency index of the drilling fluid, $\mathrm{Pas}^{\mathrm{n}}$.

When there is no leakage in the borehole, the mass balance equation of incompressible fluid is

$$\frac{\partial}{\partial r}(b\,v_i) + \frac{1}{r}(b\,v_i) + \frac{\partial b}{\partial t} = 0. \tag{5}$$

At a certain invasion time, the relationship between the change of bedding fracture opening and the change of pressure drop is

$$\frac{\partial b}{\partial t} = \frac{1}{k_n} \cdot \frac{\partial p}{\partial r}. \tag{6}$$

The flow equation of the drilling fluid with the change of the opening of the bedding fracture from the borehole wall to the bedding fracture at the finite length fracture is obtained as follows (Zhu et al., 2021):

$$\begin{aligned} &\frac{\partial b}{\partial t} - \frac{nb^{2n+1/n}}{(2n+1)^{2\mathrm{n}+1/n} c k_n {k_{ci}}^{1/n}} \cdot \frac{1}{r} \cdot \frac{\partial p}{\partial r}\left|\frac{\partial p}{\partial r}\right|^{1-\mathrm{n}/n} - \frac{n}{(2n+1)^{2\mathrm{n}+1/n} c k_n {k_{ci}}^{1/n}} \\ &\quad \cdot \frac{\partial}{\partial r}\left(b^{2n+1/n}\frac{\partial p}{\partial r}\left|\frac{\partial p}{\partial r}\right|^{1-\mathrm{n}/n}\right) = 0. \end{aligned} \tag{7}$$

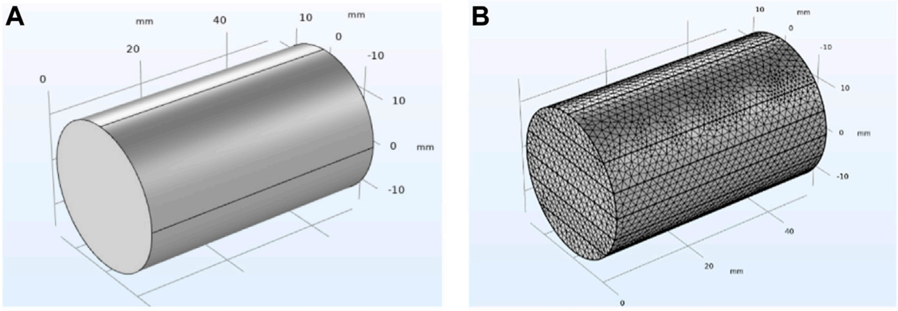

Cylindrical model

Bedding fracture

FIGURE 9
Physical model. **(A)** Cylindrical model; **(B)** bedding fracture.

3.2 Numerical simulation calculation and accuracy verification of drilling fluid invasion depth

3.2.1 Simulation prediction and accuracy analysis of invasion depth under different invasion times

According to the parameters in Table 2, the injection end pressure and confining pressure are, respectively, fixed at 5 MPa and 7 MPa, and then, the processes of drilling fluid invasion into shale under different invasion times were simulated, as shown in Figure 10i.

As shown in Figure 10i, with the extension of invasion time, the degree of fluid pressure declines along the bedding fracture (according to the variation trend of dark red, light red, yellow, light blue, and dark blue in the cloud image) is significantly higher than that along the matrix, and this rule becomes more and more obvious with the increase of invasion time. This is because the permeability, porosity, and pore size of the bedding fractures are much larger than those of the matrix. Under the action of pressure difference, the fluid pressure decreases faster when the permeability, porosity, and pore size of the shale are larger. Therefore, at the same time, the invasion depth of the drilling fluid in the bedding fractures is greater than that of the matrix (the furthest distance between the intersection points of light blue and dark blue in the cloud image and the penetration end is the invasion depth of the drilling fluid).

Also, as shown in Figure 10i, under the same conditions, the invasion degree of the drilling fluid along bedding fractures is much greater than that of matrix, and bedding fractures are more prone to deteriorate after invasion. Therefore, it is necessary to further explore the pressure variation law at each position in the bedding fracture at different invasion times so as to provide a foundation for determining the relationship between the depth and the invasion time of the drilling fluid along the bedding fracture.

The vector diagram of pressure and invasion position under different invasion times is shown in Figure 10ii, in which the invasion position of the drilling fluid in the core is taken as the abscissa and the fluid pressure in the bedding fracture calculated by the model is taken as the ordinate.

As shown in Figure 10ii, the fluid pressure between bedding fractures gradually decreases with the increase of the invasion degree under a fixed displacement time. The degree of pressure drop varies with the invasion time. When the invasion position is the same, the shorter the invasion time and the faster the pressure drop.

As shown in Figure 10ii, the distance between the invasion position when the fluid pressure is 0 MPa, and the origin is defined as the invasion depth of the drilling fluid. Error analysis was made between the calculated values and the experimental values of drilling fluid invasion depth along bedding fractures at different invasion times (Table 3).

According to the comprehensive analysis of errors, the errors between the calculated value of the model and the measured value of the experiment are within 15%, indicating that the model has good prediction accuracy. The drilling fluid invasion depth can be accurately predicted at different invasion times by the model.

3.2.2 Simulation prediction and accuracy analysis of intrusion depth under different invasion pressures and confining pressures

Due to the compaction of the overlying strata, the permeability, porosity, and pore size of the core will change under different confining and driving pressures, which will affect the invasion process of the drilling fluid along the bedding fracture. Therefore, it is necessary to predict the invasion depth of the drilling fluid along the bedding fracture under different confining and invasion pressures. Thus, the invasion process of the drilling fluid along the bedding fracture was simulated under different invasion pressures and confining pressures when the invasion time was fixed at 12 days, and the results are shown in Figure 11i.

As shown in Figure 11i, with the increase of invasion pressure and confining pressure, the degree of fluid invasion along the bedding fracture and matrix becomes smaller, and the degree of reduction along the bedding fracture is significantly higher than that of the matrix.

In order to further study the mathematical relationship between the invasion depth and invasion pressure and confining pressure in bedding fractures, the vector diagram of pressure and invasion position under different invasion pressures and confining pressures was drawn (Figure 11ii), in which the invasion position of the drilling fluid in the core was taken as the abscissa and the fluid pressure in bedding fractures calculated by the model was taken as the ordinate. As shown in Figure 11ii, under a certain invasion pressure and confining pressure, the fluid pressure between bedding fractures gradually decreases with the

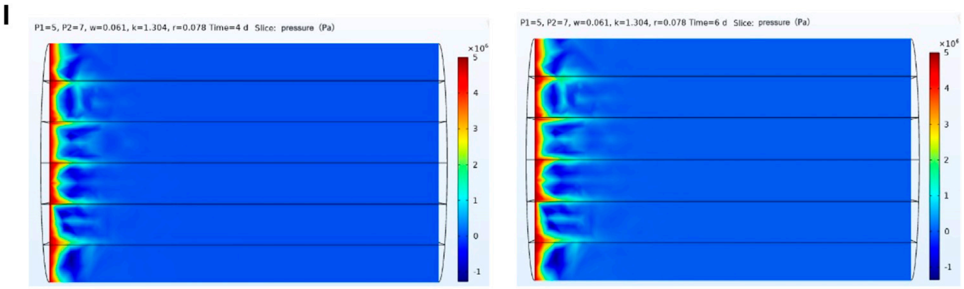

(a) 4 days (b) 6 days

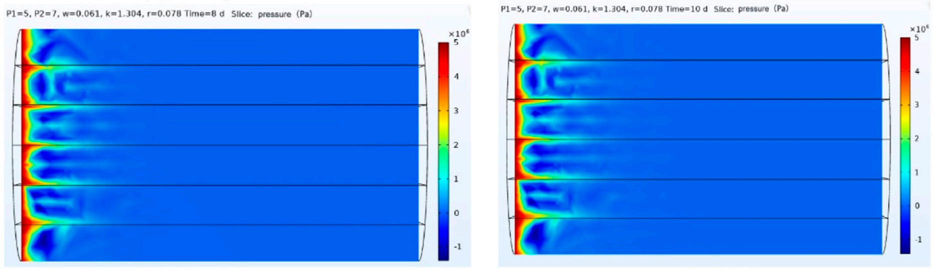

(c) 8 days (d) 10 days

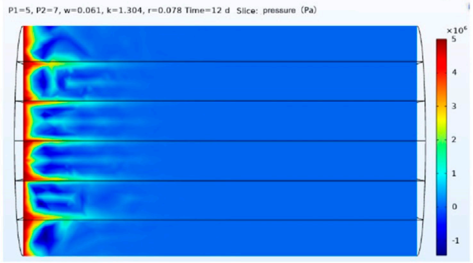

(e) 12 days

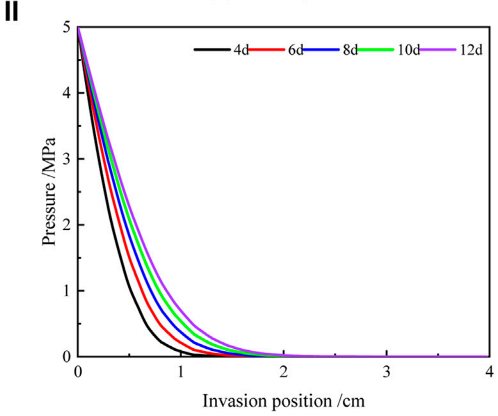

FIGURE 10
(i): Cloud diagram of the invasion effect at different invasion times. **(A)** 4 days, **(B)** 6 days, **(C)** 8 days, **(D)** 10 days, and **(E)** 12 days. **(ii)**: Changes of pressure between bedding fractures with the invasion position at different invasion times.

increase of the invasion degree. With different invasion and confining pressures, the degree of pressure drop between bedding fractures is also different. The greater the invasion pressure and confining pressure, the more obvious the pressure drop.

Error analysis was made between the calculated values and the experimental values of drilling fluid invasion depth along bedding fractures under different invasion pressures and confining pressures (Table 4).

A shown in Table 4, the errors between the simulated calculated value and the experimental measured value of the invasion depth under different invasion pressures and confining pressures are within 14%, indicating that the model has good prediction accuracy. The model can accurately predict the invasion depth of drilling fluid along the bedding fractures under different invasion pressures and confining pressures.

3.2.3 Simulation prediction and accuracy analysis of intrusion depth under different angles to the bedding plane

A major feature of stratum rational strata is that there is a set of nearly parallel stratum surfaces, and its three-dimensional spatial state

TABLE 3 Calculated and experimental values of invasion depth under different invasion times.

Invasion pressure/MPa	Confining pressure/MPa	Invasion time/day	Experimental invasion depth/cm	Calculated invasion depth/cm	Error/%
5	7	4	1.09	1.25	14.68
5	7	6	1.37	1.42	3.65
5	7	8	1.63	1.52	6.75
5	7	10	1.86	1.62	12.90
5	7	12	1.97	1.71	13.20

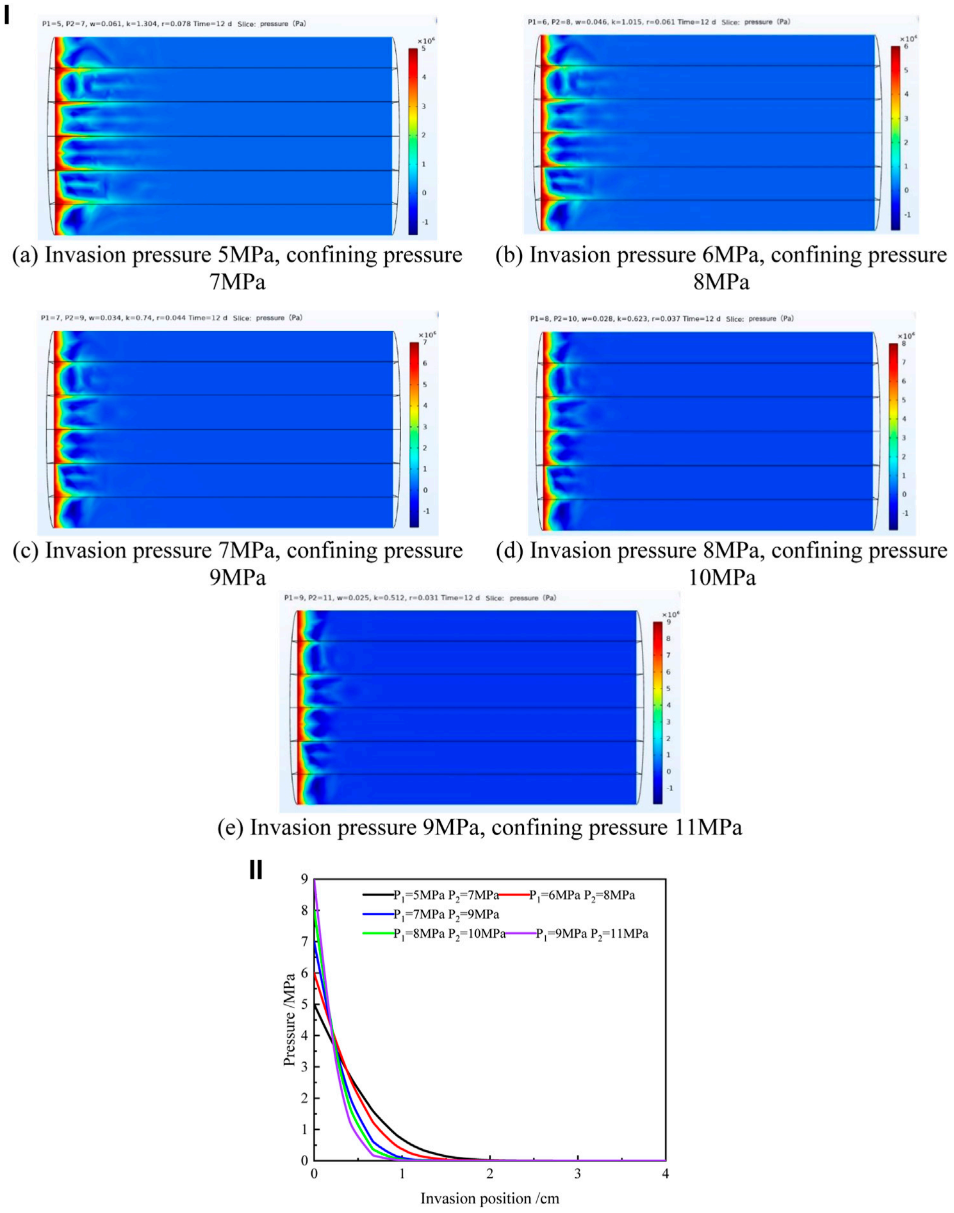

FIGURE 11
(i): Cloud diagram of the invasion effect under different invasion and confining pressures. **(A)** Invasion pressure 5 MPa, confining pressure 7 MPa, **(B)** invasion pressure 6 MPa, confining pressure 8 MPa, **(C)** invasion pressure 7 MPa, confining pressure 9 MPa, **(D)** invasion pressure 8 MPa, confining pressure 10 MPa, **(E)** invasion pressure 9 MPa, and confining pressure 11 MPa. **(ii)**: Changes of fluid pressure between bedding fractures with invasion position under different invasion and confining pressures.

TABLE 4 Calculated and experimental values of invasion depth under different invasion pressures and confining pressures.

Invasion pressure/MPa	Confining pressure/MPa	Invasion time/day	Experimental invasion depth/cm	Calculated invasion depth/cm	Error/%
5	7	12	1.93	1.70	11.9
6	8	12	1.72	1.59	7.6
7	9	12	1.43	1.47	2.8
8	10	12	1.26	1.38	9.5
9	11	12	1.15	1.31	13.9

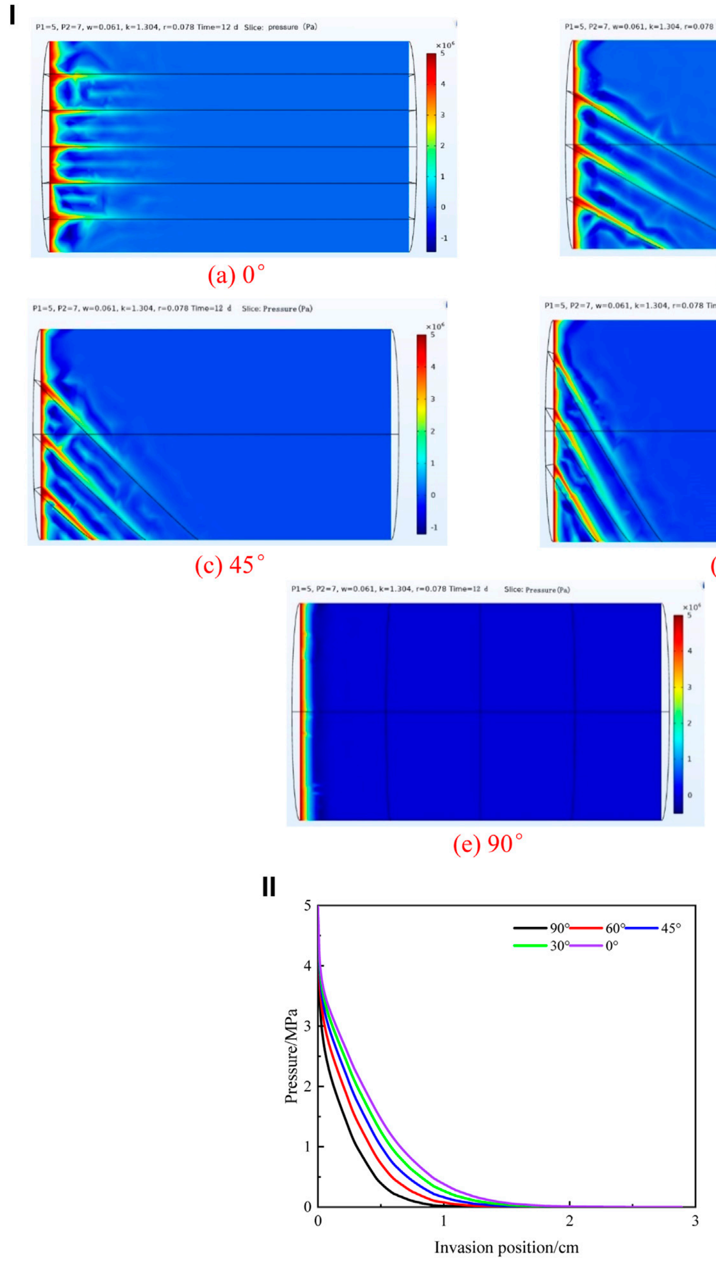

FIGURE 12
(i): Cloud diagram of the invasion effect under different angles to the bedding plane. **(A)** 0, **(B)** 30, **(C)** 45, **(D)** 60, and **(E)** 90. **(ii)**: Changes of fluid pressure between bedding fractures with the invasion position under different angles to the bedding plane.

TABLE 5 Calculated and experimental values of invasion depth under different angles to the bedding plane.

Invasion pressure/MPa	Invasion time/day	Angle to the bedding plane/°	Experimental invasion depth/cm	Calculated invasion depth/cm	Error/%
5	12	0	1.93	1.70	11.9
6	12	30	1.54	1.36	11.7
7	12	45	1.17	1.23	5.1
8	12	60	0.98	0.94	4.1
9	12	90	0.16	0.14	12.5

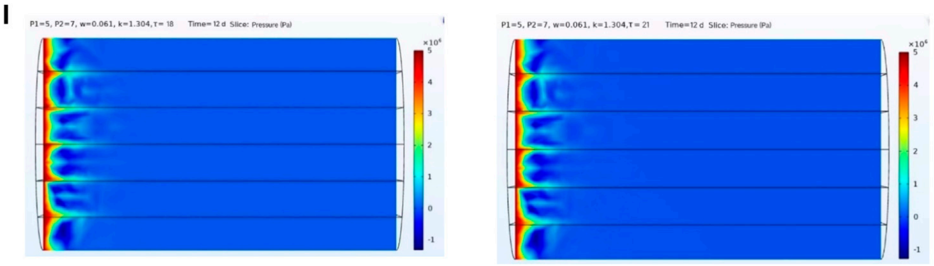

(a)τ=18 mPa·s (b) τ=21 mPa·s

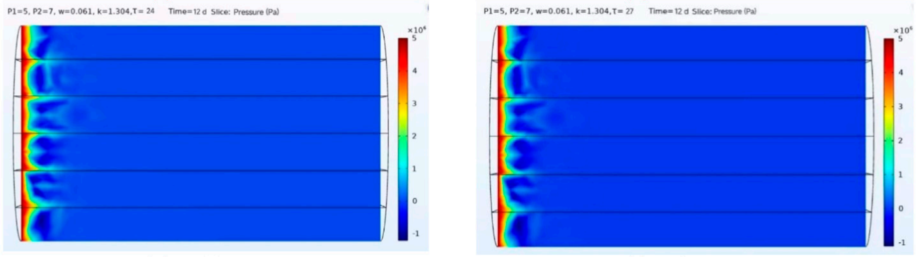

(c) τ=24 mPa·s (d) τ=27 mPa·s

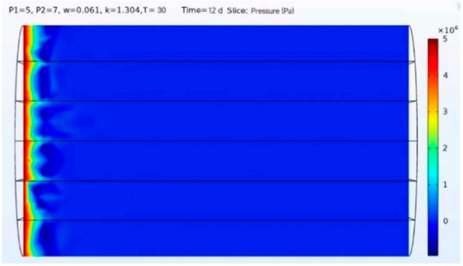

(e) τ=30 mPa·s

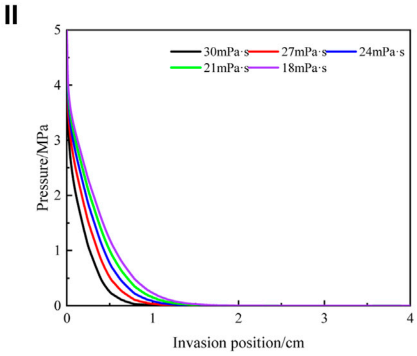

FIGURE 13
(i): Cloud diagram of the invasion effect under different viscosities of the drilling fluid. **(A)** τ = 18 mPa·s, **(B)** τ = 21 mPa·s, **(C)** τ = 24 mPa·s, **(D)** τ = 27 mPa·s, and **(E)** τ = 30 mPa·s. **(ii)**: Changes of fluid pressure between bedding fractures with the invasion position under different viscosities of the drilling fluid.

TABLE 6 Calculated and experimental values of invasion depth under different viscosities of the drilling fluid.

Invasion pressure/MPa	Invasion time/day	Viscosity of the drilling fluid/mPa·s	Experimental invasion depth/cm	Calculated invasion depth/cm	Error/ %
5	12	1.2	1.90	1.78	6.32
5	12	1.4	1.76	1.58	10.22
5	12	1.6	1.53	1.47	3.92
5	12	1.8	1.27	1.36	7.08
5	12	2.0	1.06	0.96	9.43

(production form) is generally described by the stratum surface trend, tendency, and inclination, in which the inclination of the stratum surface has a very large impact on the stability of the well wall. The weakening effects of the stratum after being subjected to the action of the drilling fluid are different when the inclination angle changes, so it is necessary to consider the influence of drilling fluid invasion along different inclination angles of the layer surface on the stability of the well wall.

According to the parameters in Table 2, the process of the drilling fluid invading to the shale at different bedding plane angles is simulated by fixing the injection end pressure, displacement confining pressure, and displacement time, as shown in Figure 12i.

The vector diagram of pressure and invasion position under different angles to the bedding plane is shown in Figure 12ii, in which the invasion position of the drilling fluid in the core is taken as the abscissa and the fluid pressure in the bedding fracture calculated by the model is taken as the ordinate.

As shown in Figure 12ii, the fluid pressure between the layers of fractures gradually decreases with the increase of the degree of intrusion during the fixed displacement time. The degree of pressure drop varies with the changes of the inclination angle. When the intrusion position is the same, the greater the inclination angle, the faster the pressure drop.

Error analysis was made between the calculated values and the experimental values of drilling fluid invasion depths along bedding fractures under different angles to the bedding plane (Table 5).

As shown in Table 5, the errors between the calculated and experimental values of invasion depth under different angles to the bedding plane are within 13%, indicating that the model has good prediction accuracy and the model can accurately predict the invasion depth of the drilling fluid along the bedding fractures under different angles to the bedding plane.

3.2.4 Simulation prediction and accuracy analysis of intrusion depth under different viscosities of the drilling fluid

According to the parameters in Table 2, the process of the drilling fluid invading shale at different viscosities of the drilling fluid is simulated by fixing the injection end pressure, displacement confining pressure, and displacement time, as shown in Figure 13i.

The vector diagram of pressure and invasion position under different viscosities is as shown in Figure 13ii, in which the invasion position of the drilling fluid in the core was taken as the abscissa and the fluid pressure in bedding fractures calculated by the model was taken as the ordinate. As shown in Figure 13ii, under a certain invasion pressure and confining pressure, the fluid pressure between bedding fractures gradually decreases with the increase of the invasion degree. With different viscosities of the drilling fluid, the degree of pressure drop between bedding fractures is also different. The greater the viscosity of the drilling fluid, the more obvious the pressure drop.

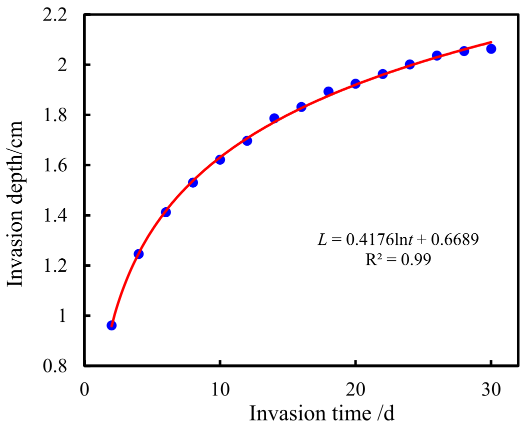

FIGURE 14
Relationship between invasion depth and invasion time of the drilling fluid along the bedding fracture.

Error analysis was made between the calculated values and the experimental values of drilling fluid invasion depth along bedding fractures under different viscosities of the drilling fluid (Table 6).

As shown in Table 6, the errors between the simulated calculated value and the experimental measured value of the invasion depth under different viscosities of the drilling fluid are within 11%, indicating that the model has good prediction accuracy. The model can accurately predict the invasion depth of the drilling fluid along the bedding fractures under different viscosities of the drilling fluid.

3.3 Analysis of drilling fluid invasion along the bedding fracture

3.3.1 Variation law of invasion depth with invasion time

When the drilling fluid has been contacting with the formation for different times, the invasion depth will change accordingly. In order to clarify the change law of drilling fluid invasion depth along bedding fractures with invasion time, the invasion pressure at this time was fixed as 5 MPa and the confining pressure was

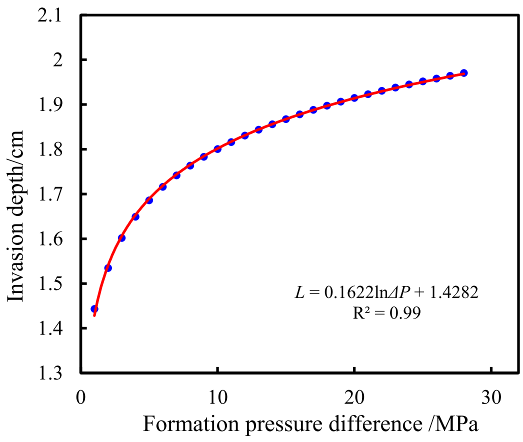

FIGURE 15
Relationship between the invasion depth of the drilling fluid along the bedding fracture and formation pressure difference.

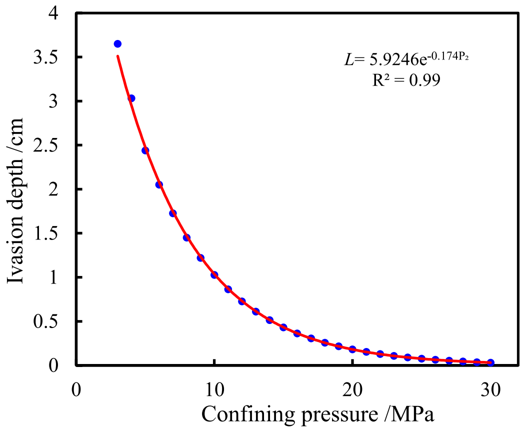

FIGURE 16
Relationship between the invasion depth of the drilling fluid along the bedding fracture and confining pressure.

7 MPa, the bedding plane angle is 0°, and the viscosity of drilling fluid is 18 mPa·s. With invasion time as abscissa and invasion depth as the ordinate, the vector diagram of invasion depth–invasion time was drawn and mathematical fitting was carried out. Compared to the fitting results of linear, power function, exponential function, and logarithmic function, it is found that the logarithmic function has the highest fitting degree, as shown in Figure 14.

As shown in Figure 14, the invasion depth gradually increased with the increase of the invasion time, but the increase in amplitude gradually slowed down and finally tended to be unchanged. This is because with the invasion of the drilling fluid into the bedding fractures, the contact area between the drilling fluid and shale pores gradually increases, and the pore resistance in the invasion process becomes more and more large (Ma et al., 2022; Wang et al., 2022), which then cancels out part of the formation pressure difference that results in the gradual reduction of the driving force of drilling fluid invasion and the growth rate of invasion depth. By fitting, it was found that the invasion depth (L) of the drilling fluid is logarithmic to the invasion time (t), and the specific functional formula is $L = 0.4176 \ln t + 0.6689$. The invasion depth of the drilling fluid along bedding fractures at any time under fixed formation pressure difference and confining pressure can be obtained by using this formula.

3.3.2 Variation law of invasion depth with formation pressure difference

The formation pressure difference is the main driving force of the drilling fluid invasion into the shale, which will certainly affect the invasion depth of the drilling fluid. In order to clarify the mathematical relationship between the invasion depth of the drilling fluid along bedding fractures and the formation pressure difference, the invasion time was fixed as 12 days, the confining pressure was 7 MPa, the bedding plane angle is 0°, and the viscosity of drilling fluid is 18 mPa·s. The vector diagram of the penetration depth–formation pressure difference was drawn with the formation pressure difference as abscissa and the invasion depth as the ordinate, and then, mathematical fitting was carried out. Compared to the fitting results of linear, power function, exponential function, and logarithmic function, it is found that the logarithmic function has the highest fitting degree, as shown in Figure 15.

The invasion depth gradually increases with the increase of formation pressure difference, but the growth rate gradually slows down. When the formation pressure difference is greater than 25 MPa, the invasion depth gradually tends to have a fixed value. This is because when the local pressure difference exceeds a certain value, the interfacial drag effect caused by the capillary force becomes particularly significant (Ma et al., 2022; Wang et al., 2022), and these interfacial drag effects are offset with formation pressure, so the invasion depth will not increase. The invasion depth of the drilling fluid is also logarithmic to the formation pressure difference (ΔP), and the specific functional formula is $L = 0.1622 \ln \Delta P + 1.4282$. The penetration depth of the drilling fluid along the bedding fracture can be obtained under any formation pressure difference with fixed invasion time and confining pressure using this formula.

3.3.3 Variation law of invasion depth with confining pressure

Due to the compaction of the overlying strata, the permeability, porosity, and pore size of the core change under different confining pressures, which will further affect the invasion process of the drilling fluid along the bedding fracture. Therefore, it is necessary to analyze the change rule of the invasion depth of the drilling fluid along the bedding fracture under different confining pressures. In order to clarify the relationship between the invasion depth of the drilling fluid along bedding fractures and confining pressure, the invasion time was fixed as 12 days, the confining pressure was 7 MPa, the bedding plane angle is 0°, and the viscosity of the drilling fluid is 18 mPa·s. With confining pressure as the abscissa and invasion depth as the ordinate, the vector diagram of invasion depth–confining pressure was drawn, and mathematical fitting was carried out. Compared to the fitting results of linear, power function, exponential function, and logarithmic function, it is found that the exponential function has the highest fitting degree, as shown in Figure 16.

As shown in Figure 16, the invasion depth of the drilling fluid gradually decreases with the increase of confining pressure and finally approaches 0. This is because with the increase of confining pressure,

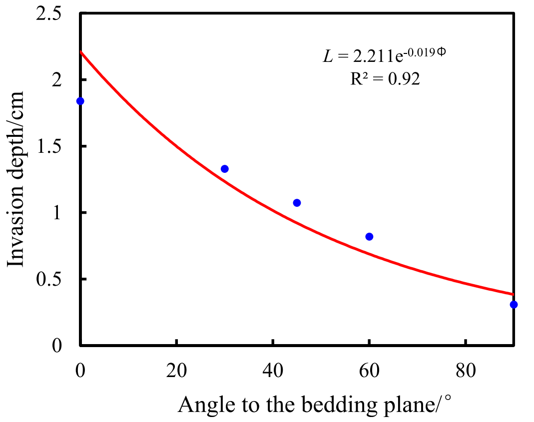

FIGURE 17
Relationship between the invasion depth of the drilling fluid along the bedding fracture and angle to the bedding plane.

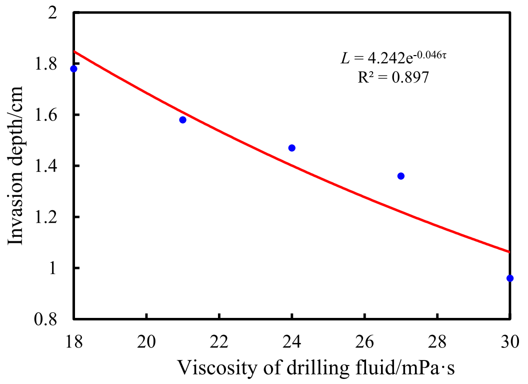

FIGURE 18
Relationship between the invasion depth of the drilling fluid along the bedding fracture and viscosity of the drilling fluid.

the pore structure of the rock is gradually compressed, then the pore size, permeability, and porosity of the core are gradually reduced, and the invasion resistance of the drilling fluid is increased, resulting in the decrease in the invasion depth. When the confining pressure increases to a certain value, the bedding fractures are pressed and closed, and the permeability approaches 0, so there is nearly no drilling fluid invading the shale reservoir. Through mathematical fitting, the mathematical relation between the invasion depth of the drilling fluid along the bedding fracture and confining pressure (P_2) is determined as $L = 5.9246e^{-0.174P2}$, and the invasion depth of the drilling fluid along the bedding fracture under any confining pressure with fixed time and formation pressure difference can be obtained by using this formula.

3.3.4 Variation law of invasion depth with the angle to the bedding plane

When the angle of the bedding plane is different, the invasion resistance will also be different. For example, when the bedding plane is 90°, the drilling fluid cannot invade along the bedding plane but only along the rock matrix. The invasion depth must be small because of the matrix with small pores. Therefore, it is necessary to analyze the variation law of invasion depth of the drilling fluid along the bedding fracture under different angles to the bedding plane. In order to clarify the relationship between the invasion depth of the drilling fluid along the bedding fracture and the bedding plane angle, the invasion time is fixed as 12 days, the invasion pressure at this time was fixed as 5 MPa, the confining pressure was 7 MPa, and the viscosity of the drilling fluid is 18 mPa·s. Taking the bedding plane angle as abscissa and invasion depth as the ordinate, the vector diagram of the invasion depth layer with the angle was drawn, and the mathematical fitting of linear, power function, exponential function, and logarithmic function was carried out. The results show that the exponential function has the highest degree of fit, as shown in Figure 17.

As shown in Figure 17, the invasion depth of the drilling fluid gradually decreases with the increase of the bedding plane angle. This is because with the increase of the angle of the bedding plane, the resistance of drilling fluid intrusion along the bedding fracture gradually increases, resulting in gradual decrease in the invasion depth of the drilling fluid along the bedding fracture. When the angle of bedding plane is 90°, the drilling fluid cannot invade along the bedding plane. Due to the small porosity of the matrix, the intrusion depth is basically unchanged. Through mathematical fitting, the mathematical relation between the invasion depth of the drilling fluid and the angle of the bedding plane (Φ) is determined as $L = 2.211e^{-0.019\Phi}$. The invasion depth of the drilling fluid along the bedding fracture under any angle to the bedding plane can be obtained by this formula.

3.3.5 Variation law of invasion depth with viscosity of the drilling fluid

The invasion resistance will be different when the viscosity of the drilling fluid is different, which will affect the invasion process of the drilling fluid along the bedding fractures. Therefore, it is necessary to analyze the variation law of invasion depth of the drilling fluid along the bedding fracture under different viscosities of the drilling fluid. In order to clarify the relationship between the invasion depth of the drilling fluid along the bedding fracture and the viscosity of the drilling fluid, the invasion time is fixed as 12 days, the displacement pressure is 5 MPa, the displacement confining pressure is 7 MPa, and the bedding plane angle is 0°. With the drilling fluid viscosity as the abscissa and the invasion depth as the ordinate, the vector diagram of invasion depth with drilling fluid viscosity was drawn, and mathematical fitting was performed. The results show that the exponential function has the highest degree of fit, as shown in Figure 18.

As shown in Figure 18, the invasion depth of the drilling fluid gradually decreases with the increase of drilling fluid viscosity. After mathematical fitting, the mathematical relation between the invasion depth of the drilling fluid along the bedding fracture and the viscosity of the drilling fluid (τ) is determined to be $L = 4.242e^{-0.046\tau}$. The invasion depth of the drilling fluid along the bedding fracture can be obtained by using this formula.

4 Conclusion

The laws of drilling fluid invasion along the shale bedding fractures were studied by experiment and numerical simulation, and the following conclusions are derived:

(1) Compared with the static immersion experiment, the method of simulating the drilling fluid invade into shale bedding fractures in the displacement experiment takes into account not only the

capillary force but also the influence of liquid column pressure difference on the process of drilling fluid invasion into bedding shale, which realizes the unidirectional invasion of the drilling fluid into shale and is closer to the actual process of drilling fluid filtration into shale.

(2) Based on fissure flow and Darcy flow physical fields, the rational model of drilling fluid invading shale bedding fractures is established and the process of drilling fluid invasion is simulated. Then, the mathematical relationships between the invasion depth and invasion time, formation pressure, confining pressure, bedding angles, and drilling fluid viscosity are defined as $L = 0.4176 \ln t + 0.6689$, $L = 0.1622 \ln \Delta P + 1.4282$, $L = 5.9246e^{-0.174P2}$, $L = 2.211\ e^{-0.019\Phi}$, and $L = 4.242e^{-0.046\tau}$. The errors between the calculated values of the drilling fluid invasion depth and the experimental values under different conditions are less than 15%, which shows highly prediction accuracy.

(3) The invasion depth of the drilling fluid along shale bedding has a positive logarithmic relationship with the invasion time and the formation pressure difference. With the increase of the invasion time and the formation pressure difference, the invasion depth gradually increases, but it grows slowly in the later stage and finally tends to be unchanged. There are negative exponential relationships between the invasion depth and confining pressure, the angle of bedding plane, and the viscosity of the drilling fluid. The invasion depths of the drilling fluid decrease when the confining pressure, the angle of bedding plane, and the viscosity of drilling fluid increase. When the bedding angle is 90°, the drilling fluid invades only along the rock matrix.

Data availability statement

The original contributions presented in the study are included in the article/Supplementary Material; further inquiries can be directed to the corresponding author.

Author contributions

HL, QW, and KZ designed research; TS, HW, and LZ performed research; QZ, CZ, and CH analyzed data; HW, FF, and YZ performed the data analyses and wrote the paper. All authors discussed the results and revised the manuscript.

Acknowledgments

The authors are grateful to the Key Laboratory of Ministry of Education P.R.C. in China for financial support.

Conflict of interest

HL, QW, LZ, and CH were employed by CNPC Engineering Technology Research Institute Co., Ltd. KZ and TS were employed by the PetroChina Daqing Oilfield Company Limited. QZ was employed by the PetroChina Qinghai Oilfield Third Oil Production Factory. CZ was employed by the PetroChina Qinghai Oilfield Drilling and Production Technology Research Institute.

The remaining authors declare that the research was conducted in the absence of any commercial or financial relationships that could be construed as a potential conflict of interest.

Publisher's note

References

Akbarpour, M., and Abdideh, M. (2020). Wellbore stability analysis based on geomechanical modeling using finite element method. *Model. Earth Syst. Environ.* 6 (2), 617–626. doi:10.1007/s40808-020-00716-x

Aslannezhad, M., Keshavarz, A., and Kalantariasl, A. (2020). Evaluation of mechanical, chemical, and thermal effects on wellbore stability using different rock failure criteria. *J. Nat. Gas Sci. Eng.* 78, 103276. doi:10.1016/j.jngse.2020.103276

Cao, H. T. (2016). *Research on fracture surface morphology and seepage characteristics based on fractal theory*. Chengdu, China: Chengdu University of Technology.

Chen, P., Ma, T. S., and Xia, H. Q. (2014). Prediction model for collapse and instability of shale horizontal wells with multiple weak planes. *Nat. Gas. Ind.* 34 (12), 87–93. doi:10.3787/j.issn.1000-0976.2014.12.012

Chen, X., Tan, C. P., and Detournay, C. (2003). A study on wellbore stability in fractured rock masses with impact of mud infiltration. *J. Petroleum Sci. Eng.* 38 (3-4), 145–154. doi:10.1016/S0920-4105(03)00028-7

Lin, H., Deng, J. G., Xie, T., Liu, H. L., Luo, C., and Liu, W. (2021). Borehole stability of middle-deep mud shale formations in Bozhong area of Bohai Oilfield. *Sci. Technol. Eng.* 21 (11), 4409–4417. doi:10.3969/j.issn.1671-1815.2021.11.016

Lin, H., Sun, X., Yuan, Y., Lai, X., Qu, H., and Luo, C. (2022). Experimental investigation on the dynamic volume changes of varied-size pores during shale hydration. *J. Nat. Gas Sci. Eng.* 101, 104506. doi:10.1016/j.jngse.2022.104506

Liu, K. (2014). *Study on hydration control method of hard and brittle shale*. Si Chuan Sheng, China: Southwest Petroleum University.

Liu, Y., Yang, C., Wang, J., Xiong, Y., and Peng, P. (2022). New insights into hydration-induced creep behavior of shale: A comparison study of brittle black shale and clayey oil shale at micro-scale. *Mar. Petroleum Geol.* 138, 105554. doi:10.1016/j.marpetgeo.2022.105554

Ma, X., Nguyen, N. N., and Nguyen, A. V. (2022). A review on quantifying the influence of lateral capillary interactions on the particle floatability and stability of particle-laden interfaces. *Adv. Colloid Interface Sci.* 307, 102731. doi:10.1016/j.cis.2022.102731

Mody, F. K., and Hale, A. H. (1993). Borehole-stability model to couple the mechanics and chemistry of drilling-fluid/shale interactions. *J. Petroleum Technol.* 45 (11), 1093–1101. doi:10.2118/25728-PA

Shi, B. Z., and Xia, B. R. (2011). Microstructure changes during hydration process of hard and brittle shale. *J. Daqing Petroleum Inst.* 35 (6), 28–34. doi:10.3969/j.issn.2095-4107.2011.06.005

Wang, L., Ma, F., He, Y., and Liu, D. (2022). The prediction of spontaneous oil-water imbibition in composite capillary. *Petroleum* 8 (1), 84–91. doi:10.1016/j.petlm.2021.07.001

Yang, H., Li, J., Zhang, G., Zhang, H., Guo, B., and Chen, W. (2022a). Wellbore multiphase flow behaviors during gas invasion in deepwater downhole dual-gradient drilling based on oil-based drilling fluid. *Energy Rep.* 8, 2843–2858. doi:10.1016/j.egyr.2022.01.244

Yang, S., Li, X., Zhang, K., Yu, Q., and Du, X. (2022b). The coupling effects of pore structure and rock mineralogy on the pre-Darcy behaviors in tight sandstone and shale. *J. Petroleum Sci. Eng.* 218, 110945. doi:10.1016/j.petrol.2022.110945

Zhu, H. Y., Dang, Y. K., Wang, G. R., Zhou, S. W., and Fu, Q. (2021). Near-wellbore fracture initiation and propagation induced by drilling fluid invasion during solid fluidization mining of submarine nature gas hydrate sediments. *Petroleum Sci.* 18 (6), 1739–1752. doi:10.1016/j.petsci.2021.09.026

frontiers | Frontiers in Earth Science

TYPE Original Research
PUBLISHED 30 January 2023
DOI 10.3389/feart.2022.1083436

OPEN ACCESS

EDITED BY
Leilei Si,
Henan Polytechnic University, China

REVIEWED BY
Erol Yilmaz,
Recep Tayyip Erdoğan University,
Turkey
Shuai Cao,
University of Science and Technology
Beijing, China

*CORRESPONDENCE
Zhiliu Wang,
6855@zut.edu.cn

SPECIALTY SECTION
This article was submitted to Economic Geology,
a section of the journal
Frontiers in Earth Science

RECEIVED 29 October 2022
ACCEPTED 01 December 2022
PUBLISHED 30 January 2023

CITATION
Wang Z, Chen L and Hu M (2023),
Experiment research and mechanism analysis on rheological properties of tailings slurry.
Front. Earth Sci. 10:1083436.
doi: 10.3389/feart.2022.1083436

Experiment research and mechanism analysis on rheological properties of tailings slurry

Zhiliu Wang[1]*, Linlin Chen[2] and Mengxin Hu[1]

[1]School of Civil Engineering and Architecture, Zhongyuan University of Technology, Zhengzhou, China, [2]Gengcun Coal Mine, Yi Ma Coal Industry Group, Mianchi, China

The particle size and content of tailings are important parameters affecting the rheological properties of tailings slurry. To explore their influence law and mechanism on rheological properties, the experiments of tailings slurry were designed and carried out under different particle sizes and content conditions. The rheological properties of the tailings slurry were quantified in the paper. The Bingham body model was used in the texperiment. The “double 30” theory (“particle size of 30.0 μm” and “content of 30%”) was proposed and expounded. The corresponding theoretical model is established to analyze the mechanism of the above results. The conclusion is as follows. The tailings slurry agreeed to different rheological models with different particle size and content. The rheological behavior of the tailings slurry conforms to the Herschel-Bulkley model for the tailings, whose particle size is no larger than 30.0 μm and content is no larger than 30%. With the increase of the content of fine tailings, its behavior agrees better with the Bingham model. The yield stress and viscosity of tailings slurry in the process of transportation are in accordance with the laws of “double 30” theory. “Particle size of 30.0 μm” and “content of 30%” is the critical point of rheological characteristics of tailings. Based on the obtained results, the corresponding theoretical model was established to discuss the mechanism. The rheological laws of tailings slurry can provide theoretical guidance for reducing pressure and preventing pipeline wear in the process of tailings cementation discharge and pipeline transportation in an iron mine.

KEYWORDS

rheological properties, yield stress, viscosity, rheological model, double 30 theory

Introduction

Mineral resources excavation contributes significantly to the world economy andmany industries depend on the provision of raw materials by it (Si et al., 2021a; Si et al., 2021b; Li et al., 2022a; Zhang et al., 2022). With the increase of mining depth, more and more waste tailings are produced (Liu et al., 2020; Ruan et al., 2021). Statistics show that every 10,000 tons of ore mined will produce 9,300 tons of tailings and 3,400 tons of waste rock (Yan et al., 2022), which not only has serious security hidden dangers, but also destroys the environment and the ecology seriously (Small et al., 2015; Falagán et al., 2016; Li et al., 2022b). In order to protect the ecological environment and make rational use of resources (Aldhafeeri and Fall 2017), tailings backfilling in mines has become an important method of tailings disposal and has extensive application prospect (Cao et al., 2018; Li et al., 2022c; Zheng et al., 2022; Ouattara et al., 2017161).

Cemented paste backfill (CPB) technology has become an effective way of backfill method to solve solid waste in mines, and received more attention in mining practices around the world (Fang and Fall 2018; Liu et al., 2018; Mangane et al., 2018; Qi et al., 2019). It is an engineered combination of tailings, cement and mixing water, which can be transported to underground stopes by pumping or gravity. The cementation discharge and pipeline transport of tailings slurry is an important challenge for CPB technology (Qi et al., 2018; Liu et al., 2019; Chen et al., 2020). It is important to determine the reasonable slurry concentration, cement-sand ratio and pipeline transportation parameters to ensure the efficient and stable operation of pipeline discharge system. Especially for high concentration slurry, the rheological properties of slurry become the key factor for stable and reliable operation of the system. If the liquidity of the paste is too poor, it will lead to pipe blocking accidents, which will seriously affect the mine's productivity. It is intended to solve the above-mentioned challenges simultaneously to investigating the rheological properties and mechanism of tailings slurry.

Long-term backfill research and practice show that the strength of backfill is positively correlated with cement-sand ratio, slurry mass fraction and curing age in a certain range. There are plenty of works dealt with the different key characteristics and multiscale behavior of cemented tailings/paste backfill with different mineral additives (Li et al., 2020; Cavusoglu et al., 2021; Kasap et al., 2022; Sari et al., 2022). However, with the increase of cement addition and slurry mass fraction, the fluidity of slurry will become worse (Wu et al., 2020; Wu et al., 2021). Currently, numerous scientists are conducting experimental studies on the rheological properties of pastes. Cheng (Cheng et al., 2020a) found that the tailing particle size significantly affects the cemented paste rheological properties. Roshan (Roshani and Fall 2020) evaluate the silica mechanism on early yield stress and viscosity of CPB. The fluidity of CTWB paste is generally characterized by the yield stress and viscosity in fluid mechanics (Wu and Cai, 2015; Deng et al., 2018). (Zhang and Qiao, 2015) concluded that the effect of cement-sand ratio and mass fraction on slurry yield stress was more significant through the rheological experiment of high-mass fraction slurry of waste rock tailing. The influencing factors of slurry rheological characteristics were studied (Xu et al., 2016; Long et al., 2017), the results showed that the content of fine particles was an important factor affecting the rheological characteristics of slurry. The minimum viscosity would appear when the ratio of coarse and fine particles decreased. To evaluate the rheological properties of tailings, many scholars have extensively conducted a large amount of work on the rheological characteristics of tailings through changing the experimental method, such as studies on the effect of the installation angle of mixing blade (Yin et al., 2010), blade resistance, and stirring method (Hale Micah et al., 2009; Just and Middendorf, 2009). Some scholars also study the rheological characteristics of tailings by means of numerical simulation (Bouvet et al., 2010; Lei et al., 2017; Rakotondrandisa et al., 2019). Computational fluid dynamics (CFD) simulations have become a trend in pipeline transportation and rheological characteristics of tailings research. Zhang (Zhang et al., 2015) developed a two-dimensional pipeline model for long distances and found that the necessary condition for self-flow transport is that the pressure value generated by gravity is greater than the pressure drop. Cheng (Cheng et al., 2020b) used CFD to investigate the effect of time and temperature on paste transport characteristics.

Especially for high concentration tailings slurry, quantifying the influence of particles and content on rheological characteristics and laws is helpful to optimize pipeline transport parameters and reduce pipeline resistance loss. It provides the basis for the design and operation of tailings cementation discharge system. However, the research on quantifing rheological characteristics and transport performance of consolidated slurry is relatively insufficient.

To solve the existing problems above effectively and reduce the transportation costs of tailings, the quantitative laws and effects of particle size and content on the rheological properties of tailings slurry should be determined and the rheological models for different particle size and content should be studied. And the mechanism of the above-mentioned rheological law need be further elucidated based on the particle structure and mechanical properties. The experiments were carried out and the mechanism are analyzed on rheological properties of tailings slurry in the work. Tailings slurry was preparated by mixing fine tailings and whole tailings. Based on the test and the rheology principles, the rheological parameters such as yield stress and viscosity of slurry are obtained. And the consilient rheology model for the tailings slurry is determined for different content conditions by rheological test of tailings slurry. The quantified rheological laws of "double 30" theory ("particle size of 30.0 μm" and "content of 30%") were proposed and expounded. The results make contribution to obtaining transportation parameters of tailings and further rheological properties research. The research above is beneficial to reduce pipe friction and transportation costs in the transportation proce.

Rheological test of tailings

Test materials and instruments

An iron ore is located in the west of Anhui Province, China with an anual production of five million t/a. New technology of

TABLE 1 Chemical constituents of the whole tailings (%).

MgO	Al_2O_3	SiO_2	CaO	Na_2O	MnO	Fe_2O_3	Sum
2.413	3.849	82.052	2.461	0.179	0.021	8.003	98.978

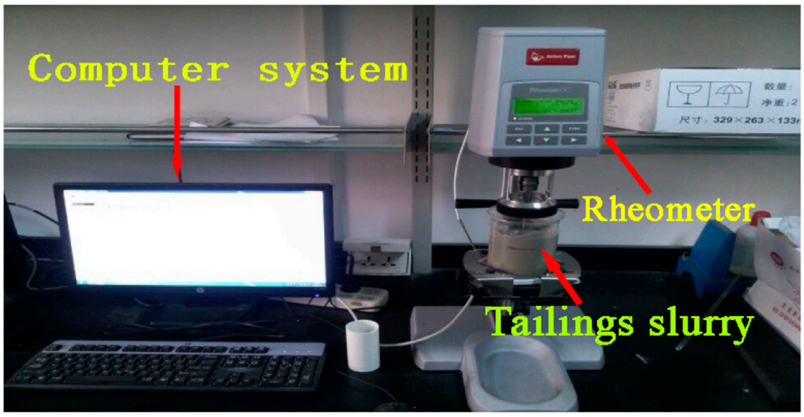

FIGURE 1
RheolabQC rheometer.

tailing cementation and discharge is applied and the whole tailings are discharged to surface. The complicated concentration dehydration process increased the transportation difficulty of high density paste, and the transportation conditions of high density paste are rigorous. The great friction resistance is generated in the transportation process of tailings, which is harmful to tailings transportation. Pressurized transporation is required and it will increase transportation costs for tailings.

Tailings from the iron mine are used as test material which have the characteristics of more fine particle size content and poorly gradation. The initial solid content of the tailings brought to the laboratory from the mine site is 74%. Varigrained tailings are mixed with the whole tailings in the test and chemical properties of tailings slury are studied including the chemical constituents of the whole tailings and the content. The measured results of chemical constituents and their contents are shown in Table.1.

The factors affecting the rheological properties of tailings slury are very complicated. The parameters, such as slurry concentration, particle size, and fine tailings content, were considered during testing. RheolabQC rheometer was used to determine the rheological parameters of tailings in this paper. It has the advantages of strong performance and simple operation, and can test rheological parameters of various fluids. The rotating speed ranges from 0.01 to 1500 1/min. Torque range is from 0.25 to 75 mN m; The shear stress ranges from 0.5 to 30 kPa. The viscosity ranges from 1 to 1000 MPas; The temperature range is from -20–180°C; The shear rate ranges from 0.01 to 4000 1/s. The angular displacement accuracy is 2 rad. The Reynolds number of laminar flow to turbulent flow is much larger than that of high concentration mortar pipeline transportation. In addition, the mortar itself has a strong internal structure. Combined with the rheological theory, the Bingham body model was used in the texperiment. The experimental equipment is shown in Figure 1. Blade rotor was used to stir tailings and the room-temperature was 25°C. In addition, measuring cylinder (500 ml), general utility balance (1000 g), and beakers were also used.

Designation of tailings physical parameters

In this experiment, the ball mill was used to grind the large particles of tailings, and the milling time was set to 30 s, 2 min 5 min, 10 min, 20 min, and 40 min, respectively. The large particles of tailings were grinded based on the ball milling time above.

The physical parameters of tailings are shown in Table.2. The Particle size distribution is in Figure 2. The curves of the weighted average of particle size *versus* mass for different particle diameter is shown in Figure 3 And in the Figure. The characteristic values of particle composition for whole tailings are as follows. d_{10}=54.27 μm, d_{30}=135.32 μm, d_{60} =200.79 μm, and the

TABLE 2 Physical parameters of tailings.

Tailings	d_{10}/μm	d_{50}/μm	D (4,3)/μm
1(Poorly gradated tailings)	54.40	178.28	168.02
2 (Grinding 40min)	1.70	8.06	10.21
3 (Grinding 20 min)	3.13	19.43	21.97
4 (Grinding 10 min)	4.21	27.95	32.87
5 (Grinding 5 min)	6.97	42.25	55.53
6 (Grinding 2 min)	10.13	63.52	81.28
7 (Grinding 30s)	12.71	79.44	98.04

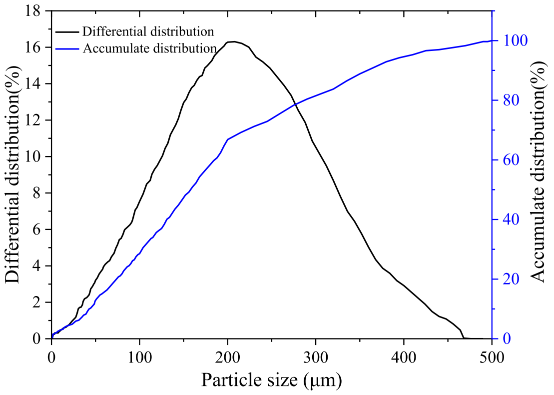

FIGURE 2
Particle size distribution diagram of the tailings.

median diameter is d_{50}=178.28 μm. The diameters of the whole tailings are mainly between 80 μm and 341 μm, then the non-uniformity coefficient C_u and the curvature coefficient Cc of tailings are calculated. C_u equals to 3.636 (less than 5), and Cc equals to 1.657. The results showed the whole tailings belong to poorly gradation, which seriously affects on the process of tailings transport such as concentration, dehydration, cementation and stabilization.

Experimental procedures

In this experiment, the optimum time interval was determined to be about 1s through multiple experiments. Note that if the time interval is too short it would cause inaccurate test results, while it would cause slurry sedimentation if the time interval is too long.

The experiment procedures were as follows:

1) In the test the concentration of tailings slurry was 75%, which was made by mixing fine tailings and whole tailings. The particle sizes of fine tailings were 10.21 μm, 21.97 μm, 28.5 μm, 30.00 μm, 32.87 μm, 55.53 μm, 81.28 μm, and 98.04 μm, respectively, the partical size of whole tailings was 168.02 μm, and the contents of fine tailings were 10%, 20%, 30%, 40%, 50%, respectively. The information about the mixing ratio of tailings slurry is in Table 3.
2) The weighed tailings and water were mixed in the beaker, then the mixture above was stirred evenly with a glass rod to get tailings slurry.
3) RheolabQC rheometer was used in the test, and the time interval was 1s. In order to reduce the test error, the data was measured at least three times in every group. The final results were obtained by taking average values. When the difference coefficient was large, When the difference coefficient is large, the data with large difference will be removeed and the test was conducted again.

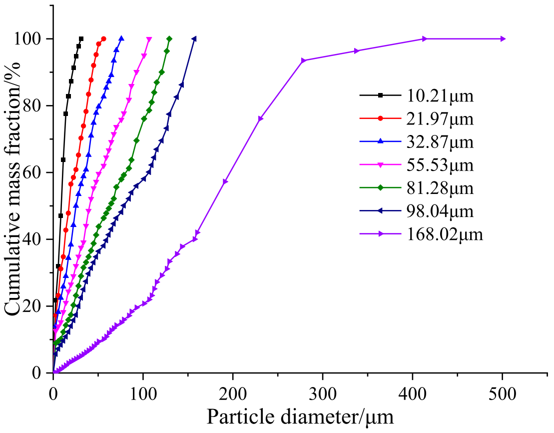

FIGURE 3
Curves for different size fraction and particle diameter.

Test results and analysis

Test results

The rheological curves of tailing slurries with different particle sizes and contents are shown in Figure 4–11. 10F90C represents the mixture of 10% fine tailings and 90% whole tailings.

It can be concluded from Figure 4 Figure 5, Figure 6, Figure 7, Figure 8, Figure 9, Figure 10 Figure 11.

1) When the shear rate of rotors is constant, the shear stress increases with the increase of the contents, and the rheological curves with different contents have the same trend. This is because the high content of fine particles and increased contact area between particles, which strengthen the

TABLE 3 Mixing ratio of tailings slurry.

Particle sizes of fine tailings(F)	10.21	21.97	28.5	30.00	32.87	55.53	81.28	98.04
	μm	μm	μm	μm	μm	μm	μm	μm
Partical size of whole tailings(C)	168.02	168.02	168.02	168.02	168.02	168.02	168.02	168.02
	μm	μm	μm	μm	μm	μm	μm	μm
Content	10F90C 20F80C 30F70C 40F60C 50F50C	10F90C 20F80C 30F70C 40F60C 50F50C	10F90C 20F80C 30F70C 40F60C	10F90C 20F80C 30F70C 40F60C 50F50C	10F90C 20F80C 30F70C 40F60C	10F90C 20F80C 30F70C 40F60C 50F50C	10F90C 20F80C 30F70C 40F60C 50F50C	10F90C 20F80C 30F70C 40F60C 50F50C
			50F50C		50F50C			

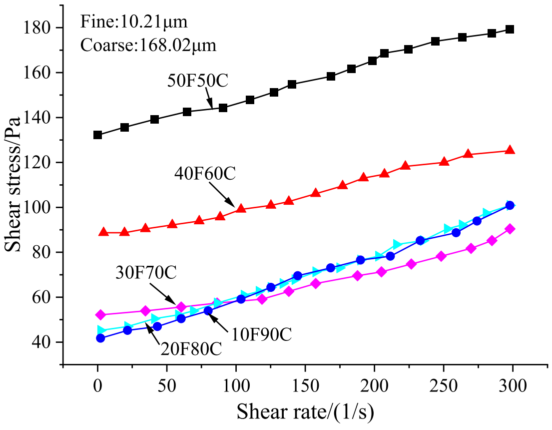

FIGURE 4
The shear stress-shear rate rheological curve of particle diameter 10.21 μm.

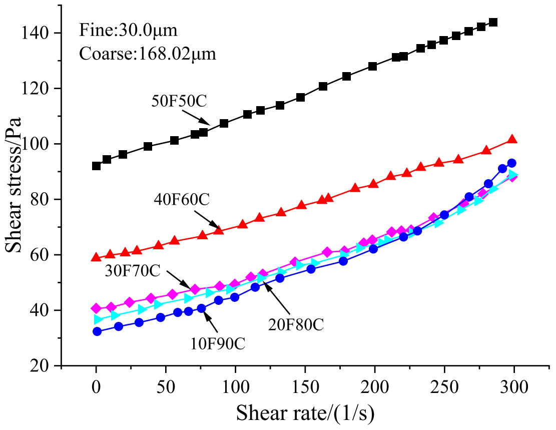

FIGURE 6
The shear stress-hear rate rheological curve of particle diameter 28.5 μm.

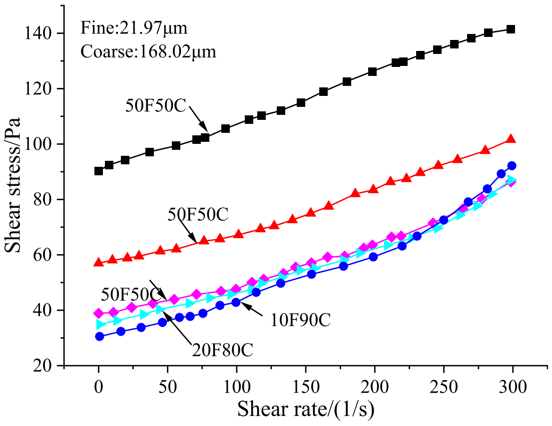

FIGURE 5
The shear stress-shear rate rheological curve of particle diameter 21.97 μm.

internal interaction of tailings slurry particles. Simultaneously, shear stress is positively correlated with shear rate. That is, the shear stress increases with the shear rate. It agrees with the results obtained by Cao et al. (2018).

2) When the particle size is less than or equal to 30.0 μm, the shear stress increases constantly with the shear rate of the rotor for the same content. The slope of curves is smaller, which means the shear stress is more stable. When the particle size is greater than 30.0 μm, the curve slope between shear stress and shear rate is larger with the same content, that is, the increase rate of shear stress is relatively larger. With the increase of contents, the shear stress also increases, but the increase range is small. For tailings with particle size of 10.21 μm, the shear stress with the content of 50% is about 2.88 times as high as that with the content of 10%. However, the shear stress with the content of 50% is almost the same as that with the content of 10% for the fine tailings with particle size of 90.04 μm. The variations show that the tailing contents

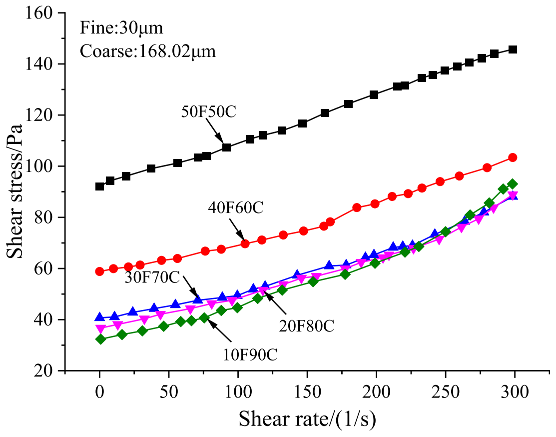

FIGURE 7
The shear stress-hear rate rheological curve of particle diameter 30.0 μm.

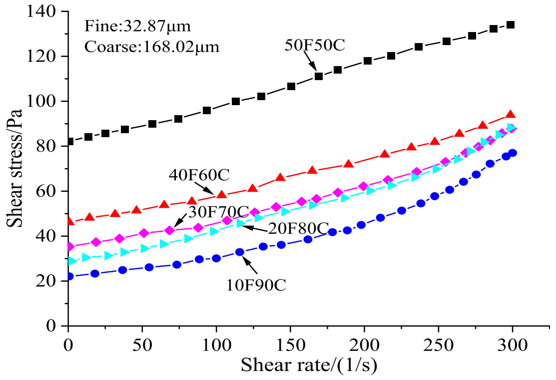

FIGURE 8
The shear stress-shear rate rheological curve of particle diameter 32.87 μm.

have less effect on the shear stress when the particle size of tailings increases to a certain value.

3) As shown in Figure 4–11, when the content of fine tailings is less than or equal to 30%, the rheological curves of the tailings are relatively concentrated and shear stress changes little. The shear stress increases more sharply with the content less than 30% compared with that with more than 30%. The flocculation of fine particles is the dominant factor leading to the yield stress of the slurry. The more the fine particles of slurry are, the more obvious the flocculation is. The increase of contact points between particles causes the increase of frictional resistance, which hinders the tailings slurry flowing. Thus, the resistance and the yield stress are larger with high content than that with low content.

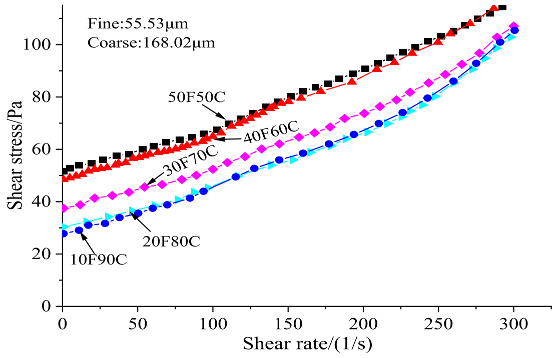

FIGURE 9
The shear stress-shear rate rheological curve of particle diameter 55.53 μm.

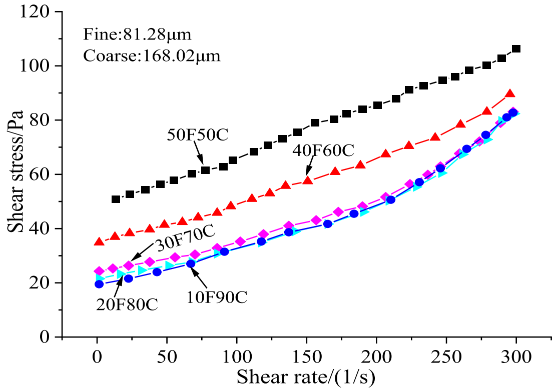

FIGURE 10
The shear stress-shear rate rheological curve of particle diameter 81.28 μm.

Test results analysis

There are many rheological models for tailings slurry, such as the Herschel-Bulkley model, Bingham model (Liu et al., 2018; Zhang et al., 2023). The slurries will conform to different rheological models when the particle size and contents are different.

Bingham model equation is defined as:

$$\tau = \tau_0 + \mu\gamma \tag{1}$$

Herschel-Bulkley equation is defined as:

$$\tau = \tau_0 + \mu\gamma^n \tag{2}$$

Where τ_0 is yield stress, Pa, μ is plastic viscosity coefficient, Pas, γ is shear rate,1/s.n is yield index.

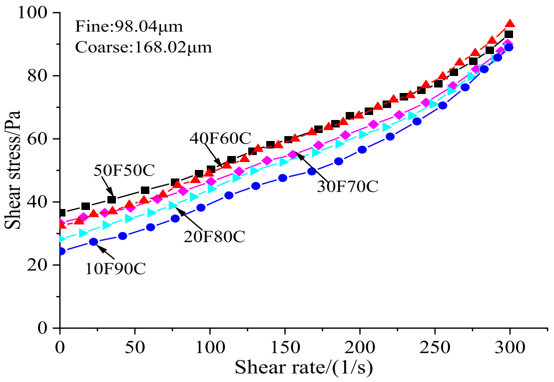

FIGURE 11
The shear stress-shear rate rheological curve of particle diameter 98.04 μm.

When $\tau_0 = 0, n = 1$, the model is Newton fluid; When $\tau_0 = 0, n < 1$, the model is Pseudo plastic fluid; When $\tau_0 = 0, n > 1$, the model is Expanding fluid; When $\tau_0 > 0, n = 1$, the model is Bingham fluid; When $\tau_0 > 0, n < 1$, the model is Pseudo plastic fluid with yield stress; When $\tau_0 > 0, n > 1$, the model is Expanding fluid with yield stress.

Based on the curves in Figure 4–Figure 11 the test results are fitted by Eq 1 and 2. As there are many fitting curves and the fitting trends are similar, fine particle size of 30 μm are taken as an example and the fitting results are shown in Table 3. It can be seen that the correlation coefficients are more than 99.4% and the following conclusions are obtained.

1) When the particle size of fine tailings is less than or equal to 30 μm and the content is less than or equal to 30%, the rheological properties of tailing slurries conform to the Herschel-Bulkley model. And will transform into Bingham model with the increase of content. This is because the particle size of fine tailings is relatively small, the structure state of tailings slurry is disassembled then reforming under the influence of shear stress, and the rate of the structure reformation increases with the extent of debonding. When the contents are more than 30%, the dynamic balance of the tailing slurry system is achieved and it has a stable plastic viscosity, thus the tailings slurry system transforms into Bingham model.
2) When the particle size is greater than 30 μm, no matter how the content of tailings slurry changes, the slurry always presents Herschel-Bulkley model without transforming into Bingham.

Expanding fluid with yield stress

Because with the increase of particle size, the collision and friction between the particles becomes the main factor increaing the viscosity of the tailings slurry.

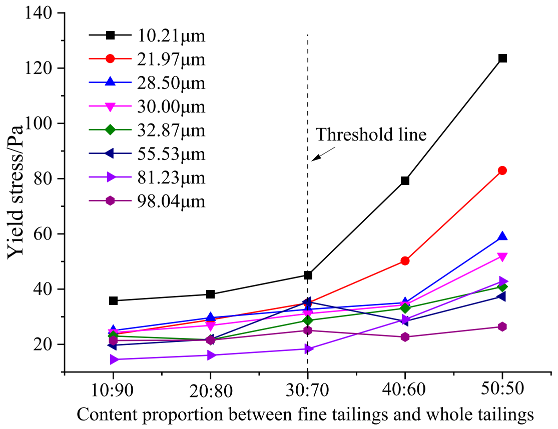

FIGURE 12
The variation curves of yield stress with different particle diameters and contents.

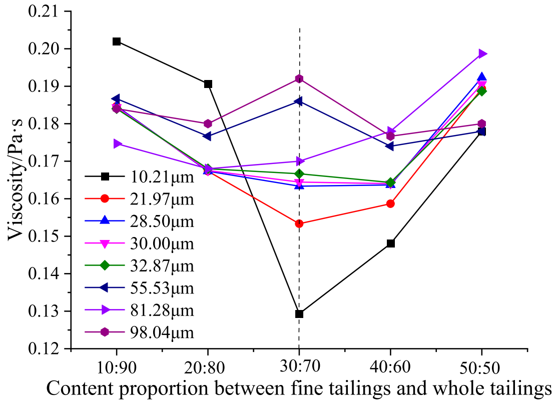

FIGURE 13
The variation curves of viscosity with different particle diameters and contents.

Yield stress and viscosity laws

Yield stress and viscosity are the main factors affecting the flow of the slurry. Therefore, the yield stress and viscosity of different particle sizes and content are analyzed in the test. The changing curves are shown in Figure 12 and Figure 13. The following conclusions are obtained from the figures above.

1) As shown in Figure 12, the yield stress of the fine tailings with size of 10.21 μm is greater than that of other particle sizes, and the change rate of yield stress gradually enlarges with the increase of content. Meanwhile, the larger the particle size is, the more stable the yield stress is. When the particle diameter is greater than 30.0 μm, the yield stress changes less with the

increase of the contents. When the particle size is less than or equal to 30 μm and the contents is less than or equal to 30%, the yield stress increases slowly. The yield stress increases rapidly when the contents are more than 30%. This is because when the particle size is small and the content is large for fine tailings, and the friction between the particles increases, thus increasing the yield stress rapidly and reducing the fluidity of tailings slurry.

2) As shown in Figure 13, when the particle size is less than or equal to 30.0 μm, the viscosities decrease with the contents of 10%, 20%, and 30%, respectively, and the smaller the particle size is, the more severe the viscosity decreases. For the particle size of 10.21 μm, the viscosity decreases to the minimum suddenly when the contents are 30%, which is due to the fact that the lubrication effect between particles is the main factor at this time. When the particle size is greater than 30 μm, the viscosity changes less and is relatively stable.
3) The viscosity and the yield stress change greatly for fine tailings with the particle size less than 30.0 μm, while that are more stable for a particle size with more than 30.0 μm. The particle size and content of fine tailings have great influence on the rheological behavior of tailings slurry.

Rheological laws and mechanism analysis

For the tailings backfilling disposal, the content and partical size of fine tailingd are not the larger the better, there exists an influence sphere. The filling and transportation parameters of tailing mortar were optimized in order to quantitatively elucidate the rheological characteristics of tailing mortar. In this part, a new law of rheological properties of tailing mortar is given, and the influence mechanism of particle size and content on the yield stress and viscosity of total tailings is deeply revealed from the microscopic perspective.

Rheological laws of tailings

From the rheological curves above, it is clear that the content of 30% and the particle size of 30.0 μm for fine tailings are the turning point of the tailings rheological properties. The parameter laws of particle size of 30.0 μm and content of 30% can be obtained.

1) The law of particle size of 30.0 μm is as follows. When the diameter is less than or equal to 30.0 μm, the yield stress varies greatly and increases with the contentr of fine tailings. While it is relatively stable when the particle size is more than 30.0 μm. The particle size of 30.0 μm is considered to be the turning point and the yield stress changed from stability to instability.
2) The law of content of 30% is as follows. In the test, the content of 30% can be considered to be the inflection point. When the particle size is less than or equal to 30.0 μm and the contents is less than 30%, the tailings viscosity decreased gradually with the increase of the contents, while it began to increase with the increase of the contents when the contents is more than 30%. The viscosity of tailings reaches a minimum value when the contents is 30%.

Mechanism analysis on tailings rheological law

The resistance functions in the flowing process for tailings slurry is as follows.

$$F = d^2 \rho u^2 f\left(R_{ep}\right) \tag{3}$$

$$\xi = \frac{8}{\pi} f\left(R_{ep}\right) \tag{4}$$

Particles are supposed spheres. Reynolds number (R_{ep}) and projected area (A) can be obtained in Eq. 5.

$$R_{ep} = \frac{du\rho}{\mu},\ \ A = \frac{\pi}{4} d^2 \tag{5}$$

Where, F *is the* resistance,N; A *is* the projected area of the particle on a plane perpendicular to the direction of motion,m^2; u is the relative velocity of the particles,m/s; d *is* rpherical particle diameter,m; ρ is fluid density,kg/m^3; ξ is resistance coefficient; μ and R_{ep} are fluid viscosity and reynolds number, respectively.

Thus, the resistance of tailings slurry can be obtained in Eq. 6.

$$F = \frac{\xi A \rho u^2}{2} \tag{6}$$

In the backfilling process, it is required to ensure that the particles can flow uniformly. The viscous resistance between the particles is the main factor affecting the flow of tailings slurry, and the resistance is related to the Reynolds number R_{ep}.

For the tailings slurry,

$$\xi = \frac{24}{R_{ep}} \tag{7}$$

By substituting Eq. 7 into Eq. 6, we can get

$$F = 3\pi\mu d u \tag{8}$$

It can be seen that when the resistance remains constant, the viscosity μ of the tailings slurry is inversely proportional to the particle size d, that is, the larger the particle size d, the smaller the viscosity μ. A triangular body model is presented among the particles, as shown in Figure 14.

Assume that the radius of large particles and fine particles are R_1 and R_2, respectively. According to the geometric tangential relation, when the large particles are tangent, the small particles

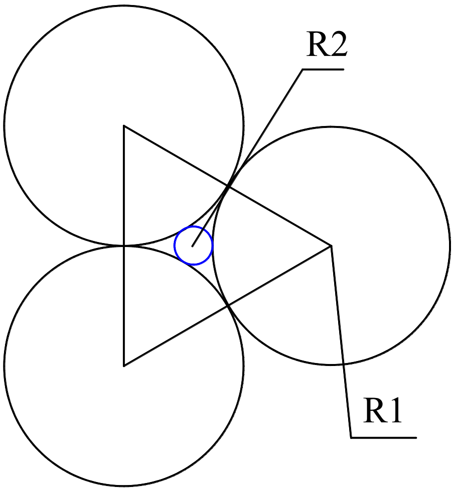

FIGURE 14
Particle arrangement.

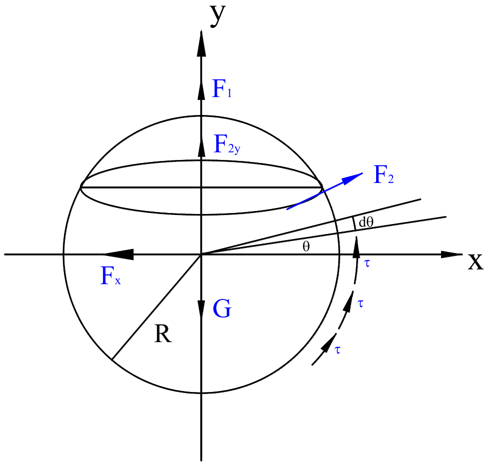

FIGURE 15
Stress analysis of tailings particles in the paste.

can be accommodated in the gap among the large particles. The relation between R_1 and R_2 is obtained in Eq. 7.

$$R_1 + 6.1R_2 \tag{9}$$

In the test, the median diameter is d_{50}=178.28 μm. The tangential particle size is 29.2 μm by using Eq. 10, where the viscosity μ of tailings is the minimum, and the particle size in the test is closest to 30.0 μm. Thus, 30.0 μm is the turning point of tailing performance, which is consistent with the above test results.

Equation 10 can be expressed using the multi-stage particle arrangement theory (Liu et al., 2017) as

$$\begin{cases} 0 < \xi_i < 1 \\ \rho' = \rho_{\max} \\ \sum_{i=1}^{n} \xi_i = 1 \end{cases} \tag{10}$$

Where ξ_i is the proportion of the ith grain grade; n is the grading number; ρ' is the packing density after particle gradation.

In the rheological test mentioned above, it can be regarded as the two-stage gradation between fine particle tailings and coarse particle tailings. The relations between porosities and percentages can be obtained in Eq. 11.

$$\begin{cases} \xi_1 = \dfrac{1-\theta_1}{1-\theta_1\theta_2} \\ \xi_2 = \dfrac{(1-\theta_2)\theta_1}{1-\theta_1\theta_2} \end{cases} \tag{11}$$

Where θ_m is the porosity of the system after grading, θ_1 and θ_2 are the porosities of the coarse and fine particles, respectively, and ξ_1 and ξ_2 are the corresponding percentages.

$$\theta_m = 1 - \frac{1-\theta_1}{[1+\theta_1(2.62k - 1.62k^2)\xi]} \tag{12}$$

Where $k = d_2/d_1$. Particle arrangement is usually between tight arrangement and free arrangement. Just assume that

$$\theta_1 = \theta_2 = \theta \tag{13}$$

According to the test, $\theta = 40\%$.Volume fraction can be estimated theoretically between coarse and fine particles porosities in Eq. 14.

$$\xi_2 = \frac{(1-\theta_2)\theta_1}{1-\theta_1\theta_2} = \frac{(1-\theta)\theta}{1-\theta^2} = \frac{\theta}{1+\theta} = \frac{0.4}{1+0.4} = 29\% \tag{14}$$

Thus, the porosity of the filling system with two-stage gradation of tailings is 29%. The calculation results agree with the experiment results in the second section.

Theoretical analysis on yield stress law

The yield stress is formed by the flocculation of fine particles in the flow process of tailings slurry. Meanwhile, the coarse particles of full tailings are sinking slowly due to the overall damping effect. When the tailings particles are regarded as spheres, the stress analysis of a sphere is shown in Figure 15. F_1 is the settlement resistance and the particle gravity is G. F_2 is the shear resistance and F_{2y} is the component of F_2 in the Y-axis direction, which is shear stress that caused by the yield stress acting on the particles.

In Figure 15, θ is the angle of sphere in the horizontal direction, dA is the differential area, which can be got in Eq. 15, F_{2y} can be obtained in Eq. 16.

$$dA = 2\pi r^2 \cos\theta \cdot d\theta \tag{15}$$

$$dF_{2y} = \tau \cos\theta dA = 2\pi r^2 \cos^2\theta \cdot \tau \cdot d\theta \tag{16}$$

The equations above are integrated in Eq. 17.

$$F_{2y} = 4\pi r^2 \tau \int_0^{\frac{\pi}{2}} \cos^2\theta \cdot d\theta = \frac{1}{4}\pi^2 d^2 \tau \tag{17}$$

$$\tau = \frac{4F_{2y}}{\pi^2 d^2} \tag{18}$$

When the shear resistance is constant, the yield stress τ is inversely proportional to particle size d according to Eq. 18. The law is consistent with the results in Figure 12. The yield stress of particle size of 10.21 μm is greater than that of other particle sizes. Furthermore, the larger the particle size is, the more stable the yield stress is.

Application of rheological laws for tailings slurry

The laws of "30.0 μm of particle size" and "30% of contents" were obtained according to the rheological test above. Rheological properties of the tailings slurry and the pipe resistance parameters were analyzed, which provide reasonable references for tailings disposal in the iron mine.

In the field of tailings disposal in the iron mine, the mine increased the content of fine tailings with a particle size less than 30.0μm, and tried to ensure that the content of fine tailings was about 30%. The results showed that the field problems were improved, such as the manufacturing difficulty of high concentration tailings slurry using the concentrated dewatering process and the harsh pipeline transportation conditions. Meanwhile, the frictional resistance generated in the tailings slurry transportation process was reduced and transportation efficiency was improved, which reduced tailings disposal cost in the field.

The particle size and content of tailings have an important effect on the yield stress and viscosity of tailings slurry. And some similar phenomena also appeared in the research results of Liu et al., (2017); Zhang et al., (2023). They thougt the stress attenuation of slurry with coarse particles is much smaller than that of slurry with finer particles. The tailings slurry agreed to different rheological models with different particle size and content. Liang et al. (2022) found similar law and pointed out that the high concentration full tailing filling slurry conforms to the characteristics of Bingham fluid in non-Newtonian fluids. The rheological characteristics and corresponding rheological theories are quantified in this study. And the "double 30" theory ("particle size of 30.0 μm" and "content of 30%") was proposed and expounded. "Particle size of 30.0 μm" and "content of 30%" is the critical point of rheological characteristics of tailings. The research results further improve the tailing transportation law, provide theoretical support for the paste filling technology of mine waste rock tailings, and are of great significance for the wide application of this technology.

A similar phenomenon is also observed for other slurries; such as cement slurries. Meanwhile, for the metal mines, the yield stress during slurry transmission can be reduced by controlling the particle size of tailings and increasing the content of fine-grained rock with particle size less than 30μm, thus reducing the transportation cost.

Conclusion

In this paper, the experiments on rheological properties of the mortar tailings were designed and carried outunder different particle sizes and content conditions. The "double 30" theory was proposed and expounded. The corresponding theoretical model is established to analyze the mechanism of the above results. The conclusion is as follows.

1) The particle size and the content of fine tailings have a significant effect on the yield stress and viscosity in the transportation process of the whole tailings slurry. When the particle size of tailings is no larger than 30.0 μm and the content is no larger than 30%, the rheological behavior of the tailings slurry conforms to the Herschel-Bulkley model. With the increase of the content of fine tailings, its behavior agrees better with the Bingham model. When the particle size is larger than 30 μm, the tailings slurry exhibits the Herschel-Bulkley model no matter how the content changes.
2) The yield stress and viscosity of tailings slurry in the process of transportation are in accordance with the laws of "double 30" theory. The theory is "particle size of 30.0 μm" and "content of 30%". That is, the particle size of 30.0 μm in the test can be regarded as a turning point of yield stress change. When the particle size of fine tailings is no larger than 30.0 μm, the yield stress changes greatly and increases with the increase of content. When the particle size is larger than 30.0 μm, the yield stress is relatively stable. The content of 30% of the tailings slurry is a turning point for the viscosity change. For tailings with the fine particle size less than or equal to 30.0 μm, the viscosity reaches the minimum with the content of 30%.
3) The mechanisms of particle size and viscosity law are analyzed from the perspective of particle arrangement and rheological mechanics of tailings. The rheological laws of tailings slurry have been successfully applied to the tailings backfilling disposal in an iron mine, and the problem of large resistance were coped with in the process of tailings transportation. The obtained laws of tailings rheology greatly improved the transportation efficiency and reduced disposal cost of tailings in the iron mine.

Data availability statement

The original contributions presented in the study are included in the article/supplementary material, further inquiries can be directed to the corresponding author.

Author contributions

Conceptualization, ZW, LC, and MH; methodology, ZW and LC; software, MH; validation, ZW and LC; formal analysis, ZW and LC; data curation, ZW and LC; writing—original draft preparation, ZW and MH; writing—review and editing, and MH; funding acquisition, ZW. All authors have read and agreed to the published version of the manuscript.

Acknowledgments

The authors sincerely thank the following agents for their financial supports: Scien-tific and Technological Project of Henan Province (222102320060), Strength Improvement Plan of the Advantageous Disciplines of Zhongyuan University of Technology (SD202232), Postograduate Education Reform and Quality Improvement Proiect of Zhongyuan University of Technology (JG202220).

Conflict of interest

The authors declare that the research was conducted in the absence of any commercial or financial relationships that could be construed as a potential conflict of interest.

Publisher's note

References

Aldhafeeri, Z., and Fall, M. (2017). Sulphate induced changes in the reactivity of cemented tailings backfill. *Int. J. Mineral Process.* 166, 13–23. doi:10.1016/j.minpro.2017.06.007

Bouvet, A., Ghorbel, E., and Bennacer, R. (2010). The mini-conical slump flow test: Analysis andnumerical study. *Cem. Concr. Res.* 40, 1517–1523. doi:10.1016/j.cemconres.2010.06.005

Cao, S., Song, W., and Yilmaz, E. (2018). Influence of structural factors on uniaxial compressive strength of cemented tailings backfill. *Constr. Build. Mat.* 174, 190–201. doi:10.1016/j.conbuildmat.2018.04.126

Cavusoglu, I., Yilmaz, E., and Yilmaz, A. O. (2021). Sodium silicate effect on setting properties, strength behavior and microstructure of cemented coal fly ash backfill. *Powder Technol.* 384, 17–28. doi:10.1016/j.powtec.2021.02.013

Chen, S., Du, Z., Zhang, Z., Zhang, H., Xia, Z., and Feng, F. (2020). Effects of chloride on the early me-chanical properties and microstructure of gangue-cemented paste backfill. *Constr. Build. Mat.* 235. doi:10.1016/j.conbuildmat.2019.117504117504

Cheng, H., Wu, S., Li, H., and Zhang, X. (2020). Influence of time and temperature on rheology and flow performance of cemented paste backfill. *Constr. Build. Mat.* 231, 117117. doi:10.1016/j.conbuildmat.2019.117117

Cheng, H. Y., Wu, S. C., Zhang, X. Q., and Wu, A. x. (2020). Effect of particle gradation characteristics on yield stress of cemented paste backfill. *Int. J. Min. Metall. Mat.* 27 (1), 10–17. doi:10.1007/s12613-019-1865-y

Deng, X., Klein, B., Tong, L., and de Wit, B. (2018). Experimental study on the rheological behavior of ultra-fine cemented backfill. *Constr. Build. Mat.* 158, 985–994. doi:10.1016/j.conbuildmat.2017.05.085

Falagán, C., Grail, B. M., and Johnson, D. B. (2016). New approaches for extracting and recovering metals from mine tailings. *Miner. Eng.* 106, 71–78. doi:10.1016/j.mineng.2016.10.008

Fang, K., and Fall, M. (2018). Effects of curing temperature on shear behaviour of cemented paste backfill-rock interface. *Int. J. Rock Mech. Min. Sci. (1997).* 112, 184–192. doi:10.1016/j.ijrmms.2018.10.024

Hale Micah, W., Freyne Seamus., F., and Russell Bruce, W. (2009). Examining the frostresistance of high performance concrete. *Constr. Build. Mater.* 23 (2), 878–888. doi:10.1016/j.conbuildmat.2008.04.006

Just, A., and Middendorf, B. (2009). Microstructure of high-strength foam concrete. *Mater. Charact.* 60 (7), 741–748. doi:10.1016/j.matchar.2008.12.011

Kasap, T., Yilmaz, E., and Sari, M. (2022). Effects of mineral additives and age on microstructure evolution and durability properties of sand-reinforced cementitious mine backfills. *Constr. Build. Mater.* 352, 129079. doi:10.1016/j.conbuildmat.2022.129079

Lei, G. L., Dong, W., Zheng, M., Guo, Z. Q., and Liu, Y. Z. (2017). Numerical investigation on heat transfer and melting process of ice with different porosities. *Int. J. Heat. Mass Transf.* 107, 934–944. doi:10.1016/j.ijheatmasstransfer.2016.11.004

Li, B., Zhang, J. X., Liu, Y. W., Qu, L., Liu, Q., Sun, Y., et al. (2022). Interfacial porosity model and modification mechanism of broken coal grouting: A theoretical and experimental study. *Surfaces Interfaces* 33(6). 10228doi:10.1016/j.surfin.2022.102286

Li, J., Cao, S., Yilmaz, E., and Liu, Y. (2022). Compressive fatigue behavior and failure evolution of additive fiber-reinforced cemented tailings composites. *Int. J. Min. Metall. Mat.* 29 (2), 345–355. doi:10.1007/s12613-021-2351-x

Li, J. J., Cao, S., and Yilmaz, E. (2022). Characterization of macro mechanical properties and microstructures of cement-based composites prepared from fly ash, gypsum and steel slag. *Minerals* 12, 6. doi:10.3390/min12010006

Li, J. J., Yilmaz, E., and Cao, S. (2020). Influence of solid content, cement/tailings ratio and curing time on rheology and strength of cemented tailings backfill. *Minerals* 10 (10), 922. doi:10.3390/min10100922

Liang, X. M., Wang, H. Y., Jiang, G. J., et al. (2022). Study on rheological properties of high concentration unclassified tailings filling slurry and resistance loss along pipeline transp. *China Mine Eng.* 51 (3), 47–53.

Liu, L., Fang, Z., Qi, C., Zhang, B., Guo, L., and Song, K. I. (2018). Experimental investigation on the relationship between pore characteristics and unconfined compressive strength of cemented paste backfill. *Constr. Build. Mat.* 179, 254–264. doi:10.1016/j.conbuildmat.2018.05.224

Liu, L., Fang, Z., Qi, C., Zhang, B., Guo, L., and Song, K. I. (2019). Numerical study on the pipe flow characteristics of the cemented paste backfill slurry considering hydration effects. *Powder Technol.* 343, 454–464. doi:10.1016/j.powtec.2018.11.070

Liu, L., Fang, Z. Y., Wang, M., Qi, C., Zhao, Y., and Huan, C. (2020). Experimental and numerical study on rheological properties of ice-containing cement paste backfill slurry. *Powder Technol.* 370, 206–214. doi:10.1016/j.powtec.2020.05.024

Liu, X. H., Wu, A. X., Wang, H. J., et al. (2017). Influence mechanism and calculation model of CPB rheological parameters. *Chin. J. Eng.* 39 (2), 190.

Long, H. C., Xia, J. X., and Cao, B. (2017). Effect of coarse/fine materials ratio on rheological Properties. *Min. Metallurgical Eng.* 37 (2), 6–10.

Mangane, M. B. C., Argane, R., Trauchessec, R., Lecomte, A., and Benzaazoua, M. (2018). Influence of superplasticizers on mechanical properties and workability of cemented paste backfill. *Min. Eng.* 116, 3–14. doi:10.1016/j.mineng.2017.11.006

Ouattara, D., Yahia, A., Mbonimpa, M., and Belem, T. (2017). Effects of superplasticizer on rheological properties of cemented paste backfills. *Int. J. Mineral Process.* 161, 28–40. doi:10.1016/j.minpro.2017.02.003

Qi, C., Chen, Q., Fourie, A., Tang, X., Zhang, Q., Dong, X., et al. (2019). Constitutive modelling of cemented paste backfill: A data-mining approach. *Constr. Build. Mat.* 197, 262–270. doi:10.1016/j.conbuildmat.2018.11.142

Qi, C., Chen, Q., Fourie, A., Zhao, J., and Zhang, Q. (2018). Pressure drop in pipe flow of cemented paste backfill: Experimental and modelingstudy. *Powder Technol.* 333, 9–18. doi:10.1016/j.powtec.2018.03.070

Rakotondrandisa, A., Danaila, I., and Danaila, L. (2019). Numerical modelling of a melting-solidification cycle of a phase-change material with complete or partial melting. *Int. J. Heat. Fluid Flow.* 76, 57–71. doi:10.1016/j.ijheatfluidflow.2018.11.004

Roshani, A., and Fall, M. (2020). Rheological properties of cemented paste backfill with nanosilica: Link to curing temperature. *Cem. Concr. Compos.* 114, 103785. doi:10.1016/j.cemconcomp.2020.103785

Ruan, Z. E., Wu, A. X., Bürger, R., Betancourt, F., Wang, Y., Wang, Y., et al. (2021). Effect of interparticle interactions on the yield stress of thickened flocculated copper mineral tailings slurry. *Powder Technol.* 392, 278–285. doi:10.1016/j.powtec.2021.07.008

Sari, M., Yilmaz, E., Kasap, T., and Guner, N. U. (2022). Strength and microstructure evolution in cemented mine backfill with low and high pH pyritic tailings: Effect of mineral admixtures. *Constr. Build. Mater.* 328, 127109. doi:10.1016/j.conbuildmat.2022.127109

Si, L., Wei, J., Xi, Y., Wang, H., Wen, Z., Li, B., et al. (2021). The influence of long-time water intrusion on the mineral and pore structure of coal. *Fuel* 290 (1). doi:10.1016/j.fuel.2020.119848119848

Si, L., Zhang, H., Wei, J., Li, B., and Han, H. (2021). Modeling and experiment for effective diffusion coefficient of gas in water-saturated coal. *Fuel* 284 (1). doi:10.1016/j.fuel.2020.118887118887

Small, C. C., Cho, S., Hashisho, Z., and Ulrich, A. C. (2015). Emissions from oil sands tailings ponds: Review of tailings pond parameters and emission estimates. *J. Petroleum Sci. Eng.* 127, 490–501. doi:10.1016/j.petrol.2014.11.020

Wu, A. X., Li, H., and Cheng, H. Y. (2021). Status and prospects of research on the rheology of paste backfill using unclassified tailings (Part 2): Rheological measurement and prospects. *Chin. J. Eng.* 43 (4), 451–459.

Wu, A. X., Li, H., and Cheng, H. Y. (2020). Status and prospects of researches on rheology of paste backfill using unclassified tailings (Part 1): Concepts, characteristics and models. *Chin. J. Eng.* 42 (7), 803–813.

Wu, D. I., and Cai, S. J. (2015). Coupled effect of cement hydration and temperature on hydraulic behavior of cemented tailings backfill. *J. Cent. South Univ.* 22 (5), 1956–1964. doi:10.1007/s11771-015-2715-3

Xu, W. B., Yang, B. G., Yang, S. L., et al. (2016). Experimental study on correlativity between rheological parameters and grain grading of coal gauge backfill slurry. *J. Central South Univ. Sci. Technol.* 47 (4), 1282–1289.

Yan, Z., Yin, S., Chen, X., and Wang, L. (2022). Rheological properties and wall-slip behavior of cemented tailing-waste rock backfill (CTWB) paste. *Constr. Build. Mater.* 324. doi:10.1016/j.conbuildmat.2022.126723126723

Yin, X. Q., Zhao, S. M., Xie, J., et al. (2010). Theoretical analysis on the setting angle of mixing blades of twin-shaft mixer. *J. wuhan Univ. Technol.* 32 (19), 141–144.

Zhang, J. X., Li, B., Liu, Y. W., Fu, J., Chen, L., et al. (2022). Dynamic multifield coupling model of gas drainage and a new remedy method for borehole leakage. *Acta Geotech.* 17 (10), 4699–4715. doi:10.1007/s11440-021-01444-x

Zhang, L. F., Wang, H. J., Wu, A. X., et al. (2023). Study of the effect of particle size on the thixotropy of tailings paste. *Chin. J. Eng.* 45 (1), 1–8.

Zhang, Q. L., Liu, Q., Zhao, J. W., et al. (2015). Pipeline transportation characteristics of filling paste-like slurry pipeline in deep mine. *Chin. J. Nonferrous Mater.* 25, 3190–3195.

Zhang, X. X., and Qiao, D. P. (2015). Rheological properties of high-density slurry with waste rock-tailings and transmission parameter optimization. *J. Kunming Univ. Sci. Technol. Nat. Sci. Ed.* 40 (3), 39–45.

Zheng, D., Song, W., Cao, S., and Li, J. (2022). Dynamical mechanical properties and microstructure characteristics of cemented tailings backfill considering coupled strain rates and confining pressures effects. *Constr. Build. Mater.* 320. doi:10.1016/j.conbuildmat.2022.126321126321

Frontiers in
Earth Science

Investigates the processes operating within the major spheres of our planet

Advances our understanding across the earth sciences, providing a theoretical background for better use of our planet's resources and equipping us to face major environmental challenges.

Discover the latest Research Topics

See more →

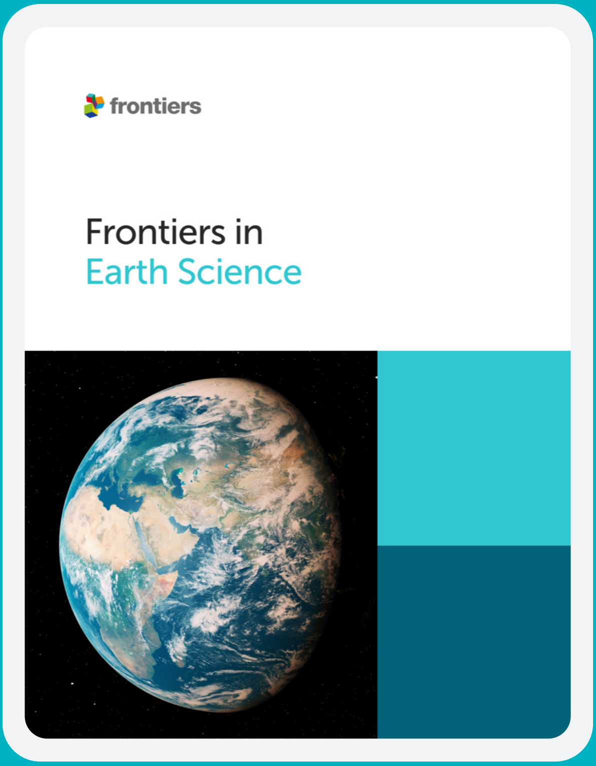

frontiers

Frontiers in
Earth Science

Frontiers

Avenue du Tribunal-Fédéral 34
1005 Lausanne, Switzerland
frontiersin.org

Contact us

+41 (0)21 510 17 00
frontiersin.org/about/contact